Evaluation and Application of FTIR spectroscopy for field study of biomass burning emissions

Smith, Thomas

Awarding institution:
King's College London

Evaluation and application of FTIR spectroscopy for field study of biomass burning emissions

By

Thomas Edward Lawrence Smith

SEPTEMBER 2012

A thesis submitted to King's College London
for the degree of Doctor of Philosophy

DEPARTMENT OF GEOGRAPHY
KING'S COLLEGE LONDON

Abstract

An average of 3.5-4.5 million square km of vegetation burns in global wildfires each year. The gases and particulates released have substantial chemical and radiative impacts, the magnitude of which depends on the specific makeup and magnitude of the emissions. This research focuses on the development, evaluation and application of field-deployed methods based around Fourier transform infrared (FTIR) spectroscopy for the assessment of the emissions from biomass burning events.

In particular, full assessment of the atmospheric effects of biomass burning generally requires spatio-temporally resolved data on the makeup and magnitude of the smoke emissions. This is usually obtained via multiplication of the amount of fuel consumed [M] by an emission factor [EF_x], representing the amount of chemical species [x] released per kilogram of dry fuel burned. Emissions factors for many species typically show wide ecosystem variations, and also vary with meteorology and fire type, increasing the uncertainty in this important variable.

When compared to established point-sampling methods, OP-FTIR spectroscopy can measure many different gases simultaneously, *in situ* and near-continuously, and can provide path-integrated amounts. Few studies, however, have investigated the accuracy of the retrievals of the main biomass burning gases (CO_2, CO and CH_4), particularly across the broad range of concentrations found in ambient air to biomass burning plumes. Laboratory gas cell experiments were first used to evaluate the accuracy of the FTIR spectrometer and spectral analysis methodology deployed to retrieving concentrations of these gases at open biomass burning sites. The findings suggest that with optimisation of the retrieval parameters, column amounts accurate to within 5% can be confidently derived.

During 2009-2011, the FTIR equipment was deployed to a number of experimental fires for the purpose of improving our understanding of emission factors. Three case studies are presented in this thesis:

1. Determining the seasonality of biomass burning emissions in Australian savanna lands - Seasonal (early- and late-dry season) emission factors were measured and

compared, revealing no evidence of seasonality of emissions, in contrast to some previous works. Instead, Modified Combustion Efficiency explains most of the variation (e.g. 95% for CH_4) in emission factors

2. Building an emissions inventory for UK fuel types - Emission factors for heather (*Calluna vulgaris*) were measured here for the first time, enabling the first measurement-based estimates of total UK biomass burning emissions for the main carbonaceous gases and selected volatile organic compounds. Typical flaming combustion emission factors for CO_2, CO, CH_4 and NH_3 are around 1711, 66.2, 2.8 and 0.53 g kg^{-1} dry fuel combusted, respectively.

3. Determining emission ratios using solar occultation FTIR spectroscopy of lofted plumes from large wildfires in the Northern Territory, Australia, and comparison of total column trace gas amounts with simultaneous and collocated measurements of Aerosol Optical Depth (AOD). The emission ratio of NH3 to CO determined from solar measurements is shown to agree with that measured on the ground using OP-FTIR. A relationship is established between total column amounts of CO and AOD, confirming that satellite-derived measures of AOD could be used as a proxy for trace gas amounts.

Further work includes an exploration of the use of field-deployed FTIR in the study of aerosols in biomass burning plumes.

Inset photo: *OP-FTIR measurements of a heathland fire smoke plume at Debdon Moor, Northumberland, UK, on 23 March 2010 (photo taken by Helen Davies)*

Acknowledgements

This thesis draws on research undertaken at a whole host of different fieldwork campaigns and laboratory studies. As such, there are a large number of people and organisations that I would like to thank individually for their direct assistance that made this work possible.

First and foremost, I would like to acknowledge the helpful comments, support and guidance provided by my two supervisors Professor Martin Wooster and Professor Sue Grimmond. Martin's support has been invaluable throughout the full course of the PhD, from first teaching me how to make OP-FTIR measurements in his back garden, through to proof reading of the final drafts of this thesis. I also acknowledge the technical support provided by Alastair Reynolds, Paul Smith, Bill Luckhurst and Trevor Blackall at King's College London. I would like to thank colleagues Maria Tattaris, Ronan Paugam, Patrick Freeborn, Josh Johnston, Helen Davies, Duick Young and Arnout van Soesbergen for their physical and intellectual support during fieldwork and down the pub at the end of a day in the office.

The work presented in this thesis relies upon analysis and retrieval software, the developers of which have each been quick to respond to queries and have provided useful insights into interpretation of my results. I would like to thank David Griffith (University of Wollongong), developer of MALT; Mike Burton (Istituto Nazionale di Geofisica e Vulcanologia), developer of FTIR_FIT; Daniel Hurtmans and Pierre-François Coheur (Université Libre de Bruxelles), developers of Atmosphit; and John Lien, developer of Essential FTIR. I would like to thank and acknowledge support from Clare Murphy (University of Wollongong) who helped with MALT retrievals and assisted my understanding of the principles and fundamentals of infrared spectroscopy. Thanks also go to Daniel Peters and Don Grainger at the University of Oxford for their advice on retrieving aerosol information from the OP-FTIR measurements.

For the accuracy assessment work carried out at the Rutherford Appleton Laboratory, I would like to thank the team at the NERC's Molecular Spectroscopy Facility, particularly Robert McPheat and Kevin Smith, for their invaluable contribution to the experimental component of this work. I am also very grateful for the expertise provided by Peter Zemek and Don Mullally (MIDAC Corporation), Clive Oppenheimer (University of Cambridge) at various points during the accuracy assessment study.

For much of the fieldwork and lab work that contributed to this thesis, it was necessary to loan an FTIR spectrometer from NERC's Field Spectroscopy Facility. I would like to thank Christopher MacLellan and Alasdair MacArthur for their support with this loan and for their wide ranging advice relating to many aspects of this work.

During the two campaigns to Arnhem Land in Australia, whole teams of people made the field trips possible. I would like to thank all those from Charles Darwin University, Bushfires NT, CSIRO, and the people of Kulnguki, who welcomed and provided for us during these campaigns. Particular acknowledgements go to Stefan Maier (Charles Darwin University), Jeremy Russell-Smith (Bushfires NT), and Mick Meyer, Garry Cook and Dick Williams of CSIRO, without whom our involvement in the Northern Territory would not have happened. During my third and extended campaign to the Darwin region, I would like to thank a number of individuals from Bushfires NT and NRETAS who assisted me with fieldwork measurements: Cameron Yates, Jay Evans, Dominique Lynch, Andrew Edwards, and Bryan Baker.

My involvement with fires in the UK was largely brought about thanks to an invitation from John Dold (Fire Research Centre) to attend the experimental fires in Northumberland. His continued support at each of the UK campaigns was invaluable. These campaigns were made possible thanks to the support of Northumberland, Manchester, and Dorset Fire and Rescue Services. In particular, I would like to thank Steve Gibson and Paul Hedley in Northumberland, Steve Yearsley in Manchester and Andy Elliott in Dorset. At the University of Liverpool, I would like to thank Katherine Allen, Rob Marrs and Mike Harris for the kind provision of their fuel load and combustion completeness data from Northumberland and the Peak District. Support also came from Matt Davies at the University of Glasgow, who also provided fuel load and combustion completeness data. I also acknowledge assistance provided by Neil Cape and Ulrike Dragosits at the Centre for Ecology and Hydrology, who assisted with the total emissions calculations.

I would like to acknowledge the financial support of the Natural Environment Research Council and the Economic and Social Research Council (studentship ES/F012551/1).

I thank my friends and family for their unconditional support and dependability. I thank Melissa for her love, support and patience over the past couple of years, and also for her help with making measurements of gas samples! Finally, I would like to thank Steve, who inspired my interest in the outdoors and my enthusiasm for geography; and my Mum, Susan, to whom this thesis is dedicated.

Table of Contents

List of Figures

CHAPTER 4: Evaluating the Accuracy, Precision and Sensitivity of OP-FTIR Trace Gas Concentration Retrievals

CHAPTER 5: Northern Territory: Seasonality of Burning Emissions and Emissions inventory

CHAPTER 6: United Kingdom: an Emissions Inventory for Heathland Burning

CHAPTER 7: Solar Occultation FTIR for Biomass Burning Emissions Measurements

CHAPTER 8: Summary, Conclusions and Future Prospects

List of Tables

List of Abbreviations

A-FTIR	Airborne Fourier Transform Infrared
ACE-FTS	Atmospheric Chemistry Experiment – Fourier Transform Spectrometer
AIRS	Atmospheric Infrared Sounder
AOD	Aerosol Optical Depth
ARSF	Airborne Reconnaisance and Surveying Facility
ASTER	Advanced Spaceborne Thermal Emission and Reflection Radiometer
AVHRR	Advanced Very High Resolution Radiometer
BRDF	Bi-directional reflectance
CCN	Cloud Condensation Nuclei
C.E.	Common Era
CF	Combustion Factor
CFC	Chlorofluorocarbon
CTM	Chemical Transport Model
DECAF	Deforestation Carbon Fluxes
DOAS	Differential Optical Absorption Spectroscopy
EF	Emission Factor
ENSO	El Niño-Southern Oscillation
ER	Emission Ratio
FOV	Field of View
FRE	Fire Radiative Energy
FRP	Fire Radiative Power
FSF	Field Spectroscopy Facility
FTIR	Fourier Transform Infrared
GC	Gas Chromatography
GFED	Global Fires Emissions Database
GOES	Geostationary Operational Environmental Satellite
GOSAT	Greenhouse gases Observing SATellite
HITRAN	High Resolution Transmission
IASI	Infrared Atmospheric Sounding Interferometer
ILS	Instrument Line Shape
IPCC	Intergovernmental Panel on Climate Change
IR	Infrared
MALT	Multi-Atmospheric Layer Transmission
MAPS	Measurement of Air Pollution from Satellites
MCE	Modified Combustion Efficiency
MM	Molecular Mass
MODIS	Moderate Resolution Imaging Spectroradiometer
MODTRAN	Moderate Resolution Atmospheric Transmission
MOPITT	Measurements of Pollution In The Troposphere
MSF	Molecular Spectroscopy Facility
NASA	National Aeronautics and Space Administration
NERC	Natural Environment Research Council
NDIR	Non-Dispersive Infrared
NLLS	Non-Linear Least Squares

NMOC	Non-Methane Hydrocarbon
OCO	Orbiting Carbon Observatory
OD	Optical Depth
OP-FTIR	Open-Path Fourier Transform Infrared
OVOC	Oxygenated Volatile Organic Compound
Pg	Petagram (1×10^{15} g)
ppb	parts per billion by volume
ppm	parts per million by volume
RAL	Rutherford Appleton Laboratory
RSC	Residual Smouldering Combustion
SO-FTIR	Solar Occultation Fourier Transform Infrared
Tg	Teragram (1×10^{12} g)
WALFA	West Arnhem Land Fire Abatement Programme

List of Chemical Symbols

C_2H_2	Acetylene
C_2H_4	Ethylene
C_2H_6	Ethane
CH_2O	Formaldehyde
CH_3Br	Methyl bromide
CH_3Cl	Methyl chloride
CH_3COOH	Acetic acid
CH_3OH	Methanol
CH_4	Methane
CO	Carbon monoxide
CO_2	Carbon dioxide
HCN	Hydrogen cyanide
HCOOH	Formic acid
InSb	Indium antimonide
KBr	Potassium bromide
MCT	Mercury Cadmium Telluride
N_2O	Nitrous oxide
NH_3	Ammonia
NO	Nitrogen oxide
NO_2	Nitrogen dioxide
NO_x	Nitrogen oxides
PAN	Polyacrylonitrile

Introduction and General Aims of the Thesis

Fire is an integral component of the Earth system. Scientists have long known that biomass burning influences the evolution of global ecosystems, the distribution and structure of vegetation, the carbon cycle, and climate (Bowman *et al.*, 2009; Crutzen *et al.*, 1979). Knowledge of the annual emissions from biomass burning is critical if we are to understand the importance of fire as a driver of anthropogenic climate change and the relative influence of pyrogenic emissions on both local and global atmospheric chemistry. In pursuit of such knowledge, two challenges exist, first, to estimate the total mass of biomass that burns each year, and second, to make accurate measurements of the relative amounts of each trace gas emitted when biomass burns in different ecosystems and environments. The aim of this thesis is to address the second of these challenges. A relatively new approach to atmospheric gas measurement, that of open-path Fourier transform infrared spectroscopy (OP-FTIR) will be presented, assessed and developed. Gas emissions data collected at over fifty fires in Australia, Canada and the UK will be analysed, and used to reveal new insights into both the measurement and understanding of biomass burning emissions.

This thesis will detail the findings of a laboratory-based accuracy assessment undertaken in June 2009, where the accuracy of OP-FTIR spectroscopy was investigated for retrievals of trace gas concentrations in quantities representative of clean air to highly polluted plumes. In addition to the accuracy assessment, six field campaigns took place during 2009, 2010 and 2011, where OP-FTIR was used to measure in-plume concentrations at fires in Alberta, Canada; Northern Territory, Australia; and in Dorset and Northumberland, UK. Data collected at fires of different intensities, burning under different fuel and meteorological conditions, and in different vegetation types, are used to address the issue of the perceived considerable variability

associated with fire emissions, particularly with respect to the emission factors (the amount of plume gases released per unit of biomass burnt).

Following the introductory Chapter, which provides an overview of biomass burning and the motivation for fire emission studies, the thesis will review the current state of biomass burning emissions measurement efforts in Chapter 2. Chapter 3 presents a concise technical introduction to OP-FTIR spectroscopy, before a substantial investigation into the precision and accuracy of the methodology for retrieving fire plume trace gas concentrations is described in Chapter 4. Chapter 5 presents the results from three field campaigns to Australia, where seasonal tropical savanna emissions were investigated. Chapter 6 presents results from a further three field campaigns to Dorset and Northumberland in the UK where emissions from a unique and unstudied ecosystem are considered. Finally, Chapter 7 focuses on solar occultation measurements of total column atmospheric gas amounts, with an accuracy assessment, similar to that undertaken in Chapter 4, and results from field measurements undertaken in Canada and Australia. The concluding Chapter outlines the main findings of the thesis and contains some thoughts about the future use of OP-FTIR for biomass burning emissions measurements.

1

Introduction to Biomass Burning: Dynamics and Climate

The oldest evidence for biomass burning on Earth comes from the fossilised charcoaled remains of small, primitive plant species found at the Ludford Lane outcrop near the Welsh borders of the United Kingdom (Glasspool *et al.*, 2004). These fossils, dating to the Silurian period, 417 to 443 million years ago, are evidence that wildfires existed in times of lower atmospheric oxygen (18% compared with 21% today) and restricted fuel supply. In the era that followed these earliest of fires, long-term changes in atmospheric oxygen concentrations appear to be the significant control on fire occurrence (Scott and Glasspool, 2006). The earliest evidence for hominid exploitation of fire suggests that our ancestors were using fire for cooking as early as 1.5 to 1.9 million years ago (Brain and Sillen, 1988; Wrangham *et al.*, 1999), with evidence of routine use beginning around 50,000-100,000 years ago (Arjamaa and Vuorisalo, 2010). However, only during the most recent 50,000 years have humans used fire for the continental-scale destruction of forests for the purposes of foraging, cultivation and colonisation (Clark *et al.*, 1989; Clark and Royall, 1996; Tinner *et al.*, 1999), beginning with Asia and Australasia, shortly followed by Europe, and eventually the Americas (Figure 1.1). The Holocene (the most recent 10,000 years) is characterised by a gradual increase in carbon dioxide (CO_2) concentration, from around 260 ppm 8,000 years ago to around 280 ppm before the industrial revolution, as recorded in Antarctic ice-core bubbles (Indermühle *et al.*, 1999). In a reconstruction of prehistoric biomass burning events using charcoal

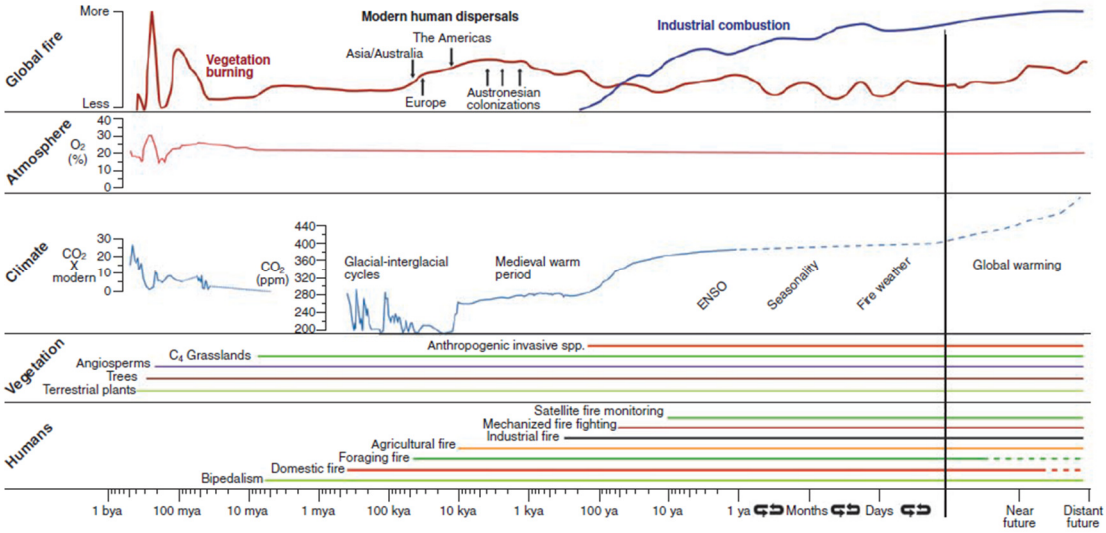

Figure 1.1 After Bowman *et al.* (2009, p. 482). "Qualitative schematic of global fire activity through time, based on pre-Quaternary distribution of charcoal, Quaternary and Holocene charcoal records, and modern satellite observations, in relation to the percentage of atmospheric O_2 content, parts per million (ppm) of CO_2, appearance of certain vegetation types, and the presence of the genus *Homo*. Dotted lines indicate periods of uncertainty."

accumulation rates, Carcaillet *et al.* (2002) suggest that human-induced fires might explain the anomalous increasing CO_2 concentrations recorded in Antarctica over the past 7,000 years (prior to the industrial revolution), providing evidence for the first significant anthropogenic influence on our planet's atmospheric composition (Ruddiman, 2003).

Today, as greenhouse gas concentrations rapidly approach double those of pre-industrial times, there remain many questions as to the significance of the role in which biomass burning plays in different environments: Do fire affected regions act as carbon sources or sinks? Are humans or climate more important in determining fire patterns (Bowman *et al.*, 2009)? Can greenhouse gas abatement be improved by practicing different land management in fire affected regions (Williams *et al.*, 2005)? These questions can be addressed, for example, by combining an understanding of biomass burning trace gas emissions, novel methods for estimating fire fuel consumption from remote sensing, regional scale plume dispersion modelling, and analysis of spatio-temporal data on human activity and land-use change. This PhD project aims to contribute to providing the tools by which these questions may be addressed, in particular those related to the quantification of the emission ratios and factors of various greenhouse gases and

reactive gases released by various types of biomass burning. This Chapter will introduce the human and climatic drivers of biomass burning and fundamental fire processes (Section 1.2) and to the influence of biomass burning on contemporary climate (Section 1.3).

1.1 Fire dynamics

1.1.1 Human and climate drivers of biomass burning

Whilst it is estimated that perhaps as little as 10% of global biomass burning is ignited by natural causes (Crutzen and Andreae, 1990), the factors contributing to the ignitability and combustability of biomass at a regional scale are primarily controlled by climatic factors acting over a range of temporal scales (Bowman *et al.*, 2009). The amplitude of wet/dry cycles is the primary control on wildfire activity (Heyerdahl *et al.*, 2002) as wet periods promote biomass growth before fire occurences in the dryer periods. Periods of warming and/or drought also increase wildfire activity (Westerling *et al.*, 2006). At annual and decadal scales, the most important climatic driver of these regional wet/dry cycles is the El Niño-Southern Oscillation (ENSO) (Swetnam and Betancourt, 1992). The El Niño phase of ENSO generally brings increased fire activity to the tropical regions of Africa, Southeast Asia, Australasia and the Americas, as well as increased activity in the boreal regions of North America and Siberia (van der Werf, 2004). During the La Niña phase of ENSO, increased fire activity can usually be found in the subtropical regions of the United States (Sherriff *et al.*, 2001) and Argentina (Veblen *et al.*, 1999).

Palaeoecological studies have shown that these regional fire regimes are not constant through time and vary at longer centennial (Swetnam, 1993; Clark, 1990) and millennial (Long *et al.*, 1998) timescales. Clark (1990) used charcoal stratigraphy and fire scars on red pine trees to identify periodicities of ~9 years up to ~44 years demonstrating a strong reliance of fire return intervals on climate, with fire occurring most frequently during the warm/dry 15th and 16th centuries (~9 year intervals), and fire occurring far less frequently during the cooler/moist Little Ice Age (with return intervals of ~25 and

~44 years). Long *et al.* (1998) used charcoal deposited in lake sediment cores to demonstrate this sensitivity to climate for longer timescales. Fire intervals during 6,850 to 9,000 years ago, when the climate was warmer than today, were around 110 years, increasing to around 230 years for the more recent cooler and moist climate.

As discussed earlier, humans are responsible for the majority of biomass fire ignitions. However, anthropogenic influences on regional fire regimes beyond the climatic oscillatory controls are primarily related to widespread destruction of fire-resistant forests and their replacement by relatively flammable pasturelands (Mouillot and Field, 2005). Historically, these changes have occurred on continental scales, with the human colonisation of Australia purported to have been responsible for the collapse of drought-adapted tree and shrubs species and nutritious grasslands, leading to a megafaunal extinction of animal species that could not adapt to the new fire-adapted desert scrub environment (Miller *et al.*, 2005). Anthropogenic land-use change continues to drive new fire regimes to this day, with deforestation of rainforests in Brazil, South-East Asia and the central plateau of Africa leading to and resulting from increased fire activity (Houghton, 1994; Nepstad *et al.*, 1999).

Globally, anthropogenic emissions of greenhouse gases from all sources may now be acting as another anthropogenic driver of biomass burning. Recent evidence suggests that climate change associated with greenhouse warming may now be resulting in net increases in fire activity due to more severe "fire weather". Higher temperatures and longer drying seasons are suggested to be causing longer, and more intense fire seasons in some regions (Running, 2006; Westerling *et al.*, 2006), as well as reducing life expectancy of trees due to drought stress (van Mantgem *et al.*, 2009).

1.1.2 Biomass combustion processes

Biomass burning is the combustion of organic material. For combustion to occur, heat, oxygen and fuel are required (the fire triangle); this occurs in wooded areas, savanna or grasslands when an ignition source comes into contact with combustible vegetation under conditions where oxygen is freely available from the ambient air. Ignition is usually caused by some source of external heat or energy (Stott, 2000) and can lead to a chain of reactions that ultimately leads to the chemical breakdown of organic material

(cellulose in the equation below) to simple molecules such as carbon dioxide (CO_2) and water (H_2O) (Trollope, 1984):

$$(C_6H_{10}O_5)_n + O_2 + \text{Kindling temperature} \rightarrow CO_2 + H_2O + \text{Heat} \quad (1.1)$$

Ignition is usually caused by some source of external heat or energy. Lightning strikes are by far the most common natural ignition source (Stott, 2000), whilst other factors, such as volcanic action (proximity to lava flows, or at a distance, from windborne hot ash) and friction (from landslides or wind action) may occasionally occur locally, but are very much less significant globally (Stott, 2000). Spontaneous combustion is also a possibility (e.g. heating of materials by solar radiation that are well insulated from heat loss), but is rare and species specific (Stott, 2000). Anthropogenic ignition sources are estimated to be responsible for around 90% of biomass burning ignitions (Crutzen and Andeae, 1990), though this estimate is very uncertain and certainly varies greatly between ecosystem types. Anthropogenic ignition sources are either intentional (e.g. burning vegetation for path clearance, hunting, grazing, agriculture, war, arson etc.), inadvertent (when intentional fires spread to areas not intended for burning, or jump breaks in vegetation intended to halt the advance of a fire), or accidental (e.g. from cigarettes, warfare) (Stott, 2000). Whilst ignition sources may provide the initial heat source, all elements of the fire triangle (combustible vegetation for fuel, and oxygen) must co-exist at the same time and in the same place of ignition for a fire to persist.

The biomass combustion process may be split into a series of stages (conceptualised in Fig. 1.2). If we consider a single vegetation stand downwind of a flaming fire front, the combustion process begins with the radiative heating of the vegetation by the fire (in addition to the normal solar heating effect). At this *pre-heating stage* the fuel is dried and pyrolysis begins as temperatures rise above ~400 K. The long complex cellulose molecules are 'cracked' to produce combustible tars (gases) and char (solid). Tars mix with the air and this mixture begins to combust at the flash point temperature (this temperature depends on the tar composition, but will be higher than 850 K) and sustains *flaming combustion* at the fire point temperature (around 50 K higher than the flash point temperature). At this stage the tars react with air to produce simple molecules including CO_2, water vapour (H_2O), methane (CH_4), oxides of nitrogen (NO, N_2O), molecular hydrogen (H_2), short hydrocarbon molecules (e.g. C_2H_2, C_2H_4) and soot

(molecular carbon, C). As increasing amounts of char is produced, relative to tar, large amounts of CO_2 and H_2O are released, stifling the flames. For some fuels this leads to *glowing combustion*, where the remaining char is burned as a solid with oxidation taking place on the surface of the fuel (rather than in the air), forming CO, which is oxidised into CO_2. When the production of flammable tars ceases, pyrolysis slows down due to decreasing temperatures, the remaining vegetation now begins *smouldering combustion*. Smouldering typically occurs at temperatures below 850 K, and is characterised by low "*combustion efficiency*" due to the temperature not being sufficient to fully oxidise the fuel carbon to CO_2 (Stott, 2000). Combustion efficiency is a measure of the amount of fuel carbon released as CO_2, and may be approximated using the *Modified Combustion Efficiency* (MCE) formula, which requires only a measurement of CO and CO_2 rather than all the carbon containing gases (Yokelson *et al.*, 2008):

$$MCE = \frac{\Delta CO_2}{\Delta CO_2 + \Delta CO} \quad (1.2)$$

Where ΔCO_2 and ΔCO represent the elevated mixing ratios of these gases (the difference between mixing ratios measured in biomass burn emissions and those in the ambient air). MCE is often expressed as a percentage. Generally, an MCE lower than 0.9 (90%) is considered a low combustion efficiency burn (Lobert *et al.*, 1991; Yokelson *et al.*, 1996).

Eventually, convective and radiative cooling will cause the biomass to stop smouldering and the fire to become extinct. Other factors, such as a sudden change in fuel moisture content or lack of fuel, will stop a fire from sustaining itself (Stott, 2000).

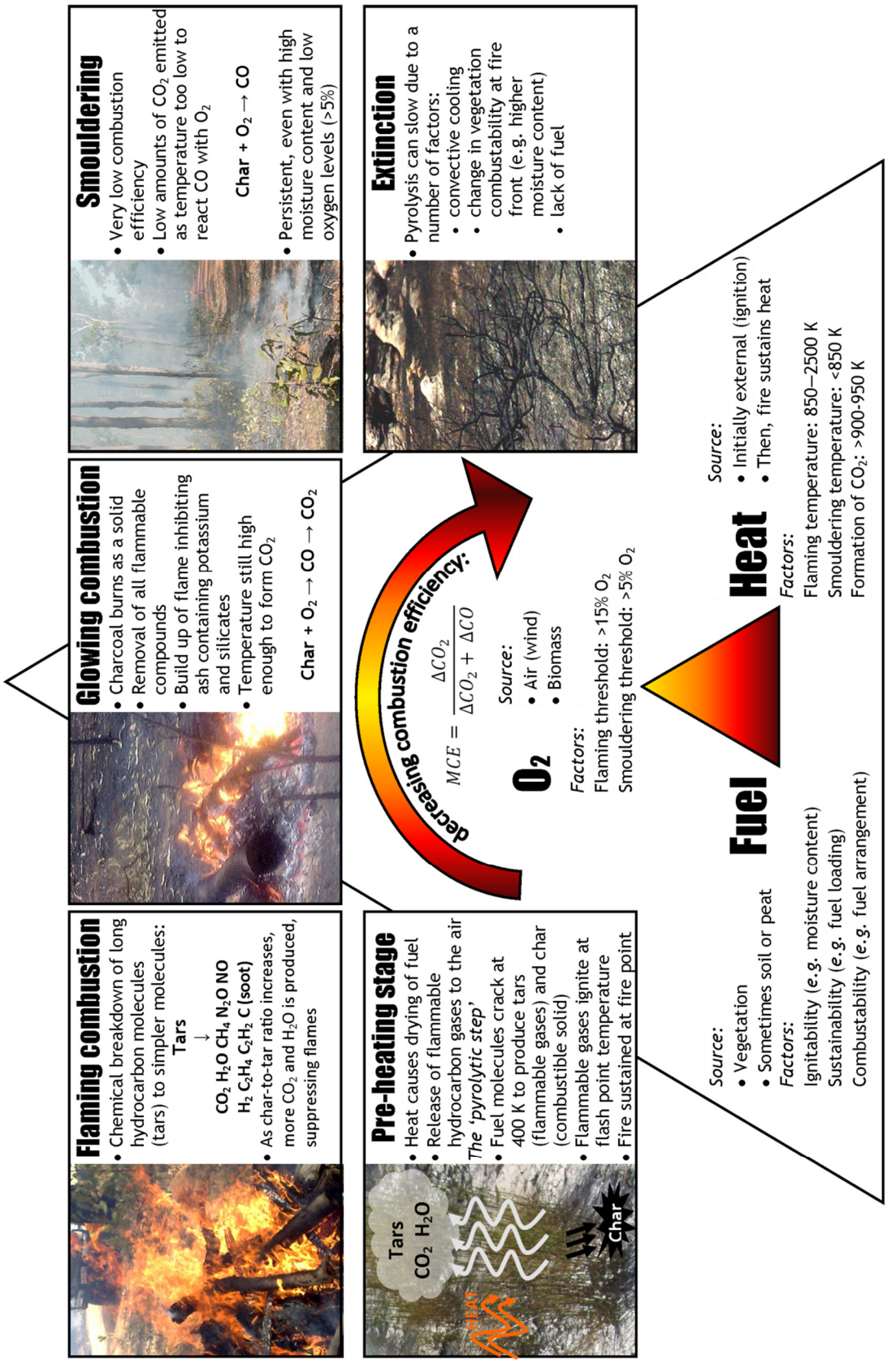

Figure 1.2 Schematic – The fire triangle and stages of combustion.

1.2 Fire and climate

Biomass burning is one of the most ancient forms anthropogenic atmospheric pollution (Ruddiman, 2003). Since the beginnings of the industrial revolution in the 18th century, biomass burning has remained a significant component of anthropogenic emissions to the atmosphere. Today, it is estimated that an average of 3.5-4.5 million km^2 of Earth's land surface biomass is burned each year (Figure 1.3) (Tansey *et al.*, 2004, Tansey *et al.*, 2007, Giglio *et al.*, 2006), with mean estimates of CO_2 emissions from biomass burning equal to around 50% of those from the combustion of fossil-fuels (Bowman *et al.* 2009). Biomass burning is postulated as being one of the main drivers of interannual variability in CO_2, CH_4 and CO (Langenfelds *et al.*, 2002), with burning in high fire activity years (e.g. 1994/1995 and 1997/1998) releasing enough of these gases to account for the anomalous pulses in CO_2 concentration observed globally (Schimel and Baker, 2002). In 1997/1998, the wildfires occurring in Indonesia (Figure 1.4) alone were estimated to have released between 0.8-2.6 petagrams of carbon (Pg C), or 13-40% of the annual global emissions from fossil fuels for the same period (Page *et al.*, 2002). Biomass burning, therefore, represents one of the most important carbon fluxes of the carbon cycle (Seiler and Crutzen, 1980), forming an integral component of tropical forest, savanna, grassland, chaparral, boreal forest and tundra ecosystems (Dwyer *et al.*, 2000).

The gases and particulates released in biomass burning plumes, along with the secondary effects of land cover change have substantial short- and long-term climatic impacts (Forster *et al.*, 2007) through changes to the composition of the atmosphere and/or through changes in the reflective properties of the affected surfaces (Bowman *et al.*, 2009). These impacts combine to affect climate through their influence on Earth's radiation budget, known as radiative forcing (Forster *et al.*, 2007). Radiative forcing, as defined by the Intergovernmental Panel on Climate Change (IPCC), may be defined as the change in net irradiance (in W m^{-2}) at the tropopause relative to preindustrial conditions at 1750 C.E. (Forster *et al.*, 2007). This section will give a brief insight into the role biomass burning plays in affecting contemporary climate through gaseous emissions (Section 1.3.1), particulate (aerosol) emissions (Section 1.3.2) and other effects caused by land cover change associated with fires (Section 1.3.3).

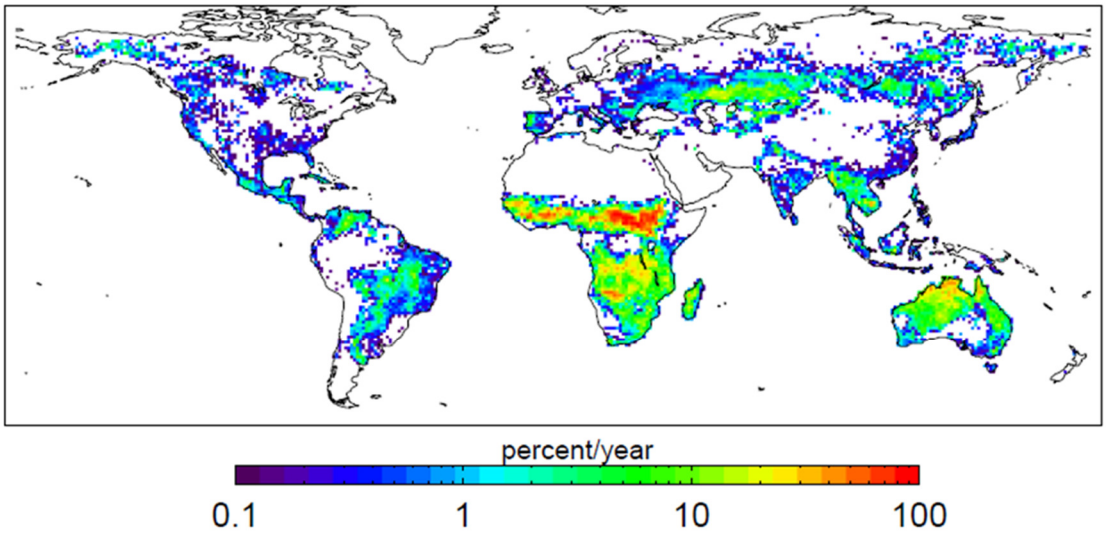

Figure 1.3 After Giglio *et al.* (2006, p. 967). 2001-2004 mean annual burned area derived from Terra MODIS (MODerate resolution Imaging Spectrometer) active fire observations.

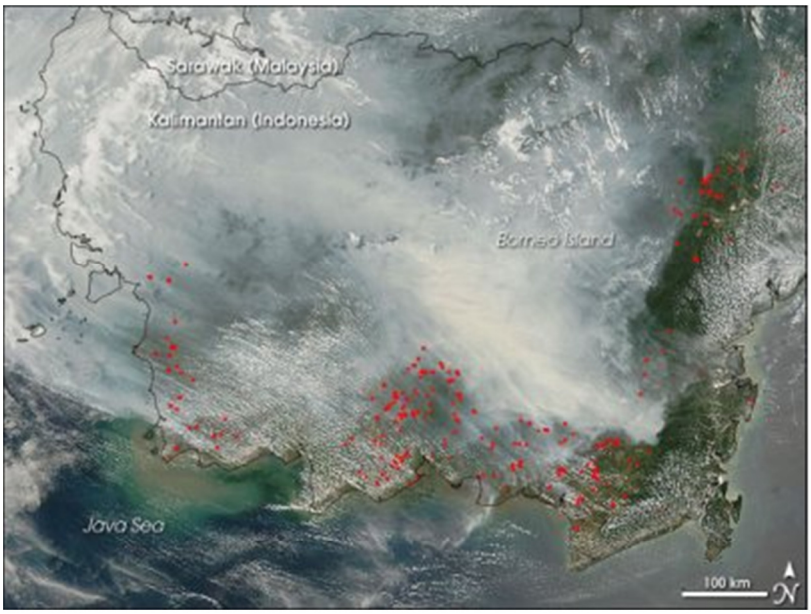

Figure 1.4 Extensive fires (red dots) burning in Kalimantan (Indonesia) on the island of Borneo during the 1997/1998 El Niño. Emissions from biomass burning in Indonesia during this period were estimated to amount to 13-40% of the annual global emissions from fossil fuel combustion during the same period (Page *et al.*, 2002). The resultant regional haze evident in this image had significant health implications for the tens of millions of humans living on Borneo and beyond (Wooster *et al.*, 2012).

1.2.1 Gaseous emissions

The amount of gas emitted from biomass burning is roughly proportionate to the amount of biomass burned, and the composition of the gases is heavily influenced by the chemical makeup of the biomass. Most plant biomass consists of 40-50% carbon, with the remaining mass consisting of hydrogen, oxygen, nitrogen (nutrients) and small amounts of sulphur, chlorine, bromine and other elements. Therefore, most gaseous emissions consist of the oxides of carbon and nitrogen (CO_2, CO, NO_2, N_2O, NO), methane and other simple hydrocarbons (CH_4, C_2H_2, C_2H_4 etc.), ammonia (NH_3) and some halogenated hydrocarbons (CH_3Br, CH_3Cl). Of these gases, the long-lived greenhouse gases (CO_2, CH_4, N_2O and the halocarbons) present the most direct influence on climate (Bowman *et al.*, 2009). Of the approximately 95% of biomass carbon that is volatised in burning (Lobert *et al.*, 1990), around 89-92% will be emitted as CO_2, with the remainder as CO (~6-10%) and CH_4 (0.3-0.5%) (Andreae and Merlet, 2001).

CO_2 emissions from biomass burning represent the single most important fire influence on contemporary climate (Bowman *et al.* 2009). Whilst it is estimated that 315 petagrams of carbon (PgC) have been released into the atmosphere since 1750 due to the burning of fossil fuels (Marland *et al.*, 2008), a further 190 Pg has been emitted by deforestation (or 38% of that from fossil fuel burning) (de Fries, 1999). Given that 50% of total deforestation CO_2 emissions are due to fires (van der Werf *et al.*, 2006), Bowman *et al.* (2009) conclude that CO_2 emissions from the permanent destruction of forests alone must account for ~19% of the total CO_2 radiative forcing (equivalent to 0.35 W m^{-2}) (Figure 1.5). Whilst this estimate does not account for any subsequenct carbon sequestration by the possible regrowth of deforested areas, Bowman *et al.* (2009) assume a steady state in the emission and sequestration of carbon from all non-deforestation fires, which may not be the case in a warming world. As discussed in Section 1.2.1, climate change may be causing increased fire activity due to higher temperatures and longer drying seasons, altering the balance between emission and sequestration.

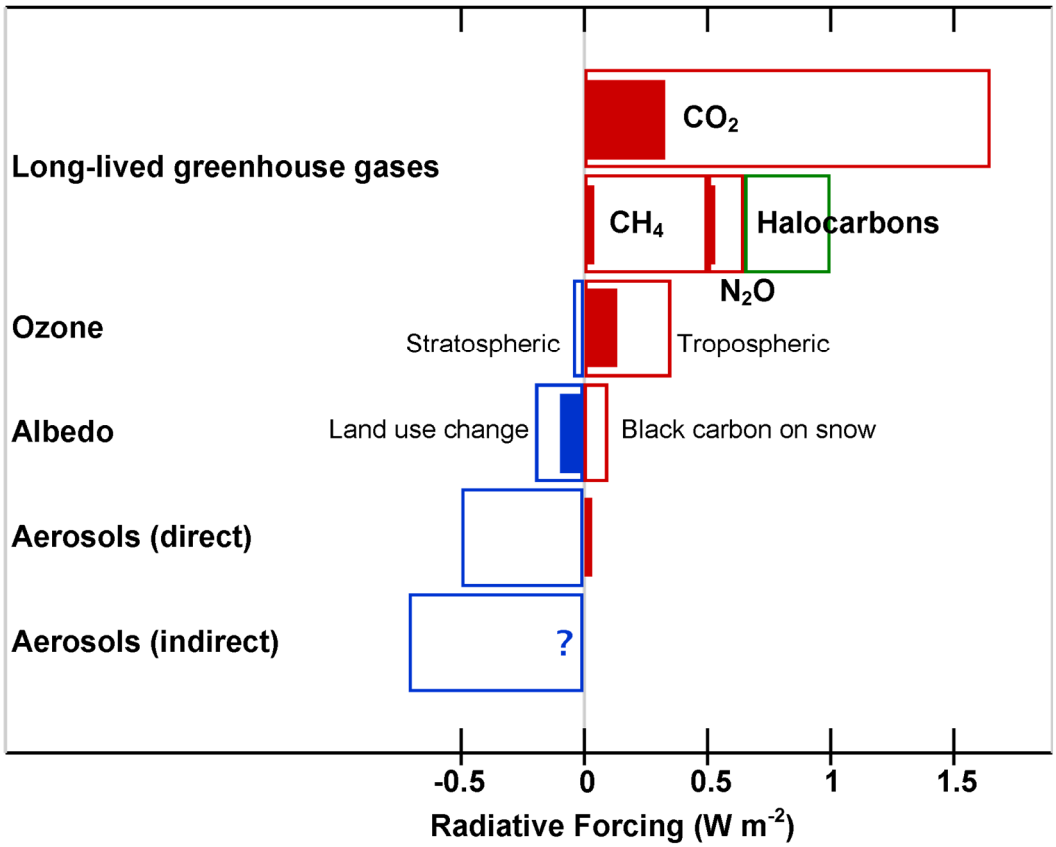

Figure 1.5 redrawn from Bowman *et al.* (2009). Estimated contribution of deforestation fires to climate change. The shaded inner bar (blue indicates cooling; red, warming) is the estimated fire contribution to the total Radiative forcing of various components of climate change identified by the IPCC (unshaded outer bar) (Forster *et al.*, 2007). CO_2 emissions, formation of ozone and the direct effects of aerosols lead to warming, whilst change in surface albedo is responsible for cooling.

By applying a similar analysis to methane emissions from deforestation and tropical peatland fires, Bowman *et al.* (2009) assume that these biomass burning sources contribute 14 Tg per year, compared to 600 Tg $year^{-1}$ from all contemporary sources and 250 Tg year from pre-industrial sources, concluding that fires contribute to approximately 4% of the total CH_4 radiative forcing. These estimates assume that anthropogenic burning has remained constant since 1750 C.E., a big assumption. Better quantification of CH_4 emissions will require improved understanding of the evolution of biomass burning emissions since 1750 C.E. (Lelieveld *et al.*, 1998). For nitrous oxide (N_2O), whilst emission factors (the amount of a particular trace gas released per unit of biomass burned) are very poorly known (Andreae and Merlet, 2001), Bowman *et al.* (2009) estimate annual emissions of ~0.36 Tg N_2O $year^{-1}$ from deforestation and tropical peatland fires, around 5% of emissions from all sources globally.

The influence on climate of the other nitrogen containing compounds produced in biomass burning is less well characterised. Estimates of nitrogen compounds emitted in biomass burning vary significantly, with the differences in emission factors of nitrogen containing compounds between vegetation types being much greater relative to those from carbon compounds (Andreae and Merlet, 2001). For example, the emission factor of ammonia (NH_3), another greenhouse gas, vary from a lower estimate of 0.6 grams per kilogram of dry matter burned (g kg^{-1}) in savanna to 1.4 g kg^{-1} in tropical forests. Similarly, the estimates of the NO emission factor, a gas important in the formation of tropospheric ozone, vary from 1.6 g kg^{-1} in tropical forests to 3.9 g kg^{-1} in savanna. Yokelson *et al.* (2007) also found a significant difference in NH_3 and NO emissions for fires from the same region in Brazil. It is suggested that the variability in nitrogenous emissions is in part controlled by the fuel nitrogen content, which varies considerably between fuel types and at different stages of vegetation growth (Lobert and Warnatz, 1993).

Biomass burning does not lead to direct emissions of ozone, however, emissions of NO_x (NO and NO_2), CO and other oxygenated organic compounds (e.g. formaldehyde) promote the production of this potent greenhouse gas. Based on emissions of NO_x, Bowman *et al.* (2009) estimate the contribution of deforestation and tropical peatland fires to account for 17% of the total radiative forcing due to tropospheric ozone, stressing that much work is needed to reduce uncertainty in this estimate. Whilst the halogenated hydrocarbons of methyl chloride (CH_3Cl) and methyl bromide (CH_3Br) are potent greenhouse gases and are released in relatively small quantities by biomass burning, their relative importance in greenhouse warming is small (Grossman *et al.*, 1997) when compared with the anthropogenic emissions of chlorofluorocarbons (CFCs) resulting from other sources (Forster *et al.*, 2007).

1.2.2 Aerosols

The net effect on radiative forcing of the direct and indirect effect of aerosols produced in biomass burning is not well understood (Schultz *et al.*, 2006). The direct effects include the scattering of light by sulphate aerosols, leading to a cooling effect. Globally, however, fires are estimated to only contribute around 2% to this effect (Bowman *et al.*,

2009). Fires have a more substantial contribution to the warming effect caused by tropospheric black carbon, however, even this effect may only account for around 0.01 W m^{-2} of radiative forcing. Uncertainties associated with the indirect effects of fire aerosol emissions are far greater. Aerosols originating from fires are believed to significantly influence cloud formation, lifetime and albedo (Bowman *et al.*, 2009). Fire aerosols can act as cloud condensation nuclei, promoting the formation of clouds, decreasing the droplet size and thus increasing their persistence and albedo (Andreae *et al.*, 2004). Conversely, the indirect effects of black carbon near fires can lead to a decrease in cloud cover due to the evaporation of clouds caused by the warming (Kaufman and Koren, 2006). To date, no global estimate of the fire aerosol effect on clouds exists. Reducing the uncertainty associated with the indirect effects of all aerosol emissions, natural and anthropogenic, is one of the biggest challenges to current climate science (Forster *et al.*, 2007).

1.2.3 Albedo effects

Biomass burning influences the albedo of a surface through a number of short- and long-term effects. The long-term effect of biomass burning on albedo is related to the widespread replacement of low albedo forests with croplands and grasslands that have a higher albedo. Considering that 50% of deforestation is attributed to fires (van der Werf *et al.*, 2006), Bowman *et al.* (2009) assume that the fire contribution to this negative forcing is 50%. On shorter timescales, the blackened surface following a fire will lead to some short-lived warming of the surface due to its low albedo (Jin and Roy, 2005), whereas at high latitudes, fires can increase the exposure of snow (by removing vegetation canopy cover) and thus increase albedo, causing cooling.

In areas removed from biomass burning activity, the effects of aerosols settling from the atmosphere can have profound albedo effects if the black carbon particles fall to coat a very high albedo surface, such as snow. The total radiative forcing from black carbon on snow is estimated to amount to around 0.1 W m^{-2} (Figure 1.5), of which around 20% is attributed to fires (Flanner *et al.*, 2007). Whilst the uncertainties associated with these albedo changes are broad and relate to both radiative uncertainties, and uncertainties regarding fire histories. Bowman *et al.* (2009) suggest that the negative forcing by land

use change is greater than the positive forcing by black carbon on snow, amounting to a net negative forcing of ~0.1 W m^{-2} (Figure 1.5).

1.3 Conclusions from Chapter 1

This Chapter began by defining biomass burning as an intrinsic component of the Earth system; a phenomenon that has probably existed since the evolution of plants. After describing the nature of biomass burning, the focus turned to the motivations to measure biomass burning emissions, these may be summarised as:

(a) Fire is endemic to many of our planet's natural environments with the biomass burned in naturally occurring fires often being replaced by new growth, sequestering the carbon emitted by the burning. Yet only 10% of wildfire ignitions are caused by natural forces such as lightning, with 90% of wildland fires started by human ignition. Human intervention has violently tipped the scales from equilibrium, with the widespread use of slash-and-burn to clear fire-resistant forests leading to a smaller terrestrial carbon pool, soil erosion, and perhaps the prevention of the future return of a forested landscape, leading to a net release of carbon to the atmosphere. The net effect of the various biomass burning influences on climate is clearly a significant positive radiative forcing (Figure 1.5), although a great deal of uncertainty is tied into these numbers. Reducing this uncertainty is one of the key goals of current biomass burning research.

(b) Global climate models that are relied upon for our prediction of future climate change require an accurate understanding of global biomass burning emissions to account for their large contribution to the global carbon cycle. This requires knowledge of the total biomass burned each year and the relative amounts of each of the relevant emitted trace gases.

(c) Climate change associated with greenhouse warming may now be resulting in net increases in fire activity due to higher temperatures, longer drying seasons and reduced life expectancy of trees due to drought stress. Accurate modelling

of future emissions and any positive feedback effect is a further motivation for biomass burning emissions research.

On the basis of these motivations to better understand and quantify global biomass burning emissions, the general aim of this study is to contribute to the development and exploitation of methods to improve the quantification of trace gas emissions from biomass burning, and in particular that of Open-Path Fourier Transform Infrared spectroscopy (OP-FTIR). The following Chapter begins by exploring some of the many approaches to measuring the phenomenon, including OP-FTIR, with a focus on local or regional scale trace gas measurement techniques, and the methodologies for translating these to estimates of total global emissions estimates. From this review, the specific objectives of the study will be derived.

A synthesis of this introductory Chapter won the Environmental Physics Group Essay Competition 2010 of the Institute of Physics (Smith, 2010)

2

Biomass Burning Emissions Characteristics and their Measurement

2.1 Development of biomass burning emissions studies

Some of the earliest records of wildfires occur in ancient Hebrew, Greek and Roman Classical literature (Rackham, 2003). Hanno, the Phoenician explorer, during his voyage around Africa in *c.* 500 B.C.E., mentions reaching '*an immense gulf, on either shore of which was a plain where by night we saw big and little fires flaming up at intervals everywhere*' (translation by Harden, 1962, believed to be a description of volcanically ignited wildfires in modern day Ivory Coast). Accounts such as these become increasingly common from the Middle Ages onwards, with evidence of fire management in the decrees and laws of 14th century Sardinia and 15th century Crete (Grove and Rackham, 2001), however, interest in wildfire was restricted to observation and management, with no evidence of interest in the smoke and its constituents. The first known scientific approach to the estimation of emissions from wildfires was made by Alexander Freiherr von Danckelman (von Danckelman, 1884, recalled by Brönnimann, 2007 and Brönnimann *et al.*, 2009), a Dutch geographer who, after observing huge savanna fires in Africa, reported that biomass burning affected cloudiness and precipitation, causing cumulus clouds and a persistent brown haze, and who argued that fires produced cloud condensation nuclei. Furthermore, von Danckelman estimated that 20% of southern Africa burns each year, and used

experimental evidence to suggest that this equated to 0.6 Gt of burnt biomass per year, astonishingly close to current satellite based estimates of 8–18% of southern Africa land area and 0.44 Gt of burnt biomass (Brönnimann *et al.*, 2009).

In the subsequent eighty years to von Danckelman's paper, the focus of the atmospheric scientific community was largely on anthropogenic fossil fuel emissions to the atmosphere, with no published study on emissions from biomass burning until the 1970s, when the effect on clouds was re-discovered (Eagan *et al.*, 1974). Radke *et al.* (1978) and Crutzen *et al.* (1979) were the first to publish quantitative measurements of the emission of CO, CO, CH_4 and other gases from airborne gas chromatography (GC) measurements. With these first measurements of gas species emissions, scientists were able to upscale their measurements in an attempt to model the global contribution of biomass burning to atmospheric composition (Crutzen *et al.*, 1979). With the discovery that biomass burning is a significant process in the global carbon cycle (Seiler and Crutzen, 1980) and with increasing information about the extent of global biomass burning available from satellite detection techniques (e.g. Dozier, 1981), a number of global initiatives were undertaken to improve the knowledge of biomass burning emissions, most notably the International Geosphere-Biosphere Programme. These led to an improved understanding of emissions of a large number of trace gas species, summarised by Delmas *et al.* (1995) and Andreae and Merlet (2001). Most recently, Akagi *et al.* (2011) performed a comprehensive review of published emissions measurements.

With the assimilation of global burnt area data (e.g. Giglio *et al.*, 2010), global estimates of fuel consumption per unit area (van der Werf *et al.*, 2006) and knowledge of emissions factors (the amount of a particular trace gas species emitted per unit of fuel burned) from a variety of biomass burning environments (Andreae and Merlet, 2001; Akagi *et al.*, 2011), work is now underway to accurately quantify global fire emissions to increasing precision and to assess the relative contribution of deforestation, and savanna, forest, agricultural and peatland fires (van der Werf *et al.*, 2010). On a regional scale, real-time fire detection is being used as a tool to drive biomass burning plume dispersion models (e.g. Kaiser *et al.*, 2009; Kaiser *et al.*, 2012) in an effort to improve forecasts of the resultant poor air quality. Despite these advances, van der Werf *et al.*

(2010) estimate that global carbon emissions uncertainties were on the order of at least 20%, with uncertainties for particular trace gas species being far greater (Akagi *et al.*, 2011).

In this Chapter, the particular trace gases released during biomass burning are considered in detail along with the metrics used to describe biomass burning emissions. Following this, a detailed review of measurement methods is presented, together with recent advances in quantifying biomass burning emissions and how these are used to model plume dispersion and global fire emissions totals.

2.2 Biomass burning trace gas products and their chemistry

Biomass burning is a significant source of a large number of important atmospheric trace gases (Crutzen *et al.*, 1979; Andreae and Merlet, 2001; Akagi *et al.*, 2011). Some of these trace gases contribute to the atmospheric greenhouse effect (e.g. CO_2, CH_4), others are important for reactive atmospheric processes (e.g. CO, CH_2O, NH_3), and many are of direct societal concern due to air quality and human health impacts (e.g. NO_x). This section identifies and describes a selection of some of the most important trace gas species emitted from biomass burning, with a focus on the relative importance of biomass burning as a source and the atmospheric fate of each gas. Average annual biomass burning and anthropogenic emissions estimates for this section are taken from the Emission Database for Global Atmospheric Research (EDGAR), release version 4.2 (EC-JRC/PBL, http://edgar.jrc.ec.europa.eu/, 2009) for the period 1999–2008 (unless otherwise cited) and are summarised in Table 2.1.

2.2.1 Direct greenhouse gases

2.2.1.1 Carbon dioxide (CO_2)

As explained in Chapter 1, CO_2 is the most important of all biomass fire emissions (Bowman *et al.*, 2009). Emissions from agricultural waste burning, savanna burning, and grassland fires are assumed to have a short carbon cycle, where the burned crops,

savanna and grasslands regrow within a year, and therefore do not contribute to a net increase in atmospheric CO_2. However, emissions of CO_2 from forest fires (anthropogenic and natural), followed by post-burn and decay are considered more permanent and are estimated to amount to 6.1 petagrams (Pg, equivalent to a gigaton, Gt) annually (average for 1999–2008), 22% of other anthropogenic sources of long-term CO_2 (28 Pg) and 17.8% of total annual long-term carbon emissions to the atmosphere (34 Pg). Incidentally, annual volcanic emissions of CO_2 amount to ~0.26 Pg (Gerlach, 2011), ~4% of forest fire CO_2 emissions, and less than 1% of total annual emissions of long-term CO_2 to the atmosphere. Biomass burning is therefore the second largest source of carbon dioxide to the atmosphere (Figure 2.1), after the energy industry sector (with 30.9% of total CO_2 emissions), and larger than both the manufacturing industry sector (12.9%) and combined road, shipping and aviation transport sources (17.2%). To estimate the contribution of biomass burning CO_2 to climate change, it is important to only include deforestation forest fires related to land-use change (when trees are not allowed to regrow), as on climate change timescales (e.g. since 1750) forest fires in regions with forest regrowth do not contribute to net increases in atmospheric CO_2. De Fries (1999) estimate that CO_2 from deforestation since 1750 amounts to ~190 Pg of carbon, compared with the 315 Pg of carbon released from the burning of fossil fuels.

As mentioned in the previous Chapter, this amounts to a total CO_2 radiative forcing of 0.35 W m^{-2} (19% of the total CO_2 radiative forcing). CO_2 is largely unreactive in the atmosphere and relies upon dissolution in the oceans for removal. Consequently the atmospheric lifetime of CO_2 is on average greater than 100 years (Forster *et al.*, 2007).

Table 2.1 Average annual biomass burning and anthropogenic emissions estimates taken from the Emission Database for Global Atmospheric Research (EDGAR), release version 4.2 (EC-JRC/PBL, http://edgar.jrc.ec.europa.eu/, 2009) for the period 1999–2008 for a series of important atmospheric trace gases. The table also indicates the percentage contribution of biomass burning total annual emissions of each trace gas, as well as estimated atmospheric lifetimes and an indication of whether the trace gas is considered a greenhouse gas (see section 2.2.1) or an ozone pre-cursor (see section 2.2.2).

	Average annual emissions by source for 1999-2008 (Tg)			**Biomass burning as % of total**	Biomass burning as % of anthro.	atmospheric lifetime	GHG	O_3 pre-cursor
Gas	Biomass Burning	Anthro-pogenic*	Total					
CO_2**	6083	28020	34104	**17.8**	21.7	5-200 yrs	yes	no
CH_4	20.9	314.9	335.8	**6.20**	6.60	12 years	yes	yes
N_2O	1.4	8.8	10.2	**13.4**	15.4	114 yrs	yes	no
CO	409.6	501.9	911.5	**44.9**	81.6	2 months	no	yes
NMVOC	28.8	131.3	160.1	**18.0**	21.9	2-40 days	no	yes
NO_x	13.4	101.8	115.2	**11.6**	13.1	1 day	no	yes
NH_3	8.2	40.6	48.7	**16.8**	20.1	hours	no	no

*Anthropogenic totals do not include anthropogenic biomass burning sources.

**Emissions of CO_2 from agricultural waste burning, savanna and grasslands are excluded from these totals due to their short carbon cycle (the burned crops, savanna, and grasslands are assumed to regrow within a year, and therefore do not contribute to a net increase in atmospheric CO_2).

2.2.1.2 Methane (CH_4)

Methane is a strong greenhouse gas with an atmospheric lifetime of 12 years and a 100-year Global Warming Potential (GWP) of 21 (Forster *et al.*, 2007), where GWP is the ratio of the amount of heat trapped by a certain mass of a particular gas for the same mass of CO_2. Unlike estimates of total CO_2 emissions from biomass burning, for which emissions from savanna, grasslands and agricultural waste burning are not considered to contribute to net increases in CO_2 as explained above, all biomass burning emissions are considered to contribute to net increases in CH_4. Emissions of CH_4 from biomass burning amount to an annual average of 20.9 teragrams (Tg, or megatons) for the period 1999-2008, 6.3% of total annual emissions to the atmosphere (336 Tg), which are dominated by agriculture (Figure 2.1b), fuel production and waste. Regionally, however, the relative importance of biomass burning for CH_4 emissions can be more significant (Figure 2.1). Biomass burning-sourced CH_4 in Australia, for example, accounts for 11.8% of the country's emissions, nearly twice the global proportion. In the Northern Territory of Australia, this proportion could be far greater due to the higher propensity for wildfires (Figure 2.1a). In central African nations, biomass burning is by

far the most important source of methane; in the Central African Republic, for example, biomass burning is responsible for 92.2% of the country's CH_4 emissions.

As a greenhouse gas, CH_4 is responsible for a radiative forcing of ~0.5 W m^{-2}, of which approximately 4% is attributed to biomass burning (Bowman *et al.*, 2009). The most effective sink of atmospheric methane is the OH hydroxyl radical in the troposphere and stratosphere, which reacts with CH_4 to produce water vapour and carbon dioxide.

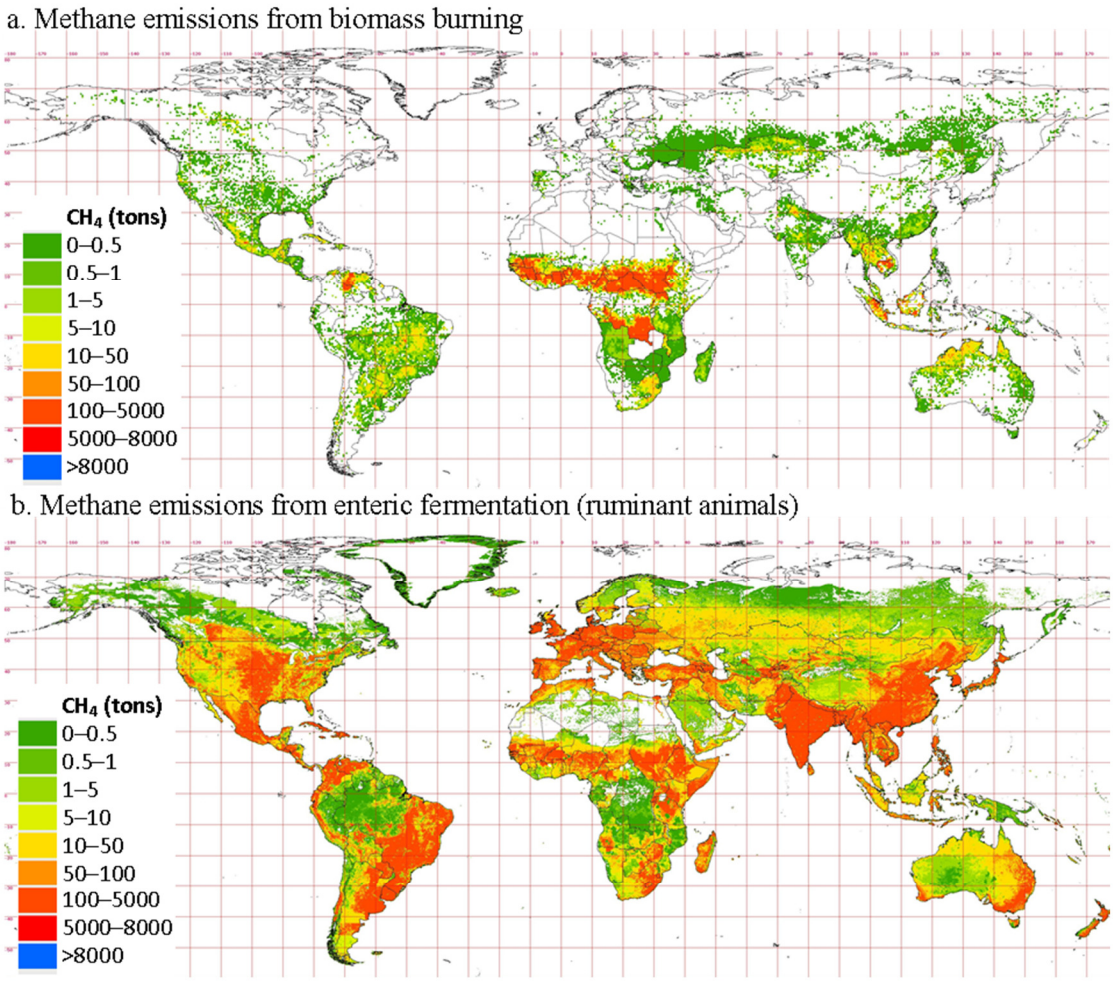

Figure 2.1 (Drawn from EC-JRC/PBL, http://edgar.jrc.ec.europa.eu/, 2009.) Global distribution of CH_4 emissions in 2008 from (a) biomass burning; and (b) enteric fermentation (ruminant digestion). On a global scale, biomass burning is responsible for 6.3% of annual methane emissions. However, regionally, biomass burning can be a far more significant source.

2.2.1.3 Nitrous Oxide (N_2O)

N_2O is an important greenhouse gas with a long atmospheric lifetime of 114 years and a GWP of 310. Biomass burning is a major source of N_2O to the atmosphere, accounting for an average of 1.4 Tg annually, 13.4% of total annual N_2O emissions (10.2 Tg), the second largest source after agricultural soils (4.4 Tg) (Table 2.1). Despite the smaller mass of emitted N_2O compared with CH_4, the radiative forcing due to N_2O from biomass burning is similar to that of CH_4 due to its greater GWP. As is the case for CH_4, the regional significance of biomass burning as a source of N_2O emissions can vary greatly depending on the abundance of fires within particular regions. The impact of N_2O, however, is global, due to its lengthy atmospheric lifetime (Forster *et al.*, 2007). The only known sink of N_2O is photolysis in the stratosphere, where N_2O is broken down to N_2 + O or reacts with atomic oxygen to produce two molecules of NO. The NO produced from N_2O subsequently reacts with ozone (O_3) to form NO_2 and O_2. This series of reactions stemming from the migration of tropospheric N_2O to the stratosphere is now considered the single most important threat to the stratospheric ozone layer (Ravishankara *et al.*, 2009).

2.2.2 Reactive gases

2.2.2.1 Carbon monoxide (CO)

Carbon monoxide is a key reactive gas in the atmosphere and is one of the principle gases involved in the formation of tropospheric ozone (O_3) and photochemical smogs. Carbon monoxide strongly affects the tropospheric concentrations of the highly reactive hydroxyl (OH) radical (Crutzen *et al.*, 1979) through the reaction:

$$CO + OH \rightarrow CO_2 + H \qquad (2.1)$$

Importantly, this reaction produces atomic hydrogen which quickly reacts with O_2 in the atmosphere to produce the peroxy radical HO_2 (Friedlander *et al.*, 1977):

$$H + O_2 \rightarrow HO_2 \qquad (2.2)$$

Peroxy radicals will then proceed to react with atmospheric NO (also emitted during biomass burning) to produce NO_2 which is subsequently photolysed to atomic oxygen and NO; the atomic oxygen reacts with O_2 to produce ozone:

$$HO_2 + NO \rightarrow OH + NO_2 \quad (2.3)$$

$$NO_2 \xrightarrow{sunlight} NO + O \quad (2.4)$$

$$O + O_2 + N_2 \rightarrow O_3 + N_2 \quad (2.5)$$

Simplified, the net effect of these reactions is:

$$CO + 2O_2 \rightarrow CO_2 + O_3 \quad (2.6)$$

Biomass burning is the principle source of carbon monoxide to the atmosphere, accounting for 410 Tg of CO annually, or 44.9% of total annual CO emissions (911 Tg) (Table 2.1). The impacts of CO are felt both regionally and globally. On a regional scale, the photochemical smogs that form downwind of fires as a consequence of the production of tropospheric ozone (as well as the presence of other biomass burning products, such as volatile organic compounds, nitrogen oxides and particulates) can have significant negative human and economic impacts. Witte *et al.* (2010) observe that CO concentrations in Moscow during the wildfire episode of 2010 reached similar levels to those seen at the 2006 El Niño wildfire event over Indonesia. The Moscow smog from the 2010 wildfires was reportedly responsible for a doubling of the death rate in the city (Zvyagintsev *et al.*, 2011). On a global scale, CO as a tropospheric ozone precursor is indirectly responsible for the warming attributed to this greenhouse gas. CO from biomass burning, along with other trace gases emitted from vegetation fires that act as O_3 precursors, is accountable for ~17% of the total radiative forcing attributed to tropospheric ozone (Bowman *et al.*, 2009).

2.2.2.2 Non-methane volatile organic compounds (NMVOCs)

Non-methane volatile organic compounds (NMVOCs) are a group of compounds that are collectively involved in complex reactions with nitrogen oxides (NO_x) in the presence of solar radiation to produce ozone (Sillman, 1999). Whilst hundreds of

compounds are considered NMVOCs, the most important biomass burning compounds include acetylene (C_2H_2), ethylene (C_2H_4), ethane (C_2H_6), methanol (CH_3OH), formaldehyde (CH_2O), formic acid (HCOOH) and furan (C_4H_4O). The principle role of NMVOCs in the O_3 formation process is similar to that of carbon monoxide, as NMVOCs react to form the peroxy radical. As described in Eqns. 2.3–2.5, the peroxy radicals (HO_2) convert nitrogen monoxide (NO) back to nitrogen dioxide (NO_2) without consuming O_3, regenerating the hydroxyl radical (OH), thus allowing sustained net O_3 formation. The relative ability of different NMVOCs in producing O_3 is variable and depends on reaction rates and intermediary reaction products (Atkinson, 2000). Akagi *et al.* (2011) highlight the importance of biomass burning as a source of NMVOC and stress the need to speciate as many of these gases as possible and estimate their total emissions. Average annual emissions of NMVOCs from biomass burning amount to ~29 Tg, 18% of total global emissions (160 Tg). Biomass burning is the third largest source of NMVOCs after transformation industries (23%) and buildings (22%).

2.2.2.3 Nitrogen oxides (NO_x)

As described above (Eqns. 2.3–2.5), NO_x is an important reactive trace gas species and is necessary for the formation of ozone and photochemical smogs. In addition to ambient levels of NO_x available for reactions with the peroxy radical formed from both CO and NMVOC emissions, NO_x is also a primary emission product from biomass burning, boosting O_3 production within fire plumes. Of the total global annual emissions of NO_x (115 Tg), biomass burning accounts for 13.4 Tg, or 12% of total annual global emissions. Globally, biomass burning is the third largest source of NO_x after transportation (41%) and the energy industries (26%) (EC-JRC/PBL, 2009). As the previous sections have highlighted, the regional significance of biomass burning as a source of NO_x can be far greater.

2.2.2.4 Ammonia (NH_3)

Ammonia is the most abundant gas-phase alkaline species in the atmosphere (Dentener and Crutzen, 1994) and is important for its ability to neutralise acidic aerosols produced from the oxidation of sulphur and nitrogen oxides. The atmospheric lifetime of NH_3 is on the order of hours due to fast dissolution into water vapour and condensation onto

and reactions with aerosols, leading to a highly heterogeneous global distribution. As a result of this heterogeneity, isolated but high volume sources of ammonia, such as biomass burning, can have a significant regional influence. Globally, biomass burning is reported to be responsible for 17% (8.2 Tg) of total annual ammonia emissions (48.7 Tg). Biomass burning is the second largest source of NH_3, after agriculture (79%).

2.2.3 Biomass burning tracer gases

A few trace gases are almost exclusively produced by biomass burning and are therefore useful as biomass burning tracers. Hydrogen cyanide (HCN) and acetonitrile (CH_3CN) were highlighted by Akagi *et al.* (2011) as tracer species. Biomass burning is the only known source of HCN, with estimates of total emissions ranging from 2.7 to 5.6 Tg annually (Li *et al.*, 2000a). The atmospheric lifetime of HCN is estimated to be 2–4 months, with ocean uptake being its main sink.

2.2.4 Summary of biomass burning trace gas products and their chemistry

This review, and the data summarised in Table 2.1, have highlighted the importance of the major biomass burning trace gas emissions for global climate (direct greenhouse warming and tropospheric ozone formation), regional air quality (tropospheric ozone formation and associated photochemical smog), and for their use as a chemical tracer of biomass burning. For many of these gases, biomass burning is responsible for a significant proportion of total global emissions, often representing one of the three largest emitters by sector for each trace gas. As Figure 2.1 shows, at a regional level, biomass burning can be the dominant source of all of these gases in areas with a high propensity for biomass burning and relatively little industrial activity. The following section will describe the metrics used for quantifying emissions of trace gases in biomass burning studies, principally those of emission ratios and emission factors, and how these are deployed to estimate total emissions.

2.3 Biomass burning emissions metrics

In a comprehensive synthesis of over 200 publications relating to biomass burning emissions measurements, Akagi *et al.* (2011) listed emission factors for a broad range of gaseous species and aerosols from biomass burning in different ecosystems (savanna, tropical forest, boreal forest, temperate forest, peatland, chaparral) and from burning in industrial/agricultural applications (charcoal making, charcoal burning, crop residues, pasture maintenance, open cooking, patsari stoves, dung burning, garbage burning). It is the convention of review papers such as Akagi *et al.* (2011), Andreae and Merlet (2001) and Delmas *et al.* (1995) to report biomass burning emissions in terms of emission factors, usually derived from emission ratios. This section explains the calculation of these important biomass burning metrics.

2.3.1 Emission Ratios

Emission Ratios (ERs) may be described as the ratio between the excess concentration of a gas species x within a fire plume (Δx) to the excess concentration of a reference gas (ΔCO_2 in the example below):

$$ER_{x/CO_2} = \frac{\Delta x}{\Delta CO_2} = \frac{(x)_{smoke} - (x)_{ambient}}{(CO_2)_{smoke} - (CO_2)_{ambient}} \quad (2.8)$$

2.3.2 Emission Factors

An Emission Factor (EF) may be defined as the amount of compound x released (M_x) per amount of dry fuel consumed in a fire ($M_{biomass}$), expressed in units of grams per kilogram (g kg^{-1}) of dry fuel consumed. Given that measurements of dry fuel consumption are often unavailable/difficult/impossible to obtain (particularly for airborne emissions measurements), $M_{biomass}$ is often approximated by using the amount of carbon species released (M_C) and an assumed fuel carbon content ($C_{biomass}$ usually equal to ~0.5):

$$EF_x = \frac{M_x}{M_{biomass}} = C_{biomass} \frac{M_x}{M_C} \quad (2.9)$$

EF_x can therefore be estimated from the concentration of species x in the smoke and the concentration of all carbon species:

$$EF_x \cong C_{biomass} \frac{[x]}{\sum([C_{CO_2}]+[C_{CO}]+[C_{CH_4}]+[C_{VOC}]+[C_{aeros}]+\ldots)} \quad (2.10)$$

Where $[x]$ is the concentration of species x and $[C_{CO2}]$ etc. are the concentrations of the carbon species in the plume. This is often referred to as the carbon mass balance technique, and was first developed by Ward and Radke (1993).

2.3.3 Modified Combustion Efficiency

The combustion efficiency (CE) of a fire is the ratio of the mass of CO_2 emitted to the total mass of carbon emitted. This metric, however, is difficult to calculate due to the requirement to measure all carbonaceous species which is often impossible. Instead, a modified version (the MCE) may be used to approximate CE, where the ratio of carbon emitted in the form of CO_2 to that emitted as CO and CO_2 is used. This approximates CE as CO_2 and CO represent the vast majority of emitted carbon (Ward and Radke, 1993):

$$\text{MCE} = \frac{\Delta CO_2}{(\Delta CO_2 + \Delta CO)} \quad (2.7)$$

As introduced in Chapter 1.2, different stages of combustion may be characterised by their MCE; consequently, the MCE metric is often used as an aid to interpretation of fire behaviour.

The following sections will review the various platforms that are used to study biomass burning emissions, identifying the key advantages and limitations of each approach, before highlighting the key measurement challenges and identifying a set of objectives that can work to address these challenges.

2.4 Measuring biomass burning emissions

The studies that contributed to the Akagi *et al.* (2011) review comprised a variety of laboratory, ground-based and airborne biomass burning emissions measurements. For most emissions, however, Akagi *et al.* (2011) emphasise the wide range of uncertainty, given that for many of the chemical species the emissions estimates are derived from only one or two published studies that may only focus on measurements from a handful of fires. In the earlier review by Andreae and Merlet (2001), the natural variability of a number of chemical species was unknown due to a lack of multiple measurements within a particular ecosystem. Since 2001, a number of studies have 'filled-in' some knowledge gaps (e.g. Bertschi *et al.*, 2003a; Sinha *et al.*, 2003; Li *et al.*, 2007; Sahai *et al.*, 2007; Yokelson *et al.*, 2007; Yokelson *et al.*, 2008; Cao *et al.*, 2008), mostly by providing dedicated emission ratios or emission factors for particular key environments, allowing Akagi *et al.* (2011) to better describe the natural variability of most of the major emitted gas species. Despite these advances, some ecosystems do not have quantified emissions (e.g. from temperate shrublands) and the high degree of natural variability within ecosystems (often larger than 50% for a given trace gas species) has yet to be fully explained. This section reviews the findings and the main methods by which gaseous emission ratios and emission factors have been measured in recent laboratory studies (Section 2.4.1), ground-based field studies (Section 2.4.2) and airborne studies (Section 2.4.3). Furthermore, this section will review developments in the satellite monitoring and estimation of biomass burning emissions over the past decade (Section 2.4.4).

2.4.1 Laboratory measurements of gaseous emissions from biomass burning

Until the 1990s, most published research into biomass burning emissions resulted from field-based or airborne sampling (recent developments in these areas are reviewed in Section 2.4.2 and 2.4.3). A potential problem with these sampling strategies is that airborne sampling tends to be biased towards the convectively lofted emissions from flaming combustion, and ground sampling towards lower efficiency emissions from smouldering combustion, missing the convective column (Griffith *et al.*, 1991) (Section

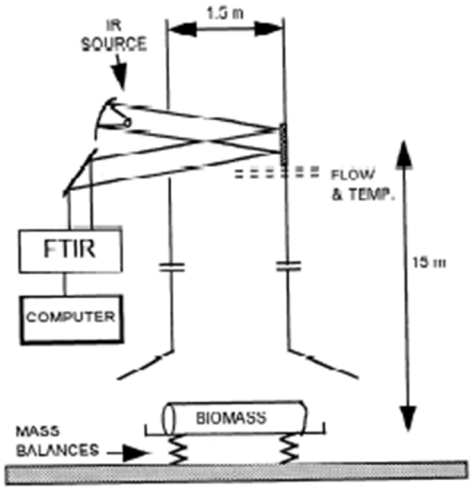

Figure 2.2 Taken from Yokelson *et al.* (1996). Schematic of the experimental arrangement used to make biomass burning emissions at the Missoula fire laboratory. Biomass is burned on a fuel bed located on the mass balances with the emissions from the fire being funnelled into a smoke stack with a sampling platform located ~15 m above the fuel bed. In this example, an IR source is used to pass an IR beam through the smoke stack which is then reflected back onto an FTIR spectrometer.

1.2.2). Furthermore, natural variability in meteorological conditions, biomass, and fire type can lead to highly variable emission ratios. Griffith *et al.* (1991) find that emissions ratios can vary by factors of 4–5 or more for fires within the same ecosystem. By burning biomass in a laboratory, it became possible to investigate the emissions from individual vegetation species under controlled conditions (e.g. Yokelson *et al.*, 2008; McMeeking *et al.*, 2009), enabling the separate characterisation of flaming and smouldering emissions (see Chapter 1.2), for example.

The majority of measurements of laboratory-based biomass burning emissions have taken place in the combustion laboratory at the Missoula Fire Sciences Laboratory, Montana (e.g. Yokelson *et al.*, 1996; Yokelson *et al.*, 1997; Goode *et al.*, 1999; Bertschi *et al.*, 2003a; Bertschi *et al.*, 2003b; Christian *et al.*, 2003; Christian *et al.*, 2004; Yokelson *et al.*, 2008). The experimental configuration of most of these studies involves the burning of measured quantities of biomass in a fuel bed (Figure 2.2), with the emissions from the fire being funnelled into a smoke stack with a sampling platform located ~15 m above the fuel bed (Yokelson *et al.*, 1997). Studies undertaken at other locations (e.g. Keene *et al.*, 2006; Cao *et al.*, 2008) employ a similar configuration. Many of the studies at Missoula employ Open-Path Fourier Transform Infrared (OP-FTIR) spectroscopy (see Chapter 3) to measure emissions of trace gases at the sampling

platform. This method, pioneered by Griffith *et al.* (1991) in relation to biomass burning emissions, exploits the spectral absorption of infrared light by gaseous emissions to identify and quantify emissions of a broad range of biomass burning emissions species. However, whilst Griffith *et al.* (1991) deployed the method to measure the constituents of smoke across a long (~100 m) pathlength, the laboratory studies in Missoula use a much shorter path of a few metres maximum.

As well as deploying OP-FTIR in the field, Griffith *et al.* (1991) also reported the first measurements of CO_2, CO, CH_4, CH_2O, N_2O, NO, NO_2 and NH_3 from laboratory biomass burning, with Yokelson *et al.* (1996) extending the number of gas species by including non-methane hydrocarbons as well as organic pyrolysis products (methanol, acetic acid, formic acid, hydrogen cyanide etc.). These studies confirmed that CO_2 was the massively dominant product of flaming combustion, whilst CO was produced in increased quantities during smouldering combustion, demonstrating that different fire types may emit compounds in very different ratios, and that these emission ratios will vary throughout the course of a single fire. Yokelson *et al.* (1996), Yokelson *et al.* (1997), and Goode *et al.* (1999) were the first to identify significant emissions of oxygenated volatile organic compounds (OVOC) from biomass burning. As discussed earlier in this Chapter, VOCs are important as they can affect ozone and hydroxyl production, suggesting an important link between biomass burning and regional scale atmospheric chemistry. Yokelson *et al.* (1997) examined measurements of smoke at different heights above the fuel bed (centimetres to 18 m above the plume), but could not find evidence of chemical reactions on this scale.

Building on earlier work at Missoula, Christian *et al.* (2003) confirmed that 70–80% of organic fire emissions were OVOC, identifying and quantifying 10 previously unmeasured species by using gas chromatography (GC) with mass spectrometry (GC-MS), flame ionization detection (GC-FID) and electron capture (GC-EC) detectors, as well as proton transfer reaction mass spectrometry (PTR-MS). In a comparison of the various techniques employed in Christian *et al.* (2003), Christian *et al.* (2004) stressed the problems of identifying OVOC using GC techniques, as chemical reactions in the volatile and concentrated smoke mixture occurred before analysis of the canisters could be undertaken. Whilst PTR-MS was much better suited to measuring low concentrations

of OVOC, OP-FTIR was better suited to measuring smaller molecules such as CO_2, CO, CH_4, other unoxidised organic compounds and NH_3, and OVOCs with high (> 1 ppm).

Besides the clear improvements in the identification and quantification of increasing numbers of chemical species in the emissions from biomass burning, laboratory burning has been used to investigate how emissions vary between different fire styles. Bertschi *et al.* (2003a) investigated Residual Smouldering Combustion (RSC) at Missoula. RSC is the process by which large diameter fuels (e.g. logs) and belowground biomass (e.g. partly decomposed leaf litter "duff") smoulder slowly (often for days to weeks) following the flaming stage of a wildfire. Laboratory conditions are ideal for measuring these as the emissions are entrained and well mixed when measured (as opposed to their swift removal by the wind in a field situation). The findings enabled a new understanding of smouldering emissions, with the authors claiming that, after accounting for RSC, the established emission factor (EF) for NH_3 from boreal forests would increase by a factor of 6, whilst the EF for NOx would halve. Savanna EFs would also be affected, with the EF of CH_4 estimated to increase by a factor of 2.5. A summary of emission factors derived from these types of laboratory studies is presented in Table 2.2 at the end of Section 2.4.

2.4.2 Field-based measurements of gaseous emissions from biomass burning

A large number of field-based ground-level measurements since the 1980s were synthesised by Delmas *et al.* (1995), Andreae and Merlet (2001) and Akagi *et al.* (2011). All of the ground-based studies contributing to these reviews involved conventional methods for atmospheric trace gas analysis, employing *in situ* point measurements (e.g. using non-dispersive infrared [NDIR] analysis for CO_2 and CO) or grab sampling, whereby samples are collected in the field before later laboratory analysis using gas chromatography (e.g. Hurst *et al.*, 1994). Generally, each gas species may require a different analytical technique and measurements are prone to small-scale localised variations (Griffith *et al.*, 1991). Furthermore, as discussed in section 2.4.1, reactive species, such as NMVOCs cannot be quantified using grab sampling as they quickly react to form secondary emissions gases within the sampling containers. Whilst

studies continue to employ these techniques, particularly to improve knowledge of emission factors from biofuel burning or agricultural residue burning (e.g. Sahai *et al.*, 2007), this section is primarily concerned with reviewing recent developments in direct field-based measurements such as OP-FTIR and solar occultation FTIR (SO-FTIR) spectroscopy. OP-FTIR is a passive methodology that provides path-integrated trace gas concentrations for a broad range of gases simultaneously, and thus overcomes many of the sampling issues associated with more conventional methods (sample handling and storage, the requirement for many point-sample replicates).

Griffith *et al.* (1991) conducted the first ground-based field measurements of biomass burning using OP-FTIR. In their study, an FTIR spectrometer was used to observe an infrared source (a gas furnace igniter coupled with a telescope) across distances of 25–200 m, above or downwind of different biomass fires. Griffith *et al.* (1991) quantified CO_2, CO, CH_4, CH_2O, NH_3 and NO_2 amongst other gases, yet subsequent use of OP-FTIR for ground-based measurements is rare. Deployment until recently has been difficult due to heavy-duty equipment, and interpretation restricted by low-precision analysis techniques (Griffith *et al.*, 1991). Recent developments in both the compaction of FTIR instruments and improvements in spectral analysis using spectral forward modelling and non-linear least squares (NLLS) methods (described further in Chapter 3) were exploited by Wooster *et al.* (2011) in a study of emissions from experimental fires in the savannah of Kruger National Park, South Africa. Wooster *et al.* (2011) build on the earlier work by Griffith *et al.* (1991), using OP-FTIR with a long 150–250 m open path to identify differences between backfire, headfire and residual smouldering combustion (RSC) emissions (Figure 2.3). Furthermore, measurements of the fires' thermal emissions were used to identify the relative amount of biomass burnt during the flaming and smouldering phases, which was used to apply weighting factors to the emission factors derived for the different combustion phases, enabling calculation of "fire-averaged" emission factors.

Bertschi *et al.* (2003b) is another of the few studies to exploit OP-FTIR in the field after Griffith *et al.* (1991), using an open-path White cell (a configuration of mirrors that allows the radiation from the infrared source to be reflected multiple times across a short pathlength) to yield a longer pathlength of 38–51 m in this particular study, see

Figure 2.4. This setup permits measurements of highly concentrated smoke when the cell is positioned in the plume, and can be used to measure the NMOC and OVOC species that are difficult to quantify using conventional sampling (e.g. GC), yet because the actual smoke sampled passes through a short path (< 1 m), the method is maybe hindered by its susceptibility to localised small-scale variations that may not be representative of the whole plume. In an interesting development, Hashmonay *et al.* (2001) used OP-FTIR and computed tomography to demonstrate a technique by which emissions *fluxes* could be estimated using multiple optical paths through a gaseous plume (in a vertical plane downwind from a source), but the method has yet to be applied to biomass burning.

One of the possible limitations of OP-FTIR spectroscopy is that it is limited to sampling smoke that advects into the infrared beam and is thus reliant on a wind-driven ground-level plume. As with other ground-based methods, this reliance on measuring emissions close to the ground opens the method up to the critique that it has a tendency to be biased towards smouldering emissions which are emitted during less intense combustion and therefore remain close to the ground (Andreae and Merlet, 2001). Furthermore, the advected smoke mixes with ambient air, diluting the biomass burning products; the consequence of which is that many of the more complex, heavier molecules lie below the detection limits of the portable low spectral resolution spectrometers (Christian *et al.*, 2003b). Christian *et al.* (2003b) suggest that FTIR is best used for the detection of CO_2, CO, CH_4, C_2H_2, C_2H_4, CH_2O, HCOOH, and NH_3, detection of more complex molecules is hampered by poor signal to noise.

Given the relative impracticalities of some OP-FTIR setups, other ground-based measurements using FTIR spectroscopy have used the sun as the source of infrared light. Measurements can be performed kilometres from the biomass burning itself as long as the sun can be viewed through the smoke affected air, but of course there must be a measurable difference between the absorption by gas species within the plume and that by the ambient atmosphere for trace gas concentrations to be quantified. Paton-Walsh *et al.* (2005) published the first emission factors derived by this technique for Australian wildfires. CO_2 emissions could not be quantified however, as no significant increase over ambient CO_2 absorption was observed. This meant that the carbon mass

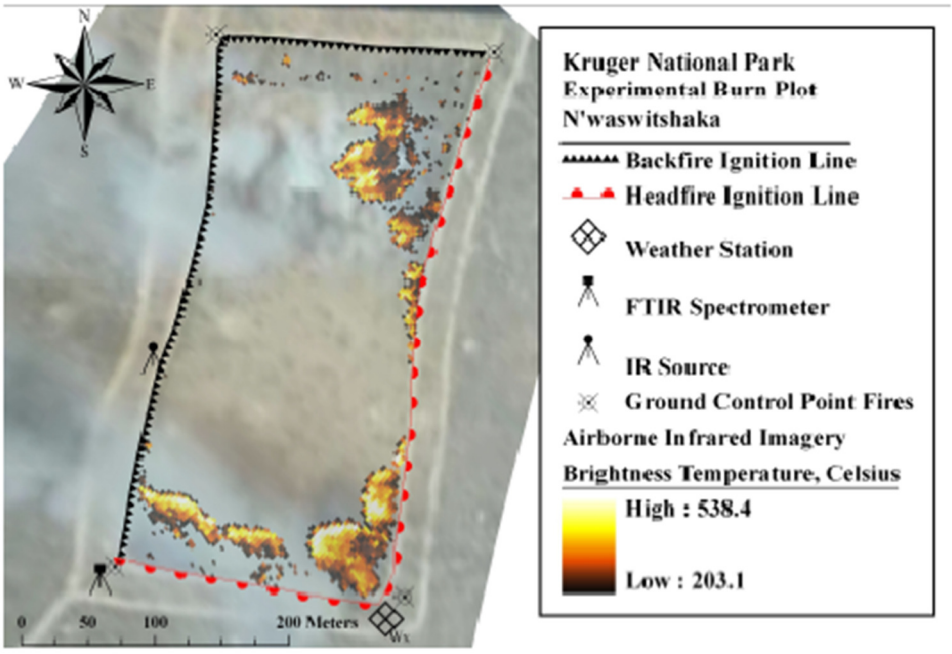

Figure 2.3 Taken from Wooster *et al.* (2011). Typical field setup deployed to study the smoke characteristics of savannah fires in southern Africa using OP-FTIR spectroscopy. The location of the FTIR spectrometer and IR source are shown. Aerial thermal imagery is superimposed on a visible aerial photograph of the fire plot. Here, the flaming front had only transited across approximately one-quarter of the total plot area. Higher brightness temperatures are generally seen at the fire fronts (location of flaming combustion), whereas lower brightness temperatures are recorded behind the fronts (smouldering combustion) where combustion rate and thus heat release is lower.

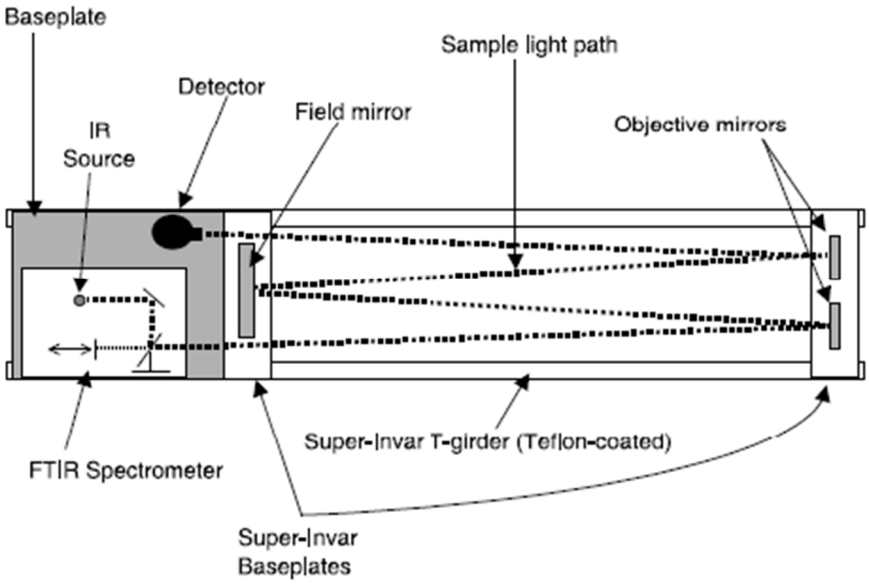

Figure 2.4 Taken from Bertschi *et al.* (2003). A simplified, top view schematic (not to scale) of the OP-FTIR cell deployed to measure the trace gas emissions from the production and use of biofuels in Zambia. The IR path is not enclosed by the cell, allowing smoke from biofuel combustion to pass freely through the path. This design has also been used in place of the simpler reflected IR beam on the measuring platform at the Missoula fire laboratory depicted in Fig. 2.2 (e.g. Yokelson *et al.* 1997).

balance approach to calculating emission factors could not be used (Equations 2.9 and 2.10). Instead, emission factors for C_2H_4, NH_3, HCOOH, H_2CO, C_2H_6, C_2H_2 and HCN were calculated from their emissions ratio to CO using the following equation:

$$EF_x = ER_{x/CO} . \left(\frac{MM_x}{MM_{CO}}\right) . EF_{CO} \quad (2.11)$$

Where EF_x is the emission factor of species x, $ER_{x/CO}$ is the molar emissions ratio of species x to CO, MM_x is the molecular mass of species x, MM_{CO} is the molecular mass of CO (28 g mol^{-1}) and EF_{CO} is the emission factor for CO (taken from Andreae and Merlet, 2001, stipulated as 107 g kg^{-1}). This study by Paton-Walsh *et al.* (2005) exposes the limitations of the solar occultation FTIR method. Without detection of enhanced CO_2 in the solar atmospheric absorption spectra of the smoke plume, it is not possible to calculate emission factors for CO_2 or CO, and emission factors for other gas species must therefore rely upon the mean emission factor for CO taken from other studies, inducing a large degree of uncertainty (±35% for the extratropical forest CO emission factor used in Paton-Walsh *et al.* [2005]). Even with such uncertainties, high spectral resolution SO-FTIR spectroscopy has since been used to provide the first estimates of methanol emissions from large biomass fires (Paton-Walsh *et al.*, 2008). Emission factors from the SO-FTIR studies are summarised in Table 2.2 at the end of Section 2.4.

Besides the estimation of emission factors, SO-FTIR spectroscopy of biomass burning plumes has been shown to be useful for deriving atmospheric profiles of gases that would otherwise be undetectable in ambient conditions (e.g. ethylene in Rinsland *et al.* [2005]), providing useful calibration data for spectral absorption line databases. Another potentially useful application of SO-FTIR is in the establishment of relationships between total column amounts of trace gases and aerosol optical depth (AOD). AOD may be described as the negative natural logarithm of the fraction of radiation (e.g. sunlight) that is not scattered or absorbed on a path through the atmosphere at a given wavelength; this is usually expressed as the negative natural logarithm of the ratio of the radiance measured on the ground (I) to that at the top of the atmosphere (I_{TOA}):

$$AOD = -\ln\left[\frac{I}{I_{TOA}}\right] \quad (2.12)$$

Paton-Walsh *et al.* (2004) establish a relationship between AOD and CO and several other trace gases (Figure 2.5) in a comparison of SO-FTIR derived total column amounts and AOD measurements made using a visible-near-infrared spectrometer (Figure 2.5). Paton-Walsh *et al.* (2005) use this relationship as a method by which total emissions from biomass burning may be quantified using AOD measurements from satellites, providing preliminary results in the form of HCN and H_2CO regional emissions mapping. Calculating total emissions of trace gases using AOD as a proxy for total column gas amounts is complicated by not knowing the age of the plume (i.e. to estimate total emissions across a week, it is necessary to avoid 'double-counting' of smoke that had been emitted on previous days). To address this, Paton-Walsh *et al.* (2010a) combine satellite observations of AOD with an atmospheric chemical transport model to calculate total daily gas emissions from biomass burning. In a case study of the Canberra wildfires of 2003, they estimate that those particular fires could account for

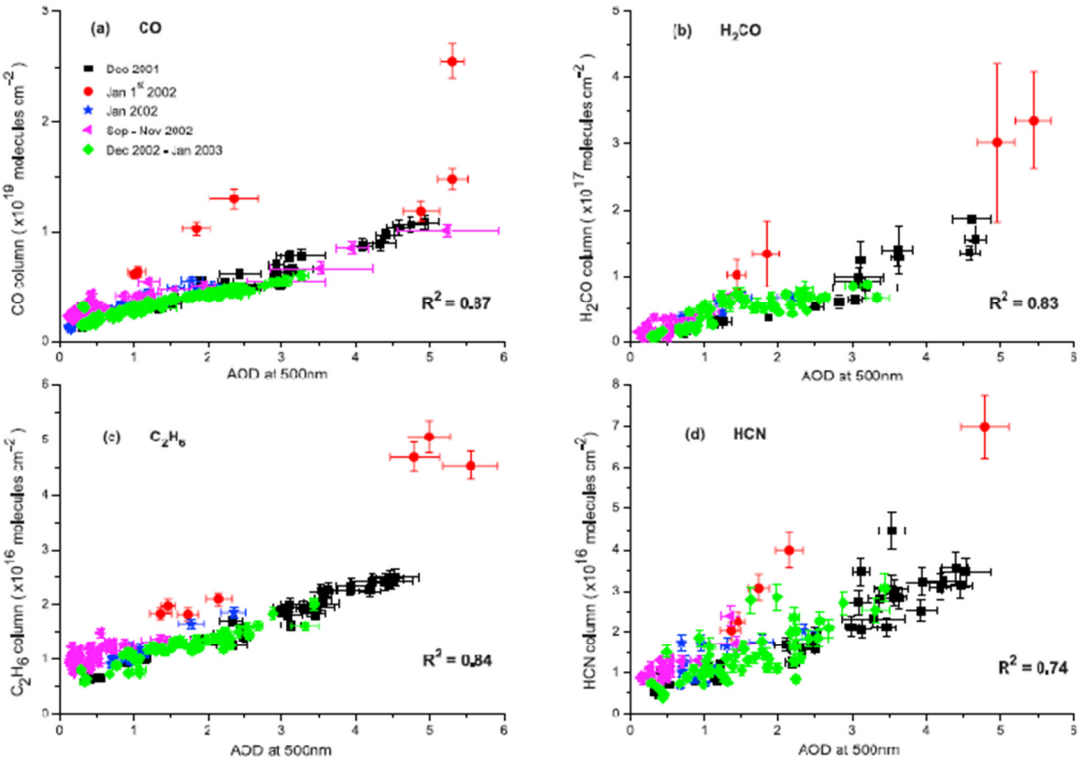

Figure 2.5 Modified from Paton-Walsh *et al.* (2005). Vertical column amounts of (a) CO, (b) H_2CO, (c) C_2H_6, (d) HCN derived from individual solar occultation FTIR spectra, plotted against simultaneous and collocated measurements of AOD. The data are coloured to distinguish different time periods. Paton-Walsh *et al.* (2005) were the first to demonstrate that AOD could be used as a proxy for total column amounts of a series of biomass burning trace gases.

3.1% of global annual emissions of CO (along with estimates for other species), albeit with a large degree of uncertainty.

2.4.3 Airborne measurements of gaseous emissions from biomass burning

The majority of data used for the calculation of ecosystem emission factors (Andreae and Merlet, 2001) are derived from measurements of biomass burning emissions by airborne (helicopter or plane) sampling techniques. In a similar trend to the laboratory studies, the evolution of airborne measurements over the past thirty years has seen the number of gases quantified rise from four or five gas species (e.g. Crutzen *et al.*, 1979) to over fifty gas species (e.g. Yokelson *et al.* 2007). As was also the case with laboratory measurements, the earliest studies solely relied on measurements from grab sampling and subsequent GC analysis (e.g. Andreae *et al.*, 1988).

Yokelson *et al.* (1999) present the results from what appears to be the first use of FTIR spectroscopy on board an aircraft (A-FTIR) for measurements of smoke from North Carolina fire plumes. Smoke was drawn into a White cell (with a total pathlength of 97.5 m) and exchanged every 7–8 seconds, giving a spatial accuracy of ~700 m. Yokelson *et al.* (1999) operated A-FTIR in conjunction with conventional analysers for CO_2, H_2O, CO, NO and O_3. A-FTIR enabled a rare quantification of OVOCs, including formaldehyde, methanol, acetic acied and formic acid, as well as ammonia. Yokelson *et al.* (1999) confirmed the findings of laboratory studies that biomass burning was an important source of OVOCs, re-emphasising the ozone and hydroxyl forming potential of these gases. Subsequent deployments of A-FTIR were undertaken by Goode *et al.* (2000) for Alaskan boreal forest fires, Yokelson *et al.* (2003) for African savanna fires and Yokelson *et al.* (2007) for tropical forests in Brazil.

Building on the work by Yokelson *et al.* (1999), Goode *et al.* (2000) also found high emissions of OVOCs and found a close relationship between these species and mass combustion efficiency (MCE), with emissions decreasing with increasing efficiency (also seen by Yokelson *et al.* [2003] and Yokelson *et al.* [2007]), suggesting that MCE could be used as a proxy for these emissions in studies that have not measured OVOCs

(i.e. studies that have not used A-FTIR). By studying smoke of different ages, these studies found noticeable increases in the ΔO3/ΔCO ratio as the plume aged, one of the predicted consequences of large emissions of OVOCs. Yokelson *et al.* (2003) found that minutes-old smoke had a negative excess ozone, implying the destruction of ambient ozone by NO and HO_2 in the plume; however, downwind, in smoke with ages 30–60 minutes, ΔO3/ΔCO increased to as much as 9%.

Most recent developments in airborne monitoring of biomass emissions have been in the quantification of previously undetected NMVOC species. Shirai *et al.* (2003) and Sinha *et al.* (2003) publish emission factors for a suite of previously undetected NMVOCs. However, by 2007, Yokelson *et al.* (2007) estimated that only ~70% of the NMVOC emissions had been quantified, stressing the need for improvement in the speciation and quantification of the remaining emissions. A summary of emission factors derived from laboratory studies since Andreae and Merlet (2001) is presented in Table 2.2 at the end of Section 2.4.

2.4.4 Spaceborne measurements of gaseous emissions from biomass burning

The earliest detection of gaseous emissions from biomass burning by spaceborne observations was by the Measurement of Air Pollution from Satellites (MAPS) instrument on board NASA space shuttle flights (Reichle *et al.*, 1986) which detected elevated levels of atmospheric CO in November 1981. It was not until December 1999, however, that the Measurements of Pollution In The Troposphere (MOPITT) instrument, on board NASA's Terra satellite, was launched, providing the first global coverage of CO monitoring (Figure 2.6). MOPITT consists of a multispectral thermal radiometer which is used to measure absorption of emitted terrestrial infrared radiation by CO and absorption of reflected solar radiation by CO and CH_4. On board gas cells containing CO and CH_4 are used to calibrate the instrument's detector.

A number of studies have used MOPITT to detect enhanced atmospheric CO due to biomass burning in a number of regions around the world, including Africa and South America (Bremer *et al.*, 2004) and North America (Lamarque *et al.*, 2003; Liu *et al.*, 2004). Liu *et al.* (2005) showed that enhanced CO could be correlated with AVHRR

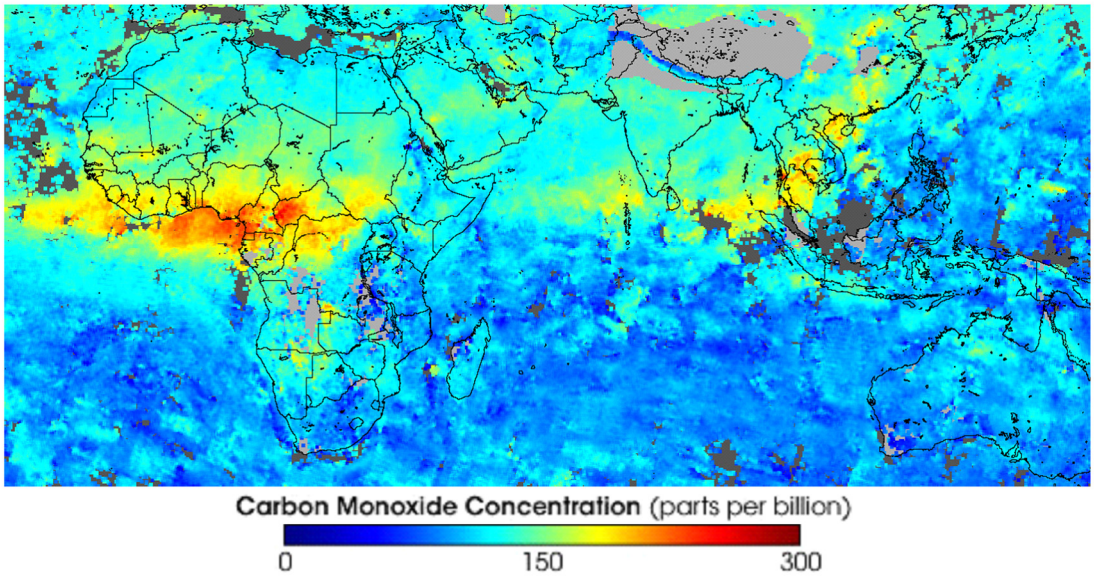

Figure 2.6 MOPITT observations of concentrations of carbon monoxide (CO) at 700 millibars (roughly 2–3 km altitude) averaged over 2–12 December 2004. High concentrations of CO (colour coded in red) are seen over the biomass burning regions of central Africa and southeast Asia, but the CO also spreads out over nearby oceans. Regions where no data are collected either due to clouds or high surface elevation (such as over the Himalayas) are coloured in grey.

"hotspot" fire detections, implying that total CO emission from fires could be estimated using MOPITT data alone, although also suggesting that estimates from MOPITT could be used as a constraint for other methods. One major disadvantage of the MOPITT instrument is its low sensitivity to CO in the boundary layer (Liu *et al.*, 2005) due to the averaging kernels that result from the CO retrieval process (Deeter *et al.*, 2003). Whilst the frequent measurement (~10 times per month) allows temporal and spatial variations of CO to be observed, a revisit time of 2–3 days and the inability to make measurements in cloud-affected pixels means that MOPITT frequently misses small scale fires. Furthermore, Liu *et al.* (2005) also show that fires need to be large (0.25° x 0.25°) for a measurable enhancement in CO to be detected. Nevertheless, despite these limitations, studies such as Turquety *et al.* (2007) have used MOPITT as an evaluation tool for assessing bottom-up models of regional scale CO emissions based on burned area methods.

Another instrument used for CO atmospheric concentration estimates is the Atmospheric Infrared Sounder (AIRS). AIRS is a high spectral resolution thermal spectrometer primarily used for temperature and humidity profiling, but its high spectral

resolution can be used to measure the absorption of terrestrial infrared radiation by certain gas species. Unlike MOPITT, AIRS has an almost daily repeat visit frequency, sampling 70% of the earth's surface every day (100% daily coverage between 45° and 80° latitude). The instrument has a 45 km field-of-view at nadir, limiting observations to large plumes in relation to biomass burning research. Yurganov *et al.* (2008) performed a comprehensive evaluation of MOPITT and AIRS retrievals of elevated CO concentrations for two regions of the world affected by biomass burning (Siberia and south-eastern Australia). In their study, Yurganov *et al.* (2008) compared MOPITT and AIRS total column CO measurements with those from a network of ground-based sun-viewing FTIR spectrometers. Their findings found that MOPITT insensitivity to CO was most profound for winter burns at higher latitudes (where the boundary layer is relatively small), with insensitivity greatest at night; the nocturnal insensitivity was also observed in the summer observations. MOPITT appears to be more accurate at lower latitudes. AIRS data (version 4) agreed qualitatively with MOPITT and ground-based observations, but 20–40% biases were found for some regions and the authors suggest that version 5 data will be more precise. In an attempt to quantify total carbon emissions (by using CO_2 and CH_4 emission ratios to CO), Yurganov *et al.* (2008) find that their top-down estimates for both CO and C are far higher (up to a factor of 2, or 150 Tg CO/a) than those from bottom-up calculations using burnt area datasets combined with fuel consumption per unit area estimates and trace gas emission factors.

Monitoring carbon dioxide emissions from biomass burning using total column measurements (either from space or using SO-FTIR) is confounded by the high ambient concentrations of the gas. Very few studies have identified enhanced CO_2 emissions signatures from space. One such study (Rajab *et al.*, 2009) used AIRS data from mega biomass fires in Indonesia 2005, where enhanced CO_2 mixing ratios were in the order of 2–4 ppm. The successful launch of the Greenhouse gases Observing SATellite (GOSAT) and the planned re-launch of the orbiting carbon observatory (OCO) should improve our future understanding of CO_2 and CH_4 emissions from biomass burning, though these systems have some difficulties in performing retrievals in the presence of enhanced aerosols, such as would be expected in biomass burning smoke.

Since 2005, a suite of spaceborne atmospheric chemistry satellite instruments have been launched. These include the the infrared Atmospheric Chemistry Experiment – Fourier Transform Spectrometer (ACE-FTS) and the Infrared Atmospheric Sounding Interferometer (IASI). ACE-FTS performs solar occultation FTIR measurements of the atmosphere measuring up to fifteen sunrises and sunsets each day using a high spectral resolution (0.02 cm^{-1}) FTIR spectrometer (Bernath *et al.*, 2005). Coheur *et al.* (2007) report the first use of ACE-FTS to detect emissions of ethylene, formaldehyde, acetone and PAN from biomass burning (previously undetected using this instrument). The measurements of a plume emanating from the east coast of Tanzania showed elevated mixing ratios for these NMVOC species, along with other biomass burning products (including CO, hydrogen cyanide, ethane and ethyne). Emission ratios calculated with respect to CO were comparable with those published by Yokelson *et al.* (2003) for African savanna regions.

IASI uses a lower spectral resolution FTIR spectrometer (0.5 cm^{-1}), with its primary objective to improve weather forecasts by providing detailed atmospheric profiles of temperature (derived from the pressure broadening of CO_2 absorption lines) and humidity (from the H_2O absorption lines). Coheur *et al.* (2009) have shown that IASI is also useful for measuring total column amounts of biomass burning emissions. In a case study of emissions from fires in Southern Siberia, Coheur *et al.* (2009) quantify total column amounts of ammonia, ethylene and a number of OVOCs yielding emission ratios for these species. Furthermore, the high temporal resolution enabled a study of the ageing of the plume, showing decreases in the ratios of reactive species NH_3, CH_3OH and C_2H_4 to CO with time, demonstrating IASI as a valuable tool in evaluating the global importance of these short-lived biomass emissions and as a tool for investigating plume 'ageing'. Although the relatively high spatial resolution (compared to other atmospheric sensors) of IASI (12 km) presents a potential for detection of relatively smaller fire plumes, the instrument has a poor temporal resolution, with a repeat cycle of 29 days (Clerbaux *et al.*, 2009). The temporal coverage will however improve with the planned launches of two more IASI instruments in 2012 and 2016 if each instrument remains in working order.

Table 2.2 Emission factors published in Akagi et al. (2011) for pyrogenic species emitted from boreal forests, tropical forests and savanna. A selection of individual studies using a variety of methodologies is also presented. See below the table for a key to each study and measurement type.

Fuel type		Boreal		Tropical				Savanna									
Study		**Ak11***	Be03	**Ak11***	Ch03	Yo08	Yo07	**Ak11***	Hu94	Be03	Ke06	Yo03	Sh03	Si03	Pw05	Wo11	Co07
Measurement type		*Mix*	*Lab*	*Mix*	*Lab*	*Lab*	*Air*	*Mix*	*Air*	*Lab*	*Lab*	*Air*	*Air*	*Air*	*SO*	*OP*	*Spa*
Carbon dioxide	CO_2	**1489 (121)**	1548	**1643 (58)**	1509	1677	1615	**1686 (38)**	1595	1685	1616	1703	1613	1700	nr	1675	nr
Carbon monoxide	CO	**127 (45)**	100	**93 (27)**	137	57	101	**63 (17)**	91	78	77	72	88	68	nr	94	nr
Methane	CH_4	**5.96 (3.14)**	5.90	**5.07 (1.98)**	7.46	1.83	5.68	**1.94 (0.85)**	2.33	3.60	nr	2.19	2.22	1.70	nr	2.50	nr
Ammonia	NH_3	**2.72 (2.32)**	4.78	**1.33 (1.21)**	5.47	3.39	1.08	**0.52 (0.35)**	0.52	0.55	0.52	0.28	nr	0.26	0.62	0.44	0.01
Acetic acid	CH_3COOH	**4.41 (2.66)**	2.52	**3.05 (0.90)**	8.05	2.84	3.43	**3.55 (1.47)**	Nr	2.81	2.14	2.42	nr	2.40	nr	nr	nr
Methanol	CH_3OH	**2.82 (1.62)**	1.37	**2.43 (0.80)**	3.79	2.23	2.57	**1.18 (0.41)**	Nr	1.74	nr	1.17	nr	1.20	2.30	nr	1.58
Ethylene	C_2H_4	**1.42 (0.43)**	1.47	**1.06 (0.37)**	1.82	1.83	0.95	**0.82 (0.35)**	0.67	0.95	nr	1.19	0.31	0.64	0.61	nr	0.05
Formaldehyde	CH_2O	**1.86 (1.26)**	1.17	**1.73 (1.22)**	1.90	0.66	1.66	**0.73 (0.62)**	0.25	1.02	nr	1.06	nr	1.10	2.60	1.80	0.07
Nitrogen oxides	NO_x	**0.90 (0.69)**	0.80	**2.55 (1.40)**	1.17	0.82	0.74	**3.90 (0.80)**	1.60	3.20	1.57	3.37	nr	3.30	nr	nr	nr
Formic acid	HCOOH	**0.54 (0.47)**	0.67	**0.79 (0.66)**	0.87	0.58	0.59	**0.21 (0.10)**	nr	0.63	0.20	0.62	nr	0.62	3.70	nr	0.54
Acetylene	C_2H_2	**0.18 (0.10)**	0.12	**0.44 (0.35)**	0.31	0.33	0.28	**0.24 (0.10)**	0.06	0.22	nr	0.26	0.24	0.22	0.34	nr	0.13
Ethane	C_2H_6	**1.79 (1.14)**	1.69	**0.71 (0.28)**	nr	nr	0.95	**0.66 (0.41)**	nr	0.44	nr	nr	0.53	0.21	0.26	nr	0.41

Study:

AM01	Andreae and Merlet (2001)
Be03	Bertschi *et al.* (2003a)
Ch03	Christian *et al.* (2003)
Yo07	Yokelson *et al.* (2007)
Yo08	Yokelson *et al.* (2008)
Hu94	Hurst *et al.* (1994b)
Ke06	Keane *et al.* (2006)
Yo03	Yokelson *et al.* (2003)
Sh03	Shirai *et al.* (2003)
Si03	Sinha *et al.* (2003)
Pw05	Paton-Walsh *et al.* (2005)
Wo11	Wooster et al. (2011)
Co07	Coheur *et al.* (2007)

Measurement type:

Lab	Laboratory measurements
Air	Airborne measurements
SO	Solar occultation FTIR
OP	Open-path FTIR
Spa	Space

*Emission factors from Akagi et al. (2011) are shown with an estimate of the natural variation in parantheses. The variability of emissions is calculated from the variety of published emission factors for a particular ecosystem.

2.5 Calculating biomass burning emissions totals

Many Earth systems science applications require an accurate understanding of global biomass burning emissions for the reasons outlined in Sect. 1.1. To achieve this understanding, it is necessary to estimate the total mass of material burned and released into the atmosphere through biomass combustion, and the relative proportions of its chemical constituents. Whilst some progress has been made recently in achieving this goal via inversion of top-down satellite measurements of atmospheric trace gases, the current state of space technology can, more readily, deliver qualitative constraints useful for comparison to bottom-up emissions modelling. The recently launched GOSAT and future missions, including OCO2, should help to refine these top-down constraints, yet accurate estimates of gas species emissions (particularly the rarer gases) are not likely to be fully quantified by top-down methods in the near future. Bottom-up methods appear likely to be to the fore for some time to come.

Conventional calculation of gaseous emissions totals, for any given biome, is based on the conceptually simple approach adopted by Seiler and Crutzen (1980), where trace gas releases are calculated using measurements and estimates of the individual components that contribute to the total amount of biomass burned, and the amount of gas emitted per unit of burned biomass. In this scheme, the total emissions of gas species x (E_x) can be approximated by the equation:

$$E_x = A \times B \times \alpha \times \beta \times EF_x \tag{2.13}$$

Where A is the annual burnt area (m^2 $year^{-1}$), B is the mass of organic matter per unit area (g m^{-2}), α is the fraction of the mass of organic matter that is above the surface and available to burn, β is the burning efficiency of the above ground organic matter (sometimes called the combustion completeness, and which represents the proportion of the available fuel that actually burns), and EF_x is the mass of gas species x released per unit burnt biomass (g kg^{-1}).

Generally, values are assigned to the above ground biomass density, burning efficiency and emission factor parameters based upon a classification of ecosystem or vegetation type. Values are drawn from databases, such as the Global Fire Emissions Database or

tables in other published literature (e.g. Andreae and Merlet, 2001). As estimates of burned area have improved via better satellite-derived products (Giglio *et al.*, 2010), focus has in part turned to improving the representativeness of the fuel consumption per unit area (van der Werf *et al.*, 2006) and the emission factors. Section 2.4 focuses on the development of emission factors for different vegetation types whilst Section 2.5.1 gives a brief review of how burnt area is estimated from satellite observations. Section 2.5.2 reviews some recent estimates of regional and global applications of emissions modelling, whilst Section 2.5.3 focuses on recent advances in modelling plume dispersion and chemistry, primarily for the purpose of air quality forecasting.

2.5.1 Estimating burned area from space

There are two main approaches to estimating burnt area using satellite observations. The first approach is the active fire method, whereby fires are detected by their thermal emission in the infrared bands of geostationary or polar-orbiting satellite sensors (e.g. Prins and Menzel, 1992). The alternative is a method by which fires are detected via the change in the land surface characteristics that occurs following a fire (i.e. the spectral reflectance difference between pre-fire vegetation and burned land) (e.g. Roy *et al.*, 1999).

Active fire detection has been shown to be possible from many satellite platforms. Fires are often much smaller than the pixel area of many of the Earth Observation (EO) instruments used (e.g. AVHRR and MODIS), but a technique for subpixel hotspot detection (and estimation of the effective size and temperature of actively burning fires) was first suggested by Matson and Dozier (1981). Generally, this technique involves identifying pixels that show a significant increase in infrared radiance over the neighbouring areas background radiance and/or a significant brightness temperature difference between the widely spaced IR channels (commonly the mid-wave IR 3-5 μm and the long-wave 8-14 μm spectral bands). Only a small area within the pixel needs to be burning, as the high temperature of combustion is sufficient to raise the average temperature of the pixel by many degrees Kelvin, even for fires covering <1% of a pixel (Matson and Dozier, 1981). The minimum absolute area for a fire to be detected is controlled by the spatial resolution of the instrument, the temperature of the fire and the

detection algorithm used. The other limiting factor is the point at which a fire saturates the detector (from which only a minimum estimate of actively burning area can be ascertained).

The popularity of active fire detection methods is reflected by the number of operational products derived from data of numerous geostationary and polar-orbiting satellite sensors. For geostationary satellites, active fire detection algorithms have been developed for GOES (Prins and Menzel, 1992) and the Spinning Enhanced Visible and Infrared Imager (SEVIRI) (Roberts and Wooster, 2007). For polar orbiting satellites, active fire detection algorithms have been developed for the Advanced Very High Resolution Radiometer (Justice *et al.*, 1996; Z. Li *et al.*, 2000b), the Along-Track Scanning Radiometer (ATSR and AATSR) (Arino and Rosaz, 1999); the Moderate Resolution Imaging Spectroradiometer (MODIS) (Kaufman *et al.*, 1998; Justice *et al.*, 2002; Giglio *et al.*, 2003) and the Advanced Spaceborne Thermal Emission and Reflection Radiometer (ASTER) (Giglio *et al.*, 2008). Whilst ASTER's low temporal resolution does not really permit burned area estimates to be derived from active fire detections, the high spatial resolution (30 m) can be useful as an evaluation tool for the lower spatial resolution instruments. Morisette *et al.* (2005) and Schroeder *et al.* (2008) both use ASTER to evaluate GOES and MODIS fire detection. One issue with using active fire detections to estimate burned area is that a pixel is only detected as having been burned if it is observed to have an active fire within it during the satellite observation (unless some form of inter-image interpolation is used) (Giglio *et al.*, 2010). This means some areas may have been burned in reality, but will remain unclassified as burned since the sensor did not observe them when the fire front was located within those particular pixels.

The Bi-directional Reflectance Distribution Function (BRDF) method relies on a sudden decrease in reflectance from a surface following a fire (Roy *et al.*, 1999). For a given day, the technique compares the reflectance of a surface with that from previous days and that predicted for the current day (depending on sun elevation angle). If a sudden decrease in reflectance is observed, and is shown to persist for the days following the initial decrease, a burned area pixel may be classified. This method, together with other methods based upon surface reflectance change, have been adapted for operational

detection of burned areas from MODIS data (Roy *et al.*, 2002; Justice *et al.*, 2002) and data from the vegetation sensor on board the Satellite Pour l'Observation de la Terre (SPOT VEGETATION) (Tansey *et al.*, 2004). Evaluation of these methods has also been performed using the Landsat Thematic Mapper (Tansey *et al.*, 2007).

Direct "burned area" detection methods do suffer from different size/saturation issues to the active fire approaches, sometimes allowing the mapping of burned areas that were too small or too large for the active fire detection method. However, they can significantly underestimate burned area in regions where low intensity fires burn underneath a tree canopy (common in wooded savanna areas or tropical rainforests) and some smaller burns are missed as sub-pixel detections are not possible with methods based on spectral reflectance measurements. Whilst the latest burned area products offer spatial resolution of up to 500 m (Roy *et al.*, 2008), there are large differences between the burned area method and active fire methods. Therefore, efforts have been made to merge these two techniques to create a multi-method approach for estimating burned area (e.g. Fraser *et al.*, 2000; Giglio *et al.*, 2010; Roberts *et al.*, 2011). The most recent Global Fire Emissions Database (GFED3), used for estimating total trace gas and aerosol emissions, estimates that global annual burned area for the period 1997–2008 varied between 330 and 431 Mha (3.3–4.3 million km^2, see Figure 2.7), with a maximum occurring in 1998 (Giglio *et al.*, 2010).

So far, this section has described the advances that have been made in reducing uncertainty in the burned area parameter of the Seiler and Crutzen (1980) emissions model. Whilst knowledge of this parameter (and of emission factors) has improved markedly over the past twenty years thanks to remote sensing, a remote sensing-based parameterisation of the parameters relating to fuel density and combustion completeness is largely lacking, with most studies relying upon uncertain land cover classifications, fuel moisture estimation and look-up tables for these values (e.g. Chang and Song, 2010) or some form of model-based methodology (e.g. van der Werf *et al.*, 2006).

A novel alternative to estimating total fuel consumption is to measure a parameter believed to be directly related to biomass consumption, namely, the remotely sensed Fire Radiative Energy (FRE) (Wooster *et al.*, 2003, 2005). Wooster *et al.* (2005) found that the Fire Radiative Power (FRP), measured using both a field spectroradiometer and

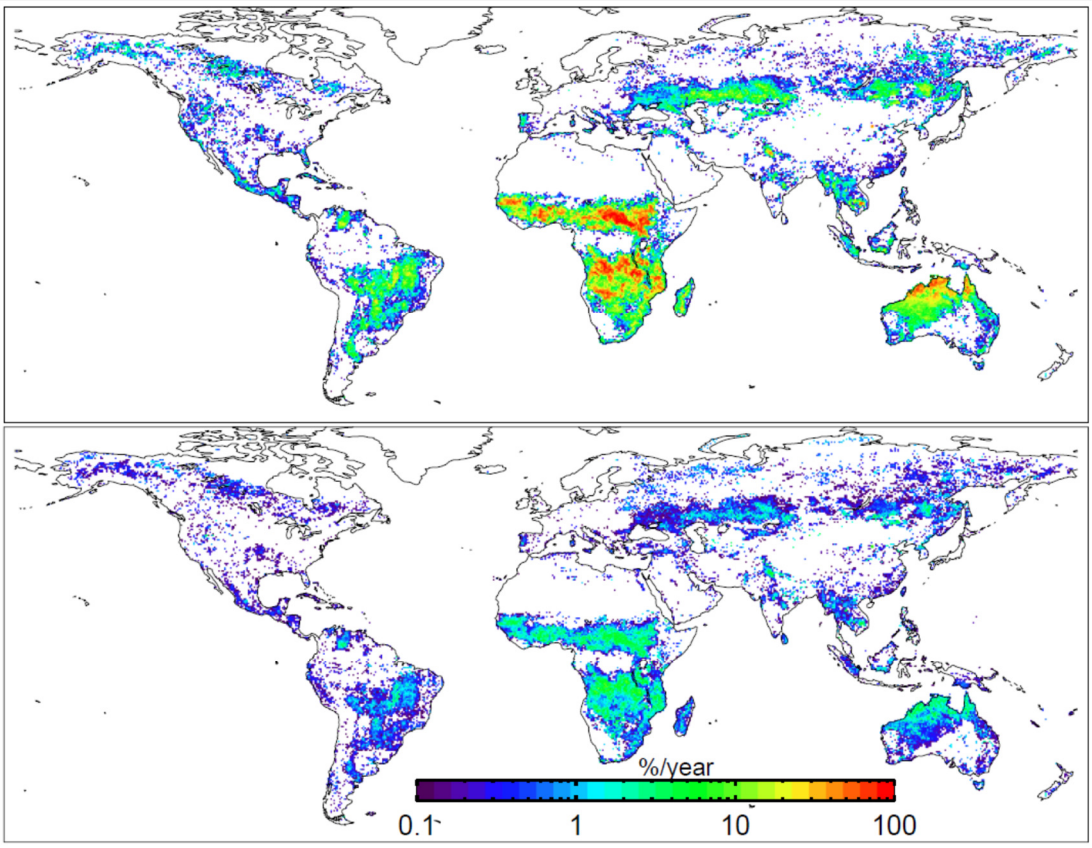

Figure 2.7 Taken from Giglio *et al.* (2010). 1997-2008 mean annual burned area (top) used in the Global Fire Emissions Database (GFED3), and associated one-sigma uncertainties (bottom), expressed as the fraction of each grid cell that burns each year.

a middle-infrared thermal imaging camera, was linearly related to the biomass loss rate during experimental fires; measurements of FRE (FRP integrated over time) can therefore be used to estimate the total biomass combusted in a fire. Given that not all of the theoretical heat yield is released radiatively, an FRE combustion factor (CF) is required to convert FRE measured at the sensor to an estimate of biomass that was burned in order to produce this radiative heat. This approach eliminates the need to estimate above ground fuel density and combustion completeness (B, A and β in Equation 2.5), simplifying the emissions model, so that emissions of gas species x (E_x) require only the remotely sensed FRE and an emissions factor (EF_x), should the value of CF be known:

$$E_x = FRE \times CF \times EF_x \tag{2.14}$$

According to Wooster *et al.* (2005) and Freeborn *et al.* (2009), *CF* thus far appears relatively constant across vegetation types.

2.5.2 Total emissions modelling

Early approaches to estimating global fire emissions relied upon estimates of biome-averaged fuel loads, fire frequency (e.g. for savanna and forest fires) and estimates of population density, along with clearing rates to estimate deforestation (Seiler and Crutzen, 1980; Crutzen and Andreae, 1990). Using these bottom-up estimates of biomass consumption with emission factors (e.g. Crutzen *et al.*, 1979), Seiler and Crutzen (1980) estimated global emissions of carbon from biomass burning to be around 1.7–3.5 Pg C $year^{-1}$, with agricultural burning as the main source of emissions (62%). Crutzen and Andreae (1990) estimated greater emissions (2–5 Pg C $year^{-1}$) with a greater contribution from deforestation and savanna burning.

With the improvement in burned area estimation thanks to improved satellite remote sensing algorithms and products (Section 2.4.1), the development of biogeochemical or dedicated fuel load models, such as Deforestation Carbon Fluxes (DECAF; de Fries *et al.*, 2008) and the Global Fire Emissions Database (GFEDv3; van der Werf *et al.*, 2010), and better emission factor estimation (Section 2.4), a number of studies have combined this information to estimate global emissions (Hoelzemann *et al.*, 2004; van der Werf *et al.*, 2006; van der Werf *et al.*, 2010), with these studies suggesting a total carbon loss due to biomass burning of between 1–3 Pg C $year^{-1}$. Some studies have concentrated on regional emissions, for example, tropical Asia (Chang and Song, 2010) and Amazonia (de Fries *et al.*, 2008), to evaluate different methodologies. Chang and Song (2010) calculated gaseous and aerosol emissions using two burned area datasets (from SPOT VEGETATION and MODIS), finding good agreement between the products, and estimating carbon emissions of between 113–168 Tg C $year^{-1}$ for tropical Asian biomass burning. De Fries *et al.* (2008) compare two biogeochemical modelling approaches (DECAF and GFEDv2) to estimating emissions from southern Amazonia caused by deforestation. Whilst DECAF estimates combustion completeness for deforested areas using satellite measurements of post-clearing fire frequency and post-clearing land use, attributing post-deforestation emissions to the original deforestation,

GFED assumes that all emissions occur at the time of initial deforestation. Consequently, estimations of emissions from deforestation vary considerably between the two methods, with DECAF attributing ~40% more emissions to deforestation (de Fries *et al.*, 2008). When all land uses are considered, total emissions agree well between the two methods (~90 Tg C $year^{-1}$).

The latest version of GFED (version 3; van der Werf *et al.*, 2010) states that the largest contributor to global fire emissions were from biomass burning in grasslands and savannas (60% when savanna woodland is included). 23% of fire carbon emissions stem from tropical deforestation, degradation and from tropical peat fires, whilst a further 15% is emitted from temperate and boreal forest fires (Figure 2.8). Van der Werf *et al.* (2010) also note that while Africa was by far the largest source of pyrogenic CO_2, emissions of gases associated with lower combustion efficiency such as CO and CH_4 in tropical America and tropical Asia were almost as high due to higher amounts of these reduced trace gases emitted per unit biomass combusted (i.e. greater emission factors) (Figure 2.9)

Pereira *et al.* (2009) present promising results for measuring biomass burning emissions using the bottom-up FRE-based method. By comparing satellite measures of FRP from GOES and MODIS with measures of Aerosol Optical Depth (AOD), Pereira *et al.* (2009) confirm the findings of earlier experimentally-based studies (e.g. Wooster *et al.*, 2005; Freeborn *et al.*, 2008) in that most fire-released energy is lost to convection and conduction. Nevertheless, radiative losses are highly detectable by satellite remote sensing, though Pereira *et al.* (2009) find poor agreement between the FRP measured by the two satellites (GOES overestimated MODIS by a factor of ~3). This disagreement is not, however, found by Xu *et al.* (2010). Pereira *et al.* (2009) find a significant correlation between FRE release rate and smoke emission rate calculated using AOD, potentially paving the way to calculate gaseous emissions using ratios between different gases and particulate matter. Routine calculation of total emissions using satellite-derived FRP data is now operational (Kaiser *et al.*, 2012).

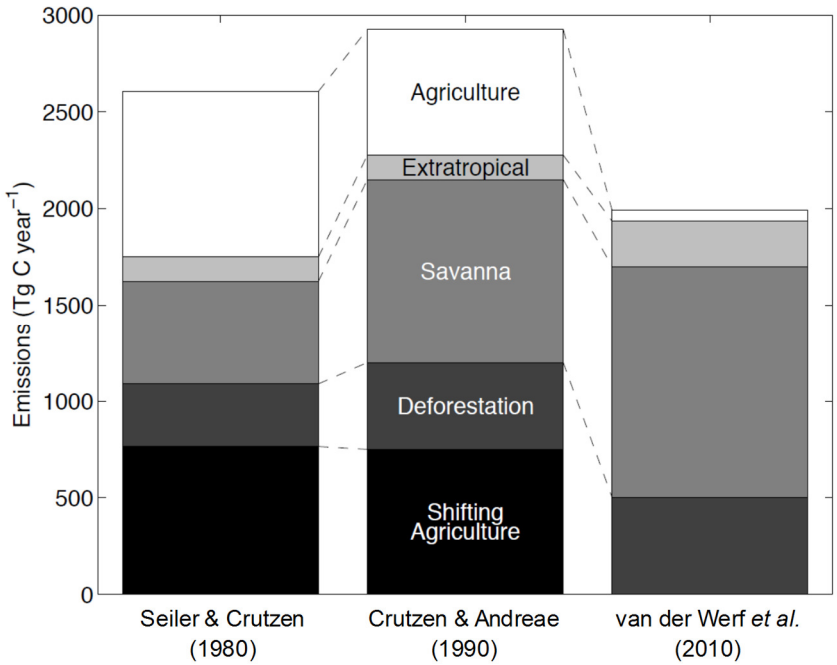

Figure 2.8 Modified from van der Werf *et al.* (2010). Partitioning of total fire carbon emissions according to Seiler and Crutzen (1980), Crutzen and Andreae (1990), and van der Werf *et al.* (2010). Van der Werf *et al.* (2010) did not separate emissions from shifting agriculture from other types of deforestation, their deforestation class includes all fire types in tropical forest regions (including tropical peat burning).

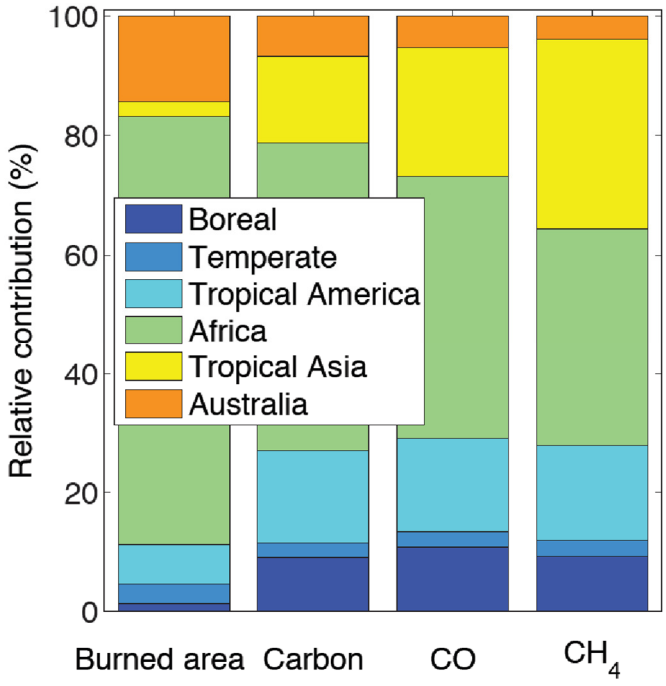

Figure 2.9 Taken from van der Werf *et al.* (2010). Relative contribution (%) from different regions to 1997–2009 average global total burned area and fire emissions of carbon, CO, and CH_4.

2.5.3 Modelling plume release and dispersion

Bottom-up modelling of biomass burning plumes involves the calculation of hourly/daily emissions inventories of gases or aerosols using Eq. 2.5, before implementing these calculated fluxes in a regional/global chemical transport model (CTM). Turquety *et al.* (2007) use daily estimates of burned area and fuel consumption along with emission factors to construct their emissions inventory at a spatial resolution of 1° × 1°. This inventory is then fed to the GEOS-Chem CTM which is used to model the smoke dispersion. To evaluate their model, Turquety *et al.* (2007) compare the model output with MOPITT retrievals of CO, generally finding good agreement between model and satellite observations (although MOPITT is known to underestimate CO at high latitudes, and this is reflected by poor agreement in this study).

Most recent advances in modelling plume dispersion have come from studies that have used an FRP approach to construct emissions inventories (eliminating the need for estimates of burned area and fuel consumption), giving rise to the potential for real-time forecasting of plumes since FRP observations can be made in almost real time. Kaiser *et al.* (2008), Kaiser *et al.* (2009), Kaiser *et al.* (2012), Sofiev *et al.* (2008) and Sofiev *et al.* (2009) and Pereira *et al.* (2009) use FRP to construct emissions inventories for use in chemical transport modelling. Kaiser *et al.* (2012) derive combustion rate (kg s m^{-2}) by scaling FRP (W m^{-2}) measured by MODIS and SEVIRI using the empirical combustion factor quoted in Wooster *et al.* (2005). Using published CO emission factors, Kaiser *et al.* (2012) estimate hourly CO emissions and uses these to drive the global GEMS reactive gas model to produce a 72 hour forecast of pyrogenic CO. Sofiev *et al.* (2009) are primarily concerned with modelling aerosol dispersion, using both an FRP and a "brightness temperature anomaly" method to derive an emissions flux for $PM_{2.5}$ and total PM. PM emissions fluxes are calculated by multiplying the 4 μm brightness temperature anomaly or the FRP by empirical conversion factors (as in Kaiser *et al.*, 2008). The emissions fluxes were used to drive the SILAM CTM and the resultant modelled plumes compared with MODIS AOD and ground-based observations. Sofiev *et al.* (2009) found that the combustion factors used to convert the temperature anomaly and FRP data to emissions of PM needed to be increased by a factor of 2–3 to fit the

observations, stressing the need for a better understanding of these combustion factors and a better evaluation of injection heights.

Pereira *et al.* (2009) calculate their own combustion factors for converting between FRE release rate and 'smoke' emission rate using GOES observations of enhanced AOD. By assigning emission factors to $PM_{2.5}$ and CO using the smoke emission rate, Pereira *et al.* (2009) model plumes of $PM_{2.5}$ and CO using a CTM for South America. A comparison with ground observations showed a very good relationship between the modelled and observed concentrations of both $PM_{2.5}$ and CO.

2.6 Summary and specific research questions

This review of gas measurement techniques illustrates the diversity of information available to those interested in modelling biomass burning emissions. The suite of measurement platforms and sampling approaches has vastly expanded trace gas speciation within biomass burning plumes, but, ultimately, each method measures something slightly different. While airborne sampling of smoke plumes are reported to reliably capture the lofted plumes from large fires (Andreae and Merlet, 2001), aircraft measurements are subject to the effects of spatial and temporal plume ageing heterogeneities, particularly for reactive trace gas species such as NMVOCs and NH_3, and are known to under-sample emissions from smouldering combustion that do not have the energy to be lofted into an airborne plume (Guyon *et al.*, 2005). Perhaps most importantly, airborne campaigns are expensive and require a great deal of planning and human resources. Conventional ground-based alternatives to aircraft measurements such as *in situ* sampling are similarly compromised by plume heterogeneities, requiring many samples to account for heterogeneous fuel arrangements (e.g. Hurst *et al.*, 1994); furthermore, if the ground samples are stored and analysed later, it is necessary to account for both ageing of the smoke within the container as well as adsorption of some trace gas species to the container walls (Christian *et al.*, 2003b). Finally, *in situ* sampling cannot be made at very intense fires (e.g. crowning forest fires) leading to claims that ground-based *in situ* sampling is biased towards smouldering emissions, under-sampling emissions from flaming combustion (Andreae and Merlet, 2001).

Careful interpretation of data collected from these various techniques is required to ensure the accurate characterisation of 'fire-averaged' emissions (Akagi *et al.*, 2011). Beyond these complications are the factors that lead to the natural variability of emissions (e.g. interactions between meterology, seasonality and combustion efficiency). As the recent study by Van Leeuwan and van der Werf (2011) shows, within-biome temporal and spatial variations in emission factors are substantial, and despite their attempts to explain these using relationships between emission factors and a number of environmental variables (tree cover density, vegetation greenness, temperature, precipitation, length of dry season), correlations between CO, CH_4 and CO_2 EFs, and MCE, were rather low, with environmental variables explaining 33%, 38%, 19%, and 34% of the variation in the reported emissions metrics. Van Leeuwen and van der Werf (2011) posit some potential explanations for the poor explanation of within-biome variability, including different measurement techniques for EFs, assumptions used to weight EFs by the amount of flaming and smouldering combustion and uncertainties in the environmental variables themselves. Explaining the large natural variability of EFs that is so pronounced in the findings of Akagi *et al.* (2011; Table 2.2) remains one of the biggest challenges for biomass burning emissions science.

It is the pursuit of this goal that forms the overall aim of this thesis. If progress is to be made towards this end, Van Leeuwen and van der Werf (2011) argue that future measurement campaigns would be more beneficial to the global modelling community if they were made over the full fire season, and paid more attention to ambient conditions. In spite of the gargantuan cost of a lengthy airborne campaign, an aircraft approach would also require ground truthing to link the emissions measurements with environmental variables influencing fires on the ground (which would be further complicated by the mixing of smoke if multiple fires were present on the ground). Instead, it is likely that a ground-based approach is needed.

As briefly reviewed above, long open-path FTIR spectroscopy provides a ground-based approach that overcomes many of the issues faced by conventional *in situ* sampling:

(a) OP-FTIR can be used to detect and quantify a wide range of gases simultaneously, without relying on a multitude of sampling devices and analysis techniques. Simultaneous measurement of multiple trace gases is important for

monitoring variations in gas ratios, a key metric in the study of biomass burning emissions.

(b) OP-FTIR can operate passively *in situ*, eliminating contamination and adsorption associated with tubing and sample containers.

(c) OP-FTIR can provide high temporal resolution (seconds) mixing ratio measurements for each measurable trace gas species.

(d) OP-FTIR provides path-integrated gas concentrations, less prone to artefacts that can occur using point-based sampling. This also means that smoke from different stages of biomass burning (i.e. flaming and smouldering emissions) can mix, so that 'fire-averaged' emission ratios ad emission factors can possibly be established without the need for knowledge of the relative amount of fuel consumed in each stage of combustion.

Despite offering many advantages over conventional sampling, the ground-based nature of the measurements suggests that the results might over-represent low-intensity smouldering emissions (Griffith *et al.*, 2001; Andreae and Merlet, 2001). This assertion is largely untested due to a lack of studies comparing ground-based measurements with those of the lofted plume (with the exception of Burling *et al.*, 2011). This is an area that will need to be addressed by this thesis if OP-FTIR is to be established as a method for making representative biomass burning emissions measurements.

The remainder of this thesis is focussed on the investigation of "long-path" OP-FTIR (i.e. using a pathlength of tens or hundreds of metres) for the purpose of measuring emissions from biomass burning. The early demonstration of this method by Griffith *et al.* (1991) and the more recent application of the method to fires in South Africa (Wooster *et al.*, 2011) indicate that the method has great potential to advance understanding of biomass burning emissions. Thanks to the reduction in size and cost of OP-FTIR equipment, and the availability of mechanically cooled detectors (rather than detectors cooled by liquid nitrogen), the method provides an opportunity to rapidly sample numerous fires at remote locations and is thus well-suited to measuring the variability of emission factors at multiple fires – the overall aim of this thesis. Towards this aim, this thesis addresses a number of specific objectives through the following research questions:

1. Can OP-FTIR spectroscopy be used to yield accurate and precise measurements of important biomass burning trace gas species spanning the full range of concentrations that might be experienced in field measurements? (addressed in Chapters 4 and 7)
2. Can ground-based OP-FTIR be used to make representative measurements of biomass burning emissions so that 'fire-averaged' emission factors can be ascertained (i.e. are ground-based OP-FTIR measurements biased towards either flaming or smouldering emissions)? (addressed in Chapters 5–7)
3. By making numerous measurements of different fires within a particular ecosystem at different times of the year, can OP-FTIR yield information on the controls of the natural variability of emissions? (addressed in Chapter 5)

These research questions are expanded further in the following Chapters. Before addressing the accuracy and precision of OP-FTIR, this thesis proceeds to present a detailed overview of the technique, methodologies for retrieving trace gas information from measurements, and how the technique might be applied to biomass burning research.

3

Open-Path FTIR Spectroscopy: Fundamentals and Technical Aspects

Whilst the application of compact, field-rugged FTIR spectrometers using long open-paths for studying fire emissions is relatively new (e.g. Wooster *et al.*, 2011), open-path spectroscopic techniques have been used in other fields of atmospheric monitoring for some decades (e.g. Herget and Brasher, 1979; Schafer *et al.*, 1995; Childers *et al.*, 2001; Grutter, 2003). This Chapter introduces this technique in detail, covering the fundamentals of infrared spectroscopy and the open-path FTIR technique in general, before addressing particular issues of its application for making measurements of biomass burning emissions, including a description of the FTIR spectrometer used for the field campaigns presented in this thesis, and an explanation of the retrieval procedure for obtaining trace gas metrics from the measured IR spectra.

3.1 Fundamentals of OP-FTIR spectroscopy

Infrared spectroscopy is a well-established tool used for the characterisation of unknown substances in both organic and inorganic chemistry. This section introduces the fundamentals of infrared absorption before focussing on infrared spectroscopy and the Fourier transform IR technique, considering the theoretical, instrumental and analytical factors relevant to the work presented in this thesis.

3.1.1 Infrared absorption

Spectroscopy is the technique used to study the interaction of electromagnetic radiation and matter. Any change in the quantised energy level of an atom or molecule will result in the absorption or emission of a photon (of electromagnetic radiation) whose energy must be exactly equal to the energy difference between the two levels (Gunzler and Gremlich, 2002):

$$\Delta E = h\,v \tag{3.1}$$

Where ΔE is equal to the allowable transition between two energy levels, h is Planck's constant (6.626×10^{-34} J s^{-1}), and v is the frequency (Hertz) of the electromagnetic radiation. Therefore, if radiation at a frequency equal to $\Delta E/h$ interacts with some matter, then the matter can be excited to a higher energy level (a transition), leading to absorption of the radiation. A source of radiation may be used to pass radiation through a material towards a detector; given that the material may absorb radiation at all frequencies corresponding to all of its allowable energy transitions, the frequencies at which the radiation intensity decreases at the detector correspond to the energy transitions in the material (Stuart, 2004).

Different frequency ranges of electromagnetic radiation are associated with different forms of energy transitions (Table 3.1). The small energy level changes arising from the reversal of spin in a nucleus or electron correspond to low frequency (long wavelength) radio waves. Higher microwave frequencies correspond to changes in the rotational energy levels of molecules. Emission and absorption features at even higher infrared frequencies correspond to changes in molecular vibrational energy levels and

Table 3.1 After Banwell and McCash (1994). Summary of the different regions of the spectrum and the corresponding nuclear, atomic and molecular energy transitions.

Spectral Region	Frequency Range (Hertz)	Wavelength Range	Molecular Changes	Energy Change (joules $mole^{-1}$)
Radiofrequency	$3x10^{6} – 3x10^{10}$	10 m – 1 cm	Spin	0.001 – 10
Microwave	$3x10^{10} – 3x10^{12}$	1 cm – 100 μm	Rotations	~ 100s
Infra-red	$3x10^{12} – 3x10^{14}$	100 μm - 1 μm	Vibrations	~ 10^{4}
Visible and UV	$3x10^{14} – 3x10^{16}$	1 μm -10 nm	Valence electrons	~ 10^{5}
X-ray	$3x10^{16} – 3x10^{18}$	10 nm – 100pm	Inner electrons	~ 10^{7}
Gamma-ray	$3x10^{18} – 3x10^{20}$	100pm – 1 pm	Nuclear	~ 10^{9} -10^{11}

accompanying rotational transitions (discussed in more detail below), termed vibrational-rotational transitions (Banwell and McCash, 1994). Visible and ultra-violet regions correspond to changes in the energy levels of valence electrons (electrons of an atom that are available for the formation of chemical bonds with other atoms), with accompanying changes in vibrational energy levels. X-ray spectroscopy measures changes involving the inner-most electrons of atoms and molecules, whilst gamma rays have the highest frequencies that correspond to changes within the nucleus.

It is the changes in vibrational-rotational energy levels and the corresponding emission and absorption of photons that is absolutely fundamental to infrared spectroscopy. The mid-infrared region, with a wavenumber range of 500–5,000 cm^{-1} (where wavenumber is the spatial frequency of a wave equal to the number of wave crests per cm, equivalent to the reciprocal of wavelength: 500–5,000 cm^{-1} is equivalent to the wavelength range 2–20 μm), is the primary region of interest for this thesis given that many atmospheric trace gases (and gaseous combustion products) have characteristic absorptions in this region of the spectrum. Molecular transitions depend upon the mass of the constituent atoms, their interatomic distances and the position of the centre of mass (Gunzler and Gremlich, 2002). Consequently, different molecules possess unique IR absorption signatures (Figure 3.1).

3.1.1.1 Pure rotational spectra

Pure rotational absorption spectra are characteristic of molecules that rotate with a permanent dipole moment so that incoming photons can interact with the molecule (Bernath, 2005). This includes molecules such as carbon monoxide (CO), hydrochloric acid (HCl) and formaldehyde (H_2CO), but excludes molecules with a centre of symmetry such acetylene (C_2H_2), methane (CH_4) and the homonuclear molecules nitrogen (N_2) and oxygen (O_2). In rotational absorption spectra, each photon is absorbed by a molecule which undergoes a transition from a lower to a higher rotational energy level (i.e. the molecule spins faster in a particular direction); the opposite is true for rotational emission spectra, where the molecule undergoes a transition to a lower rotational energy level (i.e. the molecule spins slower). In quantum mechanics the free rotation of a molecule is quantised, that is the angular momentum (J) can take only fixed values (i.e. J = 0, 1, 2, 3… etc.); therefore the rotational energy (E) can also only

take fixed values. If the molecule were to behave like a "rigid rotor" with the atoms connected by a massless non-distorting rod (Bernath, 2005), the expression for energy may be written as:

$$E = B\,J(J+1) \tag{3.2}$$

Where B, the rotational constant, is expressed as:

$$B = \left\{\frac{\hbar^2}{2I}\right\} \tag{3.3}$$

Where $\hbar$ is Planck's constant divided by 2π, and I is the moment of inertia. B is unique to a particular molecule as the moment of inertia depends upon the mass and interatomic distance:

$$I = \mu R^2 \tag{3.4}$$

Where R is the atomic bond length ($r_1 + r_2$ in Fig. 3.1) and μ is expressed as:

$$\mu = \frac{m_1 m_2}{m_1 + m_2} \tag{3.5}$$

Where m_1 and m_2 refer to the masses of the two constituent atoms of the molecule (as illustrated in Fig. 3.1). From Eqn. 3.2, it is possible to calculate the rotational energy levels for simple diatomic molecules behaving as rigid rotors (Table 3.2). As a photon can only carry one quantum of angular momentum, so J can only change by plus or minus one due to the conservation of angular momentum. Thus, the energy difference between rotational energy levels for the first six allowed absorption transitions

Table 3.2 Rotational energy levels calculated from Eqn. 3.2 for a diatomic molecule behaving as a rigid rotor.

J	Energy	$2J + 1$
0	0	1
1	2B	3
2	6B	5
3	12B	7
4	20B	9
5	30B	11
6	42B	13

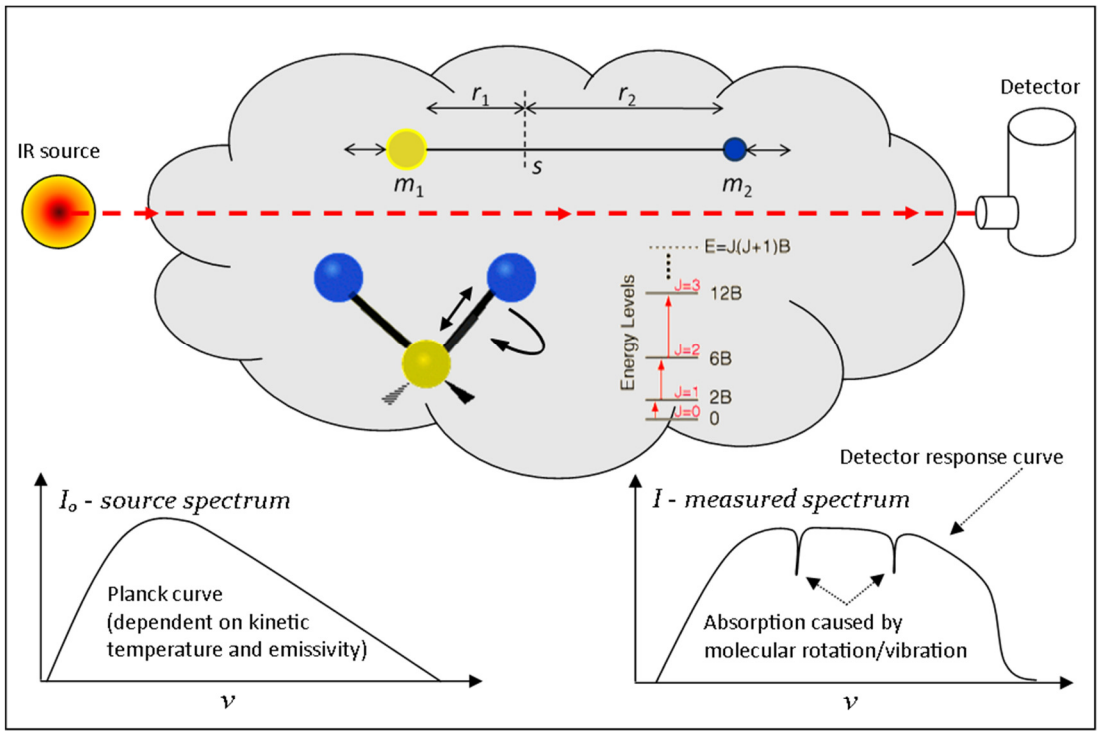

Figure 3.1 Some fundamentals of infrared absorption spectroscopy. Upper section depicts a cloud of gas molecules. Infrared absorption is caused by the vibrational-rotational transitions of the gas molecules, which is dependent on the mass of the atoms (m), the interatomic distance (r) and the position of the centre of mass (s). The lower section depicts the source radiation spectrum and the spectrum measured by the detector. The spectrum of source radiation (I_0) is a function of temperature and emissivity of the source, whilst the measured spectrum (I) is primarily a function of the detector's response and the different species and amounts of IR absorbing gases in the path.

according to the selection rule $\Delta J = \pm 1$ are:

J=0 → J=1 $\quad 2B - 0 = 2B$

J=1 → J=2 $\quad 6B - 2B = 4B$

J=2 → J=3 $\quad 12B - 6B = 6B$

J=3 → J=4 $\quad 20B - 12B = 8B$

J=4 → J=5 $\quad 30B - 20B = 10B$

J=5 → J=6 $\quad 42B - 30B = 12B$

This rigid rotor approximation gives a rotational absorption spectrum with equally spaced absorption/emission lines ($2B$ apart). In reality, centrifugal forces cause the interatomic bonds to be non-rigid (Bernath, 2005). The result is that the bond length (R in Eqn. 3.4) is longer and the moment of inertia, I, higher for greater angular momentum

(*J*). The result is that the spacing between the frequencies of higher rotational levels is reduced. The separation between the frequencies of individual rotational levels is typically less than 10 cm^{-1}.

The intensity of rotational absorption lines depends upon:

1. The transition probability (this increases approximately linearly with energy)
2. The number of molecules in the initial state available for the transition (this decreases exponentially as the energy level increases, as described by the Boltzmann distribution).
3. The degeneracy of the initial energy state $2J+1$ (see Table 3.2), this increases with energy.
4. The amount of absorbing matter (a function of concentration and pathlength).

The balance between the exponential decrease in the number of molecules available in the initial state for the transition with energy and the increase in degeneracy and transition probability with energy results in a maximum line intensity positioned above the lowest transition ($J=0 \rightarrow J=1$), with the exact location depending on the rotational constant *B* and the temperature (Bernath, 2005).

3.1.1.2 Pure vibrational spectra

Pure vibrational absorption spectra are characteristic of molecules that vibrate such that their dipole moment changes during the vibration allowing interaction with incoming photons (Steele, 2006). This includes any molecules that can undergo asymmetrical stretching vibration but once again exludes the homonuclear molecules N_2 and O_2. The molecular motion of vibration may be approximated to be sinusoidal using a simple harmonic oscillator with vibrational energy E_{vib}. As was the case with molecular rotation, the free vibration of a molecule is also quantised so that:

$$E_{\text{vib}} = hv\left\{\text{v} + \frac{1}{2}\right\} \tag{3.6}$$

Where *h* is Planck's constant, *v* is the classical vibrational frequency, and v is the vibrational quantum number (i.e. v = 0, 1, 2, 3… etc. until bond dissociation energy). From Eqn. 3.6, the energy of a single vibration of a molecule can be 0.5 *hv*, 1.5 *hv*, 2.5

hv etc. and so the step between vibrational energy levels is evenly spaced (unlike rotational energy levels). Not all transitions are allowed, the vibrational quantum number may only change by plus or minus one ($\Delta v = \pm 1$). This means that all permitted transitions amount to the same energy change, the consequence being that there is only one absorption line, at the classical vibrational frequency *v* (Steele, 2006).

In reality, vibrations are not perfectly sinusoidal. This inharmonicity permits changes in the vibrational quantum number greater than one (i.e. $\Delta v = \pm 1, \pm 2, \pm 3\ldots$ etc.) The transitions with increasing jumps in the quantum number ($\Delta v = \pm 2$, $\Delta v = \pm 3$) are called overtones (Steele, 2006). Energy separations between the fundamental and overtone vibrational levels are typically thousands of wavenumbers.

3.1.1.3 Vibrational-rotational spectra of heteronuclear diatomic molecules

At typical atmospheric temperatures, molecules may only be excited around their ground vibrational state ($\Delta v = +1$). A molecule behaving as a simple harmonic oscillator would be characterised by a single absorption line, yet molecules undergoing vibrational transitions will also change their rotational energy level (the vibrational transition leads to an instantaneous change in the molecular bond length, which in turn alters the moment of inertia, bringing about a change in the rotational energy level of the molecule). This results in a vibrational-rotational spectrum (Gunzler and Gremlich, 2002). To explain vibrational-rotational spectra, it is once again necessary to simplify things. Using the Born-Oppenheimer approximation (Bernath, 2005) which assumes that diatomic molecules undergo rotational and vibrational transitions independently of each other, the energy levels of a molecule can be approximated as the sums of the vibrational and rotational energies:

$$E_{total} = E_{vibrational} + E_{rotational} \tag{3.7}$$

So, when the equations for a perfect harmonic oscillator and a rigid rotor (described above) are combined, the energy of the rotational-vibrational transition may be described as:

$$E = hv\left(\mathrm{v} + \frac{1}{2}\right) + BJ(J+1) \tag{3.8}$$

This equation is subject to the quantum selection rules $\Delta v = \pm 1$ and $\Delta J = \pm 1$ for the independent vibrational and rotational transitions. Furthermore, a transition with $\Delta v = 0$ is also possible, corresponding to a pure rotational transition as discussed in Sect. 3.1.1.1. Under these selection rules, a transition with $\Delta v = -1$ corresponds to an emission spectrum, whereas a transition with $\Delta v = +1$ is an absorption spectrum. Both of these transitions may be accompanied by either a gain in rotational energy $\Delta J = +1$ or a loss in rotational energy $\Delta J = -1$. This combination produces a spectrum with two branches of rotational absorption lines centred over the pure vibrational frequency (Gunzler and Gremlich, 2002).

For the vibrational transition ($v=0 \rightarrow v=1$) accompanied by a gain in rotational energy ($\Delta J = +1$), the vibrational-rotational transitions occur at:

$h\nu+2B$, $h\nu+4B$, $h\nu+6B$, $h\nu+8b$… etc.

Assuming a rigid rotor and under the Born-Oppenheimer approximation, these transitions produce equally spaced absorption lines at higher frequencies than the fundamental vibrational frequency (ν), termed the R-branch (Figure 3.2).

For the vibrational transition accompanied by a loss in rotational energy ($\Delta J = -1$), the transitions occur at:

$h\nu–2B$, $h\nu–4B$, $h\nu–6B$, $h\nu–8B$… etc.

These transitions produce equally spaced absorption lines at lower frequencies than the fundamental vibrational frequency, termed the P-branch (Figure 3.2).

In real molecules, vibrational and rotational transitions do not follow the Born-Oppenheimer approximation and are not truly independent of each other (Bernath, 2005). This deviation from the Born-Oppenheimer approximation leads to P-branch lines becoming increasingly spaced as the rotational energy level increases away from the band centre, whilst the R-branch lines become increasingly closely packed further from the band centre. The intensity distribution for each vibrational-rotational band depends upon the same factors as those for pure rotational transitions (Sect. 3.1.1.1).

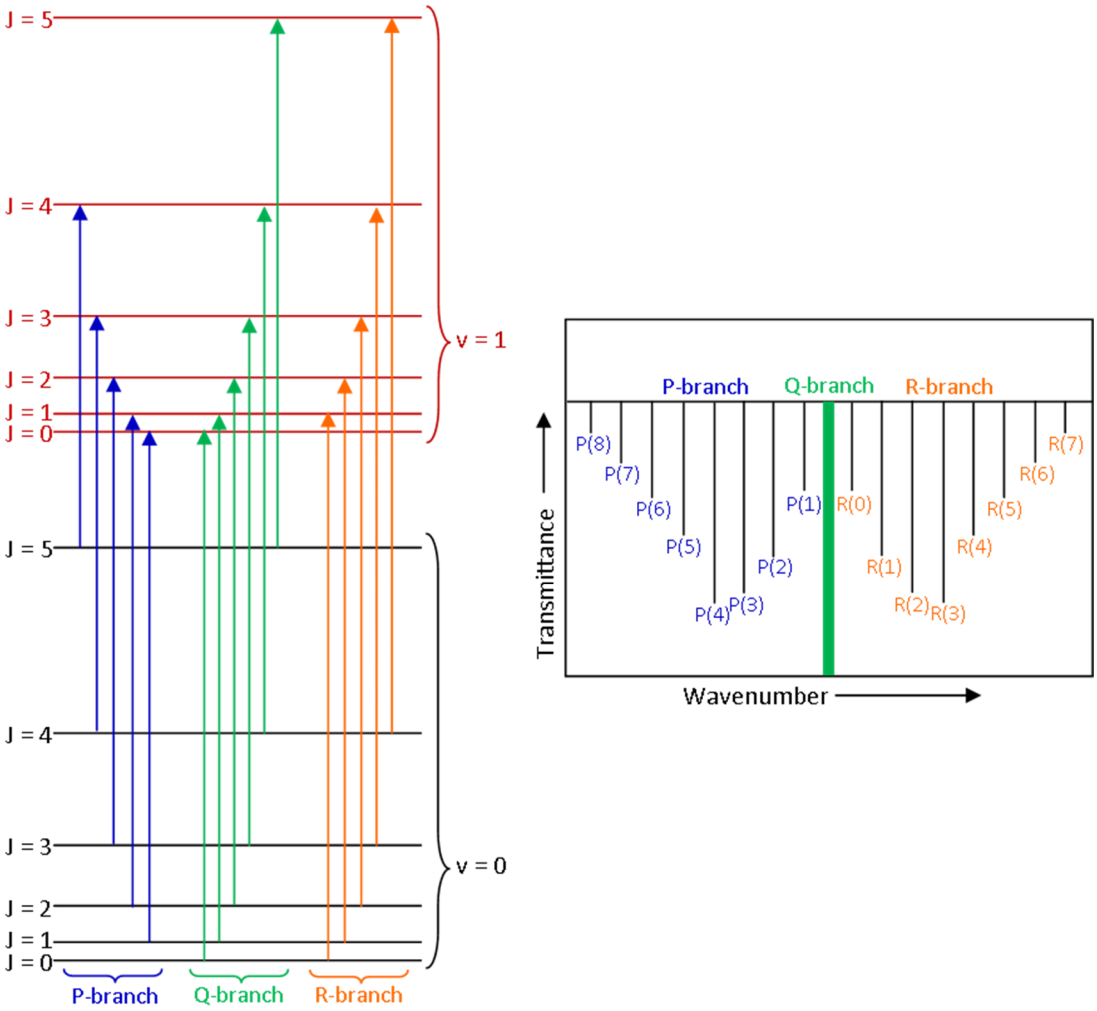

Figure 3.2 (left) Energy level diagram showing some of the vibrational-rotational transitions of a linear heteronuclear molecule. Here, the vibrational transition (v=0 → v=1) is accompanied by both a gain in rotational energy (J=0 → J=1, J=1 → J=2, J=2 → J=3… etc.) forming the R-branch and a loss in rotational energy (J=1 → J=0, J=2 → J=1, J=3 → J=2… etc.) forming the P-branch. Also shown is the Q-branch where $\Delta J = 0$ when a vibrational transition is not accompanied by a change in rotational energy (not always allowed). (right) The P-branch and R-branch spectrum are illustrated for an imaginary molecule that behaves as a rigid rotor, vibrates with simple harmonic motion and obeys the Born-Oppenheimer approximation. Each line is named using a letter referring to the branch and a number referring to the rotational quantum number (J) of the initial rotational energy state (hence why there is not a P0 line). The Q-branch, if permitted, would appear as a strong line at the pure vibrational frequency at the centre of the P- and R-branches.

3.1.1.4 Vibrational-rotational spectra of heteronuclear polyatomic molecules

Polyatomic molecules consisting of n atoms have a total of $3n$ degrees of freedom according to the Cartesian coordinates of each atom in the molecule (Steele, 2006). In a nonlinear molecule, three of these degrees are rotations, three are translational, and the remaining correspond to fundamental vibrations (the number of fundamental vibrations is therefore equal to $3n–6$); for linear molecules, two degrees are rotational and three are translational (the number of fundamental vibrations is equal to $3n–5$). For even a simple molecule such as propane (C_3H_8), this model predicts 27 fundamental vibrations (each with their own vibrational-rotational transitions). Not all transitions are possible though and the selection rules depend upon the nature of the vibrational transition (Steele, 2006). Linear polyatomic molecules can vibrate such that the dipole moment changes in parallel to the principal axis of rotation; for these types of vibrations, the selection rules are the same as for diatomic molecules. However, linear polyatomic molecules may also vibrate such that the dipole moment is changed perpendicular to the principle axis of rotation. In this case the selection rules allow $\Delta J = 0$ (i.e. the vibrational energy change $v=0 \rightarrow v=1$ can occur without accompanying change in rotational energy). For these molecules, a Q-branch (Figure 3.2) appears at the band centre between the P- and R-branches (at the pure vibrational frequency, v). The Q-branch is a particularly strong feature due to the vibrational transitions occurring from all existing rotational states at exactly the same energy change.

3.1.1.5 Absorption line shape

Heisenberg's uncertainty principle ensures that absorption lines are never monochromatic (infinitely narrow). The uncertainty in the energy level multiplied by the uncertainty in time (the lifetime of the energy level) must be greater or equal to Planck's constant over four pi:

$$\Delta E \Delta t \geq \frac{\hbar}{2} \tag{3.9}$$

The consequence for spectroscopy is that the shorter the lifetime of a particular rotational or vibrational energy level, the larger the uncertainty in the level's energy, and therefore, through Eqn. 3.1, the broader the absorption line (as the energy

uncertainty manifests as an uncertainty in the frequency of the line). This broadening of the absorption line is often referred to as 'natural broadening' and produces a Lorentzian line shape (Bernath, 2005).

In addition to this natural broadening, absorption lines undergo two further forms of broadening, Doppler broadening and pressure broadening; for atmospheric spectra, these types of broadening, caused by temperature and pressure respectively, account for several orders of magnitude more broadening than that due to natural broadening (Bernath, 2005).

Doppler broadening is caused by molecules travelling in different directions with respect to the light source (Bernath, 2005). Molecules moving towards the light source will absorb at slightly higher frequency (shorter wavelength) than molecules moving away, in a similar fashion to the blue-shift and red-shift of stars that are moving towards and away from the Earth, respectively. Doppler broadening produces a Gaussian line shape that is dependent on temperature (the velocity of molecules, and thus the strength of the Doppler effect, is a function of temperature).

Pressure broadening is caused by molecular collisions. The collisions shorten the lifetime of energy levels leading to increasing uncertainty in the level's energy (as occurs in natural broadening) producing a Lorentzian line shape (Bernath, 2005). This effect depends on the density and temperature of the gas (as higher density and temperatures increase the likelihood of collisions). Given the dependence on pressure, absorption lines for spectra that are measured through the whole atmosphere will have different line shapes depending on the vertical distribution of the absorbing gas in the atmosphere. A gas that is mainly located in the troposphere (e.g. methanol) will produce mainly broad absorption lines due to higher atmospheric pressure whereas gases residing predominantly in the stratosphere (e.g. ozone) are characterised by narrower lines due to the reduced atmospheric pressure.

For measurements at sea level (pressure is ~1,000 hPa), pressure broadening (with a Lorentzian line shape) dominates, although its effect reduces rapidly with altitude as pressure decreases. Stratospheric gases are predominantly Doppler broadened (with a Gaussian line shape), with the two forms of broadening having equal effect at

approximately 25 km altitude (Horrocks, 2001). The convolution of the two broadening line shapes produces a Voigt line shape. Radiative transfer forward models (used to model atmospheric absorption lines) use this function to model line shapes (see Sect. 3.2). One consequence of the variation in the shape and width of atmospheric absorption lines is that spectra collected through the atmosphere can be used to reveal the altitude of the absorbing gas as well as the total number of absorbing molecules in the path (referred to as the 'total column').

3.1.2 Beer-Lambert law

If the infrared-active molecules (i.e. those that can undergo vibrational-rotational transitions) in the optical path between the IR source and the detector are at a higher temperature than the IR source, then the spectral lines will be seen in emission. If, however, the molecules are cooler than the IR source, then the lines appear as spectral absorption lines (Gunzler and Gremlich, 2002). As discussed above, the intensity of an absorption line depends upon the number of molecules responsible for it (a function of the concentration of the particular trace gas species, C, and the total pathlength through the absorbing material, L) and the energy associated with the quantum mechanical transition responsible for a particular absorption line (represented by the absorption coefficient, ε, in the Beer-Lambert law below):

$$T = \frac{I}{I_0} = e^{-\varepsilon CL} \tag{3.10}$$

Where transmittance (T) is proportional to the intensity of transmitted radiation (I) divided by the intensity of the incident radiation (I_0), as illustrated in Figure 3.1.

Figure 3.3 shows a typical infrared spectrum of a biomass burning plume measured by an FTIR spectrometer (Section 3.1.3), with a number of example spectral windows containing absorption by gas molecules of interest for biomass burning research. H_2O and CO_2 absorption lines occur throughout the infrared spectrum. At spectral locations where the absorption by H_2O and CO_2 molecules is strongest, all IR energy from the source is absorbed, even over short pathlengths (metres). The 'atmospheric windows' between these major absorption bands occur at 500–1300 cm^{-1} (7–20 μm) in the long-

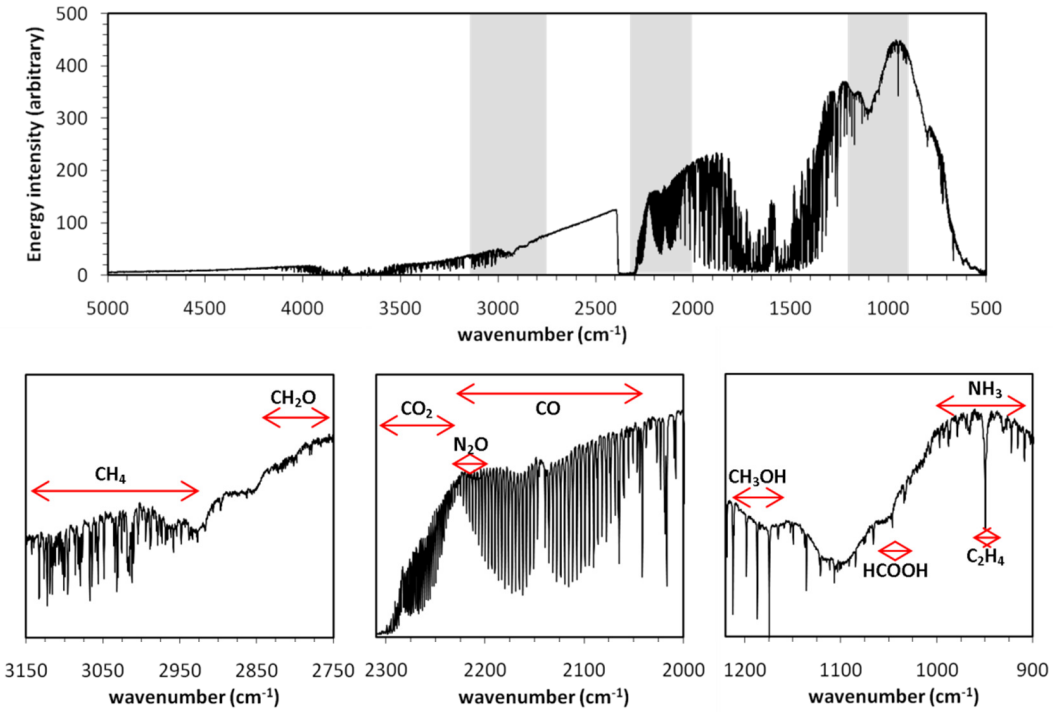

Figure 3.3 A typical infrared spectrum of a biomass burning plume showing the location of the broad H_2O and CO_2 absorption features and the atmospheric windows. The grey boxes indicate the spectral location of the three subplots. The subplots show three key spectral windows used for the retrieval of biomass burning gas species. The absorption bands of important biomass burning emissions are indicated by the red arrows. This spectrum was collected during the Northumberland field campaign (Sect. 5.1), using pathlength of 32 m.

wave infrared (LWIR), 2000–2300 cm^{-1} (4.3–5 µm) and 2400–3200 cm^{-1} (3–4.1 µm) in the mid-wave infrared (MWIR) and 4000–6000 cm^{-1} (1.6–2.5 µm) in the short-wave infrared (SWIR). As highlighted in Figure 3.3, detection of biomass burning trace gases focusses on these atmospheric windows.

3.1.3 The FTIR spectrometer

For a thorough introduction to the theory and mechanics of Fourier transform spectroscopy, see Griffiths (1975) or Griffiths and Haseth (1986). Essentially, Fourier transform spectroscopy is a method by which all frequencies of a spectrum are measured simultaneously by a detector, and resolved into intensities at individual frequencies by a mathematical transform known as a Fourier transform (after the French polemic Joseph Fourier, who developed the mathematics in the early 19th century).

To understand the basic principles of Fourier transform spectroscopy, consider a source emitting light at three different but precise frequencies (i.e. three cosine waves). At the detector, the amplitude of the measured radiation with time will be the sum of the three cosine waves. This "beat frequency" has variable amplitude as the three cosine waves constructively and destructively interfere with each other (Figure 3.4). Using the Fourier transform it is possible to resolve the components of the combined wave mathematically (Fig. 3.4). Each component wave has a frequency, amplitude and a phase; in the example using three waves, this amounts to a total of six unknowns that must be resolved from the measured composite wave. Therefore, observations of the composite wave at six points in time will yield sufficient information to solve for the six unknown components. As more and more frequencies are added, each with their characteristic three components, the combined wave becomes increasingly complex, and consequently, the required number of points needed to resolve each component increases. A computer may be used to perform a Fourier transform on complex waves to resolve each component frequency (e.g. Brault and White, 1971).

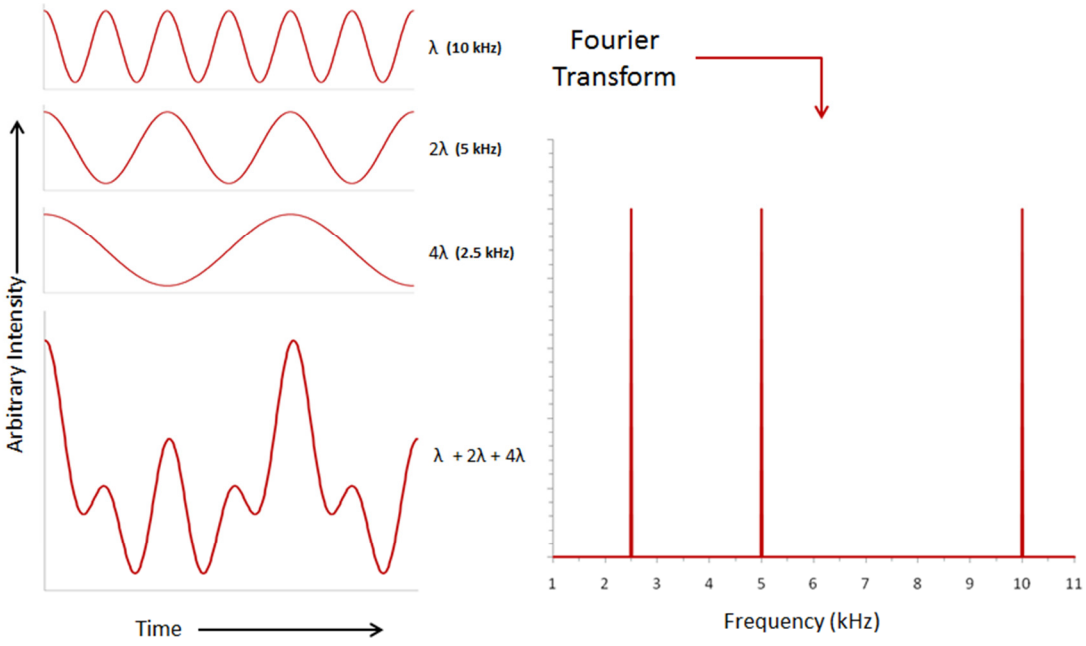

Figure 3.4 (left) Three cosine waves of different frequencies are shown at the top of the figure, the wave at the bottom of the figure illustrates the sum of the three waves – the "beat frequency". A Fourier transform of this interference pattern can be used to resolve the individual components. Here, three lines at 2.5, 5, and 10 kHz correspond to the three component frequencies.

The frequencies of infrared radiation (3×10^{12} – 3×10^{14} Hz) are far too high for detectors to respond fast enough to record time domain amplitudes directly. This problem can be overcome by using interference to modulate the IR signal at a detectable frequency (Griffiths and Haseth, 1986). Central to any FTIR spectrometer is the Michelson interferometer (Figure 3.5) which is used to produce a new signal of a much lower frequency containing the same information as the original IR signal. The interferometer splits a beam of incoming radiation into two paths; one path travels to a fixed mirror (this radiation has a fixed pathlength), whilst the other path travels to a moving mirror (this radiation has a variable pathlength). The two paths of radiation are recombined at the beam splitter where they interfere (Griffiths and Haseth, 1986). Interference will be constructive when both mirrors are at the same distance from the beam splitter, known as the zero path difference (ZPD or δ_0). For a particular wavelength, the same constructive maximum will occur if the difference in path lengths is an exact multiple of the wavelength. If the optical path difference (OPD, δ) is half the wavelength (or some odd multiple of this) then destructive interference will result. As the moving mirror moves away from the beam splitter at a constant velocity, the radiation (at a particular frequency) reaching the detector goes through a steady sequence of maxima and minima (a cosine wave) as the interference alternates between constructive and destructive phases. For a monochromatic source with frequency v, the energy arriving at the detector (I') has amplitude that varies sinusoidally as a function of the optical path difference (δ) and may be described as:

$$I'(\delta) = \tfrac{1}{2}\, I(v)\{1 + \cos(2\pi v\delta)\} \tag{3.11}$$

Where $I(v)$ is the amplitude of the radiation entering the spectrometer (i.e. before the interferometer). The varying component of this signal (I'') is simply:

$$I''(\delta) = \tfrac{1}{2}\, I(v)\cos(2\pi v\delta) \tag{3.12}$$

Given that the amplitude of a measured interferogram is affected by instrumental characteristics such as detector response, beamsplitter transmission efficiency, electrical amplifiers etc., and is therefore not simply a function of the radiation entering the spectrometer $I(v)$, the signal that reaches the detector, $I(\delta)$, is a function of instrument response, $B(v)$:

$$I(\delta) = B(v)\cos(2\pi v\delta) \tag{3.13}$$

From this equation, the signal received at the detector, I(δ), is the cosine Fourier transform (FT) of $B(v)$ (the amplitude of radiation modified by instrumental effects). Therefore, to determine $B(v)$ from the measurement of $I(\delta)$, it is necessary to take the Fourier transform of $I(\delta)$. In Equations 3.11–3.13, the incident radiation was considered monochromatic. For a continuous energy source (e.g. a blackbody radiating at all wavelengths), the interferogram in Eqn. 3.13 must be represented by an integral:

$$I(\delta) = \int_0^{+\infty} B(v)\cos(2\pi v\delta)\, dv \tag{3.14}$$

With the other half of the Fourier transform pair being:

$$B(v) = \int_{-\infty}^{+\infty} I(\delta)\cos(2\pi v\delta)\, d\delta \tag{3.15}$$

As $I(\delta)$ is symmetrical about δ=0 (the zero path difference), Eqn. 3.15 may be re-written as:

$$B(v) = \int_0^{+\infty} I(\delta)\cos(2\pi v\delta)\, d\delta \tag{3.16}$$

Of course, the maximum optical path difference (MPD) is not infinite but occurs when the moving mirror is furthest from the beam splitter. The spectral resolution of a FTIR spectrometer may be approximated using the reciprocal of the MPD (e.g. a MPD of 2 cm would result in a spectral resolution of 0.5 cm^{-1}). The implications of spectral resolution on the measured interferogram are discussed in Section 3.1.4.1.

The temporal coherence of the radiation is recorded as a function of mirror position (path difference) at discreet time intervals to produce the measured interferogram (Figure 3.6). The position of the mirror is measured using a laser and measuring its interference pattern, each peak in the laser's interference pattern indicates that the mirror has travelled half the wavelength of the laser, yielding a highly precise and accurate measurement of mirror position. The FTIR detector must respond quickly as intensity changes rapidly with the moving mirror. Typically pyroelectric detectors or cooled photon detectors must be used. Given that all frequencies emitted by the IR

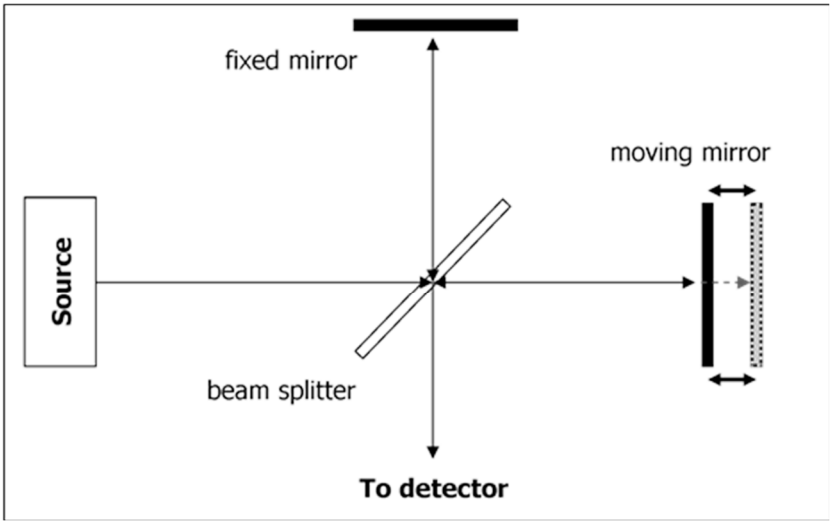

Figure 3.5 A simplified sketch of a Michelson interferometer

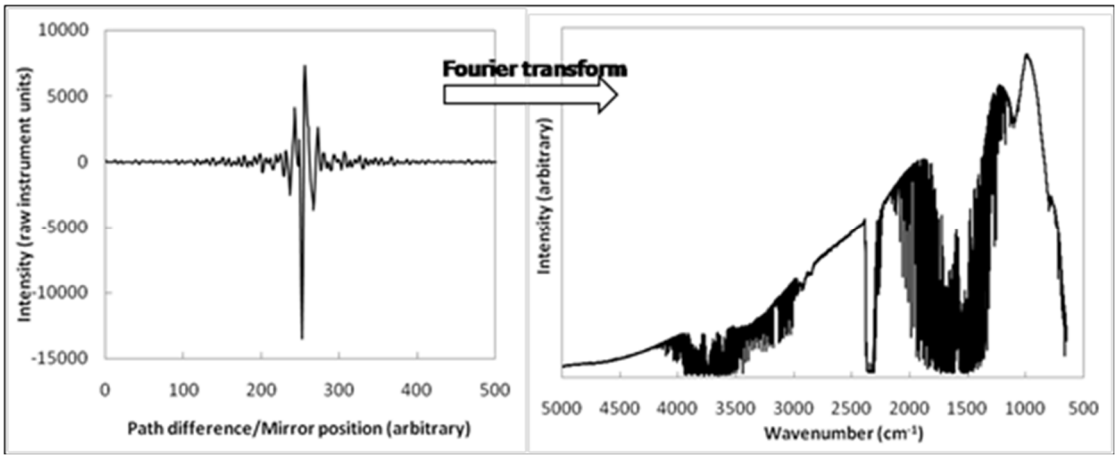

Figure 3.6 An interferogram and its corresponding single beam spectrum

source are present, the actual measured interferogram is extremely complicated (Figure 3.6). A cosine Fourier transform of the interferogram will produce a spectrum of energy intensity as a function of frequency (Figure 3.6).

All IR spectra collected for this thesis were measured using a MIDAC Corporation OP-FTIR Air Monitoring System, equipped with a Stirling-cycle cooled mercury-cadmium-telluride detector (MCT). Figure 3.7 shows a photograph of the MIDAC spectrometer along with simplified ray diagram for comparison with Fig. 3.3. The MCT detector is sensitive to IR energy from 500–5000 cm^{-1} (2–20 μm). The FTIR spectrometer records interferograms, which are later converted to 'single-beam' (SB) spectra using an inverse

fast-Fourier transform (FFT) as applied using the MIDAC Autoquant software. All MIDAC-collected spectra are recorded using 0.5 cm^{-1} spectral resolution (the MPD of the spectrometer is 2 cm). At this spectral resolution, each scan of the spectrometer mirror (each measurement) takes ~1.2 seconds. To improve the signal-to-noise ratio, it is advantageous to average (co-add) interferograms (the signal-to-noise ratio improves by the square root of the number of averaged scans). For the majority of results presented in this thesis, four or eight scans were co-added for each measurement spectrum. The field-of-view (FOV) of the spectrometer detector is ~20 mrad (although small changes in optical alignments can alter the FOV). For all measurements used in this thesis, the MIDAC FTIR spectrometer was fitted with a custom-built 76 mm Newtonian telescope equipped with gold-surfaced mirrors, reducing the FOV to 3 mrad.

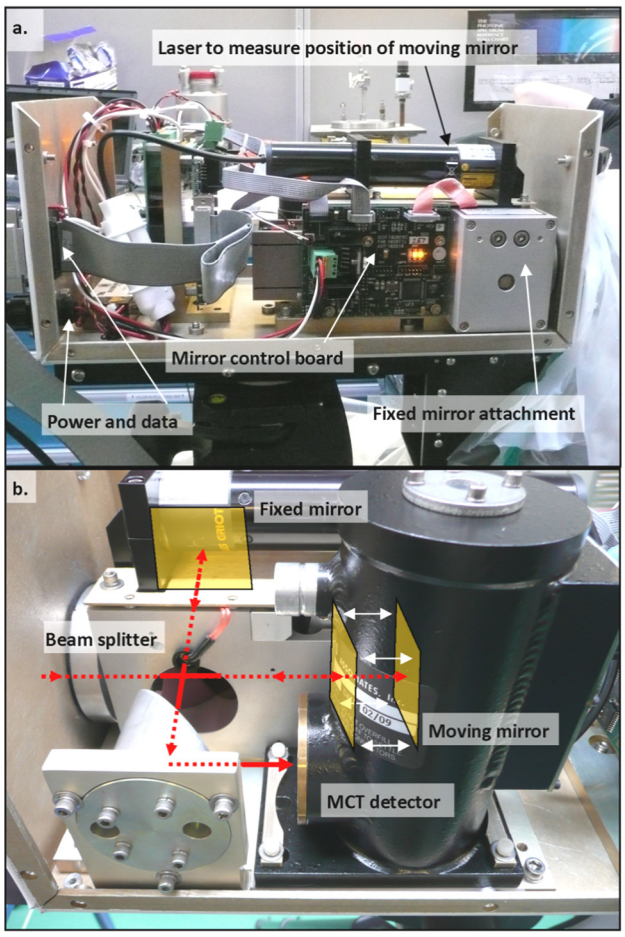

Figure 3.7 (a) Side-view of the MIDAC FTIR spectrometer with key components labelled; (b) the interferometer and MCT detector with ray diagram. The incoming light is split into two paths, one path travels to the fixed mirror, the other to the moving mirror, before the beams are recombined before being focussed onto the detector. The detector measures the interference pattern.

3.1.4 Instrument line shape and the breakdown of the Beer-Lambert Law

If an infrared spectrometer could measure true transmittance (T in Eq. 3.10), then the Beer-Lambert law relating transmittance to concentration may be used to simply calculate gas concentrations. However, the measured transmittance is affected by instrument effects and the absorption lines are convolved to the instrument line shape (ILS), so the Beer-Lambert law cannot hold true and Equation 3.10 must be re-written as:

$$T_{app} = T \otimes ILS \neq e^{-\varepsilon CL} \tag{3.17}$$

Where the apparent transmittance (T_{app}) is the true transmittance convolved to the instrument line shape (ILS) leading to deviations from the Beer-Lambert law. This convolution of true absorption line shapes to the instrument line shape is dependent on a number of instrument parameters, but primarily the spectral resolution. If the spectrometer has a spectral resolution lower than that of the theoretical line widths (a function of natural, Doppler, and pressure broadening as described in Sect. 3.1.1.5), the absorption lines will be smoothed to the lower spectral resolution of the instrument (similar to the effect shown in Figure 3.8). The theoretical strength of an absorption line (S) is equivalent to the integral of the absorption coefficient (ε) for a particular molecule over the frequency range (dv) corresponding to the transition responsible for it:

$$S = \int_0^\infty \varepsilon \, dv \tag{3.18}$$

Given that the integral of the absorption coefficient remains constant (the area of the absorption feature in Fig. 3.8), the broadening due to instrumental effects is accompanied by a reduction in the depth of the absorption line. Therefore, the measured transmission (T_{app}) is no longer linearly proportional to concentration according to the Beer-Lambert law. In addition to instrument resolution (Sect. 3.1.4.1), other effects due to interferogram processing (e.g. the apodization function discussed further in Sect. 3.1.4.2) and the finite field of view of the instrument (Sect. 3.1.4.3) also contribute to the ILS.

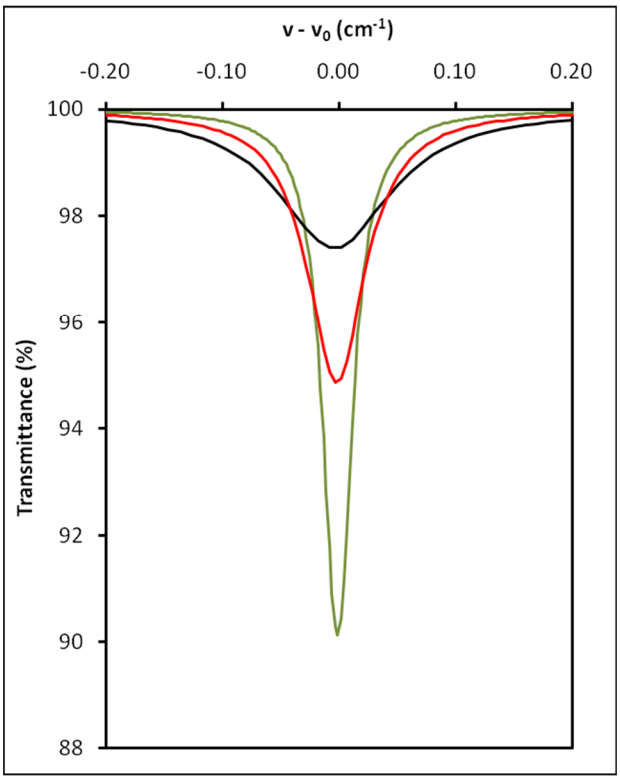

Figure 3.8 Spectral line shape as a function of pressure. Absorption lines are broadened at higher pressures and line depth is suppressed. A similar effect would be observed for spectra measured using instruments operating at a lower spectral resolution than the true line width (i.e. the true absorption line would resemble the green line, whereas a line measured by 0.5 cm^{-1} resolution spectrometer might resemble the black line).

3.1.4.1 Instrument resolution

As described above, the moving mirror cannot extend to infinity, the interferogram must therefore be truncated by the maximum optical path difference (δ_{max}). This restriction of the interferogram is mathematically equivalent to multiplying the interferogram, $I(\delta)$, by a binary (boxcar) function, $D(\delta)$, where δ is equal to 1 between δ_0 and δ_{max}, and equal to zero elsewhere. The measured spectrum, $B'(v)$, is now:

$$B'(v) = \int_0^{+\infty} I(\delta)\,\mathrm{D}(\delta)\cos(2\pi v\delta)\,d\delta \tag{3.19}$$

Given that multiplication in the Fourier (δ) domain results in a convolution in the spectral domain (v), the measured spectrum, $B'(v)$ is equivalent to the FT of $I(\delta)$ multiplied by the FT of $D(\delta)$ (Griffiths and Haseth, 1986). Recalling Eqn. 3.16, the FT of $I(\delta)$ is the true spectrum, $B(v)$; therefore the measured spectrum $B'(v)$ is the true

spectrum multiplied by the FT of the boxcar function. The Fourier transform of the boxcar function is the normalised sinc function (Figure 3.9), $J(v)$:

$$J(v) = 2\delta_{max}\frac{\sin(2\pi v\delta_{max})}{2\pi v\delta_{max}} \tag{3.20}$$

When the true spectrum is convolved to the sinc function, spectral lines are smoothed to the resolution of the width of the sinc function (Fig. 3.9), equal to $1/\delta_{max}$. The spectral resolution of a spectrometer is therefore inversely proportional to the maximum possible optical path difference (the distance over which the moving mirror travels).

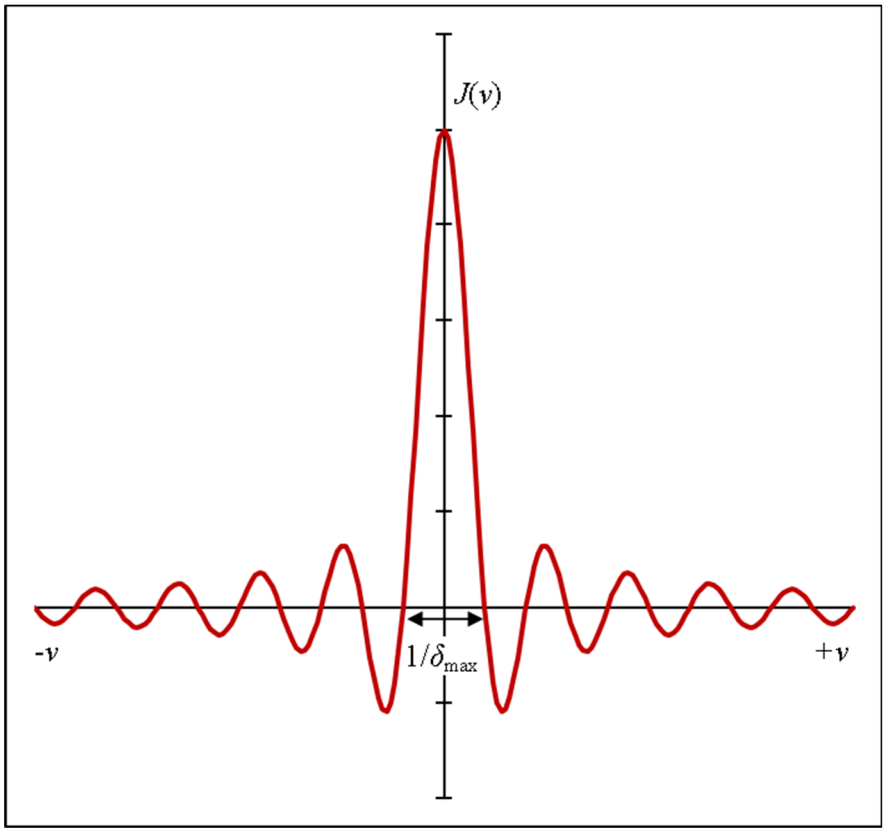

Figure 3.9 The finite optical path difference, δ, imposes the boxcar function on the measured interferogram. The normalised sinc function (above and described in Eqn. 3.20) results from the Fourier transform of the boxcar function. For a single sharp absorption line measured at a resolution ($1/\delta_{max}$) less than the half-width of the line itself, the instrument imposes this sinc function line shape on the measured absorption line.

3.1.4.2 Apodization

The sinc function that results from the FT of the boxcar function introduces some major artefacts to the spectra in the form of strong absorption line sidelobes about the central frequency of the line (Fig. 3.9). Apodizing functions are used in Fourier transform spectroscopy to suppress the amplitude of these sidelobes in the instrument line shape (Naylor and Tahic, 2007). The apodizing function, A(δ), is applied to the interferogram before the transform. Generally A(δ) is used to weight the interferogram so that A(δ) is equal to one at the zero path difference, δ_{zero}, and A(δ) is less than one elsewhere. A number of apodization functions have been used for Fourier transform spectroscopy (see Griffiths and Haseth, 1986; Naylor and Tahic, 2007). The most commonly applied form of apodization is the triangular function, where $A(\delta)$ is equal to one at δ_{zero}, but drops off linearly towards zero at $\pm\delta_{max}$:

$$A(\delta) = 1 - |\delta/\delta_{max}| \qquad \text{for } -\delta_{max} < \delta < +\delta_{max} \tag{3.21}$$

$$A(\delta) = 0 \qquad \text{for } \delta < -\delta_{max} \text{ and } \delta > +\delta_{max} \tag{3.22}$$

The triangular function reduces the amplitude of the sinc function sidelobes (Fig. 3.9), and also produces a line shape identical to that of pre-Fourier transform instruments, such as grating spectrometers with rectangular slits (Chaney, 1967).

3.1.4.3 Finite field of view

As depicted in Figure 3.5, the beam of radiation passing through the interferometer is perfectly aligned (i.e. perpendicular to the mirrors and detector). In reality, a combination of factors contribute to off-axis rays that will take a longer path through the interferometer than the central rays (Figure 3.10); this occurs due to imperfections in the collimated radiation path (e.g. from the parabolic mirrors of the transmitting or receiving telescopes) and due to the finite field of view (FOV) of the spectrometer. Light rays propagating at different angles in the interferometer will see different optical path differences (δ) (Bouchard and Tremblay, 2003) and the finite field of view of the spectrometer detector restricts the sensitivity to this off-axis radiation, effectively truncating the interferogram at an optical path difference smaller than δ_{max} (Griffiths, 1975).

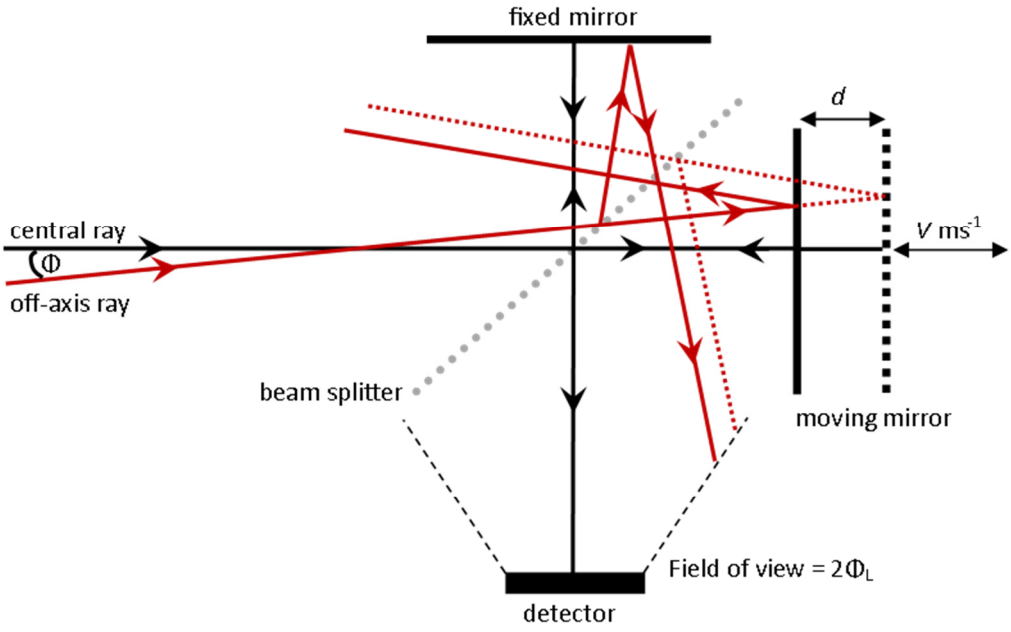

Figure 3.10 Redrawn from Horrocks (2001) Paths taken by axial and off-axis rays through the interferometer.

To understand how a restricted FOV affects the ILS, consider Figure 3.10. When the moving mirror moves a distance d, an off-axis ray with a divergence half-angle, Φ, takes a longer path through the interferometer than the central ray. The path difference l_Φ, can be calculated as follows:

$$l_\Phi = 2\frac{d}{\cos\Phi} - 2d \tag{3.23}$$

Given that Φ is small (Horrocks, 2001) a cosine expansion can be used to reduce the above equation to:

$$l_\Phi = d\Phi^2 \tag{3.24}$$

For a source of monochromatic radiation at wavelength λ, the off-axis ray will be out-of-phase with the central ray when:

$$l_\Phi = \frac{\lambda}{2} \qquad \text{i.e.} \quad d\Phi^2 = \frac{\lambda}{2} \tag{3.25}$$

This explains why the interferogram is truncated at some optical path difference shorter than the maximum path difference, as further increases in d (i.e. further movement of the mirror) adds no further information to the interferogram (Horrocks, 2001). From Eqn. 3.25, for a given off-axis ray half-angle, Φ, at wavelength λ [= v^{-1}] the path difference 2d gives the highest achievable resolution, Δv [= $(2d)^{-1}$] (Griffiths, 1975). If FOV is limited to $2\Phi_L$, the best achievable resolution is:

$$\Delta v = v\phi_L^2 \tag{3.26}$$

This dependence of the measurement resolution on frequency explains why the ILS may not stay constant across a measured spectrum. For a source of radiation over a range of wavelengths, the loss of information due to the finite FOV occurs over a range of frequencies (Horrocks, 2001). This effect appears as a multiplication of the interferogram by a sinc function. The nominal FOV of the MIDAC spectrometer used in this thesis is 20 mrad (1.15°). Misalignments to spectrometer optics and/or non-parallel source radiation will increase the effective FOV of the instrument (Horrocks, 2001). A broader FOV will lead to line broadening. Such distortions to the ILS must be accounted for when performing spectral analysis if the most accurate results are to be obtained.

3.1.5 Infrared sources

OP-FTIR absorption spectroscopy relies on a source of incident infrared radiation from a body at a temperature higher than that of the intervening gas. An ideal source should radiate at a far higher temperature than the gas of interest, and should provide energy across a range of frequencies (broadband) to enable spectral analysis (i.e. ideally a hot greybody). The majority of the spectroscopy presented in this thesis makes use of an artificial portable infrared source; although some results are also presented from spectra recorded using the sun as the source. Figure 3.11 presents photographs of the sources used in this thesis, and shows examples of the the spectra recorded using these sources.

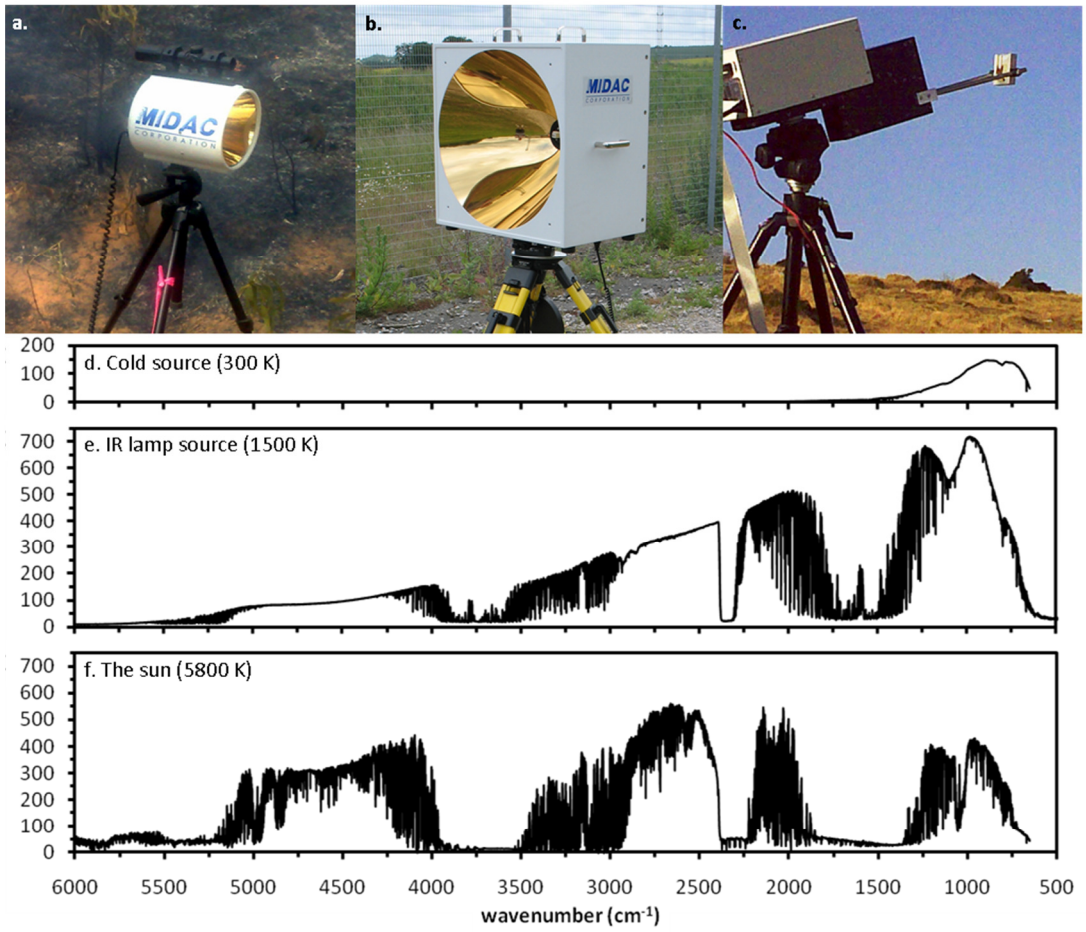

Figure 3.11 (top) Photographs of (a) small MIDAC IR source; (b) large MIDAC IR source; and (c) the MIDAC FTIR spectrometer with solar occultation attachment. (bottom) Example spectra from (d) a cold source; (e) an IR lamp source; and (f) the sun (with attenuator).

3.1.5.1 MIDAC IR sources

Two MIDAC portable IR lamps were used as sources for the work presented herein. Both consist of a 12 V silicon carbide glowbar operating at ~1500 K fitted in front of a gold plated aluminium collimator. The small lamp has a collimator diameter of ~15 cm, whilst the large lamp has a collimator diameter of ~50 cm (Figure 3.11a and b). Such IR Lamps provide a reliable source of infrared radiation with a good distribution of energy across the spectral range of interest (Figure 3.11e). The main problem with the IR lamp source is that much of the light is lost to off-axis reflections by the collimators, leading to a poor signal at distances of over 70 m for the small lamp, and ~300 m using the larger lamp. Furthermore, even when the spectrometer is operated with the telescope, some background radiation can enter the telescope FOV, adding to the source spectra

and resulting in a raised baseline at longer wavelengths caused by thermal emission from the atmosphere (Fig. 3.11d).

3.1.5.2 Solar source

Depending on cloud cover, the solar disc (~9.5 mrad) may be used as a strong source of IR radiation for FTIR spectroscopy (Figure 3.11c). The sun radiates at ~5800 K, providing more than enough energy for absorption spectroscopy across the full IR spectrum. However, the solar radiation must pass through both the solar atmosphere and the Earth's atmosphere before detection. Absorption by gases in both atmospheres caused a large degree of absorption saturation (regions of zero-energy) (Figure 3.7f). This atmospheric absorption can be modelled and accounted for in the retrieval process, and useful information about excess gas concentrations (e.g. plumes of smoke) is still achievable. Depending on the viewing geometry and the presence and thickness of scattering particles (e.g. smoke aerosols), it is often necessary to fit one or two attenuators (e.g. aluminium mesh) over the spectrometer aperture to prevent detector saturation when using the solar source.

3.1.5.3 White cell

A White cell is a multi-pass gas cell that uses a series of curved focussing mirrors to direct an incident IR beam through multiple traversals of a gas cell, before redirecting the beam to the FTIR spectrometer, enabling a total optical pathlength many times longer than the length of the gas cell, and thus increasing absorption by molecules in the cell (Figure 3.12). Multipass cells are available with pathlengths ranging from centimetres to many hundreds of metres, with or without an enclosure. A multipass cell is usually equipped with its own silicon carbide IR source. Some measurements presented in Chapter 6 of this thesis use a White cell to measure the spectra of Tedlar bag grab samples of smoke from biomass burning events in the UK. The White cell used for this thesis has an optical path length of ~22 m (40 passes of a 55 cm cell path).

Concentrations of the main trace gases CO_2, CH_4 and CO are known to be stable for many hours when held in gas cells, however, the concentration of more exotic trace gases (e.g. H_2CO, CH_3OH, NH_3) are known to decrease significantly over short

timescales (minutes) due to both chemical reactions within the cell and to deposition on to the cell walls/mirrors (Goode *et al.*, 2000). Open-path measurement, rather than White cell measurements are therefore the preferred option in most situations. Open-path measurements also sample a much larger target area than the grab samples collected for White cell analysis.

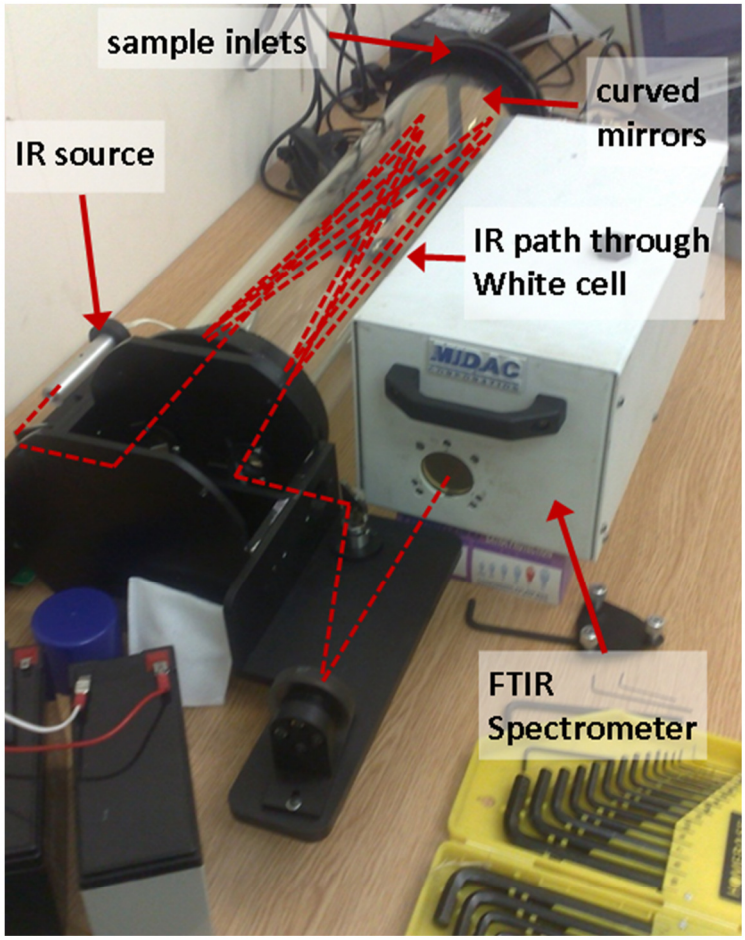

Figure 3.12 Photograph of the White cell used for this thesis with an indication of the IR beam passing through the cell (broken red line). A 12 V battery powered IR source emits IR radiation that is directed along multiple passes through the cell by a series of curved mirrors before exiting the cell and being directed into the FTIR spectrometer.

3.2 Procedure for gas concentration retrieval

3.2.1 Spectral pre-processing

Each spectral measurement used for analysis of trace gas concentrations may be derived from a series of co-added interferograms (generally 4 or 8 co-added scans are used for measurements presented in this thesis, a compromise between temporal resolution and signal-to-noise). The interferograms may be zero-filled (the spectra presented in this thesis use a zero-filling factor of 2), apodized (as described in Sect. 3.1.4.2) and corrected for asymmetries in the interferogram (Smith, 1996).

For measurements that use a bi-static approach (where the FTIR spectrometer is used to measure a distant collimated non-modulated IR source), as taken in this thesis, the measured spectrum includes radiation that has originated from the IR source (I_{SOURCE}), but also from instrument self-emission and from other ambient temperature sources (I_{AMB}) within the field of view of the receiving telescope. At the higher wavenumber regions used to retrieve gases such as CO_2, CO, CH_4, CH_2O (2,000-3,100 cm^{-1}, see Fig. 3.3), the ambient signal contribution is almost non-existent (compare the ambient spectrum in Fig. 3.11d with that of an active IR source in Fig. 3.11e). However, at wavenumber regions below ~1,500 cm^{-1}, where gases such as C_2H_4, HCOOH, CH_3OH and NH_3 are retrieved, the contribution from ambient sources becomes more significant. This ambient signal component introduces a zero-baseline offset to the measured spectra which needs to be removed prior to any trace gas retrieval as this component contains no information related to trace gas absorption (Müller *et al.*, 1999):

$$T_{app} = \frac{I}{I_{SOURCE}+I_{AMB}} \tag{3.27}$$

When I_{AMB} is small (at wavenumbers > 1,500 cm^{-1}, see Fig. 3.11d) the effect on measured transmittance is relatively minor. However, higher levels of I_{AMB} at lower wavenumbers can significantly alter the apparent transmittance (T_{app}).

To correct for this zero-baseline offset, it is necessary to make a measurement of the ambient spectrum (e.g. a spectral measurement with the active IR source turned off) and

subtract this spectrum from each measurement of the active IR source, in accordance with Müller *et al.* (1999). Wooster *et al.* (2011), who follow this methodology, confirm that subtracting the ambient signal has a large effect on retrieved concentrations of NH_3 (retrieved using a spectral window around 940 cm^{-1}); NH_3 concentrations increased by a factor of 2 due to the reduced calculated transmittance (through Eqn. 3.27). Wooster *et al.* (2011) also stress that the impact of ambient signal subtraction is smaller for retrievals of CO_2 and CO at ~2,000 cm^{-1} (<10%). During measurements of a particular fire, some changes in ambient background emission might be expected (e.g. due to changes in air temperature). The majority of measurements presented in this work took place over relatively short-lived fires (< 1 hour) and should therefore not be substantially influenced by changes in the ambient background spectrum. Nevertheless, measurements of ambient spectra were made both before and after a fire where possible, to check for any large changes in the ambient spectrum during the course of a fire.

3.2.2 Spectrum simulation and non-linear least squares fit approach

All trace gas retrievals presented in this thesis are derived using single-beam spectra analysed using a nonlinear least squares (NLLS) method combined with a radiative transfer forward modelling approach, whereby NLLS was used to fit a forward modelled spectrum to a measured spectrum, thus solving the inverse problem of returning gas concentrations from the observations. The method is quite commonly applied in OP-FTIR studies, and examples of retrieval codes include SFIT2 (Rinsland *et al.*, 1998), often used to retrieve total atmospheric column trace gas abundances (e.g. Hase *et al.*, 2006; Fu *et al.*, 2007 and Senten *et al.*, 2008), but also used for ground-based open-path studies (e.g. Briz *et al.*, 2007). A similar procedure (Burton *et al.*, 1998) has been commonly applied to the retrieval of gas concentrations from open path measurements of volcanic plumes (e.g. Oppenheimer *et al.*, 1998; Horrocks *et al.*, 1999 and Richter *et al.*, 2002). Burton *et al.* (1998) is the method used by Wooster *et al.* (2011) for analysis of FTIR spectra of biomass burning plumes in South Africa. The specific retrieval procedure used here is based on the Multi-Atmospheric Layer Transmission (MALT) model of Griffith (1996) and Griffith *et al.* (2003), whose past applications include the analysis of open-path and White cell spectra (Goode *et al.*, 1999; Goode *et al.*, 2000; Bertschi *et al.*, 2003b; Galle *et al.*, 2000; Griffith *et al.*, 2002).

The background theory to the inverse problem is detailed in Rodgers (2000). By denoting the measurement spectrum as vector **y** (the measurement vector) and the variables to be retrieved (the trace gas concentrations) as the state vector **x**, the measurement and its relation to the state vector, can be described as:

$$\boldsymbol{y} = \boldsymbol{f}(\boldsymbol{x}) \tag{3.28}$$

where $f(x)$ is the forward function, describing the physics of the measurement. It is unlikely that the physics of a system will be known and understood with full accuracy. Hence Eq. 3.5 is adapted as:

$$\boldsymbol{y} = \boldsymbol{F}(\boldsymbol{x}) + \boldsymbol{\varepsilon} \tag{3.29}$$

$F(x)$, the forward model, approximates the physics of the measurement, and ε is the measurement error. Here $F(x)$ represents the simulated single beam spectrum.

The radiative transfer forward model used to simulate the spectra $F(x)$ is detailed in Griffith (1996). To parameterise the calculation of $F(x)$ for each measured single-beam spectrum y, the user is required to decide upon an appropriate spectral window for the analysis, and *a priori* values for component trace gas concentrations, pressure, temperature, pathlength, and instrument line shape. From these, the forward model generates a synthetic single-beam spectrum as a combination of a background spectrum (modelled as a polynomial) and the effect caused by gases having IR absorption features within the spectral micro-window of interest. Calculations are performed using the HITRAN database (Rothman *et al.*, 2009), which lists absorption line positions and strengths, widths and details of pressure and temperature dependencies for the given species.

A polynomial function (the order of which is defined as a parameter by the user) is fitted to the measured spectrum and is used to simulate the 100% continuum line (i.e. the signal in the absence of the trace gas absorption). Examples of different fitted polynomial functions are shown in Figure 3.13. The forward model calculates the optical depth (OD) of the target gas at each wavenumber v as a function of the absorption coefficient at ν and the pathlength amount of each gas. A necessary parameter for this computation is the Voigt line shape - the convolution of the Doppler broadening Gaussian line shape function and the pressure broadening Lorentzian line

shape functions. The former is calculated using temperature and molecular weight, and the latter using the pressure dependence given in HITRAN. Convolving the line strengths from HITRAN with the line shape produces the absorption coefficient used to calculate the optical depth. At wavenumber v, the overall OD is taken as the sum of all calculated ODs for all absorption lines for all species. The OD is then converted to a transmission measure and convolved with the instrument line shape (ILS) and the 100% continuum line to yield the final synthetic single-beam spectrum for the spectral window of choice (Figure 3.13). The ILS is dependent on the apodization function used, the instrument field-of-view (FOV), and any modulation loss or phase error in the interferometer. These parameters can be retrieved during the NLLS fitting procedure.

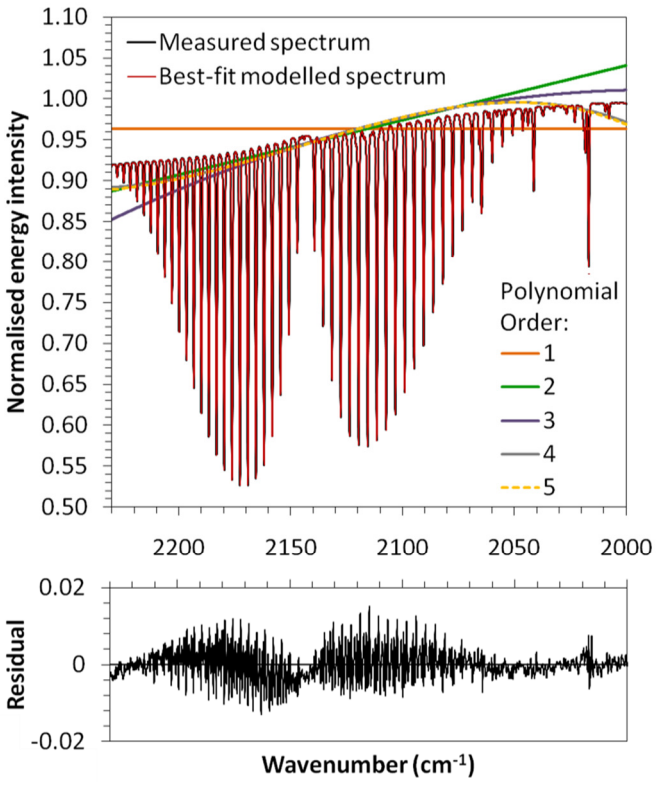

Figure 3.13 Examples of results from a measured spectrum and the best-fit modelled spectrum produced using the MALT radiative transfer forward model and nonlinear least squares (NLLS) fitting procedure described in Griffith (1996). The case shown is for 482 ppm.m of CO at a gas pressure of 1,000 hPa. (top) The measured and best-fit modelled spectra are shown to be extremely well matched, with the different background polynomial functions (orders 1-5) tested also shown. The fourth order polynomial provided the best match to the measured spectrum, and this was used to simulate the best-fit modelled spectrum shown. (bottom) The residual spectrum (i.e. the measured spectrum subtracted from the modelled spectrum), which is used to provide a measure of fitting accuracy.

The difference between the synthetic and measured spectrum yields a residual spectrum (Figure. 3.12, *bottom*); and the chi-squared (χ^2) statistic and the partial derivatives for each of the input parameters are calculated. The Levenburg-Marquardt method (Levenburg, 1944; Marquardt, 1963; Press *et al.*, 1992) is used to find the least-squares linear best fit, and thus the set of optimum gas concentrations that minimise the residual spectrum, based on pre-determined convergence criterion (χ^2 minimum).

3.2.3 Solar occultation

For the analysis of spectra collected using the sun as a source of IR radiation (presented in Chapter 7), two different retrieval procedures were used; FTIR_FIT, described in Burton (1998) and Horrocks (2001); and Atmosphit (Hurtmans *et al.*, 2005). Both of these computer codes follow a similar procedure to that described for MALT in the previous section, although there are some key differences between the approach for the analysis of solar spectra and that used by MALT for active, horizontal path spectra.

First, a different model of the atmospheric path must be used for analysis of solar spectra. For a spectrum measured using an active IR source along a horizontal path, the modelled spectrum requires only a single atmospheric pressure and temperature parameter, with uniform concentration of trace gases dispersed along the path. For a solar spectrum, however, the IR transmittance through the whole atmosphere in addition to the biomass burning plume must be modelled. To achieve this, FTIR_FIT models the atmospheric path in two stages: a 50-layer model atmosphere defined using the Fast Atmospheric Signature code (FASCODE) where the vertical profiles of pressure, temperature and trace gas concentrations are calculated using a single ground-level temperature and pressure input (Clough *et al.*, 1985); this is followed by a single pressure and temperature homogeneous plume layer. For both stages, optical depths for the relevant path profile are generated following a similar approach to MALT (described above). Atmosphit provides a more versatile approach, allowing the user to fully specify the model atmosphere to be modelled (it is therefore possible to use radiosonde measurements of actual atmospheric profiles rather than modelled profiles using ground-based measurements). Instead of the two-stage approach used in FTIR_FIT, a biomass burning plume may be represented in Atmosphit by increasing the

a priori amounts of particular biomass burning trace gases in the lowest layer of the atmospheric profile.

Second, it is important to account for absorptions within the solar atmosphere. To achieve this, both FTIR_FIT and Atmosphit use a pure exoatmospheric sun spectrum measured by the Atmospheric Trace Molecule Spectroscopy (ATMOS) experiment, a spaceborne FTIR spectrometer (Abrams *et al.*, 1996).

3.2.4 Reported error

As with other spectrally-based trace gas retrieval approaches based on forward modelling and nonlinear fitting methods (e.g. Burton, 1998), MALT, FTIR_FIT and Atmosphit report the standard error for each of the retrieved trace gas amounts and the *a priori* input parameters (this metric is termed the reported error hereafter). For each iteration of the NLLS fitting procedure, the covariance matrix is determined from the standard deviation of the residual spectrum (i.e. the synthetic spectrum subtracted from the measured spectrum). The reported error for parameter $\boldsymbol{x_i}$ is defined as the square root of the i^{th}diagonal element of the covariance matrix, and is influenced by choice of a priori fixed input parameters, model errors/lack of fit, measurement noise, amount of information (the width of the spectral window and intensity of signal within that window) and degrees of freedom (which reduces with increasing number of parameters).

The reported error is based on the quality of the fit between the measured and modelled spectra, and is in part designed to provide the user with information potentially useful in gauging the quality of the retrieval process. Most ideally the user would like to know the actual retrieval error, i.e. the true difference between the amount of trace gas present in the optical path and that reported by the retrieval procedure. This retrieval error can have both random and systematic components, and improved understanding of the relationship between the reported error and retrieval error is one of the aims of Chapter 4, along with an appreciation of the absolute accuracies able to be obtained from the method, and their sensitivity to model parameterisation uncertainty.

3.3 FTIR for biomass burning research

3.3.1 Procedure in the field

A schematic and photograph of typical field instrumentation are shown in Figure 3.14. The instrumentation is bulky, particularly when the spectrometer is operated with a large telescope or when the large IR source is used. For the field campaigns included in this thesis, a 'minimalist' setup was used. By using the spectrometer with the small, 76 mm telescope and using the small IR source, the entire OP-FTIR instrumentation, including tripods can fit into a 60 cm × 60 cm × 40 cm box, weighing less than 32 kg. Whilst this setup allows relatively easy transportation by car, the disadvantages of using a smaller telescope and IR source leads to limitations in the field as a shorter pathlength is required to minimise signal loss from the IR lamp. The portability of the spectrometer is enhanced further by the Stirling-cooled detector, overcoming logistical and portability issues associated with liquid nitrogen-cooled spectrometers. The Stirling-cooler does, however, require far more power, reducing the battery-life significantly. Consequently, a high capacity (>12 Ah) rechargeable 12 V battery was used to power the spectrometer. A 12 V battery was also used to power the IR source. A 30 Ah battery can typically power the spectrometer for 3–4 hours, or the IR source for a full day's fieldwork.

Generally, the spectrometer was operated in 'active' mode (i.e. with the IR source lamps). The spectrometer and lamp were positioned downwind of the planned experimental fires, or in some cases were positioned to form a path directly above the planned fire. This method was first described in Griffith *et al.* (1991) and used subsequently by Wooster *et al.* (2011); no other applications using a long open-path (>10 m) methodology for analysis of biomass burning plumes are known to the author. Alignment of the spectrometer and IR source was achieved by a two-step process. The spectrometer and lamp are first aligned by sight, using guide telescopes attached to both the spectrometer and lamp. Following the visual alignment, the spectrometer tripod-head was adjusted vertically and horizontally, whilst monitoring the spectrometer's signal output (the peak-to-peak voltage of the interferograms) on a laptop computer. Once the maximum signal level was ascertained (usually between 1 and 3 V), the process was repeated with the lamp. After setting up on many occasions, it becomes

possible to memorise a precise relative position to point the spectrometer and lamp for maximum signal, reducing the amount of time spent aligning to less than 10 minutes.

Once a fire was ignited, it was possible to monitor the recorded spectra using a standard laptop PC. This enabled monitoring of the alignment throughout a fire, and could also be used to confirm the presence of smoke gas species from their spectral signatures. Furthermore, a simple concentration retrieval algorithm was implemented in real-time to give an indication of CO_2, CO, CH_4 and H_2O concentrations.

When operated in solar occultation mode, the spectrometer was fitted with a mirror to direct reflected sunlight through the spectrometer aperture (see Fig. 3.11c). The

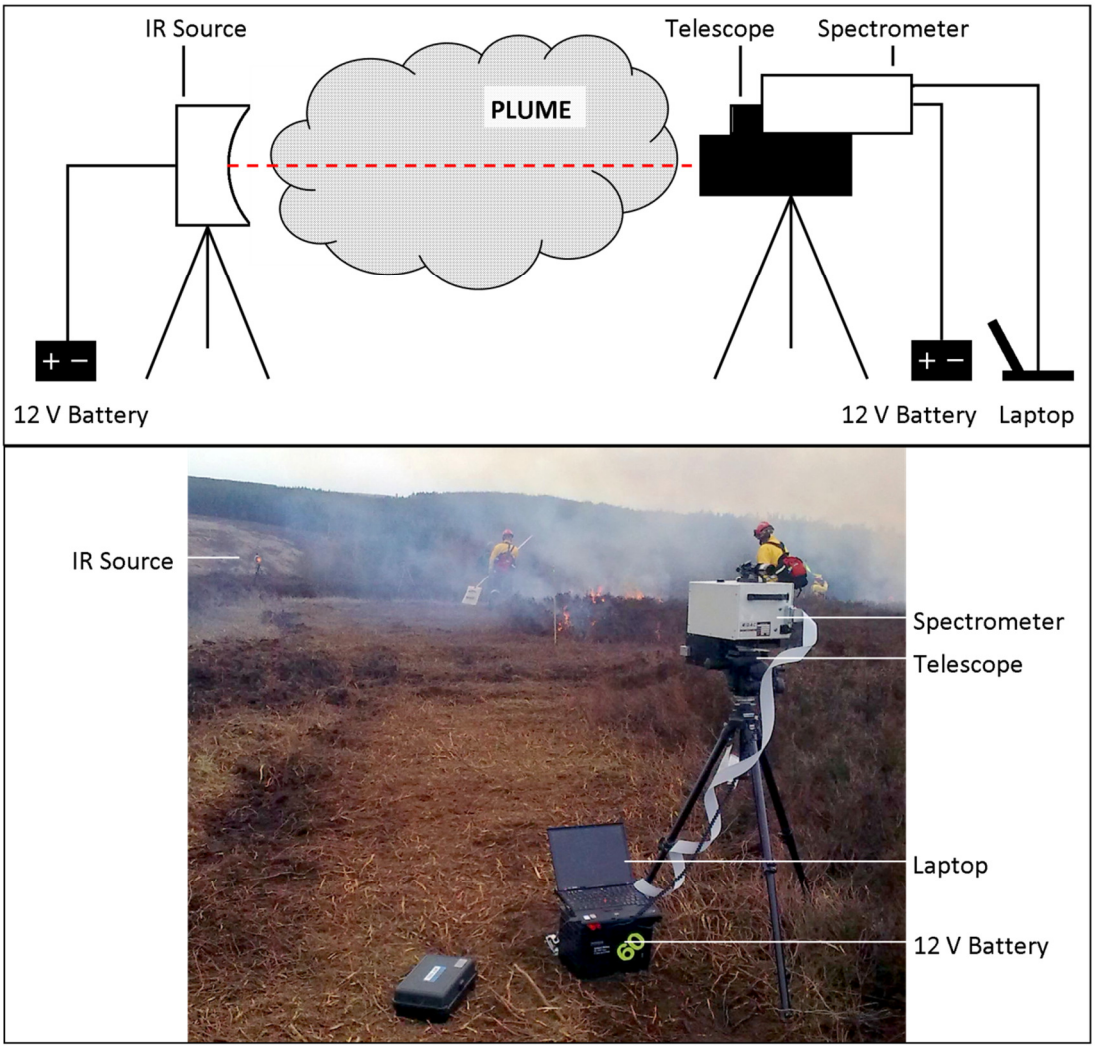

Figure 3.14 (top) Illustration showing typical instrumentation in the field. (bottom) Photograph of a typical field setup. The pathlength in this photograph is ~30 m.

attachment consists of two mirrors, a main mirror and a smaller guide mirror. The guide mirror projects the solar disc above the spectrometer aperture. After aligning the spectrometer manually using the tripod-head to maximise the signal at the detector, the position of the projected solar disc can be marked onto paper attached above the spectrometer aperture, and can be used as a reference to aid re-alignment as the position of the sun changes. Two aluminium mesh attenuators were attached to the telescope aperture to avoid detector saturation.

Temperature and pressure measurements were made routinely using a WXT510 weather station (Vaisala Oyj, Helsinki) and/or a Kestrel handheld weather station (Nielsen Kellerman, Boothryn, Pennsylvania).

3.3.2 Retrieval of biomass burning trace gas concentrations

This thesis presents the results of concentration retrievals for CO_2, CO, CH_4, C_2H_2, C_2H_4, C_2H_6, CH_2O, HCOOH, CH_3OH, NH_3, and HCN. These trace gases represent the most important direct greenhouse gas species (Chapter 2.1.1) and some of the most important ozone pre-cursor trace gases (Chapter 2.1.2) emitted from biomass burning. The retrieval procedure is detailed in Section 3.2. For each gas, a spectral window was selected that contained one of the characteristic vibrational-rotational transitions for the particular gas molecule (see Sect. 3.1.1.3). Interference with strong H_2O and CO_2 absorption at some frequencies, and the spectral response limitations of the MCT detector (650–5,000 cm^{-1}), often restrict the available transitions to one branch of an absorption band (e.g. the R-branch of HCN) or a few individual absorption lines (e.g. C_2H_6) (Table 3.3). The spectral window and background polynomial function used for the retrieval of each trace gas is listed in Table 3.3. Depending on the size of the spectral window, each spectral analysis can take between 1–6 seconds using a standard laptop PC at the time of writing. An example biomass burning plume spectrum is shown in Figure 3.15, with each subplot illustrating one of the 8 spectral windows used to retrieve the 11 trace gases listed in Table 3.3. A different set of spectral windows were used for a more limited range of trace gases for the solar occultation retrievals, these are outlined in Chapter 7.

Over the course of the seven field campaigns to experimental burns and wildfires in Australia, the UK, and Canada, ~20,000 spectra were measured. Due to this large quantity of data, it was necessary to use a systematic method for retrieving gas concentrations from bulk sets of spectra. The retrieval algorithms were run in batch mode; when anomalous features were apparent in the retrieved data, a subset of data would be manually inspected. Generally, two factors led to high reported errors and anomalous concentration retrievals. First, spectra in the dataset that had low throughput (e.g. when a person or vehicle obstructs the IR path to the spectrometer); such spectra should not be used for spectral analysis and were automatically filtered using the spectral intensity at 2,000 and 3,000 cm^{-1}. Second, some of the IR paths would occasionally be intruded by flames or very hot gases from the fire; in this case, a complicated mixture of spectral absorption and emission are present in the measured spectra. A lack of information about the distance between the flames and the spectrometer and the thickness of the flames renders such spectra useless for trace gas concentration retrieval. A manual inspection of the dataset was used to identify and remove such flame contaminated spectra. Subsequent analysis of any remaining flame contaminated spectra yielded large reported errors (>2 s.d. above normal measurements) and these errors were used to automatically remove such measurements from any further analysis and interpretation. Analysis of all 20,000 spectra for CO_2 (using the broadest spectral window) completes in ~48 hours, whilst analysis for NH_3 (a narrower spectral window) can be complted in ~8 hours using a conventional desktop PC.

Table 3.3 Spectral windows and background polynomial functions used for analysis of the biomass burning smoke plume gases.

Trace gas	Spectral window (cm^{-1})	Absorption feature	Poly.	Interfering gases
CO_2	2150-2310	$\nu 3$ (2349 cm^{-1}) P-branch	2	CO, N_2O, H_2O
CO	2150-2310	$\nu 1$ (2143 cm^{-1}) R-branch	2	CO_2, N_2O, H_2O
CH_4	2980-3090	$\nu 1$ (2917 cm^{-1}) stretch P-, Q-, & R-branch	4	H_2O
C_2H_2	710-760	$\nu 5$ (730 cm^{-1}) CH-bend, P- & R-branch	3	CO_2, H_2O, HCN
C_2H_4	900-980	$\nu 7$ (949 cm^{-1}) & $\nu 8$ (943 cm-1) CH2 wag	3	NH_3
C_2H_6	2971-3002	$\nu 10$ (2985 cm^{-1}) CH_3 stretch	3	H_2O, CH_4, C_2H_4
CH_2O	2700-2830	$\nu 1$ (2783 cm^{-1}) CH_2 stretch, P- & R-branch	4	H_2O, CH_4
HCOOH	1100-1147	$\nu 6$ (1105 cm^{-1}) C-O stretch, Q- & R-branch	4	H_2O, NH_3
CH_3OH	1000-1080	$\nu 8$ (1033 cm^{-1}) C-O stretch, P-, Q-, & R-branch	3	NH_3
NH_3	900-980	$\nu 2$ (950 cm^{-1}) deformation	3	C_2H_4
HCN	710-760	$\nu 2$ (712 cm^{-1}) bend, Q- & R-branch	3	CO_2, H_2O, C_2H_2

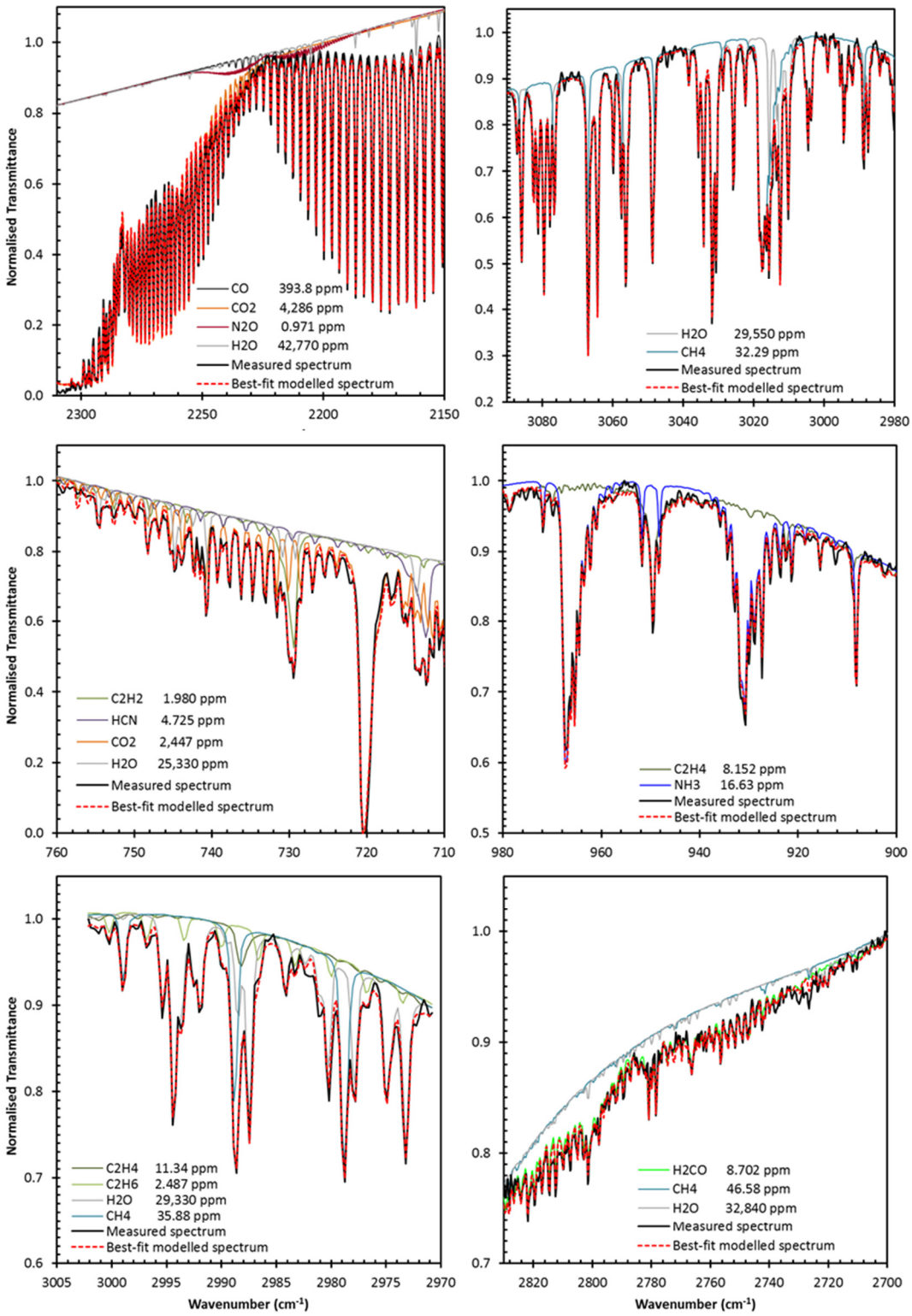

Figure 3.15 (continued on following page) Typical retrieval spectral windows for each of the trace gases listed in Table 3.3: (a) CO_2 and CO; (b) CH_4; (c) C_2H_2 and HCN; (d) C_2H_4 and NH_3; (e) C_2H_6; (f) CH_2O; (g) HCOOH; and (h) CH_3OH. The measured spectrum (black) was collected on 22 March 2010 at an experimental heather burn in Northumberland UK. The best-fit modelled spectrum is also shown (dashed red) along with each of the individually modelled trace gas spectra (multiple colours). The modelled spectrum is the sum of each of the individual trace gas spectra.

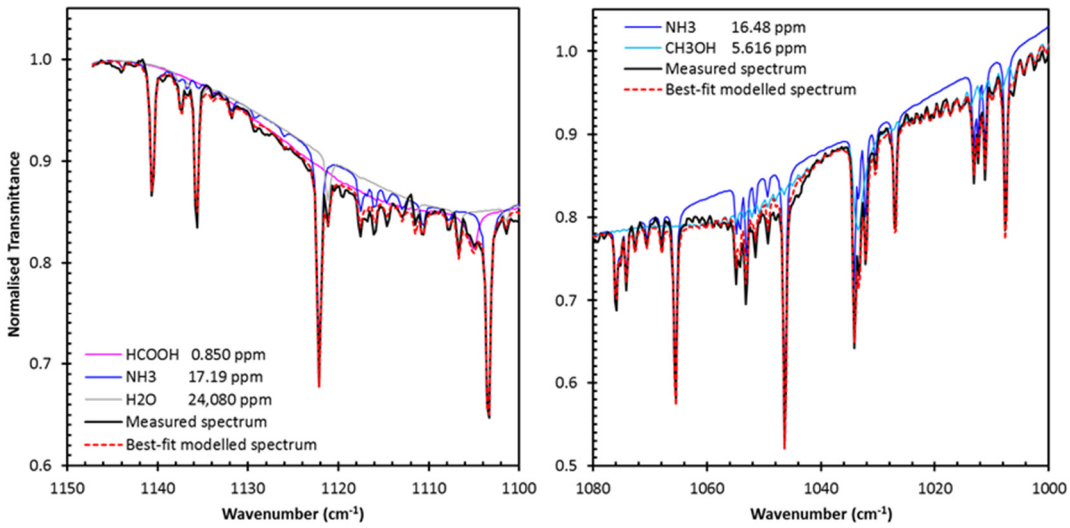

Figure 3.15 (continued from previous page)

3.3.3 Emission metrics

3.3.3.1 Emission ratios

As previously discussed in Section 2.2, the emission ratio ($ER_{x/y}$) is the molar concentration of trace gas species *x* against reference gas species *y*. As in Eqn. 2.8, the molar concentrations of *x* and *y* are normally expressed as the excess above 'background' molar concentrations (i.e. before emission, or in air not affected by emission). However, for open-path FTIR spectroscopy, this approach is complicated by the fact that the plume may typically only partially fill the optical path and thus the volumetric concentration of trace gas species *x* and *y* measured by the OP-FTIR method will be an average of the volumetric concentrations of *x* and *y* in the plume and in the ambient atmosphere (weighted by *f*, the fraction of the optical path taken by the pure plume). The fraction *f* can change greatly between measurements as the smoke plume builds and subsides (Wooster *et al.*, 2011; Horrocks, 2001):

$$x = \left[fLX_{\mathrm{p}}\right] + \left[(1-f)LX_{\mathrm{a}}\right] \tag{3.30}$$

$$y = \left[fLY_{\mathrm{p}}\right] + \left[(1-f)LY_{\mathrm{a}}\right] \tag{3.31}$$

Where X_p and Y_p are the mean volumetric concentrations of species x and y in the pure plume, respectively; and X_a and Y_a are the volumetric concentrations of the same species in the pure ambient atmosphere (expressed in units of ppmv or ppbv); L is the total path length. Equations 3.30 and 3.31 can be combined to remove dependence on the unknown and highly variable f:

$$y = \left(\frac{Y_p - Y_a}{X_p - X_a}\right) x - L\left[X_a\left(\frac{Y_p - Y_a}{X_p - X_a}\right) - Y_a\right] \quad (3.32)$$

As highlighted by Wooster *et al.* (2011), this equation is that of a straight line ($y = mx + c$), which can be obtained when the volumetric concentration of species y is plotted against that of species x, where the gradient, m, is a function of the relative abundances of the two species in the pure plume and pure atmosphere:

$$m = \left(\frac{Y_p - Y_a}{X_p - X_a}\right) \quad (3.33)$$

Given that the volumetric concentration of biomass burning gas species in the "pure" unmixed plume are far greater than those in the "pure" ambient atmosphere (i.e. $Y_p >> Y_a$ and $X_p >> X_a$). Gases with both high dry-air in-plume concentrations (e.g. 90% for CO_2, 6% for CO) according to Andreae and Merlet (2001) and low relatively lower concentrations (e.g. 0.3% for CH_4, 0.04% for NH_3) exhibit volumetric concentrations many orders of magnitude greater than in the ambient atmosphere (e.g. 0.0385% for CO_2, 0.00002% for CO, 0.00018% for CH_4, and <0.000002% for NH_3. As Wooster *et al.* (2011) find, the maximum error that can be introduced by using the gradient m to approximate $ER_{x/y}$ occurs when combinations of gases with pure plume concentrations closest those in the ambient atmosphere (e.g. CO_2 and CH_4 whose abundance in the plume is ~2300 and ~1700× higher in the plume than in the dry atmosphere, respectively). For this "worst" case, the error introduced by using Eqn. 3.33 to approximate $ER_{x/y}$ is less than 0.05% (Wooster *et al.*, 2011). Wooster *et al.* (2011) and Sawyer *et al.* (2008) conclude that emission ratios (for biomass burning and volcanic emissions respectively), can be calculated directly from the retrieved trace gas volumetric concentrations without the separation of "ambient atmosphere" and "plume" components and without the need to calculate excess abundances. Instead, the emission

ratio may be determined as the least squares linear regression slope of the species concentration versus the reference species (Yokelson *et al.*, 1999; Wooster *et al.*, 2011). This method is employed for the results presented in Chapters 5, 6, and 7.

As emission ratios are most frequently expressed with CO_2 as the reference species for flaming emissions (see Sect. 1.2.2) and with CO as the reference for smouldering emissions, both $ER_{x/CO2}$ and $ER_{x/CO}$ are reported in these Chapters. As the $ER_{x/y}$ of two trace gas species can vary substantially between different combustion stages (e.g. between flaming and smouldering combustion as outlined in Sect. 1.1.2), divergent gradients can be introduced to the *x* vs. *y* scatter plots used to calculate emission ratios. Whilst the OP-FTIR measurements used in this thesis provide spatially integrated measurements of the smoke generated by both flaming and smouldering combustion occurring simulataneously across the plot, some measurements are affected by changes in the contribution of flaming and smouldering combustion (e.g. at fire ignition when measurements are dominated by flaming emissions, and at the end of the fire when flaming has ceased and measurements are dominated by smouldering emissions). To aid interpretation of these results (discussed further in Chapters 5 and 6), a simple modified combustion efficiency (MCE, Eqn. 2.7) threshold is applied, distinguishing between measurements of emissions believed to be from the predominantly flaming or smouldering combustion stages. Following Yokelson *et al.* (1997), spectra measured with an MCE of less than 90% are classified as smouldering, whilst spectra with a higher MCE are classified as flaming.

3.3.3.2 Emission factors

The emission factors (g kg^{-1}) calculated for this thesis use a modified form of Eq. 2.9 (Ward and Radke, 1993). This approach assumes that all of the carbon released in the plume is contained in the measured carbon compounds, allowing emission factors for each trace gas species to be calculated using their respective emission ratios using a total carbon mass balance (Ward and Radke, 1993):

$$\mathrm{EF}_x = C_{biomass} \cdot 1000 \cdot \frac{MM_x}{MM_C} \cdot \frac{C_x}{C_T} \tag{3.34}$$

Where $C_{biomass}$ is the mass fraction of carbon in the fuel (0.5±0.05 in accordance with Ward *et al.*, 1996), MM_x is the molecular mass of species x (g), MM_C is the molecular mass of carbon (12 g), and C_x/C_T is the ratio of the number of moles of species x in the plume against the total number of moles of carbon, calculated as:

$$\frac{C_x}{C_T} = \frac{ER_{x/CO_2}}{\sum_{i=1}^{n}(NC_i.ER_{i/CO_2})} \tag{3.35}$$

Where NC_i is the number of carbon atoms in the compound i and the sum is over all carbonaceous species in the plume, including CO_2. As is typical of biomass burning emissions studies, not all carbon containing compounds are actually quantified in this thesis. However, the contribution of CO_2, CO and CH_4 account for the vast majority (99%) of the total carbon flux from open biomass fires (Akagi *et al.*, 2011; Keene *et al.*, 2006; Delmas *et al.*, 1995). The majority of the remaining carbon is emitted as NMVOCs (a number of which are measured for this thesis) and aerosols (Akagi *et al.*, 2011). The unmeasured trace carbon compounds and aerosols are ignored in the application of Eqns. 3.34 and 3.35 for this thesis; a simplification that is common amongst biomass burning studies, and which may inflate the resultant emission factors by only a few percent, at most (Wooster *et al.*, 2011; Andreae and Merlet, 2001; Goode *et al.*, 2000; Yokelson *et al.*, 1999).

3.3.3.3 Uncertainty estimation

Emission ratios are established only when there is a strong correlation between the two trace gas species (when the coefficient of determination, R^2, of the least squares linear regression line is greater than 0.4, in accordance with Sinha *et al.* (2003)). The emission ratio uncertainty is taken as the 95% confidence limits on the least squares linear regression line gradient. Uncertainties in the emission factors are calculated in quadrature from those associated with the trace gas emission ratios and the ±10% uncertainty in the assumed fuel carbon content.

3.3.3.4 A note on units

The number of molecules per unit volume (e.g. moles cm^{-3}) is the most common unit of concentration used for gas phase tropospheric chemistry applications (Horrocks, 1999)

and may be referred to as a mixing ratio or a volumetric concentration. Spectroscopic measurements, however, integrate across the infrared pathlength; as such, gas concentrations are retrieved as the concentration-pathlength product responsible for the particular absorption feature being studied. This measurement yields a columnar density (from integrating a volumetric density over a column) with units that are measured in molecules per cm^2. Unlike gaseous volumetric concentrations (e.g. parts per million by volume, ppm), the molecules per cm^2 unit is independent of temperature and pressure. For familiarity and for comparisons with concentrations reported in the literature, the trace gas concentrations retrieved from OP-FTIR in this study are reported as pathlength-averaged volumetric concentrations (in ppm). The equation relating ppm and molec cm^{-2} is:

$$X_i = \frac{x_i \, L \, p \, A}{R \, T} \tag{3.36}$$

Where X is the retrieved columnar density of gas i (molec cm^{-2}), x is mixing ratio of gas i (unitless), p is pressure (Pa), T is temperature (K) and L is pathlength of the sample (m), A is Avogadro's constant (6.022×10^{22} mol^{-1}) and R is the gas constant (8.315 J $[mol.K]^{-1}$). This may be simplified by collecting together Avogadro's number and the ideal gas constant, and by using units of ppm for the mixing ratio so that:

$$X_i = \frac{x_i \, L \, p}{T} \times (7.243 \times 10^{14}) \tag{3.37}$$

Units of molecules per cm^2 are only used for describing solar occultation measurements of total atmospheric columns.

3.3.4 White cell procedure

A number of grab bag samples were taken during two field campaigns in the UK. The bag sampling was used to directly sample emissions from distinct combustion phases (chiefly flaming and smouldering phases, although attempts were also made to measure pyrolysis) for use in a comparison with the open-path spatially integrated measurements (see Chapter 6 for further details). The sampling unit consisted of a sampling probe connected to a backpack mounted air pump with space for sampling bags. Flaming

combustion samples were collected by sampling close to the headfire (positioning the probe inlet ~50 cm above the flames), whilst smouldering samples were collected by sampling flameless residual combustion behind the fire front. Pyrolysis stage combustion products were also targeted in the advected smoke close to the vegetation and below the flaming combustion zone. Once collected, the bag samples were analysed in the White cell (Infrared Analysis Inc., Anaheim, California) within 1–5 days of collection (the implications of this delay are discussed in Chapter 6).

The concentration of trace gas species x within the sample bag (X_B) is the average of the volumetric concentrations of species x in the plume and in the ambient atmosphere (weighted by f, the fraction of the bag sample volume that contains the pure plume):

$$X_B = [fX_p] + [(1-f)X_a] \tag{3.38}$$

Where X_p is the mean volumetric concentration of species x the pure plume, and X_a is the volumetric concentration of the same species in the pure ambient atmosphere. Ideally, it should be possible to evacuate the White cell to a vacuum and proceed to fill the White cell with the bag sample. The retrieved concentrations for the White cell, X_C, would therefore be equal to those for the bag, X_B. However, a number of factors complicate the method for retrieval of plume trace gas concentrations using the White cell for this thesis. First, the White cell volume is 8.5 litres, whereas the Tedlar bag maximum capacity is either 5 litres or 10 litres; most of the bag samples used in this thesis would not fill the White cell. Second, the White cell could not be evacuated down to a vacuum. Instead, the White cell would be evacuated down to ~0.6 bars, before the bag sample was used to fill the White cell to ambient pressure (the White cell would be flushed with ambient air between measurements). These limitations required mixing the bag samples with ambient air from the laboratory so that the measured concentration in the cell is defined as:

$$X_C = gX_B + (1-g)X_R \tag{3.39}$$

Where g is the fraction of the gas cell volume taken by the bag sample, X_B is the volumetric concentration of species x in the bag and X_R is the volumetric concentration of species x in the laboratory. Substituting Eqn. 3.38 into Eqn. 3.39 we get:

$$X_C = gfX_p + g(1-f)X_a + (1-g)X_R \quad (3.40)$$

Re-arranging for gfX_p to get:

$$gfX_p = X_C + g(1-f)X_a + (1-g)X_R \quad (3.41)$$

When a secondary species *y* is considered for the calculation of $ER_{x/y}$ (= X_p/Y_p) we get:

$$\frac{gfX_p}{gfY_p} = \left[\frac{X_C + g(1-f)X_a + (1-g)X_R}{Y_C + g(1-f)Y_a + (1-g)Y_R}\right] \quad (3.42)$$

Where Y_p, Y_C, Y_a, and Y_R are the volumetric concentrations of species y in the pure plume, in the gas cell, in the ambient atmosphere when the bag sample was taken, and in the ambient air in the laboratory, respectively. Typically, measurements made using a handheld KANE-100 CO_2 NDIR gas analyser (Kane International, Welwyn Garden City) revealed that the volumetric concentration of CO_2 within the bag samples ranged from 5,000–10,000 ppm (0.5–1%). Given that pure plume concentrations of CO_2 are expected to be ~90% (Andreae and Merlet, 2001), it may be assumed that the fraction of the volume of the bag sample taken by the pure plume (*f*) is small (<0.015) due to efficient mixing with the ambient atmosphere before sampling. Consequently, Eqn. 3.42 may be simplified to:

$$ER_{x/y} = \frac{X_p}{Y_p} \approx \left[\frac{X_C + g(X_a - X_R) + X_R}{Y_C + g(Y_a - Y_R) + Y_R}\right] \quad (3.43)$$

As it is possible to make measurements of the ambient atmosphere when the bag sample was taken (by taking additional bag samples of the ambient atmosphere), and it is also possible to make measurements of the ambient air in the laboratory (by collecting spectra of the White cell flushed with ambient air from its surroundings), the only remaining unknown in Eqn. 3.43 is *g*, the fraction of the gas cell volume taken by the bag sample. It is possible to estimate *g* using a manometer (pressure gauge) attached to the White cell. Unfortunately, the precision of the analogue pressure gauge fitted at the time of this thesis did not allow for sufficiently precise measurements of the evacuated pressure level. Instead, the handheld CO_2 gas analyser was used to make measurements of the bag sample so that the volumetric concentration of CO_2 was known for the cell

$(X\mathrm{CO_2})_\mathrm{C}$, the bag $(X\mathrm{CO_2})_\mathrm{B}$, and the ambient air in the room $(X\mathrm{CO_2})_\mathrm{R}$. The volumetric concentration of CO_2 in the cell is described as:

$$(X\mathrm{CO_2})_\mathrm{C} = g(X\mathrm{CO_2})_\mathrm{B} + (1-g)(X\mathrm{CO_2})_\mathrm{R} \tag{3.44}$$

From the above, we can re-arrange for g, so that:

$$g = \left[\frac{(X\mathrm{CO_2})_\mathrm{C} - (X\mathrm{CO_2})_\mathrm{R}}{(X\mathrm{CO_2})_\mathrm{B} - (X\mathrm{CO_2})_\mathrm{R}}\right] \tag{3.45}$$

This then enables us to calculate g and solve Eqn. 3.43 to yield $\mathrm{ER}_{x/y}$. This methodology yields emission ratios for each individual bag sample from which emission factors can be calculated using the approach described in Sect. 3.3.3.2.

3.4 Conclusions of Chapter 3

This Chapter began with a description of the physical processes that are fundamental to infrared absorption; a phenomenon that can be measured to reveal the identity and quantity of trace gases within a gas mixture. After an explanation of how an FTIR spectrometer can be used to make measurements of infrared absorption, the focus turned to how specific gas amounts can be quantified and the relevance of this to measurements of biomass burning plumes, these may be summarised as:

(a) The composition of biomass burning plumes can be measured by infrared absorption spectroscopy. The transmission of infrared radiation is linked to the amount of a trace gas via the Beer-Lambert law. Temperature and pressure cause broadening of trace gas absorption lines and the lines are also convolved to an instrument line shape. These effects lead to a deviation from the Beer-Lambert law that must be accounted for in the analysis process.

(b) Fourier transform infrared (FTIR) spectroscopy uses a Michelson interferometer to record an interferogram (a measurement of energy intensity as a function of optical path difference). The infrared spectrum is a Fourier transform of this interferogram convolved to the instrument line shape (a function of the

maximum optical path difference, the field of view of the spectrometer and the apodization function).

(c) Open-path FTIR (OP-FTIR) spectroscopy is a portable tool that can be used in remote areas for the measurement of biomass burning plumes. The Stirling-cooled detector negates the requirement for liquid nitrogen. It is possible to fit all of the necessary OP-FTIR equipment into a single case weighing less than 32 kg that may be transported by a passenger airline as hold luggage. The FTIR spectrometer may be used to view an active infrared source or the sun as the source of IR radiation.

(d) Retrieving trace gas concentrations from a measured spectrum requires software that can forward model a spectrum, using *a priori* trace gas concentrations and atmospheric/instrument parameters that affect line shape, coupled with a fitting procedure that finds the concentrations that yield the best-fit modelled spectrum. The forward model MALT uses absorption lines from the HITRAN database (Rothman *et al.*, 2009) convolved to the instrument line shape and fitted to a background polynomial curve. The fitting procedure is an optimal estimation non-linear least squares algorithm that returns the best-fit trace gas volumetric concentrations and reports errors for each estimation. The retrieval procedure requires a user to specify a spectral window for analysis, which needs to consist of absorption lines of the trace gas of interest, but also minimise the effects of interfering trace gas species (usually H_2O).

(e) Given that the volumetric concentration of biomass burning trace gas products are far greater in the pure plume than in the ambient air, the emission ratio may be determined as the least squares linear regression slope of the target species concentration versus the reference species concentration. The emission ratios may then be used to calculate emission factors using a carbon mass balance calculation.

This Chapter has focussed on the theoretical suitability of OP-FTIR for measurements of biomass burning plumes. The following Chapter aims to test this suitability by performing a number of accuracy assessments in both field and controlled laboratory environments.

4

Evaluating the Accuracy, Precision and Sensitivity of OP-FTIR Trace Gas Concentration Retrievals

When compared to established point-sampling methods, Open-Path Fourier Transform Infrared (OP-FTIR) spectroscopy can provide path-integrated concentrations of multiple gases simultaneously, *in situ* and near-continuously. As described in the previous Chapter, trace gas concentrations can be retrieved from the measured IR spectra using a forward model coupled to a non-linear least squares fitting procedure, without requiring 'background' spectral measurements unaffected by the gases of interest. However, despite the increasing popularity of OP-FTIR as a methodology for a range of applications (Baksik *et al.*, 2007), few studies have investigated the accuracy of such trace gas concentration retrievals, particularly across a broad concentration range covering ambient to highly polluted air (e.g. from biomass burning).

This Chapter begins with two pilot studies that compare retrieved trace gas concentrations using OP-FTIR with those from other, more conventional point-based measurement approaches. The first pilot study (Section 4.1) compares OP-FTIR retrievals of near-ambient CO_2 concentrations measured in the open atmosphere with those from a standard Licor non-dispersive infrared (NDIR) analyser. The second pilot study (Section 4.2) is concerned with slightly elevated concentrations of ammonia (in an agricultural setting), where OP-FTIR measurements of NH_3 were compared with

those from several other techniques. These types of open atmosphere approaches are particularly useful for rapidly determining the sensitivity of the OP-FTIR method to the types of small variations in trace gas concentrations that can be expected in many natural situations, and for investigating volatile or 'sticky' gases, such as NH_3, that cannot be contained in a gas cell. This Chapter culminates with a comprehensive experimental assessment of OP-FTIR retrieval accuracies for a range of concentrations of CO_2, CH_4 and CO (using a gas cell containing known quantities of each gas) that might be experienced in a biomass burning environment (Section 4.3). An analysis of the sensitivity of the retrieval procedure (described in Section 3.2) to instrument parameters and environmental variables is also presented. This Chapter addresses the first thesis research question outlined in Section 2.6 concerning the accuracy and precision of OP-FTIR measurements of biomass burning trace gas species.

Section 4.2 has been published as part of von Bobrutzki et al. (2010) in Atmospheric Measurement Techniques (volume 3, issue 1, pages 91–112).

Section 4.3 (with Section 3.2.2) has also been published as Smith et al. (2011) in Atmospheric Measurement Techniques (volume 4, issue 1, pages 97–116).

4.1 Comparison of OP-FTIR with NDIR CO_2 measurements

To assess the ability of OP-FTIR methods to deliver accurate and precise gas concentrations in the ambient atmosphere, the FTIR spectrometer described in Section 3.1.4 was used to measure small changes in the concentrations of CO_2 at an urban location in central London. A calibrated Licor 840 NDIR closed-path gas analyser was used to monitor CO_2 concentrations at the same location, albeit at a point close to the spectrometer's location rather than across an open path.

4.1.1 Methodology

The MIDAC FTIR spectrometer described in Section 3.3 was used in conjunction with the small 15 cm IR source (pictured in Fig. 3.11a) in the bi-static open-path configuration across a pathlength of 65 m between the roof of the King's Building, King's College London (altitude = 26 m), where the FTIR spectrometer was situated, and the roof of the Strand Building, King's College London (altitude = 38 m), where the IR lamp was situated (Figure 4.1). The tube inlet for the Licor gas analyser was located close to the spectrometer end of the open path on the roof of the King's Building, ~2 m above the surface of the roof. Due to changes in traffic and other emissions sources, as well as changes in the ambient wind direction, temporal variations in the atmospheric CO_2 concentration can be expected over the day.

The Licor 840 gas analyser uses the non-dispersive infrared (NDIR) technique; sampled air is drawn into a temperature and pressure-controlled closed chamber where an infrared beam is passed through the air sample and the infrared absorption is measured at a single wavelength. The Licor 840 had been calibrated earlier in the day using a zero gas (pure nitrogen) and a CO_2 reference gas (air with 804.8 ppm CO_2). The Licor 840 records a CO_2 concentration measurement every 0.5 seconds, whilst the spectrometer was operating at a temporal resolution of ~10 seconds (8 co-added scans per

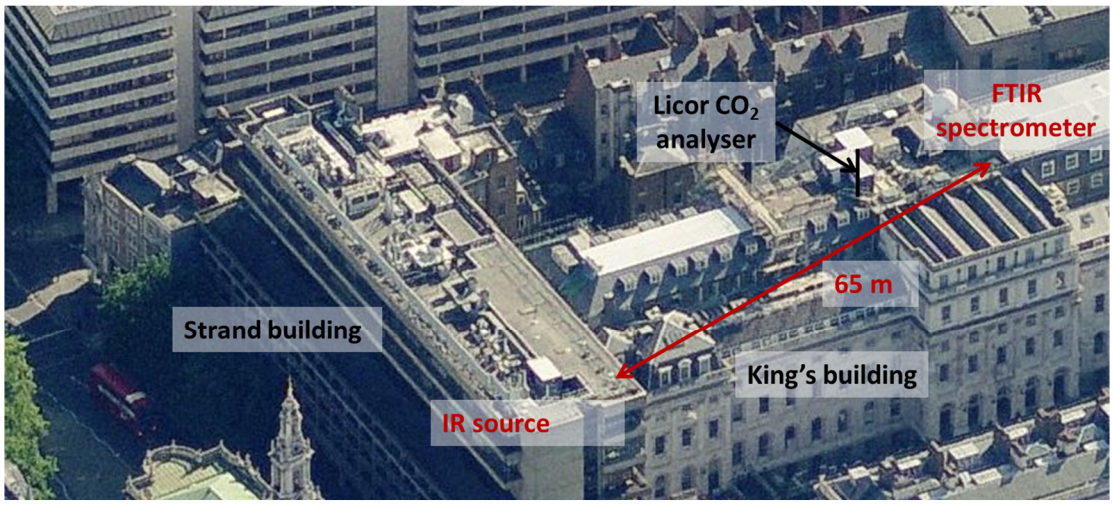

Figure 4.1 Aerial photograph of King's College London, Strand campus (Bing Maps, 2012). The annotations demark the location of the open-path between the FTIR spectrometer and the IR source and location of the Licor CO_2 gas analyser. Air temperature and atmospheric pressure measurements were made at the top of an 8 m mast on the King's Building roof.

measurement). The spectrometer was operated for just over three hours, contemporaneous with the Licor, between 11:30 and 15:00 (21 May 2009). CO_2 concentrations were retrieved from the OP-FTIR spectra using MALT (as described in the previous Chapter) with the 2150–2310 cm^{-1} spectral window (as illustrated in Figure 3.15a). Atmospheric pressure and air temperature were measured using a WXT510 weather station located at the top of an 8 m mast on the King's Building roof.

4.1.2 Results and Discussion

During the 4-hour measurement period, the Licor 840 reported a CO_2 concentration of 390–440 ppm by volume. As Figure 4.2 shows, there is a generally close agreement between the OP-FTIR and Licor CO_2 measures, and correlated concentration changes of <5 ppm are clearly apparent. Figure 4.3 shows a plot comparing the 30-second averaged CO_2 concentrations from both methods. The CO_2 concentrations derived from the OP-FTIR spectra have a small ~1 ppm negative offset when compared with the Licor 840. This offset may be due to the uncertainty associated with the pathlength, which was determined using survey maps and building heights (a decrease in the pathlength by ~20 cm would balance the 1 ppm CO_2). The spread and the apparent bias in the OP-FTIR-derived concentrations are likely to be due to the different sampling techniques. CO_2 concentrations from the Licor analyser frequently spiked to concentrations greater

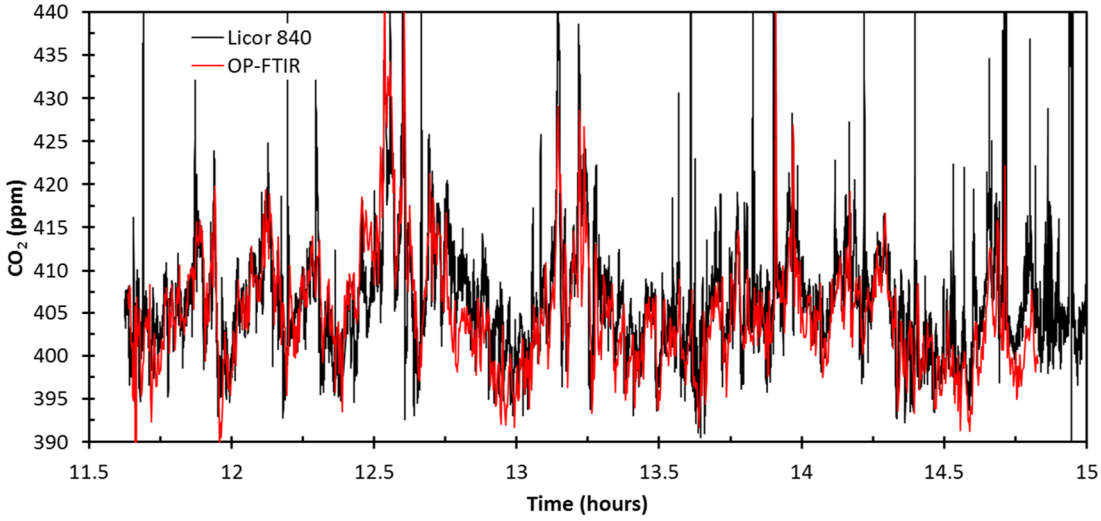

Figure 4.2 Time series of measurements of CO_2 concentrations derived from OP-FTIR spectra (red) and a Licor 840 NDIR closed-path analyser (black). OP-FTIR measureme

than 500 ppm (these spikes are constrained by the axes in Fig. 4.2), explaining some of the apparent biased 30-second mean concentrations in Fig. 4.3 (where higher concentrations were measured by the Licor). The CO_2 spikes in the Licor data are likely to be caused by microscale pockets of air emanating from windows and ventilation ducts located at various locations on the roof of the King's Building. These microscale variations observed by the Licor are not apparent in the results from the FTIR spectrometer, suggesting that the 65 m open-path was long enough to smooth out such small-scale variations.

These results encourage the suggestion that OP-FTIR spectroscopy is a viable alternative to conventional NDIR-based CO_2 monitoring for ambient/urban atmospheres (Such a conclusion has been previously reached by Grutter [2003]). For biomass burning research, however, it is important to assess the accuracy of retrievals of CO_2 and other trace gases over a very broad range of concentrations. The absolute accuracy assessment presented in Section 4.3 addresses this issue. The limitations of this ambient atmosphere pilot study related to the different sampling strategies (FTIR open-path vs. NDIR point sampling) are also addressed in Section 4.3, where a gas cell containing gas mixtures of known concentration is used.

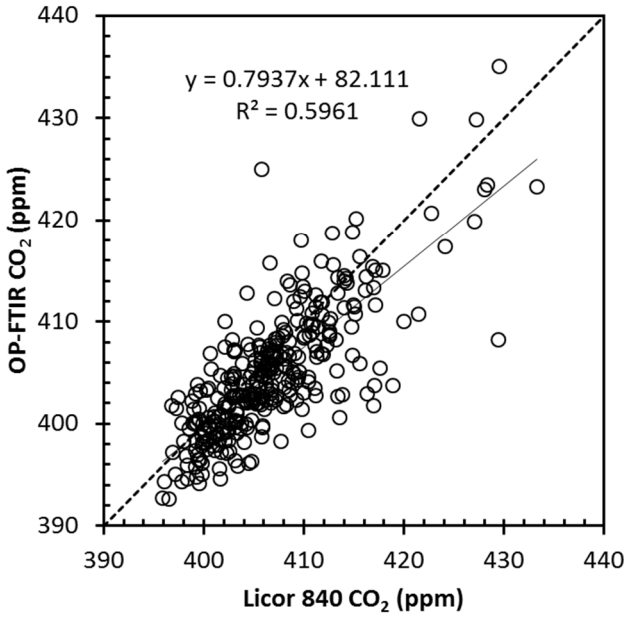

Figure 4.3 Scatter plot of 30-second averages of CO_2 concentration derived from OP-FTIR spectra and from a Licor 840 NDIR closed-path analyser (a time series of the raw data is presented in Fig. 4.2). The linear least squares regression line and the 1:1 line are also shown.

4.2 Assessment of NH_3 retrieval accuracy

This section provides a comparison between ammonia measurements made over a fertilised agricultural field in Midlothian (Scotland) using the OP-FTIR technique, and ten other NH_3 measurement approaches.

4.2.1 Methodology

The MIDAC FTIR spectrometer was used in conjunction with the large 50.8 cm IR source in the bi-static open-path configuration (with a pathlength of 102–105 m). Both the FTIR spectrometer and IR source were aligned at a height of 1.3–1.4 m above ground (Figure 4.4). Eight scans were co-added for each measured spectrum. Spectra were collected in short 3–4 hour sessions before, during, and after field fertilisation. Ten other measurement techniques were implemented by collaborating researchers at the same field site (Figure 4.5), and are listed in Table 4.1. The other measurement

Figure 4.4 Photograph of the experimental setup at the managed grassland site Easter Bush, Midlothian, Scotland; the distance between the spectrometer and lamp is 102 m.

techniques included wet-chemistry analysers, quantum cascade laser absorption spectroscopy (QCLAS), photoacoustic spectroscopy, cavity ring down spectroscopy (CRDS), chemical ionisation mass spectrometry (CIMS), and ion mobility spectrometry (IMS). The characteristics of the ammonia measurement systems deployed in the inter-comparison are summarised in Table 4.1, further details of each method can be found in the full paper describing the inter-comparison (von Bobrutzki *et al.*, 2010). The focus here is on the degree of agreement between the OP-FTIR retrievals and those from other independent methods.

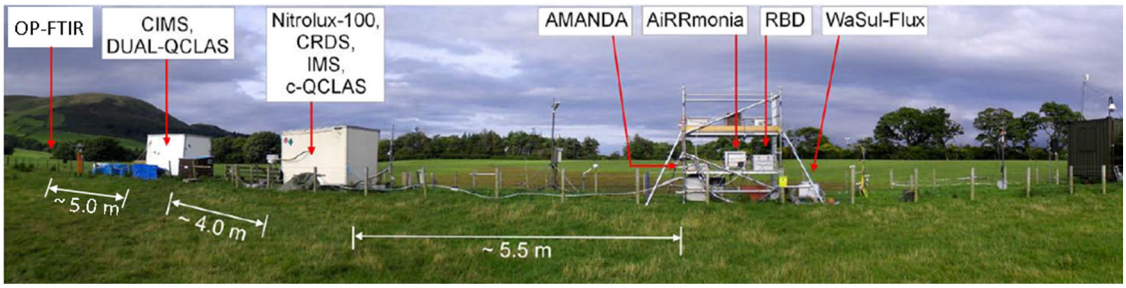

Figure 4.5 (redrawn from von Bobrutzki *et al.*, 2010) Intensively managed grassland site (Easter Bush) with array of ammonia measurement instruments. The FTIR spectrometer is not pictured, but its location when set up (as pictured in Figure 4.4 is indicated.

Table 4.1 (redrawn from von Bobrutzki *et al.*, 2010) Summary of the characteristics of each of the eleven ammonia measurement instruments.

Instrument	**Manufacturer**	**Air flow rate [l min^{-1}]**	**Time resolution/time average [s]**	**Precision [ppb]**	**Range [ppb]**	**Accuracy [%]**
RBD	Energy Research Foundation of the Netherlands (ECN)	27	2400/3600	0.02	not spec.	not spec.
AMANDA	ECN	28	450/450	0.02	0.02–500	not spec.
AiRRmonia	R&R Mechatronics	1	60/600	0.05	0.04–500	±3
DUAL-QCLAS	Aerodyne Research, Inc. (ARI)	15	0.2/60	0.018	not spec.	±54
c-QCLAS	ARI	8.9	1/60	0.05	not spec.	±10
WaSul-Flux	Hilase Ltd.	4	300–1800/ 300–1800	0.25	0.25–1,000,000	not spec.
Nitrolux-100	Pranalytica Ltd.	1.2–1.6	3/300	0.1	0.1–200	±4
CRDS	Enviro Sense10000 Analyzer, Picarro	1	3/300	0.07	0.07–25	±7
CIMS	Georgia Institute of Technology CIMS team	19.5	1/60	0.94	not spec.	±4
IMS	Bruker Daltonik	0.4	4/60	not spec.	Variable	not spec.
OP-FTIR	MIDAC Corp.	n/a	8/120	not spec.	not spec.	not spec.

NH_3 concentrations were retrieved from the OP-FTIR spectra using MALT (as described in Chapter 3) with the 900–980 cm^{-1} spectral window (as illustrated in Figure 3.15d).

4.3.2 Results and discussion

Figure 4.6 shows the NH_3 concentrations derived from the eleven different methodologies between 25 August and 30 August 2008, including those estimated from the OP-FTIR spectra via MALT. As already stated, compared with the other methods, the FTIR spectrometer was only operated for a fraction of the overall measurement period (which is reflected by the relatively small number of OP-FTIR NH_3 results shown in Fig. 4.6). Nevertheless, over 3,000 spectra were used in the retrievals of NH_3, and for the time periods when the OP-FTIR was operating, the retrieved concentrations and trends agree well with the other methods. Prior to fertilisation, concentrations of NH_3 were at the detection limit of the OP-FTIR methodology; the ammonia absorption feature at 930 cm^{-1} (see Figure 3.15d) was not apparent in the spectra and the feature at

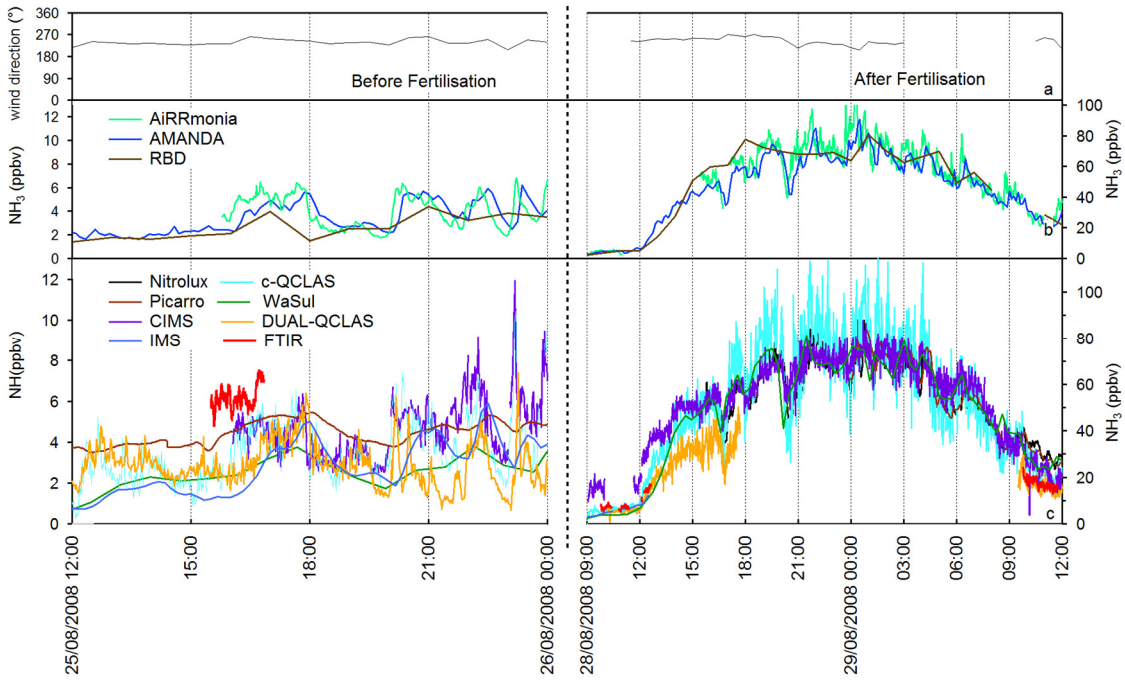

Figure 4.6 (redrawn from von Bobrutzki *et al.*, 2010) NH_3 concentrations measured by OP-FTIR (red line) and ten other ammonia measurement techniques. Compared with the other methods, the FTIR spectrometer was only operated for a fraction of the overall measurement period (which is reflected by the small amount of OP-FTIR data apparent in this plot). A summary of the NH_3 concentrations retrieved from the OP-FTIR spectra is given in Table 4.2.

960 cm^{-1} (see Figure 3.15d) was not well defined (Figure 4.7). This lack of definition in the absorption lines led to high reported errors in the retrieval algorithm (an indication of the goodness-of-fit for a particular trace gas absorption feature, as described in Sect. 3.2.4) (Table 4.2), although not necessarily a good indicator of the actual percentage error of the measurement (see Section 4.3 later). After fertilisation of the field, the absorption features at both 930 cm^{-1} and 960 cm^{-1} deepen, leading to higher retrieved ammonia concentrations and a decreased reported error (Table 4.2). The higher standard deviations for the hourly average NH_3 concentrations apparent after fertilisation are to be expected, especially considering that the spectra were collected in windy conditions.

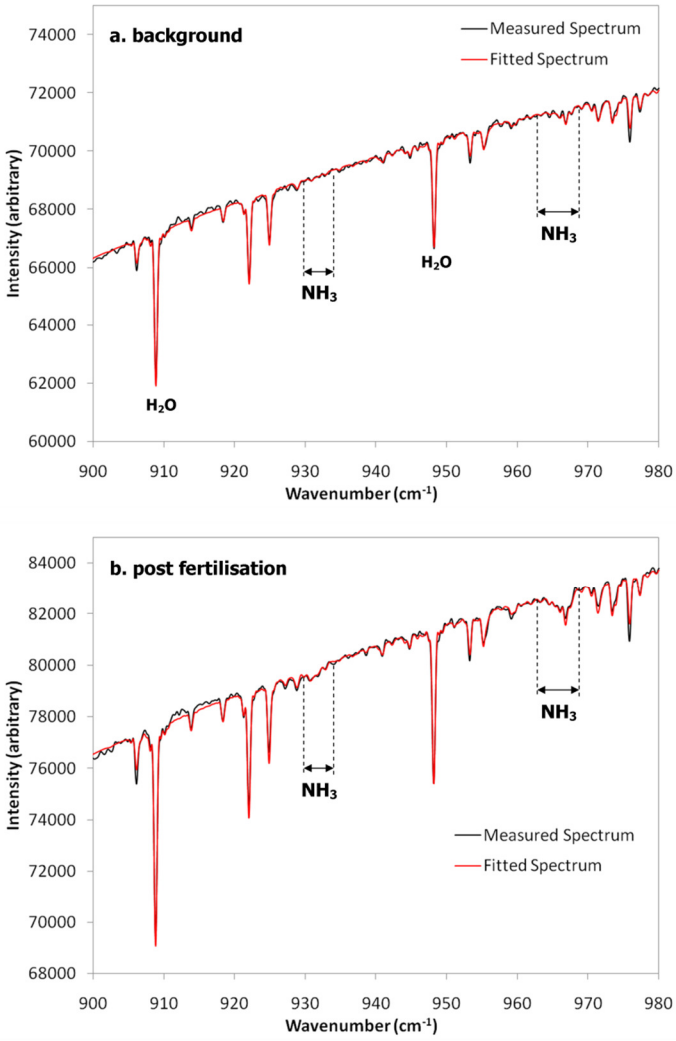

Figure 4.7 Example spectra for (a) before; and (b) after fertilisation of the field. The measured spectra (black) and best-fit modelled spectra (red) are shown. Before fertilisation, the absorption features at ~935 cm^{-1} and 965 cm^{-1} are not well defined. These features deepen after fertilisation leading to higher retrieved NH_3 concentrations using MALT.

Table 4.2 Hourly mean NH_3 concentrations retrieved from the OP-FTIR spectra. Spectra were collected before, during and after fertilisation of the field. Fertilisation occurred at ~1320 on 28 August 2008. The standard deviation of the NH_3 concentration for each on hour period is indicated along with the reported error from MALT (an indication of the goodness-of-fit between the measured trace gas absorption and that for the best-fit modelled absorption).

Date	Time	Mean concentration [ppb]	Standard deviation [ppb]	Reported Error (%)
25 August 2008	1600 - 1700	**5.30**	1.76	17.3
	1700 - 1800	**5.43**	1.38	14.4
28 August 2008	1000 - 1100	**6.51**	1.71	16.3
	1100 – 1200	**6.03**	1.65	17.0
	1200 - 1300	**6.12**	1.61	16.8
**fertilisation at ~1320*	1300 – 1400	**13.08**	2.61	10.2
29 August 2008	1000 – 1100	**19.57**	3.37	8.1
	1100 – 1200	**17.13**	3.30	8.8
	1200 – 1300	**14.79**	2.79	9.6

Figure 4.8 shows a comparison of the OP-FTIR concentration retrievals with those made by the other fast-response spectroscopic techniques. Data from the OP-FTIR agreed best with the DUAL QCLAS, although regression analysis of the OP-FTIR results with the other techniques revealed a high intercept of >3.74 ppb. The OP-FTIR data represents pathlength averages over 100 m which possibly limits comparability with the other point-source measurement techniques. Furthermore, measurements were made over a more limited concentration range. Yet, the comparison with the other fast response techniques is encouraging (Fig. 4.8). At very low concentrations, instrument noise may exceed the signal from NH_3 absorption (Fig. 4.7), which may explain the high intercept in comparison with the other detection methods, and this intercept probably represents the minimum detection limit of the OP-FTIR method.

The most important finding from this investigation with relation to biomass burning emissions of NH_3 is the apparent agreement between OP-FTIR and established point sampling methods. The agreement between methods shown here has been established for pathlength amounts (the pathlength-concentration product) of 0.4–2.0 ppm.m which are typically smaller than those which might be expected in biomass burning studies (Goode *et al.*, 2000). Unfortunately, the 'sticky' nature of ammonia prohibits an accuracy assessment based on cell measurements of known concentrations, but for CO_2, CO and CH_4 such an assessment is presented in the following section. NH_3 would coat

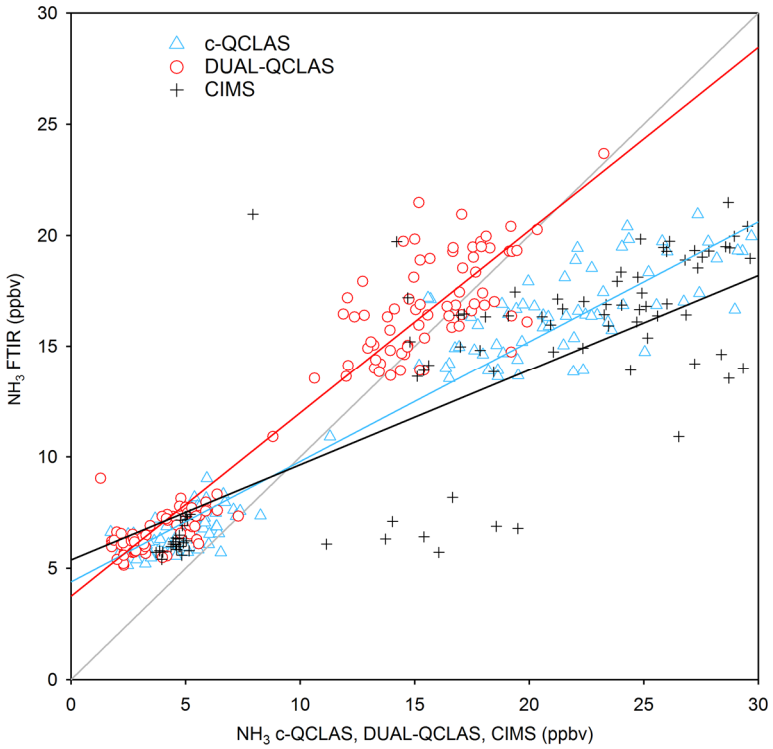

Figure 4.8 (redrawn from von Bobrutzki *et al.*, 2010) Comparison of OP-FTIR NH_3 retrievals with c-QCLAS, DUAL-QCLAS and CIMS measurements.

the cell wall in such a situation rather than remaining in gaseous form. Therefore, future comparison of OP-FTIR with other NH_3 analysis techniques at higher pathlength amounts in an open atmosphere is envisaged in future work.

4.3 Laboratory evaluation and sensitivity of OP-FTIR trace gas concentration retrievals

4.3.1 Introduction

In many applications, remote sensing of gas species presence and concentrations offer advantages over established point-sampling and/or laboratory analysis methods. Open-path (OP) Fourier Transform Infrared (FTIR) spectroscopy can be used to detect and quantify a wide range of gases simultaneously; can operate *in situ*, eliminating contamination from tubing or sample handling; can operate continuously, providing real-time data at a relatively high temporal resolution (seconds); and can be used over

long path lengths, providing path-integrated gas concentrations less prone to artefacts induced by point-based sampling and which cannot easily be acquired using alternative approaches.

A variety of analysis techniques are available to retrieve trace gas concentrations from measured single-beam spectra acquired by FTIR instrumentation. These generally involve comparing the measured spectra with reference spectra of the gas of interest under known conditions of temperature, pressure and concentration. Reference spectra may come from laboratory measurements of gases, or may be synthetically generated (e.g. Griffith, 1996) from molecular absorption databases, such as HITRAN (Rothman *et al.*, 2009). One retrieval technique involves converting the measured spectra into absorbance units and fitting the reference spectra using classical least squares (CLS) or partial least squares methods over a spectral window within which the trace gas of interest has significant features (Haaland, 1990). One difficulty with this approach can be the necessity to obtain 'background' single beam spectra unaffected by the gases of interest, these being combined with the single-beam observations of interest to derive the values of absorbance (Bacsik *et al.*, 2004). Alternatively, the single-beam reference spectra may be forward modelled and iteratively fitted to the measured spectra using nonlinear least squares (NLLS) (e.g. Griffith *et al.*, 2003). The accuracy of both methods is generally gauged via a goodness-of-fit measure between the measured and modelled/reference spectra. However, only a few published studies have determined absolute retrieval accuracies via independent accuracy assessments based on experimental methods using cells containing known gas concentrations (see Esler *et al.*, 2000; Horrocks *et al.*, 2001). This is surprising given the sensitivity of retrieval methods to analysis parameters such as spectral window position and extent, gas temperature and pressure, and instrument line shape (Hart *et al.*, 1999; Horrocks *et al.*, 2001). OP-FTIR spectroscopy is being used increasingly as a method for monitoring key carbonaceous greenhouse and tracer species such as CO_2, CH_4 and CO. Given that OP-FTIR spectroscopy of these and other trace gas species is being applied in an ever-increasing range of applications, including volcanology (Horrocks *et al.*, 1999; Oppenheimer *et al.*, 2002); urban and aircraft pollution assessment (Grutter, 2003; Grutter *et al.*, 2003; Hong *et al.*, 2004; Schäfer *et al.*, 1995, 2003) agricultural emission estimation (Childers *et al.*, 2001; Griffith *et al.*, 2002); and biomass burning investigations (Griffith *et al.*, 1991;

Yokelson et al,. 1997), it is important that the true accuracy of the method is established over the wide range of potential concentrations found in these applications. Here, an experimentally-based laboratory setup was used to determine the absolute accuracy of OP-FTIR retrievals of carbon dioxide (CO_2), carbon monoxide (CO) and methane (CH_4) made using the forward modelling approach across a concentration range encompassing both ambient air and highly polluted plumes (such as those emanating from vegetation fires, vehicle pollution or biogenic sources).

4.3.2 Background

In some cases, the accuracy of FTIR retrievals has been inferred via comparisons of the retrieved concentrations to those from more established point-sampling techniques, such as nondispersive infrared (NDIR) spectroscopy for CO_2 and CO (e.g. Gerlach *et al.*, 1998) or gas chromatography (GC) for other gases (e.g. Goode *et al.*, 1999). For laboratory biomass burning, Goode *et al.* (1999) compared FTIR concentration retrievals made using synthetic reference spectra and CLS analysis, with those from GC. CO_2 retrievals from FTIR were shown to agree to within 1% of the GC results, although FTIR retrievals of CO and CH_4 were shown to generally underestimate concentrations by ~6% when compared with GC. Gerlach *et al.* (1998) compared CO_2/SO_2 ratios derived from FTIR, NDIR and GC, finding general agreement between all three methods. Whilst these results are encouraging in terms of the apparent agreement between FTIR and alternative approaches, they only represent intercomparisons between methods essentially employing rather different sampling strategies.

To achieve a true absolute accuracy assessment for FTIR retrievals, it is necessary to measure the IR spectra of well characterised, laboratory prepared, calibrated gas mixtures and compare the gas concentrations retrieved from these measurements to the known true concentrations. Only a limited number of studies have undertaken such a procedure (e.g. Horrocks *et al.*, 2001; Esler *et al.*, 2000; Lamp *et al.*, 1997). Esler *et al.* (2000) were primarily interested in determining the precision of OP-FTIR gas analysis of CO_2, CH_4, CO and N_2O, using a sample of clean air (Southern Hemisphere 'baseline' air) introduced into a 9.8 m White cell, analysing the measured spectra using a CLS approach and synthetically generated absorbance spectra. For CO_2, the method proved

to be highly accurate giving a retrieval accuracy of 0.006% compared to GC analysis of the same sample, and for CH_4, CO and N_2O, 0.03%, 1.0% and 0.1% respectively. These excellent accuracy statistics for ambient air unfortunately were not extended to measurements covering a broader range of concentrations. Optimal retrievals made at higher concentrations (and equivalently longer pathlengths, since the method actually responds to the number of gas molecules present in the optical path) might require use of different parameterisatons of the forward model (for example the spectral window). This may be due, for example, to absorption saturation or deviations from the standard Beer-Lambert law caused by deviations in absorptivity coefficients at high concentrations due to interactions between molecules in close proximity (Zhu and Griffiths, 1998).

Lamp *et al.* (1997) generated gas mixtures using mass flow controllers to yield a broad concentration range of CH_4 (8 – 1,900 ppm.m) and CO (10 – 3120 ppm.m) in a 20 m White cell. CLS analysis of the resulting IR absorbance spectra showed a significant nonlinear relationship between measured and known concentrations. For CH_4, retrieved values were within 5% of the true concentrations below 700 ppm.m, but accuracy halved at higher concentrations. Lamp *et al.* (1997) demonstrated that use of strong absorption regions, such as the CH_4 Q-branch at 3017 cm^{-1}, can lead to reduced accuracy as concentration increases, and a switch to other microwindows might be more appropriate. CO retrievals were shown to suffer from similar nonlinearities, with concentration underestimated by more than 50% at concentrations higher than 1000 ppm.m.

An alternative to CLS-based methods is to use a nonlinear least squares (NLLS) fitting procedure (Marquardt, 1963). This approach can fit single-beam spectra directly and requires no assumption of Beer-Lambert linearity, allowing for the use of both weak and strong absorption regions (Griffith *et al.*, 2003). In a comparison between retrievals made using CLS and NLLS methods, Childers *et al.*, (2002) found that for CO_2, CH_4, NH_3 and N_2O, the CLS method generally underestimated at higher gas concentrations. To demonstrate this effect, Fig. 4.9 illustrates retrievals made here using the CLS and NLLS approach from spectra of a gas cell containing CO_2 gas of varying concentrations, topped up with nitrogen to maintain ambient pressure [the experimental method is described fully in Sect. 4.3 of this paper]. The underestimation of high CO_2

concentrations when using the CLS method is clearly evident, and is due to the aforementioned nonlinear deviation from the Beer-Lambert law.

For volcanological applications, Horrocks *et al.* (2001) used a similar experimental setup and spectral forward modelling approach to that employed here to test the accuracy of OP-FTIR retrievals of SO_2 over a wide range of absorber amounts (125 ppm.m – 10,500 ppm.m). As is the case here, instead of using a White cell to increase pathlength, Horrocks *et al.* (2001) chose to use higher mixing ratios (ppm) of SO_2, which are equivalent to a longer path according to the Beer-Lambert law:

$$\tau = \alpha L c \tag{4.1}$$

where optical depth (τ, unitless) is equal to the product of the absorption coefficient of the sample (α, $[\text{ppm.m}]^{-1}$), the path length of the sample (L, m) and the mixing ratio of the sample (c, ppm). Optical depth is related to the true transmission (T, unitless) following Eq. 4.2:

$$T = e^{-\tau} \tag{4.2}$$

The measured transmittance is the true transmittance convolved with the instrument line shape (ILS). Horrocks *et al.* (2001) found that increased retrieval accuracies were achieved as concentrations of SO_2 increased, improving from ~ 5.6% at 125 ppm.m to within 1.0% at 10,500 ppm.m. This study builds on this work by using a similar approach to establish the OP-FTIR retrieval accuracies for CO_2, CO and CH_4 at mixing ratios ranging from those found in ambient air to those found in polluted cities, biomass burning smoke and volcanic plumes, a much broader range than investigated by Esler *et al.* (2000). This study follows Horrocks *et al.* (2001) and analyse the collected IR spectra using an iterative NLLS method coupled to a forward modelling approach, specifically the Multi-Atmospheric Layer Transmission (MALT) model described in Griffith (1996) and Griffith *et al.* (2003). The work of Lamp *et al.* (1997) showed how Beer-Lambert law divergence can impact retrieval accuracy when investigating high concentration gases using spectral regions containing strong IR absorbance features. Generating retrievals from forward modelled synthetic spectra fitted to the measured spectra in the way conducted here should avoid these problems and the associated concentration underestimation illustrated in the CLS-derived results displayed Fig. 4.9.

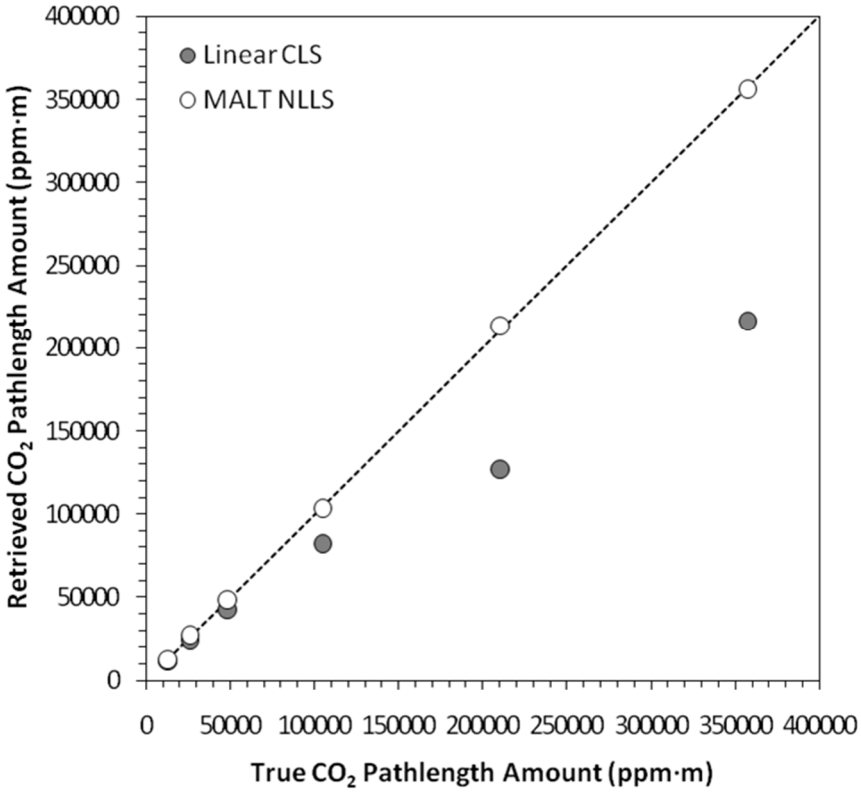

Figure 4.9 Comparison of FTIR-derived retrievals of gas-cell CO_2 pathlength amount to the true pathlength amount within the cell. Retrievals were made from the same spectra via two approaches, the Classical Least Squares (CLS) approach described in Haaland (1990) and the MALT forward model and nonlinear least squares (NLLS) fitting procedure described in Griffith (1996) and Griffith *et al.* (2003). The 1:1 line is shown, and the increasing underestimation of the CLS-based retrievals at higher pathlength amounts is clearly evident.

4.3.3 Instrumentation and setup

This study utilised facilities of the UK's Natural Environment Research Council's Molecular Spectroscopy Facility, part of the Rutherford Appleton Laboratory. A stainless steel gas cell of circular cross section was fitted with IR transparent KBr windows at each end and was filled with the sample gas at the concentration of interest before each spectral measurement. Gas cell length was 1.05 m, diameter 160 mm and IR window diameter 135 mm. The spectrometer used was a MIDAC Corporation FTIR Air Monitoring system, fitted with a mercury cadmium telluride (MCT) detector and ZnSe optics. The spectrometer was optically coupled to a 76 mm Newtonian telescope and placed to view an IR source through the IR transparent windows of the gas cell. The IR source used was a SiC globar operating at 1,100 K, positioned at the focus of a 150 mm

collimator. This setup, shown in Fig. 4.10, is very similar to that used by Horrocks *et al.* (2001), with a total pathlength of ~1.5 m, 0.5 m of which consisted of free air between the cell and spectrometer and cell and IR source, together with air inside the spectrometer housing. The CO_2 and H_2O mixing ratios in the ambient air *outside of the cell* were monitored using a calibrated LICOR 840 NDIR gas analyser. An attenuator was fitted to the FTIR spectrometer telescope to avoid MCT detector saturation, and the temperature of the gas inside the gas cell measured using a platinum resistance thermometer (PRT).

Table 4.3 lists the gas mixtures investigated. As described by the Beer-Lambert law (Eq 1), it is possible to simulate a longer OP measurement pathlength by increasing the mixing ratio of the gas sample inside the cell, since pathlength (L) and mixing ratio (c) equivalently increase the number of gas molecules in the open path over which the IR spectra are acquired. The mixing ratios used here were chosen to represent a range covering those from clean air measured over short-to-long pathlengths in the natural environment (e.g. 10–1,000 m), as well as polluted air across the same pathlength range, and range up to mixing ratios that might be found in pollutant plumes (e.g. from industrial sources or biomass burning). For example, six different CO_2 pathlength-concentration products (hereafter called pathlength amount) were used, spanning ~12,500 ppm.m to ~360,000 ppm.m. If these pathlength amounts are expressed as mixing ratios using pathlengths typically employed in the field, both the lowest and highest cell mixing ratios yield a CO_2 mixing ratio of ~420–450 ppm for a 30 m and 800 m path respectively, equivalent to typical ambient CO_2 conditions found in urban settings (e.g. Rigby *et al.*, 2008).

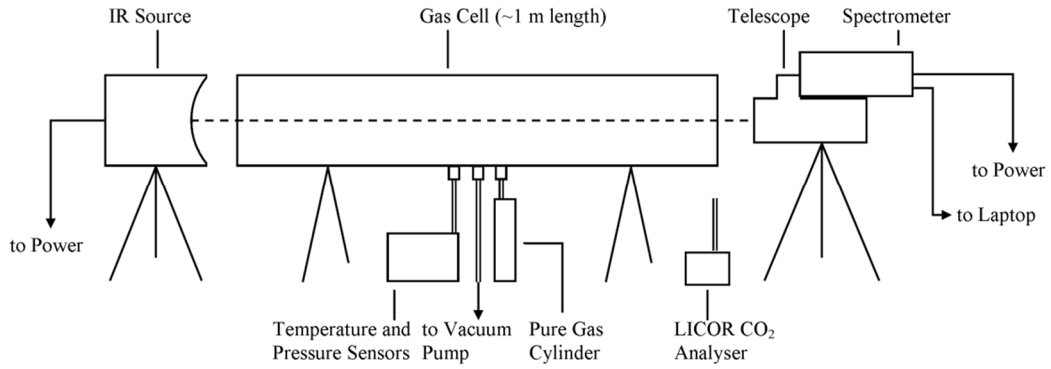

Figure 4.10 Schematic of the physical instrumentation arrangement used in this accuracy assessment.

Gas mixtures were prepared barometrically using high purity (99.9%) component gases. The barometric mixing method relied on three MKS Baratron (type 690) pressure capacitance manometers operated at three precision levels of 0.1 Pa, 10 Pa and 100 Pa with a stated accuracy of ±0.05%. The manometers were also used to test the sealing of the gas cell, recording a <1% change in cell pressure over 18 hours when filled to ambient pressure (1,000 hPa). For each gas concentration to be studied, the cell was evacuated before the sample gas (CO_2, CO or CH_4) was slowly released into the cell until the desired mixing ratio was reached. After waiting for the pressure to stabilise and noting the final pressure, the cell was filled with nitrogen to ambient pressure (1,000 hPa) and allowed to stabilise once more. After stabilisation, 10 IR spectra were measured with the FTIR spectrometer, each consisting of 8 co-added scans (a total of ~9 seconds scan time per spectra) in order to increase signal-to-noise. The relative standard deviations among each set of 10 replicate single beam spectral measurements ranged from 0.1 – 1.2%, with standard errors of the means of 0.03–0.4% for these measurement conditions. The partial pressure of the sample gas was used to calculate the true sample mixing ratio (ppm) by dividing the partial pressure of the sample gas by the final

Table 4.3 Cell mixing ratios (ppm) and equivalent pathlength amount (ppm.m) for the 1.05 m gas cell filled with CO_2, CH_4 and CO respectively, with the equivalent mixing ratios for longer atmospheric paths (assuming the same temperature, ~20°C, and pressure, ~1,000 hPa conditions) also given. For reference, ambient "clean" air mixing ratios of CO_2, CH_4 and CO are circa 385 ppm, 1.8 ppm and 0.15 ppm, respectively.

Cell mixing ratio (ppm)	Pathlength amount (ppm.m)	30 m path equivalent (ppm)	100 m path equivalent (ppm)	800 m path equivalent (ppm)
CO_2				
12014	12612	420.4	126.1	15.8
24991	26236	874.5	262.4	32.8
45799	48080	1602.7	480.8	60.1
100125	105112	3503.7	1051.1	131.4
200200	210172	7005.7	2101.7	262.7
340351	357304	11910.1	3573.0	446.6
CH_4				
51.94	54.52	1.83	0.55	0.07
92.81	97.43	3.25	0.97	0.12
168.51	176.91	5.90	1.77	0.22
270.85	284.34	9.48	2.84	0.36
490.09	514.50	17.15	5.15	0.64
CO				
18.96	19.90	0.66	0.20	0.03
244.14	256.30	8.54	2.56	0.32
459.13	482.00	16.07	4.82	0.60
1217.05	1277.67	42.59	12.78	1.60
6077.20	6379.91	212.66	63.80	7.98

ambient pressure of the gas cell. To avoid contamination by gas from the previous mixture, the lowest concentration of each gas was mixed first, working up to higher concentrations.

4.3.4 Methodology

4.3.4.1 Determination of input parameters

When performing a spectral fit, the input parameters required by the spectral forward model (MALT) can be stated as fixed constants or can be included in the fitting process. These parameters relate to the composition of the sample atmosphere (i.e. which gases are present in the sample and have absorption lines in the spectral window of interest, the concentration of these gases, and the temperature and pressure of the composition) and to the instrument line shape (i.e. spectral shift, resolution, apodisation, FOV, phase and zero-line offset). In this experiment, whilst the gas concentration was fitted, the temperature and pressure of the sample were taken from the gas cell PRT and Baratron readings respectively. Determination of instrument line shape parameters was, however, less straight forward:

- the spectral shift (correction for fractional wavenumber shifts in the position of absorption lines caused by inaccurate knowledge of the position of the interferometer moving mirror) was fitted
- the spectral resolution was fixed at the manufacturer's specification (0.5 cm^{-1})
- asymmetry in the line shape influenced by small changes in spectrometer alignment was also fitted through a variable phase error
- the field-of-view (determined by the spectrometer's collimator focal length) was initialised at the manufacturer's specification and fitted as described below to determine the effective value.

Horrocks *et al.* (2001) demonstrate that their MIDAC spectrometer's effective field-of-view of 52 mrad differed significantly from the nominally quoted 20 mrad. This assessment follows the methodology of Horrocks *et al.* (2001) to determine the field-of-view of the instrument used here, measuring the spectrum of CO gas with narrow absorption lines at low pressure (401 hPa) so that the resulting measurement is primarily a function of the absorption feature convolved with the instrument line shape. 80 scans

were co-added to create one particularly low-noise spectrum. A series of MALT retrievals were run for a single absorption line at 2082 cm^{-1}, and the field-of-view parameter optimised to give the lowest reported error, whilst all other parameters remained fixed. The FOV parameter yielding the smallest reported error for the low-pressure CO absorption line was used as a fixed input for all other retrievals conducted here. Sensitivity to this parameter was also investigated (see Sect. 4.4.3).To determine the retrieval error of the reported concentrations, it is necessary to compare the retrieved concentrations with the true concentration (i.e. to the cell concentrations listed in Table 4.3). Retrieval error is therefore here defined as the true concentration subtracted from the reported concentration, divided by the true concentration and expressed as a percentage.

One further consideration for the retrieval procedure is to account for any zero-baseline spectral offset that may result from photometric errors associated with the use of an MCT detector (Müller *et al.*, 1999). Two factors might lead to a non-zero signal in spectral regions that should otherwise exhibit complete absorption. The first is caused by scattering of radiation that has not originated from the lamp source, potentially related to imperfections in instrument optics, such as dirty mirrors. This is a common occurrence in well used field spectrometers, particularly when deployed to dusty or corrosive environments. Furthermore, if the gas cell was at a different temperature to that of the interferometer, an effect will appear in the measured spectrum. Whilst laboratory spectrometers often solve this problem by placing the interferometer before the sample cell, this is not of the case for bistatic OP-FTIR field configurations (Müller *et al.*, 1999). Neither the temperature of the gas cell nor spectrometer were controlled in this experiment, but were rather left to equilibrate to ambient temperature, and therefore small differences in temperature may have influenced the recorded spectra. The second factor which might lead to a non-zero baseline is detector saturation. MCT detectors saturate rather easily (Smith, 1995), and whilst efforts were made in this study to prevent detector saturation via use of the attenuator, some detector saturation effect may be present. Any zero-baseline offset caused by stray light or detector saturation will be apparent in spectral regions where the examined gases should absorb all incoming radiation (e.g. the CO_2 saturation band at ~2,350 cm^{-1}). If an offset was present, this amount was subtracted from the spectrum before quantitative analysis.

4.3.4.2 Spectral window and 'background' polynomial

MALT requires the user to select a suitable spectral window and an appropriate polynomial for simulating the continuum spectra. To yield the most accurate concentrations, the window must have sufficient information about the gas of interest (i.e. an absorption feature) and should ideally be in a region of the IR spectrum that minimises contaminating absorption features from other gases (though this is not essential). The order of the polynomial used to simulate the continuum spectrum needs to be carefully selected so that it does not fit broad absorption features. In this work, a series of spectral windows were tested for retrieving the concentrations of each gas (Fig. 4.11 and Table 4.4), and the window yielding the lowest retrieval errors was thus identified. Similarly, a range of polynomial orders (3rd, 4th and 5th order) were employed. Given that all three gases in this study demonstrate fine absorption structure (a number of clearly defined narrow absorption lines) within the tested spectral windows, it is unlikely that the background polynomial fit will be influenced by these, except perhaps across the narrow CH_4 spectral window.

For CO_2 (Fig. 4.11a), the widest spectral spectral window used here, 2,020–2,310 cm^{-1} (taken from Esler *et al.*, 2000) was split into two sub windows, 2,150–2,310 cm^{-1} (location of primary absorption features of $^{13}CO_2$ and $^{12}CO_2$) and 2,034–2,075 cm^{-1} (location of the weaker $^{12}CO_2$ feature, see inset in Fig. 4.11a). For each window, CO_2 retrievals were run using a background continuum spectrum simulated via a 3rd, 4th and

Table 4.4 Spectral windows used here for the retrieval of CO_2, CH_4 and CO and marked in Fig. 4.11. Also listed are the potentially interfering gases (those in brackets were not included in the forward-model spectral simulation conducted here due to the very short clean air atmosphere path used, but would generally be required over longer pathlengths in the ambient atmosphere).

Target Gas	Spectral window	Interfering gases
CO_2	2,020–2,310 cm^{-1}	H_2O (N_2O, CO)
CO_2	2,034–2,075 cm^{-1}	H_2O
CO_2	2,150–2,310 cm^{-1}	H_2O (N_2O, CO)
CH_4	2,894–3,001 cm^{-1}	H_2O
CH_4	2,980–3,090 cm^{-1}	H_2O
CH_4	3,005–3,020 cm^{-1}	H_2O
CO	2,000–2,230 cm^{-1}	H_2O (CO_2)
CO	2,039–2,057 cm^{-1}	H_2O
CO	2,142–2,241 cm^{-1}	H_2O (CO_2)

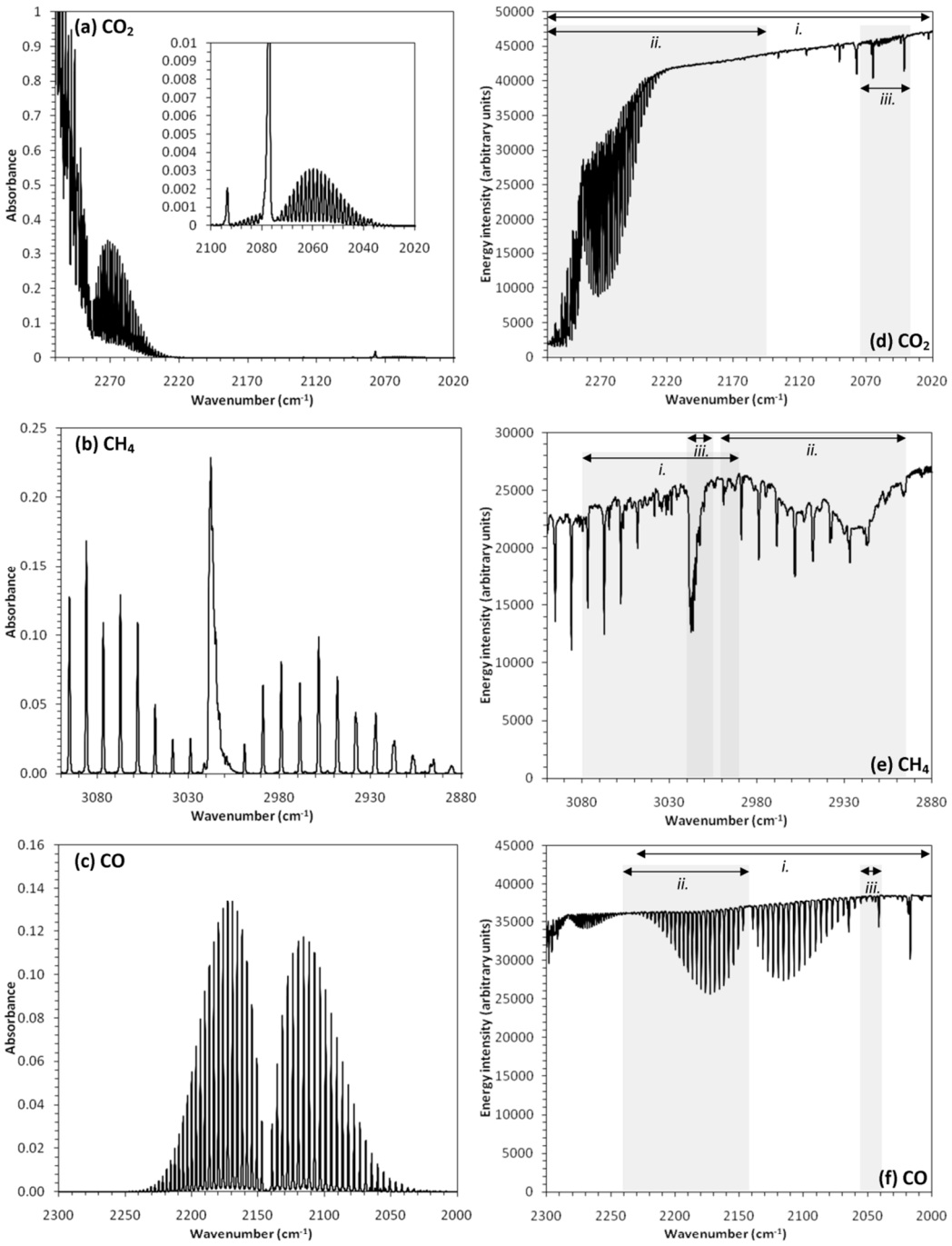

Figure 4.11 Modelled and measured spectra at 0.5 cm^{-1} wavenumber resolution for the CO_2, CH_4, and CO trace gases considered here. (left) Absorbance spectra modelled using the MALT forward model; (right) Measured FTIR single-beam spectra. The various spectral windows used to retrieve the trace gas concentrations from the measured spectra are indicated by the numbered horizontal arrows in (d), (e), (f) and are detailed in Table 4.4.

5th order polynomials. Given that water vapour was certainly present in the ambient part of the path external to the gas cell and has absorption lines in these spectral windows, H_2O was also included in the retrievals. Whilst CO and N_2O also absorb within these spectral windows, they were not present in sufficient amounts to be significant. In field situations using longer pathlengths, CO and N_2O may affect the measured signal and should therefore be included in any retrieval procedure. For CH_4, Esler *et al.* (2000) use a broad spectral window, 2,810–3,150 cm^{-1}. Unfortunately, the majority of this window is affected by a spectrometer artefact (2,800–2,990 cm^{-1}, see Fig. 4.11e), believed to be caused by residue on the instrument optics. The complexity introduced by the artefact significantly hinders the ability to model the spectrum using lower-order (<6) polynomial. Two spectral windows were therefore selected so as to exclude the effects of this artefact, a broad window (2,980–3,090 cm^{-1}), that maximises the number of CH_4 absorption lines, and a narrower window concentrating on the strongest lines (3,005–3,020 cm^{-1}). In addition, a third window, lying within the region where lines are affected by the detector artefact (2,894–3,001 cm^{-1}) was also investigated. For CO, Esler *et al.* (2000) use a broad window encompassing the entire CO absorption feature and a similar window is used here (2,000–2,230 cm^{-1}). In addition, two narrower windows, one featuring only one branch of the CO absorption feature (2,142–2,241 cm^{-1}) and the other featuring only four weaker CO absorption lines (2,039–2,075 cm^{-1}) were also investigated (Fig. 4.11c).

4.3.4.3 Sensitivity analysis and error budget

A sensitivity analysis was performed in order to determine the influence of model parameter uncertainty on retrieval accuracy. Uncertainties in temperature, pressure and spectrometer FOV were considered, which may result from field situations where the measurement conditions are less tightly controlled than is possible in the laboratory. In particular, it can be difficult to measure temperature and pressure precisely in some open-path geometries, particularly when analysing high altitude plumes, or ones where the plume is generated by high temperature volcanological or combustion-related processes. Pressure and temperature are important in the retrieval procedure as they affect the shape of gas absorption features upon which the fit between the measured and modelled spectra depends. Assumed pressure determines the Lorentzian line shape of

absorption lines in the simulated spectra. Higher pressures lead to a broadening of line widths, and the maximum line depth is suppressed. Whilst the relatively low (0.5 cm^{-1}) spectral resolution of the FTIR spectrometer used here is responsible for the majority of observed linewidths, this pressure-related broadening does also influence the retrieval process. Pressure broadening for any sample gas is also related to the other gases contained in the gas mixture.

The influence of assumed temperature is to affect the strengths of individual absorption lines and the band shape of the modelled spectra. Doppler broadening caused by the temperature-dependent distribution of molecular velocities within gases (as well as a minor influence on line broadening) contributes to the temperature dependence of lineshapes. The primary influence of temperature and pressure, however, is in the calculation of the mixing ratio (ppm) from the retrieved number of gas molecules per square cm (molecules cm^{-2}) output from the retrieval process (the absorption features present in the spectra are a direct function of the number of molecules of the target gas in the optical path). The relationship between the columnar density of a particular gas in a sample in molecules per square centimetre (X, molecules cm^{-2}) and the mixing ratio of the gas (x), pressure (p, Pa), temperature (T, K) and pathlength of the sample (L, m) is described in Eqn. 4.3, where A is Avogadro's constant (6.022×10^{22} mol^{-1}) and R is the gas constant (8.315 J $[mol.K]^{-1}$):

$$X = \frac{xLpA}{RT} \tag{4.3}$$

Any error in assumed pressure or temperature will therefore cause a proportional error in retrieved mixing ratio (x) through Eq. 4.3; whereas, retrievals in molecules cm^{-2} will only be affected by the influence of pressure and temperature errors on the forward modelled spectra. In many applications, OP-FTIR is used to investigate concentration ratios of two gases, for example CO_2:CO in biomass burning studies (Yokelson *et al.*, 1997) or SO_2:HCl in volcanological applications (Burton *et al.*, 2007), and in this case it may not be necessary to retrieve volumetric mixing ratios since the ratios of the gas amounts expressed in units of molecules cm^{-2} or ppm.m is identical. Therefore, for the sensitivity analysis conducted here, pressure and temperature-independent amounts (in molecules cm^{-2}) were used for the comparison. Pressure and temperature inputs were varied systematically by up to ±20°C and ±200 hPa respectively; ranges that might be

found over altitude differences of up to 3 km. Retrieved concentrations were compared with true concentrations to yield both the retrieval error and sensitivity to the pressure and temperature assumptions.

4.3.5 Results and Discussion

4.3.5.1 FOV determination

Figure 4.12 shows how the reported error (i.e. the MALT fitting error, quantified as a percentage of the retrieved concentration in Sect. 3.3.2) and the actual retrieval error (quantified as the percentage difference between the retrieved gas concentration and the true gas concentration in Sect. 3.3.2) varies with assumed field-of-view. Actual retrieval error is much more sensitive to FOV variations than is the reported error. The lowest reported error occurs at a FOV of 22 mrad, whereas the lowest retrieval error occurs at a FOV of 20 mrad. Assumed FOV significantly larger or smaller than the 22 mrad optimum value resulted in increasingly poor fits between the modelled and measured CO spectrum (Fig. 4.13). Unlike Horrocks *et al.* (2001), this assessment found the optimal FOV, according to the reported error, to be similar to the nominal FOV stated by the instrument manufacturer, and the 2 mrad (10%) discrepancy can be attributed to off-axis rays caused by a combination of small misalignments of spectrometer and telescope optics, and an imperfect source collimator. Horrocks *et al.* (2001) also found a discrepancy between the FOV parameter yielding the lowest reported error and those that yielded the lowest retrieval error. This discrepancy may be explained by the use of nitrogen as a buffer gas, given that line broadening coefficients in the HITRAN08 database (Rothman *et al.*, 2009) relate to the gas of interest in air, and not when mixed with nitrogen. The difference between nitrogen and air broadening is of the order of ~10%. This factor, combined with uncertainties in HITRAN, or an inability of the forward modelling and NLLS fitting procedure to accurately retrieve concentrations using a single absorption line given the relatively low spectral resolution of the instrument, may also explain this discrepancy. By retrieving concentrations using broader spectral features, the retrieved effect of instrument line shape inaccuracies on individual absorption lines are decreased. The effects of degrading the assumed spectral

resolution from the highest 0.5 cm^{-1} value were investigated, but increased the reported errors, and therefore further adjustments to this factor were not required.

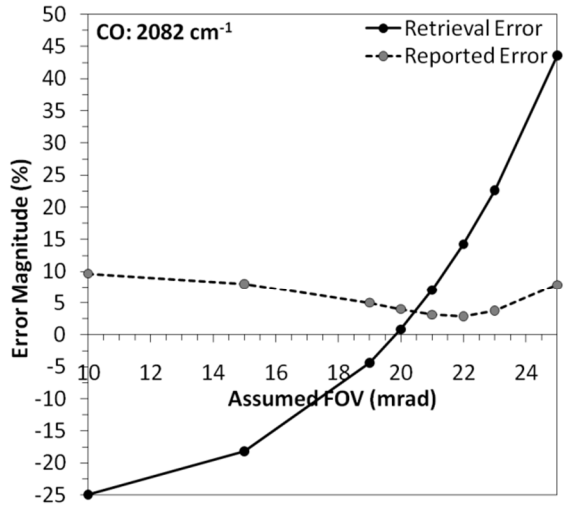

Figure 4.12 Sensitivity of the reported error (based on the fit residuals) and retrieval error (based on the difference between retrieved pathlength trace gas amount and actual pathlength trace gas amount) to assumed instrument FOV. The example is shown for CO trace gas retrievals based on the CO absorption line centred at 2082 cm^{-1} (Figure 4.13). Measurements were made at a low pressure of 400.5 hPa with a true CO mixing ratio of 1217.05 ppm. Reported error is minimised at an assumed FOV of 22 mrad, though is relatively insensitve to the FOV variations studied here. Retrieval error is, however significantly more sensitive, and assumed 20 mrad FOV yields the smallest actual retrieval error.

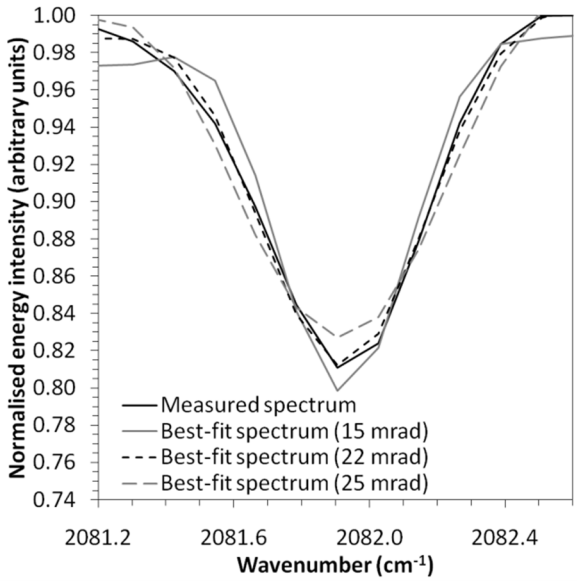

Figure 4.13 Measured single-beam spectra and best-fit modelled spectra for the CO absorption line centred at 2082 cm^{-1} at a gas pressure of 400.5 hPa. Modelled spectra were simulated assuming different fields-of-view (15-25 mrad), with the 22 mrad FOV providing the best match between the measured and modelled spectra.

4.3.5.2 Spectral window and background polynomial

Carbon Dioxide

For each gas, three spectral windows were identified containing either a broad absorption feature or a selection of individual absorption lines (Fig. 4.11 and Table 4.4). For CO_2, results shown in Fig. 4.14 indicate that the absolute retrieval error for 5 of the 6 pathlength amounts tested is at a minimum for the 2150–2310 cm^{-1} spectral window using a fourth-order polynomial, with retrieved pathlength amounts over the full range tested having a root mean squared (RMS) error of 2.4% (Fig. 4.14b). Whilst the results show little sensitivity to the use of a fourth or fifth-order polynomial, the use of a third-order polynomial leads to a noticeable increase in retrieval error. A third-order polynomial is insufficient to describe the background shape of a spectral window as wide as 2150–2310 cm^{-1}. Moreover, the background shape of this window is complicated by the CO_2 absorption feature that strengthens to saturation at 2310 cm^{-1} (Fig. 4.11a). Retrieval errors are highest for the broader, 2020–2310 cm^{-1} spectral window (Fig. 4.14a), though the reported error (not shown) is lowest for this window (0.1%, compared with 0.3% for 2150–2310 cm^{-1} and 0.9% for 2034–2075 cm^{-1}). This apparent contradiction may be explained by the presence of a large featureless baseline across most of this wider spectral window (Fig. 4.11a) leading to an overall improved fit between the modelled and measured spectrum, though not necessarily the best fit at the wavenumber location of the absorption features. A wider spectral window typically decreases the ability of any particular polynomial to model the background continuum as is the case here. There is also an additional reason why use of the broader spectral window generally leads to greater inaccuracy. This is because the zero-baseline offset can only be calculated from data collected in the CO_2 absorption saturation region (near 2350 cm^{-1}), and uncertainties in this correction will increase as the offset is applied to more distant spectral locations. The results for the narrowest spectral window (2034–2075 cm^{-1}) used here for CO_2 retrieval are less influenced by the choice of polynomial order, each having RMS errors of less than 3.7% (Fig. 4.14c). The flatter background continuum in this window, combined with the presence of fine absorption structure in the CO_2 lines, explains the reduced sensitivity to polynomial order. The inaccuracy of

the retrievals made at lower pathlength amounts in this spectral window is most likely due to the weaker nature of the absorption lines at 2034–2075 cm^{-1}.

The results clearly indicate that the choice of spectral window, coupled with an appropriate choice of background polynomial, have a strong influence on CO_2 retrieval accuracy. Broader windows typically contain more information, potentially improving the fit between the forward modelled and measured spectra. However, it is also important to ensure that the background continuum of the spectrum within the window under study can be sufficiently well represented by the chosen polynomial. The results

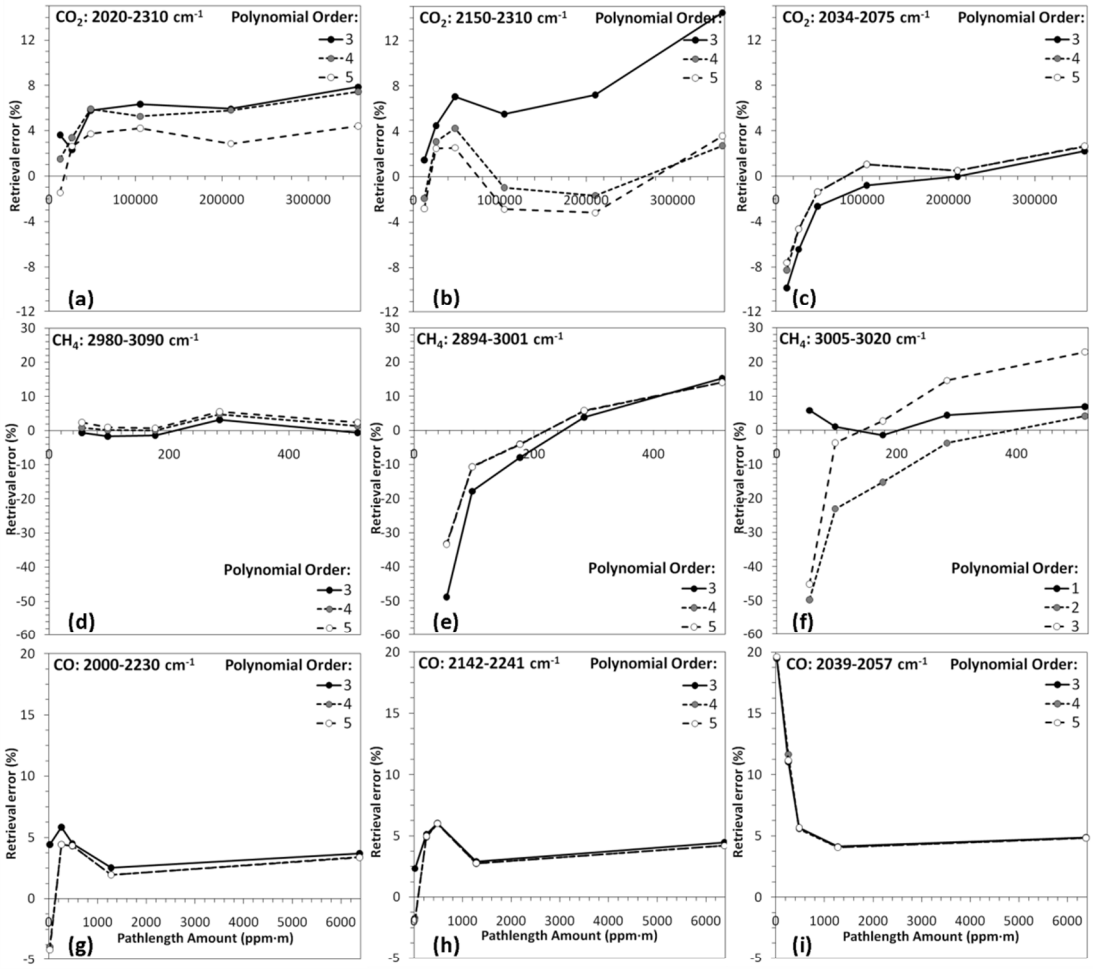

Figure 4.14 Retrieval errors for CO_2, CH_4 and CO trace gas retrievals resulting from use of the MALT forward model and NLLS fitting procedure with OP-FTIR spectra from a gas cell containing samples of these three gases over wide concentration ranges. Retrievals were made using three different spectral windows for each trace gas and three different polynomial orders. In order to aid comparison of the error magnitudes for the retrievals of each trace gas, the same y-axis range is used to display the results from the three spectral windows tested. Retrieval error magnitude is seen to vary quite widely between the different spectral windows used to retrieve the pathlength amount of a particular trace gas, and for some windows between the different polynomial orders examined.

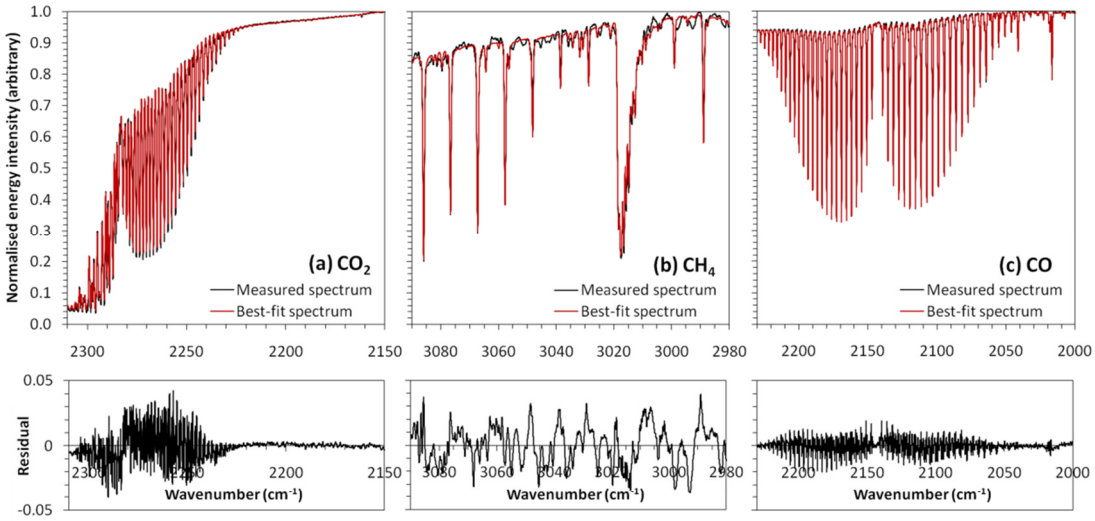

Figure 4.15 Examples of measured spectra and best-fit forward modelled spectra made using the optimum spectral windows and a fourth-order polynomial background (top), and the residual between the measured and modelled spectra (bottom) for (a) CO_2; (b) CH_4; and (c) CO. Forward modelled spectra were simulated using MALT and the best-fit modelled spectra were found using the NLLS fitting procedure.

suggest that whilst the 2020–2310 cm^{-1} spectral window used for CO_2 retrieval gives the lowest reported errors (based on the fit residuals; Sect. 3.3.2), it does not result in the lowest retrieval error. The 2150–2310 cm^{-1} spectral window, used with a fourth-order polynomial actually provides the lowest retrieval error for CO_2, ranging from -1.9% to 4.3% across all pathlength amounts tested. An example spectrum with best-fit modelled spectrum is shown in Fig. 4.15a.

Methane

As outlined in Sect. 4.3.4.2, retrievals of CH_4 were confounded by an instrument artefact in the relevant absorption region. The spectral window tested that covered this region (2894–3001 cm^{-1}) showed both large reported and retrieval errors, regardless of the polynomial order chosen (Fig. 4.14e). The lowest retrieval errors for CH_4 come instead from the 2980–3090 cm^{-1} spectral window that excludes the artefact region (Fig. 4.14d), with a fourth-order polynomial yielding an RMS error of 1.4% (Fig. 4.15b shows an example spectrum with a best-fit modelled spectrum for this spectral window). As was the case with the narrowest (2034–2075 cm^{-1}) CO_2 retrieval window, the polynomial order does not significantly influence retrieval accuracy due to the fine structure of the CH_4 absorption lines and the flat background continuum. However, for

the narrowest CH_4 retrieval window tested (3005–3015 cm^{-1}), the polynomial order has a strong influence (Fig. 4.14f) with only a first order function allowing pathlength amounts to be retrieved within an RMS error of 3.9%. Individual CH_4 absorption lines remain unresolved at the 0.5 cm^{-1} spectral resolution used here, and instead combine to appear as one large apparent absorption feature, and thus higher order polynomials incorrectly start to fit this feature as well as the background continuum.

Carbon Monoxide

Results for CO suggest that the two broadest spectral windows provide very similar retrieval accuracies, with the 2000–2230 cm^{-1} spectral window used with a fourth-order polynomial achieving an RMS error of 3.6% across all pathlength amounts tested here (slightly better than the RMS error of 3.9% for the 2142–2241 cm^{-1} spectral window). Figure 4.15c shows an example spectrum and best-fit modelled spectrum for the spectral window 2000–2230 cm^{-1}. Generally, the two narrower spectral windows overestimated pathlength amounts compared to the 2000–2230 cm^{-1} window. Retrievals for CO across all spectral windows tested here showed a lower reliance on choice of background polynomial compared to the other gases, reflecting the 'flat' background continuum across the whole CO absorption feature (Fig. 4.11f). Results from the narrower 2039–2057 cm^{-1} spectral window indicate that it is best suited to retrieval of higher pathlength amounts, with poor retrieval accuracies for pathlength amounts below 1,000 ppm.m. High reported errors (based on the fit residuals) suggest that the retrieval process performs poorly with the weak absorption lines in this spectral window, as is also the case for lower pathlength amounts of CO_2 retrieved in the 2034–2075 cm^{-1} spectral window.

4.3.5.2 Sensitivity analysis and error budget

Using the optimum set of retrieval parameters described in Sect. 4.5.2, a series of sensitivity analyses were performed. In Sect. 4.5.1, the spectrometer FOV was determined as 22 mrad. The exact FOV is difficult to determine given the fast optics and the absence of a well-defined limiting aperture. Retrievals were compared using the optimally determined FOV with those made using a FOV varied by ±10%.

Retrievals for all three gases generally show a systematic reliance upon the specified FOV (Fig. 4.16), with retrieved pathlength amounts generally increasing with assumed FOV. CO demonstrated the greatest sensitivity to FOV since the CO absorption lines are narrower than the instrument's 0.5 cm^{-1} spectral resolution and their representation is therefore strongly influenced by instrument parameters. CO_2 retrieval accuracy appears to be less sensitive to FOV uncertainty at higher pathlength amounts. This may be explained by the increasing saturation (absorption of all source energy) by strong absorption lines at higher CO_2 pathlength amounts, leaving fewer lines in the spectral window affected by errors in FOV.

The retrieval sensitivities to assumed pressure and temperature were calculated from the pressure- and temperature-independent molecular amounts (molecules cm^{-2}), rather than from the volumetric mixing ratios (ppm.m), as the latter are additionally sensitive to these parameters via the relationship used to interconvert between these two concentration units (Eq. 4.3). Figure 4.17 shows the sensitivity of the retrievals to assumed gas pressure, where it can be seen that pathlength amounts are generally overestimated when pressure is underestimated, and vice versa. As is the case with the FOV parameter, the forward modelled absorption line widths are affected by the assumed pressure (Fig. 4.19a and b). When a lower pressure is assumed, narrower lines than are actually present in the measured spectrum are modelled due to inadequate pressure broadening, causing a positive residual between the modelled spectrum and the measurement (similar to the residual spectrum in Fig. 4.19b. In order to fit the modelled spectrum to the measured spectrum, the NLLS procedure increases the concentration of the absorber to minimise this positive residual, leading to an overestimation of gas pathlength amounts, whereas the reverse is true when assumed pressure is overestimated.

For CH_4 and lower pathlength amounts of CO, the error induced by pressure uncertainties was significantly lower than for CO_2 (Fig. 4.17). As pathlength amounts increase, absorption lines deepen, causing any line shape inaccuracies due to incorrect pressure specification to be exacerbated. For CO_2, line deepening is less of an issue, given that deep absorption lines occur for all pathlength amounts in the spectral window chosen, and this explains why CO_2 retrievals shows a higher sensitivity to pressure uncertainties at all pathlength amounts, with the percentage error relatively independent

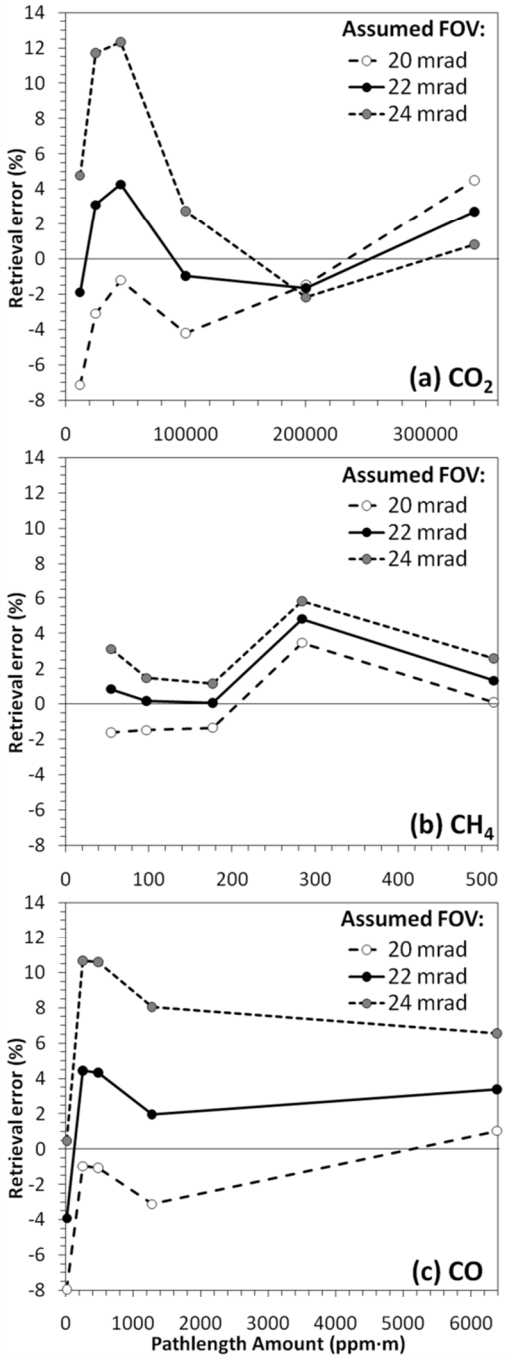

Figure 4.16 Sensitivity of trace gas concentration retrieval error to the assumed FOV for (a) CO_2, (b) CH_4, and (c) CO. Retrievals were made using the MALT forward model with a NLLS fitting procedure. The same y-axis range is used in each case to aid comparison of error magnitude between gases.

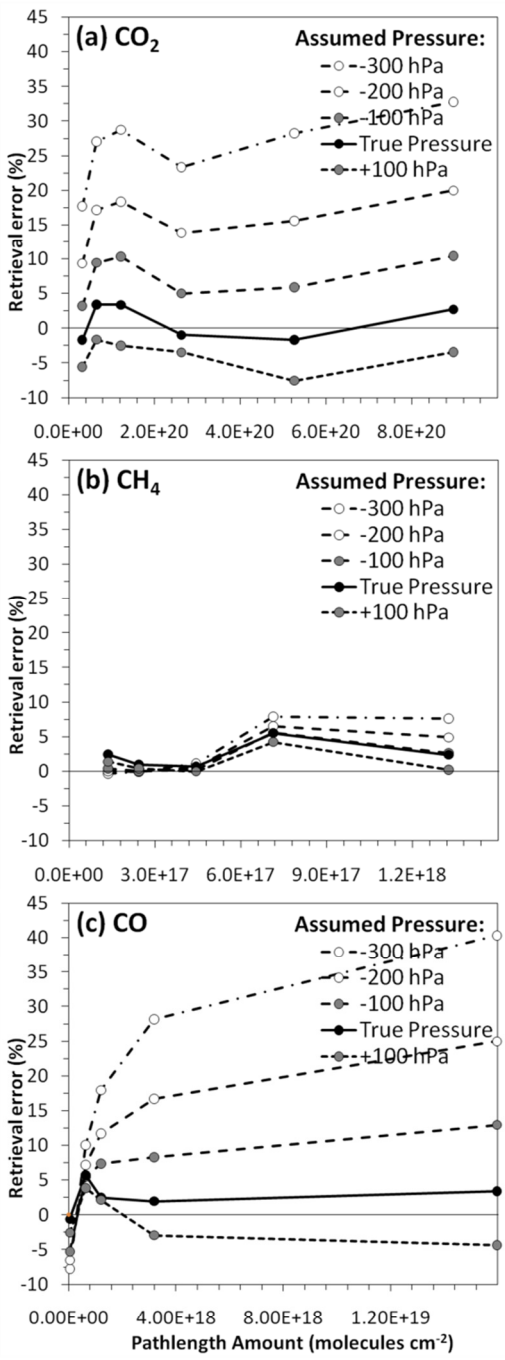

Figure 4.17 Sensitivity of trace gas concentration retrieval error to the assumed gas pressure for (a) CO_2, (b) CH_4, and (c) CO. Retrievals were made using the MALT forward model with a NLLS fitting procedure. The same y-axis range is used in each case to aid comparison of error magnitude between gases.

of actual concentration. The reported errors based on the forward modelled fit residuals show little dependence on pressure (±0.04%, ±0.01% and ±0.002% across ±100 hPa for CO_2, CH_4 and CO respectively), whereas retrieval errors show a much greater sensitivity. In field situations, pressure uncertainties are most likely to arise from uncertainty in plume height. The analysis shows that uncertainties of up to 500 m at sea level (~50 hPa) are therefore equivalent to a ±0.5% uncertainty in CH_4 and low CO pathlength amounts, but are closer to ±3% for CO_2 and higher pathlength amounts of CO.

Figure 4.18 shows the sensitivity of retrieved pathlength amount to assumed temperature. For CH_4 and CO retrievals, temperature increases lead to proportional increases in retrieved pathlength amounts, whilst for CO_2, this effect is not observed at lower pathlength amounts and is reversed for the highest pathlength amounts (above 5×10^{20} molecules cm^{-2}). These findings are best explained by the temperature dependence of spectral band shape. Changing temperature affects the envelope of the absorption band (Fig. 4.19c), with higher temperatures causing more absorption in the weaker lines that lie towards the edge of the band, and reduced absorption in the stronger lines located towards the middle of the band. Therefore, for spectral windows containing strong absorption lines located towards the middle of an absorption band, when assumed temperature is overestimated, a higher gas concentration is required for the forward modelled spectrum to best-fit the measured spectrum. When a spectral window containing weaker absorption lines at the edge of an absorption band is used, the opposite is true. For the CH_4 and CO spectral windows, these effects largely cancel each other out as the spectral windows lie across both strong and weaker lines at the middle and edge of their respective absorption bands. The greater influence of the stronger absorption lines leads to a small positive sensitivity for CH_4 and CO in the spectral windows used here. For CO_2, however, the saturation of the strongest lines towards the middle of the band means that the sensitivity of concentration retrievals to temperature is reversed.

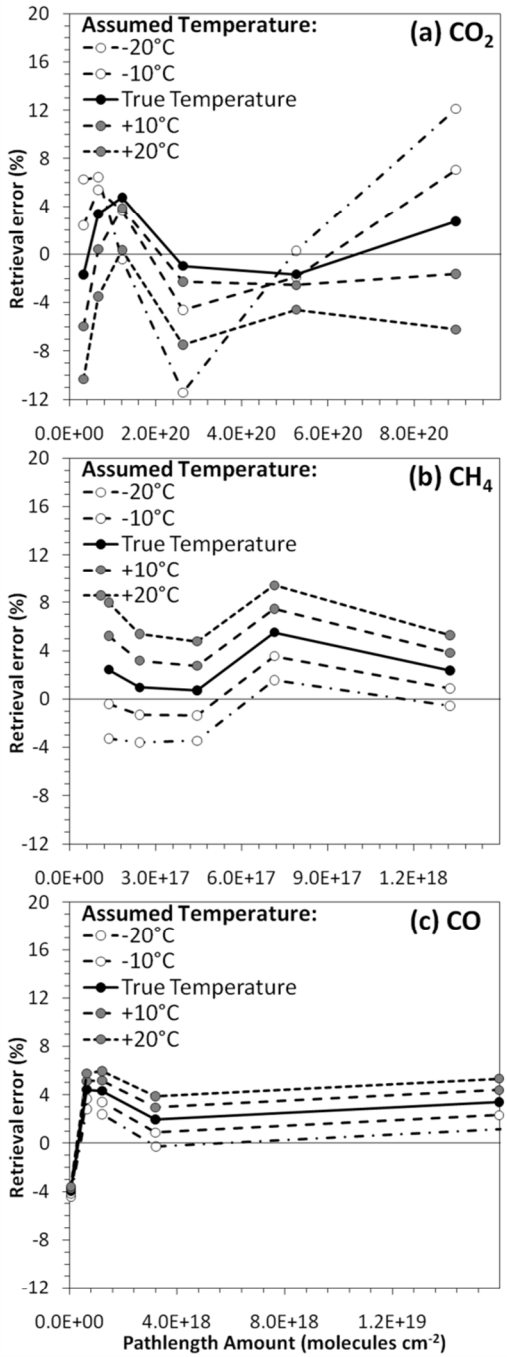

Figure 4.18 Sensitivity of trace gas concentration retrieval error to the assumed gas temperature for (a) CO_2, (b) CH_4, and (c) CO. Retrievals were made using the MALT forward model with a NLLS fitting procedure. The same y-axis range is used in each case to aid comparison of error magnitude between gases.

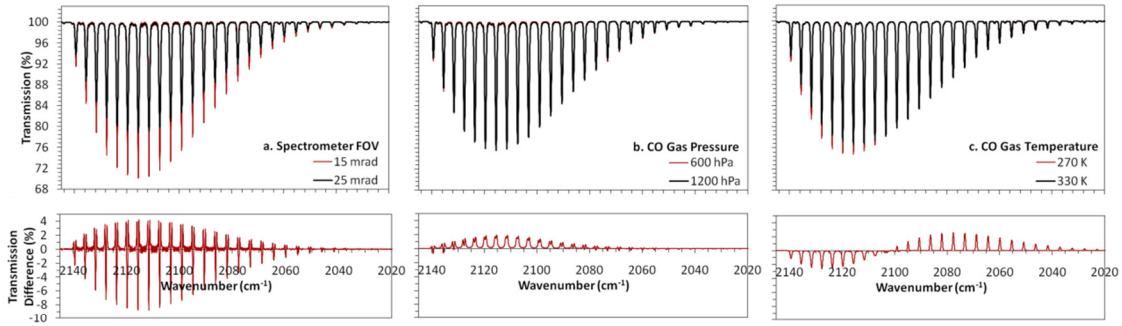

Figure 4.19 Simulated transmission spectra for CO gas at a fixed molecular amount of 6.424×10^{17} molecules cm^{-2}, along with percentage difference in transmission between the CO transmission spectra simulated using (a) an assumed FOV of 15 mrad and 25 mrad; (b) at 600 and 1200 hPa; and (c) at 270 K and 330 K. The figure focuses on the *p*-branch of the CO vibrational stretching mode absorption feature, centred at 2143 cm^{-1}. Increasing FOV leads to broader, but weaker absorption lines; increasing pressure leads to deeper and broader absorption lines; whilst increases in temperature lead to stronger absorption towards the edge of the band (wavenumbers < 2100 cm^{-1}) and weaker absorption towards the band centre (wavenumbers >2100 cm^{-1}).

4.3.5.3 Sensitivity summary

Table 4.5 summarises the findings of the sensitivity analyses and indicates to what percentage accuracy CO_2, CH_4 and CO can be retrieved assuming optimum parameterisation of the forward model. The 'worst-case' scenario (as suggested by Horrocks *et al.*, 2001) indicates that the total error due to uncertainties that could arise from incorrect retrieval parameterisation amounts to less than 8.2% for all tested pathlength amounts, with a mean of 4.8%. Generally these 'external' errors are of a similar magnitude to the additional errors that maybe introduced via the uncertainty inherent in the absorption line intensities for each gas. The HITRAN08 absorption line intensity uncertainties are reported to be between 5–10% for CO_2 and CH_4, but are lower for CO at 1–2% (Rothman *et al.*, 2009). Of course, with good meteorological measurements and careful collection of non-saturated single-beam spectra, the magnitude of the external errors can be minimised.

Errors in assumed pressure become increasingly significant at higher pathlength amounts due to the deepening of absorption lines, especially for CO_2 and CO. One solution to this problem would be to use a spectral window with weaker absorption lines; however, the results for temperature sensitivities indicate that this would increase sensitivity to the spectral band shape dependence on temperature. Errors in assumed temperature of less than 10 °C lead to errors in retrieved concentration of below 3%.

Table 4.5 Summary of errors associated with parameter uncertainty when retrieving trace gas amounts from OP-FTIR measurements using the MALT forward model (Griffith, 1996) with a NLLS fitting procedure. Errors for choice of polynomial and errors in assumed field-of-view, pressure and temperature are taken from the results presented in Figures 7, 9, 10 and 11, and are calculated using the difference between the retrievals made using the best parameter to those using the altered parameter, expressed as a percentage. Uncertainties in the HITRAN08 database (Rothman *et al.*, 2009) refer to the line intensity error specified therein.

	Retrieval Error (%), for CO_2 pathlength amounts (ppm.m):					
Source of Error	12,612	26,235	48,080	105,112	210,172	357,304
Choice of polynomial (4^{th} or 5^{th} order)	0.9	0.6	1.7	1.8	1.5	0.9
Field-of-view (best-fit or manufacturer's)	5.2	6.2	5.5	3.2	0.2	1.8
50 hPa error in assumed pressure	2.2	2.8	3.2	2.1	3.4	3.5
10°C error in assumed temperature	4.2	4.5	1.0	2.5	0.6	4.3
Total (added in quadrature)	7.1	8.2	6.7	4.9	3.8	5.9
Uncertainty in line intensities (HITRAN08)	5.0–10.0	5.0–10.0	5.0–10.0	5.0–10.0	5.0–10.0	5.0–10.0
Mean reported error	0.2	0.3	0.4	0.4	0.3	0.3
Accuracy of retrieved:true (best parameters)	-1.9	3.1	4.3	-1.0	-1.7	2.7
	Retrieval Error (%), for CH_4 pathlength amounts (ppm.m):					
Source of Error	54.5	97.4	176.9	284.3	514.5	
Choice of polynomial (4^{th} or 5^{th} order)	1.6	0.8	0.6	0.7	1.0	
Field-of-view (best-fit or manufacturer's)	2.4	1.6	1.4	1.3	1.2	
50 hPa error in assumed pressure	0.8	0.4	0.3	0.3	0.6	
10°C error in assumed temperature	2.8	2.2	2.1	1.9	1.5	
Total (added in quadrature)	4.1	2.9	2.6	2.4	2.2	
Uncertainty in line intensities (HITRAN08)	5.0–10.0	5.0–10.0	5.0–10.0	5.0–10.0	5.0–10.0	
Mean reported error	2.0	0.9	0.6	0.6	0.8	
Accuracy of retrieved:true (best parameters)	0.8	0.2	0.1	4.8	1.3	
	Retrieval Error (%), for CO pathlength amounts (ppm.m):					
Source of Error	19.9	256.3	482.0	1,277.7	6,379.9	
Choice of polynomial (4^{th} or 5^{th} order)	0.2	0.0	0.0	0.0	0.0	
Field-of-view (best-fit or manufacturer's)	4.0	5.4	5.4	5.1	2.4	
50 hPa error in assumed pressure	1.7	0.5	1.3	2.8	4.3	
10°C error in assumed temperature	0.2	0.8	0.9	1.0	1.0	
Total (added in quadrature)	4.4	5.5	5.6	5.9	5.0	
Uncertainty in line intensities (HITRAN08)	1.0–2.0	1.0–2.0	1.0–2.0	1.0–2.0	1.0–2.0	
Mean reported error	0.5	0.1	0.1	0.1	0.1	
Accuracy of retrieved:true (best parameters)	-4.0	4.4	4.3	2.0	3.4	

Greater errors are perhaps most likely to occur during studies focused on plumes from hot sources (volcanic, fire or industrial), and care should be taken to minimise sensitivity to these errors by using a broad spectral window encompassing weak and strong absorption lines and ideally targeting plumes once they have cooled to near ambient temperatures at some distance from the source region. Then, the magnitude of errors in assumed pressure and temperature that may be expected in the field should not lead to significant retrieval errors when retrieving molecular amounts (molecules cm^{-2}). However, for volumetric mixing ratios (e.g. ppm) the effect of these errors will be exacerbated through Eq. 4.3.

In this experiment, the spectrometer FOV was determined to be 10% higher than the manufacturer's nominal value of 20 mrad. Unlike gases such as SO_2, ambient and elevated pathlength amounts of CO_2, CH_4 and CO demonstrate deep absorption lines that increase their sensitivity to instrument line shape, and therefore extra care should be taken to preserve instrument optics from degradation if measurements are to target these gases.

4.3.6 Summary and implications for field measurements

This study collected single-beam spectra of a broad range of concentrations of CO_2, CH_4 and CO using OP-FTIR spectroscopy, representing mixing ratios varying from those found in the ambient atmosphere to the highly polluted plumes of biomass burning, volcanoes and industry over the equivalent pathlength of tens to hundreds of metres.

A number of spectral windows were investigated for the concentration retrieval of each gas species via a forward modelling nonlinear least squares fitting approach. Spectral windows that maximised the amount of absorption information for each gas (e.g. the number of absorption lines) typically produced the lowest reported errors (fit residuals) and the lowest actual retrieval errors when compared to the true gas cell pathlength amount. However, if broad spectral windows are to be used it is important to ensure a good background polynomial fit (used to represent the continuum radiation), and when wider windows were investigated, containing large regions showing no absorption (e.g. 2020–2310 cm^{-1} for CO_2), retrieval accuracies were diminished due to poor background

fitting. Similarly, it is important to check that broader windows do not contain spectral artefacts, such as those found here in the 2894–3001 cm^{-1} spectral window when retrieving CH_4. Such artefacts, potentially caused by substances contaminating spectrometer optics, will complicate the simulation of background shape using lower-order polynomials, and should therefore be avoided.

When using optimum parameterisation of the MALT forward model used here, the nonlinear least squares fitting procedure was able to retrieve pathlength amounts within 4.8% of the true values for all gases and pathlength amounts tested (Figure 4.20). Mean retrieval errors were 2.4%, 1.4% and 3.6% for CO_2, CH_4 and CO, respectively. A series of analyses was performed to assess the sensitivity of retrievals to uncertainties in instrument (FOV) and environmental (temperature, pressure) parameters. The uncertainties assumed were of a magnitude similar to those expected in many field situations in which OP-FTIR may be deployed. Sensitivities were shown to be different for each gas. Uncertainty in the FOV parameter had most impact on CO retrieval. The shape of the forward modelled absorption feature is therefore highly dependent on the assumed instrument FOV due to the narrowness of the CO absorption lines, which remain unresolved at the 0.5 cm^{-1} resolution used here. The sensitivity of all retrievals to FOV increased when the spectral window used for the analysis contained strong absorption lines, which occurred at higher pathlength amounts for the CH_4 and CO spectral windows, but at lower pathlength amounts for the CO_2 spectral window (where higher pathlength amounts led to absorption saturation, and therefore, a smaller number of observed absorption lines).

Generally, the results of this study indicate that reported errors, based on the residuals between the best-fit forward modelled spectra and the measured spectra, are smaller than the actual retrieval errors (Table 4.5). Reported errors should therefore not be used as a proxy for actual retrieval error. Reported errors appear most useful for the optimisation of instrument line shape, where minimising the reported error via adjustment of the assumed FOV can improve actual retrieval errors. However, errors in assumed FOV, temperature and pressure can all impart similar effects on the spectral fitting. For example, minimising reported errors by adjusting the assumed pressure could improve the spectral fit, but the same degree of improvement might be achieved by adjusting the FOV, potentially resulting in a quantitatively different retrieved

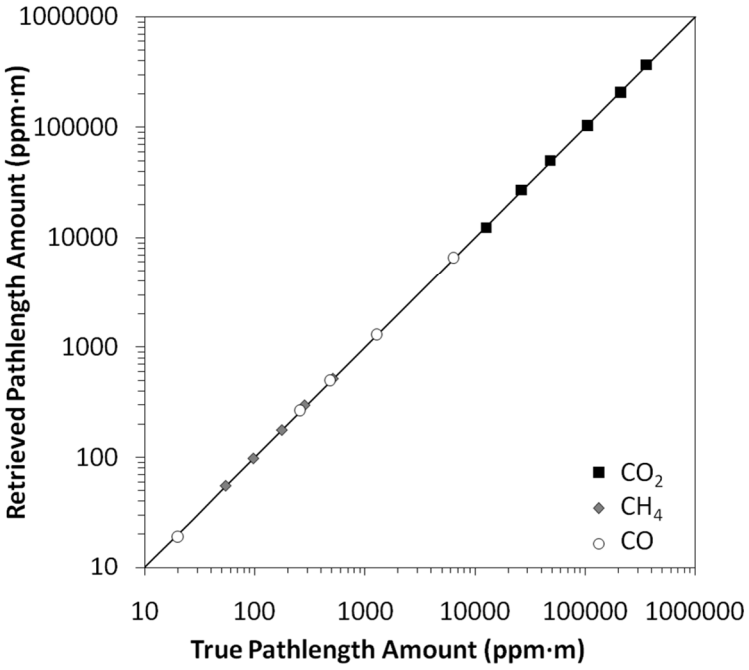

Figure 4.20 Relationship between mean retrieved pathlength trace gas amounts made using the optimum parameterisation of the MALT forward model determined herein. The 1:1 line is shown and all retrieved amounts are within 4.8% of true amounts (note logarithmic axes).

pathlength trace gas amount. These sensitivities and uncertainties suggest that proper assessment of gas temperature, pressure and instrument FOV is important for accurate gas concentration retrieval, given that errors induced by one parameter may be compensated for by adjusting the value of another parameter to minimise reported error, but that this may result in retrieval of an incorrect concentration.

Retrieval sensitivity to errors in temperature and pressure were relatively small for the magnitude of parameter uncertainty that might be expected in typical field situations. Assuming a potentially 'worst-case' scenario of a 50 hPa and 10°C error in assumed pressure and temperature, and the 10% difference in FOV found here as compared to the manufacturer's specification, pathlength amount retrievals might vary by up to 8.2% (errors added in quadrature). As discussed by Horrocks *et al.* (2001), gases that demonstrate individual absorption lines resolved by the spectrometer (as opposed to gases such as SO_2, with broad bands for which individual rotational lines cannot be resolved), are more susceptible to parameter errors affecting spectral line shape. Minimising uncertainty in these parameters is therefore paramount for retrievals of CO_2, CH_4 and CO via a combination of accurate temperature and pressure information, and

careful examination of the spectral fit. In particular, as demonstrated in this study, errors due to poor zero-baseline offset correction, incorrect pressure, temperature, and instrument line shape assumptions will all cause a poor fit when a retrieval is performed using a window containing both weak and strong absorption lines, and minimising reported errors in such a window will improve retrieval accuracy.

4.4 Conclusions of Chapter 4

The results from the two pilot studies and from the more extensive laboratory accuracy assessment presented in this Chapter confirm that a forward modelling approach, coupled with a nonlinear least squares fitting routine, can be a viable and accurate method for retrieving gas concentrations from OP-FTIR data, in this case using an MCT detector covering a wide spectral range (600–6,000 cm^{-1}).

The pilot studies found that the OP-FTIR methodology produces comparable results to those from more conventional point-based techniques (such as NDIR analysers for CO_2 and wet chemistry analysis for NH_3). Whilst these results were encouraging, the different sampling strategies (open-path vs. point-based) inhibited establishment of an absolute accuracy measure for the OP-FTIR derived CO_2 and NH_3 concentrations. The laboratory-based assessment using a gas cell filled with known gas concentrations offered a means to establish such an absolute accuracy measure. From the spectra measured at the Molecular Spectroscopy Facility (Rutherford Appleton Laboratory), the concentrations of the three most abundant carbonaceous gases in the atmosphere were retrieved to accuracies better than 5% over a very wide range of pathlength amounts (Fig. 4.20). Whilst it remains difficult to provide a quantitative measure of actual concentration retrieval error directly from the forward modelling reported errors (which are solely based on the fit residuals), the results from this study provide confidence that carefully undertaken retrievals made using the forward modelling NLLS method can provide high retrieval accuracies of a few percent or better.

5

Northern Territory: seasonality of burning emissions and emissions inventory

5.1 Introduction

Chapter 4 consisted of a thorough laboratory assessment of the absolute accuracy of the OP-FTIR method for the three most volumetrically abundant (in terms of emission amount) biomass burning carbonaceous trace gases (CO_2, CO and CH_4). Additionally, comparisons with conventional instruments for measuring NH_3 were used to help establish the accuracy of OP-FTIR for retrieving ammonia concentrations. Comparisons with measurements made by a conventional NDIR CO_2 analyser were also used to help establish the relative accuracy and precision of OP-FTIR derived CO_2 measures in the open atmosphere. Having established that concentrations of these gases can be retrieved at usable accuracies (<5 % error), the method can now be confidently applied during campaigns to measure smoke plumes at experimental fires and wildfires in the field.

This Chapter presents results from the application of OP-FTIR to the measurement of biomass burning emissions from Australian savanna fires. During July and October 2009, two trips were made to the Arnhem Land plateau of the Northern Territory, Australia, to measure emissions from experimental fires lit during the early and late dry seasons respectively. During August 2010 to October 2010, a further, longer-duration trip was made to Darwin, Australia where opportunistic visits to wildfires were used to increase the number of measured fire events. By sampling fires at different times during

the dry season, and by sampling fires from different vegetation types, it was possible to investigate the main controls on emission factors in the Australian savanna ecosystem.

Both open-path and solar spectra were collected during these field campaigns. This Chapter will focus on spectra collected in the "active" open-path mode, as these are the highest quality data and retrieved amounts have lower reported errors than those measured in the solar mode. In addition to measurements made using OP-FTIR, co-incidental point-based *in situ* (source) samples of smoke were taken during the 2009 campaigns and subsequently analysed using a variety of laboratory techniques in Darwin, allowing for a useful comparison of emission factors calculated from gas concentrations that were measured using two very different sampling strategies.

The work presented here represents the first Australian savanna emission factors calculated from gas concentrations derived from open-path FTIR spectra. Further to the accuracy assessments in the previous Chapter, this Chapter makes a direct comparison between emission factors derived from OP-FTIR and those derived from the more established *in situ* (source) sampling approach.

Sections of this Chapter have been published as part of Meyer et al. (2012) in the Journal of Geophysical Research.

5.2 Background

Estimates of the annual emissions from worldwide savanna and grassland fires amount to ~1 Pg C per year during 2000–2009, or something like 40–50% of total global annual biomass burning carbon emissions (van der Werf *et al.*, 2010). These estimates contain an uncertainty of perhaps 30% (van der Werf *et al.*, 2010), and consequently much effort has been made to refine estimates of emissions from these very significant fires (e.g. Andreae and Merlet, 2001). Despite the prevalence of savanna fires on the Australian continent, with approximately 400,000 km^2 of tropical savannas and 150,000 km^2 of arid savannas burning annually (Russell-Smith *et al.*, 2007), the focus of most

savanna emissions research has been on Africa (e.g. Bertschi *et al.*, 2003a; Yokelson *et al.*, 2003; Sinha *et al.*, 2003; Keane *et al.*, 2006). Only Hurst *et al.* (1994a) and Hurst *et al.* (1994b) and Shirai *et al.* (2003) have published emission factors from Australian savanna, as reviewed in Sect. 2.3 and Table 2.2.

The direct emissions of CO_2 from Australian savanna fires are of a similar magnitude to the national emissions of CO_2 from fossil fuel combustion. Given that CO_2 is assumed to be re-assimilated during savanna regrowth the following year, CO_2 from biomass burning is not included in the accountable greenhouse gas emissions from the Australian continent (IPCC, 2000). Emissions of nitrous oxide and methane, however, comprise 2 to 4 % of total national accountable greenhouse gas emissions (DCCEE, 2010) and are included in the accountable greenhouse gas inventory. Regionally, pyrogenic emissions of CO_2, CH_4 and N_2O can be far more significant, with emissions from fires comprising nearly 50% of the Northern Territory's accountable carbon emissions (DCCEE, 2010).

The Intergovernmental Panel on Climate Change Good Practice Guidance (IPCC, 2000) argued that:

> "*Since the emission factor for CH_4 can decrease by 50–75% as the burning season progresses, it is strongly suggested that each inventory agency collect seasonal data on the fraction of savanna area burned, the aboveground biomass density, and the fraction of aboveground biomass burned in each savanna ecosystem from the early dry season to the late dry season.*" (Section 4A1.1.3, page 4.87)
>
> [Hence]...
>
> "*It is desirable to develop the seasonal-dependent activity data and the emission factors of CH_4 and N_2O from savanna burning in various savanna ecosystems in each country if data are available. Fewer savanna areas and a smaller percentage of aboveground biomass are burned in the early dry season than in the late dry season. Therefore, as the dry season progresses in different savanna ecosystems, it is critical to monitor (i) the fraction of burned savanna area; (ii)*

> *the aboveground biomass density; (iii) the percentage of the aboveground biomass burned; and (iv) combustion efficiency.*" (Section 4A1.1.1, page 4.85)

Parties to the United Nations Framework Convention on Climate Change (UNFCCC), including Australia, are required to follow the IPCC Good Practice Guidance in their compilation of regional and national greenhouse gas emissions inventories, although few nations have implemented this particular guidance to date.

The main study of Australian emissions from savanna burning, that of Hurst *et al.* (1994b), in fact did not find any evidence for seasonal variation in methane emissions in its measurements of 15 fires across the dry seasons of 1991 and 1992 (including 3 fires in May, with the remainder in September). However, this finding appears to disagree with more recent research in Africa, with the above IPCC assertion being supported by a range of studies of fires in Southern Africa (e.g. Hoffa *et al.*, 1999; Korontzi, 2005; Korontzi *et al.*, 2003a, Korontzi *et al.* 2003b, Korontzi *et al.* 2004). The implications of this assertion by the IPCC, and its application to northern Australia, could invalidate the Northern Territory's entire approach to reducing greenhouse gas emissions from fires. Currently, in northern Australia early dry season prescribed fires are used to minimise devastating late dry season wildfires (and thus reduce area burned and fuel consumption); but under this IPCC assertion, this approach could increase rather than decrease methane emissions due to higher CH_4 emission factors from early dry season fires. Land managers and rangers would then be forced into a trade-off between these requirements to minimise the late dry season fires that pose a threat to biodiversity, life and property, and the requirements to minimise early dry season fires due to their greater emission factors for methane.

This Chapter aims to establish whether the earlier conclusions of Hurst *et al.* (1994b) about the consistency of methane emissions factors across the year are valid. To achieve this, measurements of smoke emissions from adjacent experimental plots are made in both the early and late dry season. The results presented here represent the first Australian savanna emission factors derived from *in situ* open path FTIR measurements, complete with the first direct comparison with emission factors calculated simultaneously from the more established *in situ* sampling method used in previous studies (Hurst *et al.*, 1994a; Hurst *et al.*, 1994b).

5.3 Specific objectives of this Chapter

The objectives of this Chapter aim to address the second and third thesis research questions outlined in Section 2.6. These relate to establishing whether OP-FTIR can be used to establish "fire-averaged" and whether OP-FTIR can yield information on the controls on the natural variability of emissions. These research questions are addressed through the following specific objectives:

(a) To improve information on Australian savanna burning emissions by measuring emissions from a variety of fuel types and from different times during the burning season.
(b) To determine the seasonality of savanna emissions, particularly for the important greenhouse gases, methane and nitrous oxide.
(c) To compare emission factors determined from two different measurements strategies (conventional *in situ* [point source] sampling and OP-FTIR).

5.4 Measurements of emissions

Savanna fire emissions were measured at experimental fires in July and September 2009 near Kulnguki on the Arnhem Land Plateau, Northern Territory. OP-FTIR and source sampling techniques were used at these fires. Further OP-FTIR measurements of both experimental and "wild"-fires were carried out during August to October 2010 in the cities of Darwin and Palmerston, and the Litchfield and Coomalie Shires of the Northern Territory. The flora of these areas is typical of mesic eucalyptus dominated savannas that comprise much of northern Australia, from the Kimberley region of Western Australia, through the Top End of the Northern Territory to Cape York in Queensland (Figure 5.1).

5.4.1 Site descriptions

5.4.1.1 Arnhem Land (2009)

Measurements were conducted during two field campaigns:

1. An early dry season campaign between 2 July and 7 July 2009, during which six experimental fires were measured.
2. A late dry season campaign between 30 September and 4 October 2009 during, which five experimental fires were measured.

The experimental fire sites were located near Kulnguki, in West Arnhem Shire, Northern Territory (12° 38' S 133° 55' E, Figure 5.2d), 330 km east of Darwin. One set of fires were situated on the gently undulating sandplains of the Queue landsystem (Lynch and Wilson, 1998). This landsystem is dominated by *Eucalyptus tetrodona*, *Eucalyptus miniata* and *Corymbia ferruginea* trees, with an *Acacia mimula* mid-storey.

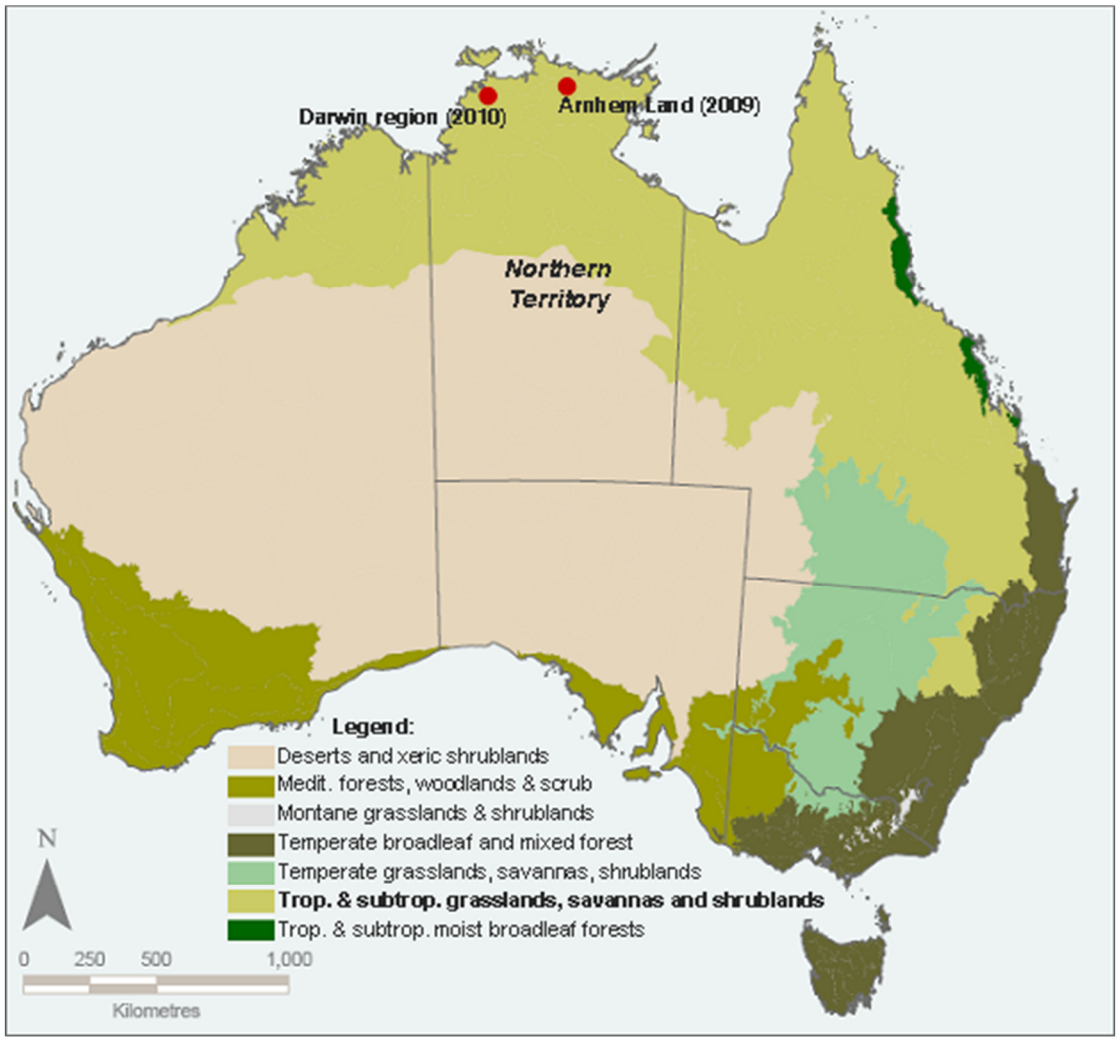

Figure 5.1 Map of Australia, showing the two field campaign locations. Both the Arnhem Land and Darwin Region campaigns are situated in the 'tropical and subtropical grasslands, savannas and shrublands' terrestrial ecoregion (Parks Australia, 2010).

The understorey mainly consists of annual or perennial sorghum grasses (*Sorghum intrans* and *Sorghum plumosum*, respectively) with a number of shrub species to about 1 m high. The vegetation of this system will be referred to as tussock grass open woodland hereafter. Another set of fires were situated on the rugged dissected quartz sandstone plateau of the Buldiva landsystem (Lynch and Wilson, 1998). Here, the dominant trees are *Eucalyptus miniata* and *Corymbia arnhemensis* with an *Acacia* spp. mid-storey. The understorey is mainly dominated by hummock grass (Spinifex, *Triodia* spp.) with a variety of shrubs. The vegetation of this system will be referred to as hummock grass open woodland. While the tussock grasses are similar to those of other savanna systems worldwide, the hummock grasses are endemic to Australia, adapted to the arid climate with a shrub-like growth form.

The climate of West Arnhem Land is tropical monsoonal, and 97% of the mean annual rainfall falls between November and April. The closest weather station, at Oenpelli (12° 20' S 133° 03' E), 100 km west-northwest of the experimental fire sites records a mean annual rainfall of 1,417 mm, with a mean maximum temperature of 30° C in July and 38° C in October.

5.4.1.2 Darwin region (2010)

A third measurement campaign to the Northern Territory was conducted during August to October in the dry season of 2010. Measurements were made at a number of wildfires, as well as experimental fires, at various locations within a region 120 km to the south/southeast of Darwin (Figure 5.2c). The opportunistic nature of this campaign allowed for emissions to be measured from a number of different savanna land systems, these included:

- The gently undulating plains of the Koolpinyah land system (Christian *et al.*, 1953), dominated by open eucalypt woodland with tussock grasses.
- The flat perennially flooded plains of the Marakai land system (Christian *et al.*, 1953), mainly consisting of tussock grasslands.
- The flat country of the Batchelor land system (Christian *et al.*, 1953), dominated by tall closed woodland with tussock and gamba (*Andropogon gayanus*) grasses.

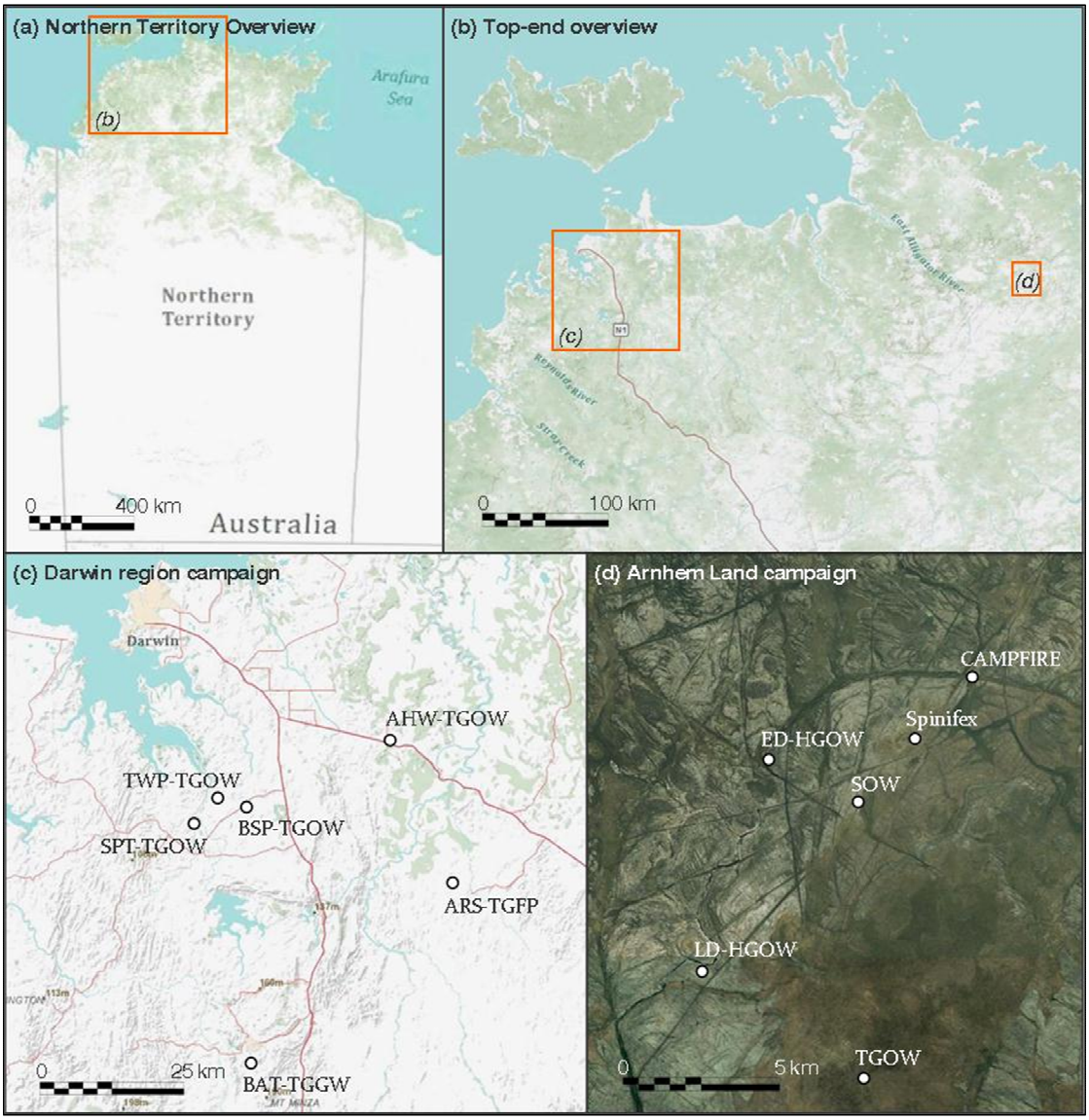

Figure 5.2 Maps showing the location of each of the fire sites discussed in this chapter (see Tables 5.1 and 5.2 for full site descriptions)

The climate of these areas is tropical monsoonal, with 95% of mean annual rainfall falling between April and November. According to the weather station at Batchelor (within 60 km of all fire measurement sites), mean annual rainfall is 1,528 mm, with a mean maximum temperature of 32° C in July and 37° C in October.

5.4.2 Fire descriptions

5.4.2.1 Arnhem Land (2009)

There were a number of classes of fires measured during the two Arnhem Land campaigns:

1. Tussock-grass open woodland (tgow)
2. Sorghum open woodland (sow)
3. Hummock-grass open woodland (hgow)
4. Isolated hummocks of Spinifex (spin) surrounded by rocky outcrops
5. Open campfire (smoke from grass, fine tree leaf litter, coarse fuels, heavy fuels and green leaves were sampled individually)

The tussock-grass open woodland and sorghum open woodland fires were conducted in a series of adjacent plots established prior to the first campaign along an access road. Each tussock-grass open woodland plot was approximately 500 m × 200 m in size, whilst each sorghum open woodland plot was approximately 100 m × 100 m in size. The dissected quartz sandstone landscape of the hummock-grass open woodland allowed for the identification of two isolated plots prior to the campaign, each with areas of 50–70 hectares, surrounded by natural fire barriers. The plots were situated in isolated country accessible only by helicopter, approximately 6–10 km from the tussock-grass plots. These experimental plots were ignited by a line ignition pattern on the upwind side of the plot, with some plots having a back fire also ignited on the downwind side of the plot. The isolated hummocks of Spinifex could be ignited individually without risk of establishing a fire front due to the surrounding rocky outcrop.

Plant species composition, fuel composition, fuel load and fuel moisture content were surveyed at each plot prior to ignition. The plots were also surveyed following each fire to determine combustion completeness. These measurements were carried out by researchers from the Commonwealth Scientific and Industrial Research Organisation (CSIRO) according to protocols described in Russell-Smith *et al.* (2009). The rate of spread for each fire was also measured by CSIRO, following the procedures outlined in Williams *et al.* (2003), from which Byram fireline intensity was determined. The characteristics of all plots, fuels and fires are given in Table 5.1.

In total, twelve experimental plots were measured during the two campaigns, seven in the early-dry season July campaign, and five in the late dry-season October campaign. Of these experimental fires, successful OP-FTIR measurements were made at ten of the plots (five in July and five in October). Additionally, source sampling was conducted on the open campfire, where fuels were fed onto a hot coal bed and burned to completion.

5.4.2.1 Darwin region (2010)

Three classes of fires were measured during the August–October 2010 Darwin region campaign:

1. Tussock-grass open woodland (tgow)
2. Tussock-grass floodplain (tgfp)
3. Tussock and gamba-grass woodland (tggw)

Unlike the purely experimental fires of the Arnhem Land campaign, most of the fires measured for the Darwin region campaign were either wildfires or "burn-off", where there was no control over the timing and pattern of ignition, with many of the fires burning over many hectares. Locations of burn-off and wildfires were identified by regular monitoring of the NAFI website (www.firenorth.org.au), which shows the locations of satellite-detected fires; and by regular phone calls to Bushfires NT (Northern Territory Government), who are responsible for supporting landholders with fire mitigation.

Wildfires were measured at the Adelaide River Station on the Marrakai Road (tgfp) on 1 October 2010; near Lambells Lagoon off the Arnhem Highway (tgow) on 1 October 2010; and at Berry Springs (tgow) on 4 October 2010. Burn-offs were measured at the Gould airstrip near Batchelor (tggw) on 11 September 2010 and at Southport (tgow) on 6 October 2010. In addition to the wildfires and burn-offs, measurements were made at a set of three experimental fires in the Territory Wildlife Park (tgow) near Berry Springs on 5 October 2010. Each of the experimental plots were approximately 130 × 80 m in size, and the fires and fire conditions from this campaign are presented in Table 5.2.

Figure 5.3 Photographs depicting the various savanna fire classes experienced during both the Arnhem Land (Arnhem) and Darwin region (Darwin) campaigns. The abbreviations in parentheses are used throughout this chapter, more details about specific fire plots are given in Tables 5.1 and 5.2.

Table 5.1 List of fires studied using OP-FTIR and source sampling during the Arnhem Land campaign (2009), with information about the plot location, OP-FTIR pathlength, fuel characteristics and meteorological variables. Fires that do not have a stated OP-FTIR path were not investigated using OP-FTIR, with measurements from source sampling available only.

Date	Local time	Dur. (min)	Site name	Veg. type	Location		OP-FTIR Path (m)	Total fuel (t ha^{-1}) and burning efficiency (%)				Weather			
					Latitude	Longitude		Fine	Coarse	Heavy	Shrub	T (°C)	RH (%)	P (hPa)	U (m s^{-1})
02-Jul-09	1430	90	ED-TGOW-A	tgow	12°44.45 S	133°53.13 E	46.4	6.0 (52)	1.1 (6)	0.52 (1)	1.03 (37)	30.6	39	997	6.0
03-Jul-09	1330	70	ED-TGOW-B	tgow	12°44.58 S	133°53.13 E	41.2	4.4 (-)	1.4 (-)	0.12 (-)	0.70 (-)	28.9	46	998	5.0
04-Jul-09	1250	40	ED-SOW-A	sow	12°39.07 S	133°53.99 E	38.5	3.5 (40)	0.7 (9)	0.17 (7)	0.65 (74)	25.6	42	1000	4.0
04-Jul-09	1400	35	ED-SOW-B	sow	12°39.12 S	133°53.95 E	38.5	- (-)	- (-)	- (-)	- (-)	26.3	41	999	4.0
05-Jul-09	1430	35	ED-SPIN	spin	12°38.32 S	133°54.75 E	22 - 27*	- (-)	- (-)	- (-)	- (-)	27.8	37	996	2.0
06-Jul-09	1300	90	ED-HGOW	hgow	12°39.49 S	133°51.49 E	-	5.7 (80)	0.8 (57)	0.16 (34)	4.77 (50)	29.0	29	996	0.6
07-Jul-09	1300	25	ED-TGOW-C	tgow	12°44.70 S	133°53.13 E	-	- (-)	- (-)	- (-)	- (-)	26.8	30	998	6.4
30-Sep-09	1400	45	LD-TGOW-A	tgow	12°44.76 S	133°53.17 E	40	6.9 (58)	1.0 (32)	0.16 (20)	0.75 (56)	34.7	34	993	4.8
01-Oct-09	1400	40	LD-TGOW-B	tgow	12°44.89 S	133°53.17 E	48.5	6.3 (62)	1.2 (18)	0.09 (18)	1.24 (51)	32.1	46	994	1.6
02-Oct-09	1430	30	LD-SOW-A	sow	12°44.92 S	133°53.13 E	51	- (-)	- (-)	- (-)	- (-)	34.3	35	995	3.2
02-Oct-09	1530	60	LD-SPIN	spin	12°38.32 S	133°54.75 E	22 - 25*	- (-)	- (-)	- (-)	- (-)	34.9	34	994	0.3
03-Oct-09	1300	90	LD-HGOW	hgow	12°43.01 S	133°50.43 E	70.5	6.4 (79)	0.7 (42)	0.21 (31)	1.09 (15)	35.2	31	1001	11.5
04-Oct-09	1330	-	CFIRE	mix	12°38.00 S	133°54.95 E	-	- (-)	- (-)	- (-)	- (-)	36.0	29	1001	5.5

*Numerous OP-FTIR paths were used for the spinifex fires

Table 5.2 List of fires studied using OP-FTIR during the Darwin region campaign (2010), with information about the plot location, fire type, OP-FTIR pathlength and meteorological variables.

Date	Local time	Dur. (min)	Site name	Fire type	Veg. type	Location		OP-FTIR Path (m)	Weather			
						Latitude	Longitude		T (°C)	RH (%)	P (hPa)	U (m s^{-1})
11-Sep-10	1430	90	BAT-TGGW	burn-off	tggw	13°04.95 S	131°02.75 E	40.0	36.2	31	1008.6	4.2
01-Oct-10	1330	70	ARS-TGFP-A	wildfire	tgfp	12°48.93 S	131°20.05 E	30.5	36.9	19	1006.8	1.7
01-Oct-10	1250	40	ARS-TGFP-B	wildfire	tgfp	12°48.93 S	131°20.15 E	34.8	36.9	19	1006.8	1.7
01-Oct-10	1400	35	ARS-TGFP-C	wildfire	tgfp	12°48.93 S	131°20.25 E	40.8	36.9	19	1006.8	1.7
01-Oct-10	1430	35	ARS-TGFP-D	wildfire	tgfp	12°48.93 S	131°20.35 E	38.0	36.9	19	1006.8	1.7
01-Oct-10	1300	90	AHW-TGOW	wildfire	tgow	12°36.32 S	131°14.57 E	34.0	34	19	1006.8	1.7
04-Oct-10	1300	25	BSP-TGOW	wildfire	tgow	12°42.19 S	131°01.43 E	29.4	36.9	31	1006.2	1.1
05-Oct-10	1400	45	TWP-TGOW-A	experiment	tgow	12°41.37 S	130°58.80 E	35.0	29.8	65	1011.4	0.6
05-Oct-10	1400	40	TWP-TGOW-B	experiment	tgow	12°41.69 S	130°58.80 E	40.0	29.8	65	1011.4	0.6
05-Oct-10	1430	30	TWP-TGOW-C	experiment	tgow	12°42.02 S	130°58.80 E	38.5	29.8	65	1011.4	0.6
06-Oct-10	1530	60	SPT-TGOW	burn-off	tgow	12°43.63 S	130°56.71 E	46.0	29.8	65	1010.6	0.1

*Duration for the wildfires and burn-off fires refers to the length of the dataset

5.4.3 Gas measurement methodology

Two different methodologies were used to ascertain savanna fire emission factors from the 2009 Arnhem Land campaign:

(1) Open-path FTIR spectroscopy adjacent to, or within the fire plot boundary (measurements and analysis performed by the author). Only OP-FTIR was used in the 2010 Darwin region campaign.
(2) *In situ* (point-source) sampling close to the emission source (within 1 m), followed by subsequent laboratory analysis of the gas samples for CH_4, N_2O, CO_2 and CO using various gas chromatographs (measurements and analysis performed by CSIRO).

Both methods rely upon sampling smoke (by point-sampling or path-sampling) at ground level.

5.4.3.1 OP-FTIR

The main technique for measuring savanna fire emissions during the three campaigns discussed here is the open-path FTIR spectroscopy methodology outlined in detail in Chapter 3 and evaluated in Chapter 4. As described in Section 3.3, the FTIR spectrometer was operated in 'active' mode, where the FTIR spectrometer and IR source were operated in a bi-static configuration, with pathlengths ranging from 22 to 70 m (Tables 5.1 and 5.2). Measurements using the solar occultation configuration were also made during the Darwin region campaign, but are not presented here and are discussed further in Chapter 7. Both the spectrometer and IR source were powered by 12 V batteries.

For most plots, the OP-FTIR path was positioned on a road, track, or fire-break downwind of the fire plot. There were, however, some exceptions. For some plots, where there was no safe location downwind of the fire plot, the OP-FTIR path was positioned over the plot, with smoke passing between the spectrometer and IR source before or after the fire front passed through the optical path. Spectra collected during the time in which the fire was burning within the open path were affected by infrared

emission from the flames; this effect precludes the retrieval of gas concentrations from spectra due to the superposition of emission and absorption lines in the spectral signatures. Consequently, all spectra affected by flame emission were removed from the analysis process. For other plots, and especially for the wildfire measurements, it was not possible to position a path beside or across the fire plot. In these situations, either the IR source, or both the spectrometer and the IR source, were positioned within the fire plot. To protect the equipment from the fire, the equipment was positioned within natural firebreaks (rocky outcrops, areas of low biomass) or artificial firebreaks (raked vegetation) with the OP-FTIR path penetrating into the fire plot, or being entirely enclosed by the fire plot (Figure 5.4).

For the experimental plots, it was possible to assemble the OP-FTIR equipment prior to each fire. Burn-offs and wildfires, by their nature, are unpredictable; identification of a position for the OP-FTIR path and assembly of the equipment took place whilst the fire was burning upwind. In one case (at the Adelaide River Station), it was possible to follow the fire along a track, assembling and reassembling paths as the fire front passed each path location. For all burns, spectra were collected using 4 co-added scans to increase signal-to-noise and to allow for a high measurement frequency (approximately one measurement every 4.5 seconds), given that most plots were small (<1 Ha) and in some cases burned quickly. Observations of atmospheric temperature and pressure (parameters required for the trace gas retrieval analysis) were made using a WXT510 weather station (Vaisala Oyj, Helsinki, Finland) at the Arnhem Land campaigns. For the Darwin region campaign, temperature and pressure readings were taken from a Bureau of Meteorology (Australian Government) weather station in Batchelor (located within 60 km of all of the burn sites).

Figure 5.4 Photographs showing the use of natural and artificial firebreaks to protect the OP-FTIR equipment during fires in which the open path between the spectrometer and IR source lay within the fire plots. (a) The FTIR spectrometer positioned on a rocky outcrop (hgow), with the fire being allowed to pass around the rocks; (b) The IR lamp protected by raked vegetation (tgfp), notice the distinction between the burnt and unburned area.

5.4.3.2 Source Sampling

The second method used to determine emission factors was the source sampling approach operated by CSIRO at the two Arnhem Land campaigns. The low intensity fires that are characteristic of savanna landscapes can be reliably sampled within close proximity to the emission source. Most of the combustion in savanna fires takes place in the flaming zone; Ward *et al.* (1996) estimated that 88% of fires sampled in African savanna had more than 70% of their emissions from flaming combustion, whilst 55% of fires had more than 90% of emissions from flaming combustion. Therefore, the sampling of smoke from within the flaming combustion zone is likely to give a good representation of average smoke composition. Here, source sampling was used to sample smoke from the flaming combustion zone, with supplementary measurements of smouldering phase combustion behind the fire and front, and from burning heavy fuels and logs. The source sampling method uses random, protracted spatial sampling near to the location where the majority of smoke production occurs to estimate average smoke composition. Whilst measurements were made of smouldering-phase combustion, the sampling method is biased towards flaming combustion.

Two specially designed backpack smoke collectors were deployed by CSIRO for the Arnhem Land campaign (Figure 5.5, photograph of backpack in use). The unit comprises a 2.5 m 12 mm diameter stainless steel sampling probe, in-line Teflon filters, and an air pump that delivers the filtered smoke sample into a 10 litre Tedlar bag, all mounted onto the backpack. Sampling is achieved by positioning the tip of the probe approximately 500 mm above the flame, within the entrainment zone. In this region, combustion should have ceased due to cooling and dilution by the entrained air, whilst the smoke concentration remains high. The sampling rate is set to approximately 1 litre per minute, leading to each sample bag containing smoke sampled over approximately 10 minutes. In addition to the Tedlar bag, the backpacks are equipped with three additional gas sampling lines; two for continuous measurement of $PM_{2.5}$, CO_2 and CO, with a third for sampling total suspended particulate matter (TSP).

Tedlar bags were used as the smoke sample storage container as they are free from well-known artefacts that can occur with stainless steel canisters. In particular, stainless steel canisters can lead to inaccurate N_2O-to-CO_2 emission ratios due to reactions catalysed at the stainless steel surface involving SO_2 (IPCC Good Practice Guidance, 2000). This artefact does not occur with glass flasks or Tedlar bags.

Depending on the fire conditions, 5–8 ten-litre smoke samples were collected by each sampling unit during each experimental fire. Samples were analysed for CO_2 and CO concentrations within 12 hours of collection using a Q-TRAK non-dispersive infrared analyser (model 7565, TSI, Shoreview, MN, USA). The sample bags were then returned to Darwin where they were analysed for CH_4, NMHC, N_2O, CO_2 and CO concentration within 3 to 5 days of collection using gas chromatography (GC). CH_4 and NMHC concentrations were measured by a Flame Ionisation Detector (FID) using a Thermo Environmental Instruments (TEI) model 55C total hydrocarbon analyser (Thermo Scientific, Franklin, MA, USA). N_2O was measured by an Electron Capture Detector (ECD) using an HP 5890 Series II Gas Chromatograph (Hewlett-Packard, Palo Alto, CA, USA). CO_2 was measured by NDIR using both a Q-TRAK and a Li-Cor model 6262 CO_2/H_2O analyser (Li-Cor, Lincoln, NE, USA). CO was measured using a Q-TRAK. Analytical precision was approximately 0.5 ppb for N_2O, 50 ppb for CH_4, 1 ppm for CO_2, and 3 ppm for CO.

Figure 5.5 Source sampling of smoke during the Arnhem Land campaign (tgow) using the specially designed backpack. Inset photograph shows the arrangement of the components of the sampling system.

Trace gas species stored in Tedlar bags can slowly exchange with the surrounding atmosphere and storage time, therefore, should be limited to a few days. Here, storage times were no longer than 5 days. Furthermore, the rate of exchange is predictable; Tedlar bags filled with camp fire smoke on each day of sampling were analysed for CH_4 and N_2O at least twice after filling, the exchange rates were found to be not significantly different for each gas. Previous studies using the same bags (C. Meyer, personal communication, 2010) indicated the same exchange rate for CO_2. Under the assumption that the permeability of the Tedlar bags to CO is similar to the other gases, emission ratios derived from the bag sampling should be independent of storage time if all gases from a single bag are analysed at approximately the same time.

5.5 Results

The prime objectives of this Chapter were to determine an emissions inventory from OP-FTIR measurements of Australian savanna fires, to compare the results from this methodology with those from the established source sampling methodology, and to ascertain whether the current Good Practice guidance (IPCC, 2000) assertion of large seasonality in methane emission factors holds true for Australian savanna fires. This

results section will focus first on the OP-FTIR measurements from both Arnhem Land campaigns and the Darwin region campaign and the resultant emission factors inventory. Results from the source sampling method are [currently] limited to those for methane and nitrous oxide, allowing for a comparison of methane emission factors with those from OP-FTIR and for a comprehensive evaluation of the seasonality of methane emissions, using both methodologies.

5.5.1 OP-FTIR

The open-path FTIR methodology (described in detail in Section 3.3) is used to retrieve trace gas concentrations in the smoke eddies passing through the infrared beam emitted by the IR lamp and measured by the FTIR spectrometer. A time series of smoke tracer concentrations near to the downwind boundary of one of the experimental fires is shown in Figure 5.6. In most of the experimental burns (with the exception of the *HGOW* plots), the fires are ignited with a back-burning fire line on the down-wind boundary of the fire plot; this moves slowly against the wind, forming a fire break. The up-wind boundary is then ignited, with the majority of the plot burning with a head-fire driven by the prevailing wind. Generally, the smoke passing through the infrared beam will have first originated from the flaming combustion in the back-burn fire line (notice the high M.C.E. in the first minute of the time series in Fig. 5.7). Immediately following the initial burst of smoke from the flaming combustion, the smoke from the flaming back-burn will be mixing with smouldering smoke, also originating from the back-burn, with increasing CO concentration and a corresponding decrease in MCE. (until time *5.78* in Fig. 5.7). As the back-burn fire line burns away from the OP-FTIR path, most of the smoke crossing the infrared beam will have been emitted from the steadily increasing area of smouldering-phase combustion, with contributions from both the flaming combustion of the head-fire and the smouldering area behind the head-fire (towards the end of the time series in Fig. 5.7, as M.C.E. decreases to ~90% and below).

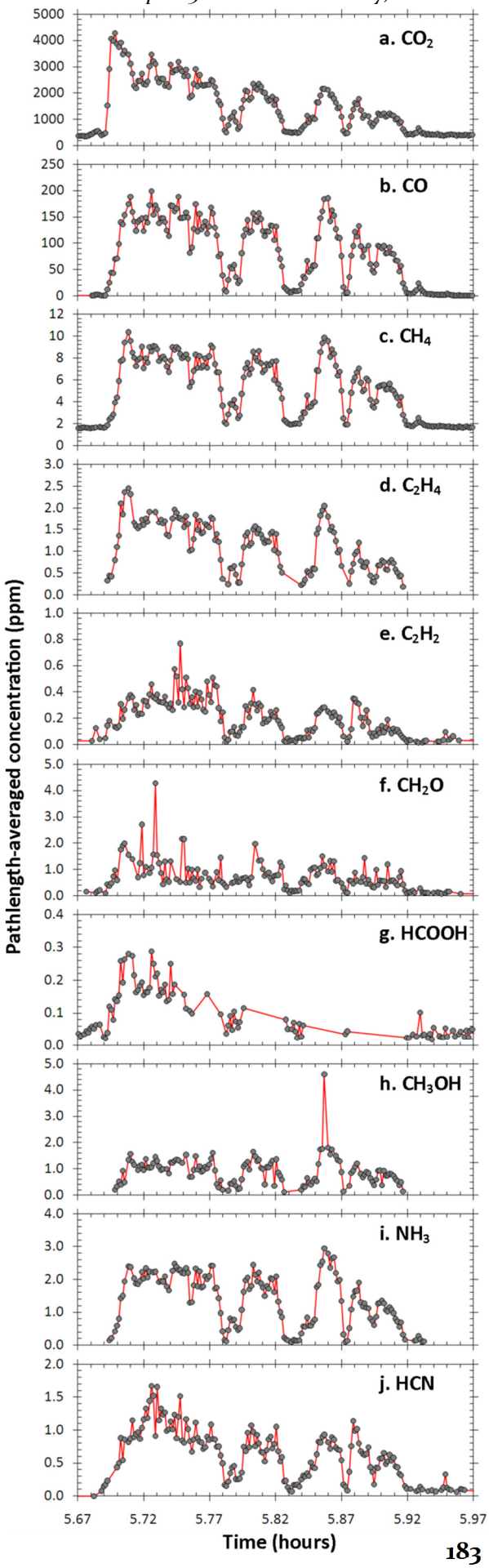

Figure 5.6 Time series of path-averaged trace gas concentrations (in ppm) for plot *LD-TGOW-A* (30 September 2009) during the late-dry season Arnhem Land campaign. Trace gas concentrations were retrieved from the OP-FTIR spectra using MALT (as described in Section 3.2). An example smoke spectrum with the best-fit modelled spectrum for each of the spectral windows used to retrieve the concentration of each of the trace gases presented in this figure can be found in Figure 3.15. Gaps in the time series of specific trace gases are due to periods of low signal-to-noise within the spectral window used for the retrieval of that particular gas.

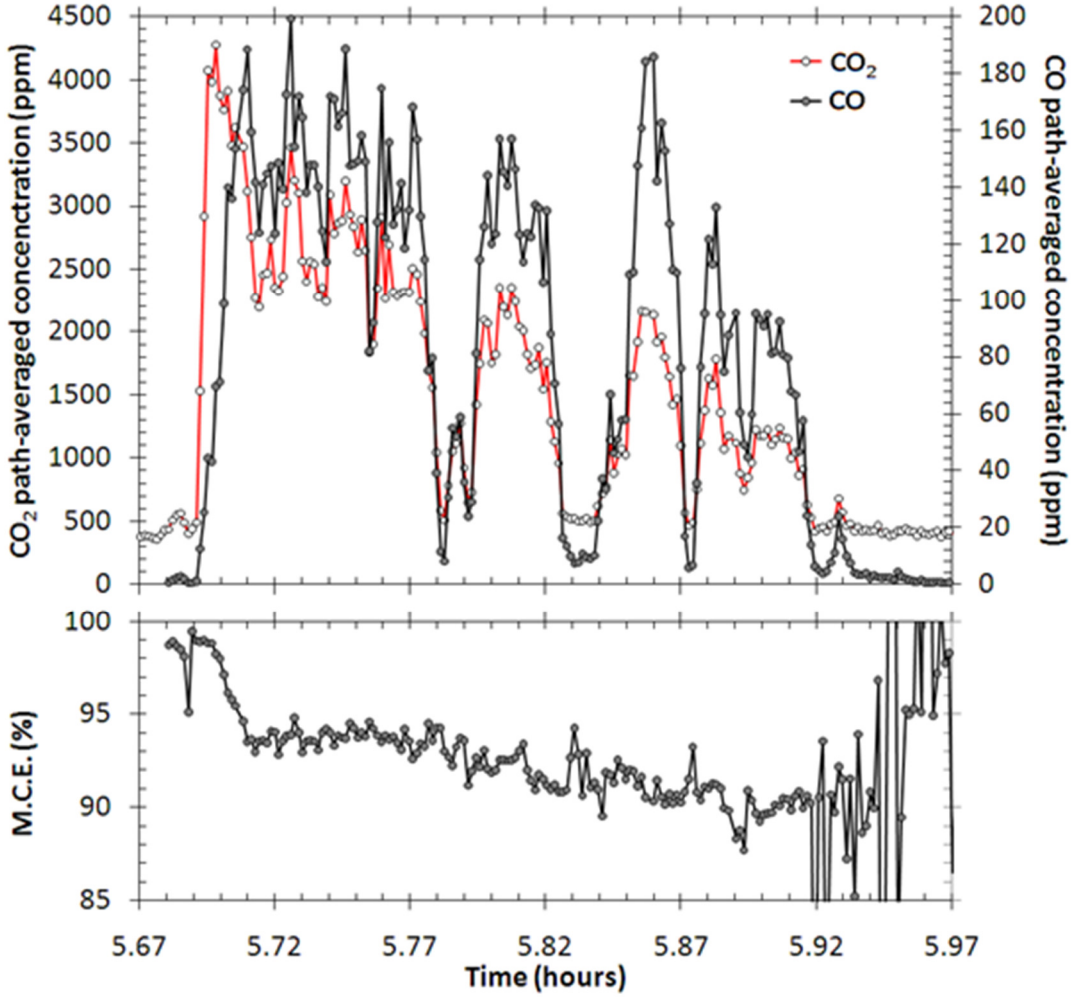

Figure 5.7 (top) Time series of retrieved CO_2 and CO pathlength averaged concentrations, and (bottom) Modified Combustion Efficiency (MCE). Only the first ~60 seconds following ignition are dominated by smoke from purely flaming combustion, with increasing contribution from the smouldering-phase combustion zone towards the end of this time series (as reflected by the decreasing MCE throughout). These data are taken from *LD-TGOW-A* (30 September 2009). The full suite of gas concentrations are presented in Figure 5.6.

5.5.1.1 Emission Ratios

The emission ratios of each trace gas relative to CO_2 are calculated from bivariate plots (as described in Section 3.3.3), where the least squares linear regression slope of the trace gas species concentration versus the CO_2 concentration is used as the emission ratio. As an example, Figures 5.8 and 5.9 show a series of trace gas concentrations (those from Fig. 5.6) plotted against CO_2 and CO, respectively. The least squares linear best fits are shown in each case, with the gradient taken as the emissions ratio [ER_{X/CO_2}

or $ER_{X/CO}$] and the 95% confidence limits on the gradient providing an estimate of the emission ratio uncertainty. As is evident in both Figures 5.8 and 5.9, and from the slope uncertainties in Table 5.3, it is clear that for most gases, there was a better correlation to CO than to CO_2 (due to their preferential production during smouldering-phase combustion). Nevertheless, the emission ratios of these species to CO_2 are required for derivation of their respective emission factors (Sect. 5.5.1.2). Following Sinha *et al.* (2003) and Wooster *et al.* (2011), the strength of the coefficient of determination (r^2) between the concentration of each target gas and that of CO or CO_2 is used to confirm whether the emission ratio for the target gas is well determined. For gases produced in high concentrations (e.g. CO, CH_4, C_2H_4, NH_3), R^2 in the figures was generally greater than 0.8, whilst rarer gases (e.g. CH_3OH, HCN, HCOOH) showed poorer correlations to CO_2 and CO, due to greater uncertainties in the retrieval process because of their low abundances and/or weaker IR absorption lines. Those species for which the coefficient of determination fell below 0.4 are assumed to have poorly determined emission ratios (Sinha *et al.*, 2003 and Wooster *et al.*, 2011). Consequently, emission ratios where R^2 fell below 0.4 were not used in the calculation of emission factors.

Given that MCE is known to decrease as the fire progresses through the plot (Figure 5.7), with a greater contribution from the increasing area of smouldering combustion, it is assumed that measurements with high MCE are of smoke that has predominantly originated from flaming combustion, whilst those measurements with low MCE are of smoke that has been predominantly produced by smouldering combustion (Yokelson *et al.*, 1996). Whilst the *within-fire* variation in emission ratios is quite limited, as shown by the confidence limits on the linear least squares regression fits in the bivariate plots (Figs. 5.8 and 5.9), this ever-changing ratio of flaming-to-smouldering smoke does lead to some variation in the emission ratio of most of the gases to CO_2 (as evident in the deviation from the linear best-fit line in most of the scatter plots). To account for this, it is necessary to calculate different emission ratios for the different combustion stages of each fire. Conventionally, laboratory studies use observations of fire activity to determine the combustion stage of emissions (e.g. Yokelson *et al.*, 1996) or an approach where the maximum rate of increase of CO emission is taken as the beginning of the smouldering stage (e.g. Lobert *et al.*, 1991). Here, measured emissions cannot be ascribed to particular combustion stages using observations due to the remote nature of

the OP-FTIR measurements; furthermore, the relative contribution to measured emissions from flaming and smouldering combustion may vary depending on changes in the wind direction, ignition pattern of the fire, and heterogeneous vegetation cover within the fire plot. Instead, the emissions measurements are split by MCE, so that measurements with high MCE (>90%) and those with low MCE (<90%) are used separately to calculate emission ratios (Figure 5.10). This 90% threshold was determined from a number of laboratory studies that have published MCE for flaming and smouldering combustion stages (e.g. Lobert *et al.*, 1991; Yokelson *et al.*, 1996; Bertschi *et al.*, 2003b). Emission ratios of each target species to both CO_2 and CO were assessed in this way and are presented in Table 5.3 and Table 5.4, respectively.

As discussed above, the *within-fire* variation in emission ratios is fairly limited, and can be constrained by splitting measurements by MCE. The *between-fire* variation, however, is larger, with the flaming emission ratio of CH_4, for example, varying from 0.0010 (for spinifex) to 0.0045 for one of the TGOW plots. Most of this variation is caused by comparison between the 'landscape' experimental fires (those that incorporate a number of fuel species, TGOW, HGOW, SOW) and the experimental fires that were conducted on the individual species of spinifex. Given that spinifex burns with high combustion efficiency (due to its high degree of curing and aerated structure), producing little smoke (see Fig. 5.3d), it is no surprise that its emissions characteristics are different from those from experimental fires containing multiple species, where vegetation that burn at different combustion efficiencies contribute to a plume-averaged efficiency (e.g. the TGOW and HGOW landscapes consist of both fine and coarse fuels, each with different structure and degrees of compaction). As the purpose of this work is to characterise landscape-averaged emissions, the emission ratios and emission factors from the spinifex fires have been excluded from calculating average emissions parameters.

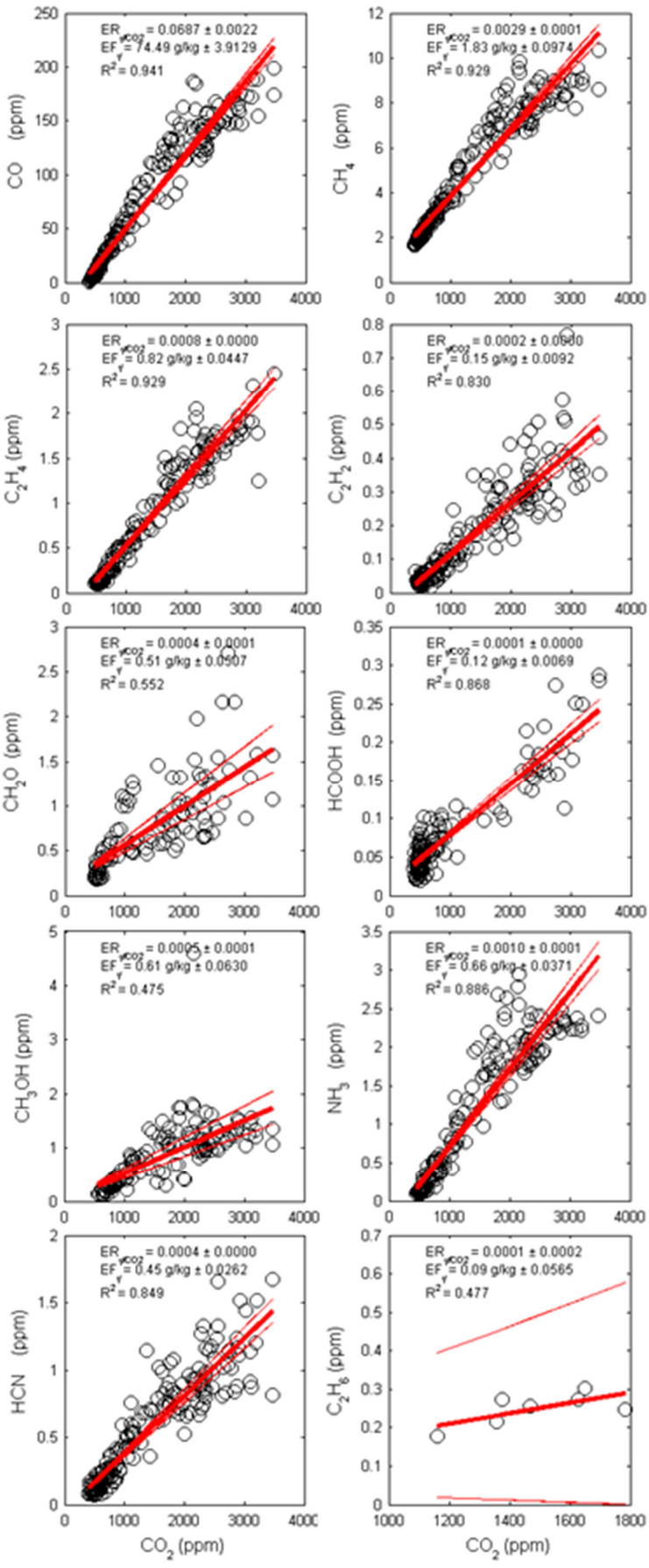

Figure 5.8 Example scatter plots of the measured trace gas pathlength-averaged concentrations used to calculate emission ratios. The data presented here are from *LD-TGOW-A* (30 September 2009). The data are presented as a time series for each trace gas in Figure 5.6. The slope of the least squares linear best fit to these data (thick red line, along with the slope uncertainty, thinner red lines) is used to derive the relevant emission ratio ($ER_{x/CO2}$). For each of the ten trace gases shown above, the emission ratio is given towards the top of each plot, along with the emission ratio uncertainty; the emission factor calculated using that emission ratio, and the R^2. The equivalent plots for emission ratios to CO are presented in Figure 5.9.

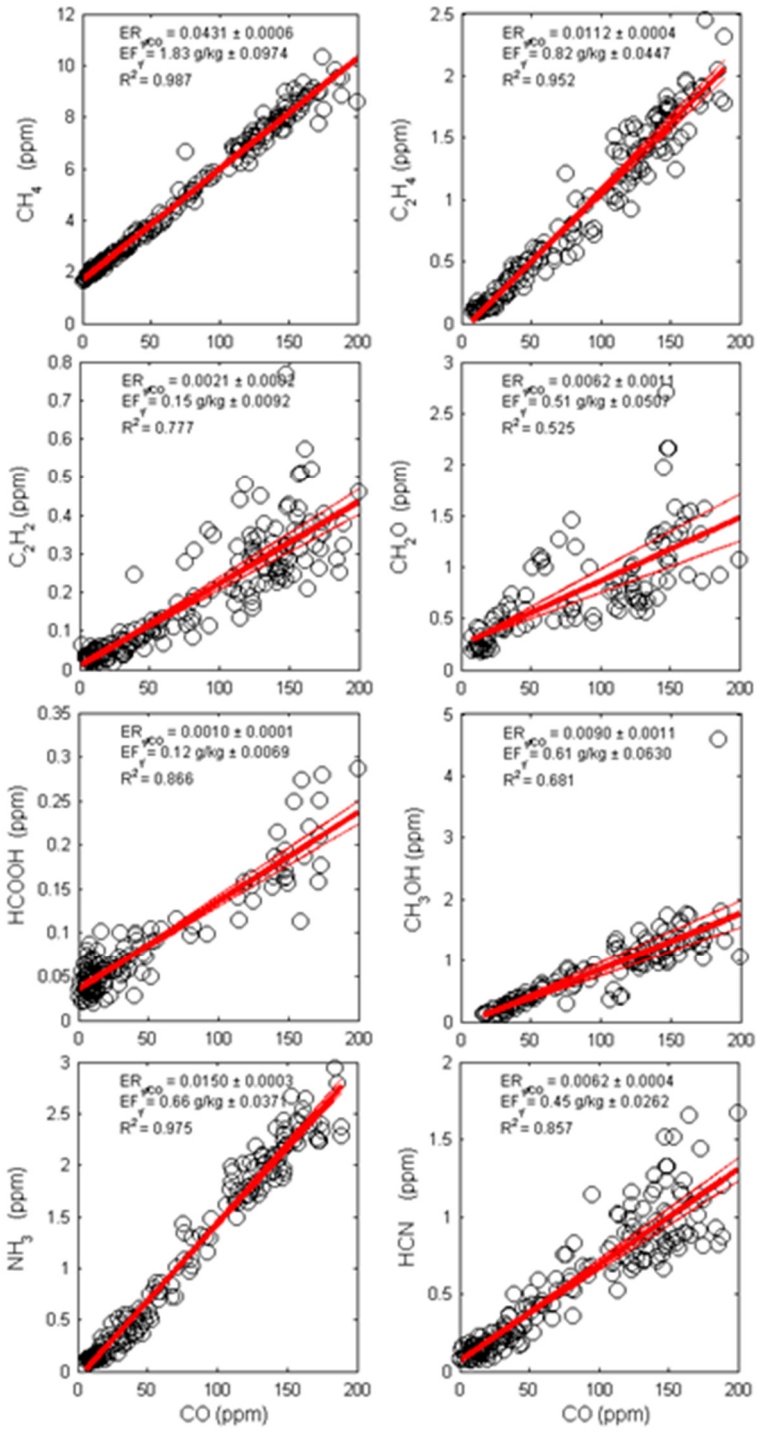

Figure 5.9 Same as Figure 5.8, but with relation to CO. Notice the higher correlation (R^2) between each of the trace gases and carbon monoxide, than between each of the trace gases and carbon dioxide (Fig. 5.8)

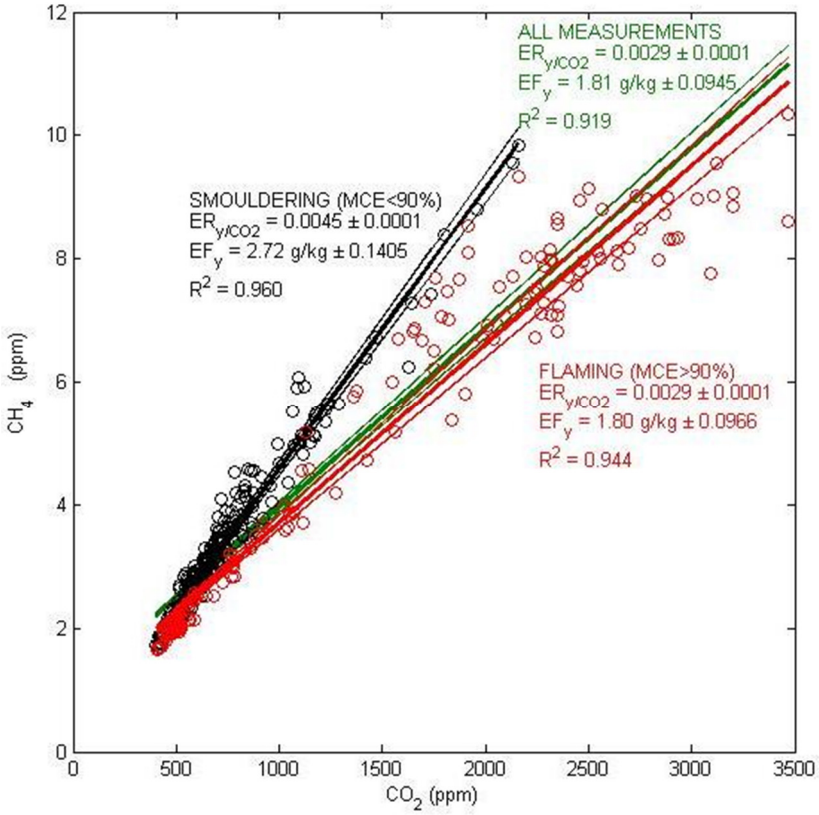

Figure 5.10 An example scatter plot of the measured pathlength-averaged concentrations of CO_2 and CH_4 (as in Figure 5.8, top right). Here, the data have been split using MCE, with measurements having an MCE greater than 90% (red) being considered separately to those with a lower MCE (black). Different emission ratios and emission factors for flaming and smouldering emissions can then be determined (also shown on the plot in red and black text respectively, the green text indicates the emission ratio and factors determined using all data). Notice the improved R^2 when the data are split into flaming and smouldering measurements (0.94 and 0.96 respectively, as opposed to 0.92 when all data considered irrespective of MCE).

The emission ratios presented in Table 5.3 ($ER_{X/CO2}$) and Table 5.4 ($ER_{X/CO}$) show the mean emission ratios for the landscape fire measurements (HGOW, SOW, TGFP, TGGW, TGOW), excluding those derived from individual species fires (SPIN). Table 5.3 confirms that the emission ratios to CO_2 (i.e. ER_{x/CO_2}), for all of the gases investigated here, are higher in the measurements characterised as 'smouldering' (MCE < 90%) than in those measurements characterised as 'flaming' (MCE > 90%). The preferential production of all studied gases (except CO_2) during the smouldering phase explains why the emission ratios are higher at lower MCE. The close correlation with CO emissions (Fig. 5.9) also explains why for all gases there is no significant difference in emission ratios to CO ($ER_{x/CO}$) between the flaming and smouldering measurements (the difference between flaming and smouldering $ER_{x/CO}$ is smaller than the standard

deviation of each ER). For formaldehyde (CH_2O), the higher emission ratio to CO during the flaming phase might be due to the production of formaldehyde during the closely-related (in space and time) pyrolysis combustion phase (Lobert and Warnatz, 1993); with some of the pyrolysed gas escaping combustion due to advective or convective winds. Conversely, formic acid (HCOOH) is only produced during the smouldering phase (Lobert and Warnatz, 1993), explaining its higher emission ratio to CO during the smouldering phase.

Table 5.3 Mean **e**mission ratios for compound *X* with respect to CO_2 ($ER_{X/CO2}$) calculated from OP-FTIR measurements at 21 tropical savanna fires over the three campaigns to the Northern Territory. The standard deviation of the emission ratios is also included.

	2009 and 2010 landscape fires	
Gas	**Flaming**	**Smouldering**
	$ER_{X/CO2}$ ± SD	**$ER_{X/CO2}$** ± SD
CO	0.0712 ± 0.0177	0.1234 ± 0.0191
CH_4	0.00306 ± 0.00094	0.00528 ± 0.00104
C_2H_2	0.00016 ± 0.00010	0.00029 ± 0.00025
C_2H_4	0.00051 ± 0.00021	0.00075 ± 0.00038
CH_2O	0.00079 ± 0.00044	0.00111 ± 0.00050
CH_3OH	0.00052 ± 0.00017	0.00087 ± 0.00041
HCOOH	0.00008 ± 0.00003	0.00016 ± 0.00010
HCN	0.00045 ± 0.00028	0.00096 ± 0.00073
NH_3	0.00124 ± 0.00147	0.00170 ± 0.00074

Table 5.4 Same as Table 5.3, but for mean emission ratios for compound *X* with respect to CO ($ER_{X/CO}$)

	2009 and 2010 landscape fires	
Gas	**Flaming**	**Smouldering**
	$ER_{X/CO}$ ± SD	**$ER_{X/CO}$** ± SD
CO_2	12.23 ± 2.68	7.44 ± 0.74
CH_4	0.0440 ± 0.0140	0.0423 ± 0.0075
C_2H_2	0.0014 ± 0.0006	0.0026 ± 0.0031
C_2H_4	0.0074 ± 0.0028	0.0060 ± 0.0059
CH_2O	0.0121 ± 0.0068	0.0094 ± 0.0051
CH_3OH	0.0073 ± 0.0059	0.0085 ± 0.0072
HCOOH	0.0018 ± 0.0017	0.0011 ± 0.0007
HCN	0.0063 ± 0.0054	0.0090 ± 0.0043
NH_3	0.0124 ± 0.0039	0.0140 ± 0.0048

Figures 5.8 and 5.9 depict smoke concentrations during a typical experimental fire. Given that a number of different vegetation types were sampled during the three Australian campaigns, with measurements made throughout the early- and late-dry season, and the likelihood that each experimental fire would have burned at different efficiencies depending on the fuel and meteorological conditions, it is important to assess the relative importance of each of these variables. Figure 5.11 includes all data from the 2009 campaigns, showing the scatter plot for CO_2 and CH_4 only, with each subplot (a–c) depicting the same data, but with each data point (i.e. each individual retrieval from 4 co-added spectra) colour-coded depending on the MCE for that data point (Fig. 5.11a); the season of the experimental fire (Fig. 5.11b); and the vegetation type of the experimental fire (Fig. 5.11c). As discussed above, the between-fire variation in emission ratios can be explained by the dependence of emission ratios on vegetation class (as is evident in Fig. 5.11c), with the spinifex (individual species) fires grouping towards the lower emission ratios and the sorghum dominated fires grouping towards the higher emission ratios. Figure 5.11a clearly demonstrates that this grouping is due mostly to the burning efficiency characteristics of these different vegetation classes, with MCE appearing to be the major control on the emission ratio slope, despite differences in vegetation classes. There is no clear pattern to discern when the data are plotted by season (Fig. 5.11b).

By sub-sampling the data in Figure 5.11a into small bins of MCE (e.g. only measurements where $80\% < \text{MCE} \leq 82\%$), it is possible to calculate a range of emission ratios depending on MCE. Figure 5.12 depicts eleven different CH_4 emission ratios to CO_2 ($ER_{CO2/CH4}$) calculated using emissions data subsampled using 2%-wide MCE bins. This figure clearly shows the strong relationship between the emission ratio of methane and the combustion efficiency, with the slope of the emission ratio decreasing with each 2% increment in MCE. These MCE-dependent emission ratios can then be used to calculate MCE-dependent emission factors, which will be discussed further in the next section.

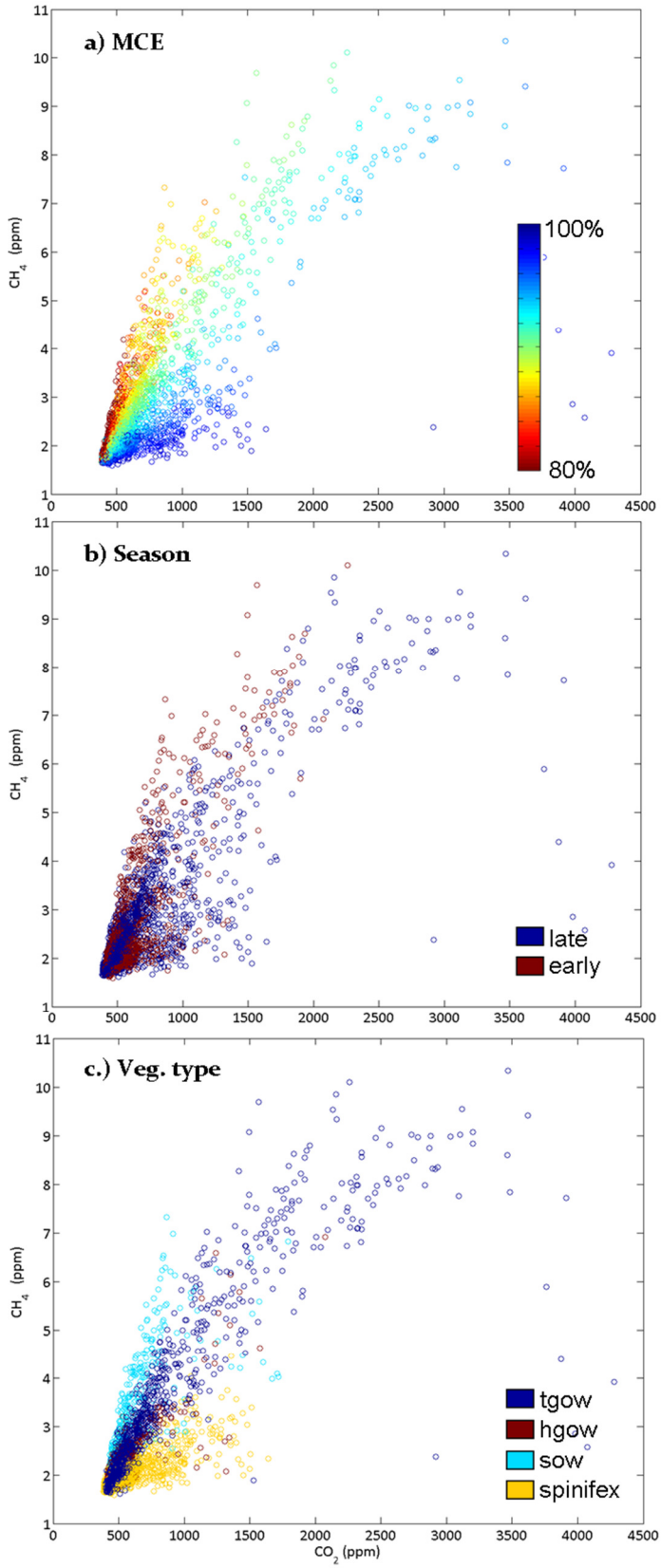

Figure 5.11 Scatter plots of the measured concentrations of CO_2 and CH_4, including all measurements made during the two Arnhem Land campaigns in 2009. All three plots show the same data, but are colour-coded differently using (a) MCE; (b) season of measurement; and (c) vegetation class.

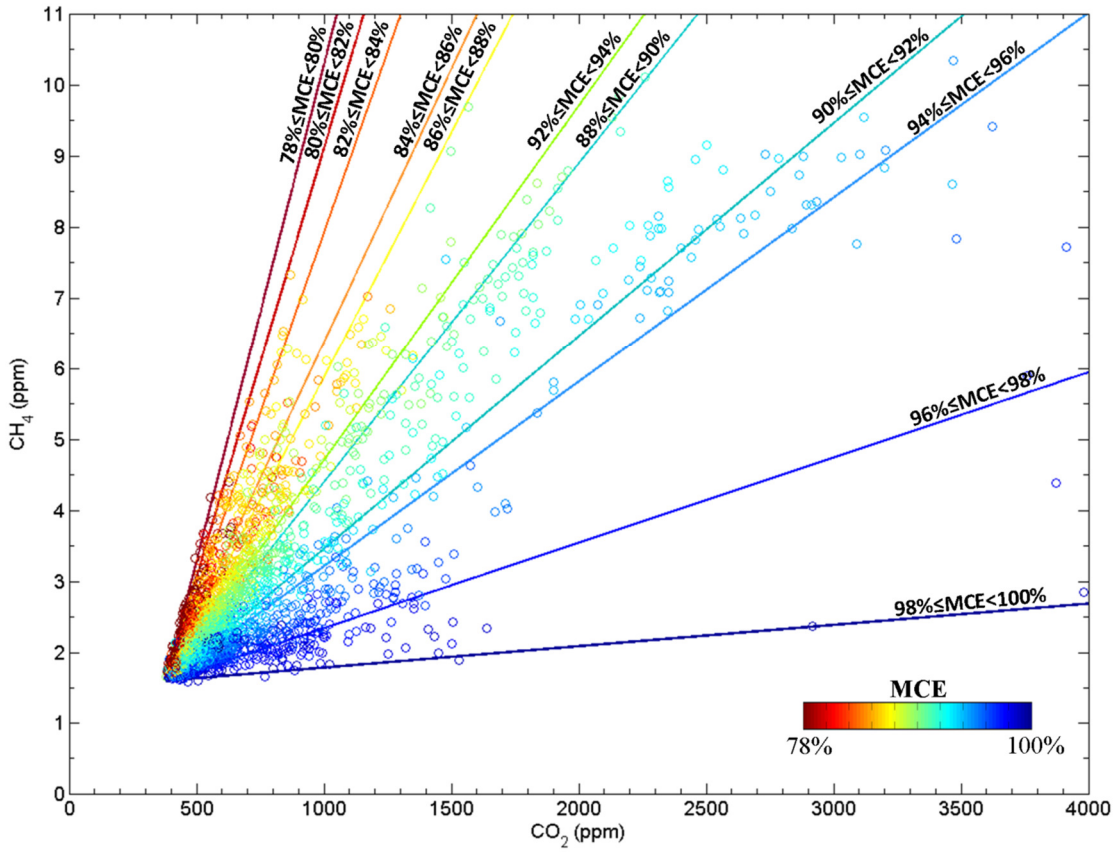

Figure 5.12 Same as Figure 5.11a, but including linear best-fit lines that have been calculated using measurements subsampled by narrow (2%) bins of MCE. Each line represents the least squares linear best fit to the subsampled emissions measurements (the MCE bin for each line is indicated on the plot). A clear relationship between the slope of the linear least squares regression lines and MCE is evident as the slope increases systematically with decreasing MCE.

5.5.1.2 Emission Factors

As discussed in Sect. 5.4.3.2, the majority of biomass burned in savanna fires takes place within the flaming combustion zone (Ward *et al.*, 1996; Wooster *et al.*, 2011). Therefore, the emission ratios determined from the measurements with high MCE (>90 %, the red line in Figure 5.10) are used to calculate "fire averaged" emission factors (using the carbon mass balance approach described in Eqns. 3.34 and 3.35), as these emission ratios should not be influenced by high proportions of smoke originating from smouldering combustion. A separate emission factor for smouldering combustion was calculated using the emission ratios derived from measurements of low MCE (<90 %) smoke. The emission factors for flaming and smouldering combustion for each of the measured fires are presented in Tables 5.5 and 5.6 respectively.

Table 5.5 Emission factors (g kg^{-1} of dry fuel burned) for flaming combustion (determined from emission ratios calculated using measurements with an MCE>90%). Uncertainties were calculated in quadrature from those associated with the trace gas emission ratios and a ±10% uncertainty in the assumed fuel carbon.

	CO_2		CO		CH_4		C_2H_2		C_2H_4		CH_2O		CH_3OH		HCOOH		HCN		NH_3	
	EF	unc	EF	unc	EF	unc	EF	unc	EF	unc	EF	unc	EF	unc	EF	unc	EF	unc	EF	unc
ED-TGOW-A	1663	± 83	103	± 6.2	2.01	± 0.15	*nr*	± *nr*	0.21	± 0.06	*nr*	± *nr*	*nr*	± *nr*	*nr*	± *nr*	0.11	± 0.01	0.13	± 0.04
ED-TGOW-B	1672	± 84	96	± 5.5	1.90	± 0.12	0.18	± 0.02	0.82	± 0.10	*nr*	± *nr*	0.71	± 0.19	*nr*	± *nr*	*nr*	± *nr*	0.53	± 0.07
ED-SOW-A	1702	± 85	76	± 5.5	1.56	± 0.13	0.05	± 0.01	0.67	± 0.10	1.75	± 0.14	0.53	± 0.12	0.19	± 0.02	*nr*	± *nr*	0.46	± 0.07
ED-SOW-B	1688	± 85	84	± 5.5	1.70	± 0.12	0.07	± 0.01	0.90	± 0.14	1.77	± 0.46	0.76	± 0.15	0.15	± 0.02	0.22	± 0.03	0.65	± 0.15
LD-TGOW-A	1715	± 86	68	± 3.7	1.67	± 0.09	0.13	± 0.01	0.75	± 0.04	0.52	± 0.05	0.44	± 0.05	0.11	± 0.01	0.39	± 0.03	0.56	± 0.04
LD-TGOW-B	1661	± 83	101	± 5.2	2.69	± 0.16	0.11	± 0.02	0.69	± 0.05	0.45	± 0.07	0.61	± 0.12	0.07	± 0.01	0.36	± 0.04	0.59	± 0.05
LD-SOW-A	1720	± 86	62	± 3.1	3.30	± 0.17	0.08	± 0.00	0.48	± 0.02	0.56	± 0.03	0.89	± 0.04	0.18	± 0.01	0.36	± 0.02	0.50	± 0.03
LD-HGOW	1708	± 85	73	± 4.2	1.81	± 0.11	0.19	± 0.02	0.40	± 0.06	0.61	± 0.28	*nr*	± *nr*	*nr*	± *nr*	0.63	± 0.05	0.36	± 0.04
BAT-TGGW	1667	± 84	88	± 4.7	2.38	± 0.14	*nr*	± *nr*	*nr*	± *nr*	*nr*	± *nr*	*nr*	± *nr*	*nr*	± *nr*	*nr*	± *nr*	*nr*	± *nr*
ARS-TGFP-B	1706	± 89	76	± 16.4	1.65	± 0.38	*nr*	± *nr*	0.32	± 0.13	*nr*	± *nr*	*nr*	± *nr*	0.15	± 0.05	0.73	± 0.29	*nr*	± *nr*
ARS-TGFP-C	1692	± 85	85	± 4.6	1.69	± 0.09	*nr*	± *nr*	0.45	± 0.04	*nr*	± *nr*	0.40	± 0.04	*nr*	± *nr*	*nr*	± *nr*	0.51	± 0.03
ARS-TGFP-D	1738	± 87	55	± 4.6	1.15	± 0.11	0.40	± 0.05	*nr*	± *nr*	*nr*	± *nr*	1.11	± 0.55	0.21	± 0.04	1.10	± 0.18	*nr*	± *nr*
BSP-TGOW	1689	± 85	86	± 4.6	1.92	± 0.11	*nr*	± *nr*	0.38	± 0.05	0.72	± 0.07	0.49	± 0.07	*nr*	± *nr*	*nr*	± *nr*	0.81	± 0.06
TWP-TGOW-A	1733	± 87	58	± 3.3	1.34	± 0.08	*nr*	± *nr*	0.36	± 0.04	1.08	± 0.08	0.78	± 1.46	*nr*	± *nr*	*nr*	± *nr*	*nr*	± *nr*
TWP-TGOW-B	1652	± 84	99	± 10.2	2.19	± 0.33	*nr*	± *nr*	0.58	± 0.10	*nr*	± *nr*	0.36	± 0.36	*nr*	± *nr*	*nr*	± *nr*	0.84	± 0.18
TWP-TGOW-C	1699	± 89	78	± 8.2	2.23	± 0.30	0.24	± 0.04	0.87	± 0.05	*nr*	± *nr*	0.64	± 0.03	*nr*	± *nr*	0.35	± 0.11	*nr*	± *nr*

Table 5.6 Emission factors (g kg^{-1} of dry fuel burned) for smouldering combustion (determined from emission ratios calculated using measurements with an MCE<90%). Uncertainties were calculated in quadrature from those associated with the trace gas emission ratios and a ±10% uncertainty in the assumed fuel carbon.

	CO_2	CO	CH_4	C_2H_2	C_2H_4	CH_2O	CH_3OH	HCOOH	HCN	NH_3
	EF unc	EF unc	EF unc	EF unc	EF unc	EF unc	EF unc	EF unc	EF unc	EF unc
ED-TGOW-A	1663 ± 83	103 ± 6.2	2.01 ± 0.15	*nr* ± *nr*	0.21 ± 0.06	*nr* ± *nr*	*nr* ± *nr*	*nr* ± *nr*	0.11 ± 0.01	0.13 ± 0.04
ED-TGOW-B	1672 ± 84	96 ± 5.5	1.90 ± 0.12	0.18 ± 0.02	0.82 ± 0.10	*nr* ± *nr*	0.71 ± 0.19	*nr* ± *nr*	*nr* ± *nr*	0.53 ± 0.07
ED-SOW-A	1702 ± 85	76 ± 5.5	1.56 ± 0.13	0.05 ± 0.01	0.67 ± 0.10	1.75 ± 0.14	0.53 ± 0.12	0.19 ± 0.02	*nr* ± *nr*	0.46 ± 0.07
ED-SOW-B	1688 ± 85	84 ± 5.5	1.70 ± 0.12	0.07 ± 0.01	0.90 ± 0.14	1.77 ± 0.46	0.76 ± 0.15	0.15 ± 0.02	0.22 ± 0.03	0.65 ± 0.15
LD-TGOW-A	1715 ± 86	68 ± 3.7	1.67 ± 0.09	0.13 ± 0.01	0.75 ± 0.04	0.52 ± 0.05	0.44 ± 0.05	0.11 ± 0.01	0.39 ± 0.03	0.56 ± 0.04
LD-TGOW-B	1661 ± 83	101 ± 5.2	2.69 ± 0.16	0.11 ± 0.02	0.69 ± 0.05	0.45 ± 0.07	0.61 ± 0.12	0.07 ± 0.01	0.36 ± 0.04	0.59 ± 0.05
LD-SOW-A	1720 ± 86	62 ± 3.1	3.30 ± 0.17	0.08 ± 0.00	0.48 ± 0.02	0.56 ± 0.03	0.89 ± 0.04	0.18 ± 0.01	0.36 ± 0.02	0.50 ± 0.03
LD-HGOW	1708 ± 85	73 ± 4.2	1.81 ± 0.11	0.19 ± 0.02	0.40 ± 0.06	0.61 ± 0.28	*nr* ± *nr*	*nr* ± *nr*	0.63 ± 0.05	0.36 ± 0.04
BAT-TGGW	1667 ± 84	88 ± 4.7	2.38 ± 0.14	*nr* ± *nr*	*nr* ± *nr*	*nr* ± *nr*	*nr* ± *nr*	*nr* ± *nr*	*nr* ± *nr*	*nr* ± *nr*
ARS-TGFP-B	1706 ± 89	76 ± 16.4	1.65 ± 0.38	*nr* ± *nr*	0.32 ± 0.13	*nr* ± *nr*	*nr* ± *nr*	0.15 ± 0.05	0.73 ± 0.29	*nr* ± *nr*
ARS-TGFP-C	1692 ± 85	85 ± 4.6	1.69 ± 0.09	*nr* ± *nr*	0.45 ± 0.04	*nr* ± *nr*	0.40 ± 0.04	*nr* ± *nr*	*nr* ± *nr*	0.51 ± 0.03
ARS-TGFP-D	1738 ± 87	55 ± 4.6	1.15 ± 0.11	0.40 ± 0.05	*nr* ± *nr*	*nr* ± *nr*	1.11 ± 0.55	0.21 ± 0.04	1.10 ± 0.18	*nr* ± *nr*
BSP-TGOW	1689 ± 85	86 ± 4.6	1.92 ± 0.11	*nr* ± *nr*	0.38 ± 0.05	0.72 ± 0.07	0.49 ± 0.07	*nr* ± *nr*	*nr* ± *nr*	0.81 ± 0.06
TWP-TGOW-A	1733 ± 87	58 ± 3.3	1.34 ± 0.08	*nr* ± *nr*	0.36 ± 0.04	1.08 ± 0.08	0.78 ± 1.46	*nr* ± *nr*	*nr* ± *nr*	*nr* ± *nr*
TWP-TGOW-B	1652 ± 84	99 ± 10.2	2.19 ± 0.33	*nr* ± *nr*	0.58 ± 0.10	*nr* ± *nr*	0.36 ± 0.36	*nr* ± *nr*	*nr* ± *nr*	0.84 ± 0.18
TWP-TGOW-C	1699 ± 89	78 ± 8.2	2.23 ± 0.30	0.24 ± 0.04	0.87 ± 0.05	*nr* ± *nr*	0.64 ± 0.03	*nr* ± *nr*	0.35 ± 0.11	*nr* ± *nr*

Mean emission factors calculated from the individual fire emission factors in Table 5.5 and Table 5.6 are listed in Table 5.7. When comparing emission factors between those for predominantly flaming sourced smoke and those for smouldering sourced smoke, only CO_2 exhibits a higher emission factor in the flaming measurements, with CO and other gases having higher emission factors in the smouldering measurements. As explained in the previous section on emission ratios, this difference is due to the preferential production (per unit mass of vegetation burned) of CO and other gases during the smouldering combustion phase.

By combining spectral retrievals from all fires, it is possible to build a detailed understanding of the relationship between MCE and emission ratios (as depicted earlier in Fig. 5.11a and Fig. 5.12). Using the method described in the previous section, the MCE-dependent emission ratios can be used to calculate MCE-dependent emission factors. Figure 5.13 shows how the emission ratios for CH_4 in Fig. 5.12 can be used to calculate the relationship between MCE and the emission factor of CH_4 (EF CH_4). Figure 5.13 highlights the relative lack of a strong seasonality in the relationship between EF CH_4 and MCE, particularly for the measurements of smoke from flaming combustion. The regression equations for the early dry season, late dry season and the combined data set for flaming combustion data are, respectively:

$$\text{EF } CH_4 = -0.284MCE + 28.3 \quad (5.1)$$

$$\text{EF } CH_4 = -0.305MCE + 30.4 \quad (5.2)$$

$$\text{EF } CH_4 = -0.304MCE + 30.3 \quad (5.3)$$

Table 5.7 Mean **e**mission factors (g kg^{-1} dry fuel burned) and their standard deviation calculated from the individual emission factors presented in Tables 5.5 and 5.6.

	2009 and 2010 landscape fires	
Gas	**Flaming**	**Smouldering**
	EF_X ± SD	**EF_X** ± SD
CO_2	1694 ± 26	1612 ± 21
CO	80 ± 15	130 ± 11.2
CH_4	1.95 ± 0.53	3.10 ± 0.59
C_2H_2	0.16 ± 0.11	0.28 ± 0.24
C_2H_4	0.56 ± 0.22	0.77 ± 0.39
CH_2O	0.93 ± 0.55	1.20 ± 0.53
CH_3OH	0.64 ± 0.22	1.04 ± 0.48
HCOOH	0.15 ± 0.05	0.27 ± 0.17
HCN	0.47 ± 0.30	0.95 ± 0.72
NH_3	0.54 ± 0.20	1.11 ± 0.42

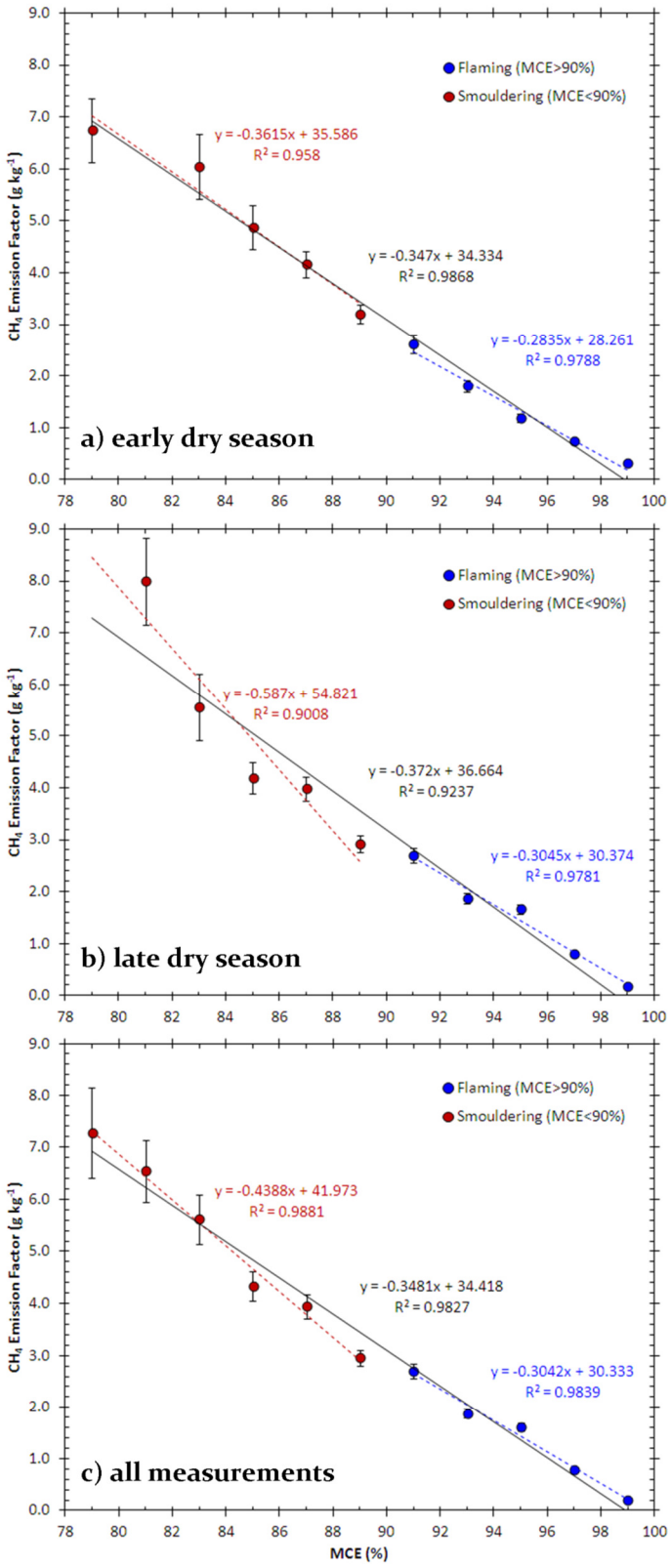

Figure 5.13 The emission factor for CH_4 (EF CH_4) for (a) all early-dry season measurements; (b) all late-dry season measurements; and (c) all measurements, grouped by MCE, calculated using the emission ratios determined from 2%-wide MCE bins (example MCE-dependent emission ratios are shown in Fig. 5.12 for CH_4). The linear least squares regression lines for flaming (MCE>90%), smouldering (MCE<90%) and all measurements are indicated using blue, red and black lines, respectively.

Whilst the slope of the linear best-fit line to the smouldering data varies between -0.362 and -0.587 for the early and late dry season, most of this variation is due to the high emission factor of the 80–82% MCE bin in the late dry season. The slope of the linear best fit to all of the data (including both flaming and smouldering) varies between -0.347 and -0.372. Considering all seasons, the linear best-fit to the data has a steeper slope for the smouldering data, implying some nonlinearity in the relationship between MCE and EF CH_4.

An alternative approach to calculating MCE-dependent emission factors from the MCE-dependent emission ratios derived from all data (e.g. Figure 5.12), is to use MCE-dependent emission ratios derived from individual fires. Figure 5.14 shows how measurements from individual fires can be categorised by MCE. The regression equations derived from this approach differ to those derived from emission ratios derived from data irrespective of vegetation class; the equations for flaming, smouldering and all data are, respectively:

$$EF\ CH_4 = -0.241MCE + 28.3 \quad (5.4)$$

$$EF\ CH_4 = -0.320MCE + 30.4 \quad (5.5)$$

$$EF\ CH_4 = -0.269MCE + 30.3 \quad (5.6)$$

For all cases, the slope of the linear best-fit is lower using this approach. This difference is due to the inherent bias that is introduced by calculating regression using the already processed data where *X* measurements have been used to derive a single point, and where *X* varies between the different samples. The data presented in Figure 5.14 does not contain information on the number of samples that were used to calculate each point. For example, only 4 early dry season spinifex measurements were used to calculate the emission ratio, and thus the emission factor for the 84–86% MCE bin, yet over 30 measurements were used to calculate the ED-TGOW emission factor for the same MCE bin. This difference is not accounted for by the linear regression.

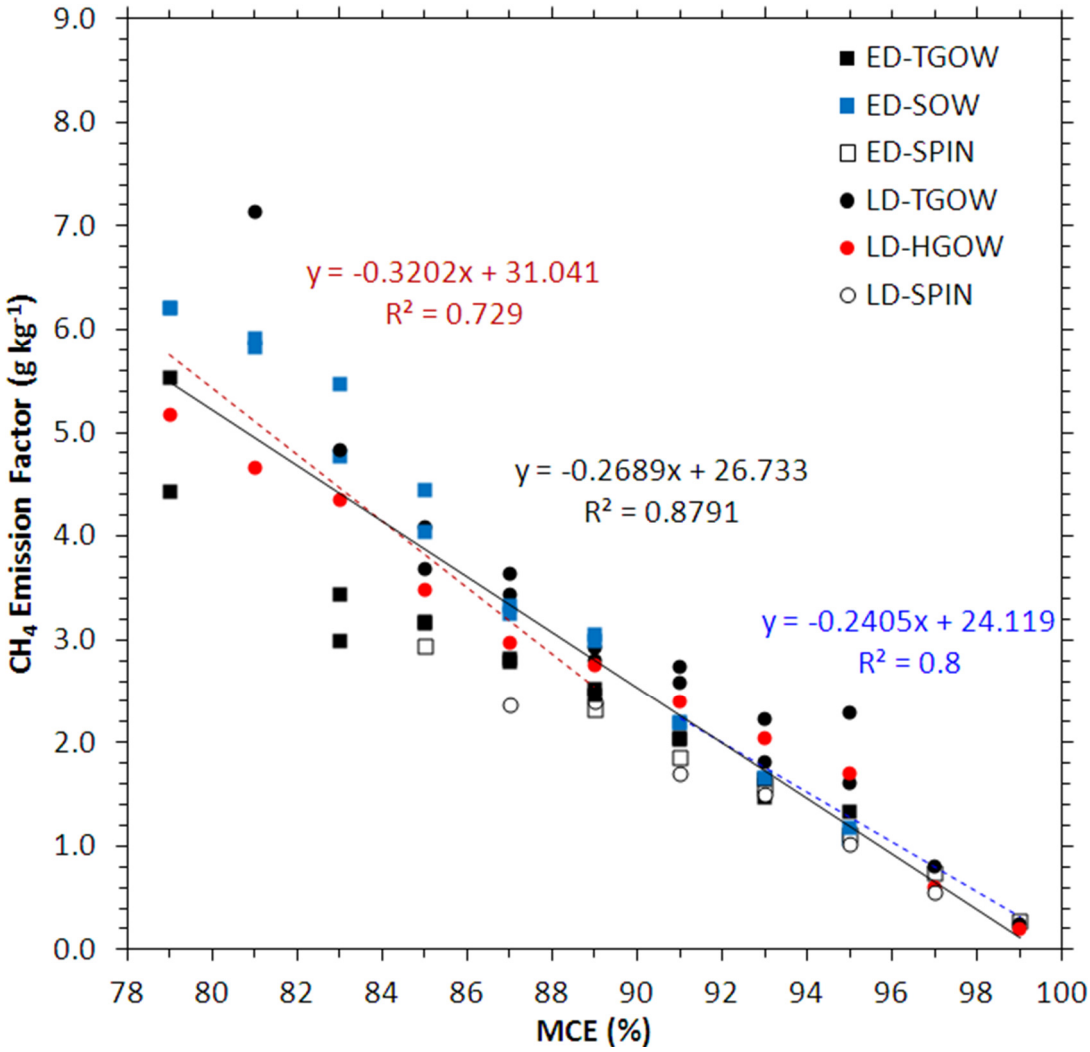

Figure 5.14 Emission factors for CH_4 for each of the experimental fires grouped by MCE. Unlike Figure 5.13 where data from *all* measurements are used to calculate EF CH_4 for each MCE-bin, the emission factors presented in this figure are calculated for each experimental fire, grouped by MCE. Early-dry season measurements are indicated using squares, late-dry season measurements are indicated using circles; different colours are used to distinguish vegetation classes.

Whilst this section has focussed on methane due to the importance of assessing seasonal emissions of this greenhouse gas, a number of other gases examined exhibit a significant relationship between MCE and EF. Figure 5.15 shows the relationship between MCE and the emission factors of CH_3OH, NH_3 and HCN.

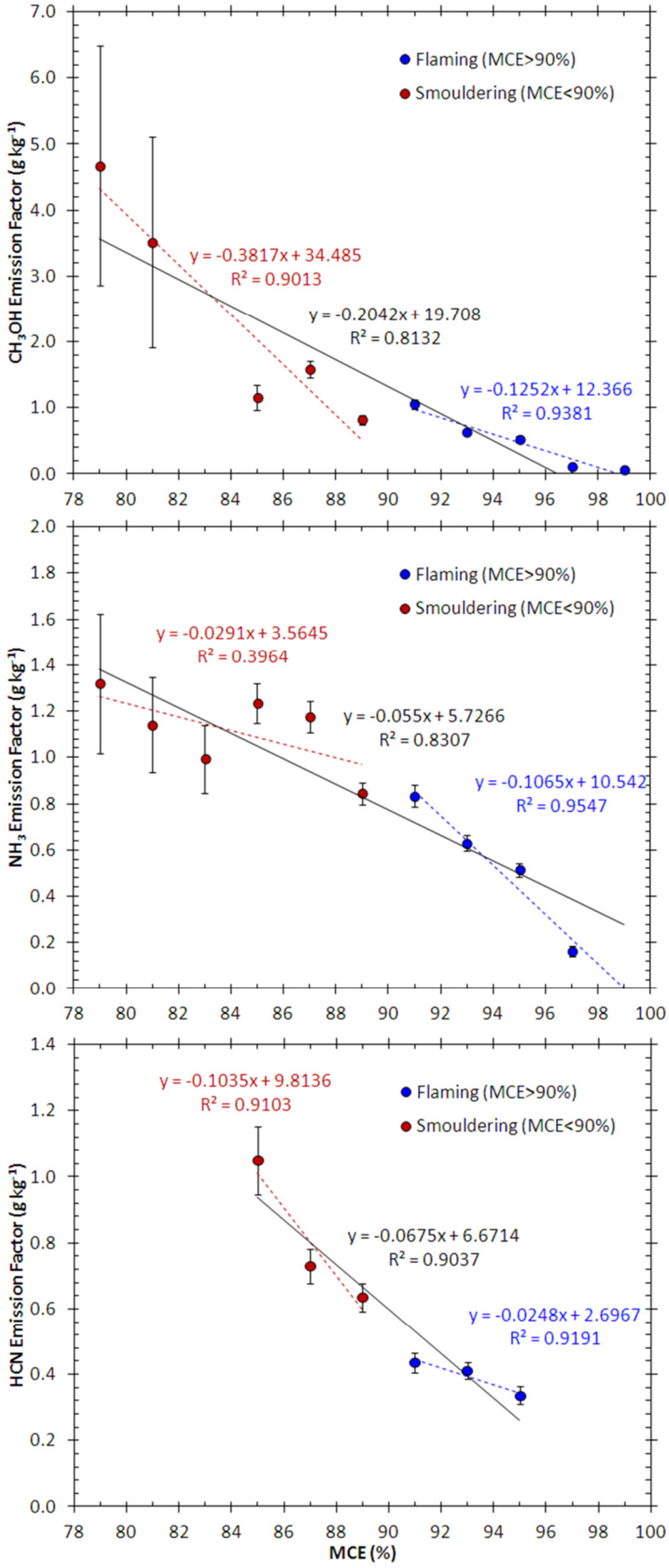

Figure 5.15 Same as Figure 5.13, but for emission factors for CH_3OH, NH_3 and HCN grouped by MCE. Each plot uses all measurements from the two 2009 Arnhem Land campaigns (as listed in Table 5.1)

5.5.2 Source sampling

Despite the capabilities of GC to measure a great number of gases in the smoke sampled during the 2009 campaigns, at the time of writing only the results for methane and nitrous oxide have been presented by CSIRO in time for this thesis. Consequently, this section will only consider these gas measurements. These measurements provide the first opportunity to perform a comparison between the established source sampling methodology and the OP-FTIR approach, and will also help address the objective concerning the seasonality of the important greenhouse gases, CH_4 and N_2O.

Unlike the OP-FTIR methodology, where emission ratios are calculated using the least squares linear regression slope of the trace gas species concentration versus the CO_2 concentration, using many measurements collected at regular intervals through time, the source sampling approach calculates emission ratios and emission factors on a *per-sample* basis where the emission ratio of trace species *i* is defined as:

$$ER_i = \frac{\Delta C_i}{\Delta CO_2} \tag{5.7}$$

Where ΔC_i is the difference between the concentration of trace species *i* in the smoke sample and its concentration in ambient air up-wind of the combustion source, ΔCO_2 is the difference between CO_2 concentration in the smoke sample and in the upwind air. Emission factors are then calculated for each sample using the carbon mass balance approach (as outlined in Eqns. 3.34 and 3.35). As was the case with the OP-FTIR measurements, the MCE and CH_4 emission factors measured using the source sampling methodology were highly correlated and varied significantly between fires (Fig. 5.16). Unlike the OP-FTIR measurements however, the source sampling also found significant *within-fire* variation, as demonstrated by the wide variation in methane emission factors and MCE for individual vegetation classes in Figure 5.14 (e.g. LD-TGOW). This discrepancy is explained by the nature of the sampling techniques, with the source sampling targeting smoke sourced from individual points burning with different efficiencies within the flaming and smouldering combustion zone, whilst the OP-FTIR measures a mixture of flaming and smouldering sourced smoke integrated across the

optical path. The two sampling methods therefore represent the characterisation of smoke using discrete vs. well mixed sampling methods.

As was also the case for the OP-FTIR measurements, the correlation between CH_4 emission factors and MCE over the flaming combustion MCE range of 88–100 % explained most of the variance in EF CH_4. The regression equations for the early dry season, late dry season and the combined data set for flaming combustion data are, respectively:

$$EF\ CH_4 = -0.265MCE + 26.4 \quad (5.8)$$

$$EF\ CH_4 = -0.253MCE + 25.2 \quad (5.9)$$

$$EF\ CH_4 = -0.263MCE + 26.2 \quad (5.10)$$

The July and October linear least squares regression lines are not significantly different. The linear least squares regression lines are shown in Figure 5.16. Figure 5.17 overlays the OP-FTIR results from Figure 5.14 onto the source sampling results presented in Figure 5.16. The majority of the MCE-dependent fire-averaged emission factors lie within the range of results from the source sampling methodology.

The variation in the emission factor for nitrous oxide (EF N_2O) was not strongly related to the MCE (Fig. 5.18), reflecting the status of N_2O as an intermediate oxidation product (Lobert and Warnatz, 1993). The EF for N_2O varied from 0.075 g kg^{-1} to 0.166 g kg^{-1} for the TGOW plots, from 0.014 g kg^{-1} to 0.190 g kg^{-1} for the HGOW plots and 0.057 g kg^{-1} to 0.149 g kg^{-1} for the spinifex plots. Therefore, in contrast to EF CH_4, EF N_2O was independent of vegetation class or combustion efficiency. Most of the variability occurred within fires and is unexplained.

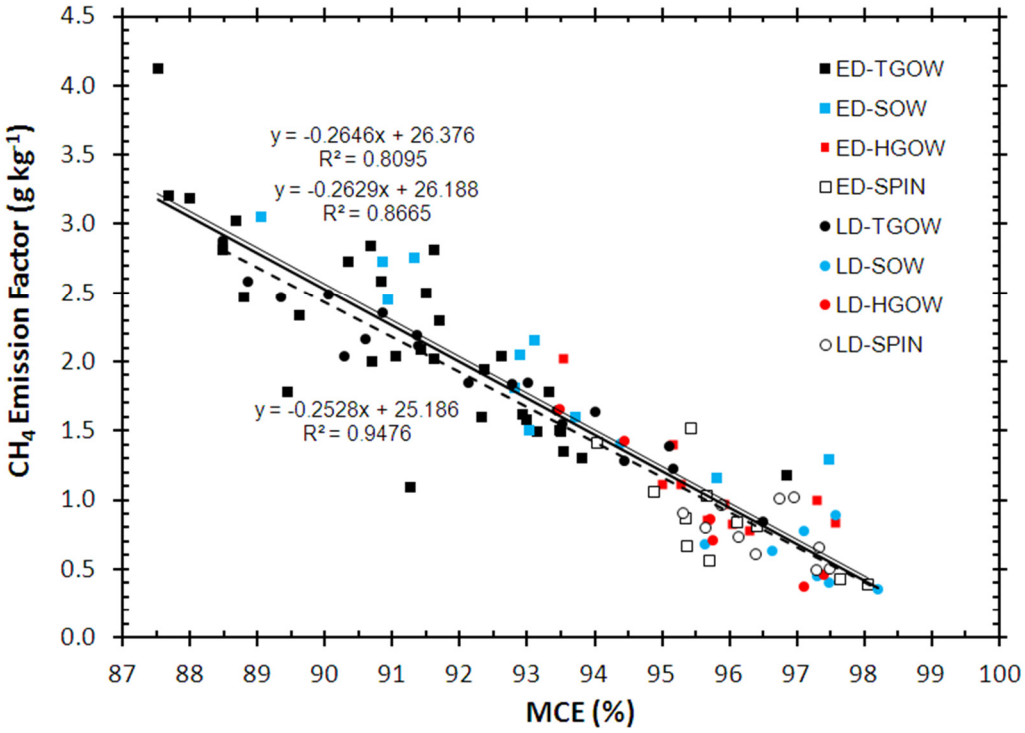

Figure 5.16 The relationship between EF CH_4 and MCE for each of the source sampling bag samples collected during both campaigns to Arnhem Land in 2009. Early-dry season measurements are indicated using squares, late-dry season measurements are indicated using circles; different colours are used to distinguish the various vegetation classes.

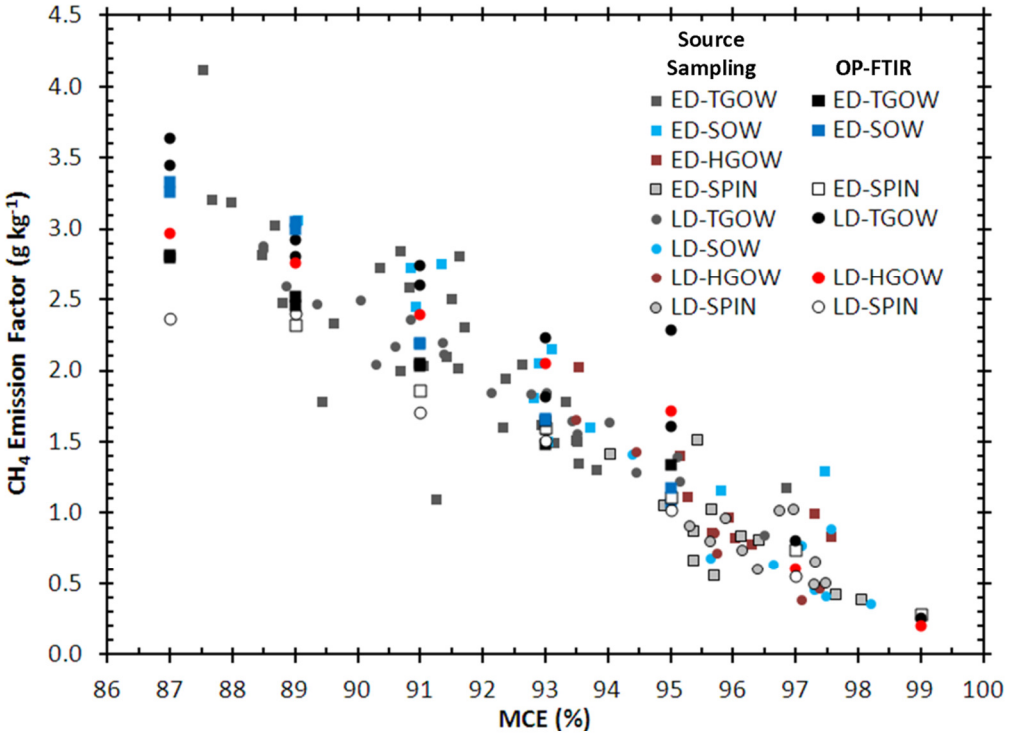

Figure 5.17 Same as Figure 5.16, but including the OP-FTIR data from Figure 5.14. All of the OP-FTIR derived emission factors, grouped into 2% MCE bins, lie within the range of emission factors determined using the independent source sampling methodology.

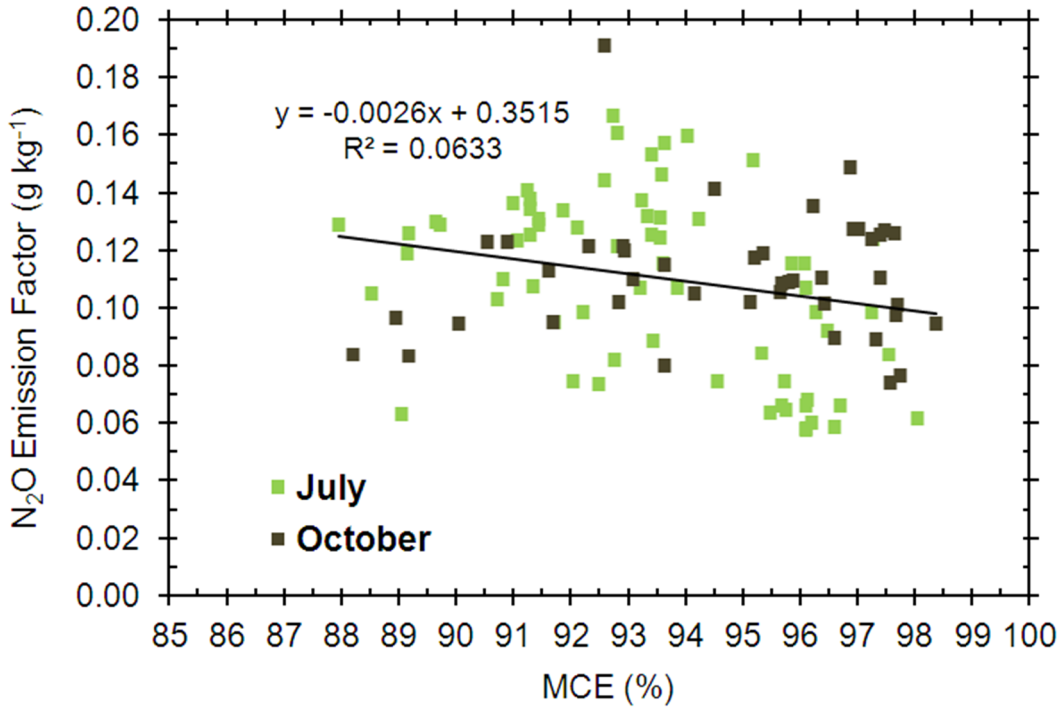

Figure 5.18 The relationship between EF N_2O and MCE for each of the source sampling bag samples collected during both campaigns to Arnhem Land in 2009.

The emission factors for CH_4 and N_2O derived from the source sampling methodology are summarised in Table 5.6, grouped by fire, by season and by vegetation class. In both OP-FTIR and source sampling approaches, this study argues that the main source of variation is within each fire, so that the concept of a fire as an entity with a defined time, and boundary is entirely arbitrary. Therefore, for the OP-FTIR approach, each measured spectrum can be considered as a valid independent replicate of emission source properties, whilst the source sampling approach considers each individual bag sample as valid independent replicates. Evidence from the source sampling approaches supports this assumption; for measurements of the TGOW vegetation class where there were several replicated fire plots (4 in the early-dry season, 2 in the late-dry season) the mean values for each season of MCE, EF CH_4 and EF N_2O (92, 2.07 and 0.13 respectively for the early-dry season and 92, 1.93 and 0.11 for the late-dry season) were almost identical to the mean of individual TGOW samples (92, 2.13 and 0.13 respectively for the early-dry season and 92, 1.93 and 0.11 for the late-dry season). An analysis of variance of the emission factors with vegetation class and then season as the 'treatments' indicates that there is no significant difference in CH_4 emission factor due to season, but there is a

highly significant effect due to vegetation class (supporting the OP-FTIR results presented in Fig. 5.11c). Nitrous oxide emissions and methane emissions, however, appear to behave differently seasonally. While EF CH_4 varies little with season across all the vegetation classes, EF N_2O does exhibit significant seasonal differences within the vegetation classes, but not consistently in the same direction. The TGOW EF N_2O declined from the early-dry season through to the late-dry season, whereas the HGOW and the spinifex EF N_2O increased over the study period. From Figure 5.18, it is clear that N_2O is not determined by combustion efficiency, but it may vary with the N:C ratio of the fuels (discussed in the following section). Changes in either the N:C ratio of the fuel components or the proportion of leaf litter and grass in the fine fuels of the TGOW/HGOW vegetation classes would cause the seasonal variation in EF N_2O observed here.

5.6 Discussion

5.6.1 Emissions inventory

The emissions factors presented here are the first to be reported from OP-FTIR measurements of tropical savannas in Australia and follow only a few ground-based (Hurst *et al.*, 1994a) and airborne studies (Hurst *et al.*, 1994b; Shirai *et al.*, 2003) of biomass burning emissions from this ecosystem. The emission factors for CH_3OH and HCOOH are the first to be reported by all methodologies (Table 5.8). The emission factors presented here have been estimated from measurements at up to 16 separate fires from a variety of vegetation types and from both controlled experimental burns and wildfires. Table 5.8 compares the emission factors reported here with those reported by previous studies of tropical savannas in Australia (listed above) and with those reported by the emission factor databases for global savanna and grasslands in Andreae and Merlet (2001) and global savannas in Akagi *et al.* (2011).

Table 5.8 Emissions factors (g kg^{-1} dry fuel burned) reported by this study and those for the same trace gases reported by previous Australian savanna studies (Hurst *et al.*, 1994a; Hurst *et al.*, 1994b; Shirai *et al.*, 2003) and by Andreae and Merlet (2001) and Akagi *et al.* (2011) who estimate global savanna emission factors by amalgamating suite of emissions studies. For this study and the Australian savanna studies, the mean and standard deviation of the emission factor is calculated from individual fires. The emission factor reported by Andreae and Merlet (2001) is the mean emission factor of all of the contributing studies, and the standard deviation is that of the studies (unless only two studies were used for a particular emission factor, in which case, the uncertainty is represented by a range). The emission factor reported by Akagi *et al.* (2011) is the mean of the contributing studies, whilst the uncertainty is an indication of the natural variability of the emission factor estimated from the reported variability in the contributing studies.

	This Study				**Australian Tropical Savanna**						**All Savanna**			
	Flaming		*Smouldering*		*Hu1994a*		*Hu1994b*		*Sh2003*		*AM2001*		*Ak2011*	
	EF	**SD**	EF	SD	EF	SD	EF	SD	EF	SD	EF	SD	EF	NV
CO_2	**1694 ±**	**26**	1612 ±	21	1595 ± 55		1595 ± 37		1613 ± 111		1646 ± 99		1686 ± 38	
CO	**80 ±**	**15**	130 ±	11	91.4 ± 27		58.9 ± 20		88 ± 8		61 ± 16		63 ± 17	
CH_4	**1.95 ±**	**0.5**	3.10 ±	0.6	2.3 ± 1.29		2.3 ± 0.79		2.2 ± 0.4		2.2 ± 0.8		1.94 ± 0.85	
C_2H_2	**0.16 ±**	**0.1**	0.28 ±	0.2	0.12 ± 0.08		0.10 ± 0.05		0.12 ± 0.02		0.27 ± 0.22		0.24 ± 0.1	
C_2H_4	**0.56 ±**	**0.2**	0.77 ±	0.4	nr ± nr		0.53 ± 0.24		0.31 ± 0.04		0.84 ± 0.46		0.82 ± 0.35	
CH_2O	**0.93 ±**	**0.6**	1.20 ±	0.5	0.26 ± 0.16		nr ± nr		nr ± nr		0.71 ± 0.42		0.73 ± 0.62	
CH_3OH	**0.64 ±**	**0.2**	1.04 ±	0.5	nr ± nr		nr ± nr		nr ± nr		1.47 ± 1.20–1.74		1.18 ± 0.41	
HCOOH	**0.15 ±**	**0.1**	0.27 ±	0.2	nr ± nr		nr ± nr		nr ± nr		0.63 ± 0.62–0.63		0.21 ± 0.10	
HCN	**0.47 ±**	**0.3**	0.95 ±	0.7	0.03 ± 0.02		0.03 ± 0.02		nr ± nr		0.23 ± 0.55		0.41 ± 0.15	
NH_3	**0.54 ±**	**0.2**	1.11 ±	0.4	1.53 ± 0.86		0.61 ± 0.39		nr ± nr		0.74 ± 0.25		0.52 ± 0.35	

5.6.1.1 Carbonaceous species

A broad range of emission factors for carbon dioxide (EF CO_2) are reported in the literature from savanna ecosystems (Table 5.8). The emission factors reported here for emissions predominantly from flaming combustion are higher than those reported by both Hurst *et al.* (1994a) and Hurst *et al.* (1994b) for northern Australian savanna fires, but fall within the standard deviation of measurements in northern Australia made by Shirai *et al.* (2003) whose mean EF CO_2 is 4.8% smaller than that reported here. The EF CO_2 reported here agrees well with those reported in Andreae and Merlet (2001 and subsequent updates in 2009), and Akagi *et al.* (2011), which draw on numerous studies in savanna ecosystems worldwide (the mean EF CO_2 reported here is only 0.5% larger than that reported by Akagi *et al.* (2011) for savanna ecosystems).

The carbon monoxide emission factor (EF CO) reported here agrees well with previous studies of biomass burning in Australian tropical savannas, which appear to be slightly higher than the global average for savannas (Akagi *et al.*, (2011) report an EF CO of 63 g kg^{-1}, whilst the mean EF CO for the Australian studies, including this one, is 80

g kg^{-1}). This might indicate that the efficiency of burning in Australian tropical savannas might be lower than the global savanna average; indeed, the global ecosystem averages include emissions from grasslands, which are believed to burn with higher MCE due to the relatively higher abundance of finer fuels than is found in woodland savannas (van Leeuwen and van der Werf *et al.*, 2011).

For the methane emission factor (EF CH_4), the EF reported here agrees with all of the previous Australian studies and the global savanna EF CH_4 (there is only a 0.5% difference between the EF CH_4 reported here and that in Akagi *et al.* [2011]). The mean emission factors of C_2H_2 and C_2H_4 are both lower than those reported by Andreae and Merlet (2001) and Akagi *et al.* (2011), and are closer to those measured in the northern Australian studies (the mean EF C_2H_2 and EF C_2H_4 for the northern Australian studies, including this one, at 0.13 g kg^{-1} and 0.47 g kg^{-1} respectively, are both about half of those reported for global savannas).

The emission factor for formaldehyde (EF CH_2O) is almost 4 times higher than the only previous study to report EF CH_2O for Australian savanna fires (Hurst *et al.* 1994a), but is in closer agreement to the estimates for global savannas (Andreae and Merlet, 2001; Akagi *et al.*, 2011). Paton-Walsh *et al.* (2010b) (who report emission ratios to CO, but not emission factors, for northern Australian fires from solar occultation FTIR measurements) also find that their emission ratio for CH_2O is far higher than that reported in Hurst *et al.* (1994a) and suggest that the discrepancy might be due to the methodology of Hurst *et al.* (1994a), whose study was based on cryogenically stored samples that may have been subject to losses of CH_2O during sampling or storage. Both the OP-FTIR methodology used here and the methodology of Paton-Walsh et al (2010b) use open-path measurements and so do not suffer from such problems associated with losses to the walls of sampling or storage equipment.

The emission factors for CH_3OH and HCOOH are the first to be reported for Australian savannas. Globally, only two savanna studies are reported in the database of Andreae and Merlet (2001), whilst the standard deviation for EF CH_3OH and EF HCOOH is high in Akagi *et al.* (2011) (35% and 48% of the mean EF, respectively). EF HCOOH reported here agrees with the latest estimates of Akagi *et al.* (2011) for global savannas, whilst EF CH_3OH is somewhat lower than those reported in both Andreae and Merlet

(2001) and Akagi *et al.* (2011). The number of studies that contribute to this 'global' average, however, is limited (only two studies for EF CH_3OH and EF HCOOH in Andreae and Merlet [2001 with 2009 updates] and five studies in Akagi *et al.* [2011]), and it is likely that the lower emission factor reported here is within the realms of natural variability for CH_3OH emissions.

5.6.1.2 Nitrogeneous species

There is a very clear discrepancy between the emission factors for HCN (EF HCN) reported here and those from Hurst *et al.* (1994a) and Hurst *et al.* (1994b). EF HCN reported here is over an order of magnitude higher than those from the previous Australian savanna studies. As was the case for EF CH_2O, Paton-Walsh *et al.* (2010b) also find their measured emission ratio of HCN to CO to be over 6 times higher and 3 times higher than that of Hurst *et al.* (1994a) and Hurst *et al.* (1994b) respectively. It is suggested that the HCN measured by Hurst *et al.* (1994a) and Hurst *et al.* (1994b) may also have been subject to losses during sample handling and storage. The EF HCN reported here agrees with measurements from other savanna ecosystems (Table 5.8) and might therefore represent the first reliable estimate of EF HCN for Australian savannas.

The emission factor for ammonia (EF NH_3) is somewhat lower than those reported in previous Australian savanna studies (Table 5.8), but is within 4% of the global savanna average reported in Akagi *et al.* (2011).

5.6.1.3 Summary of emissions inventory

The overall agreement with previous studies, particularly for the emission factors of CO_2, CO and CH_4, suggests that the method used to separate the predominantly flaming emissions from the predominantly smouldering emissions is suitable for estimating emission factors that best represent the whole-fire average (i.e. those that were calculated using measurements with an MCE>90%). As Table 5.8 illustrates clearly, many of the emission factors for the measurements deemed to be predominantly dominated by smouldering emissions (MCE<90%) are greater than those reported in other savanna studies, due to the preferential production of these gases under smouldering conditions. As the emission factors estimated from the predominantly

smouldering emissions (MCE<90%) are not representative of "pure" smouldering emissions, due to some degree of mixing with flaming emissions, it is not surprising that many of these 'smouldering' emission factors still lie within the standard deviations of the global savanna averages, which are compiled from a suite of studies that have different approaches to calculating fire-averaged emission factors.

Given that the reliability of the reported emission factors for CH_2O and HCN by Hurst *et al.* (1994a) and Hurst *et al.* (1994b) has been questioned by both Paton-Walsh *et al.* (2010b) and this study, the emission factors for CH_2O, HCN, CH_3OH and HCOOH reported here may represent the first well-measured versions for Australian savannas. For CH_3OH and HCOOH, the emission factors reported here represent one of only a few studies of these gases in savannas globally.

5.6.2 Seasonality of emissions

5.6.2.1 CH_4

In Figure 5.11, the CO_2 and CH_4 concentrations derived from each of the spectra measured during the early-dry season and late-dry season campaigns of 2009 are presented and are colour-coded by their MCE, seasonality and vegetation type. There appear to be substantial differences in the ratio of CH_4 to CO_2 across vegetation types

Table 5.9 Analysis of variance of MCE, EF CH_4 and EF N_2O derived from bag samples of emissions from flaming combustion with vegetation class and season**.**

	df	Sum of squares	Mean Square	F	P
MCE					
Veg class	2	0.0401	0.0200	56.6	0.00
Season	1	0.0065	0.0065	1.85	0.18 (ns)
Residual	93	0.0329	0.00035		
EF CH_4					
Veg class	2	0.694	0.347	51.2	0.00
Season	1	0.0170	0.0170	2.50	0.11 (ns)
Residual	93	0.630	0.007		
EF N_2O					
Veg class	2	0.563	0.281	10.4	0.00
Season	1	0.035	0.035	1.3	0.25 (ns)
Residual	93	2.518	0.027		

(Fig. 5.11c), whilst there appears to be no seasonal influence on the distribution of the spectra on the bivariate plot. As discussed above, most of the variance in the ratio of CH_4 to CO_2 can be explained by MCE (Figures 5.11a and 5.12). An analysis of variance of the emission factors calculated for each of the individual bag samples confirms that there is no seasonal change in EF CH_4, but that there are substantial and significant differences in EF CH_4 across vegetation types (Table 5.9).

Figure 5.19 presents the comparison of this study's emission factors for CH_4 (for flaming combustion measurements) with previous Australian measurements and with the emissions measured from the coarse and heavy fuels (from source sampling of emissions of selected heavier fuels fed onto a small fire). This comparison shows that the equation for the relationship between EF CH_4 and MCE appears to be true for a wide range of combustion states, but when the MCE decreases to below 88%, the relationship becomes non-linear.

Continuing the comparison with a wider range of published data; from African savanna (Cofer *et al.*, 1996; Korontzi *et al.*, 2003a; Ward *et al.*, 1996), and laboratory experiments (Kuhlbusch *et al.*, 1991), we can see that at higher MCE, with the exception of 9 outliers with much higher EF CH_4 than predicted by the MCE-EF CH_4 equation, most data lie close to the regression line (Fig. 5.20). Below an MCE thresholds of 0.88 these data are consistent with the emissions from the coarser and heavier fuels measured in this study (Figs. 5.19 and 5.20). Even EF CH_4 measured from domestic woodheaters (Gras *et al.*, 2002) fits the measurements from this study; it seems that the EF CH_4/MCE relationship is robust. The anomalous values at MCE above 90% may have been caused by sampling incompletely burned gases within the combustion zone, but the relationship is clearly non-linear over the complete domain of MCE. An exponential relationship provides a good empirical description of the combined datasets and explains 71% of the variance and asymptotes to the linear equation of the EF CH_4/MCE for the flaming combustion measurements (Fig. 5.21):

$$EF\ CH_4 = 456013e^{-0.134MCE} \quad (5.11)$$

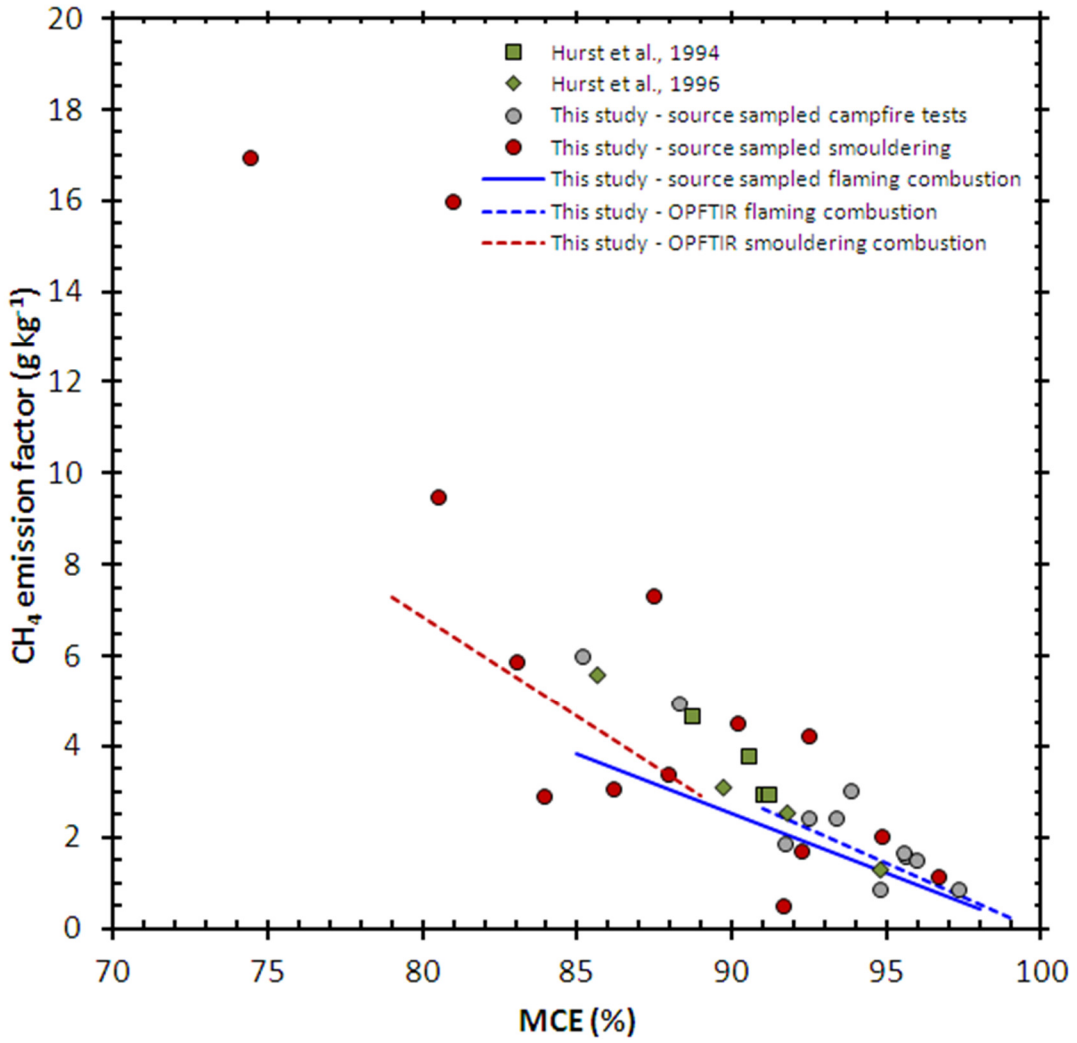

Figure 5.19 The relationship between EF CH_4 and MCE for an extended domain of MCE (70-100%). For clarity, the flaming combustion measurements for both OP-FTIR and for the source sampling are included as the least squares linear regression lines taken from Fig. 5.13c and Eqn. 5.10, respectively; The OP-FTIR 'smouldering' measurements are also included as the regression line from Fig. 5.13c. These regression lines are compared with the source sampling of pure smouldering emissions for this study (circles) and the results from Hurst *et al.* (1994) and Hurst *et al.* (1996) (squares and diamonds, respectively).

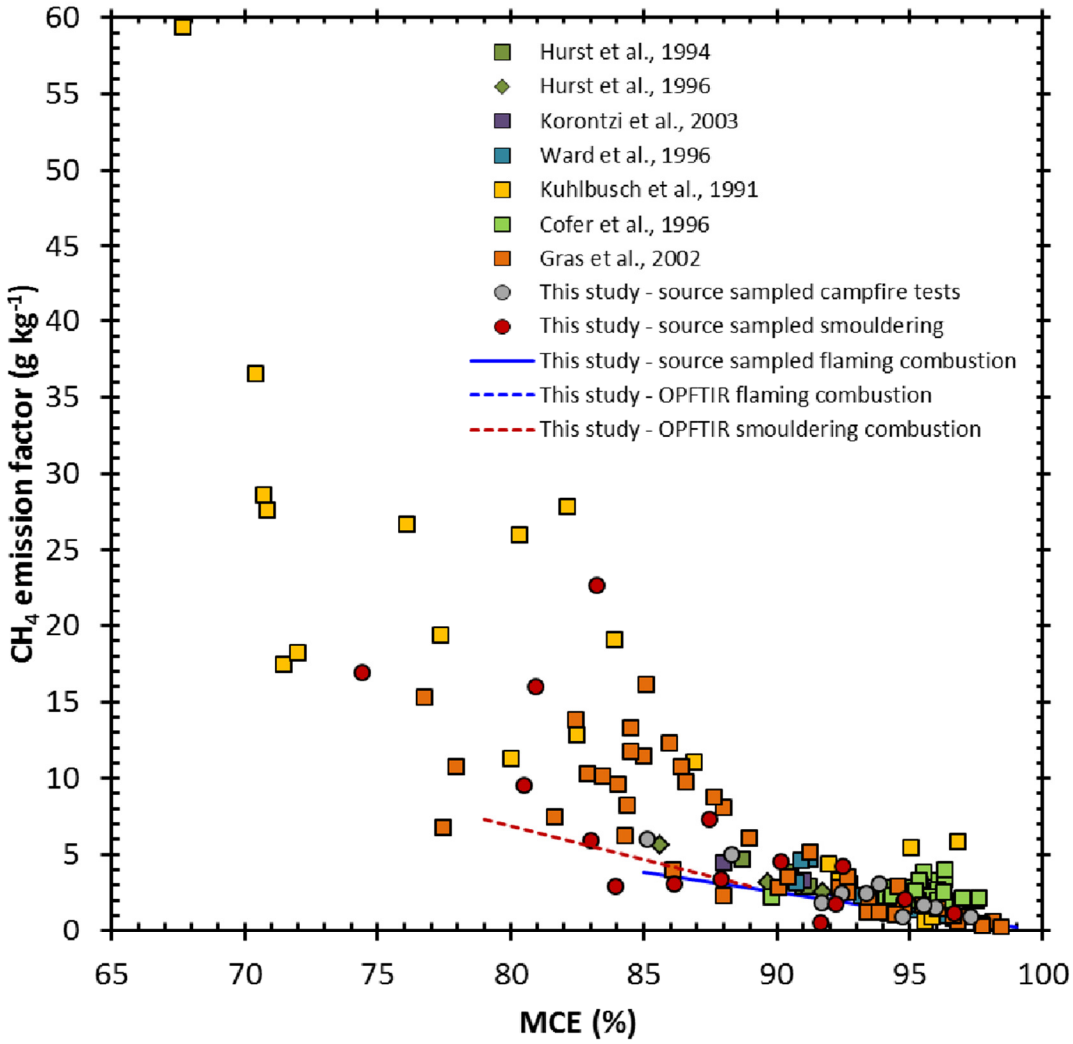

Figure 5.20 Comparison between EF CH_4 for flaming combustion and EF CH_4 from the source sampled coarse and heavy fuels, campfire tests and previously published measurements in Australian savanna woodlands and temperate forests.

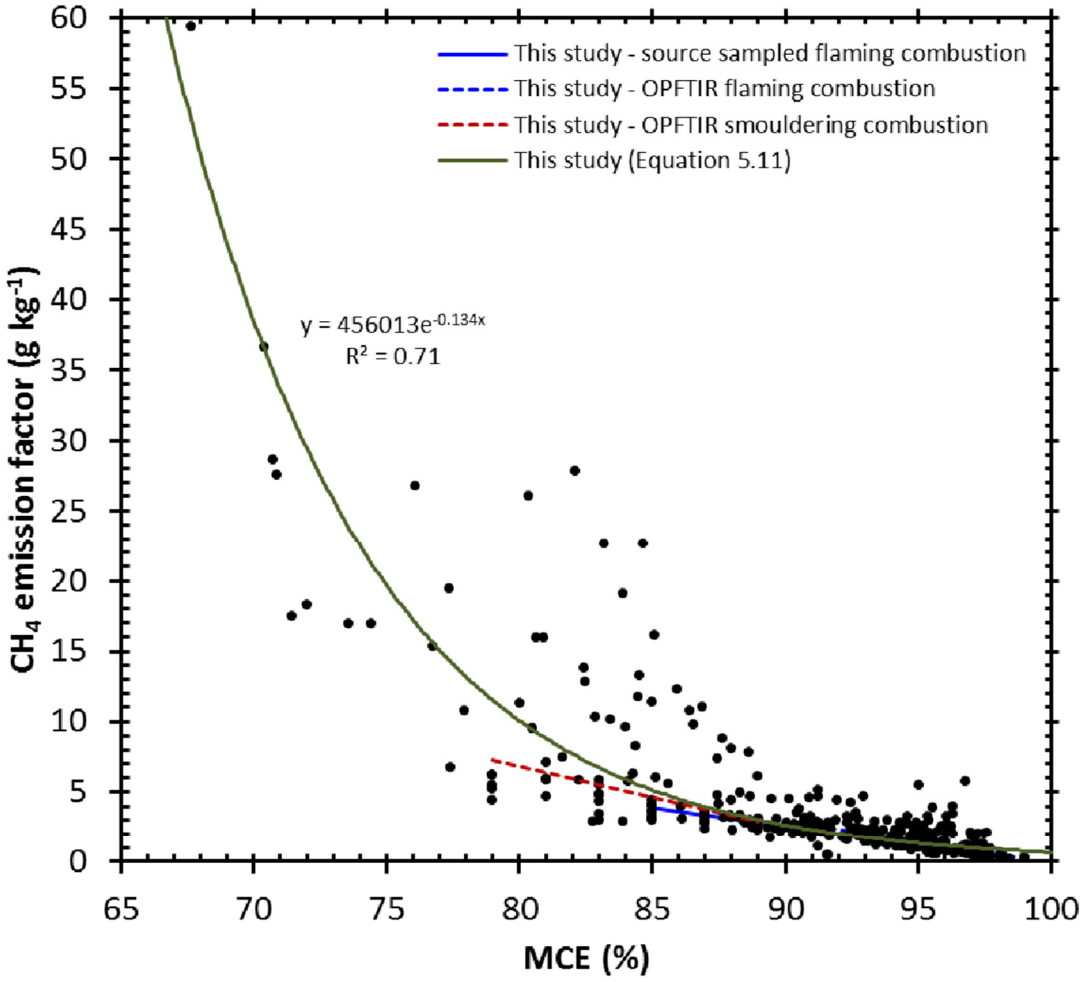

Figure 5.21 Nonlinear exponential curve fit through the comprehensive dataset comprising all data from previously published studies shown in the previous figures. The regression line is given in Eqn. 5.11.

This non-linear description of the EF CH_4/MCE relationship contradicts the convention of assuming that emission factors for organic trace gas species, including particulates are linearly dependent on MCE (Ward *et al.*, 1996; IPCC, 2000; Korontzi *et al.*, 2003a). To a first approximation, this convention is valid, but over the extended domain of MCE (e.g. Fig. 5.20) it is clearly not true. Figure 5.22 compares nonlinear equation 5.11 and the linear EF CH_4/MCE relationship established from the flaming combustion from this study with EF CH_4/MCE relationships published in a series of papers by Ward *et al.* (1996), Korontzi *et al.* (2003a) and others that have been influential in the development of the IPCC Good Practice Guidance on savanna fire emissions accounting (IPCC, 2000). However, linearising the EF CH_4 to MCE relationship beyond the MCE domain in which it is a reasonable approximation overestimates the true EF CH_4 at MCE values

measured in the Australian savanna woodlands, and thus grossly overestimates the sensitivity of EF CH_4 to any seasonal variation in MCE.

In summary, when we consider the EF CH_4 values for flaming combustion measured here, along with lower MCE measurements made using source sampling in this study, combined with previous Australian studies and with previous studies in Africa and even measurements made in laboratories, the relationship between EF CH_4 and MCE is a very robust one; approximately linear for MCE values greater than 90%, but exponential below that value.

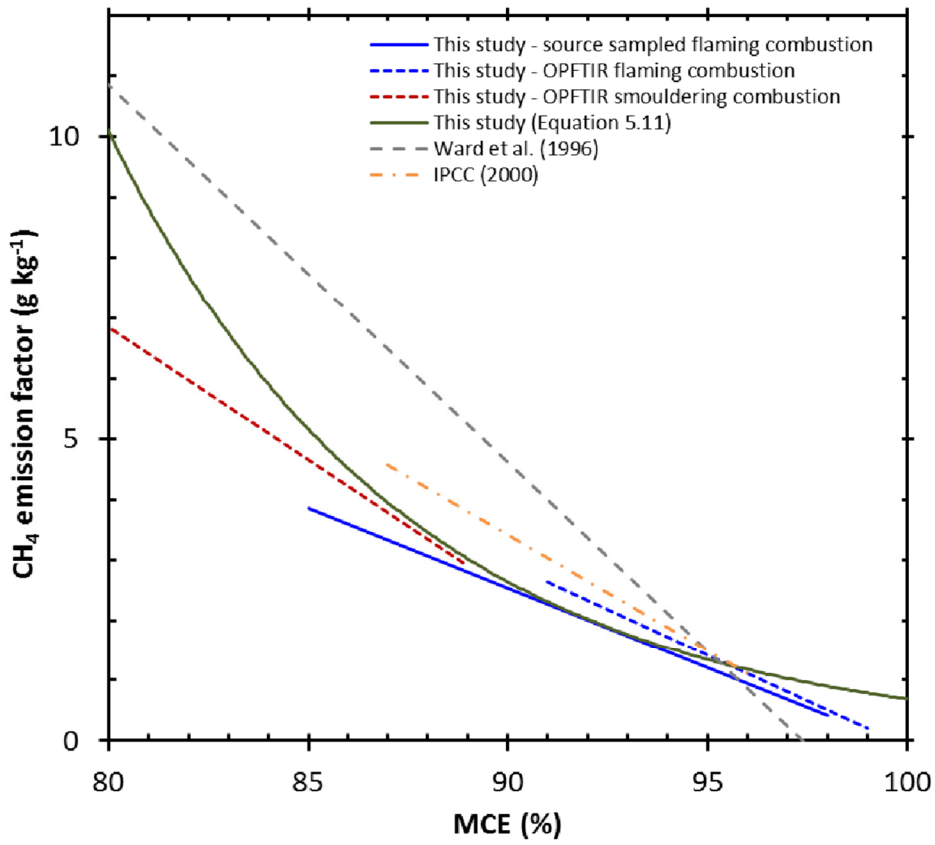

Figure 5.22 A comparison of the linear regression from the flaming combustion measurements in this study, the exponential curve through all published data and data presented here, with the EF CH_4 to MCE regressions of Ward *et al.* (1996), and the IPCC (2000) Good Practice Guidance Table 4.A2.

5.6.2.2 N_2O

As is clear from Figure 5.18 and Table 5.9, there is no seasonal change in EF N_2O. EF N_2O exhibited substantial variability between replicates and among fires from different vegetation classes. As explained earlier, this variability may arise due to the role of N_2O as an intermediate reaction product (which explains the lack of relationship between EF N_2O and MCE). N_2O can be both produced in combustion reactions (by reactions between NO and NH or NCO) or may be destroyed by collisions (i.e. by thermal decomposition) or by reaction with H_2 or OH to produce N_2 (Ogawa and Yoshida, 2005). As the net production relies upon this balance formation and destruction of N_2O, the emission rate is highly dependent on the combustion conditions and the dispersion rate of the combustible gases.

5.6.3 Comparison of OP-FTIR with source sampling

The emission factors retrieved using the OP-FTIR and source sampling methods cannot be directly compared temporally or spatially due to the spatially-integrated nature of the OP-FTIR measurements and the time-integrated nature of the source sampling method. Similarly, comparison of whole-fire emission factors for each measured fire cannot be used due to the varying amounts of flaming and smouldering emissions measured by the OP-FTIR between different fires, whilst the source sampling technique targets emissions from discrete combustion phases. Instead, it is necessary to use EF CH_4 as a function of MCE for the comparison, as described in Section 5.5.2. By sub-sampling spectra with a narrow range of retrieved MCE (the 2% bins used in Figures 5.13–5.15), it is possible to compare the emission factors retrieved from those spectra with bag samples that possess an MCE within that range (Figure 5.17). Figure 5.17 shows a remarkably good agreement between the CH_4 emission factors derived from OP-FTIR measurements and those derived from the source sampling of flaming combustion, with all OP-FTIR derived emission factors lying within the range of source sampled emission factors for each of the MCE bins. This is very encouraging, and suggests that the OP-FTIR methodology (field-portable, passive, *in situ*, and instantaneous) is a viable alternative to the established source sampling methodologies (that require many replicates and subsequent laboratory analysis). Once the results from source sampling

for other gases have been made available to the author, it will be possible to make a broader comparison of results from the two methodologies.

5.7 Conclusions and Implications

This Chapter has presented the first substantial use of OP-FTIR for measuring the emission factors of a wide range of important biomass burning trace gas products. Emissions were measured at a series of experimental fires and wildfires during three measurement campaigns throughout the burning seasons of 2009 and 2010 (spanning over three months between 2 July and 6 October). The findings of this Chapter are important for both the quantification of biomass burning emissions from savanna regions and from a methodological point of view, these are summarised below.

5.7.1 Conclusions about tropical savanna biomass burning

(a) The emission factors presented here follow only a few limited studies of Australian savannas, which is surprising given that Australian savanna burning is an important source of a number of climatologically important atmospheric trace gases at both a national and global level. Generally, the averaged emission factors presented here are in line with global savanna emission factors (e.g. Akagi *et al.*, 2011; Table 5.8), with the exception of methanol (CH_3OH) that has an emission factor of around half of that reported by Andreae and Merlet (2001) and Akagi *et al.* (2011).

(b) The emission factors for CH_2O and HCN agree with global savanna emission factors, but are substantially larger than those measured in previous studies of Australian savannas (Hurst *et al.*, 1994a; Hurst *et al.*, 1994b). As suggested by Paton-Walsh *et al.* (2010b), who also find discrepancies between their measurements of CH_2O and HCN in northern Australia and those of Hurst *et al.* (1994a) and Hurst *et al.* (1994b), the underestimation by these earlier studies is probably due to losses of CH_2O and HCN during sample handling and storage.

(c) The reported uncertainty in emission factors for individual fires (Table 5.5) and the standard deviation of the mean emission factor calculated from all of the

measured fires is large, although it is in line with the natural variability reported by Akagi *et al.* (2011).

(d) Explaining this natural variability is one of the overall aims of this thesis and one of the important scientific questions posed by those who wish to better model global biomass burning emissions (van Leeuwen and van der Werf, 2011). With a focus on the variability of CH_4 emissions, it was possible to rule out any seasonal influence on EF CH_4. Instead, the emission factor varied substantially for different vegetation classes (Figure 5.11 and Table 5.9), whilst the MCE explains the majority of this variation (Figures 5.12–5.14). MCE was shown to be an important control for a number of other gases (CH_3OH, NH_3, HCN). The variability in the emission factor of N_2O was found to be difficult to predict and probably relies upon the availability of products relating to the formation and destruction of N_2O, which in turn depend a complex relationship between combustion efficiency and meterological or convective processes.

5.7.2 Implications for OP-FTIR spectroscopy of biomass burning

Following the theoretical (Chapter 3) and controlled (Chapter 4) evaluation of the suitability of OP-FTIR spectroscopy for measurements of biomass burning emissions, this Chapter presents a number of findings that help to confirm the viability of the OP-FTIR technique as an alternative to conventional ground-based point-sampling and airborne approaches (at least for measurements of savanna fires):

(a) The methane emission factors derived from the OP-FTIR measurements agree well with those measured by CSIRO using their point-source sampling methodology. This ground-based point-sampled methodology is a well-established technique for measuring biomass burning emissions (as deployed by Hurst *et al.*, 1994a; Sahai *et al.*, 2007; Li *et al.*, 2007). The agreement between the two methodologies suggests that the open-path approach provides a spatially integrated measurement that is equivalent to many point-sourced replicates. This is clearly advantageous as the OP-FTIR methodology is passive, does not suffer from losses due to sample handling and storage, and does not require a suite of laboratory machines for analysis of the sample.

(b) The majority of the suite of emission factors presented in Table 5.7 agree with those from previous measurements in savanna ecosystems (Table 5.8). This suggests that the method used to estimate whole-fire emission factors here (only using measurements with an MCE greater than 90% in the calculation of the emission factor) is not biased towards either flaming or smouldering emissions. Future work is needed to improve this approach; ideally airborne thermal imaging measurements of the relative amount of fuel consumed by each combustion phase (as used in Wooster *et al.*, 2011) could be used to weight the whole-fire emission factors.

6

United Kingdom: an emissions inventory for heathland burning

6.1 Introduction

Whilst emissions factors from fires in the savanna and grassland ecosystems of Africa, South America and Australasia are relatively well studied, with over 30 published measurements represented in the updated (2009) emission factor database of Andreae and Merlet (2001); emission factors from fires in the temperate heathlands of western and northern Europe remain largely unknown. In Chapter 5, the OP-FTIR methodology described in Chapter 3 was used to derive seasonal emission factors for fires occurring in the savanna of northern Australia. In a confirmation of the results of the accuracy assessment presented in Chapter 4, the emission factors measured in this Australian study using the OP-FTIR agreed well with those measured using an established ground-based *in situ* point-sampling methodology. Having found the OP-FTIR method to be a robust approach for measuring emission factors in the field, this Chapter presents results from its application to estimating biomass burning emissions factors from the hitherto unstudied (in terms of EFs) heathland ecosystem.

This Chapter will focus on the establishment of a suite of emission ratios and emission factors for *Calluna vulgaris* (Scottish Heather) dominated heathland environments. Measurements presented in this Chapter were made during three fieldwork campaigns to heathlands in the UK (Northumberland and Dorset). In total, 25 fires were measured across 4 different sites, during both the early spring and summer. By measuring such a

large number of fires at different locations and throughout different seasons, this Chapter aims to characterise the broad emissions components resulting from burns in this ecosystem, for future use in total emissions modelling. The Chapter concludes with the first tentative estimates of total trace gas emissions from UK heathland burning for a series of climatically and chemically important species (i.e. CO_2, CO, CH_4, C_2H_2, C_2H_4, C_2H_6, HCOOH, CH_3OH, CH_2O, NH_3, and HCN).

In addition to the open-path measurements used for establishing the emissions inventory, a number of targeted bag samples were taken during different stages of the fires (during the flaming and smouldering stages) in both Northumberland and Dorset. These samples were analysed in a closed-path White cell using the FTIR spectrometer, enabling a comparison between point-based and path-based FTIR methodologies, building on the previous comparison with the GC-analysed samples in Australia. Finally, following the findings of a strong relationship between MCE and the emission factors of some of the trace gases investigated in Chapter 5 (methane, in particular), MCE determined using an inexpensive handheld CO_2/CO gas analyser was also compared with OP-FTIR MCE measurements.

To the author's knowledge, the work presented here represents the first ever measured emission factors for temperate heathland ecosystems, facilitating the first estimates of total biomass burning emissions from this ecosystem using direct measurements, rather than best-guess emission factors (e.g. Dragosits *et al.*, 2009). Furthermore, to the author's knowledge, this Chapter also presents the first direct comparison between the analysis of open-path and closed-path White cell spectra of smoke from the same fire, helping to further affirm the representative nature of the open-path sampling technique.

6.2 Background

Little is known about the makeup and magnitude of biomass burning emissions from temperate heathland environments, despite their predominant location in Western Europe and the widespread use of fire for land management in these regions. A number of papers on the effects of prescribed heathland burning provide evidence that suggests

regular burning of heathland in England (Yallop *et al.*, 2006), Scotland (Davies *et al.*, 2009), Italy (Borghesio, 2009), Germany (Klein *et al.*, 2009), Norway (Nilsen *et al.*, 2005; Måren *et al.*, 2010), France (Rius *et al.*, 2009), and Spain (Ojeda *et al.*, 1996). Additional to this research concerning the effects of burning on this environment, published research has also focussed on heathland fire intensity and severity (e.g. Yallop *et al.*, 2006; Davies *et al.*, 2010), the rate of spread of fires in heathland environments (e.g. Davies *et al.*, 2009) and the role of biomass burning in heathland carbon balance (e.g. Farage *et al.*, 2009).

Despite this broad range of interest in biomass burning in temperate heathlands, there appear to be no records of direct measurements of smoke emissions from these fires. In the UK alone, it is estimated that 120–360 km^2 of heather-dominated moorland is burned each year (Yallop *et al.*, 2006; Moorland Working Group, 2002). In total, approximately 3,000 km^2 of moorland is managed by controlled burning on a rotational basis (Figure 6.1). This burning of heathland ("muirburn") accounts for almost all emissions from controlled burning in the UK (Dragosits *et al.*, 2009).

Elsewhere in Europe, it is difficult to amalgamate records of burnt area due to a lack of fire reporting and difficulties associated with detecting heathland fires using remote sensing (e.g. high cloud cover, small plot sizes, rapid regeneration). Nevertheless, reports of individual fires covering areas of 50 km^2 (Rius *et al.*, 2009) suggest that the scale of burning might be similar to, or exceed, that of the UK. Furthermore, fire is increasingly being used as a management tool for the conservation of heathlands (Davies *et al.*, 2008; Borghesio, 2009) and the likelihood of future wildfires is also predicted to rise with warmer temperatures into the 21st century (McEvoy *et al.*, 2008; Albertson *et al.*, 2010).

Whilst clearly of a much lower magnitude than the emissions from African/Australian savanna or Siberian/Canadian boreal forest fires, the high human population density of Western Europe means that heathland burning is often located close to populated areas where smoke plumes can pose a health hazard, particularly for those suffering from pre-existing respiratory problems such as asthma (Rappold *et al.*, 2011). Consequently, there is national-government-level interest in the smoke constituents of heathland fires in the UK. For example, the UK's National Atmospheric Emission Inventory attempts

Figure 6.1 Aerial photography of the Derwent area of the Peak District National Park (Google Maps, 2012). This patchwork pattern, caused by intensive prescribed burning, is typical of the majority of upland moors in the UK (Yallop *et al.*, 2006).

to estimate total emissions of ammonia (NH_3) from biomass burning sources (Dragosits *et al.*, 2009). Unfortunately, due to the lack of data concerning the emission factors from heathland fires, estimates of emissions such as those in Dragosits *et al.* (2009) have to rely on emission factors from other vegetation types, with Dragosits *et al.* (2009) using a range of 1–5 g NH_3 kg^{-1} dry fuel. This approach is far from ideal, as NH_3 emission factors can vary significantly between ecosystem type (0.52–10.8 g kg^{-1}), as summarised in the 2009 updates to Andreae and Merlet (2001) and Akagi *et al.* (2011).

This Chapter aims to establish the first emissions inventory for heathland biomass burning, with the ultimate objective of helping to significantly improve the total emissions estimates from heathland biomass burning, for the benefit of both national and global emissions modelling. To achieve this, results from measurements of a large number of heathland fires at different UK sites conducted across different times of year are presented.

6.3 Specific objectives of this Chapter

(a) To establish emission factors for biomass burning in the heather-dominated heathlands of the UK.

(b) To compare emission factors determined from both open-path FTIR measurements and from FTIR spectroscopy of bag samples in a closed-path White cell.

(c) To determine whether cost-effective handheld CO_2/CO gas analysers can be used to determine MCE accurately by comparing the handheld analyser measurements of bag-sampled smoke with those made with the FTIR spectrometer and White cell.

6.4 Measurements of emissions

Measurements of heathland fires were made at experimental fires in March 2010 near Rothbury, Northumberland (NLR); in March 2011 near Longframlington, Northumberland (NLL); and in July 2011 near Dorchester, Dorset (DOR). The flora of these sites is typical of ericaceous dwarf-shrub dominated European dry heaths that can be found extensively in the western oceanic fringes of Europe (Figure 6.2a). A high proportion of European temperate heathlands occurs in the UK (Figure 6.2b) with the UK heathland being of special scientific interest due to its exceptional biodiversity (JNCC, 2012). Both the Northumberland and Dorset sites were within close proximity to designated Special Areas of Conservation (SAC).

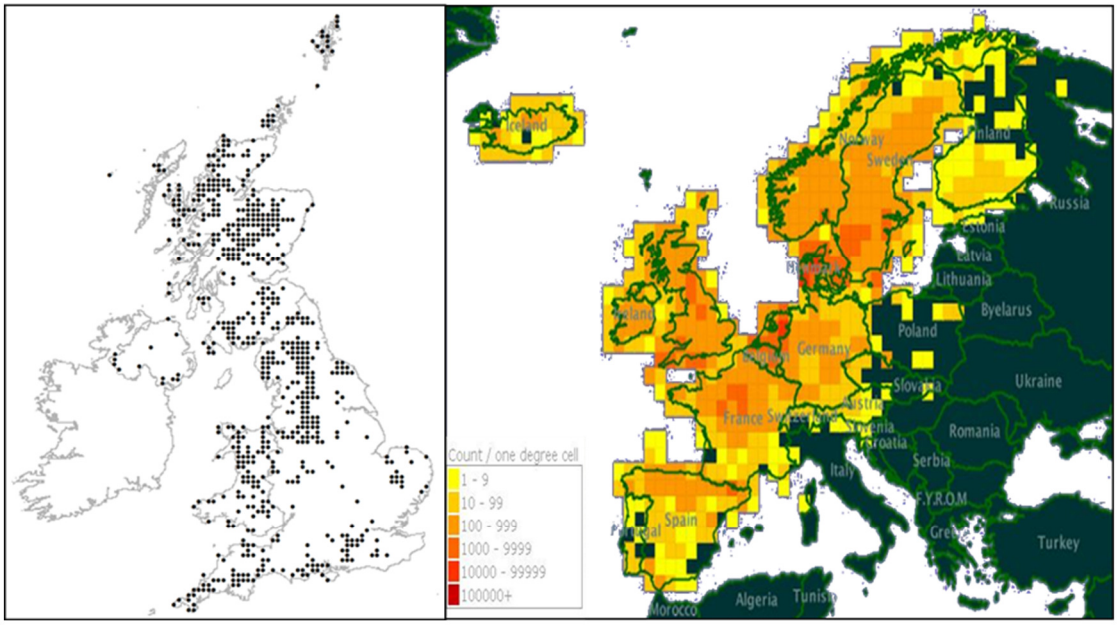

Figure 6.2 (a) Map of the UK showing the distribution of European dry heaths (taken from JNCC, 2012). The total UK extent of European dry heath is 608,022 hectares. (b) European distribution of *Calluna vulgaris* (GBIF, 2012)

6.4.1 Site descriptions

Burns at three experimental sites were studied, two in Northumberland (2010 and 2011) and one in Dorset (2011). Figure 6.3 indicates the locations of these three sites within the UK, which were all relatively close to coastal areas (within 25 km).

6.4.1.1 Northumberland (2010)

Measurements were conducted on 22–23 March 2010 at two sites near Rothbury, Northumberland. Both sites were within close proximity to the Simonside Hills Special Area of Conservation. The first site was dominated by gorse (*Ulex spp.*) and only one experimental fire was carried out here. The vegetation class for this site will be referred to as *gorse-dominated heathland* (GH). The second site, Debdon Heath, was dominated by heather (*Calluna vulgaris*), occurring in combination with other dwarf-shrubs. Five experimental fires were carried out at this site. The vegetation class for this site will be referred to as *heather-dominated heathland* (HH). Both sites were typical of European dry heathland, occurring on freely-draining, acidic to circumneutral soils with low nutrient content. Both sites were situated at ~200 m altitude.

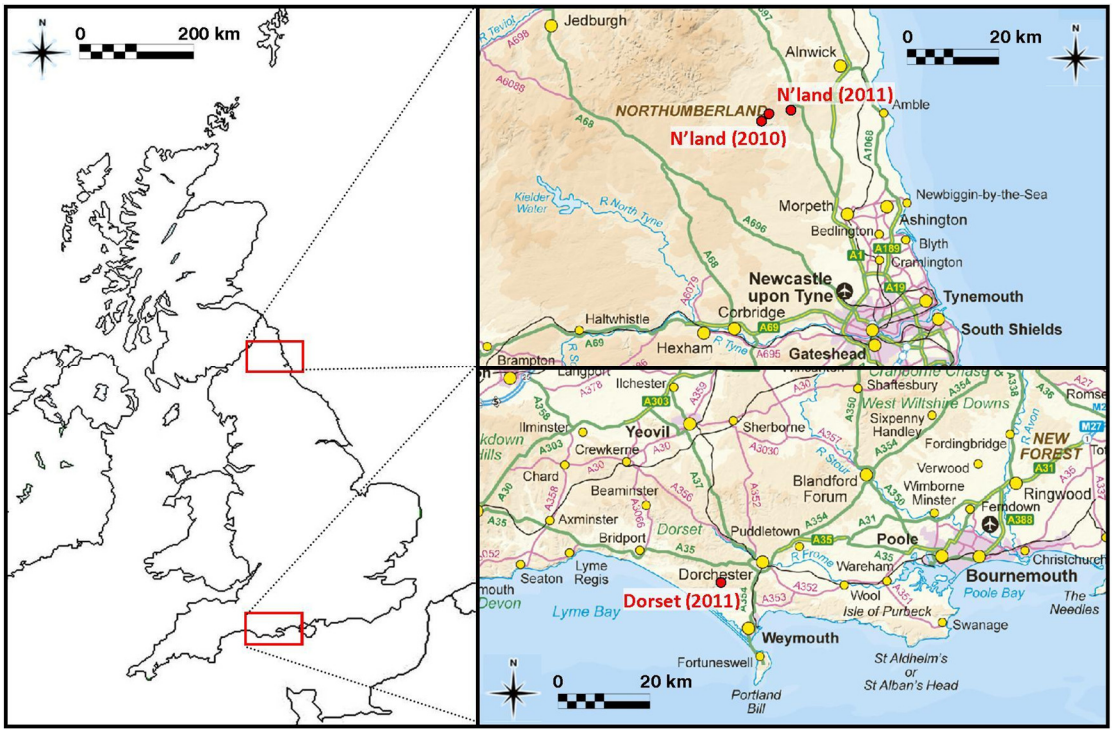

Figure 6.3 Map of the UK (*left*) showing the two campaign locations. Three sites were used for experimental fires in Northumberland (*top right*) and one site in Dorset (*bottom right*) (Bing Maps, 2012).

The climate of Northumberland is maritime temperate. The closest weather station, at Morpeth (55° 10' N 1° 41' W), 20 km southeast of the experimental fire sites, records a mean annual rainfall of 694 mm, and in March a monthly average rainfall of 55 mm and a mean maximum temperature of 8.4°C.

6.4.1.2 Northumberland (2011)

Measurements were conducted across three days between 21 and 23 March 2011 at one site, New Moor, near Longframlington, Northumberland, 16 km north-northeast of Morpeth. In total, 15 experimental fires were measured during the campaign. The site characteristics were very similar to those of the heather-dominated site from the 2010 campaign. The vegetation class for all of the experimental fires for this campaign is HH.

6.4.1.3 Dorset (2011)

This campaign was conducted across four days between 25 and 28 July 2011 at one site near Dorchester, Dorset. In total, 5 experimental fires were measured during this campaign. Unlike the Northumberland sites, which were predominantly heather, the

Dorchester site exhibited both heather-dominated and bracken-dominated vegetation, as well as some mixed plots. Experimental fires were carried out in both vegetation types; the vegetation class for these fires will be either HH, *bracken-dominated heathland* (BH) or *mixed heathland* (MH).

The climate of Dorset is maritime temperate. Climate records at Bournemouth (50° 43' N 1° 51' W), 40 km east of the experimental fire sites records a mean annual rainfall of 813 mm, with a July (the driest month) monthly average rainfall of 37 mm and mean maximum temperature of 22.0°C.

6.4.2 Fire descriptions

6.4.2.1 Northumberland (2010)

Experimental burning of two vegetation classes was measured during this first UK campaign:

1. Gorse-dominated heathland (GH, Figure 6.4a)
2. Heather-dominated heathland (HH, Figure 6.4b)

Whilst the UK can experience long periods of warm, dry conditions (usually associated with anticyclones) that create ideal conditions for severe wildfires (as in the summer of 2003 (McMorrow, 2009)), the weather during the planned experimental period in March 2010 was less than ideal. Conditions were dry enough for burning on one and a half days of the planned five day period. Nevertheless, OP-FTIR measurements were made for one burn on 22 March 2010 at a small gorse plot in spite of rain only a few hours earlier, and for a further five heather fires on 23 March 2010. This indicates the relative ease at which fires can occur in this environment, despite less than ideal conditions for combustion.

The gorse plot (the only fire that was conducted on the gorse-dominated heathland, Figure 6.4b) consisted of a small 25 × 50 m isolated clump of gorse shrubs, surrounded by mown grass, which acted as a convenient fire break. The tall nature of the gorse bushes (> 1 m), coupled with their position on a steep slope with the wind blowing upslope, allowed for a high intensity burn (see Figure 6.4a). This site consisted of a

large (300 × 500 m) area of heather through which fire breaks had been trimmed to create individual experimental plots (Figure 6.5c). The size of each fire plot ranged from around 30 × 30 m, up to 80 × 80 m. Each experimental fire was ignited using a line ignition at the downwind edge of the plot to widen the trimmed fire breaks, before a further line ignition was used on the upwind edge of the plot (Figure 6.4b). Table 6.1 gives details for each plot including ignition time, vegetation type, temperature, pressure and relative humidity.

a. Northumberland (2010): Gorse heathland (GH)
b. Northumberland (2010): Heather heathland (HH)
c. Northumberland (2011): Heather heathland (HH)
d. Dorset (2011): Heather heathland (HH)
e. Dorset (2011): Bracken/heather heathland (MH)
f. Dorset (2011): Bracken heathland (BH)

Figure 6.4 Photos depicting the various heathland fire classes experienced during the three UK field campaigns. The appreviations in parentheses are used throughout this chapter, more details about specific fire plots are given in Table 6.1 and Figures 6.5, 6.6 and 6.7.

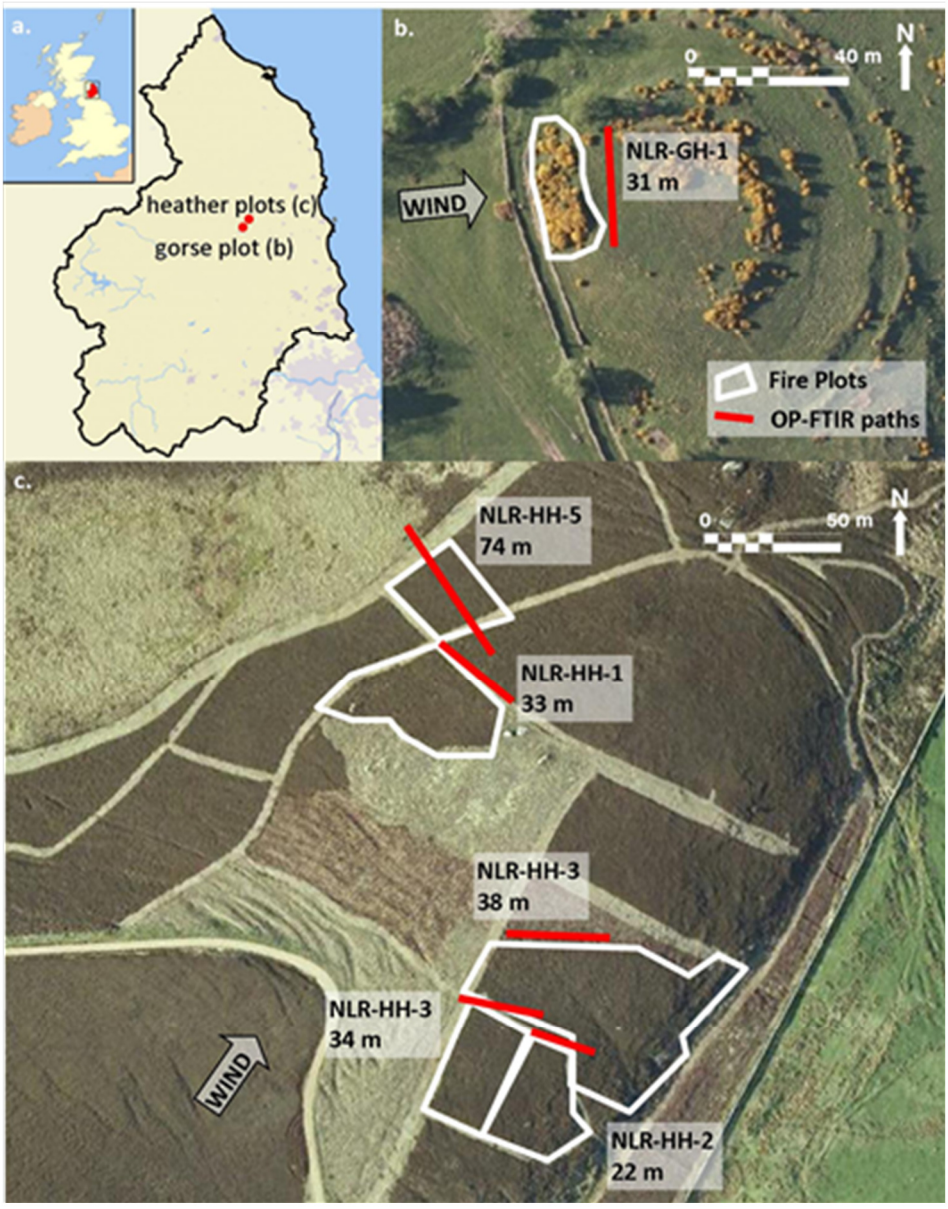

Figure 6.5 (a) Location of the Northumberland 2010 plots in the UK and Northumberland; (b) Gorse plot with OP-FTIR path; (c) the heather plots with OP-FTIR paths. Dominant wind direction is also shown. Aerial photography taken from Google Maps (2012).

Table 6.1 List of fires studied using OP-FTIR during each of the UK campaigns, with information about the plot location, fire type, OP-FTIR pathlength and meteorological variables. *indicates plots that were not measured using OP-FTIR #indicates fires that were only measured with bag sampling

Date	Local time	Dur. (min)	Site name	Veg. type	Location		OP-Path (m)	Weather			Bag sampling	
					Latitude	Longitude		T (°C)	RH (%)	P (hPa)	Flaming	Smouldering
Rothbury (2010)												
22-Mar-10	1630	10	NLR-GH-1	GH	55°18.77 N	1°56.53 W	31	8.5	50	985	No	No
23-Mar-10	1050	40	NLR-HH-1	HH	55°19.88 N	1°54.91 W	33	8.5	60	985	No	No
23-Mar-10	1208	10	NLR-HH-2	HH	55°19.79 N	1°54.87 W	22	8.5	65	985	No	No
23-Mar-10	1312	10	NLR-HH-3	HH	55°19.80 N	1°54.89 W	34	8.5	60	985	No	No
23-Mar-10	1450	30	NLR-HH-4	HH	55°19.81 N	1°54.84 W	38	8.5	70	985	No	No
23-Mar-10	1558	20	NLR-HH-5	HH	55°19.91 N	1°54.88 W	74	8.5	70	985	No	No
Longframlington (2011)												
21-Mar-11	1245	10	NLL-HH-1	HH	55°20.44 N	1°49.21 W	40	13.0	62	1014	No	Yes
21-Mar-11	1420	10	NLL-HH-2	HH	55°20.43 N	1°49.23 W	40	13.0	62	1014	No	Yes
21-Mar-11	1545	10	NLL-HH-3	HH	55°20.43 N	1°49.25 W	40	13.0	62	1014	No	No
22-Mar-11	1155	10	NLL-HH-4	HH	55°20.45 N	1°49.16 W	41	14.0	65	1021	Yes	No
22-Mar-11	1210	*	NLL-HH-5	HH	55°20.46 N	1°49.17 W	*	14.0	65	1021	No	No
22-Mar-11	1215	10	NLL-HH-6	HH	55°20.46 N	1°49.18 W	41	14.0	65	1021	No	No
22-Mar-11	1225	10	NLL-HH-7	HH	55°20.45 N	1°49.19 W	41	14.0	65	1021	No	No
22-Mar-11	1305	10	NLL-HH-8	HH	55°20.45 N	1°49.19 W	40	14.0	65	1021	No	No
22-Mar-11	1420	20	NLL-HH-9	HH	55°20.47 N	1°49.21 W	40	14.0	65	1021	No	No
22-Mar-11	1525	10	NLL-HH-10	HH	55°20.50 N	1°49.23 W	34	14.0	65	1021	No	No
22-Mar-11	1545	15	NLL-HH-11	HH	55°20.52 N	1°49.25 W	34	14.0	65	1021	No	No
22-Mar-11	1620	15	NLL-HH-12	HH	55°20.55 N	1°49.27 W	36	14.0	65	1021	No	No
23-Mar-11	1230	20	NLL-HH-13	HH	55°20.52 N	1°49.30 W	40	14.5	60	1021	Yes	Yes
23-Mar-11	1400	25	NLL-HH-14	HH	55°20.50 N	1°49.27 W	42	14.5	60	1021	Yes	Yes
23-Mar-11	1600	40	NLL-HH-15	HH	55°20.20 N	1°50.35 W	46	14.5	60	1021	Yes	Yes
Dorset (2011)												
25-Jul-11	1500	15	DOR-HH-1	HH	50°41.25 N	2°33.14 W	36	18.5	71	982	Yes	Yes
26-Jul-11	1430	30	DOR-MH-1	MH	50°41.24 N	2°33.06 W	40	19.0	49	988	Yes (×2)	Yes
27-Jul-11	1145	40	DOR-MH-2	MH	50°41.24 N	2°33.03 W	36	16.0	67	983	Yes	Yes
28-Jul-11	1215	25	DOR-BH-1	BH	50°41.27 N	2°33.03 W	44	18.0	62	995	No	No
28-Jul-11	1320	25	DOR-MH-3	MH	50°41.22 N	2°33.01 W	35	20.0	58	995	Yes	No
28-Jul-11	1530	#	BBQ	#	50°41.91 N	2°33.00 W	#	21.0	55	995	Yes (×2)	Yes (×2)

6.4.2.2 Northumberland (2011)

All of the 15 fires from the March 2011 campaign to Northumberland took place on heather-dominated heathland (Figure 6.6). The site consisted of an expansive area of heather moorland that had been trimmed into experimental plots (Figure 6.6c). A range of plot sizes were used during this campaign due to the broader requirements from other researchers on site (who were investigating fire rate-of-spread, fuel loads, combustion completeness and fuel moisture content). The smallest plots measured ~10 m × 20 m, with most plots measuring around 30 m × 30 m. The final plot to be measured (*NLL-HH-15*) was a larger plot, measuring 150 m × 70 m. The majority of these plots were ignited in a similar fashion to those during the 2010 campaign; using an initial back burn line ignition (Figure 6.5c), before igniting a line on the upwind plot edge. The characteristics of each experimental burn plot are given in Table 6.1.

6.4.2.3 Dorset (2011)

Experimental burning of three vegetation classes was measured during the campaign to Dorset in July 2011:

1. Heather-dominated heathland (HH, Figure 6.5d)
2. Bracken-dominated heathland (BH, Figure 6.5f)
3. Mixed heathland – bracken and heather (MH, Figure 6.5e)

The mixed nature of the Dorset site is apparent in aerial images of the vegetation (Figure 6.7), with distinct patches of heather (darker greens in Fig. 6.7b) amongst the bracken (lighter greens in Fig. 6.7b). Consequently, three of the five fire plots were classified as mixed heathland, with one heather-dominated and one bracken-dominated plot. Whilst not visible in Figure 6.7, the ~30 m × 30 m plots were divided using trimmed fire breaks, as was the case in both Northumberland campaigns. All plots, with the exception of *DOR-BH-1* were ignited using two-step backfire-headfire line ignitions as described above. The characteristics of each plot are given in Table 6.1.

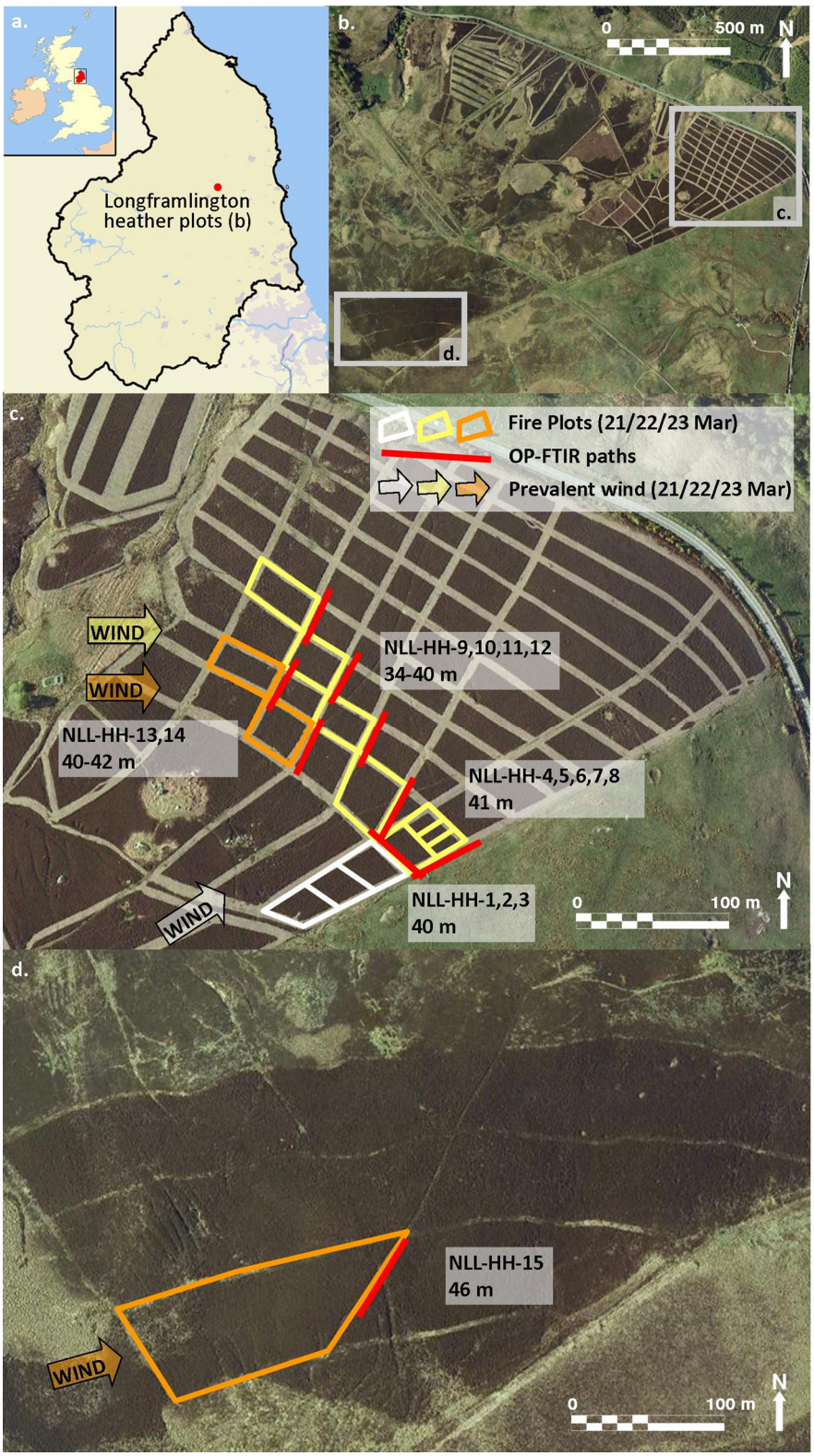

Figure 6.6 (a) Location of the Northumberland 2011 plots in the UK and Northumberland; (b) Overview of the site showing the two main locations of fire plots; (c) Map showing the 14 experimental fire plots measured for this chapter with their corresponding OP-FTIR paths. Fires were measured across three days (21-23 March), represented on the map by the white, yellow and orange plot outlines, respectively, dominant wind direction on each day is also shown using the same colours; (d) Map showing the location of NLL-HH-15 with the corresponding OP-FTIR path. Aerial photography taken from Google Maps (2012).

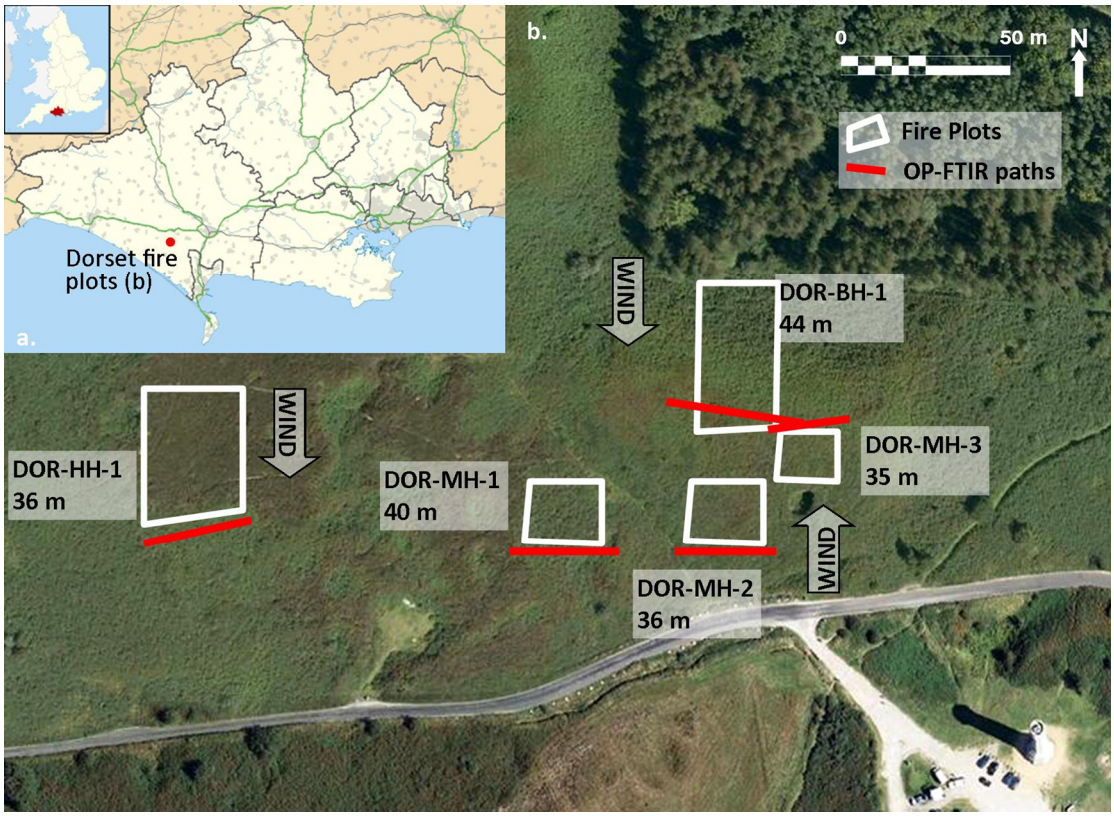

Figure 6.7 (a) Location of the Dorset 2011 plots in the UK and Dorset; (b) map showing the 5 experimental fire plots measured for this chapter with their corresponding OP-FTIR paths. The dominant wind direction (shown) was northerly (off-shore) for all plots except DOR-MH-3 where the wind was southerly (on-shore). Aerial photography taken from Google Maps (2012).

6.4.3 Gas Sampling Methodology

Two different FTIR-based methodologies were used to ascertain trace-gas emission factors for the smoke resulting from the experimental UK burns:

1. OP-FTIR spectroscopy adjacent to, or within the fire boundary (with measurements and analysis performed by the author in accordance with the methodology described in Section 3.3). This methodology was the only one used in the first (Northumberland 2010) campaign.
2. *In situ* bag sampling very close to the smoke emission source (within ~ 1 m), followed by subsequent analysis of the gas samples by FTIR analysis in a closed-path White cell constructed in part for the purpose of this experiment and described in Section 3.3.

Both methods rely upon sampling the smoke (either by path-sampling or point-sampling) close to the ground.

6.4.3.1 OP-FTIR

As in the previous Chapter on measuring emissions from Australian savanna, the main technique for measuring emission factors from the three UK campaigns discussed here is the OP-FTIR spectroscopy methodology outlined in detail in Chapter 3, evaluated in Chapter 4, and applied in Chapter 5 of this thesis. As in Australia, the FTIR spectrometer and IR source were operated in a bi-static configuration, with pathlengths for the UK measurements varying from 22 to 74 m (Table 6.1), with an average pathlength for the 25 fires of 39 m. Both the spectrometer and IR source were powered by 12 V batteries. For all experimental burns, spectra were collected using 4 co-added scans to increase signal-to-noise yet also allow for a high measurement frequency and so a good number of sample points, given that plots were small (<1 Ha), and in some cases burned quickly (<10 minutes).

For most plots, the OP-FTIR path was positioned within the trimmed fire break downwind of the fire plot, or within the adjacent plot downwind (the red lines in Figs. 6.5, 6.6 and 6.7 represent the approximate location of the OP-FTIR paths). For *DOR-BH-1* and *NLR-HH-5*, the OP-FTIR path was positioned over the plot itself. A high resolution vertical aerial photograph (Figure 6.8), taken by NERC's Airborne Research and Survey Facility (ARSF) aircraft over the experimental fire on plot *NLR-HH-3* during the Northumberland 2010 campaign, shows the typical situation of the OP-FTIR equipment layout relative to the fire plot.

6.4.3.2 Point sampling and White cell

During the two 2011 campaigns to Northumberland and Dorset, a White cell was used to analyse smoke that had been collected in Tedlar bags. As was the case with the Australian savanna fires, the relatively low intensity fires that are characteristic of heathland burning can be quite easily sampled on the ground at close proximity to the source fire. Here, *in situ* sampling was used to collect smoke from both the flaming combustion zone and smouldering combustion zone. Flaming combustion samples were

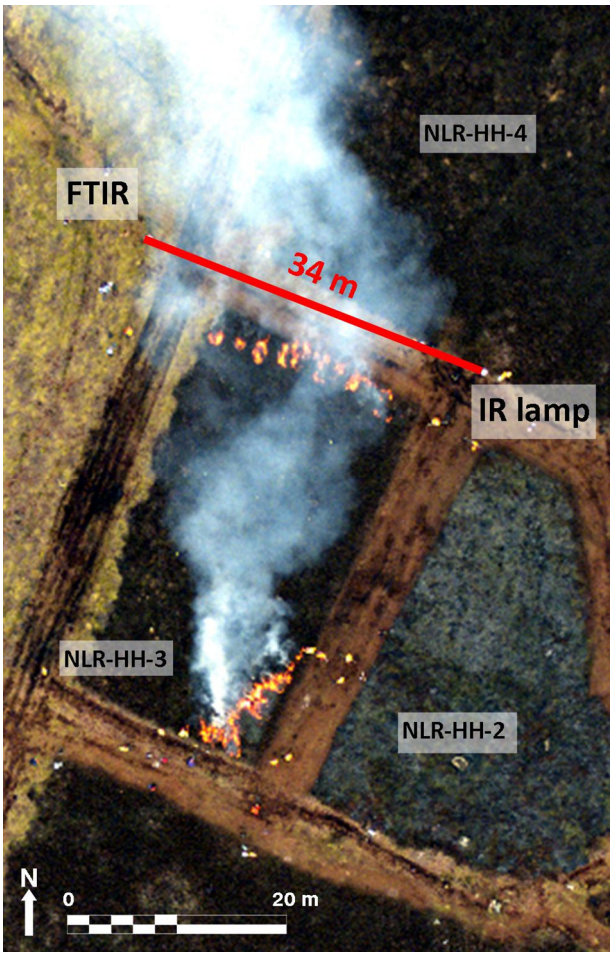

Figure 6.8 Aerial photograph of one of the experimental fires (plot NLR-HH-3 in Figure 6.5 and Table 6.1) on 23 March 2010. This photograph was taken by the NERC Airborne Research and Surveillance Facility (ARSF) aeroplane.

collected by sampling close to the headfire (Figure 6.9a), whilst smouldering samples were collected by sampling residual burning behind the fire front (Figure 6.9b). It was also possible to sample pyrolysis stage combustion products by targeting the advected smoke close to the vegetation and below the flaming combustion zone.

The sampling unit used to collect *in situ* smoke samples in Northumberland (March 2011) comprised of plastic tubing mounted on a 2.5 m cane sampling probe and connected to a handheld air pump that delivered a smoke sample into a 5 or 10 litre Tedlar bag. By July 2011, the unit was modified so that the plastic tubing ran through an extendable 1.5–3.5 m 16 mm diameter stainless steel sampling probe, with in-line Teflon filters and a backpack mounted air pump with space for the sampling bags. Samples were collected in line with the CSIRO methodology detailed in Chapter 5,

Figure 6.9 Photographs of the *in situ* point-sampling technique used for measuring (a) flaming combustion emissions; and (b) residual smouldering combustion emissions. Flaming measurements were made at ~0.5 m above the flames, whilst residual smouldering measurements were only made once flaming had ceased.

where the tip of the probe was positioned approximately 0.5 m above the flame for the flaming combustion measurements, and within the low-lying smoke for the smouldering combustion measurements. The sampling rate delivered by the pump was approximately 1 litre per minute, leading to each sample bag containing smoke being sampled for around 5–10 minutes. Given that only one sampling unit was available for the measurement campaigns, and the relatively small (and therefore quick) fires, only one sample could be collected from each combustion stage per fire. In addition to this *in situ* sampling, measurements of pure heather and pure bracken samples were also made by burning discrete samples of these fuels in an incinerator bin on site and sampling the smoke from both the flaming and smouldering combustion stages. Table 6.1 outlines which plots were sampled for flaming and/or smouldering combustion using this

methodology. In total, 11 bag samples of flaming combustion and 9 bag samples of smouldering combustion were measured, the majority of which are from heather-dominated sites. In Section 5.4.3.2, the bagged gas samples from Australia were analysed using multiple laboratory-based GC instruments some days after collection. Here, the *in situ* smoke samples were instead analysed within 8 hours of collection using a field-portable closed-path White cell system, based around the same FTIR spectrometer as that used for the OP-FTIR measurements. A full description of this 'White cell' method can be found in Section 3.3.4. Prior to analysis in the White cell, each bag sample was analysed using a KANE 100-1 CO_2 and CO gas analyser to determine the concentration of CO_2 and CO within each sample bag before mixing with ambient air in the White cell (see Section 3.3.4).

6.4.4 Biomass sampling methodology

Biomass was sampled from plots at both Northumberland campaigns (2010 and 2011) to yield measures of both fuel load (kg m^{-3}) and combustion completeness (%). Following the methodology outlined in Harris *et al.* (2011), all above-ground material was harvested before burning from 0.25 m^2 quadrats positioned within the area to be burned. After burning, vegetation from a secondary quadrat, adjacent to the first, was harvested. Pre- and post-burn samples were sorted into fractions (dwarf shrubs, litter and others), dried at 80°C and weighed to determine fuel load and combustion completeness. The resulting fuel loads and combustion completeness measures are used to calculate total heathland emissions in Section 6.6.

6.5 Results and Discussion

The objectives of this Chapter were to present an emissions inventory for the European heathland ecosystem from OP-FTIR measurements; to compare these results with those obtained from bag samples measured by the FTIR spectrometer in a White cell and with an inexpensive handheld gas analyser; and to use these measurements in conjunction with simultaneous and previous measurements of fuel loads and completeness of combustion to establish a total emissions model for the moorland ecosystem.

This results section will first focus on the OP-FTIR measurements undertaken at 25 experimental fires in the UK, presenting the final calculation of the smoke emission factors for UK heathland fuels. The results from the handheld gas analyser and White cell FTIR measurements of the 22 bagged smoke samples will then be compared with those measured using the open-path methodology. The measured fuel loads and combustion completeness are also presented here, although the total emissions modelling is considered separately in Section 6.6.

6.5.1 OP-FTIR

As described in detail in the methodologies Chapter (Sect. 3.3) and in the OP-FTIR results from the previous Chapter (Sect. 5.5.1), OP-FTIR was used to retrieve trace gas concentrations in the smoke eddies passing between the FTIR spectrometer and the IR lamp. A time series of trace gas concentrations near to the downwind boundary of one of the experimental fires from the 2010 Northumberland campaign is shown in Figure 6.10. As was the case for the experimental fires in Australia, a majority of the fires measured in the UK were ignited with a back-burning fire line on the down-wind boundary of the fire plot. As this backing-fire moves slowly against the wind, widening the fire break, the up-wind boundary is then ignited, with a majority of the plot burning with a head-fire driven by the prevailing wind.

A number of discrete fire 'stages' can be identified by evaluating the timing of peak concentrations of different trace gases in Fig. 6.10, similar to that seen in the African fires studied by Wooster *et al.* (2011) using the OP-FTIR technique. Immediately following the ignition of the backing fire, we see a burst of smoke from flaming combustion, characterised by high MCE (Fig. 6.11) of greater than 95%. As the backing-fire moves up-wind, an increasing area of the fire plot remains smouldering (residual combustion from the backing-fire), with increasing CO concentration and a corresponding decrease in MCE (until time *~16.08* in Figs. 6.10 and 6.11). As the backing-fire burns away from the OP-FTIR path there is a period of time when overall concentrations remain low due to less smoke advecting into the OP-FTIR path. At the same time, the headfire advances downwind towards the OP-FTIR path, contributing an increasing amount of smoke to the path between the spectrometer and IR lamp, causing

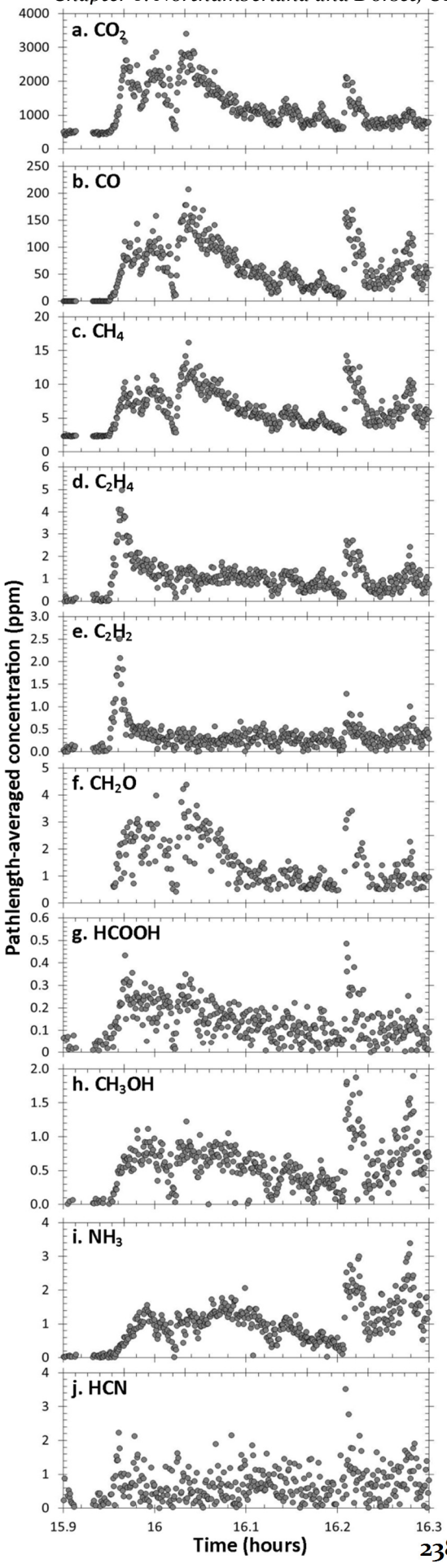

Figure 6.10 Time series of path-averaged trace gas concentrations (in ppm) for plot *NLL-HH-15* (23 March 2011) during the second Northumberland measurement campaign. Trace gas concentrations were retrieved from the OP-FTIR spectra using MALT (as described in Sections 3.2.2 and 3.3.2). An example smoke spectrum with the best-fit modelled spectrum for each of the spectral windows used to retrieve the concentration of each of the trace gases presented in this figure can be found in Figure 3.15.

moderate increases in MCE in the example of Figure 6.11 (up to time *16.2*). When the headfire meets with the backing-fire, the resultant brief increase in fire intensity (before flaming combustion ceases altogether) drives smouldering smoke from the burnt area of the plot towards the downwind boundary; this strong pulse of smoke is evident in the high concentrations measured in the OP-FTIR (particularly of signature smouldering combustion gases such as CO, CH_4, CH_3OH, HCOOH and NH_3).

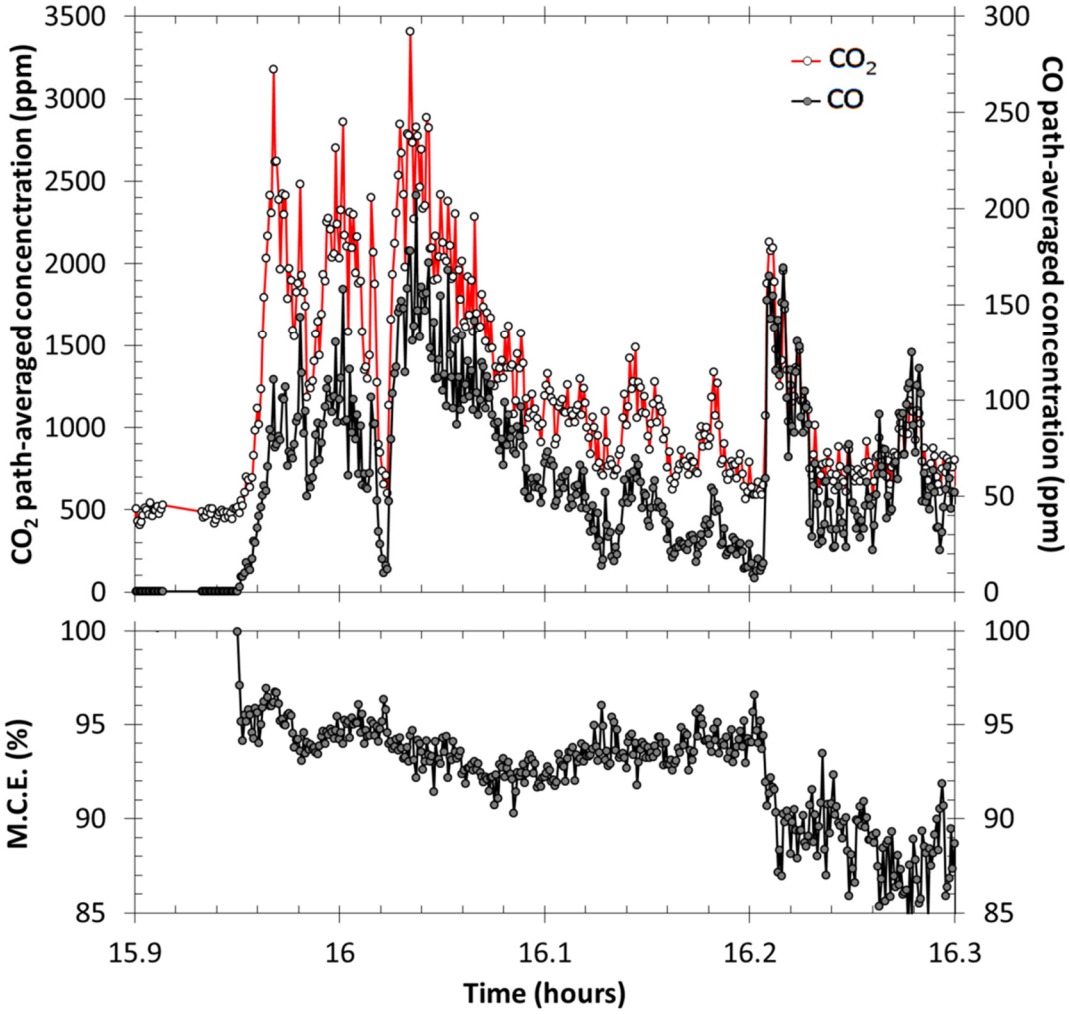

Figure 6.11 (top) Time series of retrieved CO_2 and CO pathlength averaged concentrations; and (bottom) Modified Combustion Efficiency (MCE). Smoke passing into the IR beam at the start of the fire originates from the highly efficient back burning fire ignited close to the OP-FTIR path. As the backing fire moves into the experimental plot, smouldering emissions contribute to the smoke measured by the OP-FTIR spectrometer, decreasing the retrieved MCE. As the headfire advances from the opposite side of the experimental plot, smoke from this flaming combustion increases the MCE measured in the OP-FTIR path. Finally, once the flaming ceases, a pulse of smouldering smoke is drawn into the OP-FTIR path, drastically reducing the MCE derived from the OP-FTIR spectra.

6.5.1.1 Emission Ratios

Following the methodology of the previous Chapter, emission ratios for each trace gas relative to CO_2 are calculated using the least squares linear regression slope of the trace gas species concentration versus CO_2 concentration. Unlike the Australian data, where the *within-fire* degree of scatter between trace gas concentrations and concentrations of CO_2 was minimal (e.g. Figure 5.8), there is a higher degree of scatter for many of the trace gases investigated for each UK fire (Figure 6.12). As is apparent in Figure 6.12, the scatter is not random, but rather appears to be related to the MCE (indicated by blue-to-red shading indicating high-to-low MCE), particularly for the trace gases CO, CH_4, CH_2O, CH_3OH and NH_3. Furthermore, the bivariate plots in Fig. 6.12 appear to show bimodal relationships between the concentrations of many of the trace gases and CO_2, with the lower MCE measurements (red) clearly lying on a distinguishably separate line. There are a number of factors that can help explain the patterns shown in these plots, and explain the difference between the UK measurements and those from Australia:

- The sizes of the experimental plots in the UK (usually 30 m × 30 m) were considerably smaller than those measured in Australia (typically 500 m × 200 m). Due to the smaller size of the plot, there is less opportunity for smoke from different stages of the fire to mix before entering into the optical path. Therefore, eddies of smoke passing through the infrared beam are more likely to have originated from *either* the flaming combustion of the backing-fire *or* headfire *or* the residual smouldering combustion (RSC). This lack of mixing can explain the variation in the slope of the relationship between the trace gas concentrations and CO_2 concentrations. In the Australian measurements, from the much larger plots, there would have been more opportunity for smoke to mix before passing through the OP-FTIR path, reducing the variation of this slope.
- The homogeneity of the UK fire plots also decreases the mixing of smoke from different combustion stages. In plots with mixed fuel types (the Australian plots had a mixture of leaf litter, grasses, shrubs and trees), each individual fuel type will burn with a different combustion efficiency, and perhaps flame residence time, depending on the fuel structure (e.g. fine or coarse) and moisture, with

smoke from each fuel type (and thus from differing MCE) mixing at any one time. For the homogeneous fuel types that are characteristic of the UK fires measured here, which occurred in highly managed landscapes, only one fuel type was typically burning at any one time (or at least provided the vast majority of the burning fuel at any one time). This may also help explain the existence of the bi-modal relationships between trace gas concentrations and CO_2 concentrations in these UK fire results. Such bi-modal relationships have been seen in both field studies of homogeneous vegetation plots (e.g. Wooster *et al.*, 2011) and in laboratory studies of individual species burning (e.g. Fernández-Gómez *et al.*, 2011).

Fernández-Gómez *et al.* (2011) identify the different combustion phases by using a CO vs. CO_2 plot. In their laboratory study, the flaming phase combustion (measurements with a low gradient on their plot) is clearly distinct from the smouldering combustion (with a much higher gradient), measurements that lie in between these two 'modes' are ascribed to a transition phase between flaming and smouldering. In the results presented in Figure 6.12 a similar pattern emerges (as indicated by the MCE colour coding), with the lower gradient for most gases originating from measurements with a high MCE (i.e. predominantly flaming combustion), whilst the higher gradient measurements have a lower MCE (i.e. predominantly smouldering combustion). Measurements lying in between the two modes (evident in plots of CO, CH_4, CH_2O, CH_3OH, NH_3 vs CO_2) may be ascribed to a mixture of the smoke originating from flaming and smouldering. For C_2H_2 and C_2H_4, a number of measurements with a high MCE appear to have a much higher gradient than many of the other measurements; it is possible that these measurements are influenced by high proportions of pyrolysis products in the IR path (pyrolysis emissions occur close to flaming emissions in both space and time).

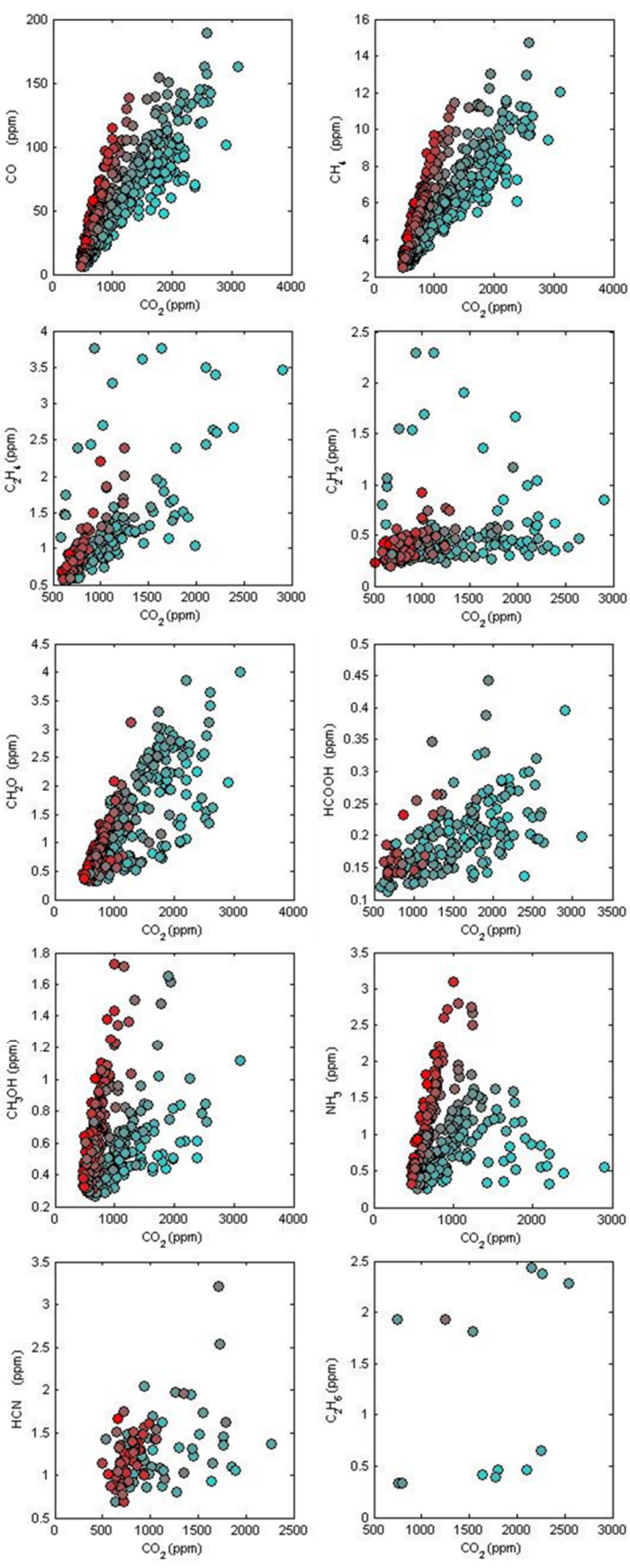

Figure 6.12 Example scatter plots of the measured trace gas concentration used to calculate emission ratios. The data presented here are for the same example fire featured in Figure 6.10 and Figure 6.11, *NLL-HH-15* (23 March 2011). The colour indicates the Modified Combustion Efficiency derived from the CO_2 and CO concentration for each individual measurement (cyan = high MCE; red = low MCE).

Only three of the 25 fire plots measured in the UK exhibited mixed fuel types, specifically those of the Dorset fires. The results from these three plots with mixed (heather and bracken) fuels enable a suitable comparison with the homogeneous plots of Northumberland (Figure 6.13). The results from a mixed heather and bracken plot

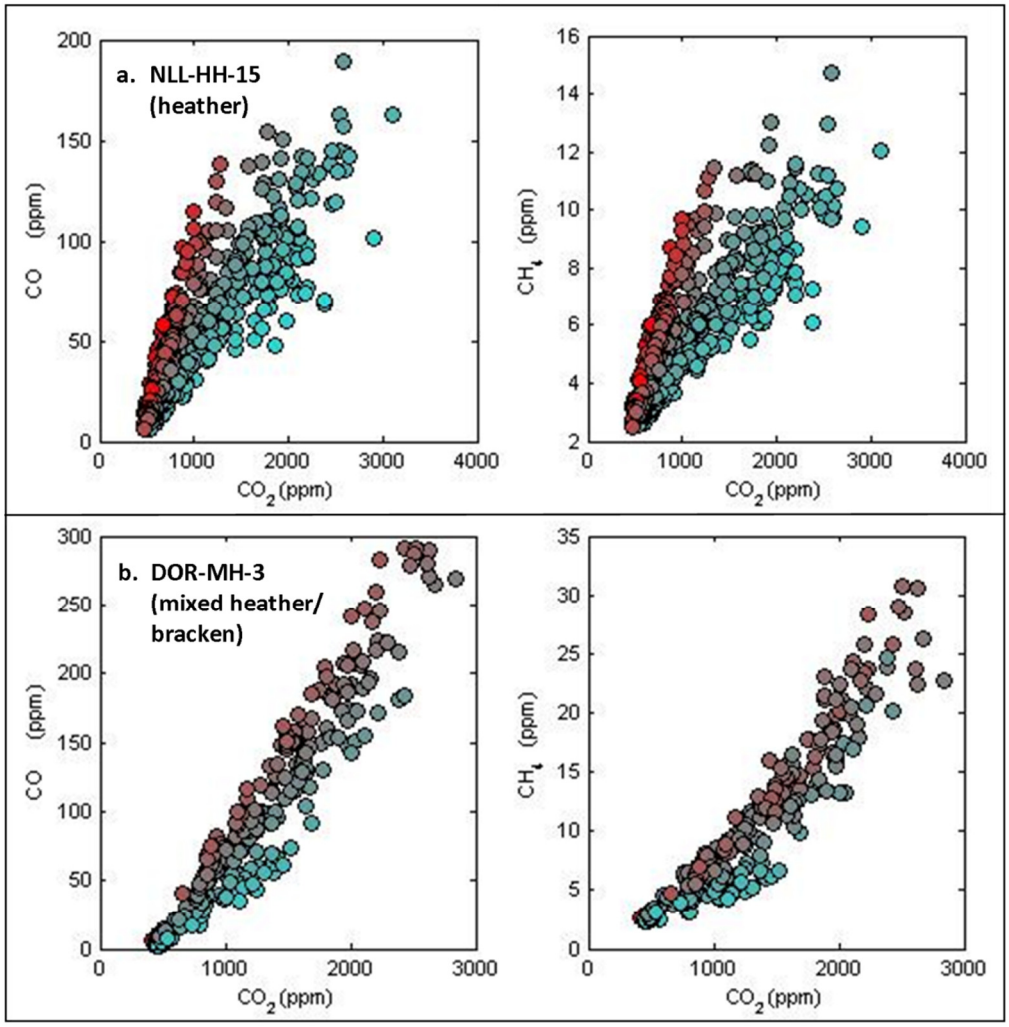

Figure 6.13 A comparison of scatter plots of the measured trace gas concentrations used to calculate emission ratios for (a) a heather-dominated heathland fire (*NLL-HH-15*); and (b) a mixed vegetation heathland fire (*DOR-MH-3*). As in Figure 6.12, the colour indicates the Modified Combustion Efficiency (cyan = high MCE; red = low MCE) The homogeneity of the heather-dominated fire plot decreases the possibility of smoke mixing from different combustion stages, leading to two distinct relationships in the scatter plot; a low gradient slope corresponding to flaming combustion, as indicated by the increasingly blue points at lower gradients; and a high gradient slope corresponding to smouldering combustion, as indicated by the increasingly red points at higher gradients. For heterogeneous vegetation cover (b), each individual fuel type will burn with a different combustion efficiency, and perhaps flame residence time, depending on the fuel structure (e.g. fine or coarse) and moisture, with smoke from each fuel type (and thus from differing MCE) mixing at any one time, reducing the strength of the bi-modal relationship evident in more homogeneous vegetation covers (a).

clearly show a smaller degree of scatter between trace gas concentrations and CO_2 concentrations.

Due to the aforementioned factors concerning the size and homogeneity of the experimental fire plots, there is a low degree of mixing of flaming and smouldering smoke, leading to high *within-fire* variation in the emission ratio of trace gas concentrations to concentrations of CO_2 (as evident in the large degree of scatter present in the example fire of Fig. 6.12). To account for this, each measurement is characterised by MCE so that measurements with high MCE (>90%) and those with low MCE (<90%) are used separately to calculate emission ratios as demonstrated in Fig. 5.10 of the previous Chapter and following previous distinctions made by Lobert *et al.* (1991); Yokelson *et al.* (1996); and Bertschi *et al.* (2003b). It was also possible to calculate *within-fire* MCE dependent emission ratios using smaller (2%) MCE bins (Figure 6.14). In the example results presented in Figure 6.14, the CH_4/CO_2 emission ratio varies from 0.0034 for smoke emanating from high efficiency burning (94–96% MCE), up to 0.0149 for smoke emanating from lower efficiency burning (80–82% MCE).

Tables 6.2 and 6.3 outline the mean emission ratios for each trace gas species to CO_2 (Table 6.2) and CO (Table 6.3) for each of the vegetation classes, and split by MCE into flaming-dominated smoke (MCE > 90%) and smouldering-dominated smoke (MCE < 90%). For all of the gases investigated (with the exception of C_2H_2 and HCN for the heather-dominated heathland, HH, vegetation class), the emission ratio to CO_2 is greater for the measurements characterised as smouldering, than those characterised as flaming. The preferential production of all gases (except CO_2) during the smouldering phase explains why the emission ratios are higher with low MCE. Only acetylene (C_2H_2) and hydrogen cyanide (HCN) emissions during the heather-dominated heathland fires appear to have higher mean $ERx/_{CO2}$ during the flaming stage of the fire. Both of these gases are pyrolysis products; the windy conditions (with gusts of over 10 m s^{-1} according to an on-site portable weather station) under which the HH fires were conducted may explain the higher $ER_{X/CO2}$ of these gases during the flaming stage, due to transport of the un-oxidised gases downwind, preventing the ignition and consequent oxidation of the gases. Other pyrolysis gases (C_2H_4, C_2H_6) exhibit small mean differences in their $ER_{X/CO2}$ between the flaming and smouldering measurements. This

suggests that emission of these gases is possible through both the transportation of pyrolysis gases during the flaming stage, and from incomplete combustion during the smouldering stage.

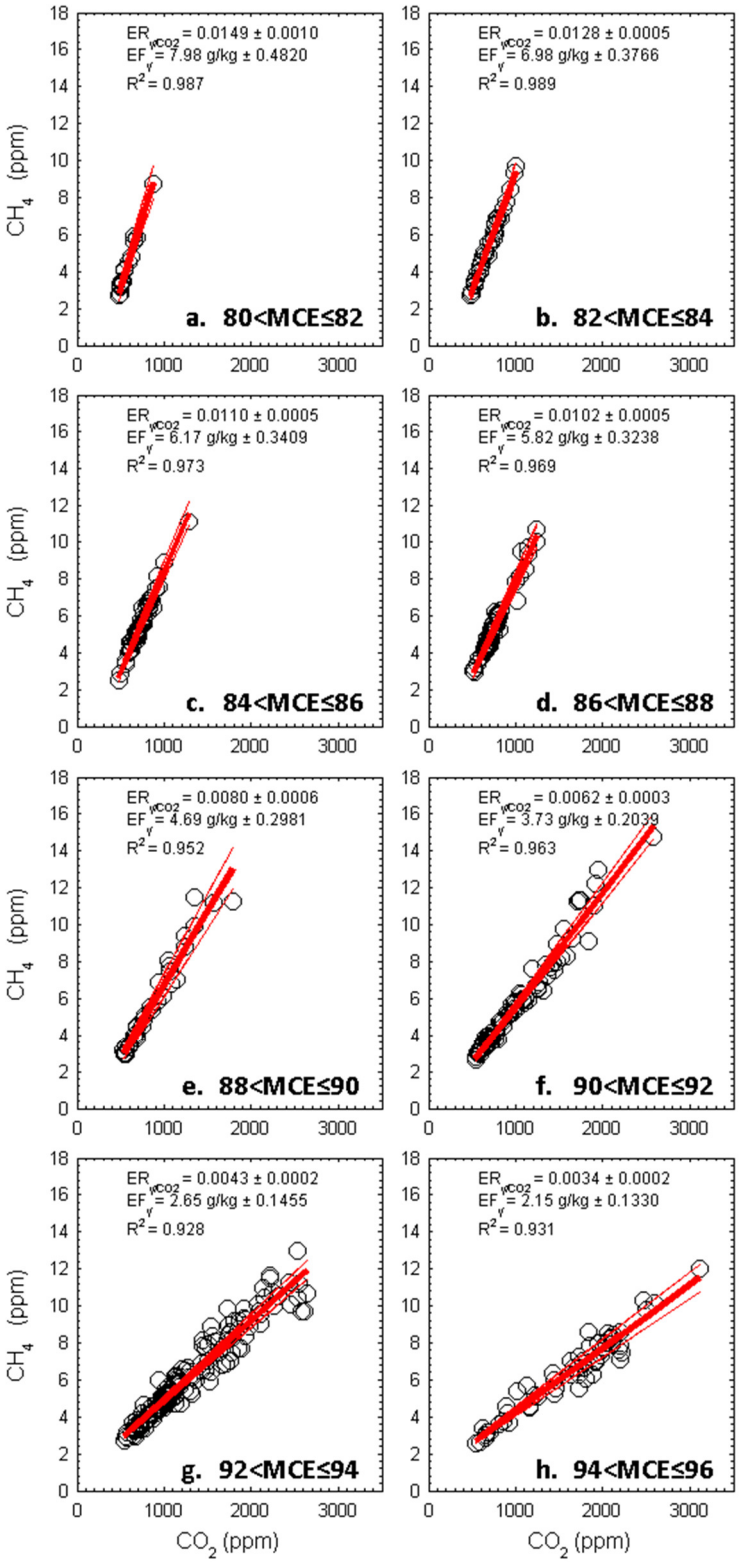

Figure 6.14 Same as the scatter plot presented for CH_4 vs. CO_2 in Figures 6.12 and 6.14a, but each individual scatter plot here (a–h) uses a subset of measurements selected using a small 2% range of MCE (indicated by a red-to-blue colour ramp in previous figures). MCE-dependent emission ratios and emission factors can then be determined. The resultant emission ratio for each MCE range is indicated at the top of each plot along with the retrieved emission factor. For example, the emission ratio for measurements with an MCE between 80% and 82% is 0.0149, with an emission factor of 7.98 g kg^{-1} dry fuel burned, whilst for measurements with a higher MCE (94–96%), the emission ratio is 0.0034, with an emission factor of 2.15 g kg^{-1}.

Table 6.2 Mean emission ratios for compound *X* with respect to CO_2 ($ER_{X/CO2}$) calculated for each heathland vegetation class and listed separately for measurements of predominantly flaming combustion (MCE>90%) and those of predominantly smouldering combustion (MCE<90%). The standard deviations of the emission ratios for each vegetation class are also indicated. In total, 21 heather-dominated heathland (HH) fires were measured, 3 mixed-vegetation heathland (MH) fires were measured, whist only one fire was measured from the gorse-dominated heathland (GH) and bracken-dominated heathland (BH) vegetation classes.

Veg:	**HH**		**MH**		**GH**		**BH**	
Flaming	$ER_{X/CO2}$	SD	$ER_{X/CO2}$	SD	$ER_{X/CO2}$	SD	$ER_{X/CO2}$	SD
CO	**0.0610**	±0.0133	**0.0952**	±0.0084	**0.0889**	-	**0.1010**	-
CH_4	**0.0046**	±0.0016	**0.0082**	±0.0011	**0.0064**	-	**0.0056**	-
C_2H_2	**0.0011**	±0.0003	**0.0006**	±0.0001	**0.0006**	-	**-**	-
C_2H_4	**0.0023**	±0.0008	**0.0023**	±0.0001	**0.0025**	-	**-**	-
C_2H_6	**0.0007**	±0.0007	**0.0002**	±0.0000	**0.0005**	-	**-**	-
HCOOH	**0.0001**	±0.0000	**0.0002**	±0.0000	**0.0002**	-	**-**	-
CH_3OH	**0.0004**	±0.0001	**0.0009**	±0.0000	**0.0010**	-	**-**	-
CH_2O	**0.0014**	±0.0005	**0.0024**	±0.0001	**0.0015**	-	**-**	-
NH_3	**0.0008**	±0.0002	**0.0016**	±0.0007	**0.0031**	-	**-**	-
HCN	**0.0005**	±0.0001	**0.0009**	±0.0000	**0.0012**	-	**-**	-
Smouldering								
CO	**0.1159**	±0.0170	**0.1253**	±0.0032	**0.1191**	-	**0.1214**	-
CH_4	**0.0084**	±0.0028	**0.0116**	±0.0010	**0.0085**	-	**0.0084**	-
C_2H_2	**0.0004**	±0.0002	**0.0013**	±0.0000	**0.0007**	-		-
C_2H_4	**0.0024**	±0.0016	**0.0035**	±0.0011	**0.0030**	-	**0.0013**	-
C_2H_6	**0.0009**	±0.0008	**nr**	-	**0.0007**	-		-
HCOOH	**0.0003**	±0.0003	**0.0002**	±0.0000	**0.0002**	-	**0.0001**	-
CH_3OH	**0.0008**	±0.0003	**0.0012**	±0.0003	**0.0017**	-	**0.0008**	-
CH_2O	**0.0022**	±0.0007	**0.0025**	±0.0007	**0.0023**	-	**0.0028**	-
NH_3	**0.0016**	±0.0008	**0.0022**	±0.0012	**0.0053**	-	**0.0015**	-
HCN	**0.0004**	±0.0001	**0.0019**	±0.0000	**0.0015**	-		-

Table 6.3 Same as Table 6.2, but for mean emission ratios for compound *X* with respect to CO ($ER_{X/CO}$)

Veg:	**HH**		**MH**		**GH**		**BH**	
Flaming	$ER_{X/CO}$	SD	$ER_{X/CO}$	SD	$ER_{X/CO}$	SD	$ER_{X/CO}$	SD
CO_2	**13.90**	±2.38	**10.01**	±0.67	**9.92**	-	**8.87**	-
CH_4	**0.0728**	±0.0135	**0.0818**	±0.0071	**0.0696**	-	**0.0114**	-
C_2H_2	**0.0068**	±0.0064	**0.0041**	±0.0020	**0.0055**	-	**nr**	-
C_2H_4	**0.0274**	±0.0119	**0.0195**	±0.0052	**0.0249**	-	**nr**	-
C_2H_6	**0.0084**	±0.0142	**nr**	-	**0.0062**	-	**0.0022**	-
HCOOH	**0.0016**	±0.0006	**0.0013**	±0.0004	**0.0021**	-	**nr**	-
CH_3OH	**0.0054**	±0.0020	**0.0080**	±0.0029	**0.0141**	-	**0.0043**	-
CH_2O	**0.0199**	±0.0057	**0.0232**	±0.0025	**0.0171**	-	**nr**	-
NH_3	**0.0069**	±0.0034	**0.0146**	±0.0051	**0.0410**	-	**0.0045**	-
HCN	**0.0054**	±0.0026	**0.0050**	±0.0015	**0.0133**	-	**nr**	-
Smouldering								
CO_2	**8.38**	±1.82	**7.53**	±0.11	**8.28**	-	**7.65**	-
CH_4	**0.0778**	±0.0347	**0.0950**	±0.0031	**0.0720**	-	**0.0617**	-
C_2H_2	**0.0036**	±0.0071	**0.0046**	±0.0033	**0.0060**	-	**0.0012**	-
C_2H_4	**0.0230**	±0.0194	**0.0211**	±0.0061	**0.0253**	-	**0.0101**	-
C_2H_6	**nr**	-	**nr**	-	**0.0057**	-	**nr**	-
HCOOH	**0.0022**	±0.0033	**0.0013**	±0.0006	**0.0020**	-	**0.0008**	-
CH_3OH	**0.0057**	±0.0045	**0.0061**	±0.0051	**0.0147**	-	**0.0060**	-
CH_2O	**0.0087**	±0.0375	**0.0233**	±0.0016	**0.0192**	-	**0.0191**	-
NH_3	**0.0131**	±0.0080	**0.0137**	±0.0080	**0.0453**	-	**0.0125**	-
HCN	**0.0037**	±0.0026	**0.0072**	±0.0057	**0.0128**	-	**0.0012**	-

Emission ratios to CO (Table 6.3) are slightly more complex. For the mixed-vegetation heathland (MH), the preferential production of all gases during the smouldering phase, and the associated close correlation between each trace gas and CO, explains why there appears no significant difference in emission ratios to CO between the flaming and smouldering measurements. Yet, for the heather-dominated heathland some gases exhibit large differences in $ER_{X/CO}$ between the flaming and smouldering measurements. These differences may be ascribed to emissions of pyrolysis products during the closely-related (in space and time) flaming phase of the fire. The difference between the preferential production of each gas during the pyrolysis and smouldering phases of the fire relative to the production of CO, which is predominantly emitted during the smouldering phase may explain the variation in $ER_{X/CO}$ (Yokelson *et al.*, 1996). From Table 6.3 it is apparent that pyrolysis gases such as C_2H_2, CH_2O and HCN have greater ER_{CO} during the flaming phase, whilst NH_3 (which is only produced during the smouldering phase, Lobert and Warnatz, 1993) has a greater ER_{CO} during the smouldering phase.

Tables 6.2 and 6.3 also give us an impression of the variability of emission ratios *within* and *between* vegetation classes. Given that measurements were made at different times of year (for example, the MH and BH plots were only measured in the UK Summer, whilst the GH plots and most of the HH plots were measured in the Spring), it is important to try to assess the relative importance of the fuel characteristics, the season of burning, and the burning efficiency on the measured emission ratios. Figures 6.15 and 6.16 include all emissions measurements from the UK fires studied herein, showing the relationship between concentrations of CO_2 and CH_4 (Fig. 6.15), and CO_2 and NH_3 (Fig. 6.16). Each of the subplots (a–c) depict the same data, but the colour of each individual measurement is determined by its MCE (Fig. 6.15a and Fig. 6.16a), time of year (Fig. 6.15b and Fig. 6.16b) and vegetation class (Fig. 6.15c and Fig. 6.16c). As evident in Table 6.2, the variation in emission ratio between vegetation classes is clearly identifiable in Figures 6.15c and 6.16c. Emission ratios of both CH_4 and NH_3 to CO_2 are clearly greater for the MH and BH vegetation classes, and smaller for HH and GH, with the vegetation classes forming distinct clusters of measurements. Determining whether this difference is due to vegetation type or time-of-year is difficult, given that MH and BH vegetation classes were only measured in the summer. Only the heather-dominated

heathland (HH) was measured during both the spring and summer. No significant difference in the emission ratios between the two seasons could be found for HH, suggesting that HH emissions do not depend on the time-of-year, at least for the samples taken here.

Figures 6.15a and 6.16a clearly demonstrate that MCE is a major control on the emission ratio slope, despite differences in the vegetation classes. These figures may also help explain some of the difference in emissions between vegetation classes. As discussed above, measurements of the mixed-vegetation heathland fuel class do not exhibit extreme MCE (dark blue or red points on Fig. 6.15a/6.16a), due to heterogeneity of the plots yielding well-mixed smoke. Measurements of the heather-dominated heathland, however, exhibit a full range of MCE, yielding a full 'envelope' of emission ratios.

An alternative to sub-sampling individual fires by small changes in MCE (as in Figure 6.14) is to take all measurements for a particular vegetation type and take sub-samples from all of the data from all fires (Figure 6.17). Figure 6.17 shows a range of emission ratios calculated for the HH vegetation class. Each emission ratio is calculated from a sub-sample of data that depends on MCE (e.g. the darkest red line was calculated using measurements where $80\% < MCE \leq 82\%$). As was found in the previous Chapter for Australian fuel types, there is a strong relationship between the emission ratio of methane to CO_2 and combustion efficiency, with the slope of the emission ratio decreasing with each 2% increment in MCE. These MCE-dependent emission ratios can then be used to calculate MCE-dependent emission factors, which are typically published alongside whole-fire emission factors in studies of biomass burning (e.g. Yokelson *et al.*, 1997; Christian *et al.*, 2003a; Goode *et al.*, 1999).

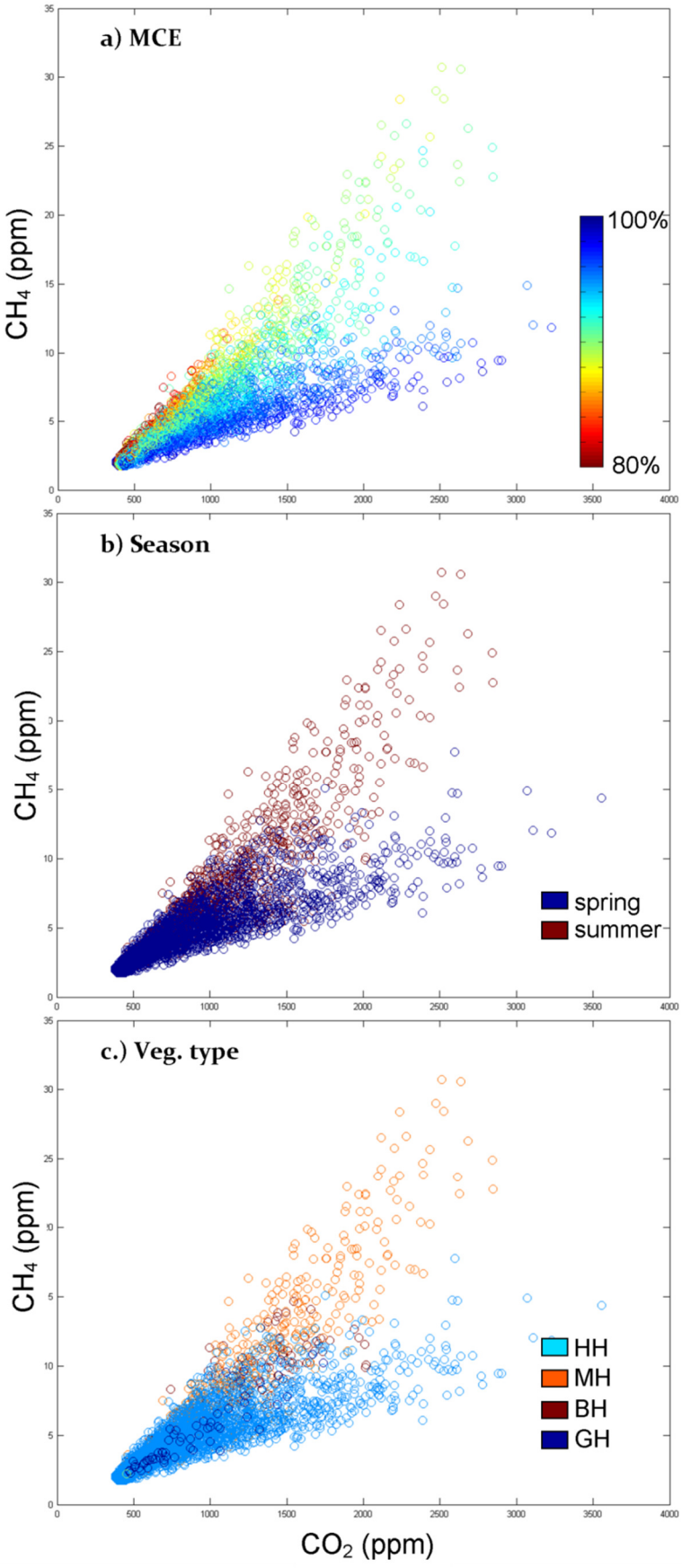

Figure 6.15 Scatter plots of the measured concentrations of CO_2 and CH_4, including all measurements of the heather-dominated heathland experimental fire plots measured during the three UK field campaigns in 2010 and 2011. All three plots shown the same data, but are colour-coded differently using (a) MCE; (b) season of measurement; and (c) vegetation class.

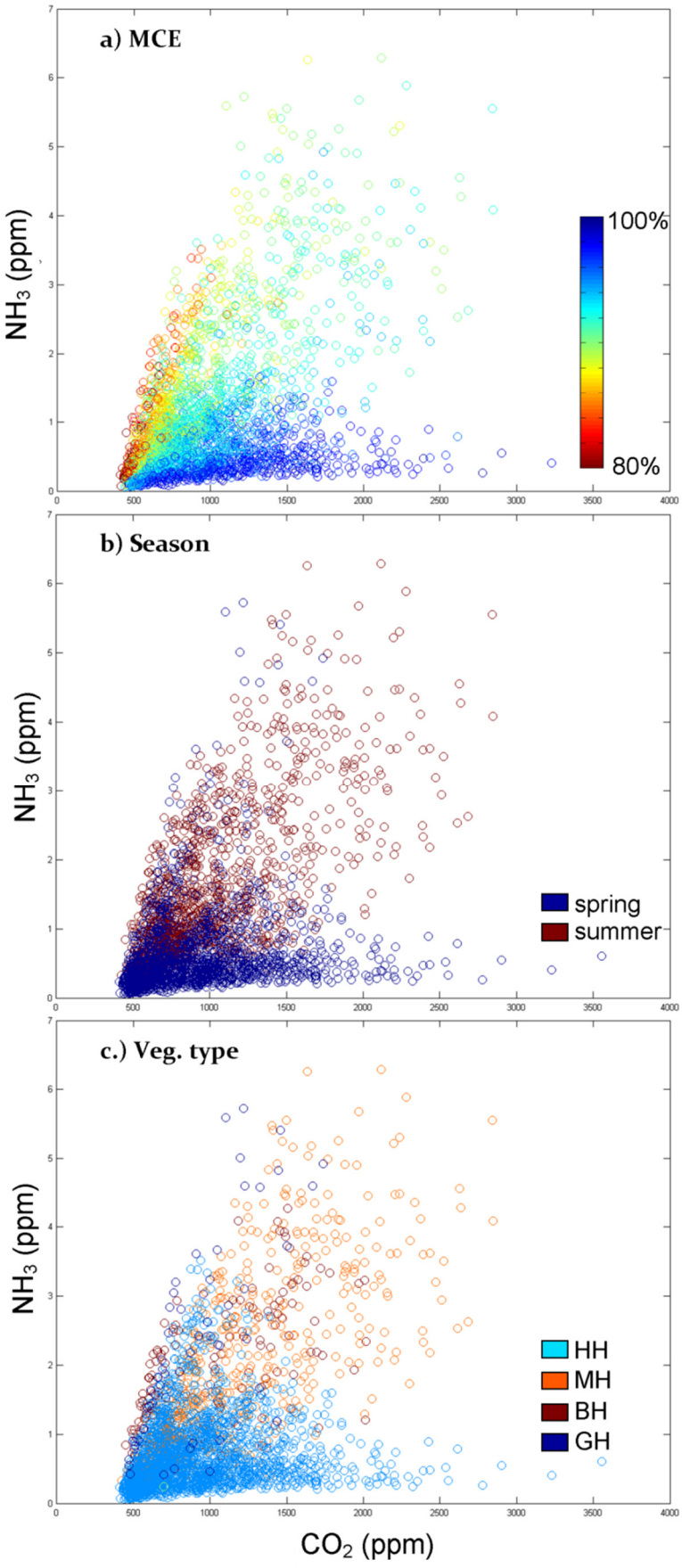

Figure 6.16 Same as Figure 6.15, but for CO_2 vs. NH_3.

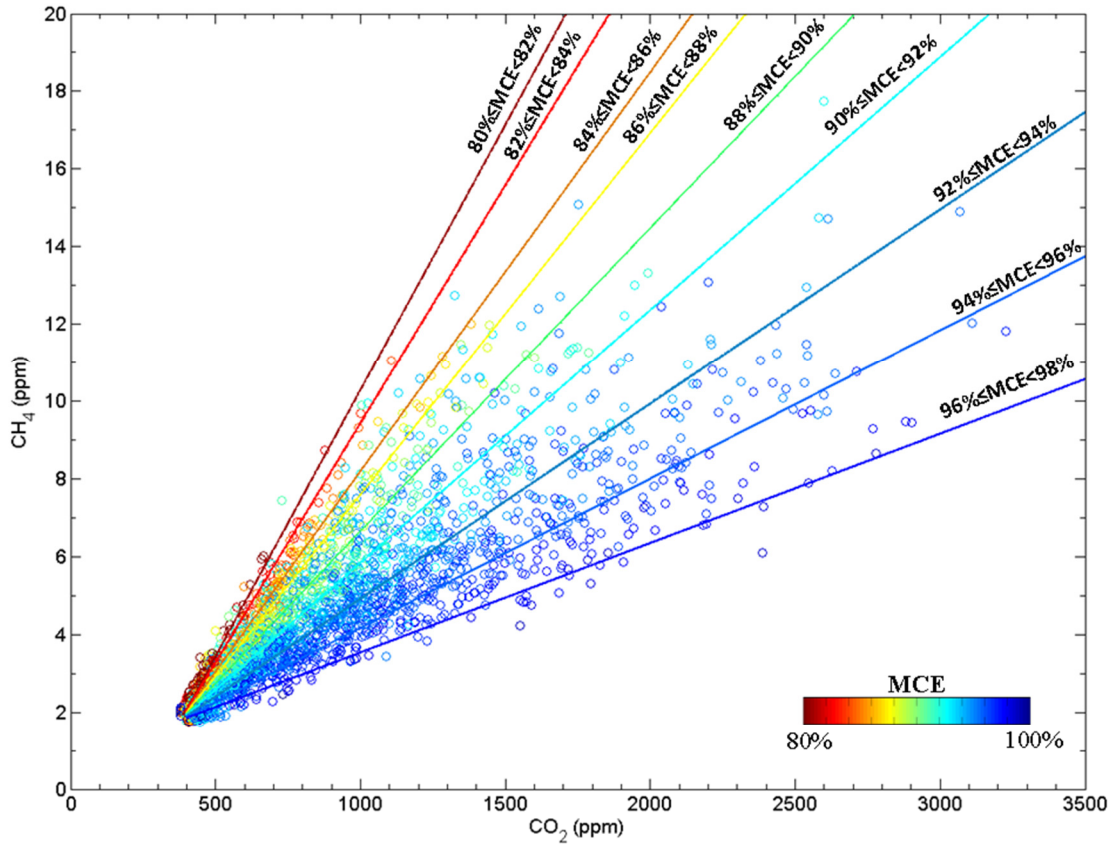

Figure 6.17 As first presented in the previous chapter, regression lines can be calculated using measurements subsampled by narrow (2%) bins of MCE. Each line represents the least squares linear best fir to the subsampled emissions measurements (the MCE bin for each regression line is indicated on the plot). A clear relationship between the slope of the regression lines ($ER_{CH4/CO2}$) and MCE is evident as the slope increases systematically with decreasing MCE.

6.5.1.2 Emission Factors

Little research has been conducted into the relative amount of biomass burnt during flaming and smouldering combustion in heathland vegetation fires. Aerial and tower-mounted thermal imagery of both the HH fires in Northumberland 2010 and at the MH fires in Dorset 2011 indicate that a majority of the thermal emission (>95%) from the heathland fires occurs within the headfire or backing fire, suggesting that these zones are most important for biomass consumption. As with the African savanna fires studied by Wooster *et al.* (2011), the smouldering phase in these fires is responsible for only a small minority of the actual fuel consumption. Two sets of emission factors are presented in Table 6.4, calculated from the 'flaming' and 'smouldering' emission ratios

of Table 6.2 (using the carbon mass balance approach described in Eqns. 3.34 and 3.35). Given that the majority of biomass burned in these heathland fires takes place within the flaming combustion zone (which is also the case for the savanna ecosystem covered in the previous Chapter), the emission factors for flaming measurements should be used for any subsequent total emissions modelling. The smouldering emission factors simply represent those for any residual smouldering combustion (RSC), and are presented in Table 6.4 for comparison. As explained in the previous section covering emission ratios, the higher emission factors for most of the non-CO_2 gas species in the predominantly RSC phase is due to the preferential production of CO and most other trace-gas species during the smouldering combustion phase. Essentially the smouldering phase of combustion in these fuels sees more CO (and most other gases apart from CO_2) released per unit of fuel burned, but since much less fuel is actually consumed in this stage compared to the flaming stages – the actual total emissions budget of all the gases is dominated by the flaming stage.

By combining measurements of trace-gas concentrations from all of the fires measured in the Northumberland and Dorset campaigns, it is possible to build a detailed understanding of the relationship between MCE and emission ratios (as depicted in Figs. 6.15a, 6.16a and 6.17). For trace-gas species that exhibit a strong relationship between their emission ratio to CO_2 ($ER_{X/CO2}$) and MCE, these MCE-dependent emission ratios (as shown in Fig. 6.17) can be used to calculate the relationship between MCE and the emission factor for each particular trace-gas species (Yokelson *et al.*, 1997; Goode *et al.*, 1999; Christian *et al.*, 2003a). Figure 6.18 shows how the emission ratios, such as those shown in Figure 6.17 can be used to calculate the relationship between MCE and the emission factor for CH_4, CH_3OH, NH_3 and HCOOH. A significant relationship between emission factors and MCE for other gases could not be established (the relationship between the emission factor for CO and MCE is nearly perfectly correlated due to the interdependence of EF CO and MCE).

Table 6.5 compares the emission factors for heather-dominated heathland (HH) and mixed-vegetation heathland (MH) with those from extratropical forest and savanna ecosystems (taken from the 2009 updates to the emission factor database of Andreae and Merlet (2001); and those from savanna and temperate forest ecosystems in Akagi *et*

al. [2011]). For HH, there are similarities to savanna emission factors for the climatically important gases CO_2, CO and CH_4, yet emission factors for these gases in MH are significantly different. This difference is likely to be due to the low curing of the vegetation components of the mixed vegetation heathland (e.g. bracken), leading to greater production of CH_4, a phenomenon that is well documented in the burning of African grasslands (e.g. Korontzi, 2005). For other gases, there are significant differences from the established ecosystems listed in Andreae and Merlet (2001) and Akagi *et al.* (2011). The emission factors for both C_2H_2 and C_2H_4 are higher than those for other ecosystems whilst the emission factor for NH_3 is lower than any of those quoted in Andreae and Merlet (2001), although it is similar to savanna ecosystems according to Akagi *et al.* (2011). This is important, given that the UK's National Atmospheric Emissions Database rely upon estimated emission factors from other ecosystems. For NH_3, for example, the NAEI use an emission factor of 2.55±1.3 g kg^{-1} (Dragosits *et al.*, 2009), five-times the emission factor measured here.

Table 6.4 Mean emission factors (g kg^{-1} dry fuel burned) and their standard deviation for each of the vegetation classes measured here. In total, 21 heather-dominated heathland (HH) fires were measured, 3 mixed-vegetation heathland (MH) fires were measured, whist only one fire was measured from the gorse-dominated heathland (GH) and bracken-dominated heathland (BH) vegetation classes.

Veg:	**HH**		**MH**		**GH**		**BH**	
	EF (g kg^{-1})		EF (g kg^{-1})		EF (g kg^{-1})		EF (g kg^{-1})	
Flaming	EF	SD	EF	SD	EF	SD	EF	SD
CO_2	**1711**	±27	**1649**	±20	**1656**	-	**1655**	-
CO	**66.2**	±13.5	**99.8**	±7.6	**93.7**	-	**106.4**	-
CH_4	**2.84**	±0.94	**4.90**	±0.60	**3.85**	-	**3.41**	-
C_2H_2	**1.07**	±0.29	**0.61**	±0.08	**0.62**	-	**nr**	-
C_2H_4	**2.46**	±0.83	**2.37**	±0.08	**2.62**	-	**nr**	-
C_2H_6	**0.47**	±0.46	**0.17**	±0.00	**0.35**	-	**nr**	-
HCOOH	**0.22**	±0.06	**0.27**	±0.06	**0.33**	-	**nr**	-
CH_3OH	**0.46**	±0.13	**1.12**	±0.01	**1.24**	-	**nr**	-
CH_2O	**1.59**	±0.55	**2.73**	±0.10	**1.72**	-	**nr**	-
NH_3	**0.53**	±0.12	**1.04**	±0.42	**2.00**	-	**nr**	-
HCN	**0.52**	±0.11	**0.93**	±0.00	**1.26**	-	**nr**	-
Smouldering								
CO_2	**1619**	±27	**1598**	±16	**1604**	-	**1612**	-
CO	**119.2**	±16.0	**127.4**	±2.4	**121.6**	-	**124.6**	-
CH_4	**4.96**	±1.61	**6.73**	±0.55	**4.96**	-	**4.91**	-
C_2H_2	**0.41**	±0.18	**1.23**	±0.00	**0.69**	-	**nr**	-
C_2H_4	**2.49**	±1.69	**3.56**	±1.12	**3.11**	-	**1.32**	-
C_2H_6	**0.58**	±0.51	**nr**	-	**0.45**	-	**nr**	-
HCOOH	**0.45**	±0.57	**0.36**	±0.05	**0.39**	-	**0.24**	-
CH_3OH	**0.96**	±0.29	**1.42**	±0.40	**2.00**	-	**0.95**	-
CH_2O	**2.44**	±0.77	**2.73**	±0.75	**2.51**	-	**3.11**	-
NH_3	**1.00**	±0.52	**1.34**	±0.74	**3.29**	-	**0.91**	-
HCN	**0.44**	±0.13	**1.81**	±0.00	**1.48**	-	**nr**	-

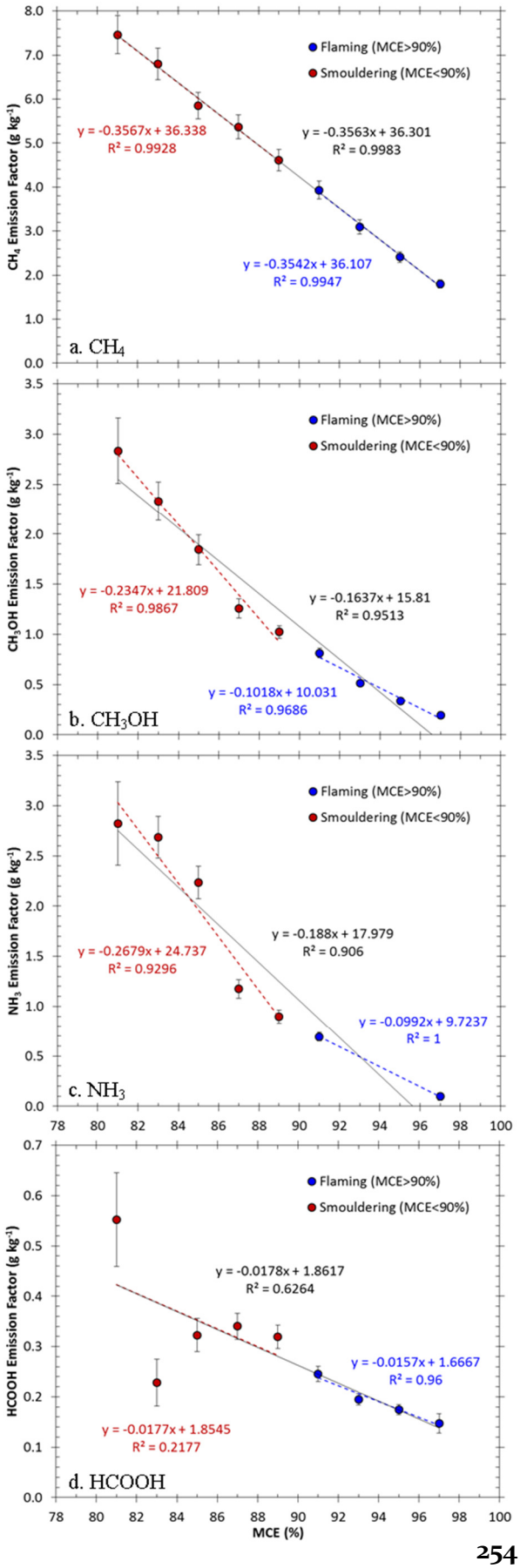

Figure 6.18 The emission factors for (a) CH_4; (b) CH_3OH; (c) NH_3; and (d) HCOOH, calculated using the emission ratios determined from 2%-wide MCE bins (example MCE-dependent emission ratios are shown in Fig. 6.17 for CH_4). The linear least squares regression lines for predominantly flaming (MCE>90%), predominantly smouldering (MCE<90%), and for all measurements are indicated using blue, red, and black lines, respectively.

Table 6.5 Emission factors (g kg^{-1} dry fuel burned) reported by this study for heather-dominated heathlands (HH) and for mixed vegetation heathlands (MH) and those for the same trace gases reported for a selection of ecosystem types in the emission factor databases of Andreae and Merlet (2001, including the 2009 updates) and Akagi et al. (2011). For this study, the mean and standard deviation of the emission factor is calculated from individual fires. The emission factor reported by Andreae and Merlet (2001) is the mean emission factor of all of the contributing studies, and the standard deviation is that of the studies (unless only two studies were used for a particular emission factor, in which case, the uncertainty is represented by a range). The emission factor reported by Akagi et al. (2011) is the mean of the contributing studies, whilst the uncertainty is an indication of the natural variability of the emission factor estimated from the reported variability in the contributing studies.

Veg:	**HH**		**MH**		**ET Forest (AM2001)**		**Savanna (AM2001)**		**Savanna (Ak2011)**		**Temp. Forest (Ak2011)**	
	EF (g kg^{-1})	EF SD	EF (g kg^{-1})	EF SD	EF (g kg^{-1})	EF	EF (g kg^{-1})	EF SD	EF (g kg^{-1})	EF nv	EF (g kg^{-1})	EF nv
CO_2	**1711**	±27	**1649**	±20	**1646**	±39	**1646**	±99	**1686**	±38	**1637**	±71
CO	**66.2**	±13	**99.8**	±7.6	**61**	±16	**61**	±16	**63**	±17	**89**	±32
CH_4	**2.84**	±0.94	**4.90**	±0.60	**2.2**	±1.8	**2.2**	±0.8	**1.94**	±0.85	**3.92**	±2.39
C_2H_2	**1.07**	±0.29	**0.61**	±0.08	**0.27**	±0.20	**0.27**	±0.22	**0.24**	±0.10	**0.29**	±0.10
C_2H_4	**2.46**	±0.83	**2.37**	±0.08	**0.84**	±0.94	**0.84**	±0.46	**0.82**	±0.35	**1.12**	±1.42
C_2H_6	**0.47**	±0.46	**0.17**	±0.00	**0.32**	±0.56	**0.32**	±0.15	**0.66**	±0.41	**1.12**	±0.67
HCOOH	**0.22**	±0.06	**0.27**	±0.06	**0.63**	0.57-0.58	**0.63**	0.62-0.63	**0.21**	±0.10	**0.35**	±0.33
CH_3OH	**0.46**	±0.13	**1.12**	±0.01	**1.47**	-	**1.47**	1.20-1.74	**1.18**	±0.41	**1.93**	±1.38
CH_2O	**1.59**	±0.55	**2.73**	±0.10	**1.71**	1.67-2.76	**1.71**	±0.42	**0.73**	±0.62	**2.27**	±1.13
NH_3	**0.53**	±0.12	**1.04**	±0.42	**0.74**	0.77-1.10	**0.74**	±0.55	**0.52**	±0.35	**0.78**	±0.82
HCN	**0.52**	±0.11	**0.93**	±0.00	**0.23**	0.23-0.66	**0.23**	±0.25	**0.41**	±0.15	**0.41**	±0.19

6.5.2 White cell

In both the Northumberland 2010 campaign and the Dorset campaign, a number of gas samples were collected in Tedlar bags for analysis in the White cell, complementing the OP-FTIR measurements of the same experimental fires. Whilst the OP-FTIR methodology yields a time series of path-averaged concentrations, the i*n situ* sampling method can be used to target particular phases of the fire, facilitating separate measurements of smoke emanating from pyrolysis-, flaming-, and smouldering-phase combustion. In total, 17 Tedlar bag smoke samples were collected and measured in the White cell, with 7 flaming combustion samples, 7 smouldering combustion samples, and 3 samples of pyrolysis products. As described in the methodology (Sect. 6.4.3.2), each smoke sample was first measured for CO_2 and CO concentrations using the calibrated KANE-100 handheld CO_2/CO gas analyser (these concentrations are listed in Table 6.6). After flushing the White cell with clean air, the smoke sample was then introduced into the White cell and the infrared absorption along the White cell path was measured using the FTIR. As each sample is introduced to the cell, the concentrations of smoke trace gases (e.g. CO) rise until the entire sample has been emptied from the Tedlar bag. Figure 6.19 shows a typical measurement, with the rise in smoke trace-gas concentrations, followed by a peak before the White cell is flushed with air. The peak concentrations, as demonstrated in Figure 6.19, are used to calculate the emission ratios for each smoke sample. One clear disadvantage with the Tedlar bag and White cell measurement approach compared to the OP-FTIR methodology is the inability to measure vapour-phase gases that readily adsorb onto the interior surface of the Tedlar bag. Despite being present in the plumes measured by OP-FTIR, NH_3, CH_2O, and HCOOH are therefore absent from the White cell measurements due to adsorption.

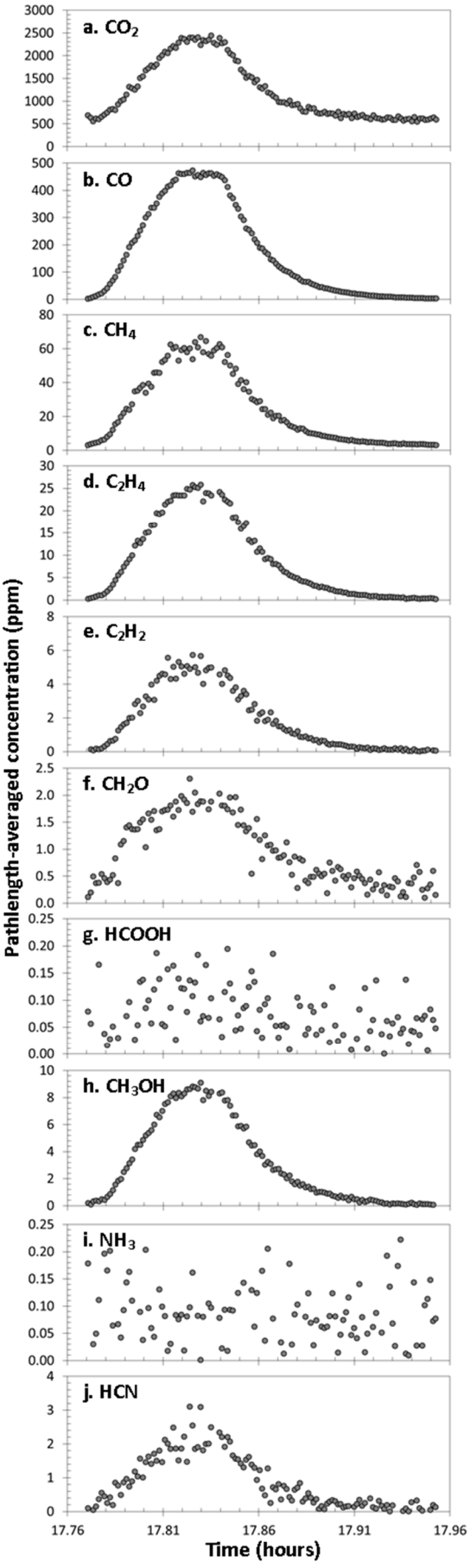

Figure 6.19 Typical time series of retrieved pathlength-averaged concentrations for a White cell sample measurement. The rise in trace-gas concentrations occurs whilst the bag sample is drawn into the semi-evacuated White cell. Once the cell reaches ambient pressure, the trace concentrations plateau. Only these peak concentrations are used to calculated emission ratios for each sample (accounting for ambient air in both the White cell and the original bag sample, using the method described in Section 3.3.4). Concentrations of HCOOH (g) and NH_3 (i) could not be reliably retrieved for any of the bag samples, probably due to adsorption of these gases onto the walls of the bag. Similarly, many of the bag samples exhibited far lower abundances of CH_2O than could be seen in the OP-FTIR data. These gases were excluded from the subsequent calculation of emission ratios and emission factors using the *in situ* bag samples.

Table 6.6 Emission ratios to CO_2 for a range of trace gases ($ER_{X/CO2}$) derived from White cell FTIR measurements of individual *in situ* bag samples of flaming, smouldering and pyrolysis combustion (indicated by '**F**', '**S**', and '**P**', respectively). To calculate emission ratios from the White cell measurements, it was necessary to measure the concentration of CO_2 in each bag sample before mixing with ambient air in the White cell (as described in Section 3.3.4). The concentrations of CO_2 and CO in the bag sample as measured by the KANE-100-1 CO_2/CO gas analyser are also indicated below.

	DOR-HH-1	DOR-MH-1	DOR-MH-1A	DOR-MH-2	DOR-MH-3	NLL-HH-13	NLL-HH-14	DOR-MH-2	BBQ-H	BBQ-B	NLL-HH-2	NLL-HH-13	NLL-HH-14	NLL-HH-15	BBQ-H	BBQ-B	NLL-HH-4
Conc. (ppm)	**F**	**F**	**F**	**F**	**F**	**F**	**F**	**S**	**S**	**S**	**S**	**S**	**S**	**S**	**P**	**P**	**P**
CO_2	5422	9472	4447	9850	3375	5952	5933	2423	6621	9631	4850	5830	5457	4339	4336	6415	4809
CO	282	580	360	860	423	335	507	606	1903	1344	992	1305	1249	1036	835	2419	791
ER_{CO2}																	
CO	0.0627	0.0808	0.1067	0.1127	0.1881	0.0760	0.1106	0.3624	0.2788	0.1566	0.2574	0.2833	0.2683	0.2782	0.2338	0.4217	0.1845
CH_4	0.0035	0.0063	0.0075	0.0094	0.0108	0.0055	0.0092	0.0290	0.0341	0.0132	0.0139	0.0244	0.0276	0.0329	0.0245	0.0260	0.0304
C_2H_2	0.0013	0.0017	0.0016	0.0019	0.0011	0.0020	0.0021	0.0004	0.0030	0.0001	0.0007	0.0017	0.0010	0.0026	0.0046	0.0015	0.0088
C_2H_4	0.0025	0.0031	0.0040	0.0045	0.0023	0.0035	0.0050	0.0052	0.0145	0.0013	0.0031	0.0061	0.0048	0.0086	0.0142	0.0064	0.0129
C_2H_6	0.0002	0.0003	0.0004	0.0004	0.0006	0.0002	0.0006	0.0025	0.0033	0.0021	0.0010	0.0020	0.0025	0.0027	0.0017	0.0019	0.0019
CH_3OH	0.0002	0.0004	0.0008	0.0007	0.0019	0.0003	0.0008	0.0076	0.0051	0.0031	0.0023	0.0042	0.0045	0.0050	0.0034	0.0037	0.0015
HCN	0.0004	0.0009	0.0012	0.0011	0.0004	0.0004	0.0006	0.0022	0.0012	0.0002	0.0007	0.0008	0.0014	0.0014	0.0015	0.0007	0.0024

Table 6.7 Emission factors for a range of trace gases calculated, using the approach described in Section 3.3.3, for each individual *in situ* bag sample using the emission ratios listed in Table 6.6. Each individual bag sample targeted flaming, smouldering, or pyrolysis combustion (these are indicated by '**F**', '**S**' and '**P**', respectively). Mean emission ratios and emission factors are summarised for the flaming, smouldering and pyrolysis samples for the HH and MH vegetation classes in Tables 6.8 and 6.9, respectively.

EF (g kg^{-1})	DOR-HH-1	DOR-MH-1	DOR-MH-1A	DOR-MH-2	DOR-MH-3	NLL-HH-13	NLL-HH-14	DOR-MH-2	BBQ-H	BBQ-B	NLL-HH-2	NLL-HH-13	NLL-HH-14	NLL-HH-15	BBQ-H	BBQ-B	NLL-HH-4
Gas	**F**	**F**	**F**	**F**	**F**	**F**	**F**	**S**	**S**	**S**	**S**	**S**	**S**	**S**	**P**	**P**	**P**
CO_2	1703	1667	1622	1610	1514	1674	1610	1291	1345	1552	1427	1375	1389	1361	1403	1245	1447
CO	68	86	110	116	181	81	113	298	239	155	234	248	237	241	209	334	170
CH_4	2.19	3.84	4.44	5.50	5.98	3.33	5.41	13.65	16.73	7.50	7.23	12.21	13.96	16.31	12.50	11.80	16.03
C_2H_2	1.36	1.69	1.58	1.79	0.97	1.98	2.05	0.33	2.39	0.10	0.63	1.40	0.83	2.09	3.81	1.07	7.57
C_2H_4	2.69	3.25	4.14	4.65	2.23	3.71	5.11	4.28	12.46	1.32	2.81	5.33	4.29	7.50	12.69	5.06	11.87
C_2H_6	0.14	0.20	0.29	0.29	0.40	0.16	0.39	1.33	1.81	1.32	0.58	1.10	1.40	1.51	0.98	0.98	1.10
CH_3OH	0.24	0.44	0.89	0.84	2.12	0.37	0.91	7.19	4.96	3.47	2.42	4.16	4.53	5.01	3.47	3.33	1.54
HCN	0.38	0.92	1.18	1.05	0.36	0.39	0.55	1.72	0.98	0.23	0.63	0.70	1.23	1.21	1.27	0.52	2.17

6.5.2.1 Emission ratios

Emission ratios were calculated from the White cell trace-gas concentrations using Eqns. 3.38 to 3.45, accounting for both the dilution of the smoke sample within the ambient air of the White cell, and the ambient air in the field during sample collection. Tables 6.6 and 6.7 present the emission ratios and factors for individual smoke samples, whilst Table 6.8 and Table 6.9 summarise the mean emission ratios for the flaming, smouldering and pyrolysis samples for the HH and MH vegetation classes, respectively.

Table 6.8 Mean emission ratios to CO_2 ($ER_{X/CO2}$) and emission factors (g kg^{-1} dry fuel burned) calculated from the individual bag samples for the heather-dominated heathland vegetation class (HH, as individually listed in Tables 6.6 and 6.7).

	$ER_{X/CO2}$		
	Flaming	**Smouldering**	**Pyrolysis**
CO	0.0831 ±0.0247	0.2732 ±0.0104	0.2092 -
CH_4	0.0036 ±0.0013	0.0074 ±0.0045	0.0135 -
C_2H_2	0.0061 ±0.0029	0.0266 ±0.0081	0.0274 -
C_2H_4	0.0018 ±0.0004	0.0018 ±0.0010	0.0067 -
C_2H_6	0.0004 ±0.0003	0.0042 ±0.0011	0.0024 -
CH_3OH	0.0004 ±0.0001	0.0011 ±0.0003	0.0020 -
HCN	0.0003 ±0.0002	0.0023 ±0.0009	0.0018 -
	EF (g kg^{-1})		
CO_2	1663 ±48	1379 ±31	1425 -
CO	87 ±23.4	240 ±5.3	189 -
CH_4	3.64 ±1.63	13.29 ±3.85	14.27 -
C_2H_2	1.80 ±0.38	1.47 ±0.77	5.69 -
C_2H_4	3.84 ±1.21	6.48 ±3.76	12.28 -
C_2H_6	0.23 ±0.14	1.28 ±0.46	1.04 -
CH_3OH	0.51 ±0.35	4.21 ±1.06	2.50 -
HCN	0.44 ±0.10	0.95 ±0.28	1.72 -

Table 6.9 Same as Table 6.8, but for the mixed-vegetation heathland (MH) vegetation class.

$ER_{X/CO2}$	**Flaming**	$ER_{X/CO2}$ **Smouldering**	**Pyrolysis**
CO	0.1221 ±0.0461	0.2595 -	0.4217 -
CH_4	0.0035 ±0.0010	0.0033 -	0.0064 -
C_2H_2	0.0085 ±0.0020	0.0211 -	0.0260 -
C_2H_4	0.0016 ±0.0003	0.0003 -	0.0015 -
C_2H_6	0.0009 ±0.0007	0.0054 -	0.0037 -
CH_3OH	0.0009 ±0.0003	0.0012 -	0.0007 -
HCN	0.0005 ±0.0001	0.0023 -	0.0019 -
		EF (g kg^{-1})	
CO_2	1603 ±65	1422 -	1245 -
CO	123 ±40.8	226 -	334 -
CH_4	4.94 ±0.98	10.58 -	11.80 -
C_2H_2	1.51 ±0.37	0.22 -	1.07 -
C_2H_4	3.57 ±1.06	2.80 -	5.06 -
C_2H_6	0.29 ±0.08	1.33 -	0.98 -
CH_3OH	1.07 ±0.73	5.33 -	3.33 -
HCN	0.88 ±0.36	0.98 -	0.52 -

Compared with the OP-FTIR CO_2 emission ratios, the Tedlar bag samples exhibit a much greater difference between the flaming and smouldering measurements. Flaming CO_2 emission ratios from the OP-FTIR measurements and from the Tedlar bag samples are similar, with the mean emission ratios from both measurement types having overlapping standard deviations for most of the gas species investigated (apart from C_2H_2 for HH, and CH_4, C_2H_2 and HCN for MH). This is encouraging, suggesting that the 90% MCE threshold (identified from previous studies) for classifying OP-FTIR measurements as 'flaming' is a good approximation for flaming emissions. Whilst C_2H_2 flaming emission ratios to CO_2 were higher for both vegetation classes, this could be due to the inadvertent sampling of pyrolysis products that may have resulted from sampling at close proximity to the flames. Smouldering CO_2 emission ratios were far greater for the Tedlar bag samples than for the OP-FTIR measurements classified as 'smouldering' (MCE<90%). This is not surprising, as the Tedlar bag sampling targeted purely residual smouldering combustion (where smoke was only sampled in the absence of flames, as can be seen in Fig. 6.9), whereas the majority of the smoke in the OP-FTIR measurements classified as 'smouldering' would have been a mixture of smoke from both flaming and smouldering combustion.

Figure 6.20 amalgamates the results from all of the OP-FTIR measurements (individual points in the scatter plots, coloured by MCE) with the emission ratios calculated from the Tedlar bag samples in the White cell (blue, red and black lines representing the flaming, smouldering and pyrolysis samples, respectively). As was evident in the mean CO_2 emission ratios of Tables 6.8 and 6.9, the majority of the flaming Tedlar bag samples (blue lines in Fig. 6.20) lie within the envelope of OP-FTIR results, towards the higher MCE (blue circles) measurements. For CO and CH_4, a small number of OP-FTIR measurements with particularly high MCE appear to have a lower emission ratio to CO_2 then the Tedlar bag samples. This is further evidence that the OP-FTIR methodology can capture the full suite of emissions from a particular ecosystem, whilst the bag sampling is limited by the number of samples and sampling conditions (smoke with a very high MCE might be difficult to sample using the bag methodology due to high intensities that characterise such activity, making it more difficult to approach and collect samples). Conversely, many of the emission ratios determined from the smouldering bag samples lie significantly beyond the OP-FTIR measurements. As

explained above, this is due to the sampling technique of targeting RSC. The OP-FTIR methodology does not effectively measure RSC due to the low level of smoke production from this phase of the fire (only a small proportion of the FTIR path may be filled by residual smouldering smoke at any one time). Clearly the bag sampling approach appears a more effective method for measuring RSC emissions; however, the relative amount of biomass consumed by this phase of the fire is small, rendering these emission ratios and resultant emission factors largely insignificant when calculating the entire emissions budget, at least in ecosystems dominated by fine fuel combustion (Wooster *et al.*, 2011).

6.5.2.2 Emission factors

The emission factors calculated for each of the individual *in situ* samples are listed in Table 6.7, whilst the mean emission factors for the heather-dominated heathland (HH) samples and mixed-vegetation heathland (MH) samples are summarised in Tables 6.8 and 6.9 respectively. When compared to the OP-FTIR derived emission factors (Figure 6.21), the emission factors for the flaming combustion samples agree well with those derived from the OP-FTIR measurements, a similar pattern to that evident in the emission ratio plots (Figure 6.20). The standard deviations of the 'flaming' emission factors derived from the *in situ* bag sample measurements overlap with those derived from the OP-FTIR for all gases, except C_2H_2 for which emission factors are consistently higher in the bag samples (the C_2H_4 emission factor is also systematically higher in the bag samples, although the standard deviation does overlap with the OP-FTIR emission factor). The higher abundance of C_2H_2 and C_2H_4 in the bag samples might be due to inadvertent sampling of incomplete combustion products (i.e. pyrolysis stage emissions); C_2H_2 and C_2H_4 are both produced during pyrolysis (Burling *et al.*, 2010).

As predicted by the disparity between the smouldering emission ratios measured for the *in situ* bag samples and those derived from the OP-FTIR data, the emission factors for all of the non-CO_2 gases for the bag samples are far greater than those for the OP-FTIR data. As explained above, this disparity is due to the inability of the OP-FTIR methodology to effectively measure "pure" residual smouldering combustion; the OP-FTIR measurements classified as predominantly smouldering contain some influence from flaming emissions.

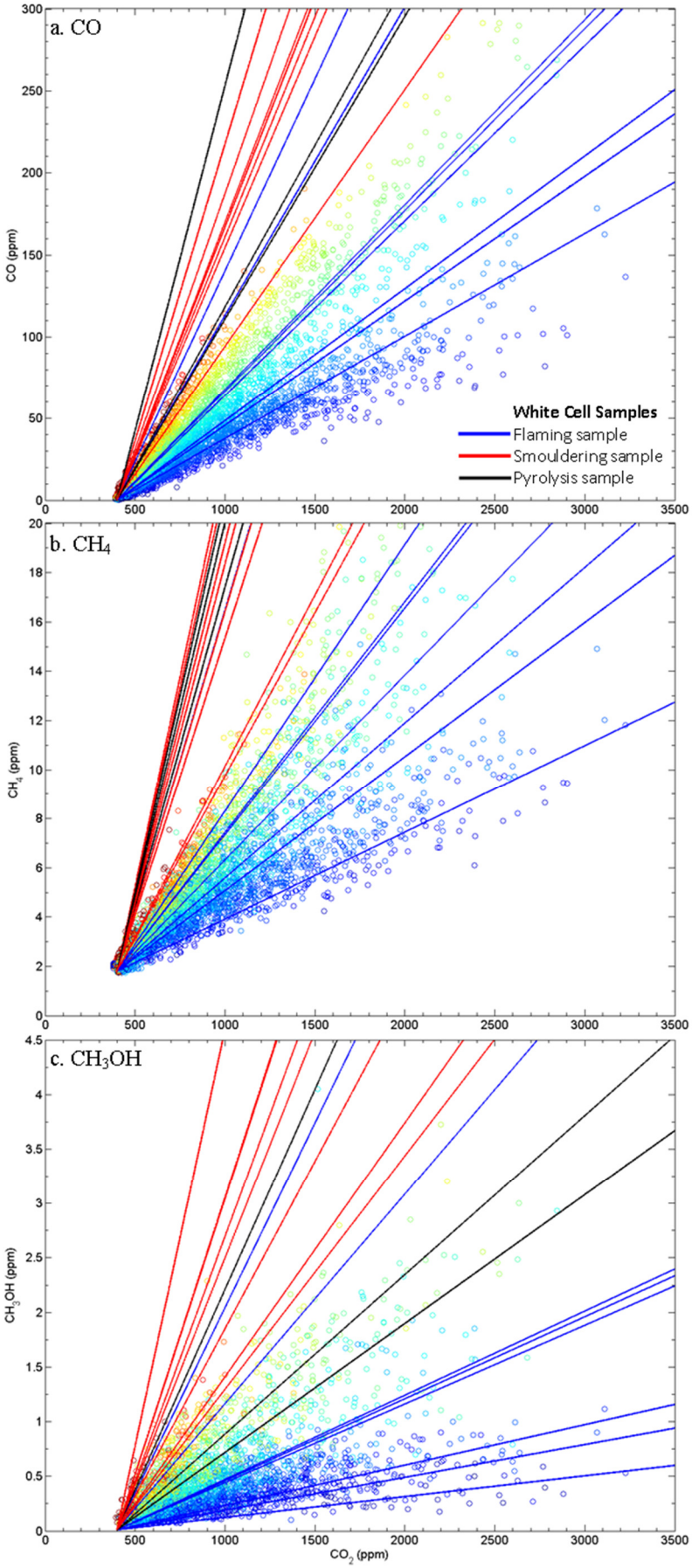

Figure 6.20 These scatter plots illustrate all of the measurements made using OP-FTIR at each of the 21 heather-dominated heathland fires and the 3 mixed-vegetation heathland fires (small circles colour-coded by MCE as in Figure 6.17). Overlaying the OP-FTIR data are lines used to represent the emission ratios derived from the *in situ* bag samples taken during the *HH* and *MH* experimental fires. The blue lines indicate samples that were collected during the flaming stage of the fire; the red lines indicated samples of residual smouldering combustion (RSC); whilst the black lines indicate samples collected from pyrolysis combustion. This is repeated for (a) CO; (b) CH_4; (c) CH_3OH; (d) C_2H_2; (e) C_2H_4; and (f) HCN. For most of these trace gases, the *in situ* bag samples of flaming combustion exhibit similar emission ratios to those present in the OP-FTIR data. The *in situ* bag sample measurements of smouldering combustion, however, appear to have mostly higher emission ratios than those for the OP-FTIR data. This is due to the targeted sampling of RSC for the *in situ* samples, whilst the smoke sampled by the OP-FTIR consisted of predominantly smouldering smoke, but mixed with some smoke from flaming combustion.

Figure 6.20 (continued)

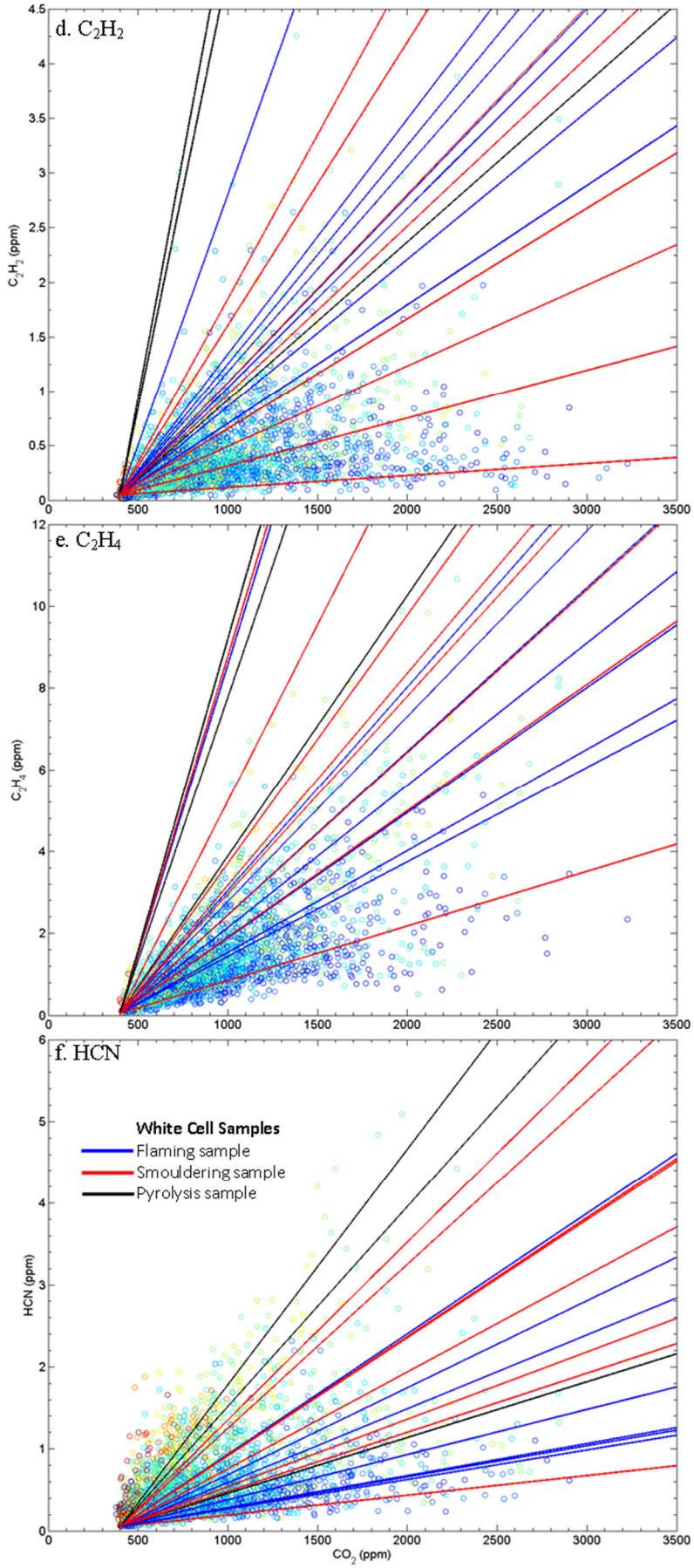

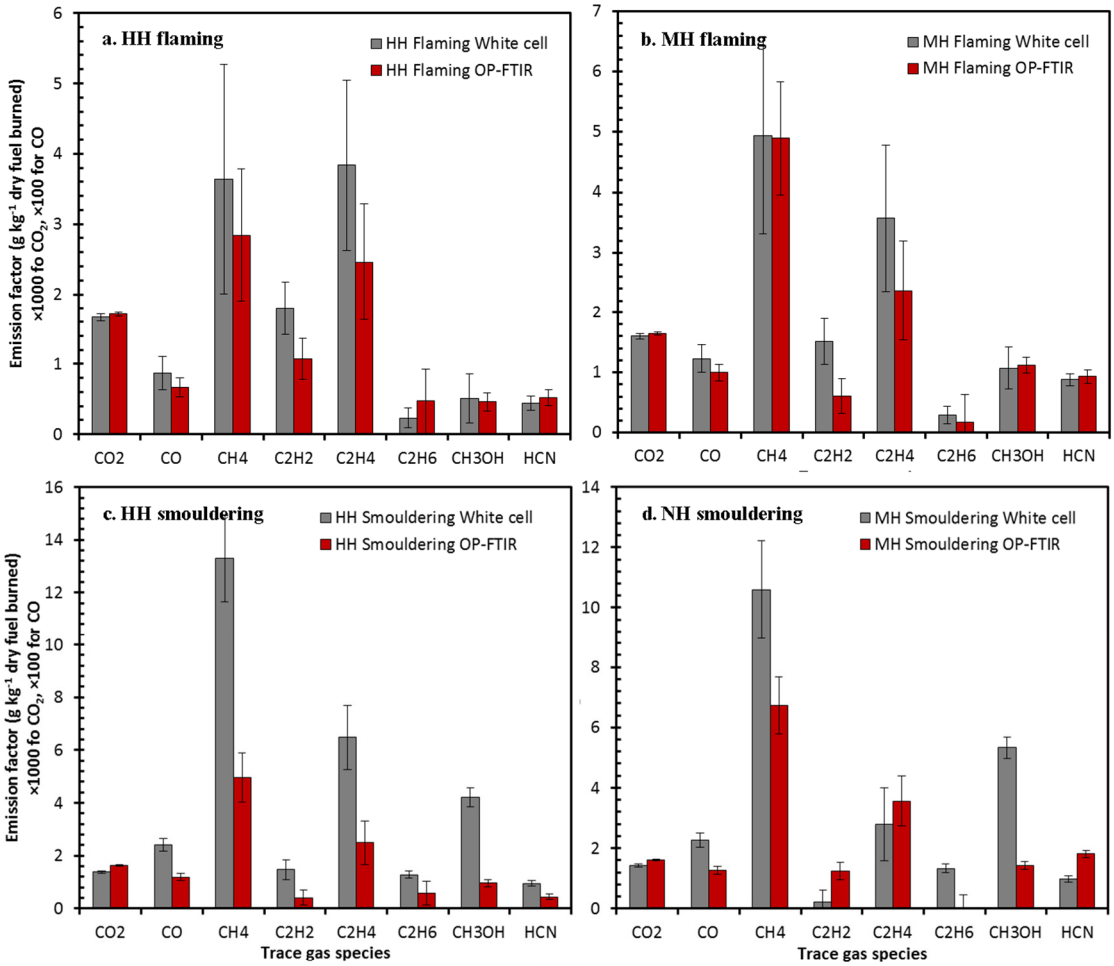

Figure 6.21 Comparison of mean emission factors (g kg^{-1}) for flaming and smouldering emissions from the heather-dominated heathland (HH) and mixed-vegetation heathland vegetation classes derived from the White cell FTIR measurements of *in situ* bag samples and those derived from the OP-FTIR spectra. The mean and standard deviation of the White cell emission factors is calculated from the individual bag samples, whilst the mean and standard deviation of the OP-FTIR emission factors is calculated from each of the individual fires measured using OP-FTIR. The emission factors for CO_2 and CO are adjusted by a scaling factor for comparison with the other trace gases.

6.5.3 MCE from CO_2/CO gas analyser

Many trace gas emission factors have been shown to be related to MCE (Figure 6.18 in this Chapter, and Figure 5.15 in the previous Chapter, as well as in a number of other previous studies (Yokelson *et al.*, 1997; Goode *et al.*, 1999; Christian *et al.*, 2003a)). Potentially, low-cost and compact CO_2/CO gas analysers (such as the KANE-100-1 used to measure the *in situ* bag samples in this Chapter) could be used to measure CO_2 and CO concentrations when other more sophisticated methodologies are unavailable.

The MCE retrieved from the CO_2 and CO measurements could be used to predict emissions of other gases if their relationship to MCE for a particular vegetation type was known. In a simple test of the accuracy of the handheld CO_2/CO analyser, Figure 6.22 compares the emission ratio of CO to CO_2 ($ER_{CO/CO2}$) calculated using the handheld analyser measurements of the *in situ* bag samples (Table 6.6) with the $ER_{CO/CO2}$ for the same samples derived from the FTIR spectra collected in the White cell. The strong agreement between the handheld instrument and the measurements using the FTIR spectrometer (Figure 6.22) is encouraging and suggests that handheld analysers could be used to calculate MCE, which itself could act as a proxy for emissions of other gases (such as CH_4, NH_3, CH_3OH, HCN) through relationships established elsewhere between MCE and the emission factors of these gases (e.g. Yokelson *et al.*, 1997; Goode *et al.*, 1999; Christian *et al.*, 2003a; and in Sections 5.5.1 and 6.5.1 of this thesis).

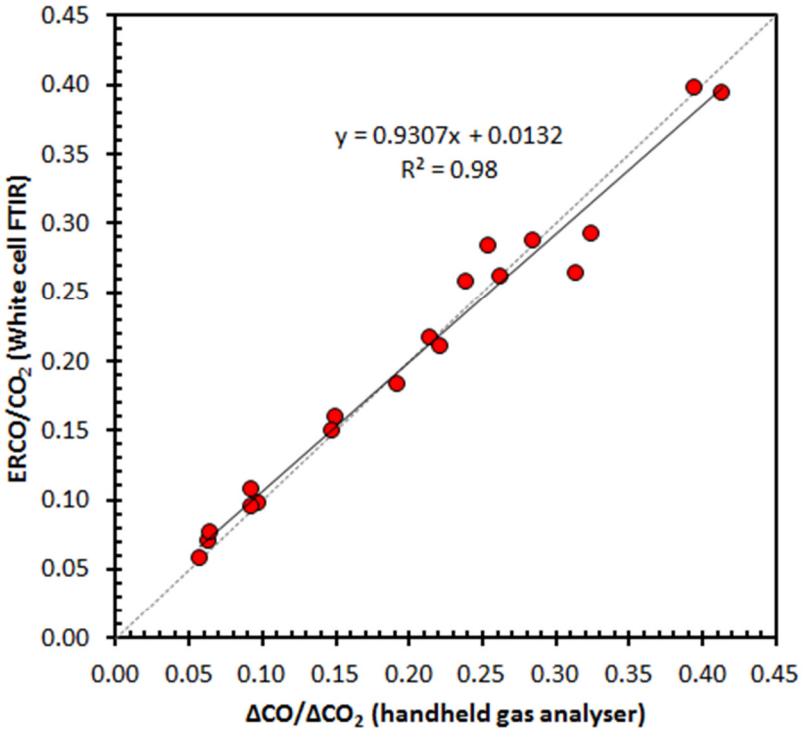

Figure 6.22 Comparison of $ER_{CO/CO2}$ determined from handheld gas analyser measurements of the *in situ* bag samples with $ER_{CO/CO2}$ retrieved from the FTIR measurements of the same *in situ* bag samples in the White cell.

6.5.4 Fuel loads and combustion completeness

The mean fuel load (including heather, litter and mosses) measured using destructive sampling (Harris *et al.*, 2011) at the Northumberland plots was 3.22 kg m^{-2} with a standard deviation of 0.81 kg m^{-2}. Statistics summarising the measured fuel loads are presented in the box plots of Figure 6.23, where measurements from the Northumberland campaigns are compared with previous research performed by the University of Liverpool (K. Allen, R. Marrs, and M. Harris, personal communication) at Howden Moor in the Peak District National Park (UK) and by Legg *et al.* (2010) at Crubenmore Estate in the Cairngorms National Park (UK). Legg *et al.* (2010) classify their measurements by fuel category determined by the growth stage of the heather (building, late building, mature). According to the relationship between the fuel category and canopy height for each fire site in Legg *et al.* (2010), the Northumberland canopy heights mostly fall into the "late building" category; the fuel loads measured in Northumberland agree well with those from Legg *et al.* (2010) for the same fuel category. The measurements at Howden Moor, however, were of a range of fuel categories (building, late building and mature). Despite this, the fuel loads at Howden Moor are substantially smaller than those measured for the Northumberland campaigns presented here, and those measured by Legg *et al.* (2010) in the Cairngorms. Both the Northumberland measurements presented here and those in Legg *et al.* (2010) include heather, "fine fuels", "litter" and "mosses" in the fuel load calculations; the Howden Moor measurements simply refer to "all biomass". It must therefore be assumed that the variability presented is Figure 6.23 is real and that this variability in heathland fuel loads needs to be accounted for in the total emissions calculations presented in Section 6.6.

The mean combustion completeness measured at the Northumberland plots was 57.4% with a standard deviation of 15.3%. Summary statistics for the Northumberland measurements and those performed at Howden Moor (K. Allen, R. Marrs, and M. Harris, personal communication) and at Crubenmore Estate (Legg *et al.*, 2010) are presented in Figure 6.24. Whilst the Northumberland measurements of combustion completeness agree with those made at Howden Moor, the combustion completeness is somewhat higher than that published in Legg *et al.*, (2010), where the combustion

completeness of the "late building" sites averages 34.2% with a standard deviation of 2%. It must also be assumed that this range of combustion completeness is within the natural variability of heathlands; this variability must also be accounted for in any estimate of total emissions from heathland burning.

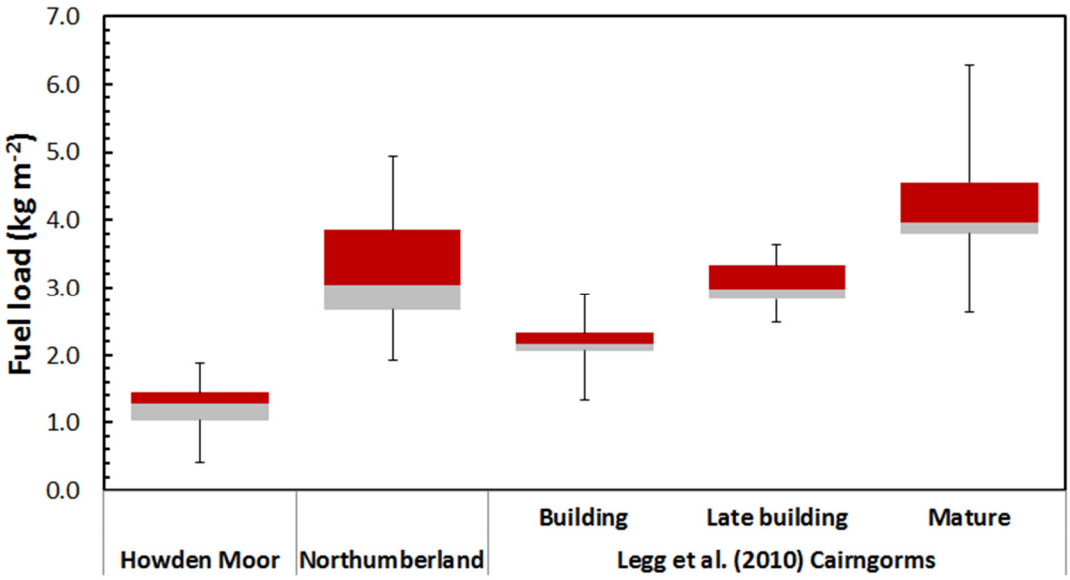

Figure 6.23 Fuel load (kg m^{-2}) measured at the Northumberland campaigns (n=35) covered by this Chapter compared with fuel loads measured at other heathland sites in the UK. These include measurements were made at Howden Moor (n=30) in the Peak District National Park (K. Allen, R. Marrs, and M. Harris, personal communication) and those published in Legg *et al.* (2010) measured in the Cairngorms National Park (n=26).

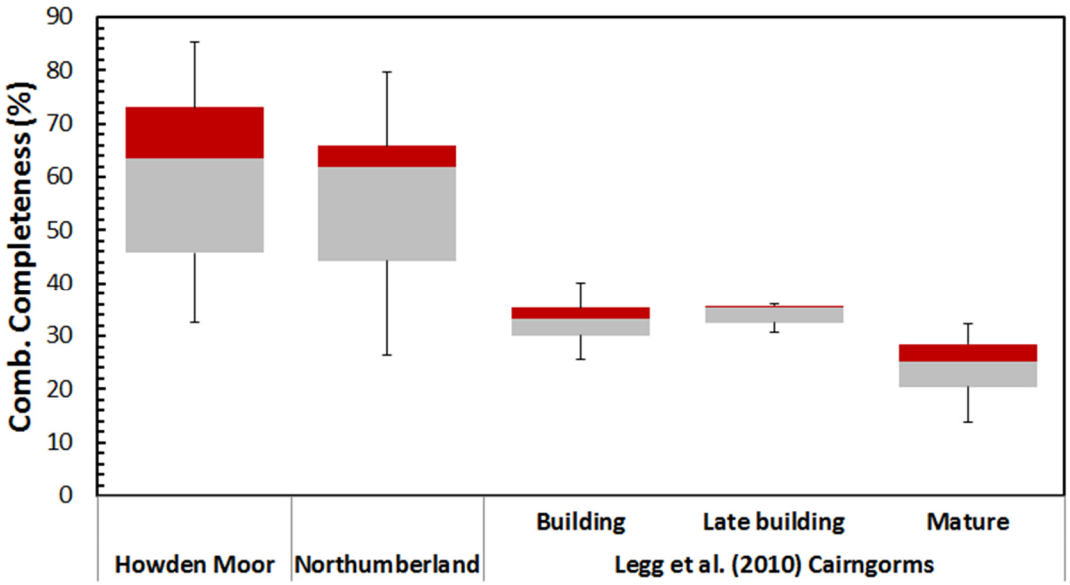

Figure 6.24 Same as Figure 6.23, but for combustion completeness

6.6 Total emissions modelling for UK heathlands

Previous attempts to estimate total emissions of specific trace gas species from biomass burning in the UK have relied upon best-guess estimates of the relationship between that available fuel and the amount of a particular trace gas released per unit mass of fuel burned, in a report for the UK's National Atmospheric Emissions Inventory covering non-agricultural NH_3 emissions for 2007, Dragosits *et al.* (2009, p.7) state that:

> *"As there are no data available from specific measurements of emissions from heather burning, the estimates have to be based on the available fuel"*

The report estimates that controlled heather burning emits 2.1 g NH_3-N per square metre of burnt heather (with a range of 0.95–3.89 g NH_3-N m^{-2}) using published emission factors for other ecosystems. It is possible to convert this unit into an NH_3 emission factor (g NH_3 kg^{-1} dry fuel burned) if we know the assumed fuel load (kg m^{-2}). The ancillary data to the NAEI report (U. Dragosits, personal communication) reveals that the assumed fuel load is 1±0.5 kg m^{-2}. The best estimate NH_3 emission factor used by the NAEI can therefore be calculated as 2.55 g NH_3 kg^{-1} dry fuel burned (2.1 g NH_3-N kg^{-1} dry fuel burned). As mentioned earlier, this is substantially higher than the NH_3 emission factor presented in this Chapter for heather-dominated heathland. Furthermore, recent studies of heathland fuel loads (Legg *et al.*, 2010; and those presented in Figure 6.23 of this Chapter) suggest that fuel loads are higher than those used in the NAEI report. This Section attempts to update the emissions estimates for biomass burning in the NAEI, for NH_3 and the other gases covered by this Chapter. Total emissions of trace gas species x (E_x) are calculated using a modified form of Equation 2.13 (Seiler and Crutzen, 1980):

$$E_x = A \times B \times \alpha \times EF_x \qquad (6.1)$$

Where the emissions of trace gas species x (E_x, g) is equal to the product of burned area (A, m^2), fuel load (kg m^{-2}), combustion completeness (unitless fraction), and the emission factor of trace gas species x (EF_x) as listed in Table 6.4.

6.6.1 Burned area

Since the ban on field burning of cereal straw and stubble in England and Wales, and strong discouragement of this practice in Scotland and Northern Ireland (NetRegs.org.uk, 2012), emissions from controlled biomass burning in the UK are now assumed to be dominated by the burning of heather moorlands (Dragosits *et al.*, 2009).

According to an aerial photography survey of 7.5% of Scotland, around 20% of the Scottish moorlands appeared to be regularly burned (or 3% of the total land area of Scotland), equivalent to ~2,400 km^2 (Moorland Working Group, 2002), assuming a burning frequency of 15 years, this amounts to a total annual burned area of ~160 km^2 in Scotland. In an aerial photography survey covering 2% of England's land area, Yallop *et al.* (2006) estimate that 114 km^2 of English moorlands are burned each year. No estimates of burned area could be found for Wales or Northern Ireland.

Given the lack of burned area data for Wales and Northern Ireland, and the reliance on knowledge of burning frequency (which can be highly variable according to Dragosits *et al.* (2009)) to estimate annual burned area in Scotland, it is necessary to use a substantial uncertainty range for burned area. Dragosits *et al.* (2009) assume an annual burned area of 200 km^2, with an uncertainty range of 120–360 km^2. Here, UK burned area is assumed to be the sum of the Scottish and English estimates of the Moorland Working Group (2002) and Yallop *et al.* (2006) (274 km^2) with an uncertainty estimate of ±50% (274±137 km^2).

6.6.2 Fuel load

As shown in Section 6.5.4, fuel loads are highly variable and depend upon the growth stage of the heather when burned. Here, the mean fuel load of all available measurements (Figure 6.23) is used (2.53 kg m^{-2}), with an estimate of uncertainty based on the standard deviation of all measurements (1.22 kg m^{-2}). This estimate is substantially larger than that used in the NAEI (Dragosits *et al.*, 2009) which assumes a fuel load of 1 kg m^{-2}, although this does not appear to be based on published fuel loads.

6.6.3 Combustion completeness

As is the case for fuel load, measured combustion completeness varies substantially within and between studies (Figure 6.24). Here, the mean combustion completeness calculated from all available measurements is used (49.4%), with an estimate of uncertainty based on the standard deviation of all measurements (19.5%).

6.6.4 Emission factors

Given that it is assumed that the majority of controlled biomass burning in the UK occurs on heather-dominated heathlands, the emission factors for this vegetation class, listed in Table 6.4, are used for the total emissions calculations. Two scenarios are used for assigning emission factors to the total emissions calculations. The first approach uses the "flaming" emission factors listed in Table 6.4 under the assumption that the majority of fuel is combusted in the flaming phase of the fire (i.e. when MCE is greater than 90%). The second approach assumes some modest 20% contribution to total emissions from the smouldering phase (here the weighted average of the "flaming" and "smouldering" emission factors are used). The emission factors and their associated uncertainties for these two scenarios are listed in Table 6.10.

Table 6.10 Emission factors (g kg^{-1} fuel burned) used for the calculation of total emissions from UK controlled biomass burning. Emission factors for Scenario 1 are taken directly from this Chapter's results presented in Table 6.4 and assume that the vast majority of the fuel is burned when the MCE is greater than 90%. Scenario 2 is a weighted average of the "flaming" and "smouldering" emission factors presented in Table 6.4, and assumes a modest 20% contribution to total emissions from smouldering combustion (MCE<90%).

	Scenario 1 EF (g kg^{-1})		**Scenario 2** EF (g kg^{-1})	
	EF	SD	EF	SD
CO_2	**1711**	± 27	**1693**	± 27
CO	**66.2**	± 13.5	**76.8**	± 14
CH_4	**2.84**	± 0.94	**3.26**	± 1.07
C_2H_2	**1.07**	± 0.29	**0.94**	± 0.27
C_2H_4	**2.46**	± 0.83	**2.47**	± 1.00
C_2H_6	**0.47**	± 0.46	**0.49**	± 0.47
HCOOH	**0.22**	± 0.06	**0.27**	± 0.16
CH_3OH	**0.46**	± 0.13	**0.56**	± 0.16
CH_2O	**1.59**	± 0.55	**1.76**	± 0.59
NH_3	**0.53**	± 0.12	**0.62**	± 0.20
HCN	**0.52**	± 0.11	**0.50**	± 0.11

6.6.5 Total emissions from UK controlled biomass burning

The parameters outlined throughout the previous sections were used as coefficients in Equation 6.1 to calculate total emissions (in metric kilotonnes, kt, equivalent to 1 gigagram, Gg) for each of the trace gases outlined in Table 6.10. Table 6.11 presents the results of this calculation, and thus represents the first emissions inventory for controlled biomass burning calculated using *measured*, rather than "*best-guess*" emission factors for the heather-dominated moorland ecosystem.

The total emissions of CO_2, CO, CH_4, NMVOCs (the summed total of C_2H_2, C_2H_4, $C2H_6$, HCOOH, CH_3OH, CH_2O) and NH_3 from controlled biomass burning emissions in the UK are compared with estimates of total emissions of these gases from all biomass burning activity (including agricultural waste burning) from the Emission Database for Global Atmospheric Research (EDGAR), release version 4.2 (EC-JRC/PBL, http://edgar.jrc.ec.europa.eu/, 2009) for the period 1999–2008. EDGAR does not discriminate between different forms of agricultural burning, whilst the results presented in this Chapter are for controlled landscape fires only (i.e. excluding waste burning).

Table 6.11 Total emissions from controlled biomass burning in the UK for a suite of trace gases. Total emissions were calculated using Equation 6.1 with burned area, fuel load, combustion completeness and emission factor parameters as explained in Sections 6.6.1–6.6.4. The emission uncertainties were calculated from the percentage uncertainties for each parameter added in quadrature. Differences between the two emission factor scenarios (Table 6.9) are small when compared to the overall uncertainty largely introduced by uncertainties in burned area and fuel combusted. Finally, the total emissions calculated here are compared with those from EDGAR (EC-JRC/PBL, 2009) (although emissions in EDGAR include agricultural waste burning) and Dragosits *et al.* (2009).

	EF Scenario 1 emissions (kt)	**EF Scenario 2 emissions (kt)**	**EDGAR v4.2**	**Dr09**
CO_2	**586** ± 469	**580** ± 464	1320	*nr*
CO	**22.7** ± 18.7	**26.3** ± 21.6	93.1	*nr*
CH_4	**0.973** ± 0.842	**1.118** ± 0.967	2.270	*nr*
C_2H_2	**0.367** ± 0.309	**0.321** ± 0.273	*nr*	*nr*
C_2H_4	**0.843** ± 0.731	**0.845** ± 0.758	*nr*	*nr*
C_2H_6	**0.161** ± 0.203	**0.169** ± 0.210	*nr*	*nr*
HCOOH	**0.075** ± 0.064	**0.091** ± 0.092	*nr*	*nr*
CH_3OH	**0.158** ± 0.134	**0.192** ± 0.163	*nr*	*nr*
CH_2O	**0.545** ± 0.474	**0.603** ± 0.523	*nr*	*nr*
NMVOC	**2.148** ± 1.916	**2.221** ± 2.018	5.51	*nr*
NH_3	**0.182** ± 0.151	**0.214** ± 0.184	1.061	0.511
HCN	**0.178** ± 0.147	**0.173** ± 0.143	*nr*	*nr*

The large differences between the total emissions estimated here and those in EDGAR (EC-JRC/PBL, 2009) are probably explained by the inclusion of agricultural waste burning in the EDGAR estimates (hence the larger emissions for all trace gases in EDGAR). Nevertheless, a comparison of the relative emissions of each trace gas reported in EDGAR with those reported here reveals some agreement between the two inventories. The only published study of controlled biomass burning emissions in the UK known to the author is that of the NAEI (Dragosits *et al.*, 2009). Dragosits *et al.*, (2009) estimate total NH_3 emissions to be 0.511 kt (with an uncertainty ranging from 0.134–1.702 kt). The estimate reported here (0.182±0.151 kt) substantially reduces the previous range of estimated emissions for NH_3 and lies towards the lower end of that estimated in Dragosits *et al.*, (2009). A summary of the parameters used by the approach presented here and that of Dragosits *et al.*, (2009) is presented in Figure 6.25.

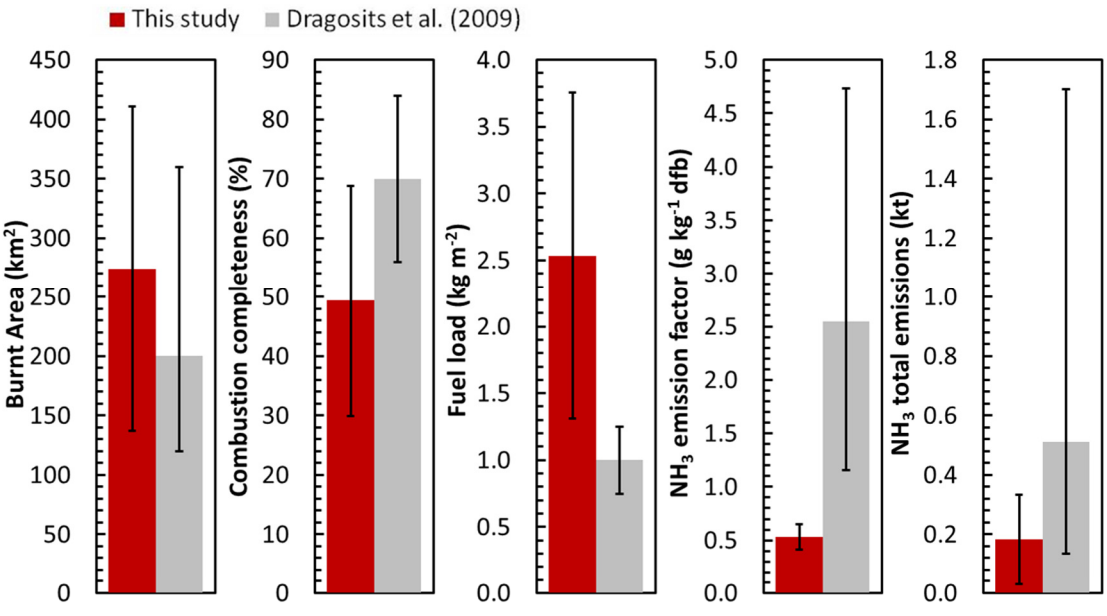

Figure 6.25 Comparison of total emissions modelling parameter values used in this study with those used for the National Atmospheric Emissions Inventory (Dragosits *et al.*, 2009) for NH_3. This figure in particular highlights the importance of having a measured emission factor for UK heathland burning, rather than a "best-guess" emission factor as used in Dragosits *et al.* (2009). Estimated total NH_3 emissions from this study have a far smaller range of uncertainty than the current estimate in the NAEI.

6.7 Conclusions and Implications

This Chapter has presented the first investigation into the emission factors of a wide range of trace gases for the heather-dominated moorland environment (an ecosystem that extends beyond the UK into much of western Europe (Figure 6.2). Measurements at 27 experimental fires have characterised emissions from different vegetation assemblages and at different times of year. The main findings of this Chapter are important from both an atmospheric emissions and a methodological perspective, these are summarised below.

6.7.1 Conclusions about biomass burning in temperate heathlands

(a) This Chapter presents the first emission factor and total emissions inventories for controlled biomass burning in the UK. Previous work has relied upon "best-guess" estimates of emission factors which have been shown to be substantially different to those measured for this thesis (Table 6.5).

(b) As indicated by the vast range of uncertainty in the total emissions of NH_3 in the UK's National Atmospheric Emissions Inventory (Figure 6.25, there was a clear need for measurements of emission factors appropriate for UK heathlands. It is hoped that the measurements reported here can significantly improve estimates of total emissions from biomass burning in the UK. In the case of NH_3 emissions, the uncertainty range has been reduced by a factor of five (Figure 6.25).

6.7.2 Implications for OP-FTIR spectroscopy of biomass burning

The findings of this Chapter build on those from the previous Chapters and further strengthen the viability and reliability of the OP-FTIR biomass burning methodology:

(a) By comparing all of the OP-FTIR measurements with the emission ratios calculated from *in situ* bag samples of smoke collected at different stages of the fire (i.e. during flaming combustion, and during residual smouldering combustion once all flaming had ceased), it is clear that the OP-FTIR technique is not biased towards smouldering emissions (Figure 6.20). Indeed, the emission

ratios derived from the bag samples of flaming combustion lie within the range of emission ratios that can be obtained from the OP-FTIR measurements. This suggests that source sampling might omit measurements of the highest MCE emissions due to the difficulty of getting close to the severest flaming; the "remote" nature of the OP-FTIR methodology appears more suitable for measuring high-MCE emissions than does the direct sampling approach.

(b) Conversely, a majority of the emission ratios determined from the bag samples of residual smouldering combustion lay beyond the envelope of the OP-FTIR measurements, yielding far higher emission ratios and thus, emission factors, than the OP-FTIR derived metrics. This is explained by the nature of the *in situ* bag sampling, which was targeted at "pure" smouldering (as depicted in the photograph in Figure 6.9b). The spatially integrated measurements made using the OP-FTIR technique will always include some contribution by flaming combustion. It may be possible to measure *pure* residual smouldering combustion using the OP-FTIR if the infrared path were adjusted to be closer to the surface and above the smouldering material, increasing the likelihood of the RSC smoke intercepting the IR path. However, the RSC stage was typically short lived, and given that the vast majority of fuel is consumed during the flaming stage of the fire, determining the emission factors for RSC is considered a low priority.

(c) In summary, a number of findings from this and the previous Chapter suggest that the OP-FTIR methodology is suitable for making measurements that characterise the emission factors of a landscape without apparent bias towards lower combustion efficiency (smouldering) emissions:

- A full range of MCE is detected in the OP-FTIR measurements, with some measurements exceeding 99% MCE.
- Measurements of flaming emissions from above the flaming zone (and thus capturing the lofted emissions) have similar emission ratios to those measured by the OP-FTIR methodology in both the Australian campaign (where bag samples were analysed independently by CSIRO) and in the UK campaigns reported here (where bag samples were analysed in the White cell using the FTIR spectrometer).

- There is agreement between the OP-FTIR derived emission factors for Australian savannas and those for other savanna ecosystems (the majority of which were measured using airborne campaigns).
- Finally, many of the plumes measured by the OP-FTIR during the UK campaigns were heavily wind-driven resulting in the bulk of the plume being driven sideways into the OP-FTIR IR path (see the photographs in Figure 6.4). In these situations, ground-based measurements downwind probably provide the best sampling platform to characterise whole-fire emissions.

7

Solar occultation FTIR for biomass burning emissions measurements

7.1 Introduction and Background

In the previous Chapters covering fire emissions measurements made in northern Australia and Northumberland, UK, it has been argued that ground-based sampling techniques (such as OP-FTIR and bag sampling) can be used to measure emission factors representative of both flaming and smouldering combustion, enabling the characterisation of landscape-scale emissions. One of the criticisms of ground-based emissions measurements, however, is that by being mostly unable to sample the lofted convective plume, they might be biased towards lower fireline intensity (and thus, lower combustion efficiency) emissions (Griffith *et al.*, 1991; Andreae and Merlet, 2001; Bertschi *et al.*, 2003a; Guyon *et al.*, 2005). The only published study using simultaneous ground-based and airborne measurements of vegetation fire smoke from the same fires (Burling *et al.*, 2011) appears to confirm this bias, with the ground measurements characterised by emission factors for hydrocarbon and oxygenated organic species up to ten times higher than those found in the lofted plume measurements. However, the sampling strategy employed by Burling *et al.* (2011, p.12202) on the ground was specifically targeted at the residual smouldering combustion emissions (akin to the smouldering bag sampling in Chapters 5 and 6), with seemingly little or no attempt to measure flaming combustion emissions on the ground:

> *"After the initial flame front had passed through an area of the [experimental fire] unit and flame-induced convection was no longer lofting the emissions, numerous spot sources of thick white smoke were typically observed contributing to a dense ground-level layer of smoke often confined below the canopy. The ground-based sampling consisted of acquiring FTIR snapshots of the emissions from as many scattered point sources as were accessible"*

Whilst the methodologies used in both Chapters 5 and 6 of the current work are indeed limited to ground sampling, with no attempt to particularly measure 'lofted' emissions, it is clear from the results that emissions from a full range of combustion efficiencies are sampled. This is without recourse to airborne sampling devices, and solely relies on ground-based OP-FTIR measurements of the wind-driven *advected* plume, accompanied by close-proximity bag sampling of areas of *both* flaming and smouldering combustion. Given that airborne emissions measurements were not taken at the experimental fires covered by the earlier Chapters, we cannot rule out the possibility that higher MCE emissions were missed by the ground-based sampling, although this is unlikely (and probably unimportant) given that MCEs of 99% were measured using the ground sampling methods. However, it is the case that the fires measured in Chapters 5 and 6 were of relatively low fireline intensities (typical fireline intensities range from 500–8,000 kW m^{-1} in northern Australian savanna fires (Williams *et al.*, 1999) and 75–3,400 kW m^{-1} for UK heathland fires (Davies *et al.*, 2010)) compared to large scale forest fires (typical fireline intensities for forest fires range from 4,000–50,000 kW m^{-1}, but can exceed 60,000 kW m^{-1} (Stocks and Kauffman, 1997)) for example, and in the case of the latter phenomena ground-based sampling might be expected to have more difficulties in sampling the full range of smoke emissions (since the fires will be difficult to approach on the ground, and much of the smoke may well be driven into a near vertically rising plume). Therefore, a further problem with the ground-based approach maybe that for very intense fires (e.g. crowning forest fires), it can be very difficult and/or prohibited to make close proximity measurements, restricting these OP-FTIR methodologies used in Chapters 5 and 6 to deployment at lower-intensity fires. Without airborne measurement capabilities, one solution to this issue is to make ground-based solar occultation FTIR (SO-FTIR) measurements of the convective lofted plume. This solution also offers an "easy-to-deploy" alternative to

airborne monitoring of *convected* emissions for the comparison with simultaneous open-path measurements of *advected* emissions.

Only one research group, based at the University of Wollongong, appear to be using SO-FTIR for the routine monitoring and study of biomass burning plumes (Paton-Walsh *et al.*, 2004; Paton-Walsh *et al.*, 2008; Paton-Walsh *et al.*, 2010a; Paton-Walsh *et al.*, 2010b), yet these measurements are made using stationary high spectral resolution FTIR spectrometers located at fixed research stations, confining measurements to well-mixed plumes from remote fires. The high spectral resolution of the FTIR spectrometers used in these studies permits the detection of excess concentrations of a suite of trace gases despite the well-mixed dispersive nature of the smoke plumes. Paton-Walsh *et al.* (2010b) estimate that plume ages varied from 3 hours up to over 24 hours (chemical ageing of the smoke can occur on these timescales, see Table 2.1), although on one occasion a plume originated from a fire within ~5 km of the research station. This Chapter aims to test the suitability of lower spectral resolution, highly portable FTIR spectrometers for SO-FTIR measurements of biomass burning plumes, and explores the ability to exploit the mobile nature of such instruments (e.g. the MIDAC FTIR spectrometer) to perform SO-FTIR measurements within close proximity to large fires, enabling a comparison with OP-FTIR measurements within the same ecosystem.

Finally, due to the nature of SO-FTIR spectroscopy, simultaneous ground-based spectral measurements of aerosol optical depth (AOD) made along the same line of site to the sun can be used alongside SO-FTIR to explore potential relationships between excess total column amounts of trace gases and excess AOD, both caused by the presence of smoke (e.g. Paton-Walsh *et al.*, 2004; Paton-Walsh *et al.*, 2005). For example, Paton-Walsh *et al.* (2004) establish a relationship between 500 nm AOD, measured using an Ocean Optics OD2000 grating spectrometer, and total column abundances of CO, HCN, H_2CO and NH_3, measured using a co-located Bomem DA8 high resolution FTIR spectrometer. Paton-Walsh *et al.* (2004) proceed to apply this relationship to satellite-derived aerosol optical depth maps (from MODIS) to determine total amounts of these gases in fire-affected regions of SE Australia. By combining portable AOD measurement devices with the portable SO-FTIR system, and deploying these at close proximity to fires, this Chapter aims to explore such relationships further,

including at sites experiencing far higher AODs than can be observed at remote research stations.

7.2 Specific objectives of this Chapter

(a) Determine the accuracy of total column retrievals of CO_2 and CO amounts representative of biomass burning plumes from low spectral resolution (0.5 cm^{-1}) SO-FTIR spectra.

(b) Investigate whether portable SO-FTIR is a viable method for measuring emission ratios and emission factors for biomass burning plumes.

(c) Determine whether portable handheld measurements of plume AOD can be paired with simultaneous measurements of total column amounts using SO-FTIR.

7.3 Evaluating the accuracy and sensitivity of SO-FTIR total column amount retrievals

7.3.1 Introduction and background

Infrared solar occultation measurements are usually made by high spectral resolution (e.g. 0.02 cm^{-1}) FTIR spectrometers based at continuously operated research stations. Examples include the systems that form the Total Carbon Column Observing Network (TCCON, Wunch *et al.*, 2011) and the Network for the Detection of Atmospheric Composition Change (NDACC, Hannigan *et al.*, 2009). TCCON stations record solar spectra in the near-infrared spectral region (1.2–2.4 μm, ~8,300–4,200 cm^{-1}) where a number of spectral windows can be used to retrieve column amounts of CO_2, CH_4, N_2O, HF, CO, H_2O and HDO (TCCON, 2012). Additional detectors and/or spectrometers may be used at particular stations to extend the number of detectable trace gas species. TCCON stations at Wollongong and Darwin, both in Australia, provide the data for previously published solar occultation studies of biomass burning plumes (Paton-Walsh *et al.*, 2004; Paton-Walsh *et al.*, 2008; Paton-Walsh *et al.*, 2010b). Here, a range of

detectors (Si, InGaAs, InSb, HgCdTe) have been used to maximise the range of detectable trace gas species.

TCCON observations are intended for the validation of space-borne measurements of total column abundances from satellites such as the Greenhouse Gases Observing Satellite (GOSAT), the Scanning Imaging Absorption Spectrometer for Atmopheric Cartography (SCIAMACHY) and the forthcoming Orbiting Carbon Observatory (OCO-2), and to provide a link between such satellite observations and ground-based in-situ measurements (Wunch *et al.*, 2011). Given that the TCCON observations relied on spectroscopic parameters that were not known with sufficient accuracy to compute total columns that could be used in combination with *in situ* measurements, the primary goal of the TCCON network was to determine the accuracy of total column retrievals (Wunch *et al.*, 2010) so that they could be calibrated to World Meteorological Organization (WMO) standards.

Generally, total column abundances obtained from ground-based solar occultation measurements are assessed for their accuracy using aircraft profile data (e.g. Wunch *et al.*, 2010; Messerschmidt *et al.*, 2011; Sussmann *et al.*, 2011). Wunch *et al.* (2010) present a calibration of TCCON data using a series of WMO standard in-situ profiles measured aboard aircraft over five TCCON stations (Park Falls, USA; Lamont, USA; Lauder, New Zealand; Darwin, Australia; and Tsukuba, Japan). Their findings suggest that systematic bias in the TCCON data for each of the studied gases (e.g. a 1.1% underestimation of column-averaged CO_2) could be corrected by applying a single, global correction factor to the measurements of each gas (see Table 5 in Wunch *et al.*, 2010). Further calibration flights were carried out over European TCCON sites by Messerschmidt *et al.* (2011) in order to confirm the findings of Wunch *et al.* (2010) for the calibration of TCCON column-averaged CO_2 retrievals. Messerschmidt *et al.* (2011) confirmed that the FTIR measurements at the European TCCON sites were consistently biased 1.1% ± 0.2% low with respect to WMO standards.

Very few studies appear to use lower spectral resolution (0.5 cm^{-1}) FTIR instruments (such as the MIDAC M2000 series used for the research presented in Chapters 4–6) for solar occultation measurements. Petri *et al.* (2012) recently performed a comparison between a relatively low resolution spectrometer (a Bruker IFS 66 operating at

0.11 cm^{-1}) and a TCCON station spectrometer, demonstrating that the former instrument can yield fairly precise measurements of column-averaged CO_2 (0.32%) and CH_4 (0.46%), in fact offering a similar precision to that of the TCCON station spectrometers. Petri *et al.* (2012) envision that the more portable, lower cost nature of the lower spectral resolution instruments could lead them to be exploited by a wider network of future ground stations.

The only examples of studies that use a truly portable 0.5 cm^{-1} resolution instrument for solar measurements appear to be those by a group at the Universidad Nacional Autónoma de México (UNAM) in Mexico City, Mexico (Stremme *et al.*, 2009; Grutter *et al.*, 2010) and those by the Cambridge Volcanology Group (Oppenheimer *et al.*, 1998; Horrocks, 1999; Burton *et al.*, 2001; Duffell *et al.*, 2001; Burton *et al.*, 2003). In Horrocks (1999), solar occultation spectroscopy using a MIDAC M2000 series FTIR spectrometer in the field is used to yield the emission ratio between HCl and SO_2 at Masaya Volcano, Nicaragua. Whilst the emission ratio agreed with open-path measurements made at the same volcano, there was no comparison of the solar retrievals to further independent measurements that could provide a proper accuracy assessment. Despite being made by a low resolution instrument, the measurements made in Mexico City by Stremme *et al.* (2009) and Grutter *et al.* (2010) were made at a fixed research station on the UNAM campus. Grutter *et al.* (2010) demonstrate how continuous measurements of total column CO can be used in combination with meteorological measurements of mixing layer height and wind fields to determine sources of CO. Excess concentrations of CO_2 and CH_4, however, were not large enough to distinguish sources of these species. Stremme *et al.* (2009) use both solar and lunar occultation spectroscopy to study the diurnal trend of CO in Mexico City, discovering large daily and diurnal variations over the city. Stremme *et al.* (2009) also perform a crude experimental evaluation of the retrieved CO column; a measurement precision of ~5% for each measurement was estimated by taking the average difference of consecutive measurements. However, Stremme *et al.* (2009) highlight that sensitivity to parameters such as spectrometer field-of-view are high, with retrievals using different ILS parameters leading to 25% differences in total column amounts. To check whether the CO column retrieval from their solar spectra was accurate, Stremme *et al.* (2009) used the cylindrical housing of their spectrometer's telescope as a makeshift gas cell by

sealing the telescope aperture with an IR transparent film. Over a short time period, when the solar zenith angle did not change greatly, successive injections of large amounts of CO (5 ml per injection) were added into the telescope housing each minute. The resultant linear increase in the retrieved CO total column amount, and the correlation with the estimated amount of CO within the telescope housing (Figure 6 in Stremme *et al.*, 2009), were used to evaluate the correctness of the retrieval methodology. Despite the apparently decent retrieval accuracy, Stremme *et al.* (2009) list a number of limitations to their approach; including a high degree of uncertainty concerning the amount of CO actually injected into the cell, the uncertain free volume in the telescope housing, and the rate of removal of CO through small holes or leaks in the setup.

In Chapter 4, an extensive accuracy assessment of gas concentrations retrieved from OP-FTIR spectra was performed using a gas cell filled with known concentrations of CO_2, CH_4 and CO (Smith *et al.*, 2011). For that study, the FTIR was positioned to view a fixed IR source placed at the opposite end of an IR-transparent cell filled with the gas of interest, in an attempt to extend the OP-FTIR methodology previously used for validation of SO_2 retrievals by Horrocks *et al.* (2001). Here this methodology is extended further, arranging the IR-transparent cell so that a mirror directs sunlight through the gas cell and into the FTIR spectrometer's telescope, in a geometry that allows the quantitative validation of the OP-FTIR setup and addresses the limitations of the Stremme *et al.* (2009) study. This design is used to determine the precision and accuracy of solar retrievals of both CO_2 and CO total column amounts.

7.3.2 Instrumentation and setup

Following the initial evaluation of the OP-FTIR methodology undertaken in Section 4.3, also discussed in Smith *et al.* (2011), a second experiment at RAL MSF was conducted to evaluate the precision and accuracy of SO-FTIR CO_2 and CO total column retrievals. As described in Chapter 4.2, a stainless steel cylindrical gas cell was fitted with IR-transparent windows (length = 1.05 m; diameter = 160 mm; window diameter = 135 mm) and used to contain gas mixtures of known amounts of CO_2 and CO. During a short two-day window of semi-cloud free weather in April 2011, it was possible to make measurements of a series of gas cell mixtures using the sun as the IR source. To

make solar occultation measurements of the gas cell, sunlight was directed through the cell using a mirror (Figure 7.1). As used throughout Chapters 4–6, the MIDAC M2000 series FTIR spectrometer, optically coupled to a 76 mm Newtonian telescope, was placed to view the reflected sunlight through the IR transparent windows of the gas cell. An attenuator was fitted to the FTIR spectrometer telescope to avoid MCT detector saturation. The temperature of the gas inside the gas cell was measured using a calibrated platinum resistance thermometer (PRT).

Table 7.1 lists the gas mixtures investigated here. Large amounts of CO_2 and CO were injected into the gas cell to simulate lower concentrations over longer pathlengths (in accordance with the Beer-Lambert law). Airborne measurements of young smoke plumes (within 0.2–27 km from the head fire) indicate that concentrations of CO_2 within a plume may be ~50–150 ppm (15–40%) higher than ambient concentrations, whilst CO concentrations can be 1–4 ppm (400–1,000%) higher than ambient concentrations (Hobbs *et al.*, 2003). Ground-based SO-FTIR measurements of CO by Paton-Walsh *et al.* (2004) also find that biomass burning plumes account for a 100–2,000% increase over ambient CO total column amounts. The amounts of CO_2 and CO used here were thus chosen to represent the range of excess concentrations that might be expected when viewing the sun through a wildfire or prescribed fire smoke plume,

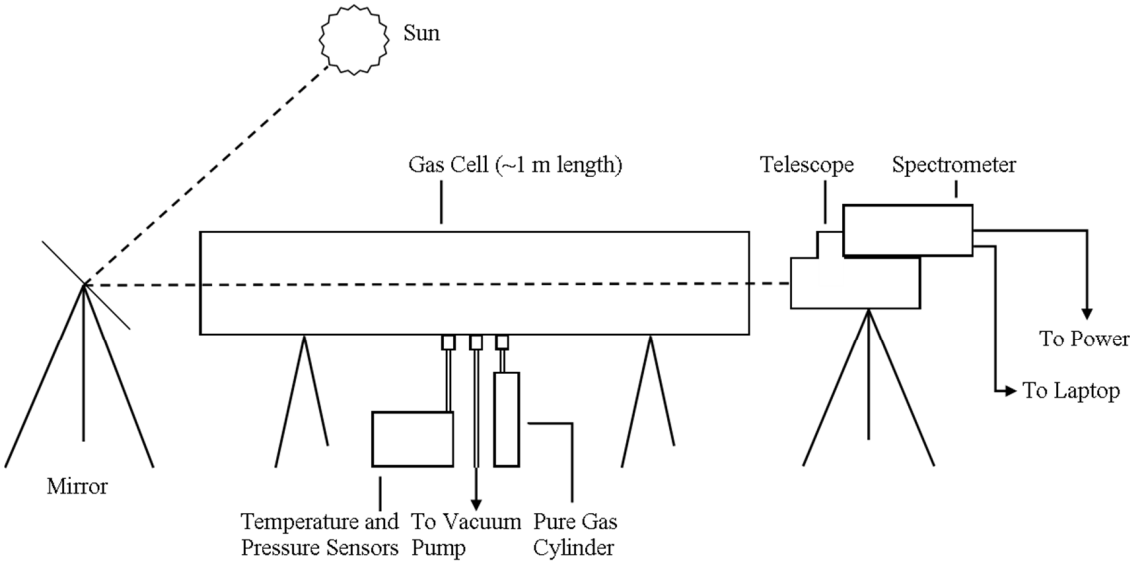

Figure 7.1 Schematic of the physical instrumentation arrangement used for the solar occultation measurements of the gas cell at RAL MSF. Measurements were also made of the solar spectrum without the presence of the gas cell.

assuming a range of plume sizes.

As described in Chapter 4, gas mixtures were prepared barometrically using high purity (99.9%) component gases. The barometric mixing method relied on three MKS Baratron (type 690) pressure capacitance manometers operated at three precision levels of 0.1 Pa, 10 Pa and 100 Pa with a stated accuracy of 0.05%. For each gas amount to be measured, the cell was evacuated before the sample gas (CO_2 or CO) was slowly released into the cell until the desired amount was reached. After waiting for the pressure to stabilise and noting the final partial pressure, the cell was filled with nitrogen to ambient pressure (1,000 hPa) and allowed to stabilise once more. The partial pressure of the sample gas was used with the temperature and pressure measurements to calculate the amount (molec cm^{-2}) of each mixture within the gas cell (using Eqn. 4.3). Given the constant motion of the Sun relative to the Earth, continual adjustments were made to the alignment of the spectrometer and mirror to maximise the signal at the detector. Consequently, spectra were collected without scan averaging due to the rapidly changing signal. Varying numbers of spectra were collected for each gas cell mixture, depending on successful alignment with the sun and periods of temporary cloud cover. Measurements were made both with and without the cell in the path, so that background levels of CO_2 and CO could be retrieved. A selection of 24 spectra with consistent, apparently good quality signals were made for each gas cell mixture (with and without

Table 7.1 Cell mixing ratios (ppm) and equivalent cell amount (molecules cm^{-2}) for the 1.05 m gas cell filled with CO_2 and CO, with the equivalent mixing ratios for longer atmospheric paths (giving an indication of the excess concentration that each cell amount equates to for different plume sizes).

Cell mixing ratio (ppm)	Cell Amount (molec cm^{-2})	500 m plume equivalent (ppm)	1,000 m plume equivalent (ppm)	1,500 m plume equivalent (ppm)
CO_2				
99671	2.615×10^{20}	209	105	70
200591	5.251×10^{20}	421	211	140
303214	7.935×10^{20}	637	318	212
408161	1.068×10^{21}	857	428	286
600400	1.299×10^{21}	1261	630	420
CO				
1258	3.287×10^{18}	2.64	1.32	0.88
2508	6.555×10^{18}	5.27	2.63	1.76
4990	1.304×10^{19}	10.48	5.24	3.49
10032	2.629×10^{19}	21.06	10.53	7.02

the cell); and these spectra were co-added to produce a final spectrum, and background spectrum, for each gas mixture.

7.3.3 Retrieval and accuracy assessment methodology

Total column amount retrievals were made using two atmospheric radiative transfer forward modelling and fitting programs, FTIR_FIT (Burton, 1998) and Atmosphit (Hurtmans *et al.*, 2005). The procedure for total column amount retrieval using these types of retrieval codes is explained in detail in Chapter 3.2.3.

To assess the accuracy of retrievals of excess CO and CO_2 column amounts, it was first necessary to calculate the amount of CO and CO_2 contained within the cell. To achieve this, background measurements (without the gas cell) were made immediately before and after the measurements that contained the gas cell in the optical path. The retrieved amounts for the background atmospheric measurements (M_{ra}) closest in time (to minimise changes in the pathlength through the atmosphere) to that of the gas cell measurements were subtracted from the retrieved amounts for the gas cell measurements (M_{rc}), yielding a retrieval of the amount of gas contained within the cell. The accuracy of this retrieved gas cell amount is defined as the true amount subtracted from the retrieved amount ($M_{rc} - M_{ra}$), divided by the true amount (M_{true}), expressed as a percentage:

$$Accuracy\ of\ retrieved\ White\ cell\ amount = \frac{(M_{rc} - M_{ra}) - M_{true}}{M_{true}} \times 100 \qquad (7.1)$$

7.3.3.1 Determination of input parameters

As with MALT (Section 3.2), when performing a retrieval using either Atmosphit or FTIR_FIT, the input parameters required by the spectral forward model can be stated as fixed constants, or can be included in the fitting process. In addition to the parameters required for MALT (regarding the composition of the sample atmosphere and the instrument line shape), retrievals of total column amounts from SO-FTIR spectra require information about the entire atmospheric profile. To achieve this, FTIR_FIT models the atmospheric path using a 50-layer model atmosphere defined using the Fast Atmospheric Signature code (FASCODE) where the vertical profiles of pressure, temperature and trace gas concentrations are calculated using a single ground-level

temperature and pressure input (Clough *et al.*, 1985). For Atmosphit, a standard mid-latitude summer atmosphere, as used in the Moderate Resolution Atmospheric Transmission (MODTRAN, Spectral Sciences Inc., 2012) model is used. Atmosphit also requires *a priori* multiplication factors for gases of interest for each layer of the atmospheric profile. To improve retrievals of CO, the *a priori* multiplication factor in the lowest level of the atmosphere was adjusted to 10 for the CO measurements. Whilst FTIR_FIT does not allow for adjustments to the *a priori* amounts, the user is expected to indicate which gases are contained within a ground-level plume as well as the interfering atmospheric gases. Determination of instrument line shape parameters were treated the same way as in Chapter 4:

- The spectral shift was fit by both programs
- The spectral resolution was fixed at the spectrometer's manufacturer's specification (0.5 cm^{-1})
- The field-of-view was fixed at 23 mrad, in accordance with the findings of Chapter 4.2.5.

Due to rapid changes in measured signal between each collected spectrum, it is not possible to correct for any zero-baseline offset (due to the continuously changing background). Atmosphit does not have the capability to correct for this effect. FTIR_FIT can be used to correct for this effect if the spectral window of interest contains a saturated spectral line. Given that including zero-baseline offset in the fitted procedure improves the resulting spectral fit, FTIR_FIT was used to correct for this offset where possible.

7.3.3.2 Spectral window and 'background' polynomial

Following the methodology of Chapter 4.2, a series of spectral windows were tested for retrieving the total column amounts of CO and CO_2. High resolution instruments typically use several narrow "micro-windows" (e.g. Senten *et al.*, 2008) for total column retrievals from solar spectra. Spectra with 0.5 cm^{-1} resolution do not show completely separated CO or CO_2 absorption lines, wider spectral windows are therefore needed to maximise spectral information (Echle *et al.*, 2000), and to improve estimation of the background slope and the columns of any interfering trace gas species. Petri *et al.*

(2009), who also used a 0.5 cm^{-1} resolution instrument, use a 50 cm^{-1} spectral window (2,110–2,160 cm^{-1}) as a compromise between obtaining sufficient information and limiting computational requirements. Here, we evaluate the accuracy of retrievals using the spectral windows previously evaluated for OP-FTIR spectra in Chapter 4.2 (Table 7.2). An additional window for retrieving CO (2,049–2,080 cm^{-1}) was also used in the evaluation, as suggested by P. Coheur (contributor to Atmosphit; personal communication, 2011). Atmosphit does not have an option for adjusting the polynomial used to calculate the background 100% continuum (fixed to a 3rd-order polynomial), and the polynomial order was in fact kept constant for both Atmosphit and FTIR_FIT.

7.3.4 Results and Discussion

Examples of solar occultation spectra collected under the conditions depicted in Figure 7.1 are shown in Figure 7.2. From consideration of these it is clear that whilst clear spectral differences between each gas mixture are identifiable in the case of CO (Fig. 7.2a), there seems little to distinguish between the spectra in the case of CO_2 (Fig. 7.2b). Indeed, some individual CO_2 absorption lines exhibit a deeper absorption with the gas cell present (e.g. at 2,050 cm^{-1}), whilst other lines appear to have the opposite signature (e.g. at 2,056 cm^{-1}). The precision of the CO_2 retrievals (the standard deviation of all total column retrievals made at the same gas cell mixing ratio) was always worse than 5%, using both Atmosphit and FTIR_FIT. Therefore the uncertainty due to precision for the retrieved cell amount ($M_{rc} - M_{ra}$) is worse than 10%. As the amount of CO_2 in the cell equates to between 3% and 16% of the total amount of CO_2 in the atmospheric column, the apparently poor performance of the CO_2-targeted spectroscopy effectively impedes any really useful retrieval attempt (the fluctuation in retrieved CO_2 amount between consecutive measurements was larger than the CO_2 amounts used in the gas cell). Given that even the largest wildfire smoke plumes may only enhance total atmospheric column CO_2 by around 10% (e.g. a 2,000 m plume with CO_2 levels 150 ppm above ambient mixing ratios (Goode *et al.*, 2000)), it seems unlikely that useful retrievals of excess CO_2 from biomass burning could be made using this instrumentation and measurement setup. A higher spectral resolution instrument and an automatic solar tracking facility may be required to significantly improve measurement

precision. The remainder of this section will focus on the accuracy and precision of the CO retrievals.

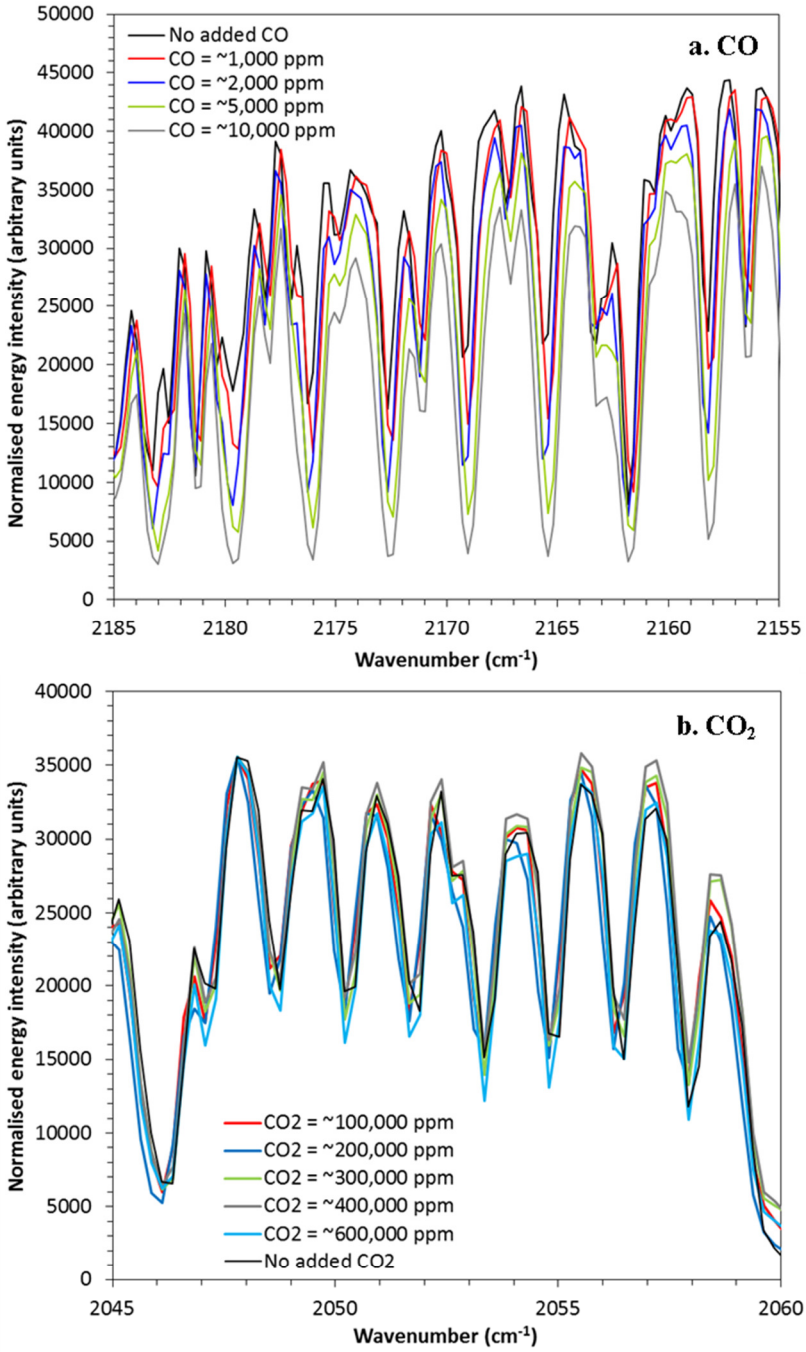

Figure 7.2 Solar occultation spectra measured at RAL MSF, the coloured lines record spectra measured using the instrumentation illustrated in Fig. 7.1 (i.e. with a gas cell containing varying amounts of CO at ambient pressure); whilst the black line is a spectrum measured without the gas cell. (a) The extra absorption caused by the CO in the gas cell is clearly evident in the gas cell spectra; (b) excess CO_2 does not appear to lead to discernible changes in spectral absorption. The proportion of CO_2 contained in the gas cell compared with the total column amount of CO_2 ranges from ~3% to ~16%.

Four spectral windows were identified containing either a broad absorption feature or a selection of individual absorption lines (Table 7.2 and Fig. 4.4 in Chapter 4). For CO, results shown in Figure 7.3 indicate that cell amounts are most accurately retrieved by Atmosphit using the 2,142–2,241 cm^{-1} spectral window, with retrieved cell amounts over the full range tested having a root mean squared (RMS) error of 0.94% (Fig. 7.3c). FTIR_FIT performs best using the 2,000–2,230 cm^{-1} spectral window, with an RMS of 3.74% (Fig. 7.3b). The 2,034–2,075 cm^{-1} spectral window yielded the worst results for both Atmosphit and FTIR_FIT, with RMS errors of 54.2% and 58.4% respectively. A number of spectral lines saturate in this narrow spectral window (Figs. 7.4e and 7.4f), leading to a poorer overall fit by the modelled spectrum.

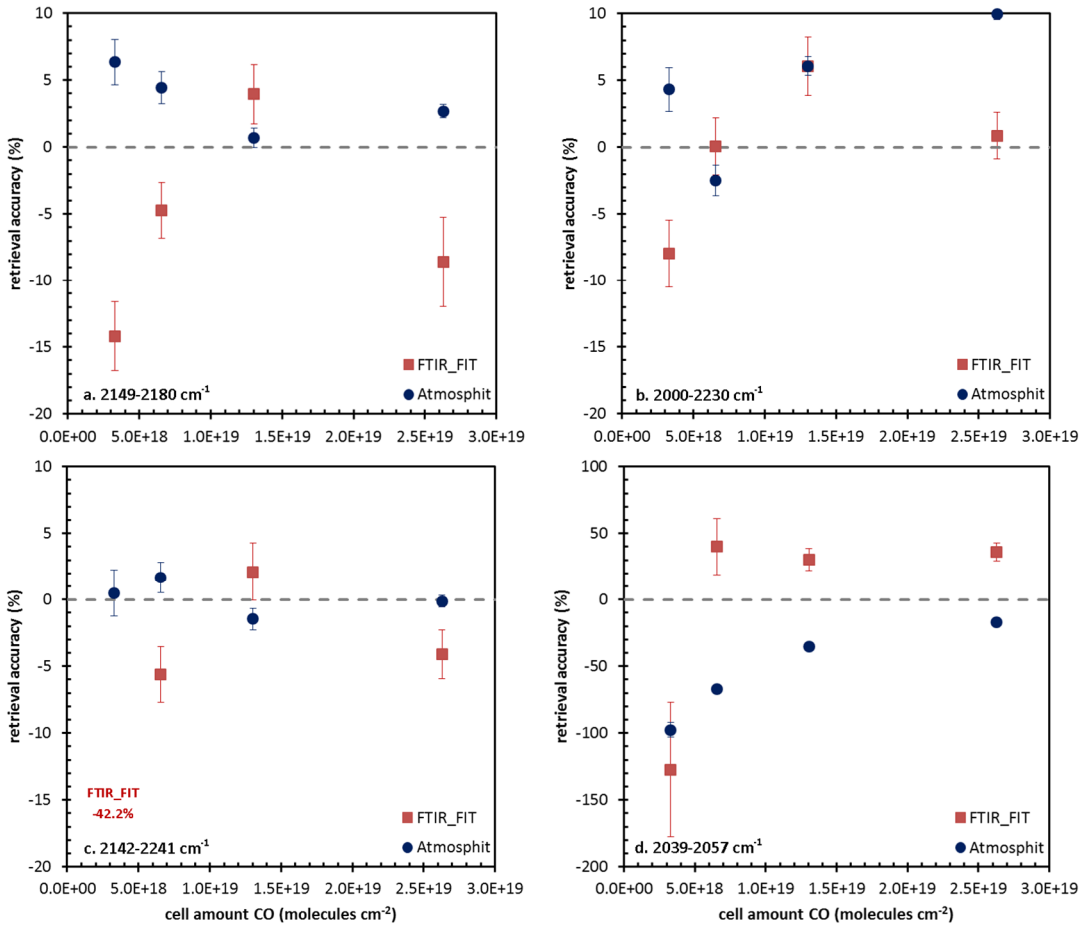

Figure 7.3 Retrieval accuracy (calculated using Eqn. 7.1) for CO cell amounts resulting from use of FTIR_FIT (red squares) and Atmosphit (blue circles) with solar occultation FTIR spectra through a gas cell containing different amounts of CO. Retrievals were made using four spectral windows. In order to aid comparison of the retrieval accuracies, the same y-axis range is used to display the results from the four spectral windows tested (apart from d. 2,039 – 2,057 cm^{-1} where the errors were far larger than for the other windows). Excluding the 2,039 – 2,057 cm-1 window, retrieval accuracies are fairly consistent for both Atmosphit and FTIR_FIT.

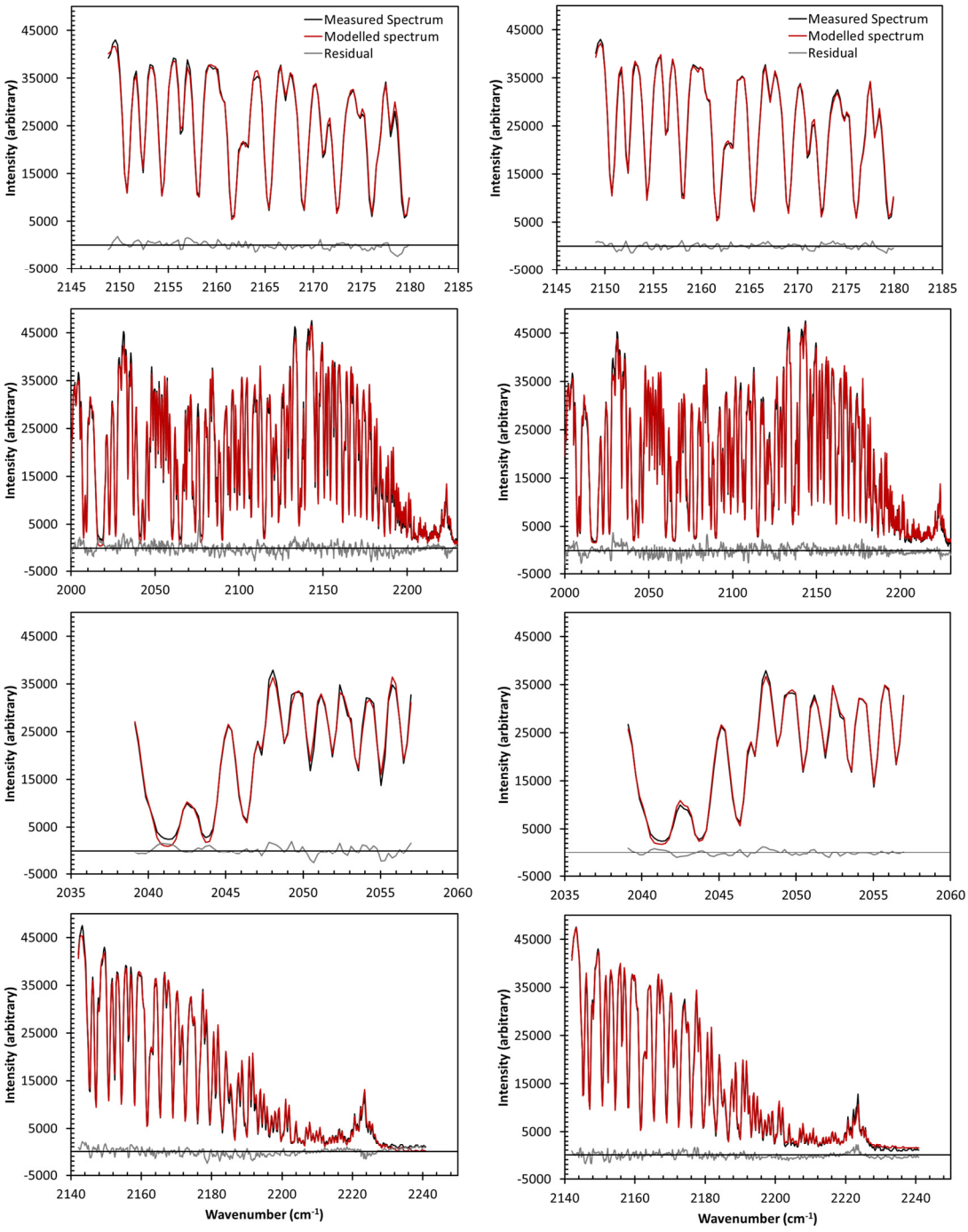

Figure 7.4 Examples of measured SO-FTIR spectra (black lines) and best-fit modelled spectra (red lines) simulated and fitted using Atmosphit (left) and FTIR_FIT (right) for each of the spectral windows (top to bottom). The residual between the measured and modelled spectra (grey lines) is also included.

Despite large variations in the retrieved cell amount accuracy between different spectral windows, the reported error (an indication of the goodness-of-fit from the retrieval codes, represented by the error bars in Figure 7.3) was low in all cases (except for the 2,034–2,075 cm^{-1} spectral window, for which both Atmosphit and FTIR_FIT indicated poor fits). For example, the reported errors for the 2,000–2,230 cm^{-1} and the 2,142–2,241 cm^{-1} spectral windows were 4.28% and 4.35% respectively for FTIR_FIT, and 1.95% and 2.07% respectively for Atmosphit. When the 2,034–2,075 cm^{-1} spectral window is excluded, the results suggest that the other spectral windows, when used with Atmosphit can yield accurate retrievals (< 6%). However, the window with the lowest reported error (i.e. the best spectral fit) in Atmosphit (2,000–2,230 cm^{-1}) does not result in the best accuracy (2,142–2,241 cm^{-1}). For FTIR_FIT, only the 2,000–2,230 cm^{-1} window yields an accuracy of less than 6% (3.74%), although this does correspond to the window with the best spectral fit (lowest reported error). The 2,142–2,241 cm^{-1} window also performs well for three of the four cell amounts (Fig. 7.3c).

7.3.5 Summary and implications for field measurements

Due to the volume of data collected in the field, with each hour of observations consisting of ~2,400 spectra (there are over 12,000 spectra in the datasets used for this Chapter) and length of time to analyse each spectrum in Atmosphit (between 3–6 minutes), analysing all spectra using Atmosphit is currently not viable due to computational restrictions. FTIR_FIT (which can analyse up to 3 spectra each second using a standard laptop computer) was therefore chosen to analyse the large datasets collected in the field. A small subset of field spectra exhibiting a range of retrieved column amounts of CO (using FTIR_FIT) were also analysed using Atmosphit; this cross validation is presented in Section 7.5.3.

Whilst FTIR_FIT did not achieve the level of accuracy seen in the results from Atmosphit (Figure 7.5), the linear response to changing cell amount and a lack of bias across the full range of the investigated CO cell amounts indicates that FTIR_FIT is a suitable alternative when using the 2,000–2,230 cm^{-1} spectral window. Furthermore, FTIR_FIT retrievals of total column CO from 82 consecutively measured spectra (a measurement time of ~2 minutes) were used to estimate the precision of the FTIR_FIT method (Figure 7.6). The mean CO amount of 2.78×10^{18} molec cm^{-2} had a standard

deviation of 7.24 × 10^{18} molec cm^{-2} (equivalent to a precision of 2.60%). Given that a smoke plume from biomass burning may enhance total column CO by as much as 2,000% (Paton-Walsh *et al.*, 2004), a total column precision of 2.60% for CO should be sufficient for measuring excess CO over a range of plume sizes.

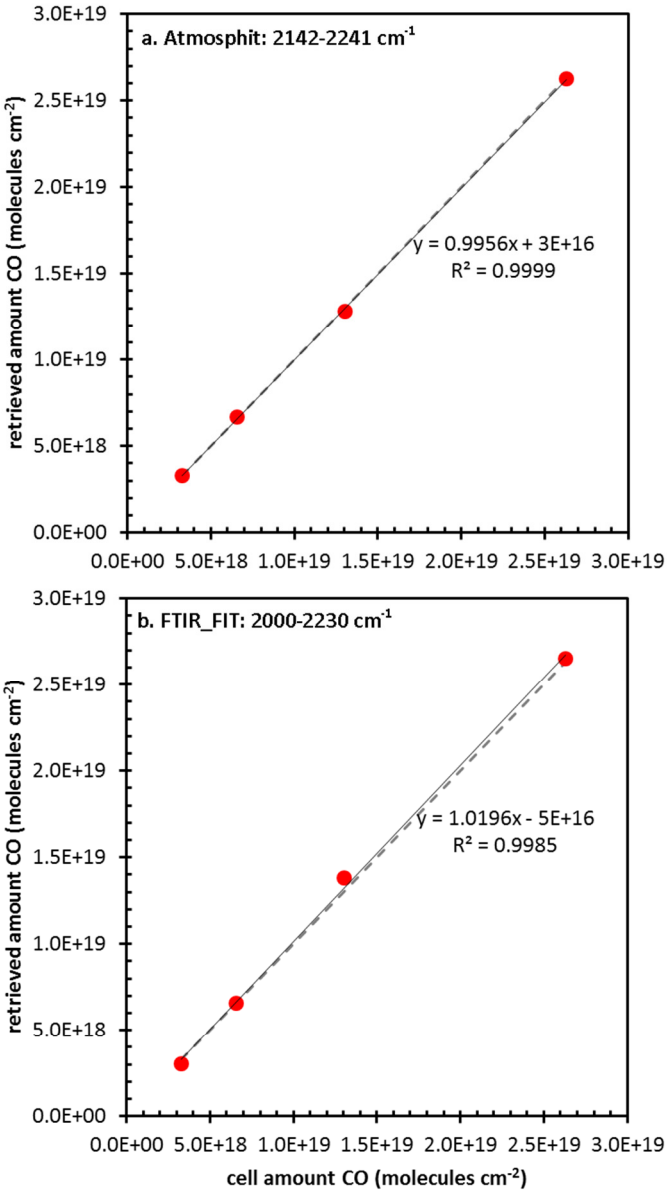

Figure 7.5 Relationship between retrieved CO cell amount using the optimum spectral window for (a) Atmosphit (2,142-2,241 cm^{-1}); and (b) FTIR_FIT (2,000-2,230 cm^{-1}). The line and equation of best-fit are shown (dashed line). The 1:1 line is also shown (solid line); all retrieved amounts are within 1.68% of true amounts for Atmosphit and within 7.96% of true amounts for FTIR_FIT.

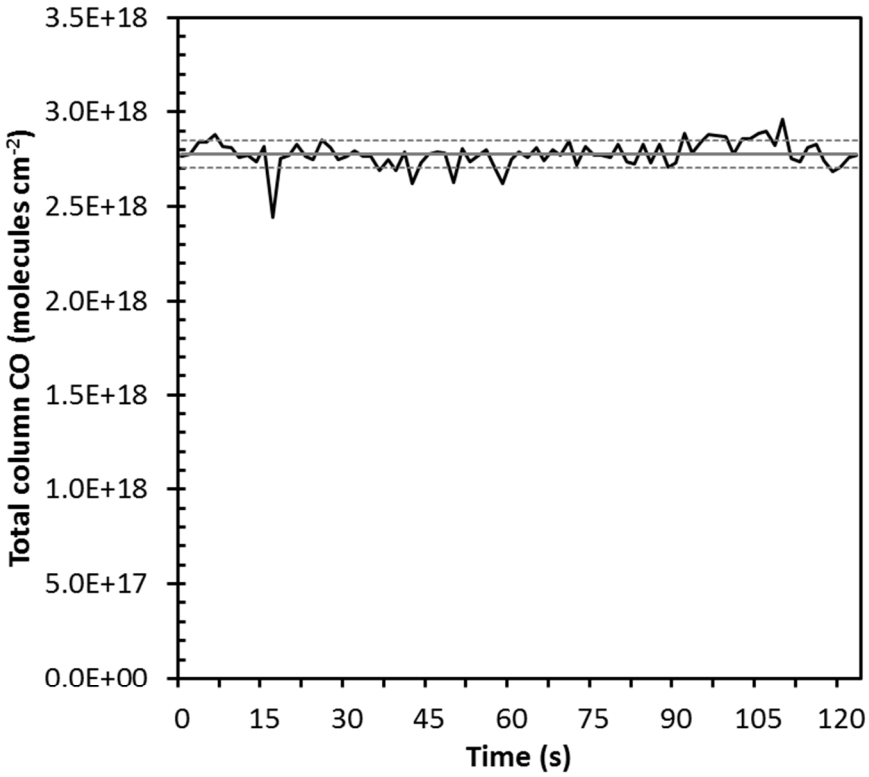

Figure 7.6 Retrieved ambient total column CO amount (molecules cm^{-2}) for 82 spectra collected using one scan for each spectrum (total time = ~120 seconds). Retrievals were made using FTIR_FIT with the 2,000-2,230 cm^{-1}) spectral window. The mean total column amount (grey solid line) is also shown with the standard deviation from the mean (grey broken line): $2.78 \times 10^{18} \pm 7.24 \times 10^{16}$ (equivalent to a precision of 2.60%).

7.4 Field case-study: Alberta, Canada

In June 2009, solar occultation measurements of a large biomass burning plume were made in Banff National Park, Alberta, Canada (Figure 7.7). This section presents an overview of this measurement campaign and the results of retrievals of CO and NH_3 amounts from the SO-FTIR spectra using the method outlined in Sect. 3.3.

7.4.1 Site and fire description

SO-FTIR measurements were made during prescribed forest fires on 2, 3, and 4 June 2009, in a 50 km^2 plot of forest due east of Saskatchewan Crossing, Banff National Park, Alberta, Canada (Figure 7.7). The long distance between the intensely burning

fires (> 400 m) and the FTIR spectrometer meant that OP-FTIR measurements were not possible. Furthermore, the plume tended to rise vertically (due to strong convection), with very little advection by the wind, pointing out a limitation of the horizontal OP-FTIR geometry under these conditions. SO-FTIR measurements were therefore both possible and desirable, although inhibited by increasing cloud cover on 3 and 4 June. The results presented in this section are from one fire on 2 June 2009, when clear skies

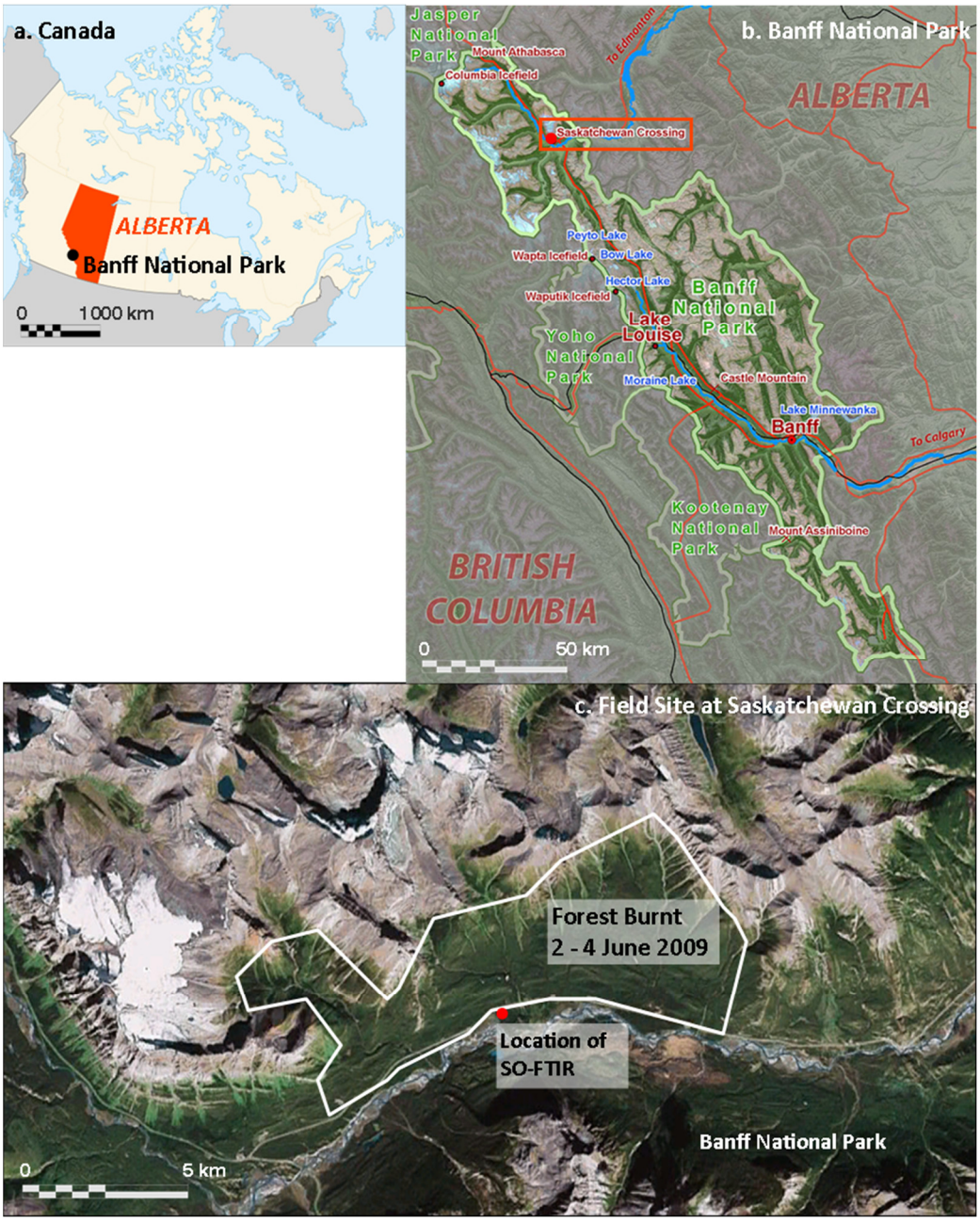

Figure 7.7 (a) Location of Banff National Park in Alberta, Canada; (b) Location of the field site at Saskatchewan Crossing within Banff National Park; (c) aerial photograph of the field site and location of the SO-FTIR measurements. Aerial photograph taken from Google Maps (2012).

allowed for the collection of over 1,000 spectra. Figure 7.8 shows a photograph of the measurement setup. Ambient temperature and air pressure measurements were made using a Kestrel handheld weather station, recording a 2 m mean air temperature during the fire of 10°C, and mean air pressure of 860 mb (unadjusted for the 1,400 m altitude).

Figure 7.8 Photograph of FTIR spectrometer measuring solar occultation spectra. A small mirror extended in front of the spectrometer telescope reflects light from the sun into the spectrometer. The plume from the large prescribed burn to the right of the photograph has obscured the sun. The location of the spectrometer is mapped in Figure 7.7c.

7.4.2 Results and discussion

For this case study test, total column amounts of carbon monoxide (CO) and ammonia (NH_3) were retrieved from the SO-FTIR spectra using FTIR_FIT (Burton, 1998) (Figure 7.9). Whilst it should be possible to retrieve other trace gas species from SO-FTIR spectra (e.g. HCN, CH_2O, C_2H_2, C_2H_4), these were not retrieved due to limitations of the FTIR_FIT software (which was initially intended for research into volcanic emissions). The ability to retrieve these other trace gas species will be added to future releases of FTIR_FIT (M. Burton, personal communication). As predicted by Section 7.3, excess CO_2 due to fire emissions could not be discerned in the SO-FTIR spectra due to its large background amount and the relatively low measurement precision; CO must therefore be used as the reference gas. For CO, the 2,000–2,230 cm^{-1} spectral window was used for the retrieval (the optimal window from Sect. 7.3). NH_3 was retrieved using the same spectral window used for OP-FTIR measurements (900–980 cm^{-1}) thanks to a lack of saturation in this window even when measuring the total atmospheric column.

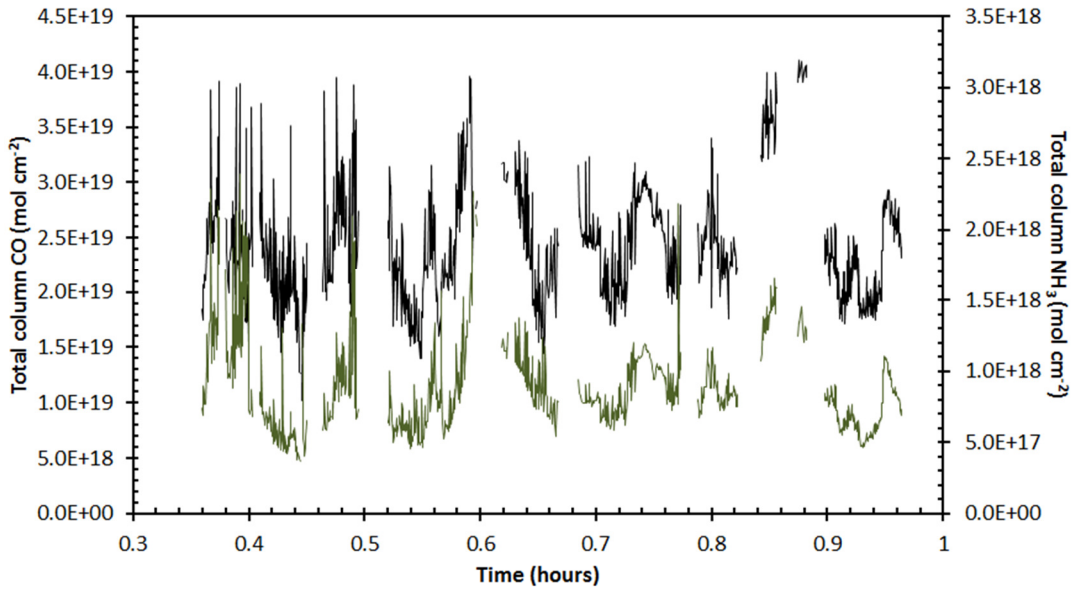

Figure 7.9 Time series of total column amounts of CO and NH_3. Spectra were collected over one hour for a large prescribed fire near Saskatchewan Crossing, Banff National Park, Alberta, Canada (Fig. 7.7). This figure demonstrates that the low spectral resolution SO-FTIR technique used here is adequate for measuring variations in both CO and NH_3 in biomass burning plumes, and thus is able to be used to estimate an emission ratio for these species (Fig. 7.10). Gaps in the data above correspond to times when adjustments were made to the alignment of the spectrometer with the sun.

The emission ratio of NH_3 to CO was calculated from the bivariate plot of CO and NH_3 total column amounts (the same method as used for the OP-FTIR methodology described in Section 3.3.3), where the least squares linear regression slope between the two gases is used as the emission ratio (Figure 7.10). The NH_3 emission ratio to CO for the one Canadian fire measured here is 0.0279±0.0012. The only previously published emission ratio of NH_3 to CO for Boreal forests appears to be that of Goode *et al.* (2000) who measured an average emission ratio of 0.0158±0.0070 using airborne FTIR at four Alaskan fires (although the emission ratio for one fire was 0.0258). One explanation for the higher emission ratio measured here might be the close proximity of the SO-FTIR measurements to the emissions source (< 500 m) where the smoke may have only aged by less than a minute; the airborne FTIR measurements by Goode *et al.* (2000) are of a mixture of aged plumes and measurements closer to the fire, where NH_3 might have been dissolved by moisture and aerosols in the air (Goode *et al.*, 2000).

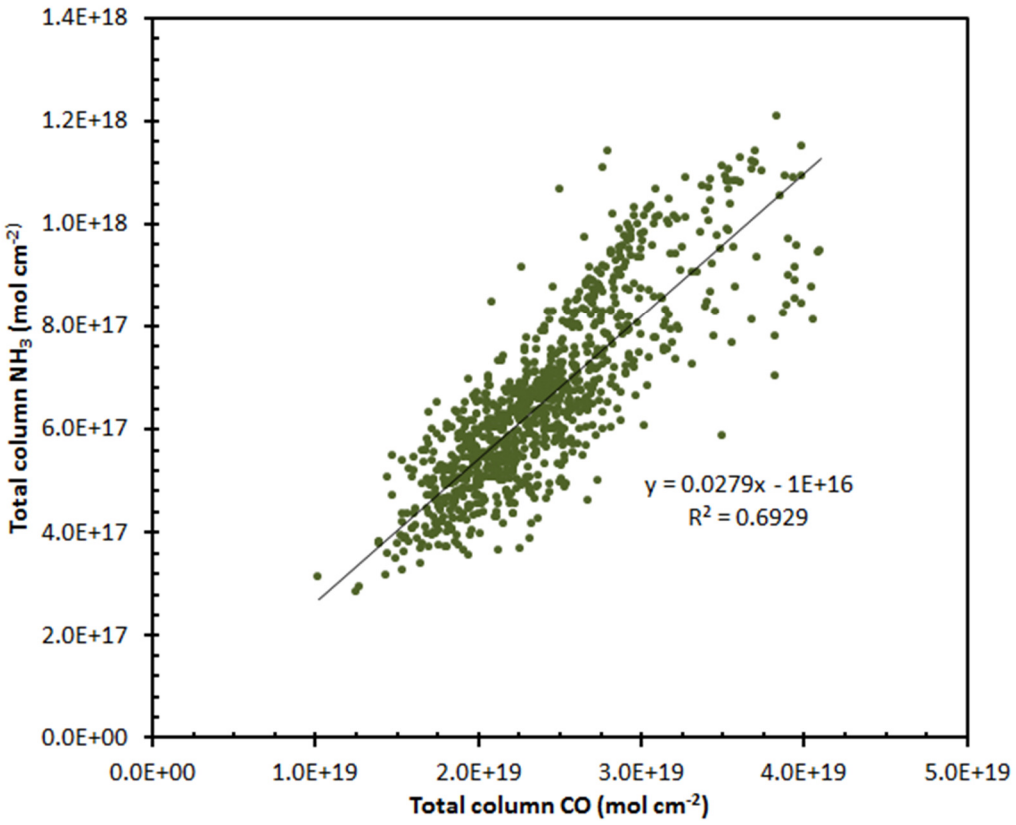

Figure 7.10 Total column amounts of CO vs. NH_3 for the prescribed forest fire at Saskatchewan Crossing, Banff National Park, Alberta, Canada. The ratio between CO and NH_3 is similar to that reported by Goode *et al.* (2000), who measured NH_3:CO emission ratios ranging 0.0122–0.0257 for Alaskan biomass burning plumes using airborne FTIR.

These limited measurements suggest that SO-FTIR using field portable, low spectral resolution spectrometers provides a suitable method for measuring biomass burning plumes in the field, without the reliance on aircraft or permanent research station facilities. Furthermore, the SO-FTIR measurements have the advantage of being integrated across the length of the plume along the solar path to the spectrometer, providing a representative sample of 'whole-fire' emissions that is difficult to achieve using expensive airborne sampling.

7.5 Field case-study: Northern Territory, Australia

Further to the OP-FTIR measurements carried out during the three campaigns to Australia's Northern Territory in 2009 and 2010 (Chapter 5), additional SO-FTIR measurements were made during the 2010 campaign in the Darwin region (Figure 7.11). A three month measurement campaign maximised the opportunity to measure accessible wildfires which occurred at locations that permitted safe, solar occultation geometry measurements to be made. In addition to the SO-FTIR measurements during this campaign, measurements of Aerosol Optical Depth (AOD) were also made using a Microtops sun photometer (Solar Light Company, Glenside, Pennsylvania). This permitted a comparison between total trace gas column amounts and AOD. This section presents SO-FTIR and AOD measurements from four fires in the Darwin region.

7.5.1 Site and fire descriptions

Measurements were made at five locations for four fires within 200 km of Darwin, Northern Territory, Australia (Figure 7.11 and Table 7.2). Two classes of fire were measured using the SO-FTIR methodology; tussock-grass open woodland (tgow) and tussock-grass floodplain (tgfp). Unlike the majority of fires measured using the OP-FTIR technique (in both Chapters 5 and 6), each of the fires measured using SO-FTIR were true wildfires. Locations of wildfires were identified by regular monitoring of the North Australian Fire Information (NAFI) website (www.firenorth.org.au), which shows the location of satellite-detected fires; and by regular phone calls to Bushfires NT

(Northern Territory Government), who are responsible for supporting landholders with fire mitigation.

Wildfires were measured at Howard Springs on Bastin Road (tgfp) on 13 September 2010 (Figure 7.12); at two locations near Bridge Creek off the Stuart Highway (tgow) on 21 September 2010; at Southport on Mira Road (tgow) on 6 October 2010; and near Lee Point off Lee Point Road (tgfp) on 15 October 2010. A list of fires and fire conditions measured using SO-FTIR is presented in Table 7.2. Due to the nature of these wildfires, the distance between the FTIR deployment location and the fire location was estimated (Table 7.2). Generally, the measurement distance was within 1.5–4 km of the fire front (with the exception of Lee Point, where measurements were made adjacent to and within 100 m of the fire front).

As previously discussed, the climate of the Darwin region is tropical monsoonal, with 95% of mean annual rainfall falling between April and November. According to the weather station at Batchelor (within 120 km of all fire measurement sites), mean annual rainfall is 1,528 mm, with a mean maximum temperature of 32°C in July and 37°C in August.

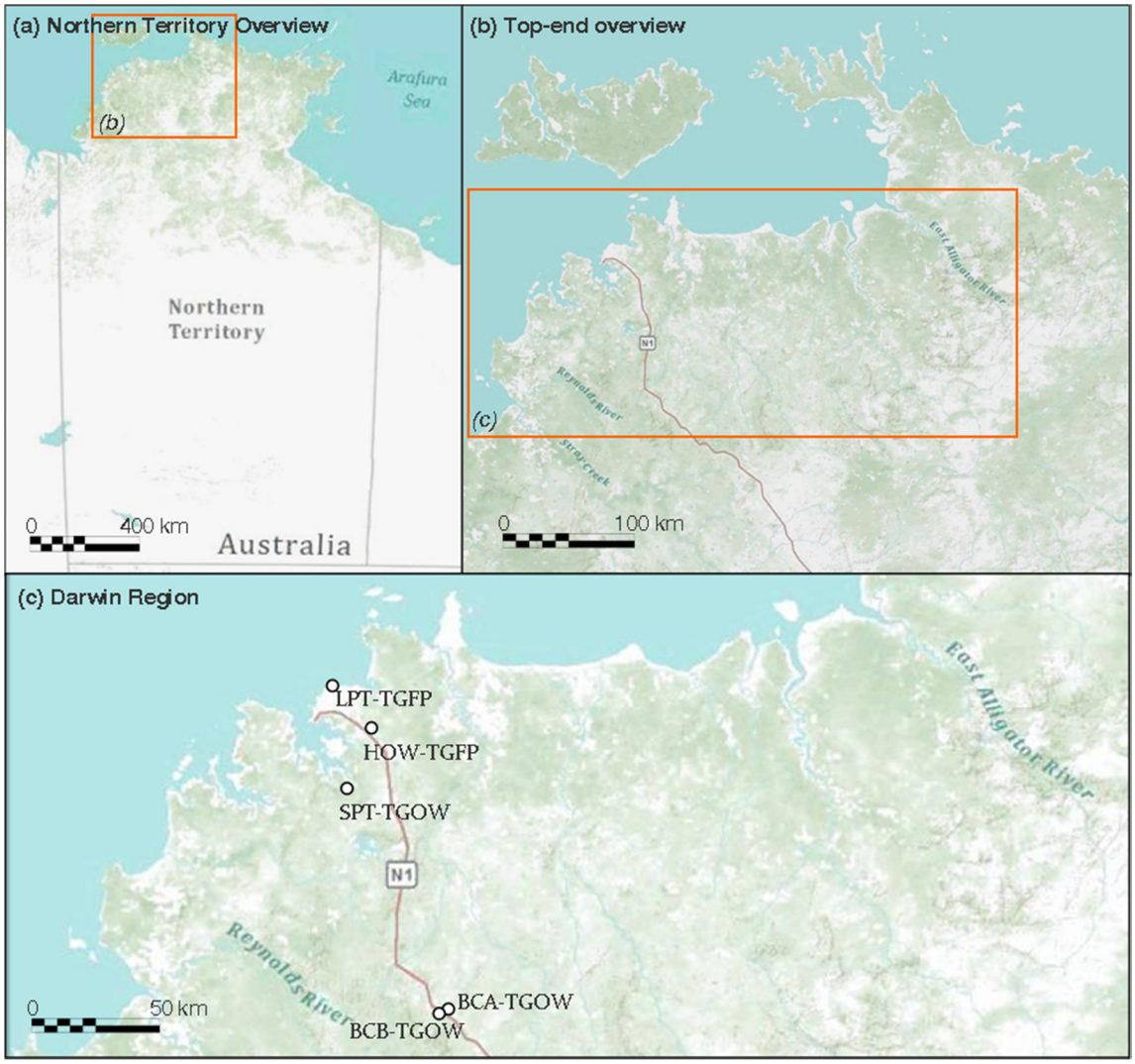

Figure 7.11 Maps showing the location of each of the fire sites measured using SO-FTIR: (a) Location of the Top-end region of the Northern Territory, Australia; (b) location of the Darwin region; (c) SO-FTIR measurement locations (see Table 7.2 for full site description).

Table 7.2 List of fires studied using SO-FTIR during the Darwin region campaign (2010), with information about the measurement location, vegetation type, and meteorological variables. The duration indicates the length of time of data collection. The location of each fire is mapped in Fig. 7.11.

Date	Local time	Dur. (min)	Site name	Veg. type	Location		Weather		
					Latitude	Longitude	T (°C)	RH (%)	P (hPa)
13-Sep-10	1400	150	HOW-TGFP	tgfp	12°30.53 S	131°03.54 E	32.7	15	1012.7
21-Sep-10	1210	50	BCA-TGOW	tgow	13°23.13 S	131°17.36 E	34.8	34	1009.5
21-Sep-10	1500	60	BCB-TGOW	tgow	13°24.55 S	131°17.39 E	35.9	48	1009.5
06-Oct-10	0950	50	SPT-TGOW	tgow	12°43.62 S	130°56.72 E	29.2	63	1008.4
15-Oct-10	1500	50	LPT-TGFP	tgfp	12°21.20 S	130°54.28 E	35.8	32	1004.9

Figure 7.12 Photograph of FTIR spectrometer measuring solar occultation spectra at the Howard Springs wildfire (13 September 2010, see Fig. 7.11 for fire location and Fig. 7.3 for further details).

7.5.2 SO-FTIR results: FTIR_FIT

As with the measurements in Canada, spectra measured at the four fires in the Northern Territory were analysed for total column CO and NH_3 using FTIR_FIT (Figure 7.13). The resultant emission ratio (NH_3:CO) for each fire vary from 0.0085 ± 0.0068 to 0.0162 ± 0.0019, whilst the emission ratio when all spectra are considered together (Figure 7.14) is 0.0135 ± 0.0055. This emission ratio is remarkably similar to the average NH_3 emission ratio to CO measured from the OP-FTIR methodology (0.0127 ± 0.0021) at 23 fires with similar vegetation characteristics (Chapter 5). This emission ratio is also similar to those reported by Hurst *et al.* (1994a) (0.016 ± 0.010, with a range of 0.006–0.043); and Hurst *et al.* (1994b) (0.026 ± 0.010, with a range of 0.014–0.056). Both of the Hurst *et al.* papers derive emission ratios from airborne FTIR measurements of tropical savanna in the Top-End of the Northern Territory and form the only published measurements of this ecosystem.

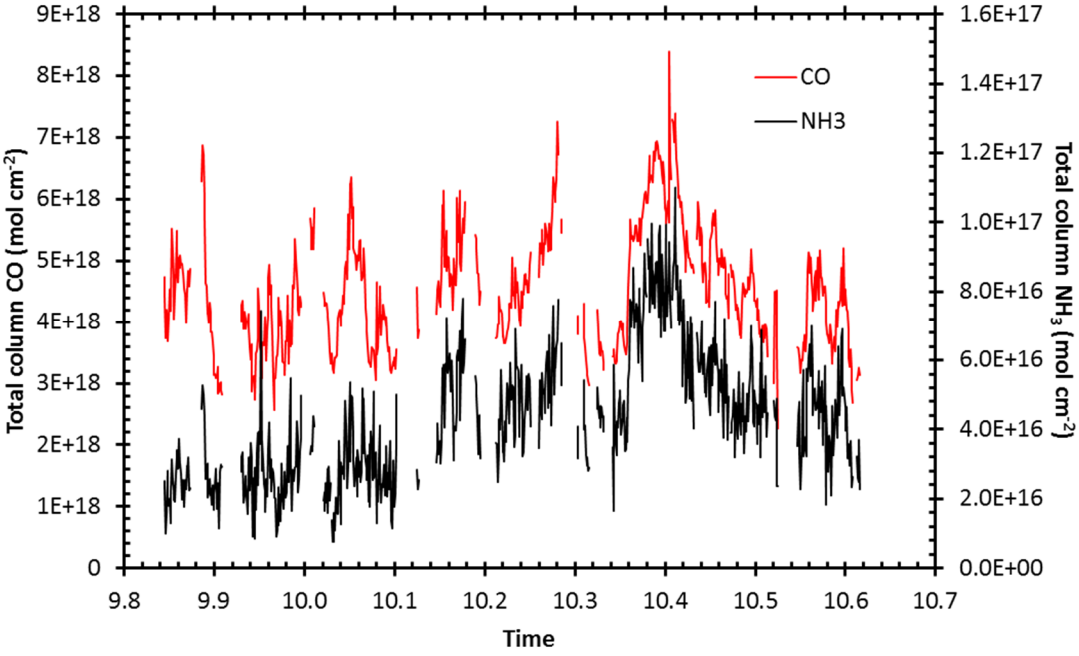

Figure 7.13 Time series of total column amounts of CO and NH_3 for the Southport wildfire (Fig. 7.11c) on the morning of 6 October 2010. A good correlation between CO and NH_3 can be used to establish an emission ratio for these species (Fig. 7.14 and Table 7.3). Gaps in the data above correspond to times when adjustments were made to the alignment of the spectrometer with the sun.

Table 7.3 NH_3 emission ratios to CO for each of the fires measured using SO-FTIR. Emission ratio to CO is calculated from bivariate plots (as described in Section 3.3.3), where the least squares linear regression slope of NH_3 vs. CO total column amounts is used as the emission ratio (Fig. 7.14). The stated uncertainties are derived from the 95% confidence limits on the slope gradient. The strength of the coefficient of determination (R^2) is also shown. When all measurements are used for the linear least squares regression (as shown in Fig. 7.14), the NH_3 emission ratio to CO is 0.0135 ± 0.0055, as opposed to the average of the five fires: 0.0119 with a standard deviation of 0.0030.

Fire	NH_3/CO emission ratio ± slope uncertainty	R^2
Southport	0.0162 ± 0.0019	0.653
Howard Springs	0.0134 ± 0.0012	0.697
Bridge Creek A	0.0118 ± 0.0010	0.760
Bridge Creek B	0.0085 ± 0.0068	0.420
Lee Point	0.0095 ± 0.0084	0.564
All measurements	**0.0135 ± 0.0055**	**0.720**

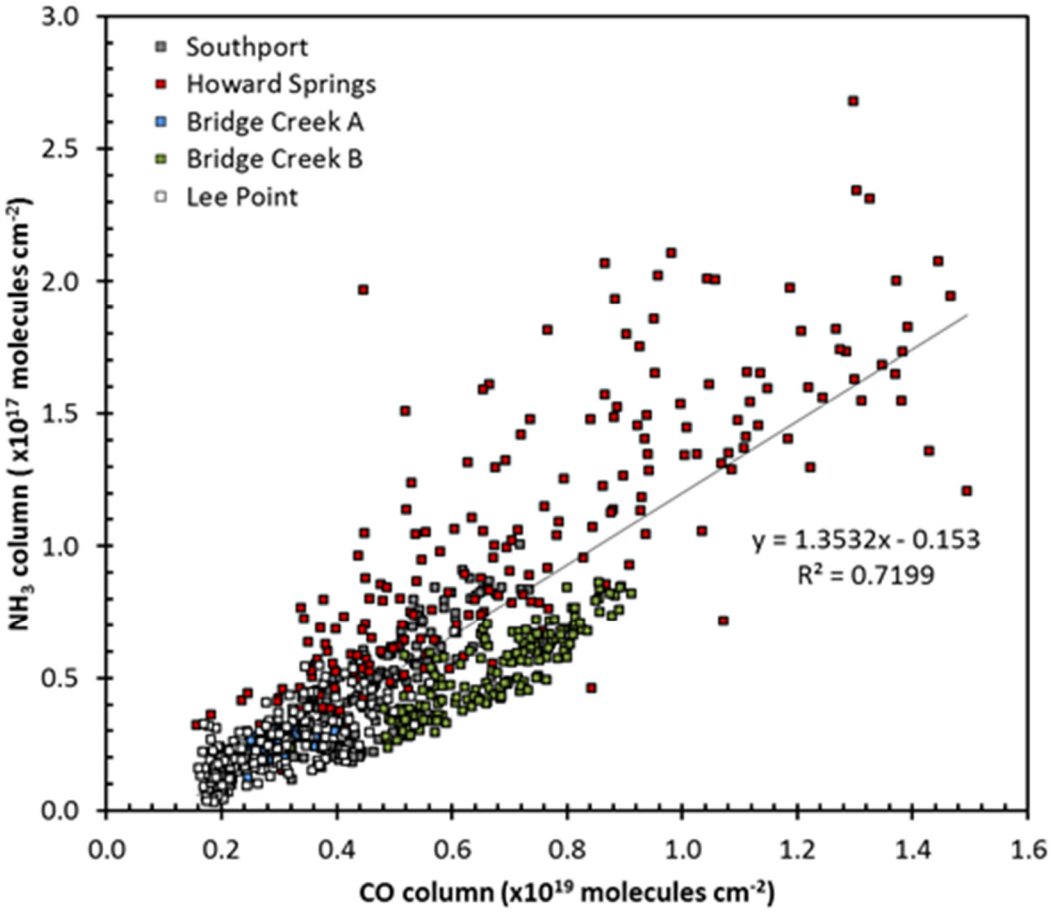

Figure 7.14 Bivariate scatter plot of the total column amounts of CO and NH_3 for each of the four fires measured at five locations using SO-FTIR. The linear least squares regression line for all data is shown. This equates to an NH_3 emission ratio to CO of 0.0135 ± 0.0055.

7.5.3 SO-FTIR results: cross validation with Atmosphit

Twelve spectra were selected from the Howard Springs SO-FTIR dataset for analysis in Atmosphit. The twelve spectra were selected from within the full range of CO column amounts retrieved using FTIR_FIT. The optimised spectral window for retrievals of CO in Atmosphit (2,141–2,242 cm^{-1}, see Section 7.3.4) was used for CO, whilst the 900–980 cm^{-1} spectral window was used for retrievals of NH_3 (as used in the OP-FTIR analysis and for the analysis using FTIR_FIT described above). Figure 7.15a shows good agreement between the two retrieval algorithms for CO, with negligible bias and a small positive offset for the Atmosphit retrievals. Retrievals of NH_3 were problematic in Atmosphit for spectra with apparently lower column amounts of NH_3 as retrieved using FTIR_FIT (Figure 7.15b); a successful fit was achieved for 7 of the 12 spectra, with the

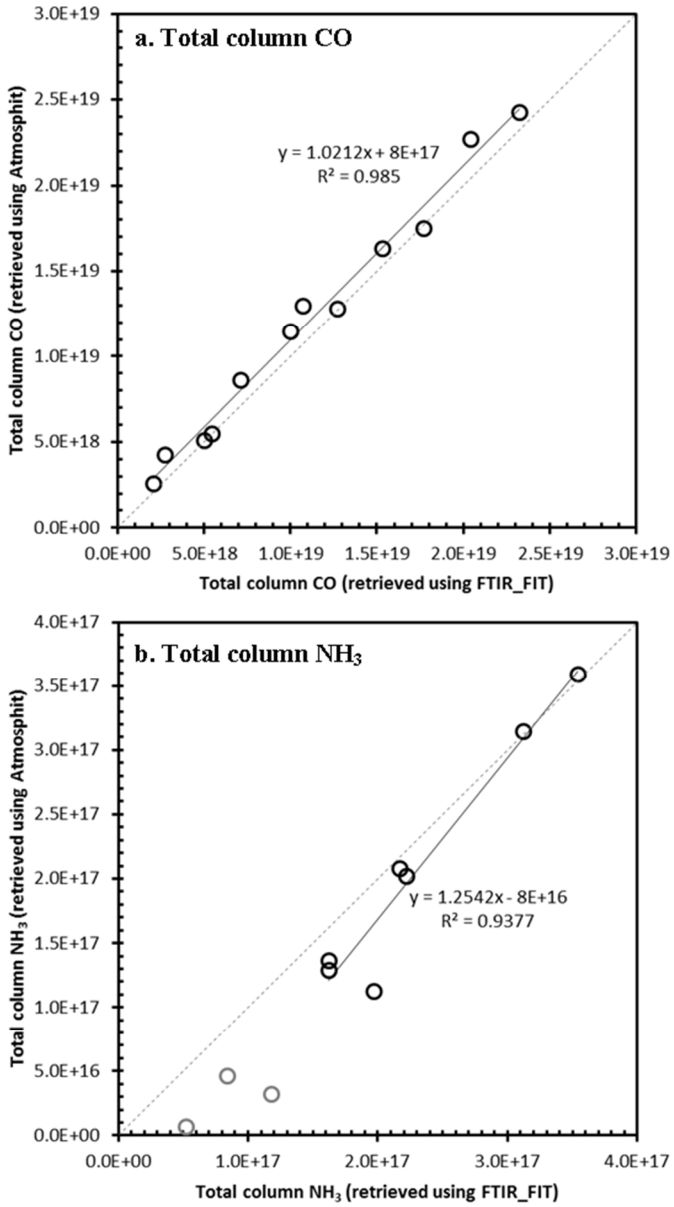

Figure 7.15 A comparison of total column retrievals of (a) CO; and (b) NH_3 using FTIR_FIT (*x-axis*) and Atmosphit (*y-axis*). The least squares linear best fit to the retrievals is shown (solid black line) along with the 1:1 line (dashed grey line).

remaining spectra achieving a poor fit (and resulting in substantially smaller retrieved NH_3 amounts than those retrieved using FTIR_FIT) or failing to fit altogether. For larger NH_3 column amounts, the two methods agree better, with the two largest amounts of NH_3 agreeing to within 2%.

The retrieved further gas column amounts (e.g. HCN, CH_2O, C_2H_2, C_2H_4) using Atmosphit proved problematic. The spectral micro-windows used by Paton-Walsh *et al.*

(2005) (typically smaller than one wavenumber for spectra with a resolution of 0.004 cm^{-1}) could not be used for the analysis here, due to the limited spectral resolution of the MIDAC FTIR spectrometer (0.5 cm^{-1}). Instead, attempts were made to use similar spectral windows to those used for the OP-FTIR analysis (Table 3.3). Unfortunately, severe H_2O saturation from atmospheric water vapour affected each of these spectral windows, effectively dwarfing any potential signal from the other target gases. This is a potentially limiting factor for the use of SO-FTIR in the study of biomass burning emission ratios and emission factors. Further work is needed, particularly tests in cooler/less humid environments where H_2O saturation is likely to be less of an issue, to rule out the possibility of using SO-FTIR at 0.5 cm^{-1} resolution for gases other than CO and NH_3.

7.5.4 Correlation of total column amounts with AOD

At each of the five SO-FTIR measurement locations, simultaneous and collocated measurements were also made using a Microtops II sun photometer. The Microtops II sun photometer consists of five specialised narrow field-of-view radiometers designed to measure solar irradiance at five wavelength bands (centred at 440, 675, 870, 936, 1020 nm). The Microtops II employs a multi-detector arrangement, with each wavelength filter fixed in front of a dedicated solid-state detector (silicon photodiodes); consequently, all bands are measured simultaneously. Given that the total optical depth recorded by a sun photometer is the sum of aerosol optical depth (AOD) and Rayleigh optical depth (which depends on wavelength and local pressure at the measurement site) (Mather *et al.*, 2004), the Microtops II performs an automatic correction for Rayleigh scattering and outputs AOD at the five wavelengths. Both the laptop controlling the FTIR spectrometer and the Microtops II sun photometer were time synchronised using GPS time. Given that the measurement time for the Microtops II (~8 seconds depending on solar alignment) was longer than that for the SO-FTIR (~1.5 seconds), an average of the SO-FTIR measurements for each Microtops II measurement was used for comparison. Due to their simultaneous operation at the same location (separated by less than 5 m at any one time), it may be assumed that the Microtops II and FTIR spectrometer are in the same alignment with the sun.

Figure 7.16 shows a time series of total column CO and AOD at the Southport wildfire. A relationship is clearly evident in the data, with simultaneous peaks and minor changes evident in both the SO-FTIR and Microtops II measurements. Figure 7.17 shows the total column amounts of both CO and NH_3 plotted against AOD at each of the Microtops II wavelengths, with each plot showing each of the five measurement locations. AOD measurements at the Lee Point fire did not correlate well with trace gas concentrations. This may be explained by the proximity of the measurements to the wildfire. Unlike the measurements at Southport, Howard Springs and Bridge Creek, where measurements were conducted at a distance of 1 to 3 km from the fire front, the measurements at Lee Point were conducted adjacent to the fire front. A lack of relationship between AOD and trace gas amounts at this fire were probably due to large, swift changes in plume composition that could not be resolved by the somewhat different measurement times of the two instruments.

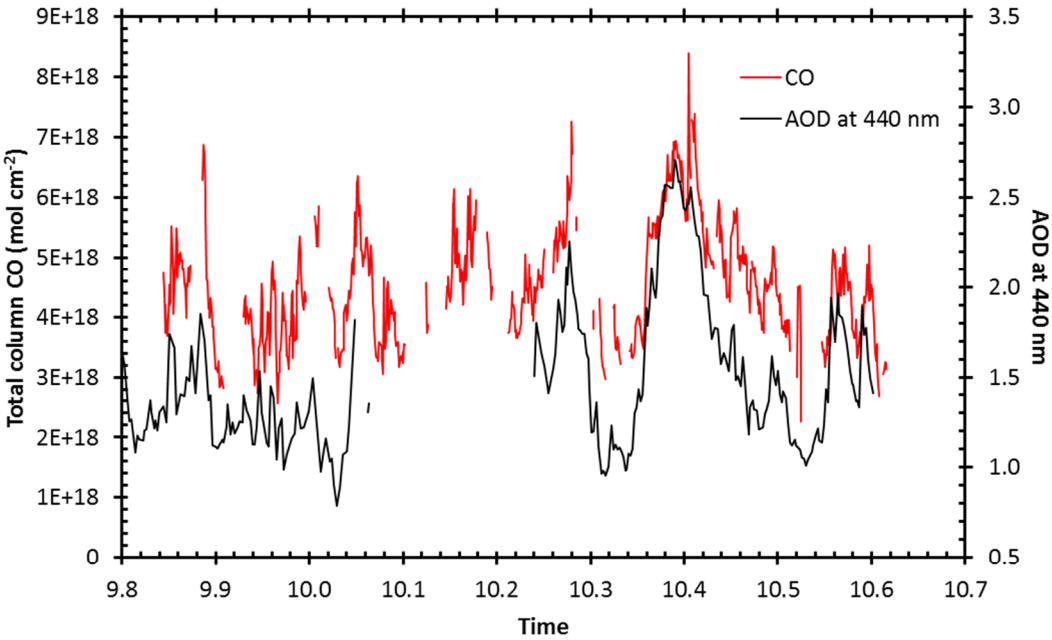

Figure 7.16 Time series of total column CO derived from SO-FTIR spectra and AOD at 440 nm measured using the Microtops sun photometer at the Southport wildfire (a time series of total column CO and NH_3 for the same fire can be seen in Fig. 7.13). There is a strong relationship between total column CO and AOD (Fig. 7.16) which implies that AOD may be used as a proxy for fire emissions. Gaps in the data above correspond to times when adjustments were made to the alignment of the spectrometer or sun photometer with the sun.

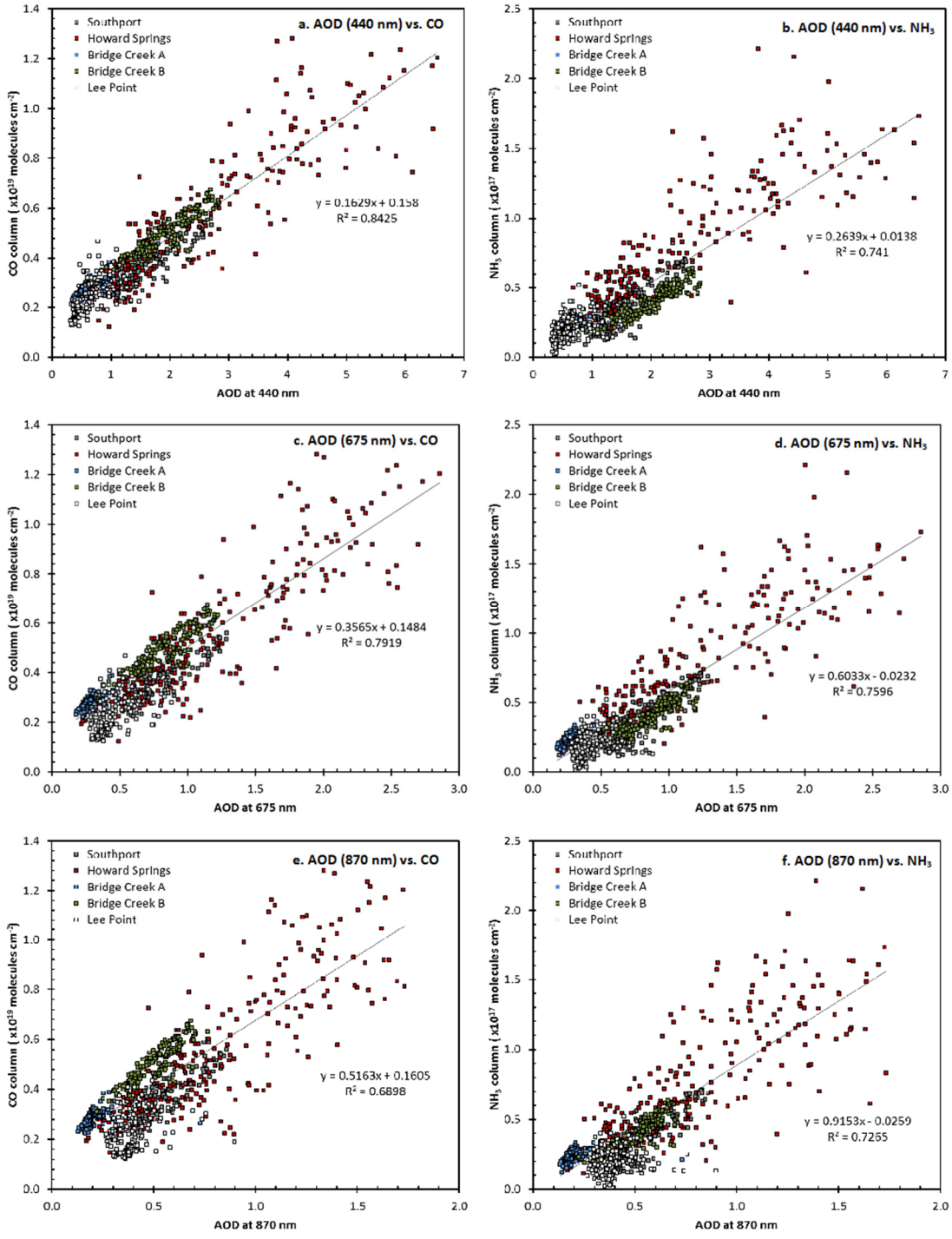

Figure 7.17 (continued on next page) Vertical column amounts of carbon monoxide (left) and ammonia (right) plotted against AOD at five wavelngths (440, 675, 870, 936, 1020 nm). The measurements were made at four Northern Territory tropical savanna wildfires in September and October 2010. The linear least squares regression line is also shown. Measurements from the Lee Point fire (white squres) were excluded from the linear regression due to a high degree of scatter in the data. A lack of a significant relationship between AOD and the trace gases at the Lee Point fire might be explained by the close proximity of the measurement to the fire (where quick changes in the composition of the plume may have hindered the methodology applied here due to the different measurement times required by the FTIR spectrometer and the Microtops sun photometer).

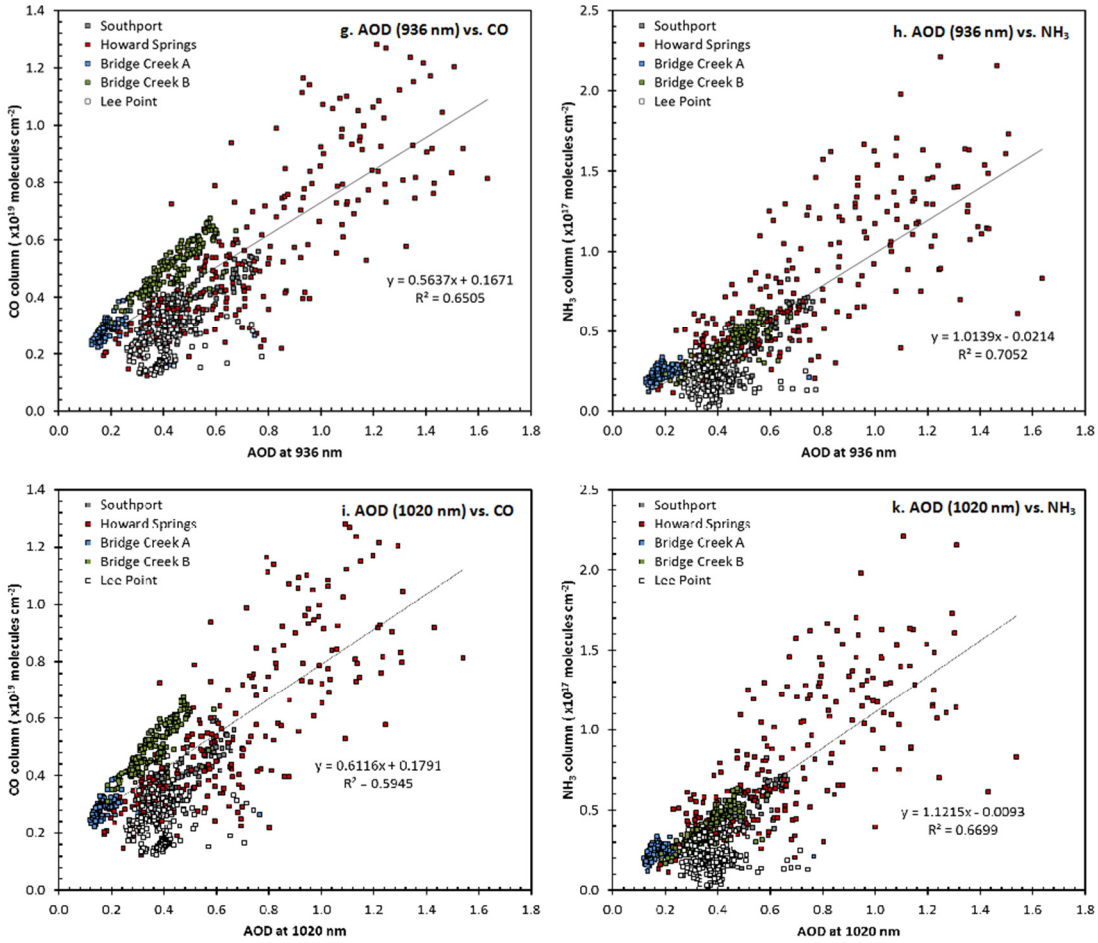

Figure 7.17 (continued from previous page)

The strength of correlation between both column CO and NH_3 and AOD is wavelength dependent, as might be expected due to the size distribution of the smoke particles. The aerosol size distribution of biomass burning particles is known to be bi-modal (Remer *et al.* 1998) with a fine particle volume peak at ~130 nm and a second coarser volume peak at ~10 µm. This distribution explains the stronger correlation to CO at shorter sun photometer wavelengths (with R^2 = 0.84 at 440 nm, compared with R^2 = 0.59 at 1020 nm; Figure 7.17 shows the decrease in mean AOD with wavelength for each fire). The relationship between AOD at 440 nm and vertical columns of both CO and NH_3 is consistent for each of the fires measured here, although the magnitude of discrepancies between the fires increases with wavelength, possibly due to the lower AOD at longer wavelengths.

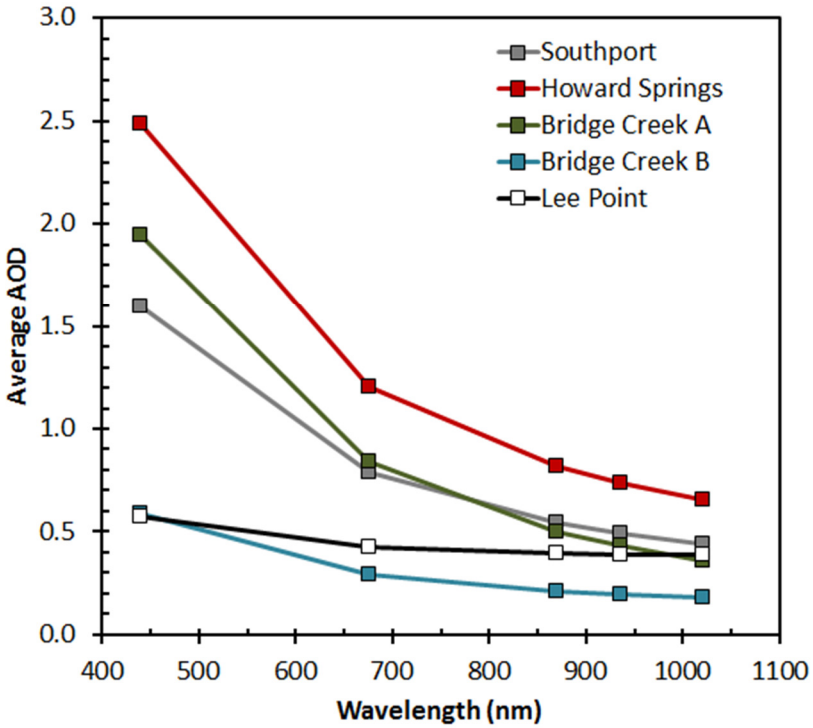

Figure 7.17 Mean AOD at each of the five wavelengths measured by the Microtops II sun photometer for each of the five measurement locations in the Darwin region, Northern Territory, Australia. The aerosol size distribution of biomass burning particles is known to peak below 1 µm (Remer *et al.*, 1998; Kaufman *et al.*, 2002; Abel *et al.*, 2003; Reid *et al.*, 2005), which explains the decline in AOD with increasing wavelength. The strength of the relationship between AOD and trace gases related to biomass burning (as presented in Fig. 7.16) also decreases with increasing wavelength.

When all data are considered (excluding those from Lee Point), the relationship between vertical column amount of CO and AOD at 440 nm is CO = (1.62AOD + 1.58) × 10^{18} molecules cm^{-2} with a correlation coefficient of R^2 = 0.84. This compares to the relationship established by Paton-Walsh *et al.* (2010b) for smoke plumes over Darwin of CO = (1.7AOD + 1.3) × 10^{18} molecules cm^{-2} with a correlation coefficient of R^2 = 0.65 and CO = (1.5AOD + 1.5) × 10^{18} molecules cm^{-2} with a correlation coefficient of R^2 = 0.87 for southeast Australian forest fires (Paton-Walsh *et al.*, 2005) (where AOD was measured at 500 nm). The relationship between NH_3 and AOD at 440 nm is NH_3 = (2.64AOD + 0.14) × 10^{16} molecules cm^{-2} with a correlation coefficient of 0.74. This differs significantly from the relationship established for southeast Australian forest fires (Paton-Walsh *et al.*, 2004), where NH_3 = (1.1AOD + 0.8) × 10^{16} molecules cm^{-2}, although there is a larger degree of scatter in the data presented in Paton-Walsh *et al.* (2004), with an R^2 of 0.57. This large discrepancy is likely to be due to the relatively

short half-life of NH_3 in the atmosphere (~hours, depending on ambient aerosol and water vapour concentrations). Where Paton-Walsh *et al.* (2004) were measuring plumes that had aged by hours/days, in which time NH_3 may have been scavenged by water vapour and aerosols, the plumes measured for this study in the Northern Territory were young (minutes), where water vapour and aerosol scavenging would have been minimal, accounting for the higher multiplicand in the regression equation and the stronger correlation.

7.7 Conclusions and Implications

This Chapter has explored the use of a highly portable methodology for measuring both trace gas and aerosol emissions from biomass burning plumes. Whilst previous research has shown that low spectral resolution FTIR spectrometers can be used to make precise measurements of total column carbon monoxide (Stremme *et al.*, 2009; Grutter *et al.*, 2010), this Chapter has made the first quantitative attempt to assess the *accuracy* of such instruments, finding that excess amounts of CO contained within a ground-level plume can be retrieved to a better than 5% accuracy (Section 7.3) when using Atmosphit. Whilst excess plume amounts of CO_2 could not be discerned from the accuracy assessment spectra or those collected in the field, it has been shown that emission ratios of NH_3 to CO can be reliably ascertained from measurements of biomass burning plumes. Furthermore, the NH_3:CO emission ratio agrees with both the OP-FTIR results from Chapter 5 of this thesis (calculated from ground-based measurements in the same tropical savanna ecosystem) and with the only published emission ratios for this ecosystem (the airborne FTIR measurements of Hurst *et al.*, 1994a; Hurst *et al.*, 1994b). This result helps to confirm that the OP-FTIR methodology can be used to measure both flaming and smouldering emissions under these types of fire conditions, and does not appear to be biased towards smoke originating from smouldering combustion. Further work is needed to extend the analysis to include other biomass burning trace gas species, although water vapour saturation throughout most of the spectrum may limit this capability.

The co-located and simultaneous measurements of AOD show how this portable methodology can be extended to establish a strong relationship between AOD and the

trace gas amounts. The relationship between AOD at 440 nm reported here agrees well with previous AOD and trace gas column measurements over Darwin (Paton-Walsh *et al.*, 2010b). Previous studies have found a good agreement between ground-based sun photometer measurements of AOD (as used in this Chapter) and satellite measurements of AOD (Schmid *et al.*, 2003). If the ground-level AOD measurements match well with satellite-measurements of AOD, then spaceborne measurements of AOD from instruments such as MODIS (Edwards *et al.*, 2006) and MISR (e.g. Diner *et al.*, 2001) could therefore be used as a proxy for trace gas columns (Paton-Walsh *et al.* 2004).

The added portability and higher temporal resolution of the SO-FTIR methodology used here could be exploited in future campaigns to assess both the evolution of plume characteristics (e.g. by making a longitudinal transect of large plumes) and to measure in regions that are not well covered by permanent measuring stations with the ability to measure both AOD and trace gas columns at the same location.

8

Summary, Conclusions and Future Prospects

8.1 Summary of main conclusions

The overall aim of this thesis has been to contribute to improving our knowledge of emissions to the atmosphere from biomass burning in different ecosystems and environments. Towards this, the work has confirmed that Open-Path Fourier Transform Infrared (OP-FTIR) spectroscopy is a highly effective and valuable technique for the measurement of trace gas emissions from biomass burning, with the application of this method to field data collected at over fifty fires during seven field campaigns. En route, the thesis has presented analysis of the precision and accuracy of both the long open-path methodology using an IR lamp, and an alternative approach using the sun (Solar Occultation FTIR, SO-FTIR). Following this brief review of the content of the previous Chapters, this Chapter will address the specific research questions outlined in Chapter 2 before commenting on avenues for future research, both towards greater understanding of biomass burning emissions, and towards the further development of the FTIR spectroscopy method itself in relation to biomass burning applications.

The introductory Chapter sets this thesis in context, providing several motivations for the measurement of biomass burning emissions, including the academic pursuit of a greater understanding of biomass combustion dynamics as well as the wider aim of investigating the environmental effects of biomass burning (particularly those related to greenhouse warming and ozone formation), and the pragmatic goal of emissions monitoring for smoke plume hazard mitigation. Chapter 2 reviewed a series of

approaches to measuring biomass burning emissions, highlighting OP-FTIR as a promising novel technique among other field, laboratory and airborne methods.

Chapter 3 offers a technical introduction to infrared spectroscopy and the FTIR spectrometer before addressing the applicability of infrared spectroscopic techniques to ground-based field measurements of biomass burning trace gas emissions. The MIDAC spectrometer used throughout this work is described as being particularly portable and rugged and suitable for field measurements using similarly portable active infrared sources or even the sun. Example spectra are shown to contain the identity and concentrations of a series of important biomass burning trace gas products present in the optical path (CO_2, CO, C_2H_2, C_2H_4, C_2H_6, HCOOH, CH_2O, CH_3OH, HCN and NH_3). This information can be retrieved using atmospheric absorption forward models coupled with optimal estimation fitting routines for specific spectral windows. The retrieved concentrations of trace gases could then be used to calculate important biomass burning emissions metrics such as modified combustion efficiency (MCE), emission ratios and emission factors. Results from comparisons with established trace gas measurement equipment and a thorough laboratory accuracy assessment are presented in Chapter 4. OP-FTIR retrievals of CO_2 and NH_3 were successfully cross-validated with other measurement techniques whilst the results of the accuracy assessment were encouraging, confirming retrievals of CO_2, CO and CH_4 spanning broad concentration ranges (i.e. from ambient to highly polluted) to be accurate to within 5% of their known concentrations.

Having established the theoretical suitability of OP-FTIR for biomass burning applications in Chapter 3 and evaluated OP-FTIR retrievals of important biomass burning products in Chapter 4, Chapter 5 presents the application of the technique to field measurements at fires in the Northern Territory, Australia. Measurements at a series of experimental fires and wildfires at three campaigns in 2009 and 2010 were used to determine emission factors for a suite of important trace gases (listed above). These represent the first reliable emission factors for CH_2O, CH_3OH, HCOOH and HCN to be measured for the Australian savanna ecosystem, and one of only a handful of studies of the other trace gases for this ecosystem. By comparing measurements of emissions from different vegetation types and during different burning seasons, it was

possible to explain that most of the variability in emission factors was due to the modified combustion efficiency as a result of different vegetation types, rather than different times of year. In addition to OP-FTIR measurements, point-source *in situ* bag sampling was also carried out by CSIRO. Results from their analyses of methane emissions agree very well with the OP-FTIR results, further strengthening the validity of OP-FTIR as a useful tool for biomass burning applications.

Following successful field deployment to Australia, the OP-FTIR technique was applied to the hitherto un-measured emissions from heathland fires in the UK. Chapter 6 presents the results from numerous fires carried out during three campaigns to UK heathlands. The results provide the first measurement-based emission factors that should improve estimates of total national and international emissions from biomass burning in heathland and moorland ecosystems. In an attempt to model total emissions from controlled biomass burning in the UK, it was shown that the new emission factors reported here could significantly reduce uncertainties in current estimates. Chapter 6 also presents the results of concurrent measurements of *in situ* bag samples collected during distinct combustion phases. Analyses of these bag samples in a multi-pass IR White cell were used to show that the OP-FTIR methodology successfully captures the full-range of emissions from flaming combustion, whilst targeted bag samples were shown to be a more effective way of sampling residual smouldering combustion.

In an extension of the open-path methodology, Chapter 7 presents analysis of ground-based solar absorption spectra taken through smoke plumes originating from tropical savanna fires in the Northern Territory, Australia. The emission ratio of NH_3 to CO for these lofted plumes is shown to be similar to that measured for similar fires on the ground using the OP-FTIR in Chapter 5. Furthermore, the measured trace gas amounts of CO and NH_3 are shown to correlate well with simultaneous, co-located measurements of Aerosol Optical Depth (AOD). As such, this Chapter builds on previous work to suggest that AOD can be used as a proxy for CO and potentially for a series of other trace gases using their emission ratios to CO.

8.2 Summary of results related to the research questions

In Chapter 2 a number of specific research questions were posed. These are restated again below (in italics), followed by a discussion of how the thesis has addressed each question and a summary of results related to each.

1. *Can OP-FTIR spectroscopy be used to yield accurate and precise measurements of important biomass burning trace gas species spanning the full range of concentration that might be experienced in field measurements?*

Pilot studies were conducted where trace gas concentrations of CO_2 and NH_3 retrieved from OP-FTIR spectra were compared with those derived via more established measurement techniques. For CO_2, OP-FTIR measurements of the ambient urban atmosphere were compared with those from a recently calibrated Licor 840 closed-path NDIR CO_2 analyser (LI-COR Biosciences, Lincoln, Nebraska). They were shown to agree well, exhibiting a similar precision to the Licor 840 and lacking any significant bias or offset. For NH_3, spectra were collected at a recently fertilised agricultural site, and the FTIR-retrieved NH_3 concentrations compared to those from a host of other analytical techniques. Whilst the OP-FTIR dataset was substantially smaller than those for most of the other instruments, and only covered low concentrations of NH_3, the available data confirmed that the OP-FTIR derived amounts agreed with the other methods. This work contributed to an inter-comparison of the various NH_3 measurement techniques published as:

> Von Bobrutzki, K., Braban, C.F., Famulari, D., Jones, S.K., Blackall, T., **Smith, T.E.L.**, Blom, M., Coe, H., Gallagher, M., Ghalaieny, M., McGillen, M.R., Percival, C. J., Whitehead, J.D., Ellis, R., Murphy, J., Mohacsi, A., Pogany, A., Junninen, H., Rantanen, S., Sutton, M.A., Nemitz, E. (2010) Field inter-comparison of eleven atmospheric ammonia measurement techniques. *Atmospheric Measurement Techniques* **3**: 91–112.

To more carefully assess the absolute accuracy of OP-FTIR technique for trace gas retrievals, a laboratory experiment was conducted where the FTIR was positioned to view a fixed IR source placed at the opposite end of an IR-transparent cell filled with

known amounts of CO_2, CO and CH_4 respectively. The target concentrations of these gases were varied by two orders of magnitude, and with careful parameterisation of the retrieval model (optimised spectral window, instrument line shape, and assumed gas temperature and pressure), concentrations for all target gases were able to be retrieved to within 5% of true values. This was the case for the full range of concentrations examined. Sensitivity to the aforementioned parameter inputs was also investigated. Retrieval accuracy was shown to still remain better than 10%, even with realistic uncertainties in atmospheric pressure and temperature or the type that might arise when studying plumes in field situations. This work was published in:

> **Smith, T.E.L.**, Wooster, M.J., Tattaris, M., Griffith, D.W.T. (2011) Absolute accuracy and sensitivity analysis of OP-FTIR retrievals of CO_2, CH_4, and CO over concentrations representative of "clean air" and "polluted plumes". *Atmospheric Measurement Techniques* **4**: 97–116.

Through this combination of cross-validation with other measurement techniques and an absolute accuracy assessment performed under controlled laboratory conditions, this thesis has established that OP-FTIR can be used to yield accurate and precise measurements of CO_2, CO, and CH_4 spanning the full range of concentrations that might be experienced in field measurements of biomass burning plumes. Absolute accuracy of many other important biomass burning products is problematic due to the difficulties in measuring these gases in controlled environments, where for example adsorption becomes an issue (e.g. for NH_3, CH_2O, CH_3OH, HCN). Further cross-validation work is required to test the absolute accuracy of OP-FTIR retrievals of these gases, although the passive nature of the OP-FTIR methodology should yield better accuracy than established techniques that rely upon sample handling and storage.

2. *Can ground-based OP-FTIR be used to make representative measurements of biomass burning emissions so that "fire-averaged" emission factors can be ascertained (*i.e. *are ground-based OP-FTIR measurements biased towards either flaming or smouldering emissions)?*

Given that the proportion of smoke in the measurement path originating from different areas of combustion having differing modified combustion efficiencies will vary over

time, depending on the position of the measurements, the wind direction and speed, and the position of flaming fronts (backing fires and head fires), emission factors representative of a landscape cannot be derived simply by taking the mean results from all the measured spectra. Instead, some form of normalisation is needed to produce an emission factor that best represents the conditions under which the majority of the vegetation burns. Wooster *et al.* (2011), determined emission factors for discrete stages of savannah fires (e.g. for the backing fire, the head fire and for residual smouldering combustion). Working in southern Africa, aerial thermal imagery of the fire was used to prove that the overwhelming majority of the vegetation fuel was burned during flaming combustion. As such, it is the emission factors for the flaming stages of the fire that provide the best approximation to the total "fire averaged" emission factor. In laboratory studies of biomass burning it is possible to measure smouldering and flaming emission factors separately, and weight these by the amount of fuel that was combusted during each stage (e.g. Yokelson *et al.,* 1997). This is not possible in the field, and for this thesis aerial thermal imagery was not generally available. Thus the proportion of vegetation burned during the flaming and smouldering stages could not be determined for the fires studied here. It was therefore necessary to assume that the Australian savanna fires measured in Chapter 5, and the heathland fires measured in Chapter 6, behave in a similar way to those measured by Wooster *et al.* (2011) in terms of the majority of the fuel being burned during the flaming rather than the smouldering combustion. Previous work in savannas (e.g. Ward *et al.,* 1996), together with personal observations in Australia and in UK heathlands, support this assumption.

Instead of identifying individual spectra as originating from a particular fire stage (as was done in Wooster *et al.,* 2011 using the airborne imagery and ground-observer reports), this thesis takes the approach of Lobert *et al.,* (1991); Yokelson *et al.,* (1996) and Bertschi *et al.* (2003b) and assigns each measured spectrum to "flaming" or "smouldering" stage based on its MCE, as derived from the retrieved CO_2 and CO concentrations. After consideration of numerous literature MCE values for flaming and smouldering combustion, an MCE threshold of 90% was used to classify each spectrum as either originating from "*predominantly flaming*" combustion or "*predominantly smouldering*" combustion. According to the aforementioned assumption that the majority of vegetation burns during flaming combustion in savannah environments

(Ward *et al.,* 1996; Wooster *et al.,* 2011), the emission factor derived from the "*predominantly flaming*" spectra was taken to be representative of the "whole-fire" emissions. The same was done for the UK heathland measurements, and a number of steps were taken to try to assess the validity of this approach:

(i) The emission factors determined using the MCE thresholding method for the savanna fires in Australia were compared with those published for other savanna environments. An agreement between the emission factors reported in this thesis and those reported for both Australian and African savannas (Chapter 5), suggests that the threshold method delivers appropriate metrics.

(ii) Emission factors determined from *in situ* bag samples of smoke resulting directly from flaming combustion were shown to agree with those derived from the OP-FTIR spectra that were classified as *predominantly flaming* (Chapters 5 and 6). Importantly, MCE determined from the bag samples of flaming combustion were shown to lie *within* the range of MCE measured by the OP-FTIR, implying that OP-FTIR may in fact be more useful for measuring the highest MCE emissions originating from the most intense stages of the fire that might be missed by grab sampling (Chapter 6).

(iii) The emission ratio of NH_3 to CO determined using solar occultation measurements of the lofted plumes from Australian savanna fires (Chapter 7) agrees rather well with the emission ratio measured using the ground-based OP-FTIR method in the same vegetation type.

Whilst these findings are encouraging, and suggest that the "flaming threshold" approach may be valid for estimating "whole-fire" emission factors, further work is needed to confirm the hypothesis that the vast majority of vegetation burns during conditions of flaming combustion, particularly in the understudied heathland fires.

3. *By making numerous measurements of different fires within a particular ecosystem at different times of the year, can OP-FTIR spectroscopy yield information on the controls of the natural variability of emissions?*

The key Figures that address this question are the bivariate plots of concentrations of specific trace gases (e.g. CH_4) versus those of CO_2 from all data from a particular ecosystem (e.g. Figure 5.11 for Australian savannas, and Figures 6.15 and 6.16 for UK heathlands). The ability to take thousands of "smoke samples" (using each individual spectrum) permits a detailed description of the range of emission ratios that can exist for a particular ecosystem. By attributing each sample (each spectrum) to a particular vegetation class, time of year, or MCE, it is possible to make an assessment of the controls on the emission ratio variability. In the Australian campaign, the distribution of measurements on the CH_4 *vs*. CO_2 plot (Figure 5.11) was clearly a function of vegetation type, with spectra from different vegetation classes clustering in different locations on the scatter plot. The reason for the clustering could be explained by the different MCE under which each vegetation class predominately burns. Essentially, the emission factor for CH_4 could be expressed as a function of MCE, which in turn appears dependent on the vegetation fuel class rather than the season in which the fire occurred. This conclusion is supported by simultaneous co-located independent measurements of smoke emissions at the Australian savanna fires, made using *in situ* bag samples and subsequent gas chromatography. These data, provided by CSIRO, show good agreement with the MCE-dependent emission factors derived from the OP-FTIR measurements. These findings have been published as:

> Meyer, C.P., Cook, G.D., Reisen, F., **Smith, T.E.L.**, Tattaris, M., Russell-Smith, J., Maier, S.W., Yates, C.P., Wooster, M.J. (2012) Direct measurements of the seasonality of emission factors from savanna fires in northern Australia. *Journal of Geophysical Research* **117** (D20305), doi: 10.1029/2012JD017671.

In addition to the published academic papers listed above, it is envisaged that three further papers will be published. The first will focus on the OP-FTIR-derived emission factors for tropical Australian savannas (Chapter 5). The second will cover the heathland emission factors (Chapter 6), and will address methodological issues relating and the determination of “fire-averged” emission factors from OP-FTIR data. The third will be a shorter paper covering the solar occultation methodology and the relationship between total column trace gas amounts and aerosol optical depth, as measured in the Northern Territory (Chapter 7).

8.3 Recommendations for future work

In concluding this Chapter, it is important to point out the advances that could still be made to the methodology and types of measurement approach that have been developed and described in this thesis. These are described below, along with some ideas for future prospects that have arisen during the process of this work.

- Further confirmation of the method used to estimate representative emission factors is needed. This requires measurements of the relative mass of vegetation burned during flaming and smouldering combustion. Given that fire radiative power (FRP) is correlated with biomass consumption in the fire (Wooster *et al.,* 2005), aerial thermal imaging of fires can be used to determine the ratio of biomass consumed during each stage of a fire (as per Wooster *et al.,* 2011). FRP data are available for a few of the fires investigated in this thesis. Preliminary investigations suggest that the assumption that a majority of biomass is consumed during flaming (i.e. high MCE) combustion is valid for both the Australian savanna fires and the UK heathland fires. Further work on this topic is needed however.
- Further work is needed to confirm or deny that differences between the composition of the lofted plume and that of the advected plume exist (Andreae and Merlet, 2001; Guyon *et al.*, 2005). In addition to further solar occultation measurements (Chapter 7), there are plans to take samples within the lofted plume using Unmanned Aerial Vehicles (UAVs) for subsequent analysis by FTIR in the White cell described in Section 3.3.4.
- An alternative method of deriving emission factors is to use emission fluxes. If the total mass of each trace gas emitted from a fire can be measured, the resulting emission factors are by definition for the whole fire. Estimating total emissions from a fire using OP-FTIR would require an open path that encompasses the full width of the fire plume, and possibly more detailed wind measurements to assist with plume dispersal modelling. It may be advantageous to deploy multiple paths through the plume using two or more FTIR spectrometers for such a study.
- Currently the solar occultation method used with the 0.5 cm^{-1} resolution spectrometer used here appears limited to retrieving only the total column abundances of CO and NH_3 (Chapter 7); retrieval of further gases is impeded by

water vapour saturation in the measured spectra. Further measurements are needed of biomass burning plumes in less humid environments (e.g. perhaps high latitude mountainous regions), where water vapour saturation should be less of an issue. A higher spectral resolution instrument is also a possibility, but this would compromise portability (and raise costs).

- A possible improvement to the OP-FTIR methodology deployed herein is to use a modulated IR source (Griffiths *et al.,* 1991). This requires housing the IR source within the spectrometer, and passing the IR radiation through the interferometer, along the open path before reflecting the IR beam back towards the spectrometer's detector. Only the modulated IR beam is measured by the detector, removing contamination of the signal by background radiation (which requires subtracting in the methodology of this thesis), and by infrared emission from flames within the path. However, this again may compromise portability, by for example requiring a large retro-reflector rather than the (relatively small) IR lamp currently used.
- In the process of reviewing collected data following an experimental fire, it was noticed that the broadband signal at the detector (i.e. across the full wavenumber range) was variable, and would decrease during the course of a particular fire (Figure 8.1). Furthermore, the signal loss appears to correlate with the concentration of carbon monoxide in the open path (Figure 8.2), suggesting that the signal losses are a function of fire emissions, and are not 'random' fluctuations caused for example by the wind. The broadband signal losses are thus attributed to scattering by aerosols in the open path. The broadband signal losses are also frequency dependent, with increasing signal loss at higher wavenumbers (Figure 8.3). This is in agreement with the suggestion that scattering by aerosols should increase with frequency (Eck *et al.*, 1999). This finding posits the possibility that OP-FTIR could be used to determine the mass of aerosols within the open-path (albeit knowledge of the frequency size distribution of the smoke particles would be required). If this were possible, then aerosol emission factors could likely be determined, via an adaptation of carbon mass balance approach used for the trace gases.

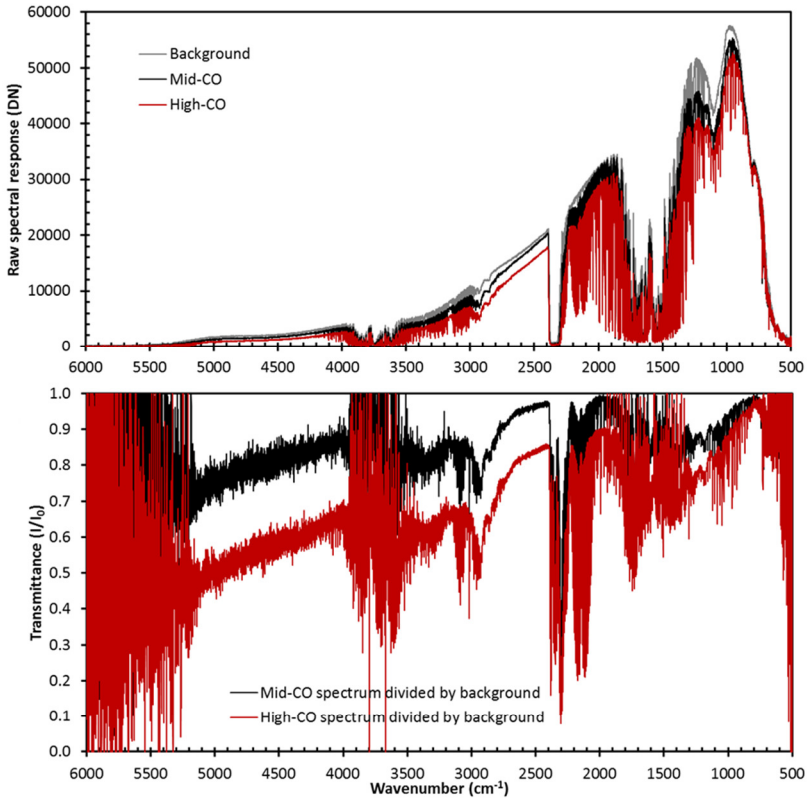

Figure 8.1 (top) Single-beam spectra from before a fire (background) and during a fire (mid-CO and high-CO). The broadband signal clearly decreases during the fire, the decrease also appears to be proportional to the amount of CO in the path. (bottom) transmittance calculated by dividing the fire spectra by the background spectrum. As predicted by the fact that aerosol scattering increases with frequency, broadband transmission decreases at higher frequencies (from almost 1 at 1,000 cm^{-1}, to ~0.5 at 5,000 cm^{-1} for the high-CO spectrum.

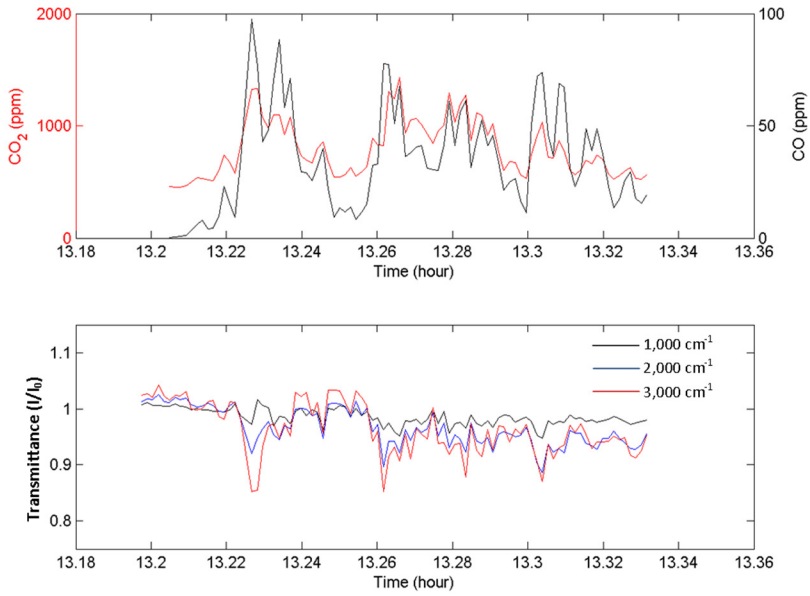

Figure 8.2 (top) time series of CO_2 (red line) and CO (black line); (bottom) time series of broadband transmittance at 1,000 cm^{-1}, 2,000 cm^{-1}, and 3,000 cm^{-1}. The drops in transmission coincide with peaks in CO_2 and CO and are strongest at 3,000 cm^{-1}.

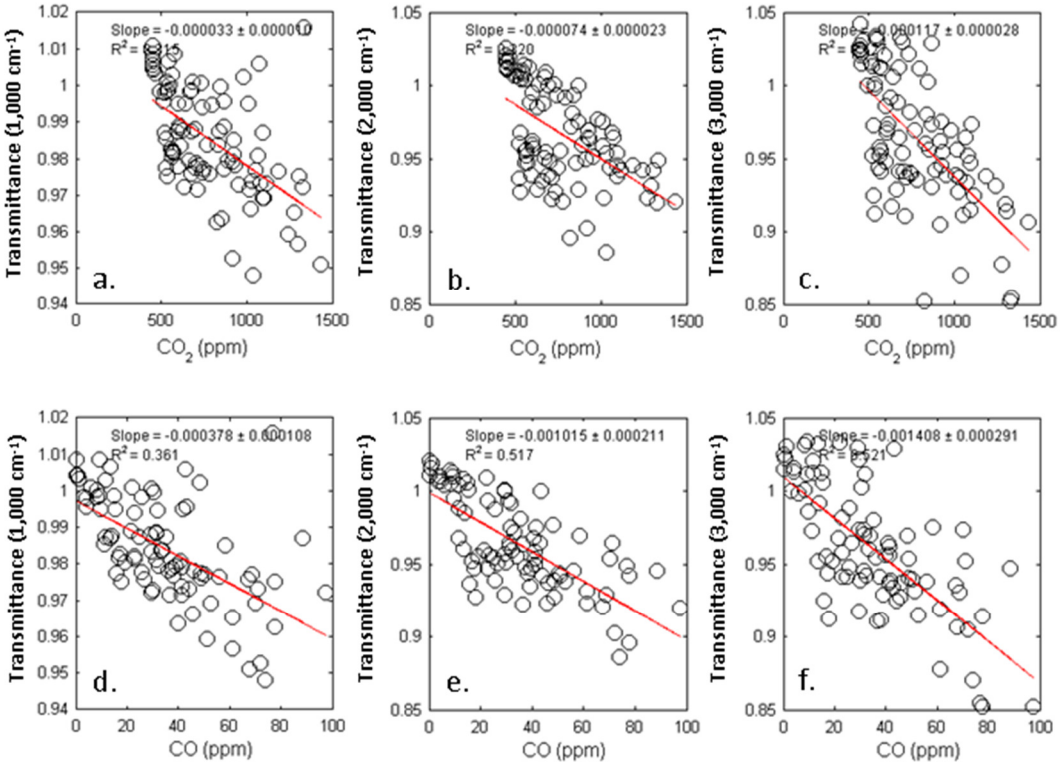

Figure 8.3 Scatter plots comparing retrieved pathlength-averaged concentrations of CO_2 (a–c) and CO (d–f) with transmittance at 1,000 cm^{-1}, 2,000 cm^{-1}, and 3,000 cm^{-1}. The relationship is strongest between CO and transmittance at 3,000 cm^{-1} (R^2 = 0.521).

8.4 Concluding remarks

Biomass burning is a phenomenon affecting global atmospheric composition, chemistry and climate. Inventories of biomass burning emissions are thus important, and biomass burning has been recognised as a major source of anthropogenic atmospheric pollution, having detrimental influences on human health over large parts of the world (Johnston *et al.,* 2012). For some trace gases (perhaps most notably carbon monoxide), biomass burning emissions rival those from fossil fuel combustion (Bowman *et al.*, 2009). The majority of research into biomass burning emissions has focussed on southern African savannas, North American boreal forests, and South American deforestation areas. Research has tended to avoid measurements during local peak fire months (van Leeuwen and van der Werf, 2011). By deploying a relatively unused methodology (long path OP-FTIR), which has only been deployed at fires by Griffith *et al.* (1991) and

Wooster *et al.* (2011), at over fifty new fires, this thesis has contributed to a better understanding of Australian savanna emissions (a relatively understudied ecosystem) and has also presented the first measurements of emissions from heathlands. Future deployments to other understudied ecosystems (e.g. tropical peatlands, whose emissions have a potentially huge regional and global impact [van Leeuwan and van der Werf, 2011]) are anticipated. Despite some limitations (the number of trace gas species is limited to those reported in this thesis), OP-FTIR should be considered a viable complement, and perhaps sometimes competitor, to airborne emissions measurements. Having demonstrated the robustness and portable nature of the approach, it is hoped that OP-FTIR can be used to address further issues relating to the spatial and temporal representativeness of fire emissions worldwide, including in ecosystems yet to be well characterised.

References

Abel, S.J., Haywood, J.M., Highwood, E.J., Li, J., Buseck, P.R. (2003) Evolution of biomass burning aerosol properties from an agricultural fire in southern Africa. *Geophysical Research Letters* **30**(15): 1783, doi:1029/2003GL017342.

Abrams, M.C., Goldman, A., Gunson, M.R., Rinsland, C.P., Zander, R. (1996) Observations of the infrared solar spectrum from space by the ATMOS experiment. *Applied Optics* **35**(16): 2747–2751.

Akagi, S.K., Yokelson, R.J., Wiedinmyer, C., Alvarado, M.J., Redi, J.S., Karl, T., Crounse, J.D., Wennberg, P.O. (2011) Emission factors for open and domestic biomass burning for use in atmospheric models. *Atmospheric Chemistry and Physics* **11**: 4039–4072.

Albertson, K., Aylen, J., Cavan, G., McMorrow, J. (2010) Climate change and the future occurrence of moorland wildfires in the Peak District of the UK. *Climate Research* **45**: 105–118.

Andreae, M.O., Browell, E. V., Garstang, M., Gregory, G. L., Garriss, R. C., Hill, G., F., Jacob, D. J., Pereira, M. C., Sachse, G. W., Setzer, A. W., Silve Dias, P. L., Talbor, W. R., Torres, A. L., Worsy, S. C. (1985) Biomass-burning emissions and associated haze layers over Amazonia.

Andreae, M.O., Merlet, P. (2001) Emission of trace gases and aerosols from biomass burning. *Global Biogeochemical Cycles* **15**(4): 955–966.

Andreae, M.O., Rosenfeld, D., Artaxo, P., Costa, A.A., Frank, G.P., Longo, K.M., Silva-Dias, M.A.F. (2004) Smoking rain clouds over the Amazon. *Science* **303**: 1337–1342.

Arino, O., Rosaz, J.M. (1999) 1997 and 1998 World ATSR fire atlas using ERS-2 ATSR-2 data. In Neuenschwander, L.F., Ryan, K.C., and Goldberg, G.E. (Eds.). *Proceedings of the Joint Fire Science Conference. University of Idaho and the International Association of Wildland Fire, Boise, Idaho*, (pp. 177–182).

Arjamaa, O., Vuorisalo, T. (2010) Gene-culture coevolution and human diet (2010) *American Scientist* **98**(2): 140–147.

Atkinson, R. (2000) Atmospheric chemistry of VOCs and NO_x. *Atmospheric Environment* **34**(12–14): 2063–2101, doi:10.1016/S1352-2310(99)00460-4.

Bacsik, Z., Mink, J., and Keresztury, G. (2004) FTIR spectroscopy of the atmosphere I. Principles and methods. *Applied Spectroscopy Reviews* **39**: 295–363.

Bacsik, Z., Mink, J., and Keresztury, G. (2007) FTIR Spectroscopy of the atmosphere Part 2. Applications. *Applied Spectroscopy Reviews* **40**: 327–390.

Banwell, C., McCash, E. (1994) *Fundamentals of Molecular Spectroscopy*. McGraw Hill, New York.

Bernath, P.F. (2005) *Spectra of Atoms and Molecules*. Oxford University Press, New York.

Bernath, P.F., McElroy, C.T., Abrams, M.C., Boone, C.D., Butler, M., Camy-Peyret, C., Carleer, M., Clerbaux, C., Coheur, P., F., Colin, R., DeCola, P., DeMaziere, M., Drummond, J.R., Dufour, D., Evans, W.F.J., Fast, H., Fussen, D., Gilbert, K., Jennings, D.E., Llewellyn, E.J., Lowe, R.P., Mahieu, E., McConnell, J.C., McHugh, M., McLeod, S., D., Michaud, R., Midwinter, C., Nassar, R., Nichitiu, F., Nowlan, C., Rinsland, C.P., Rochon, Y.J., Rowloands, N., Semeniuk, K., Simon, P., Skelton, R., Sloan, J.J., Soucy, M.A., Strong, K., Tremblay, P., Turnbull, D., Walker, K.A., Walkty, I., Wardle, D.A., Wehrle, V., Zander, R., Zou, J. (2005) Atmospheric Chemistry Experiment (ACE): Mission overview. *Geophysical Research Letters* **32** L15S01: doi:10.1029/2005GL022386.

Bertschi, I.T., Yokelson, R.J., Ward, D.E., Christian, T.J., Hao, W.M. (2003a) Trace gas emissions from the production and use of domestic biofuels in Zambia measured by open-path Fourier transform infrared spectroscopy. *Journal of Geophysical Research* **108**(D13): 8469.

Bertschi , I., Yokelson, R. J., Ward, D. E., Babbitt, R. E., Susott, R. A., Goode, J. G., Hao, W. M. (2003b) Trace gas and particle emissions from fires in large diameter and belowground biomass fuels. *Journal of Geophysical Research* **108**: 8472, doi:10.1029/2002JD002100.

von Bobrutzki, K., Braban, C.F., Famulari, D., Jones, S.K., Blackall, T., Smith, T.E.L., Blom, M., Coe, H., Gallagher, M., Ghalaieny, M., McGillen, M.R., Percival, C.J., Whitehead, J.D., Ellis, R., Murphy, J., Mohacsi, A., Pogany, A., Junninen, H., Rantanen, S., Sutton, M.A., Nemitz, E. (2010) Field inter-comparison of eleven atmospheric ammonia measurement techniques. *Atmospheric Measurement Techniques* **3**: 91–112.

Borghesio, L. (2009) Effects of fire on the vegetation of a lowland heathland in North-western Italy. *Plant Ecology* **201**: 723-731.

Bouchard, J.-P., Tremblay, P. (2003) High resolution measurements of the instrument line shape function of Fourier-transform spectrometers. *11th International Workshop on Atmospheric Science from Space using Fourier Transform Spectrometry.* October 8–12, 2003, Bad Wildbad, Germany.

Bowman, D.M.J.S., Balch, J.K., Artaxo, P., Bond, W.J., Carlson, J.M., Cochrane, M.A., D'Antonio, C.M., DeFries, R.S., Doyle, J.C., Harrison, S.P., Johnston, F.H., Keeley, J.E., Krawchuk, M.A., Kull, C.A., Marston, J., Moritz, M.A., Prentice, I.C., Roos, C.I., Scott, A.C., Swetnam, T.W., van der Werf, G.R., Pyne, S.J. (2009) Fire in the Earth system. *Science* **324**: 481–484.

Brain, C.K. and Sillen, A. (1988) Evidence from the Swartkrans Cave for the earliest use of fire. *Nature* **336**: 464–467.

Brault, J.W., White, O.R. (1971) The analysis and restoration of astronomical data via the fast Fourier transform. *Astronomy and Astrophysics* **13**: 169.

Bremer, H., Kar, J., Drummond, J.R., Nichitu, F., Zou, J., Liu, J., Gille, J.C., Deeter, M.N., Francis, G., Ziskin, D., Warner, J. (2004) Spatial and temporal variation of MOPITT CO in Africa and South America: A comparison with SHADOZ Ozone and MODIS Aerosol. *Journal of Geophysical Research* **109**: D12304.

Brönnimann, S. (2007) Fires and climate linked in nineteenth century. *Nature* **448**: 992.

Brönnimann, S., Volken, E., Lehmann, K., Wooster, M. (2009) Biomass burning aerosols and climate – a 19th century perspective. *Meteorologische Zeitschrift* **18**(3): 349–353.

Burling, I.R., Yokelson, R.J., Griffith, D.W.T., Johnson, T.J., Veres, P., Roberts, J.M., Warneke, C., Urbanski, S.P., Reardon, J., Weise, D.R., Hao, W.M., de Gouw, J. (2010) Laboratory measurements of trace gas emissions from biomass burning of fuel types from the southeastern and southwestern United States. *Atmospheric Chemistry and Physics* **10**: 11115–11130.

Burling, I.R., Yokelson, R.J., Akagi, S.K., Urbanski, S.P., Wold, C.E., Griffith, D.W.T., Johnson, T.J., Reardon, J., Weise, D.R. (2011) Airborne and ground-based measurements of trace gases and particles emitted by prescribed fires in the United States. *Atmospheric Chemistry and Physics* **11**: 12197–12216.

Burton, M.R. (1998) *Remote sensing of the atmosphere using Fourier transform spectroscopy*, PhD thesis, Department of Chemistry, University of Cambridge.

Burton, M.R., Oppenheimer, C., Horrocks, L.A., Francis, P.W. (2001) Diurnal changes in volcanic plume chemistry observed by lunar and solar occultation spectroscopy. *Geophysical Research Letters* **28**(5): 843-846, doi:10.1029/2000GL008499.

Burton, M.R., Allard, P., Muré, F., Oppenheimer, C. (2003) FTIR remote sensing of fractional magma degassing at Mount Etna, Sicily. *Geological Society, London, Special Publications* **213**: 281–293. Doi:10.1144/GSL.SP.2003.213.01.17.

Burton, M.R., Allard, P., Mure, F., and La Spina, A. (2007) Magmatic gas composition reveals the source depth of slug-driven strombolian explosive activity. *Science* **317**: 227–230.

Briz, S., de Castro, A.J., Díez, S., López, F., Schafer, K. (2007) Remote sensing by open-path FTIR spectroscopy. Comparison of different analysis techniques applied to ozone and carbon monoxide detection. *Journal of Quantitative Spectroscopy & Radiative Transfer* **103**: 314–330.

Cao, G., Zhang, X., Gong, S., Zheng, F. (2008) Investigation on emission factors of particulate matter and gaseous pollutants from crop residue burning. *Journal of Environmental Science.* **20**: 50–55.

Carcaillet, C., Almquist, H., Asnong, H., Bradshaw, R.H.W., Carrión, J.S., Gaillard, M.-J., Gajewski, K., Haas, J.N., Haberle, S.G., Hadorn, P., Müller, S.D., Richard, P.J.H., Richoz, I., Rösch, M., Sánchez Goñi, M.F., von Stedingk, H., Stevenson, A.C., Talon, B., Tardy, C., Tinner, W., Tryterud, E., Wick, L., Willis, K.J. (2002) Holocene biomass burning and global dynamics of the carbon cycle. *Chemosphere* **49**: 845–863.

Childers, J.W., Thompson Jr, E.L., Harris, D.B., Kirchgessner, D.A., Clayton, M., Natschke, D.F., and Phillips, W.J. (2001) Multi-pollutant concentration measurements around a concentrated swine production facility using open-path FTIR spectrometry. *Atmospheric Environment* **35**: 1923–1936.

Childers, J.W., Phillips, W.J., Thompson Jr, E.L., Harris, D.B., Kirchgessner, D.A., Natschke, D.F., and Clayton, M. (2002) Comparison of an innovative nonlinear algorithm to classical least-squares for analyzing open-path Fourier transform infrared spectra collected at a concentrated swine production facility. *Applied Spectroscopy* **56**(3): 325–336.

Chaney, L.W. (1967) *Fundamentals of Fourier Transform Spectroscopy*. The University of Michigan, College of Engineering, Department of Aerospace Engineering, High Altitude Engineering Laboratory Technical Report. The University of Michigan, Ann Arbor.

Chang, D., Song, Y. (2010) Estimates of biomass burning emissions in tropical Asia based on satellite-derived data. *Atmospheric Chemistry and Physics* **10**: 2335–2351.

Christian, C.S., Stewart, G.A., Noakes, L.C., Blake, S.T. (1953) General Report on Survey of Katherine-Darwin Region, 1946. *Land Research Series No. 1*. Commonwealth Scientific and Industrial Research Organization, Australia, Melbourne.

Christian, T. J., Kleiss, B., Yokelson, R. J., Holzinger, R., Crutzen, P. J, Hao, W. M., Saharjo, B. H., Ward, D. E. (2003) Comprehensive laboratory measurements of biomass-burning emissions: Emissions from Indonesian, African and other fuels. *Journal of Geophysical Research* **108**: D23, 4719, doi:10.1029/2003JD003704.

Christian, T. J., Kleiss, B., Yokelson, R. J., Holzinger, R., Crutzen, P. J, Hao, W. M., Shirai, T., Blake, D. R. (2004) Comprehensive laboratory measurements of biomass-burning emissions: 2. First intercomparison of open-path FTIR, PTR-MS, and GC-MS/FID/ECD. *Journal of Geophysical Research* **109**(D02311): doi:10.1029/2003JD003874.

Clark, J.S. (1990) Fire and climate change during the last 750 yr in northwestern Minnesota. *Ecological Monographs* **60**(2): 135–159.

Clark, J.S., Merkt, J., Müller, H. (1989) Post-glacial fire, vegetation, and human history on the northern Alpine forelands, south-western Germany. *Journal of Ecology* **77**: 897–925.

Clark, J.S., Royall, P.D. (1995) Transformation of a northern hardwood forest by Aboriginal (Iroquois) fire: Charcoal evidence from Crawford Lake, Ontario, Canada. *The Holocene* **5**, 1–9.

Clerbaux, C., Boynard, A., Clarisse, L., George, M., Hadji-Lazaro, J., Herbin, H., Hurtmans, D. Pommier, M., Razavi, A., Turquety, S., Wespes, C. Coheur, P.-F. (2009) Monitoring of atmospheric composition using the thermal infrared IASI/MetOp sounder. *Atmospheric Chemistry and Physics* **9**: 6041–6054.

Clerbaux, C., Boynard, A., Clarisse, L., Turquety, S., Hurtmans, D., Clerbaux, C. (2009) IASI measurements of reactive trace species in biomass burning plumes. *Atmospheric Chemistry and Physic* **9**: 5655–5667.

Clough, S.A., Kneizys, F.X., Shettle, E.P., Anderson, G.P. (1985) Atmospheric radiance and transmittance. In: *Sixth Conference on Atmospheric Radiation.* American Meteorological Society, Boston, MA, 141-144.

Cofer, W.R.I., Levine, J.S., Winstead, E.L., Cahoon, D.R., Sebacher, D.I., Pinto, J.P., Stocks, B.J. (1996) Source composition of trace gases released during African savanna fires. *Journal of Geophysical Research* **101**: 23597–23602.

Coheur, P. F., Herbin, H., Clerbaux, C., Hurtmans, D., Wespes, C., Carleer, M., Turquety, S. Rinsland, C. P., Remedios, J., Hauglustaine, D., Boone, C. D., Bernath, P. F. (2007) ACE-FTS observation of a young biomass burning plume: First reported measurements of C_2H_4, C_3H_6O, H_2CO and PAN by infrared occultation from space. *Atmospheric Chemistry and Physics* **7**: 5437–5446.

Crutzen, P.J., Andreae, M.O. (1990) Biomass burning in the tropics: Impacts on atmospheric chemistry and biogeochemical cycles. *Science* **239**: 1669–1678.

Crutzen, P.J., Heidt, L.E., Krasnec, J.P., Pollock, W.H., Seiler, W. (1979) Biomass burning as a source of atmospheric gases CO, H_2, N_2O, NO, CH_3Cl and COS. *Nature* **282**: 253–256.

von Danckelman, A. (1884) Die Bewölkungsverhältnisse des südwestlichen Afrikas. *Meteorologische Zeitschrift* **1**: 301–311.

Davies, G.M., Gray, A., Hamilton, A., Legg, C.J. (2008) The future of fire management in the British uplands. *International Journal of Biodiversity Science and Management* **4**: 127–147.

Davies, G.M., Legg, C.J., Smith, A.A., MacDonald, A.J. (2009) Rate of spread of fires in *Calluna vulgaris*-dominated moorlands. *Journal of Applied Ecology* **46**: 1054–1063.

Davies, G.M., Smith, A.A., MacDonald, A.J., Bakker, J.D., Legg, C.J. (2010) Fire intensity, fire severity and ecosystem response in heathlands: factors affecting the regeneration of *Calluna vulgaris*. *Journal of Applied Ecology* **47**: 356–365.

DCCEE (2010) Australian national greenhouse accounts: National Inventory Report 2008 Volume 1, Rep., 279 pp, Department of Climate Change and Energy Efficiency, Commonwealth of Australia, Canberra.

Deeter, M.N., Emmons, L.K., Francis, G.L., Edwards, D.P., Gille, J.C., Warner, J.X., Khattatov, B., Ziskin, D., Lamarque, J.-F., Ho, S.-P., Yudin, V., Attié, J.-L., Packman, D., Chen, J., Mao, D., Drummond, J.R. (2003) Operational carbon monoxide retrieval algorithm and selected results for the MOPITT instrument. *Journal of Geophysical Research* **108**(D14): 4399.

Delmas, R., Lacaux, J.P., Brocard, D. (1995) Determination of biomass burning emission factors: methods and results. *Environmental Monitoring and Assessment* **38**: 181–204.

Dentner, F.J., Crutzen, P.J. (1994) A three-dimensional model of the global ammonia cycle. *Journal of Atmospheric Chemistry* **19**: 331–369.

Diner, D.J., Abdou, W.A., Bruegge, C.J., Conel, J.E., Gaitley, B.J., Helmlineter, M.C., Kahn, R.A., Martonchik, J.V., Pilorz, S.H., Holben, B.N. (2001) MISR aerosol optical depth retrievals over southern Africa during the SAFARI-2000 Dry Season Campaign. *Geophysical Research Letters* **28**(16): 3127–3130, doi:10.1029/2001GL013188.

Dozier, J. (1981) A method for satellite identification of surface temperature fields of subpixel resolution. *Remote Sensing of Environment* **11**: 221–229.

Dragosits, U., Luk, J., Sutton, M.A. (2009) Ammonia emissions from UK non-agricultural sources in 2007: Contribution to the National Atmospheric Emission Inventory. NERC/Centre for Ecology & Hydrology, 16pp. (Report Number: AS 08/08, CEH Project number: C03614).

Duffell, H., Oppenheimer, C., Burton, M. (2001) Volcanic gas emission rates measured by solar occultation spectroscopy. *Geophysical Research Letters* **28**(16): 3131–3134, doi:10.1029/2000GL012425.

Dwyer, E., Pinnock, S., Grégoire, J.-M. and Pereira, J.M.C. (2000) Global spatial and temporal distribution of vegetation fire as determined from satellite observations. *International Journal of Remote Sensing* **21**: 1289–1302.

Eagan, R.C., Hobbs, P.V., Radke, L.F. (1974) Measurements of cloud condensation nuclei and cloud droplet size distributions in the vicinity of forest fires. *Journal of Applied Meteorology* **13**: 553–557.

EC-JRC/PBL (European Commission, Joint Research Centre/Netherlands Environmental Assessment Agency) (2009) Emission Database for Global Atmospheric Research (EDGAR), release version 4.0. [online] http://edgar.jrc.ec.europa.eu [last accessed: 23 September 2012].

Echle, G., von Clarmann, T., Dudhia, A., Flaud, J.-M., Funke, B., Glatthor, N., Kerridge, B., López-Puertas, M., Martin-Torres, F.J., Stiller, G.P. (2000) Optimized spectral microwindows for data analysis of the Michelson interferometer for passive atmospheric sounding on the environmental satellite. *Applied Optics* **39**: 5531–5540.

Eck, T.F., Holben, B.N., Reid, J.S., Dubovik, O., Smirnov, A., O'Neill, N.T., Slutsker, I., Kinne, S. (1999) Wavelength dependence of the optical depth of biomass burning, urban, and desert dust aerosols. *Journal of Geophysical Research* **104**(D24): 31333–31349.

Edwards, D.P., Emmons, L.K., Gille, J.C., Chu, A., Attié, J.-L., Giglio, L., Wood, S.W., Haywood, J., Deeter, M.N., Massie, S.T., Ziskin, D.C., Drummond, J.R. (2006) Satellite-observed pollution from Southern Hemisphere biomass burning. *Journal of Geophysical Research* **111**: D14312, doi:10.1029/2005JD006655.

Esler, M.B., Griffith, D.W.T., Wilston, S.R., and Steele, L.P. (2000) Precision trace gas analysis by FT-IR spectroscopy 1. Simultaneous analysis of CO_2, CH_4, N_2O and CO in air, *Analytical Chemistry* **72**(1): 206–215.

Farage, P., Ball, A., McGenity, T.J., Whitby, C., Pretty, J. (2009) Burning management and carbon sequestration of upland heather moorland in the UK. *Australian Journal of Soil Research* **47**: 351–361.

Fernández-Gómez, I., de Castro, A.J., Guijarro, M., Madrigal, J., Aranda, J.M., Diez, C., Hernando, C., López, F. (2011) Characterization of forest fuels in a Mass Loss Calorimeter by short open-path FTIR spectroscopy. *Journal of Quantitative Spectroscopy and Radiative Transfer* **112**(3) 519–530.

Flanner, M.G., Zender, C.S., Randerson, J.T., Rasch, P.J. (2007) Present-day climate forcing and response from black carbon in snow. *Journal of Geophysical Research* **112**: D11202.

Forster, P., Ramaswamy, V., Artaxo, P., Berntsen, T., Betts, R., Fahey, D.W., Haywood, J., Lean, J. D.C. Lowe, Myhre, G., Nganga, J., Prinn, R., Raga, G., Schulz, M., van Dorland, R. (2007) Changes in Atmospheric Constituents and in Radiative Forcing. In: *Climate Change 2007: The Physical Science Basis. Contribution of Working Group I to the Fourth Assessment Report of the Intergovernmental Panel on Climate Change* Eds. Solomon, S., D. Qin, M. Manning, Z. Chen, M. Marquis, K.B. Averyt, M. Tignor and H.L. Miller. Cambridge University Press, Cambridge, United Kingdom and New York, NY, USA.

Fraser, R.H., Li,Z., Cihlar J. (2000) Hotspot and NDVI Differencing Synergy (HANDS): A new technique for burned area mapping over boreal forest. *Remote Sensing of Environment* **74**: 362–379.

Freeborn, P.H., Wooster, M.J., Roberts, G., Malamud, B.D., Xu, W. (2009) Development of a virtual fire product for Africa through a synthesis of geostationary and polar orbiting satellite data. *Remote Sensing of Environment* **113**(8): 1700–1711.

de Fries, R.S., Field, C.B., Fung, I., Collatz, G.J., Bounoua, L. (1999) Combining satellite data and biogeochemical models to estimate global effects of human-induced land cover change on carbon emissions and primary productivity. *Global Biogeochemical Cycles* **13**(3): 803–815.

de Fries, R.S., Morton, D. C., van der Werf, G. R., Giglio, L., Collatz, G. J., Randerson, J. T., Houghton, R. A., Kasibhatla, P.K., Shimabukuro, Y. (2008) Fire-related carbon emissions from land use transitions in southern amazonia. *Geophysical Research Letters* **35**: L22705, doi:10.1029/2008GL035689.

Friedlander, S.K., Altshuler, B., Bayes, K.D., Eschenroeder, A.Q., Hackney, J.D., Heck, W.W., McCarroll, J.R., McNesby, J.R., Miller, P.R., Mueller, P.K., Murphy, S.D. (1977) *Medical and Biologic Effects of Environmental Pollutants: Ozone and other photochemical oxidants.* Committee on Medical and Biologic Effects of Environmental Pollutants, Division of Medical Sciences, Assembly of Life Sciences, National Research Council, National Academy of Sciences, Washington D.C.

Fu, D., Walker, K.A., Sung, K., Boone, C.D., Soucy, M.-A., and Bernath, P.F. (2007) The portable atmospheric research interferometric spectrometer for the infrared, PARIS-IR. *Journal of Quantitative Spectroscopy & Radiative Transfer* **103**: 362–370.

Galle, B., Bergquist, B., Ferm, M., Törnquist, K., Griffith, D.W.T., Jensen, N. O., and Hansen, F. (2000) Measurement of ammonia emissions from spreading of manure using gradient FTIR techniques. *Atmospheric Environment* **34:** 4907–4915.

GBIF (Global Biodiversity Information Facility) (2012) *Calluna vulgaris* [online] available from: http://data.gbif.org/species/2882482/ [last accessed 24 September 2012].

Gerlach, T.M., McGee, K.A., Sutton, A.J., and Elias, T. (1998) Rates of volcanic CO_2 degassing from airborne determinations of SO2 emission rates and plume CO_2/SO_2: Test study at Pu'u 'O'o cone, Kilauea volcano, Hawaii. *Geophysical Research Letters* **25**: 2675–2678.

Gerlach, T.M. (2011) Volcanic versus anthropogenic carbon dioxide. *Eos* **92**(24): 201–202.

Glasspool, I.J., Edwards, D., Axe, L. (2004) Charcoal in the Silurian as evidence for the earliest wildfire. *Geology* **32**(5): 381–383.

Giglio, L., Csiszar, I., Restás, A., Morisette, J.T., Schroeder, W., Morton, D., Justice, C.O. (2008) Active fire detection and characterization with the Advanced Spaceborne, Thermal Emission and Reflection radiometer (ASTER) *Remote Sensing of Environment* **112**: 3055–3063.

Giglio L., Descloitres, J., Justice, C.O., Kaufman Y.J. (2003) An enhanced contextual fire detection algorithm for MODIS. *Remote Sensing of Environment* **87**: 273–282.

Giglio, L., van der Werf, G.R., Randerson, J.T., Collatz, G.J. and Kasibhatla, P. (2006) Global estimation of burned area using MODIS active fire observations. *Atmospheric Chemistry and Physics* **6**: 957–974.

Giglio, L., Randerson, J.T., van der Werf, G.R., Kasibhatla, P.S., Collatz, G.J., Morton, D.C., DeFries, R.S. (2010) Assessing variability and long-term trends in burned area by merging multiple satellite fire products. *Biogeosciences* **7**: 1171–1186.

Goode, J.G., Yokelson, R.J., Susott, R.A., and Ward, D.E. (1999) Trace gas emissions from laboratory biomass fires measured by open-path Fourier transform infrared spectroscopy: Fires in grass and surface fuels. *Journal of Geophysical Research – Atmospheres* **104**(D17): 21,237–21,245.

Goode, J. G., Yokelson, R. J., Ward, E. D., Susott, R. A., Babbitt, R. E., Davies, M. A. (2000) Measurements of excess O_3, CO_2, CO_3, CH_4, C_2H_4, C_2H_2, HCN, NO, NH_3, HCOOH, CH_3 COOH, HCHO and CH_3OH in 1997 Alaskan Biomass Burning Plumes by Airborne Fourier (A-FTIR). *Journal of Geophysical Research* **103** (D17): 22,147–22,166.

Gras, J.L., Meyer, C.P., Weeks, I.A., Gillett, R.w., Galbally, I.E., Todd, J., Carnovale, F., Joynt, R.C., Hinwood, A., Berko, H., Brown, S. (2002) *Emissions from Domestic Solid Fuel Appliances*. Environment Australia, Canberra.

Griffith, D.W.T. (1996) Synthetic calibration and quantitative analysis of gas-phase FTIR spectra. *Applied Spectroscopy* **50**: 59–70.

Griffith, D.W.T., Mankin, W.G., Coffey, M.T., Ward, D.E., Riebau, A. (1991) FTIR remote sensing of biomass burning emissions of CO_2, CO, CH_4, CH_2O, NO, NO_2, NH_3 and N_2O. In: *Global Biomass Burning* Ed. Levine, J.S. The MIT Press, Cambridge, Massachusetts, pp. 230–239.

Griffith, D.W.T., Leuning, R., Denmead, O.T., and Jamie, I.M. (2002) Air-land exchanges of CO_2, CH_4 and N_2O measured by FTIR spectrometry and micrometeorological techniques. *Atmospheric Environment* **36**: 1833–1842.

Griffith, D.W.T., Esler, M.B., Paul Steele, L., and Reisinger, A. (2003), Non-linear least squares: high precision quantitative analysis of gas phase FTIR spectra, paper presented at 2nd Intl. Conference on Advanced Vibrational Spectroscopy, Nottingham.

Griffiths, P.R. (1975) *Chemical Infrared Fourier Transform Spectroscopy*. Wiley-Interscience, New York.

Griffiths, P.R., De Haseth (1986) Fourier Transform Infrared Spectrometry, in *Chemical Analysis* 83, Elving *et al.* (eds.). John Wiley & Sons, New York.

Grossman, A.S., Grant, K.E., Blass, W.E., Wuebbles, D.J. (1997) Radiative forcing calculations for CH_3Cl and CH_3Br. *Journal of Geophysical Research* **102**(D12): 13651–13656.

Grove, A.T., Rackham, O. (2001) *The nature of Mediterranean Europe: An ecological history.* New Haven, CT: Yale University Press.

Grutter, M. (2003) Multi-gas analysis of ambient air using FTIR spectroscopy over Mexico City. *Atmosféra* **16**: 1–13.

Grutter, M., Flores, E., Basaldud, R., and Ruiz-Suárez, L.G. (2003) Open-path FTIR spectroscopic studies of the trace gases over Mexico City. *Atmospheric and Oceanic Optics* **16**(3): 232–236.

Grutter, M., Stremme, W., Garcia, A.R. (2010) CO surface emissions from solar absorption IR spectroscopy. In: *Fall Meeting of the American Geophysical Union 2010*, abstract #A13F-0285.

Gunzler, H. Gremlich, H.-U. (2002) IR Spectroscopy, Wiley-VCH, Weinheim, pp.361.

Guyon, P., Frank, G.P., Welling, M., Chand, D., Artaxo, P., Rizzo, L., Nishioka, G., Kolle, O., Fritsch, H., Silva, Dias, M.A.F., Gatti, L.V., Cordova, A.M., Andreae, M.O. (2005) Airborne measurements of trace gas and aerosol particle emissions from biomass burning in Amazonia. *Atmospheric Chemistry and Physics* **5**: 2989–3002.

Haaland, D.M. (1990) Multivariate calibration methods applied to quantitative FT-IR analyses. In *Practical Fourier Transform Infrared Spectroscopy, Industrial and Laboratory Chemical Analysis*, edited by Ferraro, J.R., and Krishnan, K., pp. 395–468, Academic, San Diego.

Harden, D.B. (1962) *The Phoenicians.* Thames and Hudson.

Harris, M.P.K., Allen, K.A., Le Duc, M.G., Eyre, G., Marrs, R.H. (2011) Prescribed fire characteristics and biomass reduction on upland moorland. *Aspects of Applied Biology* **108**: 171–178.

Hart, B.K., Berry, R.J., and Griffiths, P.R. (1999) Effects of resolution, spectral window, and background on multivariate calibrations used for open-path Fourier transform infrared spectrometry. *Field Analytical Chemistry and Technology* **3**(2): 117–130.

Hase, F., Demoulin, P., Sauval, A.J., Toon, G.C., Bernath, P.F., Goldman, A., Hannigan, J.W., and Rinsland, C.P. (2006) An empirical line-by-line model for the infrared solar transmittance spectrum from 700 to 5000 cm^{-1}. *Journal of Quantitative Spectroscopy & Radiative Transfer* **102** 450–463.

Hashmonay, R. A., Natshke, D. F., Wagoner, K. (2001) Field evaluation of a method for estimating gaseoud fluxes from area sources using open-path Fourier transform infrared. *Environmental Science and Technology* **35**: 2309–2313.

Heland, J., and Schäfer, K. (1998) Determination of major combustion products in aircraft exhausts by FTIR emission spectroscopy. *Atmospheric Environment* **32**(18): 3,067–3,072.

Herget, W.F., Brasher, J.D. (1979) Remote measurement of gaseous pollutant concentrations using a mobile Fourier transform interferometer system. *Applied Optics* **18**(20): 3404–3420.

Heyerdahl, E.K., Brubaker, L.B., Agee, J.K. (2002) Annual and decadal climate forcing of historical fire regimes in the Interior Pacific Northwest, USA. *The Holocene* **12**(5): 597–604.

Hobbs, P.V., Sinha, P., Yokelson, R.J., Christian, T.J., Blake, D.R., Gao, S., Kirchstetter, T.W., Novakov, T., Pilewskie, P. (2003) Evolution of gases and particles from a savanna fire in South Africa. *Journal of Geophysical Research* **108**(D13): 8485, doi:10.1029/2002JD002352.

Hoelzemann, J.J., Schultz, M.G., Brasseur, G.P., Granier, C., Simon, M. (2004) Global Wildland Fire Emission Model (GWEM): Evaluating the use of global area burnt satellite data. *Journal of Geophysical Research – Atmospheres* **109**: D14S04.

Hoffa, E.A., Ward, D.E., Hao, W.M., Susott, R.A., Wakimoto, R.H. (1999) Seasonality of carbon emissions from biomass burning in a Zambian savanna. *Journal of Geophysical Research* **104**: 13841–13853.

Hong, D.W., Heo, G.S., Han, J.S., and Cho, S.Y. (2004) Application of the open path FTIR with COL1SB to measurements of ozone and VOCs in the urban area. *Atmospheric Environment* **38**: 5,567–5,576.

Horrocks, L.A. (2001) *Infrared spectroscopy of volcanic gases at Masaya, Nicaragua*. PhD thesis, The Open University.

Horrocks, L. A., Burton, M.R., and Francis, P. (1999) Stable gas plume composition measured by OP-FTIR spectroscopy at Masaya Volcano, Nicaragua, 1998–1999. *Geophysical Research Letters* **26**(23): 3,497–3,500.

Horrocks, L.A., Oppenheimer, C., Burton, M.R., Duffell, H.J. (2001) Open-path Fourier transform infrared spectroscopy of SO_2: An empirical error budget analysis, with implications for volcano monitoring. *Journal of Geophysical Research* **106**(D21): 27,647–27,659.

Houghton, R.A. (1994) The worldwide extent of land-use change. *Bioscience* **44**: 305–313.

Hurst, D.F., Griffith, D.W.T., Cook, G.D. (1994a) Trace gas emissions from biomass burning in tropical Australian savannas. *Journal of Geophysical Research* **99**(D8): 16441–16456.

Hurst, D.F., Griffith, D.W.T., Carras, J.N., Williams, D.J., Fraser, P.J. (1994b) Measurements of trace gases emitted by Australian savanna fires during the 1990 dry season. *Journal of Atmospheric Chemistry* **18**: 33–56.

Hurtmans, D., Barret, B., Coheur, P.-F., Clerbaux, C. (2005) Atmosphit: a new tool for simulating and inverting atmospheric spectra. *12th International Workshop on Atmospheric Science from Space using Fourier Transform Spectrometry.* May 18–20, 2005, Quebec, Canada.

Indermühle, A., Stocker, T.F., Joos, F., Fischer, H., Smith, H.J., Wahlen, M., Deck, B., Mastroianni, D., Tschumi, J., Blunier, T., Meyer, R., Stauffer, B. (1999) Holocene carbon-cycle dynamics based on CO_2 trapped in ice at Taylor Dome, Antarctica. *Nature* **398**: 121–126.

IPCC (International Panel on Climate Change) (2000) Good Practice Guidance and Uncertainty Management in National Greenhouse Gas Inventories, IPCC National Greenhouse Gas Inventories Programme, Technical Support Unit, Kanagawa, Japan.

Ito, A., Sillman, S., Penner, J.E. (2007) Effects of additional nonmethane volatile organic compounds, organic nitrates, and firect emissions of oxygenated organic species on global tropospheric chemistry. *Journal of Geophysical Research* **112**: D06309.

Jin, Y., Roy, D.P. (2005) Fire-induced albedo change and its radiative forcing at the surface in northern Australia. *Geophysical Research Letters* **32**(13): L13401.

JNCC (Joint Nature Conservation Committee) (2012) UK Lowland Heathland Habitats [online] available from: http://jncc.defra.gov.uk/page-1432 [last accessed 24 September 2012].

Johnston, F.H., Henderson, S.B., Chen, Y., Randerson, J.T., Marlier, M., DeFries, R.S., Kinney, P., Bowman, D.M.J.S., Brauer, M. (2012) Estimated global mortality attributable to smoke from landscape fires. *Environmental Health Perspectives* **120**(5): 695–701.

Justice, C., Giglio, l., Boschetti, L., Roy, D., Csiszar, I., Morrisette, J., Kaufman, Y. (2006) MODIS Fire Products. MODIS Algorithm Technical Background Document: Fires, EOS ID #2741.

Justice, C.O., Kendall, J.D., Dowty, P.R., Scholes, R.J. (1996) Satellite remote sensing of fires during the SAFARI campaign using NOAA AVHRR data. *Journal of Geophysical Research* **101**(D23): 23851–23863.

Kaiser, J.W., Suttie, M., Flemming, J., Morcrette, J.-J., Boucher, O., Schultz, M.G. (2008) Global real-time fire emission estimates bases on space borne fire radiative power observations. *Current Problems in Atmospheric Radiation* CP1100: 645–648.

Kaiser, J.W., Boucher, O., Doutriaux-Boucher, M., Flemming, J., Govaerts, Y.M., Gulliver, J., Heil, A., Jones, L., Lattanzio, A., Morcrette, J.-J., Perrone, M.R., Razinger, M., Roberts, G., Schultz, M.G., Simmons, A.J., Suttie, M., Wooster, M.J. (2009) Smoke in the air *ECMWF Newsletter No. 119 – Spring 2009* 9–15.

Kaiser, J.W., Heil, A., Andreae, M.O., Benedith, A., Chubarova, N., Jones, L., Morcrette, J.-J., Razinger, M., Schultz, M.G., Suttie, M., van der Werf, G.R. (2012) Biomass burning emissions estimated with a global fire assimilation system based on observed fire radiative power. *Biogeosciences* **9**: 527–554.

Kaufman, Y.J., Justice, C.O., Flynn, L.P., Kendall, J.D., Prins, E.M., Giglio, L., Ward, D.E., Menzel, W.P., Setzer, A.W. (1998) Potential global fire monitoring from EOS-MODIS. *Journal of Geophysical Research* **103**(D24): 32215–32238.

Kaufman, Y.J., Tanré, D., Boucher, O. (2002) A satellite view of aerosols in the climate system. *Nature* **419**: 215–223.

Kaufman, Y.J., Koren, I. (2006) Smoke and pollution aerosol effect on cloud cover. *Science* **321**: 655–658.

Keene, W. C., Lobert, J. M., Crutzen, P. J., Maben, J. R., Scharffe, D. H., Landmann, T., He´ly, C., Brain, C. (2006) Emissions of major gaseous and particulate species during experimental burns of southern African biomass. *Journal of Geophysical Research* **111**: D04301, doi:10.1029/2005JD006319.

Klein, S., Jaegar, U.G., Tischew, S. (2009) Use of fire for conservation and regeneration of complexes of heather and dry grasslands in the landscape of porphyry outcrops in the lower Saale-valley. *Hercynia* **42**(2): 217–238.

Korontzi, S. (2005) Seasonal patterns in biomass burning emissions from southern African vegetation fires for the year 2000. *Global Change Biology* **11**: 1680–1700.

Korontzi, S., Justice, C.O., Scholes, R.J. (2003a) Influence of timing and spatial extent of savanna fires in southern Africa on atmospheric emissions. *Journal of Arid Environments* **54**: 395–404.

Korontzi, S., Ward, D.E., Susott, R.A., Yokelson, R.J., Justice, C.O., Hobbs, P.V., Smithwick, E.A.H., Hao, W.M. (2003b) Seasonal variation and ecosystem dependence of emission factors for selected trace gases and PM2.5 for southern African savanna fires. *Journal of Geophysical Research* **108**(D24): 7-1 to 7-14.

Korontzi, S., Roy, D.P., Justice, C.O., Ward, D.E. (2004) Modeling and sensitivity analysis of fire emissions in southern Africa during SAFARI 2000. *Remote Sensing of Environment* **92**: 255–275.

Kuhlbusch, T.A., Lobert, J.M., Crutzen, P.J., Warneck, P. (1991) Molecular nitrogen emissions from denitrification during biomass burning. *Nature* **351**: 135–137.

Lacey, C.J., Walker, J., Noble, I.R. (1982) Fire in Australian tropical savannas. In: *Ecology of Tropical Savannas* Huntley, B.J., Walker, B.H. (Eds.), pp. 246–272, Springer-Verlag, Berlin.

Lamarque, J.-F., Edwards, D.P., Emmons, L.K., Gille, J.C., Wilhelmi, O., Gerbig, C., Prevedel, D., Deeter, M.N., Warner, J., Ziskin, D.C., Khattatov, B., Francis, G.L., Yudin, V., Ho, S., Mao, D., Chen, J., Drummond, J. (2003) Identification of CO plumes from MOPITT data: Application to the August 2000 Idaho-Montana forest fires. *Geophysical Research Letters* **30**(13): 1688.

Lamp, T., Radmacher, M., Weber, K., Gärtner, A., Nitz, R., Bröker, G. (1997) Calibration of an open-path FTIR spectrometer for methane, ethylene and carbon monoxide using a fixed 20 m multi pass cell. *Proceedings of SPIE* Bd. 3107: 126–136.

Langenfelds, R.L., Francey, R.J., Pak, B.C., Steele, L.P., Lloyd, J., Trudinger, C.M., Allison, C.E. (2002) Interannual growth rate variations of atmospheric CO_2 and its $\delta^{13}C$, H_2, CH_4, and CO between 1992 and 1999 linked to biomass burning. *Global Biogeochemical Cycles* **16**(3): 1048.

van Leeuwen, T.T., van der Werf, G.R. (2011) Spatial and temporal variability in the ratio of trace gases emitted from biomass burning. *Atmospheric Chemistry and Physics* **11**: 3611–3629.

Legg, C., Davies, G.M., Gray, A. (2010) Comment on: 'Burning management and carbon sequestration of upland heather moorland in the UK'. *Australian Journal of Soil Research* **48**: 100–103.

Lelieveld, J., Crutzen, P.J., Dentener, F.J. (1998) Changing concentration, lifetime and climate forcing of atmospheric methane. *Tellus* **50B**: 128–150.

Levenburg, K. (1944) A method for the solution of certain non-linear problems in least squares. *The Quarterly of Applied Mathematics* **2**: 164–168.

Li, Q., Jacob, D.J., Bey, I., Yantosca, R.M. (2000a) Atmospheric hydrogen cyanide (HCN): Biomass burning source, ocean sink? *Geophysical Research Letters* **27**(3): 357–360.

Li, X., Wang, S., Duan, L., Hao, J., Li, C., Chen, Y., Yang, L. (2007) Particulate and trace gas emissions from open burning of wheat straw and corn stoves in China. *Environmental Science Technology* **41**: 6052–6058.

Li, Z., Kaufman, Y.J., Ichoku, C., Fraser, T., Trischenki, A., Giglio, L., Jin, J., Yu, X. (2000b) A review of AVHRR-based active fire detection algorithms: Principles, limitations and recomendations. Canada Centre for Remote Sensing, Ottawa, Canada, and NASA Goddard Space Flight Center, Greenbelt, MD. pp. 1–50.

Liu, J., Drummond, J. R., Li, Q., Gille, J. C., Ziskin, D. C. (2005) Satellite mapping of CO emission from forest fires in northwest America using MOPITT measurements. *Remote Sensing of Environment* **95** 502–516.

Lobert, J.M, Scharffe, D.H., Hao, W.M., Crutzen, P.J. (1990) Importance of biomass burning in the atmospheric budgets of nitrogen-containing gases. *Nature* **346**: 552–554.

Lobert, J.M., Scharffe, D.H., Hao, W.M., Kuhlbusch, T.A., Seuwen, R., Warneck, P., Crutzen, P.J. (1991) Experimental evaluation of biomass burning emissions: Nitrogen and carbon containing compounds. In: *Global Biomass Burning: Atmospheric, Climatic and Biospheric Implications*. Ed: Levine, J.S., MIT Press, Cambridge, Massachusetts.

Lobert, J.M., Warnatz, J. (1993) Emissions from the combustion process in vegetation. In: *Fire in the Environment: The Ecological, Atmospheric, and Climatic Importance of Vegetation Fires* Eds. Crutzen, P.J., Goldammer, J.G., pp. 15–37, John Wiley, New York.

Long, C.J., Whitlock, C., Bartlein, P.J., Millspaugh, S.H. (1998) A 9000-year fire history from the Oregon Coast Range, based on a high-resolution charcoal study. *Canadian Journal of Forest Research* **28**(5): 774–787.

Lynch, B.T., Wilson, P.L. (1998) Land systems of Arnhem Land, Rep., 168 pp, Natural Resources Division, Northern Territory Department of Lands, Planning and Environment, Palmerston.

van Mantgem, P.J., Stephenson, N.L., Byrne, J.C., Daniels, L.D., Franklin, J.F., Fulé, P.Z., Harmon, M.E., Larson, A.J., Smith, J.M., Taylor, A.H., Veblen, T.T. (2009) Widespread increase of tree mortality rates in the western United States. *Science* **323**: 521–524.

Matson, M., and Dozier, J. (1981) Identification of subresolution high temperature sources using a thermal IR sensor. *Photogrammetric Engineering and Remote Sensing* **47**: 1311–1318.

Måren, I.E., Janovský, Z., Spindelböck, J.P., Daws, M.I., Kaland, P.E., Vandvik, V. (2010) Prescribed burning of northern heathlands: *Calluna vulgaris* germination cues and seed-bank dynamics. *Plant Ecology* **207**: 245–256.

Marland, G., Boden, T.A., Andres, R.J. (2008) In: *Trends: A Compendium of data on Global change.* Oak Ridge National Laboratory, U.S. Department of Energy, Oak Ridge.

Marquardt, D. (1963) An algorithm for least-squares estimation of nonlinear parameters. *SIAM Journal on Applied Mathematics* **11**: 431–441. doi:10.1137/0111030.

Mather, T.A., Tsanev, V.I., Pyle, D.M., McGonigle, A.J.S., Oppenheimer, C., Allen, A.G. (2004) Characterization and evolution of tropospheric plumes from Lascar and Villarrica volcanoes, Chile. *Journal of Geophysical Research* **109**: D21303, doi:10.1029/2004JD004937.

McEvoy, D., Cavan, G., Handley, J., McMorrow, J., Lindley, S. (2008) Changes to climate and visitor behaviour: Implications for vulnerable landscapes in the North West region of England. *Journal of Sustainable Tourism* **16**(1): 101–121.

McMeeking, G. R., Kreidenweis, S. M., Baker, S., Carrico, C. M., Chow, J. C., Collett Jr., J. L., Hao, W. M., Holde, A. S., Kirchstetter, T. W., Malm, W. C., Moosmüller, H., Sullivan, A. P., Wold, C. E. (2009) Emissions of trace gases and aerosols during the open combustion of biomass in the laboratory. *Journal of Geophysical Research* **114:** D19219.

McMorrow, J. (2009) Fire and climate change in UK moorlands and heaths. Paper presented at 'Creating a new prosperity: Fresh approaches to ecosystem services and human well-being', 4th September 2009, Royal Geographical Society, London, FRESH Seminar 6. [Online] Available from: http://www.nottingham.ac.uk/fresh/documents/Julia%20McMorrow.pdf [last accessed: 29 June 2010].

Messerschmidt, J., Geibel, M.C., Blumenstock, H., Chen, H., Deutscher, N.M., Engel, A., Feist, D.G., Gerbig, C., Gisi, M., Hase, F., Katrynski, K., Kolle, O., Lavric, J.V., Northold, J., Palm, M., Ramonet, M., Rettinger, M., Schimidt, M., Sussmann, R., Toon, G.C., Truong, F., Warneke, T., Wennberg, P.O., Wunch, D., Xueref-Remy, I. (2011) Calibration of TCCON column-averaged CO_2: the first aircraft campaign over European TCCON sites. *Atmospheric Chemistry and Physics* **11**(21): 10765–10777.

Meyer, C.P., Cook, G.D., Reisen, F., Smith, T.E.L., Tattaris, M., Russell-Smith, J., Maier, S.W., Yates, C.P., Wooster, M.J. (2012) Direct measurements of the seasonality of emission factors from savanna fires in northern Australia. *Journal of Geophysical Research* **117**(D20305), doi: 10.1029/2012JD017671.

Miller, G.H., Fogel, M.L., Magee, J.W., Gagan, M.K., Clarke, S.J., Johnson, B.J. (2005) Ecosystem collapse in pleistocene Australia and a human role in megafaunal extinction. *Science* **309**: 287–290.

Moorland Working Group (2002) *Scotland's Moorland: The Nature of Change*. Battleby: Scottish National Heritage.

Mouillot, F., Field, C.B. (2005) Fire history and the global carbon budget: a 1 degrees x 1 degrees fire history reconstruction for the 20th century. *Global Change Biology* **11**: 398–420.

Morisette, J. T., Giglio, L., Csiszar, I., Setezer, A., Schroeder, W., Morton, D., Justice, C. O. (2005) Validation of MODIS active fire detection products derived from two algorithms. *Earth Interactions* **9**(9).

Müller, U., Kurte, R., and Heise, H.M. (1999) Investigation of photometric errors in FTIR-spectra obtained in open-path monitoring. *Journal of Molecular Structure* **482–483**: 539–544.

Naylor, D.A., Tahic, M.K. (2007) Apodizing functions for Fourier transform spectroscopy. *Journal of the Optical Society of America* **24**(11): 3644–3648.

Nepstad, D.C., Verissimo, A., Alencar, A., Nobre, C., Lefebvre, P., Schlesinger, P., Potter, C., Moutinho, P., Lima, E., Cochrane, M., Brooks, V. (1999) Large scale impoverishment of Amazonian forests by logging and fire. *Nature* **398**: 505–508.

NetRegs.org.uk (2012) Straw and stubble burning. Environmental Guidance For Your Business in Northern Ireland and Scotland. Scottish Environment Protection Agency, Northern Ireland Environment Agency. [online] available from: http://www.netregs.org.uk/library_of_topics/waste/waste_treatment_processes/straw__stubble_burning.aspx [last accessed: 24 September 2012]

Nilsen, L.S., Johansen, L., Velle, L.G. (2005) Early stages of *Calluna vulgaris* regeneration after burning of coastal heath in central Norway. *Applied Vegetation Sciences* **8**: 57–64.

Ogawa, M., Yoshida, N. (2005) Nitrous oxide emission from the burning of agricultural residue. *Atmospheric Environment* **39**(19): 3421–3429.

Ojeda, F., Marañón, T., Arroyo, J. (1996) Postfire regeneration of a Mediterranean heathland in southern Spain. *International Journal of Wildland Fire* **6**(4): 191–198.

Oppenheimer, C., Francis, P., Burton, M.R. Madejewsky, A.J.H., and Boardman, L. (1998) Remote measurement of volcanic gases by Fourier transform infrared spectroscopy. *Appl. Phys. B. Lasers Opt.* **67**: 505–516.

Oppenheimer, C., Burton, M.R., Durieux, J. and Pyle, D.M. (2002) Open-path Fourier transform spectroscopy of gas emissions from Oldoinyo Lengai volcano, Tanzania. *Optics and Lasers in Engineering* **37**: 203–214.

Palmer, P. I., Suntharalingam, P., Jones, D. B. A., Jacob, D. J., Streets, D. G., Fu, Q., Vay, S. A., Sachse, G. W. (2006) Using CO_2: CO correlation to improve inverse analyses of carbon fluxes. *Journal of Geophysical Research* **11**: D12318, doi:10.1029/2005JD006697

Parks Australia (2010) Terrestrial Ecoregions in Australia [online] available from: http://www.environment.gov.au/parks/nrs/science/pubs/ecoregions.pdf [last accessed: 24 September 2012].

Paton-Walsh, C., Jones, N. B., Wilson, S. R., Meier, A., Deutscher, N., Griffith, D. W., Mitchell, R., Campbell, S. (2004) Trace gas emissions from biomass burning inferred from aerosol optical depth. *Geophysical Research Letters* **31**(5)

Paton-Walsh, C., Jones, N. B., Wilson, S. R., Haverd, V., Meier, A., Griffith, D. W. T., Rinsland, C. P. (2005) Measurements of trace gas emissions from Australian forest fires and correlations with coincident measurements of aerosol optical depth. *Journal of Geophysical Research* **110**: D24305, doi:10.1029/2005JD006202.

Paton-Walsh, C., Wilson, S. R., Jones, N. B., Griffith, D. W. T. (2008) Measurement of methanol emissions from Australian wildfires by ground-based solar Fourier transform spectroscopy. *Geophysical Research Letters* **35**(8).

Paton-Walsh, C., Emmons, L. K., Wilson, R. S. (2010a) Estimated total emissions of trace gases from the Canberra wildfires of 2003: A new method using satellite measurements of aerosol optical depth and the MOZART chemical transport model. *Atmospheric Chemistry and Physics* **10**: 5739–5748.

Paton-Walsh, C., Deutscher, N.M., Griffith, D.W.T., Forgan, B.W., Wilson, S.R., Jones, N.B., Edwards, D.P. (2010b) Trace gas emissions from savanna fires in northern Australia. *Journal of Geophysical Research* **115**: D16314, doi:10.1029/2009JD013309.

Page, S.E., Siegert, F., Rieley, J.O., Boehm, H.-D., V., Jaya, A., Limin, S. (2002) The amount of carbon released from peat and forest fires in Indonesia during 1997. *Nature* **420**: 61–65.

Pereira, G., Freitas, S. R., Moraes, E. C., Ferreira, N. J., Shimaburko, Y. E., Rao, V. B., Longo, K. M. (2009) Estimating trace gas and aerosol emissions over South America: Relationship between fire radiative energy released and aerosol optical depth observations. *Atmospheric Environment* **43**: 6388–6397.

Petri, C., Warneke, T., Jones, N., Ridder, T., Messerschmidt, J., Weinzierl, T., Geibel, M., Northolt, J. (2012) Remote sensing of CO_2 and CH_4 using solar absorption spectrometry with a low resolution spectrometer. *Atmospheric Measurement Techniques* **5**: 1627–1635.

Press, W. H., Teukolsky, S.A., Vetterling, W.T., and Flannery, B.P. (1992) *Numerical Recipes*, Cambridge University Press.

Prins, E. M., Menzel, W. P. (1992) Geostationaty satellite detection of biomass burning in South America. *International Journal of Remote Sensing* **13**(15): 2783–2799.

Radke, L.F., Stith, J.L., Hegg, D.A., Hobbs, P.V. (1978) Airborne studies of particles and gases from forest fires. *Journal of the Air Pollution Control Association* **28**: 30–34.

Rackham, O. (2003) Fire in the European Mediterranean. *Arid Lands Newsletter no. 54 November/December 2003.* [Online] available from: http://ag.arizona.edu/OALS/ALN/aln54/rackham.html [last accessed: 6 June 2010]

Rajab, J. M., MatJafri, M. z., Lim, h. S., Abdullah, K. (2009) Satellite mapping of CO_2 emissions from forest fires in Indonesia using AIRS measurements. *Modern Applied Science* **3** (12).

Rappold, A.G., Stone, S.L., Cascio, W.E., Neas, L.M., Kilaru, V.J., Carraway, M.S., Szygman, J.J., Ising, A., Cleve, W.E., Meredith, J.T., Vaughan-Batten, H., Deyneka, L., Devlin, R.B. (2011) Peat bog wildfire smoke exposure in rural North Carolina is associated with cardio-pulmonary emergency department visits assessed through syndromic surveillance. *Environmental Health Perspectives* **119**(10) 1415–1420.

Ravishankara, A.R., Daniel, J.S., Portmann, R.W. (2009) Nitrous Oxide (N_2O): The dominant ozone-depleting substance emitted in the 21st century. *Science* **326**: 123–125.

Reichle, H.G., Connors Jr., V.S., Holland, J.A., Hypes, W.D., Wallio, H.A., Casas, J.C., Gormsen, B.B., Saylor, M.S., Hesketh, W.D. (1986) Middle and upper tropospheric carbon monoxide mixing ratios as measured by a satellite-borne remote sensor during november 1981. *Journal of Geophysical Research* **91**: 10865–10888.

Reid, J.S., Koppmann, R., Eck, T.F., Eleuterio, D.P. (2005) A review of biomass burning emissions part II: intensive physical properties of biomass burning particles. *Atmospheric Chemistry and Physics* **5**: 799–825.

Remer, L.A., Kaufman, Y.J., Holben, B.N., Thompson, A.M., McNamara, D. (1998) Biomass burning aerosol size distribution and modelled optical properties. *Journal of Geophysical Research* **103**(D24): 31879–31891.

Richter, D., Erdelyi, M., Curl, R.F., Tittel, F.K., Oppenheimer, C., Duffell, H.J., and Burton, M. (2002) Field measurements of volcanic gases using tunable diode laser based mid-infrared and Fourier transform infrared spectrometers. *Optics and Lasers in Engineering* **37**: 171–186.

Rigby, M., Toumi, R., Fisher, R., Lowry, D., and Nisbey, E.G. (2008) First continuous measurements of CO_2 mixing ratio in central London using a compact diffusion probe. *Atmospheric Environment* **42**: 8,943–8,953.

Rinsland, C.P., Nicholas, B.J., Connor, B. J., Logan, J. A., Pougatchev, N. S., Goldman, A., Murcray, F. J., Stephen, T. M., Pine, A. S., Zander, R., Mahieu, E., and Demoulin, P. (1998) Northern and southern hemisphere ground-based infrared spectroscopic measurements of tropospheric carbon monoxide and ethane. *Journal of Geophysical Research* **103**(D21): 28,197–28,218 doi:10.1029/98JD02515.

Rinsland, C.P., Paton-Walsh, C., Jones, N.B., Griffith, W.T. Goldman, A., Wood, S.W., Chiou, L., Meier, A. (2005) High spectral resolution solar absorption measurements of ethylene (C_2H_4) in a forest fire smoke plume using HITRAN parameters: Tropospheric vertical profile retrieval. *Journal of Quantitative Spectroscopy & Radiative Transfer* **96**: 301–309.

Rius, D., Vanniére, B., Galop, D. (2009) Fire frequency and landscape management in the northwestern Pyrenean piedmont, France, since the early Neolithic (8000 cal. BP). *The Holocene* **19**: 847–859.

Roberts, G.J., Wooster, M. J. (2008) Fire detection and fire characterization over Africa using Meteosat SEVIRI. *IEEE Transactions on Geoscience and Remote Sensing* **49**(4): 1200–1218.

Roberts, G.J., Wooster, M.J., Freeborn, P.H., Xu, W. (2011) Integration of geostationary FRP and polar-orbiter burned area datasets for an enhanced biomass burning inventory. *Remote Sensing of the Environment* **115**: 2047–2061.

Roberts, J.M., Veres, P., Warneke, C., Neuman, J.A., Washenfelder, R.A., Broown, S.S., Baasandorj, M., Burkholder, J.B., Burling, I.R., Johnson, T.J., Yokelson, R.J., de Gouw, J. (2010) Measurement of HONO, HNCO, and other inorganic acids by Negative-Ion Proton-Transfer Chemical-Ionization Mass Spectrometry (NI-PT-CIMS): Application to biomass burning emissions. *Atmospheric Measurement Techniques Discussions* **3**: 301–331.

Rodgers, C.D. (2000) *Inverse Methods for Atmospheric Sounding: Theory and Practice.* World Scientific Publishing Co. Ltd. Singapore.

Rothman, L.S., Gordon, I.E., Barbe, A., Chris Benner, D., Bernath, P.F., Birk, M., Boudon, V., Brown, L.R., Campargue, A., Champion, J.-P., Chance, K., Coudert, L.H., Dana, V., Devi, V.M., Fally, S., Flaud, J.-M., Gamache, R.R., Goldman, A., Jacquemart, D., Kleiner, I., Lacome, N., Lafferty, W.J., Mandin, J.-Y., Massie, S.T., Mikhailenko, S.N., Miller, C.E., Moazzen-Ahmadi, N., Naumenko, O.V., Nikitin, A.V., Orphal, J., Perevalov, V.I., Perrin, A., Predoi-Cross, A., Rinsland, C.P., Rotger, M., Šimečková, M., Smith, M.A.H., Sung, K., Tashkun, S.A., Tennyson, J., Toth, R.A., Vandaele, A.C., and Vander Auwera, J. (2009) The *HITRAN* 2008 molecular spectroscopic database. *Journal of Quantitative Spectroscopy & Radiative Transfer* **110**: 533–572.

Roy, D.P. (1999) Multi-temporal active-fire based burn scar detection algorithm. *International Journal of Remote Sensing* **20** (15): 1031–1038.

Roy, D.P., Lewis, P.E., Justice, C.O. (2002) Burned area mapping using multi-temporal moderate spatial resolution data - a bi-directional reflectance model-based expectation approach. *Remote Sensing of Environment* **83**: 263–286.

Roy, D.P., Boschetti, L., Justice, C.O., Ju, J. (2008) The Collection 5 MODIS Burned Area Product – Global evaluation by comparison with the MODIS Active Fire Product. *Remote Sensing of Environment* **112**: 3690–3707.

Ruddiman, W.F. (2003) The anthropogenic greenhouse era began thousands of years ago. *Climatic Change* **61**: 261–293.

Running, S.W. (2006) Is global warming causing more, larger wildfires? *Science* **313**: 927–928.

Russell-Smith, J., Yates, C.P., Whitehead, P.J., Smith, R., Craig, R., Allan, G.E., Thackway, R., Frakes, I., Cridland, S., Meyer, C.P., Gill, A.M. (2007) Bushfires 'down under': patterns and implications of contemporary Australian landscape burning. *International Journal of Wildland Fire* **16**: 361–377.

Russell-Smith, J., Murphy, B.P., Meyer, M.C.P., Cook, G.D., Maier, S., Edwards, A.C., Schatz, J., Brocklehurst, P. (2009) Improving estimates of savanna burning emissions for greenhouse accounting in northern Australia: limitations, challenges, applications. *International Journal of Wildland Fire* **18**: 1–18.

Sahai, S., Sharma, C., Singh, D. P., Dixit, C. K., Singh, N., Sharma, P., Singh, K., Bhatt, S., Ghude, S., Gupta, V., Gupta, R. K., Tiwari, M.K., Garg, S. C., Mitra, A. P., Gupta, P. K. (2007) A study for development of emissions factors for trace gases and carbonaceous particulate species from in situ burning of wheat straw in agricultural fields in India. *Atmospheric Environment* **41**: 9173–9186.

Sawyer, G.M., Carn, S.A., Tsanev, V.I., Oppenheimer, C., Burton, M. (2008) Investigation into magma degassing at Nyiragongo volcano, Democratic Republic of the Congo. *Geochemistry, Geophysics, Geosystems* **9**(Q02017): doi:10.1029/2007GC001829.

Schafer, K., Haus, R., Heland, J., and Haak, A. (1995) Measurements of atmospheric trace gases by emission and absorption-spectroscopy with FTIR. *Berichte der Bunsen-Gesellschaft – Physical Chemistry Chemical Physics* **99**(3): 405–411.

Schafer, K., Jahn, C., Sturm, P., Lechner, B., and Bacher, M. (2003) Aircraft emission measurements by remote sensing methodologies at airports. *Atmospheric Environment* **37**: 5261–5271.

Schimel, D., Baker, D. (2002) The wildfire factor. *Nature* **420**: 29–30.

Schmid, B., Redermann, J., Russell, P.B., Hobbs, P.V., Hlavka, D.L., McGill, M.J., Holben, B.N., Welton, E.J., Campbell, J.R., Torres, O., Kahn, R.A., Diner, D.J., Helmlinger, M.C., Chu, D.A., Robles-Gonzalez, C., de Leeuw, G. (2003) Coordinated airborne, spaceborne, and ground-based measurements of massive thick aerosol layers during the dry season in southern Africa. *Journal of Geophysical Research* **108**: 8496, doi:10.1029/2002JD002297.

Schroeder, W., Prins, E., Giglio, L., Csiszar, I., Schmidt, C., Morisette, J., Morton, D. (2008) Validation of GOES and MODIS Active Fire Detection Products Using ASTER and ETM+ Data. *Remote Sensing of Environment **112**: 2711–2726.*

Schultz, M., Textor, C., Kinne, S., Balkanski, Y., Bauer, S., Berntsen, T., Berglen, T., Boucher, O., Dentener, F., Guibert, S., Isaksen, I.S.A., Iversen, T., Koch, D., Kirkevag, A., Liu, X., Montenaro, V., Myhre, G., Penner, J.E., Pitari, G., Reddy, S., Seland, O., Stier, P., Takemura, T. (2006) radiative forcing by aerosols as derived from the AeroCom present-day and pre-industrial simulations. *Atmospheric Chemistry and Physics* **6**: 5225.

Scott, A.C., Glasspool, I.J. (2006) The diversification of paleozoic fire systems and fluctuations in atmospheric oxygen concentration. *Proceedings of the National Academy of Sciences of the United States of America* **103**(29): 10861–10865.

Seiler, W., Crutzen, P.J. (1980) Estimates of gross and net fluxes of carbon between the biosphere and the atmosphere from biomass burning. *Climate Change* **2**: 207–247.

Senten, C., De Mazière, M., Dils, B., Hermans, C., Kruglanski, M., Neefs, E., Scolas, F., Vandaele, A.C., Vanhaelewyn, G., Vigouroux, C., Carleer, M., Coheur, P.F., Fally, S., Barrer, B., Baray, J.L., Delmas, R., Leveau, J., Metzger, J.M., Mahieu, E., Boone, C., Walker, K.A., Bernath, P.F., and Strong, K. (2008) Technical Note: New ground-based FTIR measurements at Ile de La Réunion: observations, error analysis, and comparisons with independent data. *Atmospheric Chemistry and Physics* **8**: 3,483–3,508.

Sherriff, R.L., Veblen, T.T., Sibold, J.S. (2001) Fire history in high elevation subalpine forests in the Colorado Front Range. *Ecoscience* **8**(3): 369–380.

Shirai, T., Blake, D. R., Meinardi, S., Rowland, F. S., Russell-Smith, J., Edwards, A., Kondo, Y., Koike, M., Kita, K., Machida, T., Takegawa, N., Nishi, N., Kawakami, S., Ogawa, T. (2003) Emission estimates of selected volatile organic compounds from tropical savanna burning in northern Australia. *Journal of Geophysical Research* **18**: D38406, doi:10.1029/2001JD000841.

Sillman, S. (1999) The relation between ozone NO_x and hydrocarbons in urban and polluted rural environments. *Atmospheric Environment* **33**(12): 1821–1845, doi:10.1016/S1352-2310(98)00345-8.

Sinha, P., Hobbs, P.V., Yokelson, R.J., Bertschi, I.T., Blake, D.R., Simpson, I.J., Gao, S., Kirchstetter, T.W., Novakov, T. (2003) Emissions of trace gases and particles from savanna fires in southern Africa. *Journal of Geophysical Research* **108**(D13): 8487. doi:10.1029/2002JD002325.

Smith, B.C. (1996) *Fundamentals of Fourier Transform Infrared Spectroscopy* CRC Press, New York, pp. 224.

Smith, A. M. S., Wooster, M.J. (2005) Remote classification of head and backfire types from MODIS fire radiative power and smoke plume observations. *International Journal of Wildland Fire* **14**: 249–254.

Smith, T.E.L. (2010) Not just recycled sunlight: Biomass burning and its influence on global climate change. *Winner of the Environmental Physics Group Essay Competition 2010*, Institute of Physics, London. [online] Available from: http://www.iop.org/activity/groups/subject/env/prize/file_52569.pdf [last accessed: 26 September 2012].

Smith, T.E.L., Wooster, M.J., Tattaris, M., Griffith, D.W.T. (2011) Absolute accuracy and sensitivity analysis of OP-FTIR retrievals of CO_2, CH_4 and CO over concentrations representative of "clean air" and "polluted plumes". *Atmospheric Measurement Techniques* **4**: 97–116.

Sofiev, M., Vankevich, R., Lanne, M., Koskinen, J., Kukkonen, J. (2008) On integration of a fire assimilation system and a chemical transport model for near-real-time monitoring of the impact of wild-land fires on atmospheric composition and air quality. *Modelling, Monitoring and Management of Forest Fires, WIT Transactions on Ecology and the Environment* **119**: 343–351.

Sofiev, M., Vankevich, R., Lotjonen, M., Prank, M., Petukhov, V., Ermakova, T., Kukkonen, J. (2009) An operational system for the assimilation of the satellite information on wild-land fires for the needs of air quality modeling and forecasting. *Atmospheric Chemistry and Physics* **9**: 6833–6847.

Steele, D. (2006) *Infrared Spectroscopy: Theory. Handbook of Vibrational Spectroscopy*. Wiley Online Library [online] available from: http://dx.doi.org/10.1002/0470027320.s0103 [last accessed: 24 September 2012].

Stocks, B.J., Kauffman, J.B. (1997) Biomass consumption and behavior of wildland fires in boreal, temperatre, and tropical ecosystems: Parameters necessary to interpret historic fire regimes and future fire scenarios. In: *Sediment Records of Biomass Burning and Global Change*. Ed: J.S. Clark. Springer-Verlag Berlin, Heidelberg.

Stott, P. (2000) Combustion in tropical biomass fires: A critical review. *Progress in Physical Geography* **24**: 355–377.

Stremme, W., Ortega, I., Grutter, M. (2009) Using ground-based solar and lunar infrared spectroscopy to study the diurnal trend of carbon monoxide in the Mexico City boundary layer. *Atmospheric Chemistry and Physics* **9**: 8061-8078.

Stuart, B.H. (2004) *Infrared Spectroscopy: Fundamentals and Applications*. John Wiley & Sons, New York.

Sussmann, R.F., Forster, F., Rettinger, M., Jones, N.B. (2011) Strategy for high-accuracy-and-precision retrieval of atmospheric methane from the mid-infrared FTIR network. *Atmospheric Measurement Techniques* **4**(9): 1943–1964.

Swetnam, T.W., Betancourt, J.L. (1992) Temporal patterns of El Niño/Southern Oscillation – wildfire teleconnections in the southwestern United States. In *El Niño: Historical and Paleoclimatic Aspects of the Southern Oscillation* Eds: Diaz, H.F. and Markgraf, V. Cambridge University Press, Cambridge.

Swetnam, T.W. (1993) Fire history and climate change in giant sequoia groves. *Science* **262**: 885–889.

Tansey, K., Grégoire, J.-M., Stroppiana, D., Sousa, A., Silva, J., Pereira, J.M.C., Boschetti, L., Maggi, M., Alessandro Brivio, P., Fraser, R., Flasse, S., Ershov, D., Binaghi, E., Graetz, D. and Peduzzi, P. (2004) Vegetation burning in the year 2000: Global burned area estimates from SPOT VEGETATION data. *Journal of Geophysical Research* **109**(D14): doi:10.1029/2003.JD003598.

Tansey, K., Gregoire, J-M., Pereira, J.M.C., Defourny, P., Leigh, R., Pekel, J-F., Barros, A., Silva, J., van Bogaert, E., Bartholomé, E. and Bontemps, S. (2007) L3JRC – A global, multi-year (2000-2007) burnt area product (1 km resolution and daily time steps) *Remote Sensing and Photogrammetry Society Annual Conference 2007*. Newcastle upon Tyne, UK, 11–14 September 2007.

TCCON (Total Column Carbon Observation Network) (2012) TCCON wiki [online] available from: https://tccon-wiki.caltech.edu/ [last accessed: 24 September 2012].

Tinner, W., Hubschmid, P., Wehrli, M., Ammann, B., Conedera, M. (1999) Long-term forest fire ecology and dynamics in southern Switzerland. *Journal of Ecology* **87**: 273–289.

Trollope, W.S.W. (1984) Fire in savanna. In *Ecological Effects of fire in South African Ecosystems*. Eds. Booysen, P. de V., Tainton, N.M. Springer-Verlag, Berlin, 151–175.

Turquety, S., Logan, J.A., Jacob, D. J., Hudman, R.C., Leung, F.Y., Heald, C.L., Yantosca, R. M., Wu, S., Emmons, L.K., Edwards, D.P., Sachse, G. W. (2007) Inventory of boreal fire emissions for North America in 2004: Importance of peat burning and pyroconvective injection. *Journal of Geophysical Research* **112**: D12S03, doi: 1029/2006JD007281.

Veblen, T.T., Kitzberger, T., Villalba, R., Donnegan, J. (1999) Fire history in northern Patagonia: The roles of humans and climatic variation. *Ecological Monographs* **69**(1): 47–67.

Ward, D.E. and Hao, W.M. (1991) Projections of emissions from burning of biomass for use in studies of global climate change and atmospheric chemistry. In *Proceedings, 1991 National Air and Waste Management Association, June 24–29*, Vancouver, BC and Pittsburgh, PA: Air and Waste Mangament Association, 91–128.

Ward, D.E., Radke, L.F. (1993) Emissions measurements from vegetation fires: A comparative evaluation of methods and results. In *Fire in the Environment: The Ecological, Atmospheric, and Climatic Importance of Vegetation Fires*, Eds. P.J. Crutzen, J.G. Goldammer, pp. 53–76, John Wiley & Sons Ltd., New York.

Ward, D.E., Hao, W.M., Susott, R.A., Babbitt, R.E., Shea, R.W., Kauffman, J.B., Justice, C.O. (1996) Effect of fuel composition on combustion efficiency and emission factors for African savanna ecosystems. *Journal of Geophysical Research* **101**: 23569–23576.

van der Werf, G.R., Randerson, J.T., Collatz, G.J., Giglio, L., Kasibhatla, P.S., Arellano Jr., A.F., Olsen, S.C., Kasischke, E.S. (2004) continental-scale partitioning of fire emissions during the 1997 to 2001 El Niño/La Niña period. *Science* **303**: 73–77.

van der Werf, G.R., Randerson, J.T., Giglio, L., Collatz, G.J., Kasibhatla, P.S., Arellano Jr., A.F. (2006) Interannual variability in global biomass burning emissions from 1997–2004. *Atmospheric Chemistry and Physics* **6**: 3423–3441.

van der Werf, G.R., Randerson, J.T., Giglio, L., James Collatz, G.J., Kasibhatla, P.S., Morton, D., DeFries, R. (2010) The improved Global Fire Emissions Database (GFED) version 3: Contribution of savanna, forest, deforestation, and peat fires to the global fire emissions budget. *Geophysical Research Abstracts* **12**: EGU2010–13010.

van der Werf, G.R., Randerson, J.T., Giglio, L., James Collatz, G., Mu, Mingquan, Kasibhatla, P.S., Morton, D.C., DeFries, R.S., Jin, Y., van Leeuwen, T.T. (2010) global fire emissions and the contribution of deforestation, savanna, forest, agricultural, and peat fires (1997–2009) *Atmospheric Chemistry and Physics* **10**: 11707–11735.

Westerling, A.L., Hidalgo, H.G., Cayan, D.R. and Swetnam, T.W. (2006) Warming and earlier spring increase western U.S. forest wildfire activity. *Science* **313**: 940–944.

Williams, R.J., Cook, G.D., Gill, A.M., Moore, P.H.R. (1999) Fire regime, fire intensity and tree survival in a tropical savanna in northern Australia. *Australian Journal of Ecology* **24**: 50–59.

Williams, R.J., Gill, A.M., Moore, P.H.R. (2003) Fire behaviour. In: *Fire in tropical savannas: The Kapalga experiment*. Ed: A.N. Anderson, G.D. Cook, R.J. Williams. Springer-Verlag, New York.

Williams, R.J., Carter, J., Duff, G.A., Woinarski, J.C.Z., Cook, G.D. and Farrer, S.L. (2005) Carbon accounting, land management, science and policy uncertainty in Australian savanna landscapes: Introduction and overview. *Australian Journal of Botany* **53**: 583–588.

Witte, J.C., Douglass, A.R., Duncan, B.N., da Silva, A., Torres, O. (2010) Satellite observation highlights of the 2010 Russian wildfires. NASA Technical Reports Server (NTRS) [online] available from: http://ntrs.nasa.gov/search.jsp?R=20110007963 [last accessed: 23 September 2012].

Wooster, M.J., Zhukov, B., Oertel, D. (2003) Fire Radiative Energy for quantitative study of biomass burning: Derivation from the BIRD experimental satellite and comparison to MODIS fire products. *Remote Sensing of Environment* **86**: 83–107.

Wooster, M.J., Roberts, G., Perry, G.L.W. (2005) Retrieval of biomass combustion rates and totals from Fire Radiative Power observations: FRP derivation and calibration relationships between biomass consumption and Fire Radiative Energy release. *Journal of Geophysical Research* **110**: D24311, doi:10.1029/2005JD006318.

Wooster, M.J., Freeborn, P.H., Archibald, S., Oppenheimer, C., Roberts, G.J., Smith, T.E.L., Govender, N., Burton, M., Palumbo, I. (2011) Field determination of biomass burning emission ratios and factors via open-path FTIR spectroscopy and fire radiative power assessment: headfire, backfire and residual smouldering combustion in African savannahs. *Atmospheric Chemistry and Physics* **11**: 11591–11615.

Wooster, M.J., Perry, G.L.W., Zoumas, A. (2012) Fire, drought and El Niño relationships on Borneo (Southeast Asia) in the pre-MODIS era (1980–2000). *Biogeosciences* **9**: 317–340.

Wrangham, R., Jones, J.H., Laden, G., Pilbeam, D. And Conklin-Brittain, N.L. (1999) The raw and the stolen: Cooking and the ecology of human origins. *Current Anthropology* **40**(5): 567–594.

Wunch, D., Toon, G.C., Wennberg, P.O., Wofsy, S.C., Stephens, B.B., Fischer, M.L., Uchino, O., Abshire, J.B., Bernath, P., Biraud, S.C., Blavier, J.-F.L., Boone, C., Bowman, K.P., Browell, E.V., Campos, T., Connor, B.J., Daube, B.C., Deutscher, N.M., Diao, M., Elkins, J.W., Gerbig, C., Gottlieb, E., Griffith, D.W.T., Hurst, D.F., Jiménez, R., Keppel-Aleks, G., Kort, E.A., Macatangay, R., Machida, T., Matsueda, H., Moore, F., Morino, I., Park. S., Robinson, J., Roehl, C.M., Sawa, Y., Sherlock, V., Sweeney, C., Tanaka, T., Zondlo, M.A. (2010) Calibration of the Total Carbon Column Observing Network using aircraft profile data. *Atmospheric Measurement Techniques* **3**: 1351–1362.

Wunch, D., Wennberg, P.O., Toon, B.J., Connor, B.J., Fisher, B., OSterman, G.B., Frankenberg, C., Mandrake, L., O'Dell, D.W., Ahonen, P., Biraud, S.C., Castano, R., Cressie, N., Crisp, D., Deutscher, N.M., Eldering, A., Fisher, M.L., Griffith, D.W.T., Gunson, M., Heikkinen, P., Keppel-Aleks, G., Kyrö, E., Lindenmaier, R., Macatangay, R., Mendonca, J., Messerschimidt, J., Miller, C.E., Morino, I., Northolt, J., Oyafuso, F.A., Rettinger, M., Robinson, J., Roehl, C.M., Salawitch, R.J., Sherlock, V., Strong, K., Sussmann, R., Tanaka, T., Thompson, D.R., Uchino, O., Warneke, T., Wofsy, S.C. (2011) A method for evaluating bias in global measurements of CO_2 total columns from space. *Atmospheric Chemistry and Physics* **11**(23): 12317–12337.

Xu, W., Wooster, M.J., Roberts, G., Freeborn, P. (2010) New GOES imager algorithms for cloud and active fire detection and fire radiative power assessment across North, South and Central America. *Remote Sensing of Environment* **114**(9): 1876–1895.

Yallop, A.R., Thacker, J.I., Thomas, G., Stephens, M., Clutterbuck, B., Brewer, T., Sannier, C.A.D. (2006) The extent and intensity of management burning in the English uplands. *Journal of Applied Ecology* **43**: 1138–1148.

Yokelson, R.J., Griffith, D.W.T., Ward, D.E. (1996) Open-path Fourier transform infrared studies of large-scale laboratory fires. *Journal of Geophysical Research* **101**(D15): 21067–21080.

Yokelson, R.J., Susott, R., Darold, E., Reardon, J., Griffith, D.W.T. (1997) Emissions from smouldering combustion of biomass measured by open-path Fourier transform infrared spectoscopy. *Journal of Geophysical Research* **102** (D13): 18865–18877.

Yokelson, R.J., Goode, J. G., Ward, D. E., Susott, R. A., Babbit, R. E., Wade, D. D., Bertschi, I., Griffith, D. W. T., Hao, W. M. (1999) Emissions of formaldehyde, acetic acid, methanol, and other trace gases from biomass fires in North Carolina measured by airborne Fourier transform infrared spectroscopy. *Journal of geophysical Research* **104**(D23): 30,109–30,125.

Yokelson, R.J, Bertschi, I. T., Christian, T. J., Hobbs, P. V., Ward, D. E., Hao, W. M. (2003) Trace gas measurements in nascent, aged, and cloud-processed smoke from african savanna fires by airborne Fourier transform infrared spectroscopy. (A-FTIR) *Journal of Geophysical Research* **108** (D13): 8478 doi:10.1029/2002JD002322

Yokelson, R.J., Karl, T., Artaxo, P., Blake, D.R., Christian, T.J., Griffith, D.W.T., Guenther, A., Hao, W.M. (2007) The Tropical Forest and Fire Emissions Experiment: Overview and airborne fire emission factor measurements. *Atmospheric Chemistry and Physics* **7**: 5175–5196.

Yokelson, R.J., Christian, T. J., Karl, T. G., Guenther, A. (2008) The Tropical Forest and Fire Emissions Experiment: laboratory fire measurements and synthesis of campaign data. *Atmospheric Chemistry and Physics* **8**: 3509–3527.

Yurganov, L.N., Wallace McMillan, W., Dzhola, A.V., Grechko, E.I., Jones, N.B., van der Werf, G.R. (2008) Global AIRS and MOPITT CO measurements: Validation, comparison, and links to biomass burning variations and carbon cycle. *Journal of Geophysical Research* **113**: D09301: doi:10.1029/2007JD009229

Zhang, S., NASA, Penner, J. E., Torres, O. (2005) Inverse modeling of biomass burning emissions using Total Ozone Mapping Spectrometer Aerosol Index for 1997. *Journal of Geophysical Research* **110** : D21306 doi:10.1029/2004JD005738.

Zhu, C., and Griffiths, P.R. (1998) Extending the range of Beer's law in FT-IR spectrometry. Part I: Theoretical study of Norton-Beer apodization functions. *Applied Spectroscopy* **52**(11): 1,403–1,408.

Zvyagintsev, A.M., Blum, O.B., Glazkova, A.A., Kotel'nikov, S.N., Kuznetsova, I.N., Lapchenko, V.A., Lezina, E.A., Miller, E.A., Milyaev, V.A., Popikov, A.P. (2011) Air pollution over European Russia and Ukraine under the hot summer conditions of 2010. *Izvestiya Atmospheric and Oceanic Physics* **47**(6): 699–707.